Theses and Dissertations

1-1-2013

# Structural Health Monitoring of Composite Laminates Using Piezoelectric and Fiber Optics Sensors

Catalin Roman
*University of South Carolina*

Follow this and additional works at: http://scholarcommons.sc.edu/etd

# Structural Health Monitoring of Composite Laminates

# Using Piezoelectric and Fiber Optics Sensors

by

Catalin Roman

Bachelor of Science
"Gheorghe Asachi" Technical University of Iasi, Romania, 2003

Master of Science
University of Bridgeport, 2007
_____

Submitted in Partial Fulfillment of the Requirements

For the Degree of Doctor of Philosophy in

Mechanical Engineering

College of Engineering & Computing

University of South Carolina

2013

Accepted by:

Victor Giurgiutiu, PhD, Major Professor

Yuh Chao, PhD, Committee Member

Lingyu Yu, PhD, Committee Member

Paul Ziehl, PhD, Committee Member

Matthieu Gresil, PhD, Committee Member

Lacy Ford, PhD, Vice Provost and Dean of the Graduate Studies

## ACKNOWLEDGEMENTS

## MOTIVATION

Nowadays, the composite materials are being used in more and more industries such as aerospace, naval and automotive. They slowly replace the traditional ferrous materials due to their great properties (lightness, better resistance to stress and shocks, longer life etc.).

One common way to inspect such materials is to use ultrasonic nondestructive evaluation methods (NDE) which allow examining complex structures without damaging them. NDE allows the detection of damage before it becomes a major problem. In the aerospace industry, for example, detection techniques for delaminations, cracks and corrosions are so vital that they can sometimes make the difference between life and death, being able to prevent catastrophic failures and adding a new edge of safety and a lower maintenance and operating cost for the airplanes. In recent decades, the trend is to move towards NDE methods with embedded ultrasonic sensors instead of the conventional coupled transducers ones.

# ABSTRACT

This research proposes a new approach to structural health monitoring (SHM) for composite laminates using piezoelectric wafer active sensors (PWAS) and fiber optic bragg grating sensors (FBG). One major focus of this research was directed towards extending the theory of laminates to composite beams by combining the global matrix method (GMM) with the stiffness transfer matrix method (STMM). The STMM approach, developed by Rokhlin et al (2002), is unconditionally stable and is more computationally efficient than the transfer matrix method (TMM). Starting from theory, we developed different configurations for composite beams and validated the results from the developed analytical method against experimental data. STMM was then developed for pristine composite beam and delaminated composite beam. We studied the influence of the bonded PWAS by looking at their mode frequencies and amplitudes via experiments and simulations with different sensor positions on pristine and damaged beams, with different delamination sizes and depths.

We also extended the TMM and the electro-mechanical (E/M) impedance method for applications to the convergence of TMM of beam vibrations. The focus was on the high-accuracy predictive modeling of the interaction between PWAS and structural waves and vibration using a methodology as in Cuc (2010). We expanded the frequency resonances of a uniform beam from the range of 1-30 kHz previously

studied by Cuc (2010) to a higher frequency range of 10-100 kHz and performed the reliability and accuracy analysis (error rates) of all available theoretical models (modal expansion, TMM, and FEM) given experimental data for the uniform beam specimen.

Another focus of this research was to explore the use of FBG for fiber composites applications. We performed tests that vary the load on the free end in order to understand the behavior of composite materials under tensile forces and to extend results to ring sensor applications. The last part this research focused on developing a novel acousto-ultrasonic sensor that can detect acoustic emission (AE) events using optical FBG sensing combined with mechanical resonance amplification principles. This method consists of a sensor that can detect the ultrasonic out of plane motion with preference for a certain frequency (300 kHz).

Finally, we introduced the concept of a FBG ring sensor for a Navy application, which can provide significant improvements in detecting vibrations. We use a laser vibrometry tool (PSV-400-3D from Polytec) to study the mode shapes of the sensor ring under different resonance frequencies in order to understand the behavior of the ring in the frequency band of interest (300 kHz) and further compare these results and shapes with FEM predictions (ANSYS WB). Our experiments proved that the concept works and a ring sensor that can reach the first resonance at any desired frequency could be built. This work was finalized with an invention disclosure for a novel acousto-ultrasonic FBG ring sensor (Disclosure ID No. 00937).

The dissertation ends with conclusions and suggestions for future work.

# TABLE OF CONTENTS

# LIST OF FIGURES

# PART I - STATE OF THE ART

## 1. LITERATURE REVIEW OF VIBRATION ANALYSIS BY MODAL EXPANSION

In this section, we present a brief introduction to the vibration theory (modal expansion). The modal expansion method consists of determining the axial and flexural frequencies using MATLAB, which combined give the frequency response function. We follow the approach of Giurgiutiu (2008) to calculate the admittance and impedance.

To proceed with this method, we consider a PWAS transducer attached to a structure as in

Figure *1*. When we apply a voltage to the PWAS of length $l_P$ at $x_1$ and $x_2$ from the left side, the PWAS expands and contracts by amount $\varepsilon_P$. The tension created by the PWAS produces a reaction force $F_P$ from the beam to the PWAS, that in turn, produces an opposite reaction force from the PWAS to the beam. The force produced by the sensor $F_P$ brings an axial force $N_F$ and a bending moment $M_F$ at the center of the beam (neutral axis). The harmonic excitation of the PWAS with a high frequency signal induces in the structure standing or travelling waves.
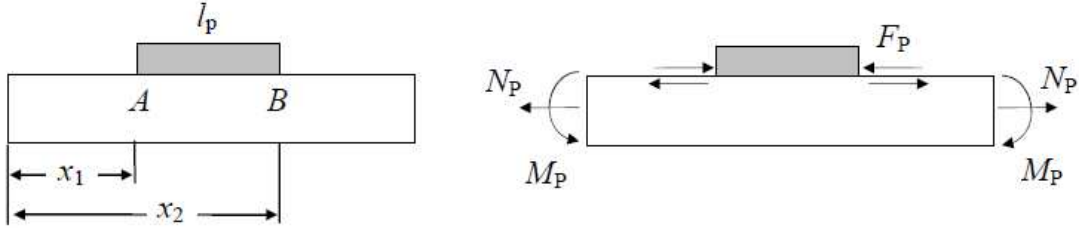
*Figure 1: Forces and moments created by a PWAS bonded to a beam structure*
*Source: Cuc (2010)*

In order to determine the axial force and the bending moment we begin from

the force generated by the PWAS ($F_P$ is the complex amplitude):

$$F_P = Ae^{i\omega t + \varphi} = Ae^{i\varphi} \cdot e^{i\omega t} = \hat{F}_P e^{i\omega t} \tag{1.1}$$

The axial force and bending moment at locations $x_1$ and $x_2$ are written as:

$$N_P = F_P = \hat{N}_P e^{i\omega t} \tag{1.2}$$

$$M_P = \frac{h}{2} F_P = \frac{h}{2} \hat{F}_P e^{i\omega t} = \hat{M}_P e^{i\omega t} \tag{1.3}$$

We use the Heaviside function:

$$H(x - y_1) - H(x - y_2) = \begin{cases} 0 & x < x_1 \\ 1 & x_1 \le x \le x_2 \\ 0 & x > x_2 \end{cases} \tag{1.4}$$

The axial force and bending moment at any point $x$ on the beam are provided by:

$$N_P(x,t) = \hat{N}_P \left[ H(x - x_2) - H(x - x_1) \right] e^{i\omega t} \tag{1.5}$$

$$M_P = \hat{M}_P \left[ H(x - x_2) - H(x - x_1) \right] e^{i\omega t} \tag{1.6}$$

2

## 1.1 Axial Vibrations

In this part, we consider the free axial vibrations of a uniform elastic bar of length $l$ cross-sectional area $A$, mass $m$, and axial stiffness $EA$ as in Figure 2. We look for the beam response under forced axial vibration.
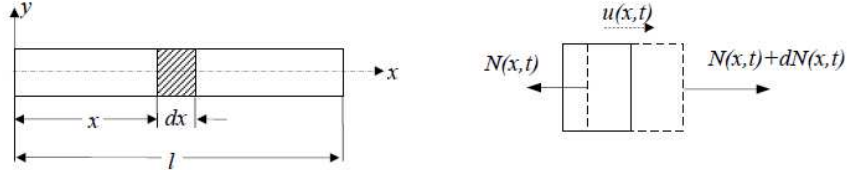


**Figure 2: Flexural vibration of a uniform bar**
**Source: Cuc (2010)**

From the summation of forces in the $x$ axis the equation of motion can be derived:

$$N(x,t) + dN(x,t) - N(x,t) = \rho A \ddot{u}(x,t) \tag{1.7}$$

and $N = \sigma A = EA \dfrac{\partial u}{\partial x} = EAu'$ the equation of motion for free axial vibrations can be written as:

$$EAu''(x,t) - \rho A \ddot{u}(x,t) = 0 \tag{1.8}$$

Define

$$c = \frac{E}{\rho} \tag{1.9}$$

Hence Eq. (1.8) becomes

$$c^2 u''(x,t) - \ddot{u}(x,t) = 0 \tag{1.10}$$

In order to find a solution for (1.8) we use the method of separation of variables.

$$u(x,t) = U(x)T(t) = U(x)e^{i\omega t} \tag{1.11}$$

We look for the steady-state solution $U(x)$. We substitute (1.8) into (1.7) and differentiate and obtain a second order differential equation:

3

$$c^2 U''(x) + \omega^2 U(x) = 0 \tag{1.12}$$

Equation (1.12) admits the general solution in the form:

$$U(x) = C_1 \sin \gamma x + C_2 \cos \gamma x \tag{1.13}$$

Where $\gamma = \dfrac{\omega}{c}$ represents a harmonic oscillation similar to a wave, as such $\gamma$ is also called the wave number. The two constants $C_1$ and $C_2$ are determined from the boundary conditions (i.e. free-free, clamped-free, etc.). For the free-free case the boundary conditions are:

$$U'(0) = 0$$
$$U'(l) = 0 \tag{1.14}$$

We differentiate(1.12), substitute into (1.13) and solve the characteristic equation for the eigenvalues $\gamma_j$ and the general solution yields the mode shapes in the form:

$$U_j(x) = C_j \cos \gamma_j x, \quad \gamma_j = j\frac{\pi}{l}, \quad j = 1,2,3,\ldots\ldots \tag{1.15}$$

where $C_j$ is calculated as $C_j = \sqrt{2/ml}$ and the mode shapes satisfy the orthogonality property:

$$\int_0^l U_m(x) U_n(x)\, dx = \delta_{mn} = \begin{cases} 1 & ,m = n \\ 0 & ,m \neq n \end{cases} \tag{1.16}$$

For forced vibrations, the equation of motion takes the form

$$EAu''(x,t) - \rho A\ddot{u}(x,t) = N_P'(x,t) \tag{1.17}$$

Next, we assume the modal expansion

$$u(x,t) = \sum_j C_j U_j(x) e^{i\omega t}, \quad j = 1,2,3,\ldots \tag{1.18}$$

Here, the constants $C_j$ are the modal participation factors and $U_j(x)$ are the modes shapes that satisfy (1.12). We substitute the modal expansion (1.18) into the equation of motion (1.17) and get:

$$-\omega^2 \rho A \sum_j C_j U_j(x) e^{i\omega t} - EA \sum_j C_j U_j(x) e^{i\omega t} = N_P'(x,t)$$

(1.19)

From (1.19) $N_P'(x,t)$ is derived and substituted into (1.18) and we get

$$-\omega^2 \rho A \sum_j C_j U_j(x) - EA \sum_j C_j U_j''(x) = \hat{N}_P \left[ \delta(x-x_2) - \delta(x-x_1) \right]$$

(1.20)

From equation(1.20),

$$U_j''(x) = -\frac{\rho \omega_n^2}{E} U(x)$$

(1.21)

We substitute (1.20) in (1.19) and get

$$\sum_j \left[ C_j \left( \omega_n^2 - \omega^2 \right) U_j(x) \right] = \frac{\hat{N}_P}{\rho A} \left[ \delta(x-x_2) - \delta(x-x_1) \right]$$

(1.22)

We multiply with $U_k(x)$ on both sides and take the integral over the length of the beam of (1.22) and get

$$\int_0^l U_k(x) \sum_j \left[ C_j \left( \omega_j^2 - \omega^2 \right) U_j(x) \right] dx$$
$$= \int_0^l U_k(x) \frac{\hat{N}_P}{\rho A} \left[ \delta(x-x_2) - \delta(x-x_1) \right] dx$$

(1.23)

By rearranging the terms

$$\sum_j C_j \left( \omega_n^2 - \omega^2 \right) \int_0^l U_j(x) U_k(x) dx = \int_0^l U_k(x) \frac{\hat{N}_P}{\rho A} \left[ \delta(x-x_2) - \delta(x-x_1) \right] dx$$

(1.24)

Using the orthogonality property of mode shapes (1.15) and the property of the delta function

5

$$\int_{-\infty}^{+\infty} f(x)\delta(x-a)dx = f(a)$$

(1.25)

Equation (1.24)becomes

$$\sum_j C_j\left(\omega_j^2 - \omega^2\right) = \frac{\hat{N}_P}{\rho A}\left[U_k(x_2) - U_k(x_1)\right]$$

(1.26)

Then, the modal participation factors $C_j$ can be expressed as

$$C_j = \frac{1}{\omega_j^2 - \omega^2}\frac{\hat{N}_P}{\rho A}\left[U_k(x_2) - U_k(x_1)\right]$$

(1.27)

Using equation(1.18), the axial vibration response becomes

$$u(x,t) = \frac{\hat{N}_P}{\rho A}\sum_j \frac{U_j(x_2) - U_j(x_1)}{\omega_j^2 - \omega^2}U_j(x)e^{i\omega t}$$

(1.28)

For a damped system with the hysteretic damping coefficient $g$ , equation becomes

$$u(x,t) = \frac{\hat{N}_P}{\rho A}\sum_j \frac{U_j(x_2) - U_j(x_1)}{(1+ig)\omega_j^2 - \omega^2}U_j(x)e^{i\omega t}$$

(1.29)

### 1.2 FLEXURAL VIBRATIONS

In this part, we analyze a portion of a beam that undergoes flexural vibrations under the excitation of an external force per unit length of the beam $f(x,t)$ as in Figure 3. We consider the flexural displacement $w$ for the flexural vibration of a uniform elastic bar of length $l$, mass $m$ and flexural stiffness $EI$ .
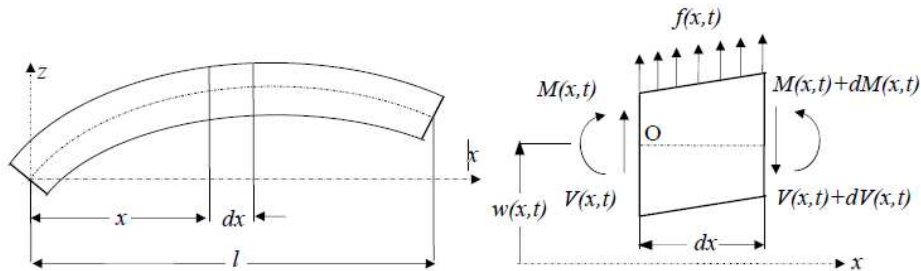


Figure 3: Flexural vibration of a uniform bar

From the free-body diagram, we have the equation of motion in the $z$ direction and the

moment equation about the $y$ axis through the point $O$ as:

$$V(x,t) + f(x,t)dx - \left[V(x,t) + dV(x,t)\right] = m\,\ddot{w}(x,t)$$

(1.30)

$$f(x,t) - V'(x,t) = \rho A(x)\ddot{w}(x,t)$$

(1.31)

$$M(x,t) + dM(x,t) + f(x,t)dx \cdot \frac{dx}{2} - \left[V(x,t) + dV(x,t)\right]dx - M(x,t) = 0$$

(1.32)

Neglecting the terms involving second order in $dx$

$$M'(x,t) - V(x,t) = 0 \Rightarrow V(x,t) = M'(x,t)$$

(1.33)

Applying the Euler-Bernoulli elementary beam theory, the relation between bending

moment and deflection is:

$$M(x,t) = EI(x)w''(x,t)$$

(1.34)

Using equations (1.34) and (1.33) and substituting in (1.31) the equation of motion for a

uniform beam undergoing flexural vibrations under a force $f(x,t)$ can be expressed as:

$$\rho A\ddot{w}(x,t) + EIw''''(x,t) = f(x,t)$$

(1.35)

For free vibrations, $f(x,t) = 0$ and the equation of motion becomes

$$\rho A\ddot{w}(x,t) + EIw''''(x,t) = 0$$

(1.36)

Define

$$a^4 = \frac{EI}{\rho A}$$

(1.37)

Hence, Eq. (1.36) becomes

$$a^4 w'''' + \ddot{w} = 0$$

(1.38)

Using the separation of variables method, we obtain a solution:

$$w(x,t) = W(x)T(t) = W(x)e^{i\omega t}$$

(1.39)

We substitute (1.39) in (1.36) we obtain a fourth order differential equation

$$W''''(x) - \gamma^4 W(x) = 0, \quad \gamma = \left(\frac{m}{EI}\right)^{1/4}\sqrt{\omega}$$

(1.40)

(1.40) admits the general solution in the form

$$W(x) = Ce^{\lambda x} u_P = \left(u_3^L - u_2^R\right) - \frac{h}{2}\left(\varphi_3^L - \varphi_2^R\right)$$

(1.41)

We substitute (1.41) in (1.40) and the solution is:

$$W(x,t) = C_1 \sin \gamma x + C_2 \cos \gamma x + C_3 \sinh \gamma x + C_4 \cosh \gamma x$$

(1.42)

where $C_1, C_2, C_3, C_4$ are constants from the boundary conditions.

In order to calculate the total flexural displacement for a uniform bar under a moment excitation $M_P$ the equation of motion is

$$\rho A \ddot{w}(x,t) + EIw''''(x,t) = -M_P''(x,t)$$

(1.43)

We assume the modal expansion

$$w(x,t) = \sum_j C_j W_j(x) e^{i\omega t}$$

(1.44)

where $W_j(x)$ are orthonormal mode shapes satisfying the free vibration differential equation (1.36) We differentiate $w(x,t)$ and $M_P$ and get

$$\ddot{w}(x,t) = -\omega^2 \sum_j C_j W_j(x) e^{i\omega t}$$

$$w''''(x,t) = \sum_j C_j W_j''''(x) e^{i\omega t}$$

(1.45)

$$M_P''(x,t) = \hat{M}_P\left[\delta'(x-x_2) - \delta'(x-x_1)\right] e^{i\omega t}$$

(1.46)

We substitute (1.46) and (1.45) into (1.43)

$$\rho A \ddot{w}(x,t) + EIw''''(x,t) = -\hat{M}_P\left[\delta'(x-x_2) - \delta'(x-x_1)\right]$$

(1.47)

8

We multiply (1.46) by $W_k(x,t)$ and take the integral over the length of the beam

$$\int_0^l W_k(x)\left[\rho A\ddot{w}(x,t)+EIw''''(x,t)\right]dx = -\hat{M}_P\int_0^l W_k(x)\left[\delta'(x-x_2)-\delta'(x-x_1)\right]dx$$
(1.48)

We use the property of the $\delta$ function

$$\int_a^b f(x)\frac{d}{dx}\delta(x-g)dx = -\int_a^b \delta(x-g)\frac{df(x)}{dx}dx = -\frac{d}{dx}f(g)$$
(1.49)

RHS of (1.48) becomes

$$-\hat{M}_P\int_0^l W_k(x)\left[\delta'(x-x_2)-\delta'(x-x_1)\right]dx = -\hat{M}_P\left[W_k'(x_1)-W_k'(x_2)\right]$$
(1.50)

and since the mode shapes $W_k(x)$ satisfy the free flexural vibration equation (1.50) we get

$$EIW''''(x)-\omega_k^2\rho AW_k(x)=0,\quad EIW''''(x)=\omega_k^2\rho AW_k(x)$$
(1.51)

LHS of (1.50) becomes

$$\int_0^l W_k(x)\left[\rho A\ddot{w}(x,t)+EIw''''(x,t)\right]dx = \sum_j C_j\left(\omega_j^2-\omega^2\right)\rho A\int_0^l W_k(x)W_j(x)dx$$
(1.52)

where $\int_0^l W_k(x)W_j(x)dx=1$ as per the orthogonality property of the mode shapes. We use (1.51) and (1.47) and substitute in (1.47)

$$\sum_j C_j\left(\omega_n^2-\omega^2\right)\rho A = -\hat{M}_P\left[W_k'(x_1)-W_k'(x_2)\right]$$
(1.53)

the modal participation factors $C_j$ are

$$C_j = -\frac{\hat{M}_P}{\left(\omega_j^2-\omega^2\right)\rho A}\left[W_k'(x_2)-W_k'(x_1)\right]$$
(1.54)

We substitute (1.54) into (1.44) and the flexural response of the beam becomes

9

$$w(x,t) = -\frac{\hat{M}_P}{\rho A} \sum_j \frac{W_j'(x_2) - W_j'(x_1)}{(\omega_j^2 - \omega^2)} W_j(x) e^{i\omega t}$$

(1.55)

For a damped system with the hysteretic damping coefficient g (1.55) becomes

$$w(x,t) = \frac{\hat{M}_P}{\rho A} \sum_j \frac{W_j'(x_1) - W_j'(x_2)}{(1+ig)\omega_j^2 - \omega^2} W_j(x) e^{i\omega t}$$

(1.56)

## 1.3 MODAL ANALYSIS WITH ANSYS WORKBENCH

Another way to determine the natural frequencies and modeshapes of a beam is through FEM analysis. We perform the analysis in ANSYS Workbench software and determine the natural frequencies (Figure 4) and the modeshapes. Figure 5 to Figure 17 present all natural frequencies and mode shapes for a uniform beam between 10 to 100 kHz.

| No. | Frequency |
|-----|-----------|
| 1. | 14.38 KHz (Flexural) |
| 2. | 19.96 KHz (Flexural) |
| 3. | 26.24 KHz (Axial) |
| 4. | 26.39 KHz (Flexural) |
| 5. | 33.65 KHz (Flexural) |
| 6. | 41.73 KHz (Flexural) |
| 7. | 50.63 KHz (Flexural) |
| 8. | 52.48 KHz (Axial) |
| 9. | 60.36 KHz (Flexural) |
| 10. | 70.93 KHz (Flexural) |
| 11. | 78.71 KHz (Axial) |
| 12. | 82.38 KHz (Flexural) |
| 13. | 94.79 KHz (Flexural) |

*Figure 4: ANSYS Workbench natural frequencies (range 10 to 100 kHz)*
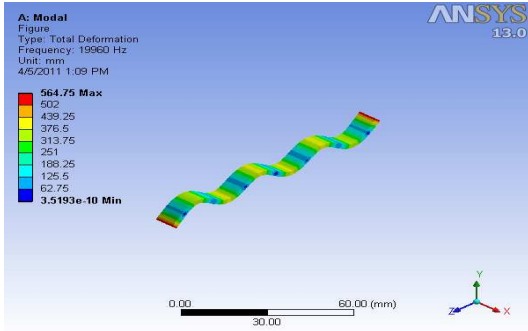
*Figure 5: Flexural (14.38 kHz)*
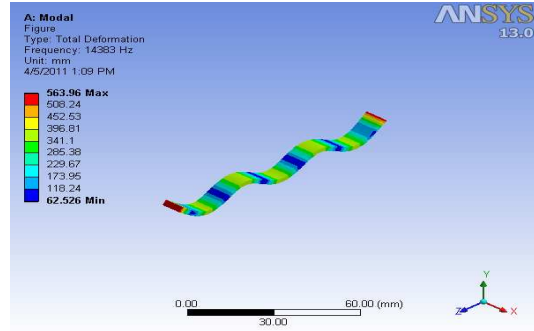


*Figure 6: Flexural (19.96 kHz)*
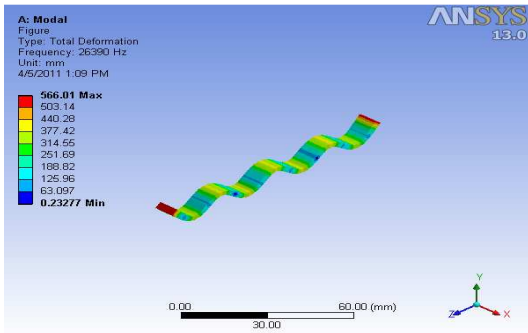


*Figure 7: Axial (26.24 kHz)*
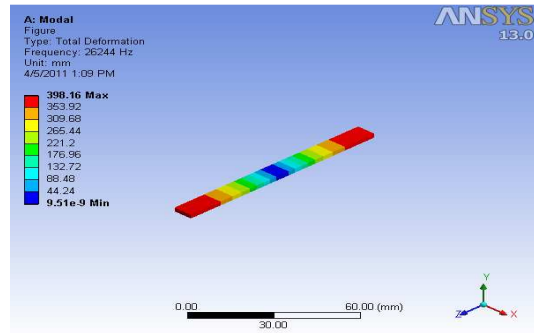


*Figure 8: Flexural (26.39 kHz)*
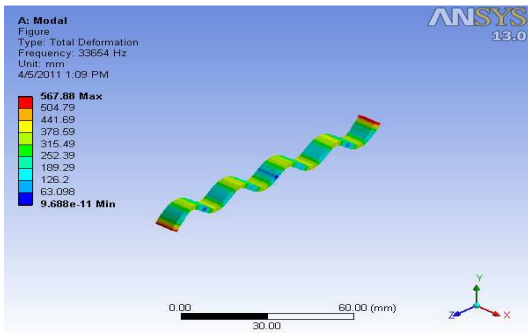


*Figure 9: Flexural (33.65 kHz)*
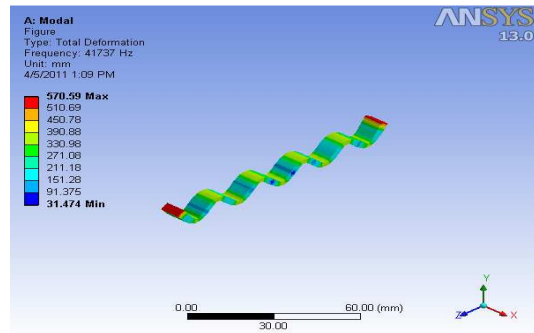


*Figure 10: Flexural (41.73 kHz)*
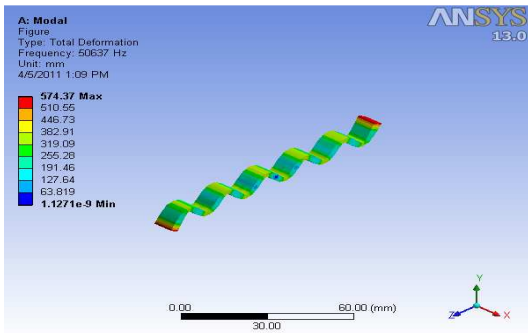


*Figure 11: Flexural (50.63 kHz)*
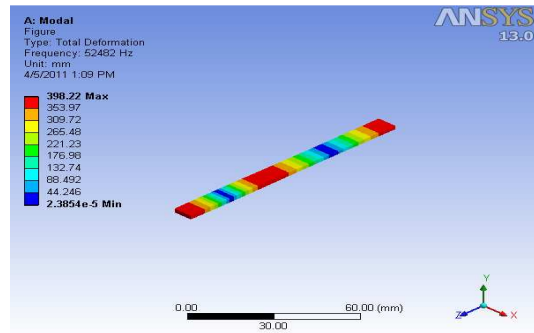


*Figure 12: Axial (52.48 kHz)*

11
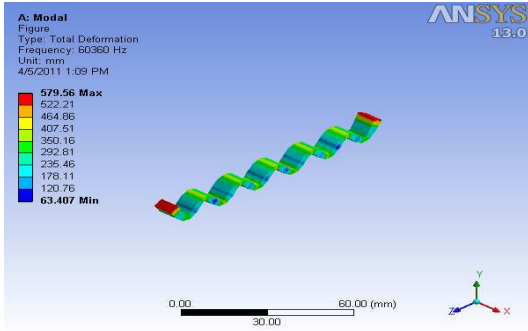
*Figure 13: Flexural (60.36 kHz)*
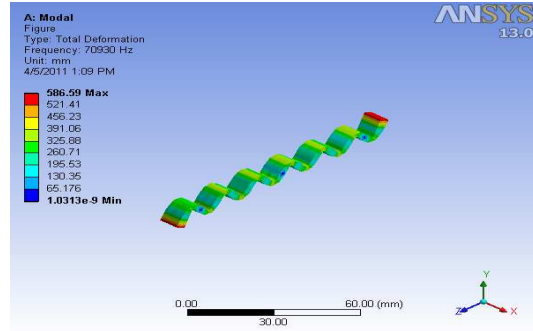


*Figure 14: Flexural (70.93 kHz)*
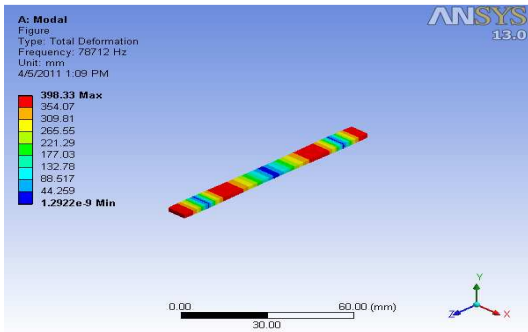


*Figure 15: Axial (78.71 kHz)*
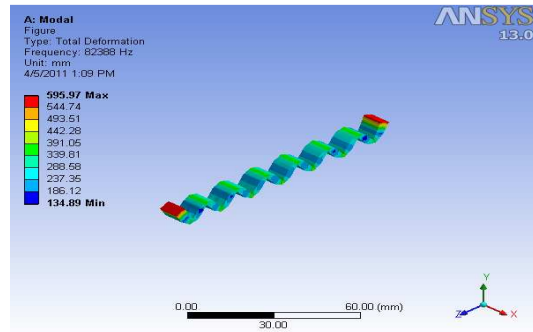


*Figure 16: Flexural (78.71 kHz)*
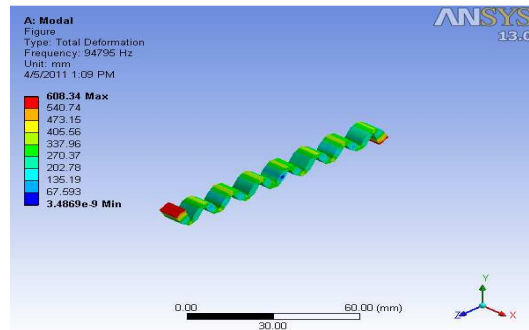


*Figure 17: Flexural (94.79 kHz)*

As per results in Figure 5 to Figure 17, all mode shapes match the modal expansion solution and the experimental results.

In order to assess whether there are differences between the ANSYS WB and the modal expansion solution in regards to the mode shapes, we compare separately the axial and flexural modes. We look at the numbers and location of the modes in the modeshape. Analysis of Figure 18 allows us to conclude that they coincide.

| | Analytical | nodes | FEM | nodes |
|---|---|---|---|---|
| **AXIAL VIBRATIONS (10 - 100) Khz** | | | | |
| **Nu** | **Frequencies (f) - (fU) Hz** | | | |
| 1 | **25400** | | **26244** | |
| 2 | **50800** | | **52482** | |
| 3 | **76200** | | **78712** | |
| 4 | 101600 | | 104930 | |
| | | | | |
| **FLEXURAL VIBRATIONS (10 - 100) KHz** | | | | |
| **Nw** | **Frequencies (f) - (fW) Hz** | | | |
| 1 | 1062.6 | 2 nodes - sym | 1096.4 | 2 nodes - sym |
| 2 | 2929.2 | 3 nodes -antisym | 2929.2 | 3 nodes -antisym |
| 3 | 5742.4 | 4 nodes - sym | 5886.7 | 4 nodes - sym |
| 4 | 9492.5 | **5 nodes - antisym** | 9683.9 | **5 nodes - antisym** |
| 5 | 14180 | **6 nodes - sym** | 14383 | **6 nodes - sym** |
| 6 | 19805 | **7 nodes - antisym** | 19960 | **7 nodes - antisym** |
| 7 | 26368 | **8 nodes - sym** | 26390 | **8 nodes - sym** |
| 8 | 33868 | **9 nodes - antisym** | 33654 | **9 nodes - antisym** |
| 9 | 42306 | **10 nodes - sym** | 41737 | **10 nodes - sym** |
| 10 | 51682 | **11 nodes - antisym** | 50637 | **11 nodes - antsym** |
| 11 | 61995 | **12 nodes - sym** | 60360 | **12 nodes - sym** |
| 12 | 73245 | **13 nodes - antisym** | 70930 | **13 nodes - antisym** |
| 13 | 85433 | **14 nodes - sym** | 82388 | **14 nodes -sym** |
| 14 | 98558 | **15 nodes -antisym** | 94795 | **15 nodes -antisym** |
| 15 | 112620 | 16 nodes - sym | 108230 | 16 nodes - sym |

*Figure 18: Analytical versus WB modes*

## 2. Literature Review of Lamb Waves for Non-Destructive Evaluation (NDE)

The ultrasonic NDE and SHM methods are used for detection of damage in different structures. The majority of the methods using ultrasonic waves to detect damage and are based on the same principles: a transmitter is used to create ultrasonic waves in the structure and the waves travel through the structure and are picked up by a receiver. In practice, the most commonly used waves to detect damage are P-waves which travel through the thickness of the structure, and guided Lamb waves which travel parallel to the surface of the structure.

Lamb waves (guided waves) are a better alternative for ultrasonic inspection and detection of cracks, corrosion, and disbonds/delaminations in various structures than conventional transducers which are a time consuming process since they can travel over large distances with little loss in amplitude, are sensitive to different types of defects, and are capable to propagate along curved structures and can reach enclosed or hidden areas.

### 2.1 Literature Review of Wave Propagation Theory

As per the Webster dictionary, waves are "disturbances or variations that transfers energy progressively from point to point in a medium and that may take the form of an elastic deformation or of a variation of pressure, electric or magnetic

intensity, electric potential, or temperature." A classification of different types of waves in elastic solids is shown in Table 1.

*Table 1: Wave types in elastic solids (Source: Giurgiutiu (2008), Table 5.1 page 130)*

| Wave Types | Motion Shape |
|---|---|
| 1. Pressure Waves (P) - longitudinal, compressional, dilatational, axial | Parallel to the surface of the structure |
| 2. Shear Waves (S) - transverse, distortional | Perpendicular to the surface of the structure |
| 3. Flexural Waves | Elliptical; plane sections remain plane |
| 4. Rayleigh Waves (bending) | Elliptical; amplitude decays quickly with depth |
| 5. Lamb Waves (guided, plates) | Elliptical; free-surface conditions satisfied at the top and bottom surface |

### 2.1.1 PRESSURE WAVES (P)

Pressure waves or P-waves (Figure 19) propagate parallel to the surface of the structure. In pressure waves, a transmitter and receiver are positioned on opposite sides of the structure in a "through-transmission" setup and an ultrasonic transducer (coupled to the structure through couplant, water, or air) serves as the transmitter or receiver. As per Giurgiutiu and Cuc (2004), if the wave transmitted between the emitter and receiver crosses a damaged area, it can be dispersed, attenuated, or shifted in time. Damage can be identified and measured by analyzing these changes. However using this type of waves, damage perpendicular to the surface can be difficult to detect.
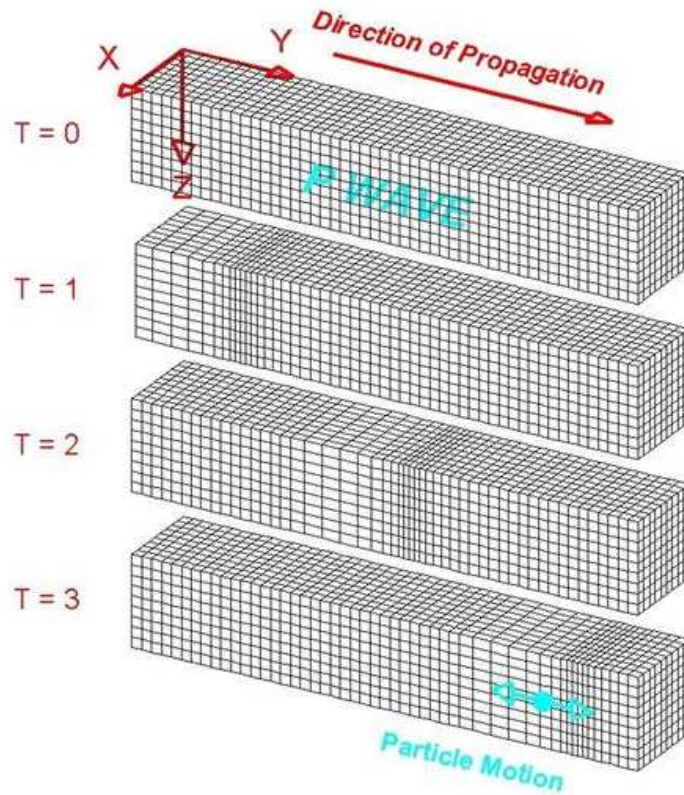
*Figure 19: P-wave that travels through a medium by means of compression and dilation. In this figure, particles are represented by cubes in this mode (Source: Lawrence Braile, http://www.geo.mtu.edu/UPSeis/waves.html)*

According to the p-wave theory, the particle displacement in a pressure wave can be written as:

$$u_x(x,t) = u_0 \cdot e^{i(kx-\omega t)} \tag{2.1}$$

where:

$k$ is the wave number

$\omega$ is the angular frequency

The wave number can be written in terms of the wave speed $c$ and the angular frequency $\omega$ as:

$$k = \frac{w}{c} = \frac{2\pi}{\lambda} \tag{2.2}$$

The particle displacement can be also written in terms of the wave length $\gamma$.

16

$$u_x(x,t) = u_0 \cdot e^{iw\left(\frac{x}{c}-t\right)} = u_0 \cdot e^{i2\pi\left(\frac{x}{\lambda}-\frac{t}{T}\right)}$$

(2.3)

where $\gamma = cT$ and $T = \dfrac{1}{f} = \dfrac{2\pi}{\omega}$ is the period of oscillation.

For a three-dimensional free solid, the wave speed $c$ for a p-wave is:

$$c_p = \sqrt{\frac{\lambda + 2\mu}{\rho}}$$

(2.4)

Where:

$\lambda = \dfrac{\nu E}{(1+2\nu)(1+\nu)}$ and $\mu = \dfrac{E}{2(1+\nu)}$ are the Lamé constants

$E$ is the Young's modulus

$\upsilon$ is the Poisson ratio

$\rho$ is the density.

For a two-dimensional plate with free top and bottom surfaces, the longitudinal wave speed becomes:

$$c_p = \sqrt{\frac{1}{1-v^2}\frac{E}{\rho}}$$

(2.5)

And for a one-dimensional slender bar the longitudinal wave speed is:

$$c = \sqrt{\frac{E}{\rho}}$$

(2.6)

### 2.1.2 SHEAR WAVES (S)

Shear waves or S-waves (Figure 20) propagate perpendicularly to the surface of the structure.
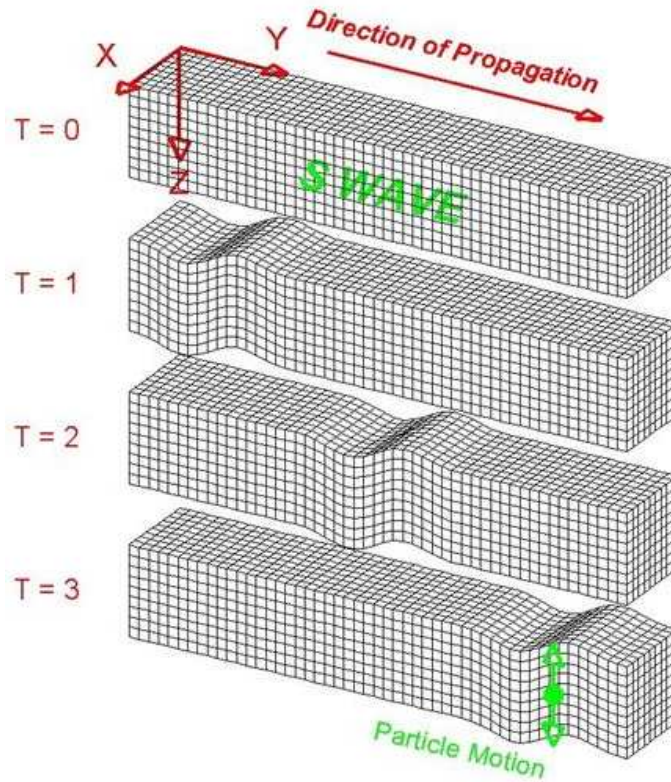
*Figure 20: Wave that travels through a medium. In this figure, particles are represented by cubes in this mode (Source: Lawrence Braile, http://www.geo.mtu.edu/UPSeis/waves.html)*

The particle displacement can be expressed as:

$$u_y(x,t) = u_0 e^{i(k_s x - \omega t)}$$

(2.7)

where the wave number $k_S = \omega / c_S$

In terms of the Lamé constants the wave speed of the shear waves can be expressed as:

$$c_S = \sqrt{\frac{\mu}{\rho}}$$

(2.8)

### 2.1.3 FLEXURAL WAVES

As per Giurgiutiu (2008) and Cuc (2010), flexural waves appear due to bending actions (Figure 21). The Bernoulli-Euler beam theory assumes that plane sections remain plane after deformation, but shear deformation and rotary inertia effects are ignored. The Kirchhoff plate theory assumes that straight normals to the mid-surface remain

18

straight after the deformation takes place but. The two theories imply a linear distribution of axial displacement across the thickness.
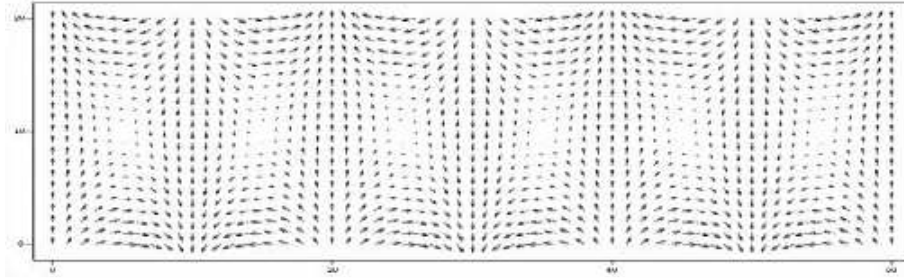


*Figure 21: Simulation of flexural waves (Source: Giurgiutiu, 2008)*

The axial and vertical displacements $u_x$ and $u_y$ for a beam can be determined as:

$$u_x = -yu'_y \tag{2.9}$$

We consider a harmonic expression for the vertical displacement as follows:

$$u_y(x, y, t) = u_0 e^{i(k_F x - \omega t)} \tag{2.10}$$

And the in-plane displacement field across the thickness becomes:

$$u_x(x, y, t) = y \frac{\partial}{\partial x} u_0 \cdot e^{i(k_F x - \omega t)} = ik_F u_0 \cdot e^{i(k_F x - \omega t)} \tag{2.11}$$

The flexural wave number $k_F$ in terms of the geometric and materials properties is:

$$k_F = \sqrt{\frac{\omega}{a}} \tag{2.12}$$

where

$$a = \sqrt{\frac{EI}{\rho A}} = \sqrt{\frac{E}{\rho} \frac{bh^3}{12bh}} = \frac{h}{2} \sqrt{\frac{1}{3} \frac{E}{\rho}} \tag{2.13}$$

The flexural wave speed is:

$$c_F = ak_F = \sqrt{a\omega} \tag{2.14}$$

According to equation (2.14), the wave speed is frequency dependent. If the wave speed is a function of frequency the wave is called dispersive.

19

### 2.1.4 RAYLEIGH WAVES

Rayleigh waves or surface waves (Figure 22) propagate close to the surface of the structure, and the motion amplitude decreases quickly with depth. The effective depth of penetration into the material is less than a wavelength.
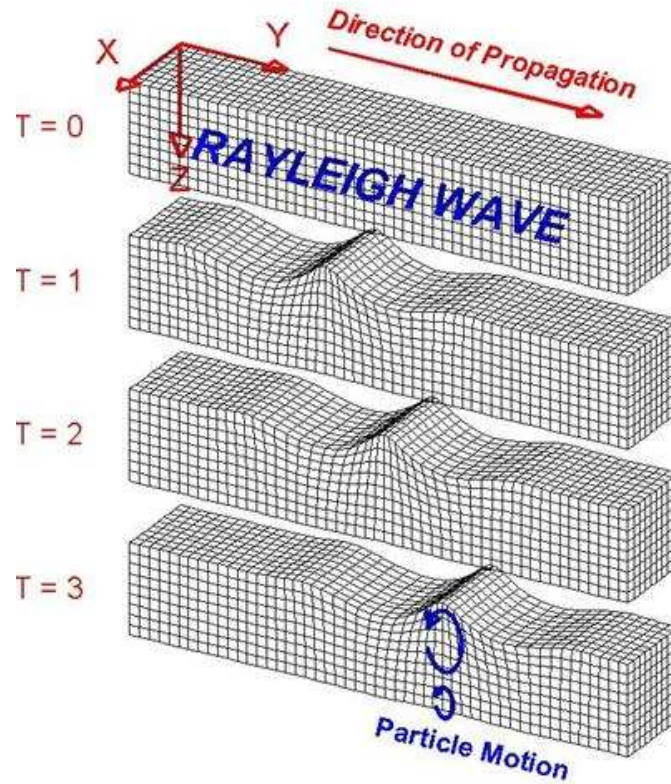


*Figure 22: Rayleigh Wave that travels through a medium. In this figure, particles are represented by cubes in this mode (Source: Lawrence Braile, http://www.geo.mtu.edu/UPSeis/waves.html)*

The two components of the Rayleigh wave $u_x$ and $u_y$ are calculated using an approximated equation for the wave velocity:

$$c_R = c_S \left( \frac{0.87 + 1.12\nu}{1+\nu} \right)$$

(2.15)

The Rayleigh wave number is $k_R = \omega / c_R$ and the components $u_x$ and $u_y$ are:

$$u_x(x,y,t) = u_0 k_R \left( e^{-qy} - \frac{2qs}{k_R^2 + s^2} e^{-sy} \right) e^{i(k_R x - \omega t)}$$

(2.16)

$$u_y(x,y,t) = iu_0 q \left( e^{-qy} - \frac{2k_R^2}{k_R^2 + s^2} e^{-sy} \right) e^{i(k_R x - \omega t)}$$

(2.17)

Where $q = \sqrt{k_R^2 - k_P^2}$ and $s = \sqrt{k_R^2 - k_S^2}$.

## 2.1.5 LAMB WAVES

### 2.1.5.1 LAMB WAVE EQUATIONS

In order to derive the Lamb wave equations we consider a traction-free surface plate with thickness $2d$ in which straight crested Lamb waves are propagating (Figure 23).
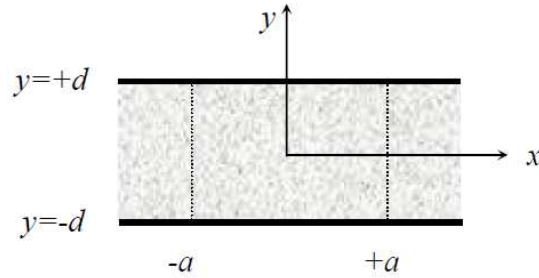


**Figure 23: Plate of thickness 2d, with a PWAS of width 2a, under harmonic loading on the top surface (Giurgiutiu, 2008)**

We make the following assumptions:

$z$-invariant motion

$u_z = 0$ (P+SV waves only)

$u_x \neq 0; u_y \equiv 0$

traction-free surface

$\sigma_{zx} = \sigma_{yz} = 0$

$\sigma_{xx} \neq 0; \sigma_{yy} \neq 0; \sigma \neq 0; \sigma_{xy} \neq 0$

21

The potentials of the pressure $P$ and shear vertical $SV$ waves are:

$$\phi(x, y, t) = f(y)e^{i(\zeta x - \omega t)}$$

(2.18)

$$H_z(x, y, t) = ih(y)e^{i(\zeta x - \omega t)}$$

(2.19)

Where

$f(y)$ describes the motion in the y–direction

$i(\zeta x - \omega t)$ describes the motion in the x-direction

The wave equation in terms of the two potentials can be written as:

$$\nabla^2 \phi = \frac{1}{c_P^2} \ddot{\phi}$$

(2.20)

$$\nabla^2 H_z = \frac{1}{c_S^2} \ddot{H}_z$$

(2.21)

Where

$c_P^2 = (\lambda + 2\mu)/\rho$ is the speed of the pressure wave;

$c_S^2 = \mu/\rho$ is the speed of the shear vertical wave;

$\lambda, \mu, \rho$ are the two Lame constants and the density, respectively.

The displacements in the $x$ and $y$ directions are:

$$u_x = \frac{\partial \phi}{\partial x} + \frac{\partial H_z}{\partial y}$$

(2.22)

$$u_y = \frac{\partial \phi}{\partial y} + \frac{\partial H_z}{\partial x}$$

(2.23)

After derivations and applying the boundary conditions, we arrive at the two differential equations:

$$f''(y) + \eta_P^2 f(y) = 0$$
$$h''(y) + \eta_S^2 h(y) = 0$$

(2.24)

22

The general solutions for the equations (2.24)are:

$$f(y) = A\sin(\eta_P y) + B\cos(\eta_P y)$$
$$h(y) = C\sin(\eta_S y) + D\cos(\eta_S y) \tag{2.25}$$

where $\eta_P^2 = \dfrac{\omega^2}{c_P^2} - \zeta^2$; $\eta_S^2 = \dfrac{\omega^2}{c_S^2} - \zeta^2$, and $\zeta$ are the directional wave numbers.

Substituting equations (2.25) in equation (2.18) and equation(2.19), we obtain the two

potentials as:

$$\phi(x,y,t) = \left[A\sin(\eta_P y) + B\cos(\eta_P y)\right]e^{i(\zeta x - \omega t)} \tag{2.26}$$

$$H_z(x,y,t) = \left[C\sin(\eta_S y) + D\cos(\eta_S y)\right]e^{i(\zeta x - \omega t)} \tag{2.27}$$

The displacements are:

$$u_x = i\left[\zeta\left(A\sin\eta_P y + B\cos\eta_P y\right) + \eta_S\left(C\cos\eta_P y - D\sin\eta_P y\right)\right]e^{i\psi} \tag{2.28}$$

$$u_y = \left[\eta_P\left(A\cos\eta_P y - B\sin\eta_P y\right) + \zeta\left(C\sin\eta_S y + Dcon\eta_S y\right)\right]e^{i\psi} \tag{2.29}$$

where $\psi = \zeta x - \omega t$

The two non-zero stresses are:

$$\sigma_{yy} = (\lambda + 2\mu)\left(\frac{\partial^2\phi}{\partial x^2} + \frac{\partial^2\phi}{\partial y^2}\right) - 2\mu\left(\frac{\partial^2\phi}{\partial x^2} + \frac{\partial^2 H_z}{\partial x \partial y}\right) \tag{2.30}$$

$$\sigma_{xy} = 2\mu\left(\frac{\partial^2\phi}{\partial x \partial y} - \frac{\partial^2 H_z}{\partial x^2} + \frac{\partial^2 H_z}{\partial y^2}\right) \tag{2.31}$$

After calculation they are:

$$\sigma_{xy} = \mu\left[\left(\zeta^2 - \eta_S^2\right)\left(A\sin\eta_P y + B\cos\eta_P y\right) + 2\zeta\eta_S\left(C\cos\eta_S y - D\cos\eta_S y\right)\right]e^{i\psi} \tag{2.32}$$

$$\sigma_{xy} = i\mu\left[2\zeta\eta_P\left(A\cos\eta_P y - B\cos\eta_P y\right) + \left(\zeta^2 - \eta_S^2\right)\left(C\sin\eta_S y + D\cos\eta_S y\right)\right]e^{i\psi} \tag{2.33}$$

**2.1.5.2 SYMMETRIC AND ANTI-SYMMETRIC LAMB MODES**

Lamb waves or guided plate waves are ultrasonic waves that travel parallel to the surface of the structure. There are two different types of lamb waves: symmetric (Figure 24) and anti-symmetric (Figure 25). For each propagation type, there are different modes shapes, based on the solutions of the Rayleigh-Lamb equation. The symmetric modes are denoted as $S_0, S_1, \ldots,$ while the anti-symmetric modes are denoted as $A_0, A_1, \ldots$. The wave motion for the two cases, symmetric and anti-symmetric is presented in Figure 24 and respectively Figure 25.
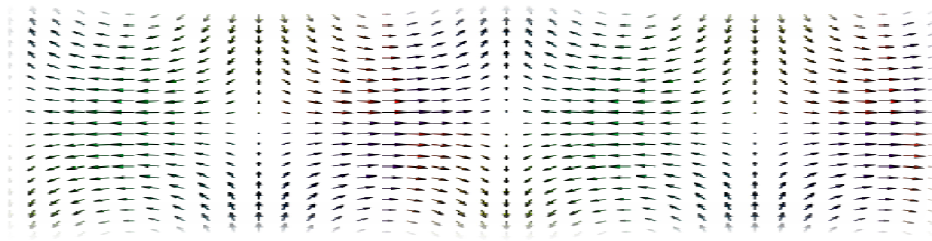


*Figure 24: Simulation of Lamb wav,: symmetric $S_0$ mode (Source: Giurgiutiu, 2008)*
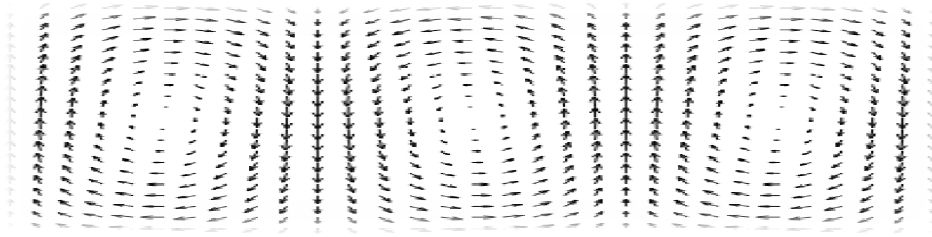


*Figure 25: Simulation of Lamb waves,: anti-symmetric $A_0$ mode (Source: Giurgiutiu, 2008)*

Symmetrical Lamb modes are similar to axial waves. The displacement of particles is shown in Figure 26.
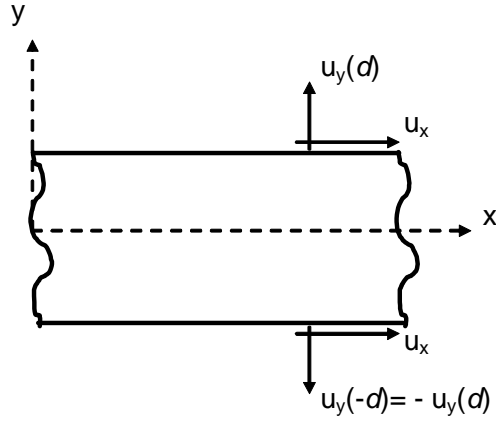
*Figure 26: Displacement of particles for a symmetric Lamb wave*
*Source: Cuc (2010)*

We use equations (2.28), (2.29) and (2.31) and apply the boundary conditions at

$$y = \pm d; \quad \sigma_{yy} = \sigma_{xy} = 0.$$

We obtain a homogeneous system of linear equations. The characteristic equation is:

$$\left( \xi^2 - \eta_S^2 \right) \tan \left( \eta_S d \right) + 4 \eta_S \eta_P \zeta^2 \tan \left( \eta_P d \right) = 0 \tag{2.34}$$

From equation (2.34) the Rayleigh-Lamb frequency equation can be derived in the form:

$$\frac{\tan \eta_S d}{\tan \eta_P d} = - \frac{4 \eta_S \eta_P \zeta^2}{\left( \zeta^2 - \eta_S^2 \right)^2} \tag{2.35}$$

Anti-symmetrical Lamb modes are similar to flexural waves. The displacement is shown

in Figure 27.



25

We use equations(2.32),(2.33) and (2.35) and apply the boundary conditions at

$$y = \pm d; \sigma_{yy} = \sigma_{xy} = 0$$

We obtain a homogeneous system of linear equations. The characteristic equation is:

$$\left(\zeta^2 - \eta_S^2\right)\tan\left(\eta_P d\right) + 4\eta_S\eta_P\zeta^2 \tan\left(\eta_S d\right) = 0$$

(2.36)

The Rayleigh-Lamb frequency equation for the anti-symmetric mode is:

$$\frac{\tan\eta_S d}{\tan\eta_P d} = -\frac{\left(\zeta^2 - \eta_S^2\right)^2}{4\eta_S\eta_P\zeta^2}$$

(2.37)

Equation (2.36) and equation (2.37) can be combined as follows:

$$F\left(\zeta,\omega\right) = \frac{\tan\eta_S d}{\tan\eta_P d} + \left[\frac{4\eta_S\eta_P\zeta^2}{\left(\zeta^2 - \eta_S^2\right)^2}\right]^{\pm 1} = 0, \quad \begin{cases} +1 = symmetric \\ -1 = antisymmetric \end{cases}$$

(2.38)

### 2.1.5.3 DISPERSION OF LAMB WAVES

Lamb waves exhibit velocity dispersion, that is, the wave speed is contingent on the product of frequency and thickness of the plate in which the Lamb waves are traveling.

Figure 28 ilustrates this by cosidering a tone burst which consists of a carrier frequency (tone) and has a short duration in time (burst). The initial signal is a sinusoidal having ten complete cycles. Figure 28 also shows the frequency spectrum of the tone burst signal where $f_c$ is the dominant frequency.
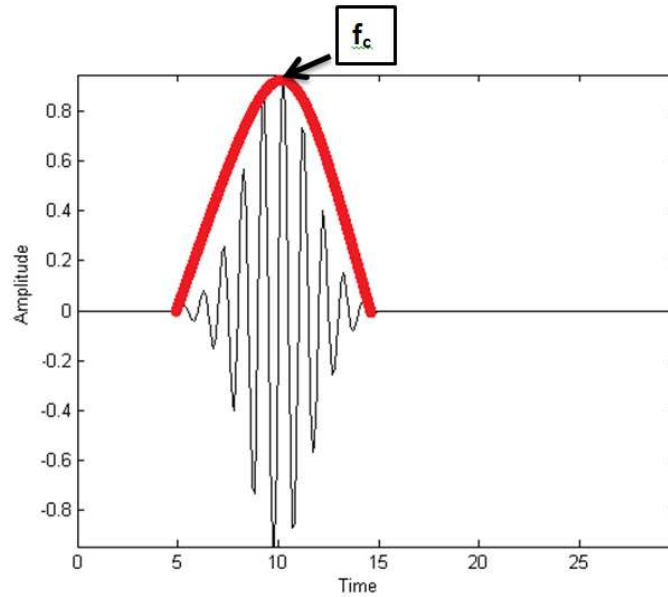
*Figure 28: Ten-count sine tone burst and frequency spectrum of the tone burst signal (shown in red)*

For a case of non-dispersive wave propagation, the shape of the wave remains the same and the wave speed is constant, while for a case of dispersive wave propagation, each frequency component travels with a different speed and the grade of dispersion is contingent on the spectrum bandwidth.

## 2.2 LAMB WAVES FOR CRACK DETECTION

In the last decade, there has been a large amount of research on the interaction of Lamb waves with cracks in different structures. Alleyne and Cawley (1992) studied how Lamb waves interact with damage and used FEM to study the interaction of individual Lamb waves with simulated damages (represented by notches). They found that the theory and the experimental results are in concord and that the sensitivity of Lamb waves to particular notches depended on the frequency-thickness product, the mode type (symmetric or anti-symmetric), the mode order and the geometry of the

27

notch. In their paper, the transducers used in the experiments were conventional wideband ultrasonic immersion transducers as per Figure 29.
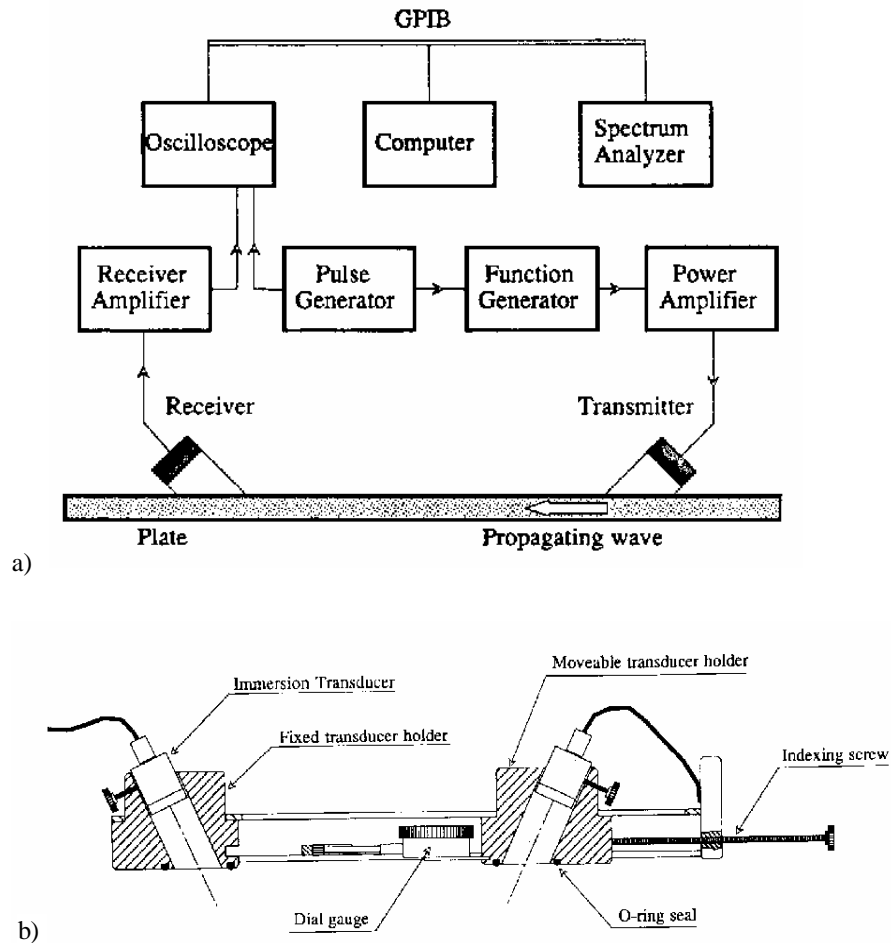




*Figure 29: (a) Schematic diagram of the experimental setup;*
*(b) Schematic of the Lamb wave test rig*
*Source: Alleyne and Cawley (1992)*

Literature shows that the propagation of Lamb waves and the interaction with damages can be modeled using various simulation techniques such as finite difference equations (FDE), finite element analysis (FEM), boundary element methods (BEM), spectral element methods (SEM), and local interaction approach simulation (LISA).

An important strand of lamb waves' research looks at the scattering of Lamb waves from defects. Although tomographic image techniques can normally be utilized to

extract the location, shape, and the extent of flaws in structures, the scattering of Lamb waves from severe defects introduces artifacts that make the tomographic reconstruction difficult. McKeon and Hinders (1999) used the Mindlin's higher order plate theory to explain the scattering of S0 Lamb waves from a cylindrical through hole in an aluminum plate. Their theoretical model predicted that for three holes with increasing radii, the lobes with maximum amplitude are located at 1800, and 900 and 2700. The experimental results using a "point source" solution showed a good correlation with the theoretical model, and confirmed that scattering is important when the hole size is larger than the beam size.

Valle et al. (2001) studied the propagation of guided circumferential waves in a metallic hollow cylinder and the interaction of the guided waves with a simulated crack. As part of their approach, they used guided waves to both locate and size the crack. First, the crack was sized using a scattering formula developed by Auld and modified to analyze transient signals. Second, the crack was located using the backscattered signal and applying a time-frequency digital signal processing technique (reassigned spectrogram). The processed signal is then compared with signals obtained from a pristine cylinder (without cracks). In order to model the scattering of guided circumferential waves caused by a crack and to calculate the transient response of the wave guides the authors used the commercial FEM code ABAQUS. They presented that the results for both crack sizing and crack locating are dependent on the frequency of the input signal and that for detecting multiple cracks, both the Auld's formula and the reassigned spectrogram must be utilized.

Another strand of research focuses on the identification of the location and the size of defects which entails the use of faster and more efficient numerical methods than FEM. Clezio et al. (2002) used a modal decomposition method to solve problems of Lamb wave scattering. They focus on the interaction of the first symmetric Lamb mode, S0, with vertical cracks in an aluminum plate placed in vacuum. The cracks are symmetric with respect to the middle plane of the aluminum plate. The reflection and transmitted coefficients and the crack motion were predicted and compared against FEM calculations and experimental data. In the experiments, they used an 8 mm-thick aluminum plate (Figure 30a) with three double notches of 0.7 mm width and height varying from 25%, 50%, and 75% of the plate thickness.
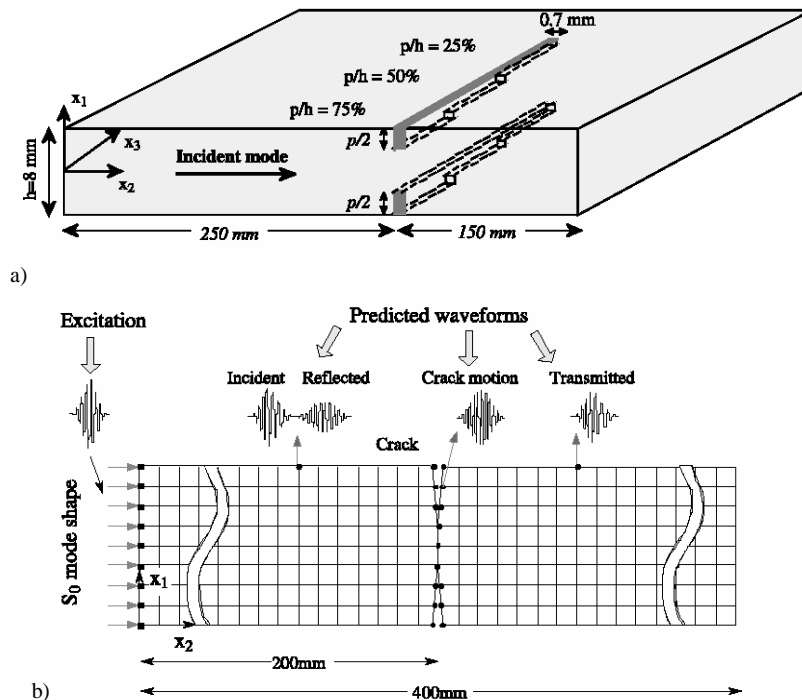


Figure 30: (a) Aluminum plate with symmetrical double surface notches;
(b) Schematic of the FE model with a double surface crack
Source: Clezio et al. (2002)

30

Authors use a frequency of the excitation (incident mode S0) of 0.14 MHz, so that the frequency-thickness product was 1.12 MHz, below the S1 mode cut-off frequency. Based on this fact and the symmetry of the problem no mode conversion was obtained.
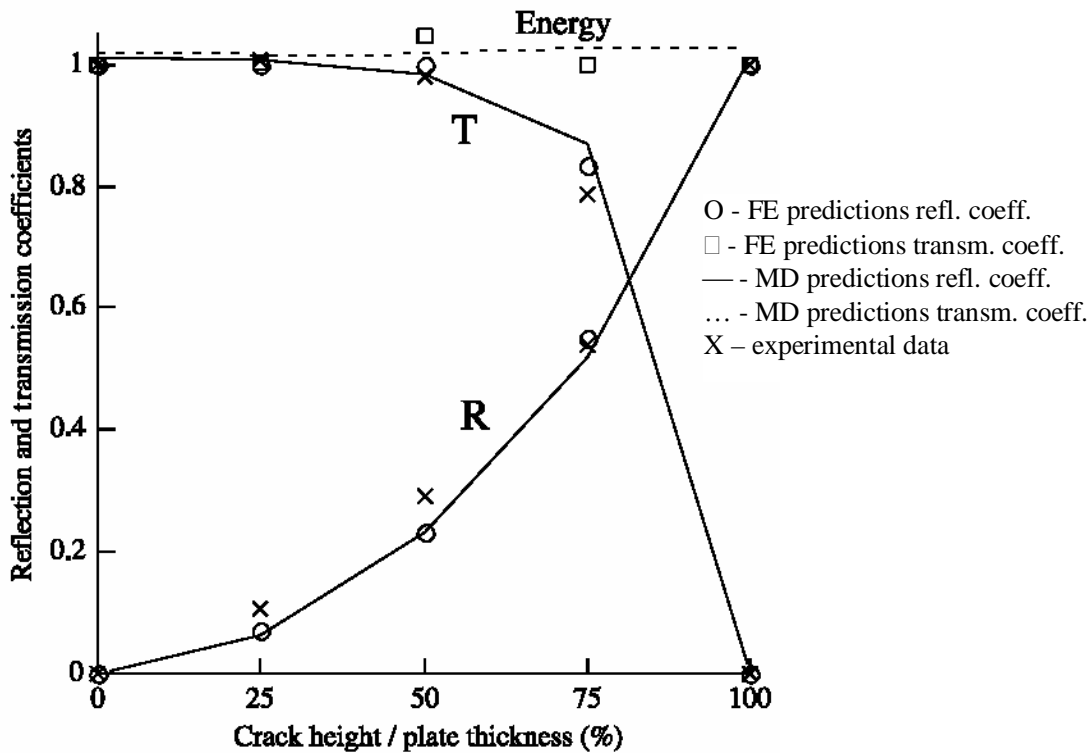


*Figure 31: Reflection and transmission coefficients vs. crack height/plate thickness; FEM predictions, modal decomposition (MD) predictions and experimental results*
*Source: Clezio et al. (2002)*

Clezio et al. (2002) found that there is accord between the predictions and the experimental data as per Figure 31. Besides, the results using modal decomposition method were very similar to those obtained using the FEM but the computational time was about 100 times smaller when using the modal decomposition method.

Grondel et al. (2002) used Lamb waves to examine riveted aluminum lap-joints during cyclical loading. As part of their approach, they excited and received Lamb waves using piezoelectric transducers coupled onto the aluminum plates. Authors used

symmetrical aluminum multi-riveted plates 750x300x2 mm fastened by six rows of a total of 84 rivets as specimens. They were manufactured in such a way to ensure crack initiation from the central rivets, as shown in Figure 32a. The piezoelectric transducers were bonded symmetrically with respect to the middle strap joint as shown in Figure 32b. The excitation consisted of a 5 cycle sinusoidal tone burst at 400 kHz. The received signal was processed using the short Fourier transform.
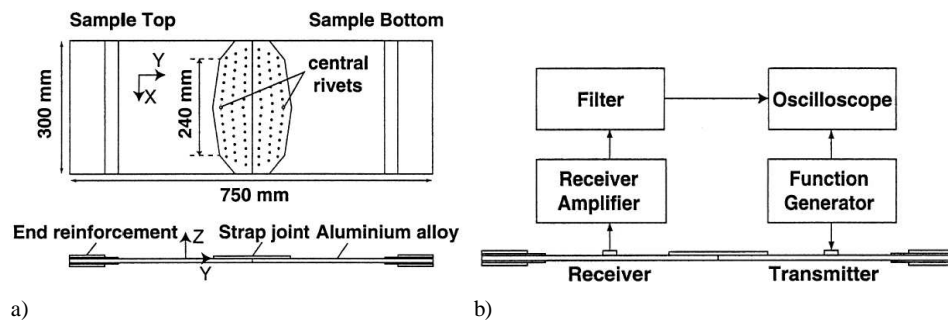


*Figure 32: (a) Schematic description of the metallic specimen;*
*(b) experimental Lamb wave set-up*
*Grondel et al. (2002)*

Grondel et. Al (2002) results confirmed the emergence of a 8 mm crack around the central rivet at 107,000 cycles. Also, they observe a variation in the distribution of the energy between 100,000 and 107,000 (Figure 33) and an even stronger one between 107,000 cycles and 180,000 cycles.
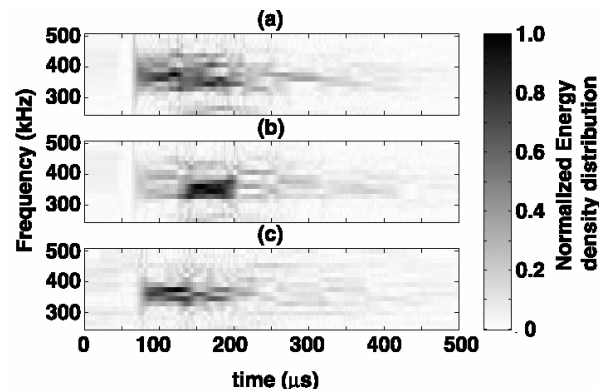


*Figure 33: Time-frequency analysis of the Lamb wave signal during fatigue loading:*
*(a) at 100,000 cycles; (b) at 107,000 cycles; (c) at 180,000 cycles*
*Source: Grondel et al. (2002)*

The ultrasonic inspection techniques can be very time consuming and labor intensive and as a result a lot of recent research focuses on building fast and low-cost structural health monitoring systems. These systems are meant to allow for an inspection of the structure without interrupting the service of the aircraft or the machinery and eliminate the labor-intensive inspection and the need to disassemble and re-assemble good structural parts, process during which accidental damage can be induced in the healthy structure. The new SHM systems should have low weight, low cost, low maintenance and require as little as possible change in the host structure.

In the area of structural health monitoring systems, Ihn and Chang (2004) developed a piezoelectric based built-in diagnostic technique for monitoring fatigue crack growth in metallic structures. Their proposed method consists of three components: diagnostic signal generation, signal processing and damage interpretation as shown in Figure 34.
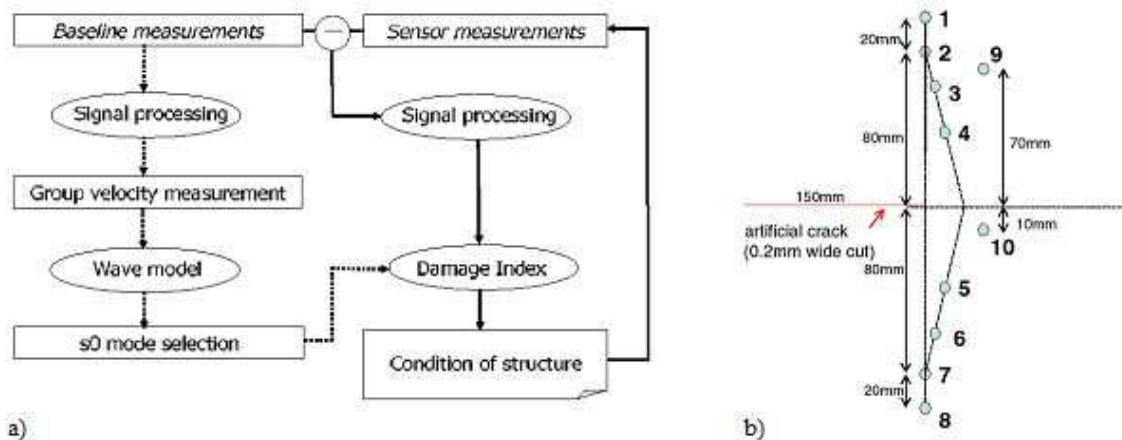


*Figure 34: (a) Crack detection scheme; (b) experimental set-up*
*Source: Ihn and Chang (2004)*

Authors used an excitation signal consisted of a 5-count sine burst signal. Lamb waves were generated in the structure by surface mounted piezoelectric actuators. The raw signals are processed using MATLAB, and the envelope of the signal is extracting by

applying the short time Fourier transform (STFT) to the initial signal. The time of flight (TOF) information can now be extracted. When Lamb waves travel over damage areas scattering occurs and the energy of the scattered signal can provide good information about the crack propagation. Based on these assumptions, Ihn and Chang (2004) developed a damage index (DI) defined as the ratio of the scatter energy contained in the S0 mode wave-packet to the baseline energy contained in the S0 mode wave-packet:

$$DI = \left( \frac{\int_{t_i}^{t_f} \left| S_{SC}\left(\omega_0,t\right)\right|^2 dt}{\int_{t_i}^{t_f} \left| S_{SC}\left(\omega_0,t\right)\right|^2 dt} \right)^{\alpha} \cong \left( \frac{Scatter\ energy\ of\ S_0\ \mathrm{mode}}{Baseline\ energy\ of\ S_0\ \mathrm{mode}} \right)^{1/2}$$

(2.39)

Figure 35 shows the crack detection scheme and the experimental set-up. The experiments were carried on a 3.175 mm thick aluminum plate with a 0.2 mm wide notch cut. The length of the notch was increased and the sensor measurements at different notch lengths were taken.
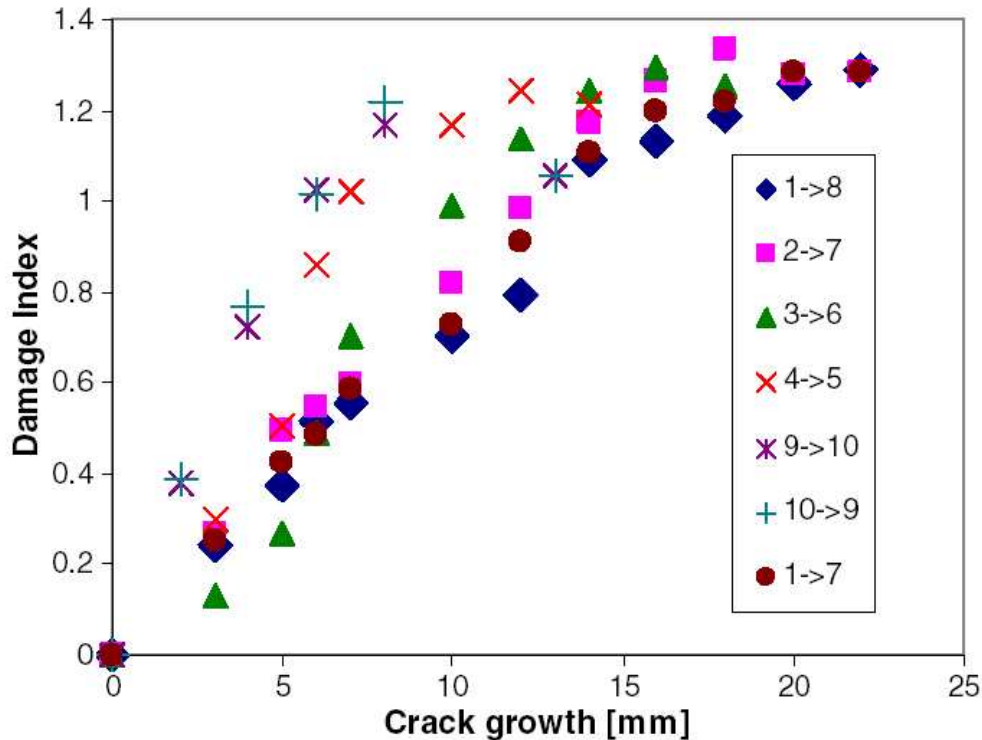
*Figure 35: Damage index vs. crack growth*
*Source: Ihn and Chang (2004)*

The Ihn and Chang (2004) results showed that the proposed damage index measured from the piezo-ceramic sensors was in good accord with the actual fatigue crack growth obtained from visual inspection of the specimen (Figure 35). The disadvantage of their proposed method is that it is sensitive to the noise and the signal to noise ratio of the received signal must be high.

## 2.3 LAMB WAVES FOR CORROSION DETECTION

Metals corrosion can cost a lot of money (in the United States alone costs are estimated to be about $300 billion a year, or approximately 3.2% of the U.S. GDP1) and in some cases corrosion accelerated fatigue failures can have catastrophic results (e.g. tragic example of that occurred in 1988 when a nineteen-year old Boeing 737 lost a

---

[1] Boyd D. Howard, Kenneth Gibbs and James B. Elder III, Corrosion detection devices, Westinghouse Savannah River Company, Army Corrosion Summit, 2004

35

major portion of its upper fuselage in full flight at 24,000 feet). A variety of Non-Destructive Evaluation (NDE) methods have become available that are good candidates for the detection of corrosion: visual, ultrasonic, radiographic, electromagnetic, acoustic transducer scanning, thermo graphic inspection, and ground penetrating radar. In the oil and chemical industries in particular, because of the insulation layer that covers the pipes, detection of hidden corrosion in aged pipes is particularly difficult. Moreover current technologies involving point-by-point inspection are expensive because of the need to remove the insulation layer. Hence, there is a lot of recent research that focuses on the development of a quick and reliable method for detection of corrosion under the insulation layer.

Ever since a few decades ago, researchers began to look at using ultrasonic guided waves for tubes inspection (Thomson et. Al (1972), Silk et, al (1979)) and a major focus was on the inspection of heat exchanger tubing. Other studies looked at the interaction of Lamb waves with defects in plates and pipe structures. Lowe et al (1998) developed a method in which guided waves propagate in the walls of thin pipes, and capture the reflected signals from defects. Authors used the pulse-echo configuration and in parallel with the experiments, conducted analytical and numerical studies. Their testing scheme utilized a pulse-echo arrangement from a single location on a pipe as per Figure 36a. The waves were excited and received using a ring transducer made by dry-coupled piezoelectric elements distributed around the circumference.
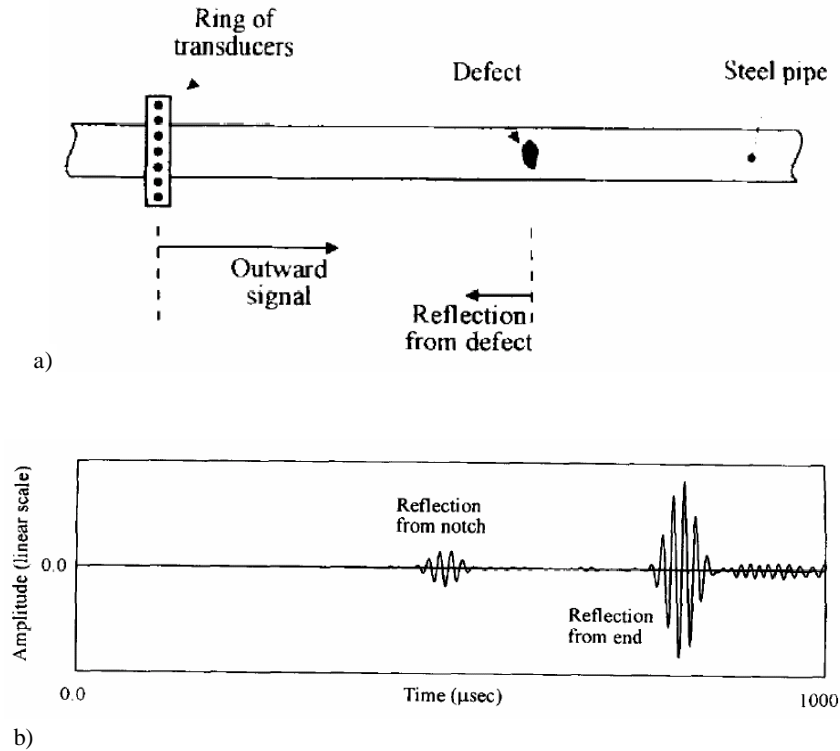
**Figure 36: (a) Pulse-echo set-up for pipe inspection using Lamb waves;**
**(b) Reflection from a through-thickness notch extending around of the circumference of a pipe**
**Source: Lowe et al. (1998)**

They used as an excitation signal a longitudinal $L(0,2)$ axially symmetric mode at 70 kHz since this mode is non-dispersive over a wide bandwidth around the 70 kHz frequency. This mode is sensitive to internal or external defects. Their results showed a clear reflection from the notch and as well as the reflection from the end of the pipe.

Corrosion poses a threat also in the aerospace industry. Conventional through-the-thickness ultrasonic methods for corrosion inspection of large surfaces using point-by-point examination can be tedious and time consuming. Besides, the disadvantage of this method is that the corrosion will create irregular surfaces and the echo signals are unclear and hard to interpret.

Recent research lead to the development of new ultrasonic inspection methods using guided waves (Lamb waves). These provided more measurable features related to

37

the interaction between guided waves and defects and hence contain more information about the flaws in structures. Rose et al. (1995, 1998, and 2002) did extensive work in the NDE for corrosion detection in pipes and plates using guided waves. Zhu et al. (1998) conducted an experimental study of hidden corrosion using guided waves, combined with a boundary element method (BEM) numerical simulation. Their experimental work involved both corrosion simulated specimens and real corrosion specimens. The BEM method was used to simulate the guided wave scattering, mode cutoff, and conversion phenomena. Based on the BEM method they proposed a quantitative technique to measure the hidden corrosion depth and compare the results with those obtained experimentally. They used two types of aluminum corrosion specimens: plates with simulated corrosion prepared by a machine cutting and real corrosion plates prepared by controlled electrochemical procedure (Figure 37). The experimental set-up is appears in Figure 38.
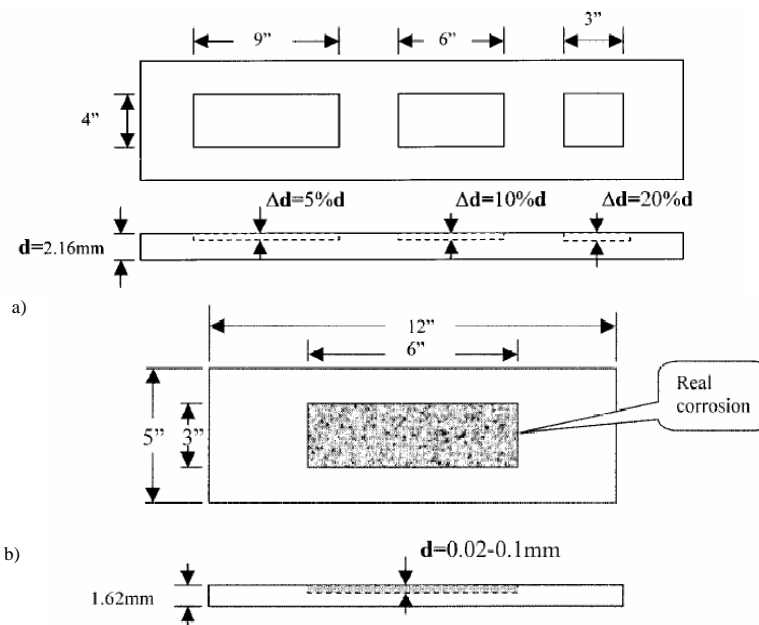


*Figure 37: (a) Corrosion simulated specimen; (b) real corrosion specimen*
*Source: Zhu et al. (1998)*

In order to produce and detect guided waves (Lamb waves) Zhu et. al (1998) used a pair of wedge transducers and both through-transmission and pulse-echo method and the plexi-glass wedges were specially conceived to decrease the effect of multi-reflection inside the wedges.
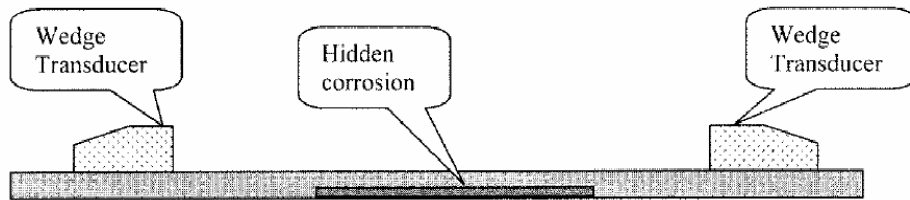


***Figure 38: Experimental set-up: oblique incidence and reception for through-transmission***
***Source: Zhu et al. (1998)***

They used a tone burst signal as well as a shock device to generate different guided waves required for mode selection and feature extraction. The time domain results showed a clear difference between the A3 Lamb mode in the pristine specimen (no corrosion) and the corroded specimen Figure 39a and the same difference for the S5 Lamb mode between the pristine and corroded specimen, Figure 39b.
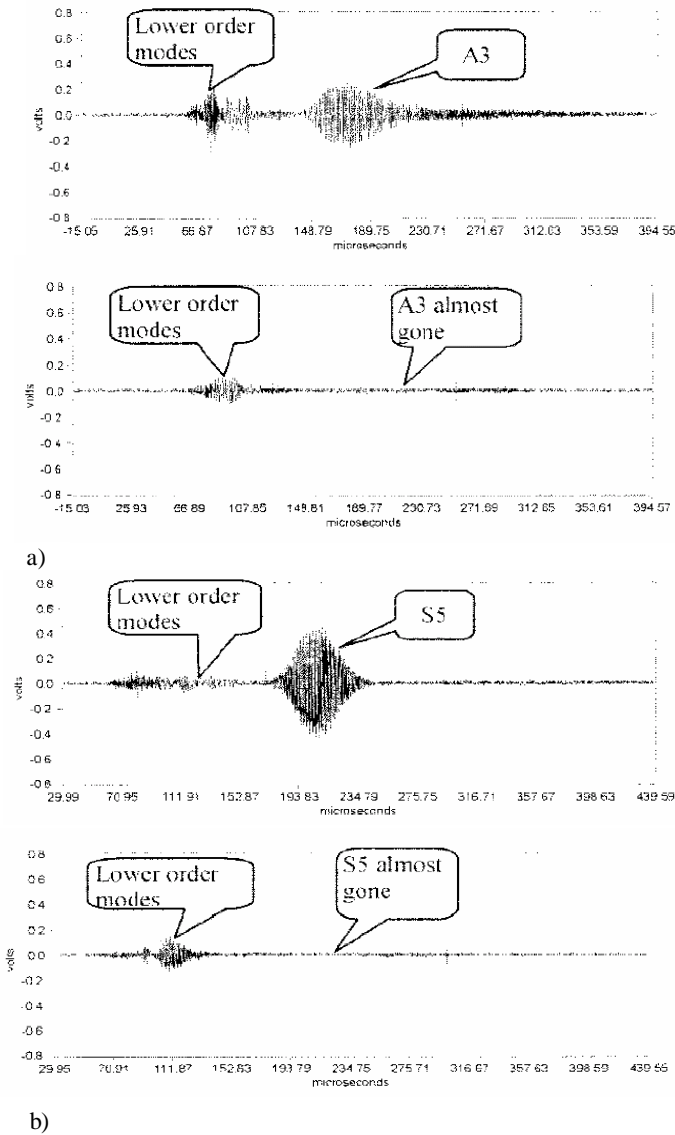
***Figure 39: Transmitted signals with and without 5% corrosion thickness:***
***(a) A3 mode at 4.39 MHz and 25o incidence; (b) S5 mode at 6.37 MHz and 25o incidence***
***Source: Zhu et al. (1998)***

Authors used the boundary element model (BEM) to determine the transmission

and reflection coefficients for different corrosion depths (Figure 40).
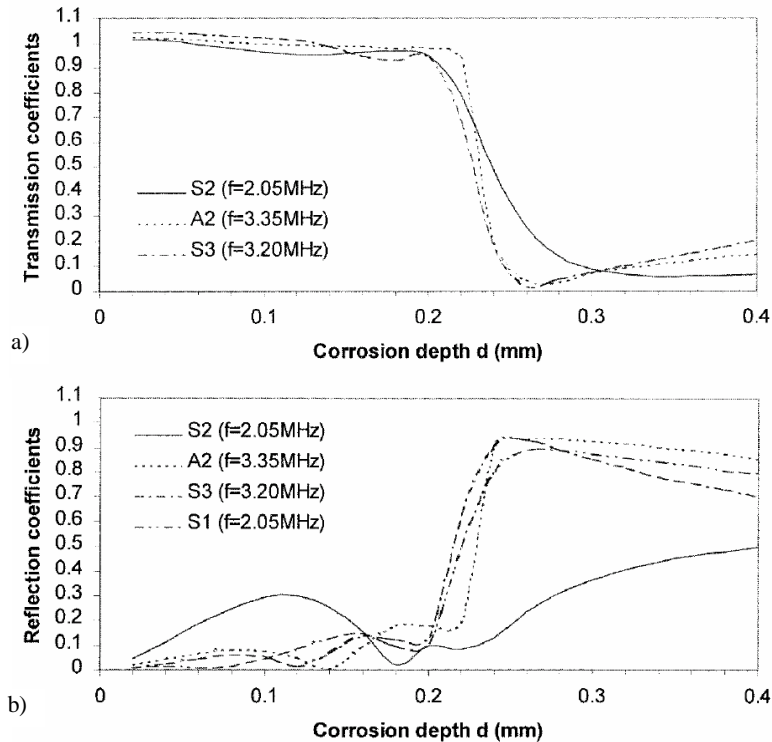
***Figure 40: (a) Transmission coefficients for the S2, A2, and S3 incidence vs. corrosion depth;***
***(b) Reflection coefficients for the S2, A2, and S3 incidence vs. corrosion depth***
***Source: Zhu et al. (1998)***

The results obtained by Zhu et al. (1998) can be used to establish a vector feature to be used in pattern recognition analysis.

Rose et al. (2002) also focused on the phase velocity, frequency wave resonance tuning and mode selection. They presented a mathematical model for the propagation of waves in hollow cylinders and also the numerical and experimental results. They found out that as a result of tuning it is possible to improve penetration power despite the coating layers and to detect difficult defect shapes.

## 2.4 LAMB WAVES FOR DISBOND/DELAMINATION DETECTION

Composite materials are starting to play a very important role in aerospace, naval, and automotive industries. There are currently many approaches for the damage detection in composite materials, however they can be divided into two main

41

categories: structural health monitoring (SHM) and nondestructive evaluation (NDE). An SHM system is a bonded system of fixed sensors which are permanently attached to the structure and monitoring can be either on demand or continuous. An NDE approach consists of inspecting a structure with adjustable and moveable sensors that systematically check the structure for damage when not in use. While an SHM system has the benefit of being able to monitor a structure while it is in service, tracking the growth of damage and providing a frequent report of the state of the structure, some capabilities are sacrificed so the system can be attached to the structure (cost, size, and weight need to be considered). NDE has the benefit of being able to use large, expensive equipment for damage detection; however the drawback is that the structure needs to be taken offline for the inspection.

Since delamination is the most important defect in composite materials, there is a large body of recent research that focuses on mathematical models that can predict delamination location.

Hanneman and Kinra (1991) focused on the study of uniaxial, steady state time harmonic wave propagation in adhesively bonded joints. They derived an exact formula for the transmission coefficient $H'(w)$ and studied the natural frequencies of the bond as a function of normalized adhesive thickness. To determine the transfer function of the bond, they considered a three-layer plate immersed in an elastic fluid (water). Authors found that the sensitivity of the transfer function $H'(w)$ is higher at odd resonance modes and thus the odd resonances are more sensitive to changes in the material properties and thickness of the adhesive layer than the even resonances.

Rose et al. (1994) used ultrasonic guided waves for NDE of adhesively bonded structures and developed a double spring hopping probe (DHSP) to introduce and receive Lamb waves. Their method was used to inspect a lap splice joint of a Boeing 737-222. They used a pair of variable angle beam transducers in order to excite the Lamb waves. Preliminary results showed the capability of through transmission for disbond detection using the symmetric mode S0 at 1.455 MHz frequency and the anti-symmetric mode A1 at 3.525 MHz. They found severe corrosion area using the DHSP hand held. Lowe and Cawley (1994) studied the applicability of plate wave techniques for inspection of adhesive and diffusion bonded joints. Problems addressed by them were related to the measurement of the cohesive properties (the material properties of the adhesive layer) and the measurement of the adhesion properties (the quality of bonding at the two interfaces between the adhesive and the metal parts). Authors found that the Lamb wave techniques are limited by their strong sensitivity to the material properties and the thickness of the adherents and that they are relative insensitive to those of the adhesive layer.

Lee et al. (2003) studied the problem of wave propagation in a diffusion bonded model using spectral elements (SE) and a new local interaction simulation approach (LISA) for numerical modeling. The novelty of their work was the sensor/actuator configuration consisting of five different layers of materials with one piezo-ceramic element generating a thickness mode vibration. The five layers were: two electrodes used for actuating and sensing (Sonox P5), two copper layers, and in the middle a couplant layer. The experiments validated the numerical simulation, showing that the

actuator/sensor configuration could operate either in S0 or A0 mode using an excitation frequency of 260.5 and 100 kHz, respectively. However the coupling layer distorts the wave propagation, due to its low impedance at the interface point and low speed within the couplant medium. Kwon et al. (2003) focuses on the reliability of piezoelectric monitoring of adhesive joints. They tested a single lap adhesively bonded tubular joint during a torsional fatigue test. Their results showed that the piezoelectric properties of the joint are related to the crack propagation and that the measured electric flux density is a good estimator of the failure strain, and are sensitive to the maximum stress or strain in the layer rather than the average stress.

Another area of research focuses on repair patches which are widely used in the aircraft industry for small repairs of the aircraft fuselage in order to extend the operational life of aging aircrafts. Chiu et al. (2000) focused on the development of a smart system which will provide information on the in-service performance of the repair and the associated structure. Their results showed the possibility to use piezoelectric elements to develop a smart patch, and use the impedance measurements to detect the presence of damage. For impedance measurements the sensor/actuator must be located close to the damaged area. Galea et al. (2001) described two in-situ health monitoring systems, one consisting of a piezoelectric polyvinylidene fluoride (PVDF) film-based, and the second one consisting of an electrical –resistance strain gauge-based sensing system and the methods were tested on a composite bonded patch applied to an F/A-18 aircraft. The "smart patch" approach described was to detect disbond growth in a safe life zone of the patch where disbonds are unacceptable, and to

monitor the damage growth in a damage tolerant region. The method used to assess the "health" of the patch was to measure the load transfer in the safe-life zone. This was achieved by monitoring the ratio of $\frac{\text{patch strains}}{\text{strain in the component}}$ during the service life. Any decrease in this ratio was an indication of the disbonding of the patch. The results showed that the concept of "smart patch" approach for an autonomous health monitoring system is viable. However, more work is to be done to minimize the power requirements of the system, and to develop other confidence building indicators.

Recently, Koh and Chiu (2003) did a numerical study of the disbond growth of a composite repair patch. As part of their approach, they used impedance method and the transfer function method to identify typical disbond growth shapes and sizes underneath the repair patch. The results showed it is possible to obtain information about the location, type, and severity of disbond by using signal processing techniques and via strategic placement of the PWAS.

Even more recently, Kudela and Ostachowitz (2009) developed a numerical model that can predict wave propagation behavior in delaminated structural elements such as beams and plates. They considered signals of propagating waves excited by PWAS and registered at some points of a structure and compared damaged state signals with reference signals. They found that delamination occurred. The essence of their proposed model is that only a small amount of degrees of freedom is necessary to predict the behavior of propagating waves in a composite structural element with delamination. The scheme of their model is shown in Figure 41.
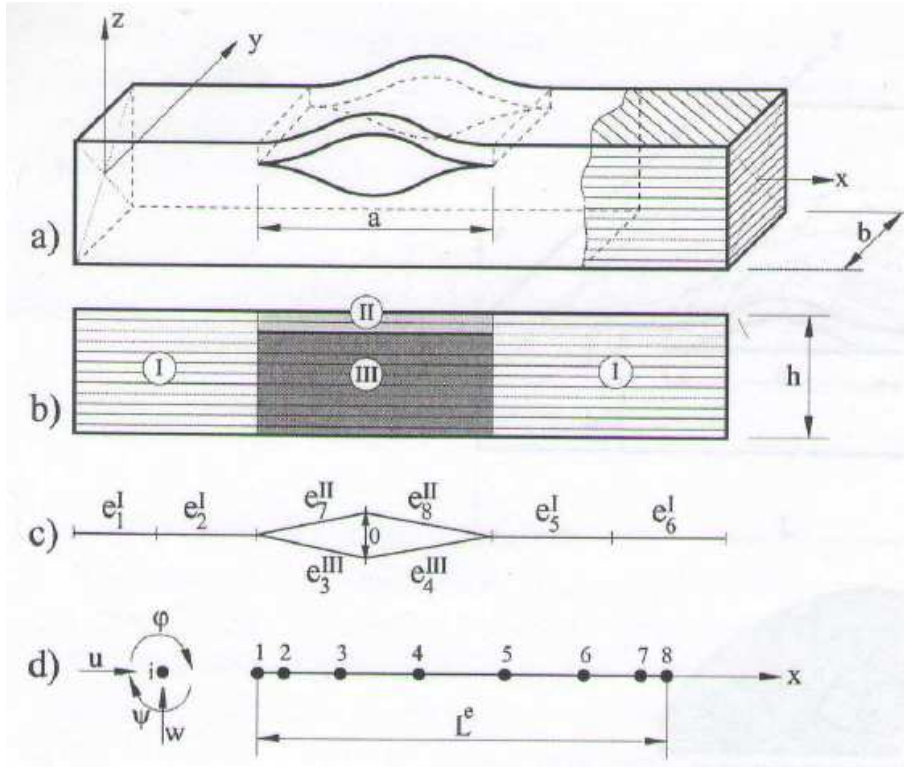
*Figure 41: Scheme of models: a) part of a delaminated composite beam;*
*b) the cross-section of a beam near the delamination tips;*
*c) region of delamination modeled by separated spectral elements;*
*d) a beam spectral finite element. Source: Kudela and Ostachowitz (2009)*

### 2.4.1 ELECTROMECHANICAL (E/M) IMPEDANCE METHOD

The resistance of a structure to an applied force is called the mechanical impedance. The mechanical impedance method is the primary method for detecting disbonds in laminated structures and delaminations in composite materials up to a depth of 6 mm (Giurgiutiu, 2008).

$$Z(\omega) = \frac{F(\omega)}{v(\omega)}$$

(2.40)

where:

$Z(\omega)$ is the mechanical impedance as it varies with frequency, $\omega$

$F(\omega)$ is the applied harmonic force

46

$v(\omega)$ is the induced velocity

The mechanical impedance analysis (MIA) is used in the nondestructive testing community to test bonded structures like composites materials and can determine changes in the local stiffness.

The electromechanical (E/M) impedance is very similar to the MIA technique, but it comes with several key advantages for structural health monitoring (SHM) use (Giurgiutiu, 2008). While, the E/M impedance method uses piezoelectric wafer active sensors (PWAS) to create an in-plane strain excitation the MIA method uses a transducer to create a normal force excitation. Also, while the MIA method uses the force and velocity measurements to calculate the structural impedance, the PWAS is coupled to the structure and the electrical impedance measured at the electrodes is a direct reflection of the structural impedance. Finally, the thin, non-intrusive nature of the PWAS and its simple measurement method makes the E/M impedance method a viable SHM method.

Giurgiutiu (2008) showed that by combining the axial displacements and flexural displacements at each point of the beam for different frequencies, we can calculate the E/M impedance (Figure 42). We can identify the resonant frequencies by looking at the peaks on the admittance plot. The peaks shift when defects appear in the structure so we can immediately identify them.
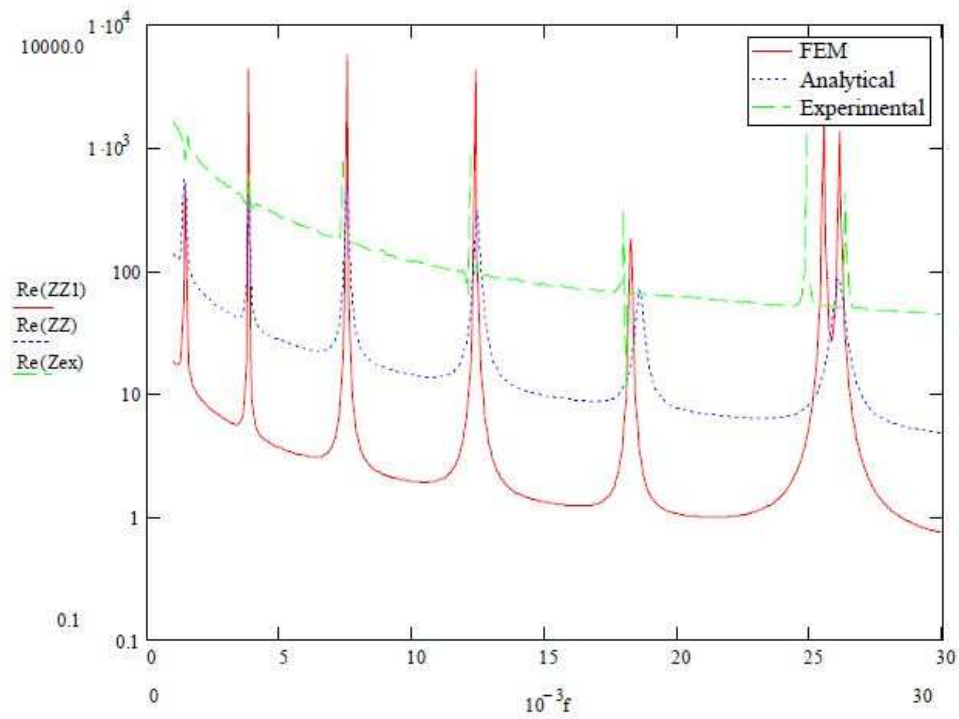
*Figure 42: Comparison of real part of impedance on simple beam elements;*
*Source: Giurgiutiu et al. (2008)*

# 3. LITERATURE REVIEW OF PIEZOELECTRIC WAFER ACTIVE SENSORS (PWAS) FOR STRUCTURAL HEALTH MONITORING (SHM)

## 3.1 INTRODUCTION TO STRUCTURAL HEALTH MONITORING (SHM)

As noted in Giurgiutiu (2008), structural health monitoring (SHM) is an area of increasing interest and praiseworthy for novel and groundbreaking approaches. In the United States, a considerable amount of money is spent each year (more than $200 billion) on the maintenance of plant equipment and facilities and aging infrastructure since approximately a third of all bridges in the US national inventory, are either in need of repairs, or replacement ("structurally deficient" or "functionally obsolete") , deeming them an on–going concern. Structural health monitoring systems is a solution as when it is installed on the aging infrastructure could ensure increased safety and reliability but also save significant costs. Moreover, for existing structures, SHM can replace scheduled maintenance with as–needed maintenance, can forecast the remaining life of the structure and preclude occasional and unexpected maintenance. For new structures, SHM included from the early design stage can reduce the life–cycle cost.

SHM is an emerging research area with applications in many other fields such as for example, aerospace and civil infrastructure systems. SHM can ensure they will remain possible in service for an extended period, beyond their design life but also makes possible condition–based maintenance inspection for them instead of schedule–driven inspections. Therefore, SHM is a revolutionizing new way to monitor a structure

for the length of its life and, when applied correctly and timely, can lead to considerable savings in weight, size, and cost.

### 3.2 PIEZOELECTRIC WAFER ACTIVE SENSORS (PWAS) THEORY

Recently developed piezoelectric wafer active sensors (PWAS) can improve significantly structural health monitoring, damage detection, and nondestructive evaluation. Piezoelectric wafer active sensors (PWAS) are inexpensive transducers that operate on the piezoelectric principle (Giurgiutiu, 2008). Their main role is to convert electric energy to mechanical energy or mechanical energy back to electrical energy. Initially, PWAS were used for vibrations control[2] and later researchers (Tzou and Tseng (1990); Lester and Lefebvre (1993)) modeled the piezoelectric sensor/actuator design for dynamic control or damage detection (Banks et al. (1996)). In SHM, the use of PWAS has followed three main approaches: (a) modal analysis and transfer function; (b) electromechanical (E/M) impedance (Chaudhry et al.(1994), Ayres et al. (1996), Park et al. (2001), Giurgiutiu et al. (1997–2002)); (c) wave propagation (Dupont et al. (2000), Osmont et al. (2000), Diamanti, Hodgkinson, and Soutis (2002)). PWAS have been used under various names for bonded ultrasonic testing for structural health monitoring. PWAS are a type of ultrasonic transducers that are bonded to the structure and operate on the piezoelectric principle coupling electrical and mechanical variables.

$$\varepsilon_{ij} = S^E_{ijkl}\sigma_{kl} + d_{kij}E_k \tag{3.1}$$

$$D_j = d_{jkl}\sigma_{kl} + \varepsilon^\sigma_{jk}E_k \tag{3.2}$$

---

[2] E.g., Crawley et al. (1987, 1990) and Fuller et al. (1990)

Equations (3.1) and (3.2) show how the mechanical strain, $\varepsilon_{ij}$, and stress, $\sigma_{kl}$, and electrical field, $E_k$, and displacement, $D_j$, relate, where $S_{ijkl}^E$ is the mechanical compliance of the material at zero electrical field $(E = 0)$, $\sigma_{kl}$ is the stress, $\varepsilon_{jk}^\sigma$ is the dielectric constant at zero stress $(\sigma = 0)$, and $d_{jkl}$ is the induced strain coefficient (mechanical strain per unit electric field). In order to create in-plane strain from a transverse electric field or vice versa, the $d_{31}$ property is utilized by the PWAS.

Figure 43 shows the schematic of a PWAS with coupling and in-plane shear stress.
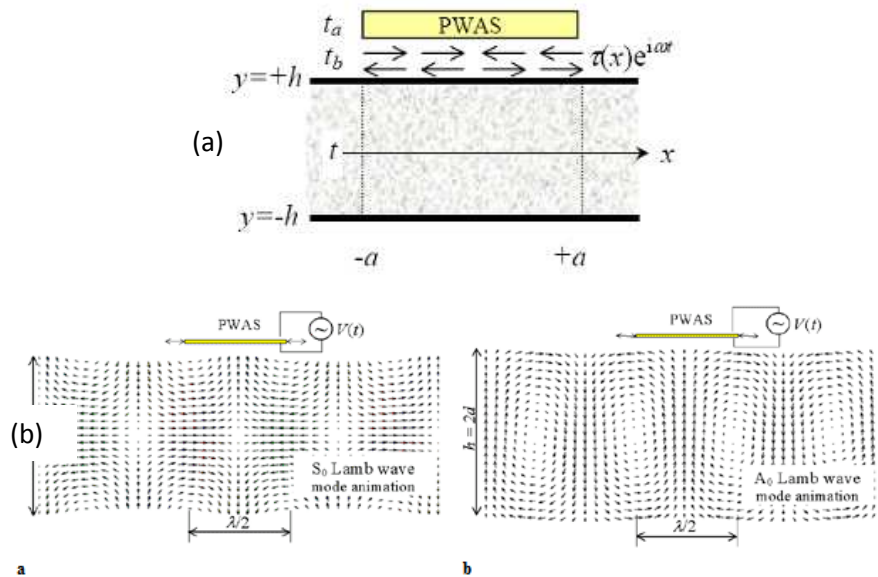


***Figure 43: (a) Schematic of the PWAS shows the coupling of the in-plane shear stress;***
***(b) PWAS interaction with SO and AO Lamb modes.***
***Source: Giurgiutiu (2008) and Giurgiutiu (2003)***
***http://www.tms.org/pubs/journals/JOM/0301/Giurgiutiu/Giurgiutiu-0301.html***

PWAS performance exceeds that of conventional resistance strain gages because PWAS are active devices that can monitor the structure at will, whereas strain gages are

passive devices that can only listen to the structure. Besides, PWAS can address high–frequency applications at hundreds of kHz and beyond.

PWAS present some important functionalities. First, in their functions as high–bandwidth strain sensors and exciters, PWAS convert directly mechanical energy to electrical energy, in their function as high–bandwidth strain exciters and act very well as an embedded generator of waves and vibration, being called "active sensors". Second, in their function as resonators, PWAS can perform resonant mechanical vibration under direct electrical excitation. Third, as embedded modal sensors, PWAS can directly measure the high–frequency modal spectrum of a support structure achieved with the E/M impedance method.

There are four ways that the PWAS can be used for structural health monitoring with propagating guided waves, (a) pitch-catch and (b) pulse-echo, (c) Thickness mode and (d)impact/AE detection as shown in Figure 44.
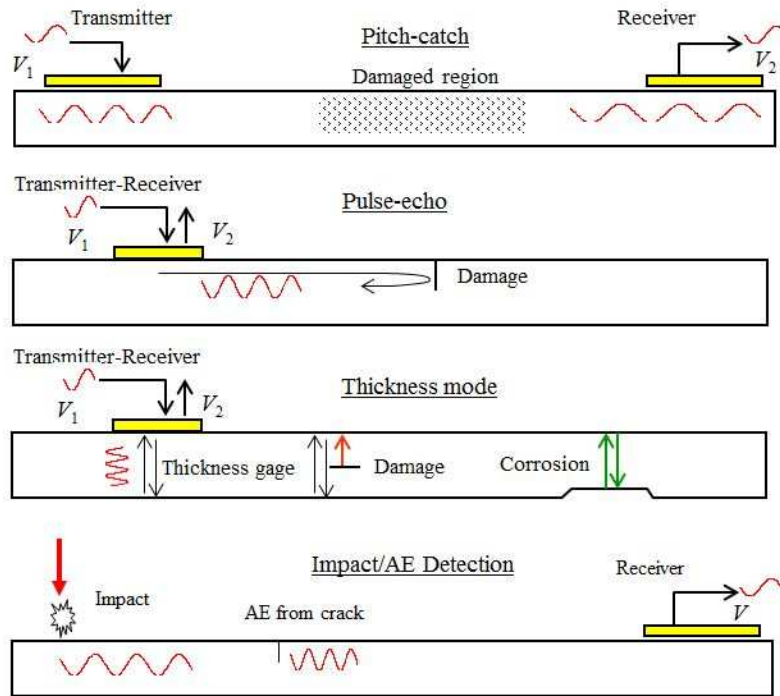
*Figure 44: PWAS Modes of Operation*
*Source: Giurgiutiu et al., US patents: 7,174,255/2007; 7,024,315/2006; 6,996,480/2006*

We now elaborate more on the two most used modes of operation: the pitch-catch method and the pulse-eco.

The pitch-catch method can be used to detect structural changes that take place between a transmitter transducer and a receiver transducer. Typically, one PWAS first acts as a transmitter while the other PWAS acts as receivers. Then another PWAS acts as a transmitter while all the others act as receivers. This "pitch-catch" pattern is continued until waves have been transmitted and received from every PWAS on the structure. These collected signals constitute the first scan and form the benchmark to which all future scans are compared. This method detects damage from the changes in the lamb waves travelling through a damaged region. More precisely, damage that has developed in the structure between the PWAS pairs can be detected by comparing a current scan (after the damage was incurred) with the original benchmark can. Lamb wave change as

53

it travels through a damaged area. It can become more dispersed or even change speed. The pitch-catch method can detect delaminations, cracks, disbonds in joints or impact damage.

The pulse-echo method uses only one transducer. Thus, a PWAS bonded to a structure can both transmit and receive waves. More precisely, the PWAS is first to used transmit the wave into the structure and then if the wave hits a deflect zone, a part of the wave will be reflected back by the damaged zone and will be captured by the PWAS. The collected signals can be compared to the baseline signal and damage can be found. In order for the pulse-echo method to be successful, the transmitted wave needs to reflect off of the damage. Different types of damage reflect the Lamb wave differently.

Damage through the thickness will reflect the largest percentage of the transmitted wave. The pulse-echo method is successful at detecting cracks but not very successful to detect delaminations.

### 3.2.1 CONSTRAINED PWAS

When attached to a structure, a PWAS is constrained by the structure and its dynamic behavior is altered. Let us consider that a structure constraining a PWAS is represented by an unspecified dynamic structural stiffness, $k_{str}$. Because the dynamic structural stiffness is frequency dependent, the interaction mode with the PWAS will also be frequency dependent and can change the PWAS resonances. As shown in Giurgiutiu (2008), the structural dynamics can overpower the inherent PWAS dynamics, in which case, the PWAS E/M impedance will follow the dynamics of the structure and the PWAS becomes a sensor of the dynamical modal behavior of the structure.

### 3.2.1.1 ONE-DIMENSIONAL ANALYSIS OF A CONSTRAINED PWAS

As in Giurgiutiu (2008), let us consider a PWAS of length $l_a$, thickness $t_a$, and width $b_a$, undergoing longitudinal expansion, $u_1$, induced by the thickness polarization electric field, $E_3$.

The electric field is formed by the application of a harmonic voltage $V(t) = \hat{V}e^{i\omega t}$ between the top and bottom surface electrodes. The resulting electric field, $E = V / t$, is assumed uniform w.r.t. $x_1$ ($\partial E / \partial x_1 = 0$). We assume the length, width, and thickness have widely separated values ($t_a << b_a << l_a$) such that the length, width, and thickness motions are basically uncoupled.

The constitutive equations of the piezoelectric material are

$$S_1 = s_{11}^E T_1 + d_{31}E_3$$
$$D_3 = d_{31}T_1 + \varepsilon_{33}^T E_3$$

(3.3)

where

$S_1$ is the strain

$T_1$ is the stress

$D_3$ is the electrical displacement (charge per unit area)

$SE$ is the mechanical compliance at zero field

$\varepsilon$ is the dielectric constant at zero stress

$d_{31}$ is the induced strain coefficient, i.e., mechanical strain per unit electric field.

When the PWAS is bonded to the structure, the structure will constrain the PWAS motion with a structural stiffness, $k_{str}$. Here we focus on the study of an elastically constrained PWAS as shown in Figure 45.
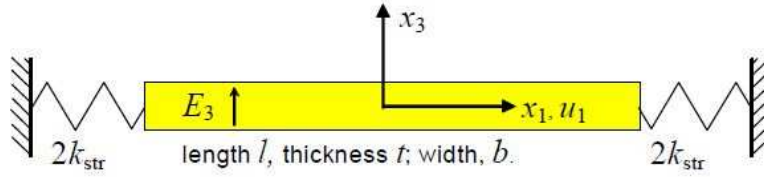
The overall structural stiffness applied to the PWAS has been divided into two equal components applied to the PWAS ends. The values of these components are $2k_{str}$ each, so that

$$k_{total} = \left[ \left( 2k_{str} \right)^{-1} + \left( 2k_{str} \right)^{-1} \right]^{-1} = k_{str} \tag{3.4}$$

The boundary conditions applied at the PWAS ends balance the stress resultant, $T_1 b_a t_a$, with the spring reaction force, $2k_{str} u_1$:

$$T_1 \left( \frac{1}{2} l_a \right) b_a t_a = -2k_{str} u_1 \left( \frac{1}{2} l_a \right)$$

$$T_1 \left( -\frac{1}{2} l_a \right) b_a t_a = 2k_{str} u_1 \left( -\frac{1}{2} l_a \right) \tag{3.5}$$

The strain–displacement relation is

$$S_1 = u_1' \tag{3.6}$$

By replacing equations (3.3) and (3.6) in (3.5) we obtain

$$u_1' \left( +\frac{1}{2} l_a \right) b_a t_a + k_{str} \frac{r}{\frac{1}{2} l_a} u_1 \left( \frac{1}{2} l_a \right) = d_{31} E_3$$

$$u_1' \left( -\frac{1}{2} l_a \right) b_a t_a - k_{str} \frac{r}{\frac{1}{2} l_a} u_1 \left( \frac{1}{2} l_a \right) = d_{31} E_3 \tag{3.7}$$

56

The quasi–static PWAS stiffness is

$$k_{PWAS} = \frac{A_a}{s_{11}^E l_a}$$

(3.8)

and the stiffness ratio is

$$r = \frac{k_{str}}{k_{PWAS}}$$

(3.9)

Equation (3.7) can be rewritten as

$$u_1'\left(\frac{1}{2}l_a\right)b_a t_a = -2k_{str}\frac{s_1^E}{bt}u_1\left(\frac{1}{2}l_a\right) + d_{31}E_3$$

$$u_1'\left(-\frac{1}{2}l_a\right)b_a t_a = 2k_{str}\frac{s_1^E}{bt}u_1\left(-\frac{1}{2}l_a\right) + d_{31}E_3$$

(3.10)

### 3.2.1.2 MECHANICAL RESONANCE

We replace Newton's law of motion, $T_1' = \rho \cdot \ddot{u}$, and the strain–displacement

relation, $S1 = u_1'$, into equation (3.3) and obtain the axial waves equation:

$$\ddot{u}_1 = c_a^2 u_1''$$

(3.11)

Where

$\ddot{u} = \partial u / \partial t$

$u' = \partial u / \partial x$, and

$c_a^2 = 1/\rho s_{11}^E$ is the piezoelectric material wave speed

The general solution of (3.11) is

$$u_1(x,t) = \hat{u}_1(x)e^{i\omega t}$$

(3.12)

where

$$\hat{u}_1(x) = \left(C_1 \sin \lambda x + C_2 \sin \lambda x\right)$$

(3.13)

And $\gamma = \omega / c_a$ is the wavenumber.

The constants $C1$ and $C2$ can be obtained from the boundary conditions. By replacing the general solution equation (3.13) into the boundary conditions (3.10), we obtain the following linear system in $C1$ and $C2$:

$$\frac{1}{2}l\gamma\left(C_1\cos\frac{1}{2}\lambda l - C_2\sin\frac{1}{2}\lambda l\right) + r\left(C_1\sin\frac{1}{2}\lambda l + C_2\cos\frac{1}{2}\lambda l\right) = \frac{1}{2}l\cdot d_{31}\hat{E}_3$$

$$\frac{1}{2}l\gamma\left(C_1\cos\frac{1}{2}\lambda l + C_2\sin\frac{1}{2}\lambda l\right) - r\left(-C_1\sin\frac{1}{2}\lambda l + C_2\cos\frac{1}{2}\lambda l\right) = \frac{1}{2}l\cdot d_{31}\hat{E}_3$$

$$\text{(3.14)}$$

By rearranging, we obtain

$$\frac{1}{2}l\gamma\left(\cos\frac{1}{2}\lambda l + r\sin\frac{1}{2}\lambda l\right)C_1 + \left(-\frac{1}{2}\gamma l\sin\frac{1}{2}\lambda l + r\cos\frac{1}{2}\lambda l\right)C_2 = \frac{1}{2}l\cdot d_{31}\hat{E}_3$$

$$\frac{1}{2}l\gamma\left(\cos\frac{1}{2}\lambda l + r\sin\frac{1}{2}\lambda l\right)C_1 + \left(+\frac{1}{2}\gamma l\sin\frac{1}{2}\lambda l - r\cos\frac{1}{2}\lambda l\right)C_2 = \frac{1}{2}l\cdot d_{31}\hat{E}_3$$

$$\text{(3.15)}$$

By substituting the definitions $u_{ISA} = d_{31}\hat{E}_3 I_a$ and $\phi = \frac{1}{2}\gamma l_a$, we get a linear system in $C_1$ and $C_2$.

$$(\varphi\cos\varphi + r\sin\varphi)C_1 - (\varphi\sin\varphi - r\cos\varphi)C_2 = \frac{1}{2}u_{ISA}$$

$$(\varphi\cos\varphi + r\sin\varphi)C_1 + (\varphi\sin\varphi - r\cos\varphi)C_2 = \frac{1}{2}u_{ISA}$$

$$\text{(3.16)}$$

We assume the system determinant is different from zero and the solution can be obtained by subtracting the first equation from the second:

$$2(\varphi\sin\varphi - r\cos\varphi)C_2 = 0$$

$$\text{(3.17)}$$

$C_2 = 0$. By adding the two equations, we obtain:

$$2(\varphi\cos\varphi + r\sin\varphi)C_1 = 2\frac{1}{2}u_{ISA}$$

$$\text{(3.18)}$$

Thus

$$C_1 = \frac{1}{2}u_{ISA}\frac{1}{(\varphi\cos\varphi + r\sin\varphi)}, \quad C_2 = 0$$

$$\text{(3.19)}$$

We substitute $C_1$ and $C_2$ and $\phi = \frac{1}{2}\gamma l_a$ into equation (3.13) and get

$$\hat{u}_1(x) = \frac{1}{2}u_{ISA}\frac{\sin\gamma x}{\frac{1}{2}\gamma l\cos\frac{1}{2}\gamma l + r\sin\frac{1}{2}\gamma l} \tag{3.20}$$

### 3.2.1.3 ELECTRICAL RESPONSE

Let us consider a constrained PWAS under harmonic electric excitation from Figure 46.
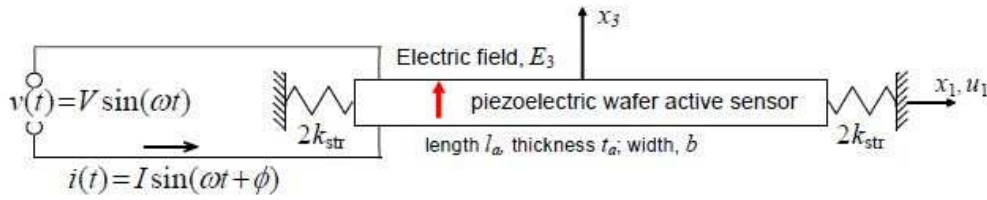


*Figure 46: Schematic for the electrical response analysis of a constrained PWAS under harmonic electric excitation; Source: Giurgiutiu (2008)*

The electrical displacement equation is

$$D_3 = d_{31}T_1 + \varepsilon_{33}^T E_e \tag{3.21}$$

Equation (3.3) yields the stress as function of strain and electric field

$$T_1 = \frac{1}{s_{11}^E}\left(S_1 - d_{31}E_3\right) \tag{3.22}$$

The electric displacement can be expressed as

$$D_3 = \frac{d_{31}}{s_{11}^E}\left(S_1 - d_{31}E_3\right) + \varepsilon_{33}^T E_3 \tag{3.23}$$

By substituting the strain–displacement relation of equation (3.6) we get

$$D_3 = \frac{d_{31}}{s_{11}^E}\cdot u_1' - \frac{d_{31}^2}{s_{11}^E}\cdot E_3 + \varepsilon_{33}^T E_3 \tag{3.24}$$

i.e.

59

$$D_3 = \varepsilon_{33}^T E_3 \left[ 1 - k_{31}^2 \left( 1 - \frac{u_1'}{d_{31} E_3} \right) \right]$$

(3.25)

where

$k_{31}^2 = d_{31}^2 / (s_{11}^E \varepsilon_{33}^T)$ is the electromechanical coupling coefficient. By integrating equation

(3.25) over the electrodes area $A = bl$ we obtain the total charge.

Equation (3.3) can be re-rewritten as

$$D_3 = \frac{d_{31}}{s_{11}^E}\left( u_1' - d_{31} E_3 \right) + \varepsilon_{33}^T E_3 = \varepsilon_{33}^T E_3 \left[ 1 + k_{31}^2 \left( \frac{u_1'}{d_{31} E_3} - 1 \right) \right]$$

(3.26)

By integrating equation (3.26) over the area of the piezoelectric wafer we get the total

charge

$$Q = \int_{-\frac{l_a}{2}}^{+\frac{l_a}{2}} \int_{-\frac{l_a}{2}}^{+\frac{l_a}{2}} D_3 \, dx \, dy = \varepsilon_{33}^T \frac{b_a l_a}{t_a} V \left[ 1 + k_{31}^2 \left( \frac{1}{l_a} \frac{1}{d_{31} E_3} u_1 \Big|_{\frac{1}{2}l}^{\frac{1}{2}l} - 1 \right) \right]$$

(3.27)

We assuming harmonic time dependence as in Giurgiutiu (2008) ($Q = \hat{Q}e^{iwt}$) and get

$$Q = C\hat{E}_3 \left\{ 1 + k_{31}^2 \left( \frac{1}{l_a} \frac{1}{d_{31} E_3} \left[ \hat{u}_1\left( \frac{1}{2}l \right) - \hat{u}_1\left( \frac{1}{2}l \right) \right] - 1 \right) \right\}$$

(3.28)

where $C$ is the conventional stress–free capacitance of the PWAS and is given by

$$C = \varepsilon_{33}^T \frac{b_a l_a}{t_a}$$

(3.29)

Using the definitions $u_{ISA} = d_{31}\hat{E}_3 I_a$ and $\hat{V} = \frac{\hat{E}_3}{t_a}$, we obtain

$$\hat{Q} = C\hat{V} \left[ 1 - k_{31}^2 + k_{31}^2 \left( \frac{\hat{u}_1\left( \frac{1}{2}l \right) - \hat{u}_1\left( -\frac{1}{2}l \right)}{u_{ISA}} \right) \right]$$

(3.30)

We obtain the electric current as the time derivative of the electric charge

$$I = \dot{Q} = i\omega Q \tag{3.31}$$

Thus

$$\hat{I} = i\omega C\hat{V}\left[1 - k_{31}^2 + k_{31}^2\left(\frac{\hat{u}_1\left(\frac{1}{2}l\right) - \hat{u}_1\left(-\frac{1}{2}l\right)}{u_{ISA}}\right)\right] \tag{3.32}$$

and the admittance, $Y$, is the ratio between the current and voltage and is thus

$$Y = \frac{\hat{I}}{\hat{V}} = i\omega C\left[1 - k_{31}^2 + k_{31}^2\left(\frac{\hat{u}_1\left(\frac{1}{2}l\right) - \hat{u}_1\left(-\frac{1}{2}l\right)}{u_{ISA}}\right)\right] \tag{3.33}$$

We define the displacement solution as

$$\hat{u}_1(x) = \frac{1}{2}u_{ISA}\frac{\sin\gamma x}{\varphi\cos\varphi + r\sin\varphi} \tag{3.34}$$

Therefore, the term of equation (3.33) that contains $\hat{u}_1$ becomes

$$\hat{u}_1\left(\frac{1}{2}l\right) - \hat{u}_1\left(-\frac{1}{2}l\right) = \frac{1}{2}\frac{\sin\frac{1}{2}\gamma l - \left(\sin\frac{1}{2}\gamma l\right)}{\varphi\cos\phi + r\sin\phi} = \frac{1}{2}2\frac{\sin\phi}{\varphi\cos\phi + r\sin\phi} = \frac{1}{r + \phi\cot\phi} \tag{3.35}$$

where $\phi = \frac{1}{2}\gamma l_a$.

When substituting, we obtain

$$Y = \frac{\hat{I}}{\hat{V}} = i\omega C\left(1 - k_{31}^2 + k_{31}^2\frac{1}{r + \phi\cot\phi}\right) \tag{3.36}$$

or

$$Y = \frac{\hat{I}}{\hat{V}} = i\omega C\left[1 - k_{31}^2\left(1 - \frac{1}{r + \phi\cot\phi}\right)\right] \tag{3.37}$$

The admittance is purely imaginary, and consists of a capacitive admittance,

$i\omega C$, modified by the effect of piezoelectric coupling between mechanical and electrical

variables, while the impedance, $Z$, is the ratio between the voltage and current and can be written as

$$Z = \frac{\hat{V}}{\hat{I}} = \frac{1}{i\omega C}\left[1 - k_{31}^2\left(1 - \frac{1}{r + \phi\cot\phi}\right)\right]^{-1}$$
(3.38)

We arrived at the admittance and impedance expressions for a PWAS constrained by the structural substrate with an equivalent stiffness ratio $r$. If we consider equations (3.36) and (3.37), the structural stiffness ratio, $r$, is additive to the PWAS resonance term, $\varphi\cos\varphi$. Moreover, these two equations suggest that both structural resonances and PWAS resonances will be in the admittance and impedance frequency spectra. When the PWAS is used in a frequency sweep, the structural stiffness, $k_{str}$, will change with frequency, being in the range from zero for structural resonances to extreme values for structural anti–resonances.

### 3.2.1.4 FREE PWAS

In the case of a free piezoelectric wafer, we have $k_{str} = 0$. Here, the admittance and impedance expressions for a free PWAS are recuperated. Indeed, as the $r$ term in the denominator of equations (3.36) and (3.37) cancels, we obtain

$$Y_{free} = i\omega C\left[1 - k_{31}^2\left(1 - \frac{1}{\phi\cos\phi}\right)\right]$$
(3.39)

$$Z_{free} = \frac{1}{i\omega C}\left[1 - k_{31}^2\left(1 - \frac{1}{\phi\cos\phi}\right)\right]^{-1}$$
(3.40)

These are equivalent to the previously determined expressions for the admittance and impedance expressions of a free piezoelectric wafer.

### 3.2.1.5 FULLY CONSTRAINED PWAS

$$Y_{blocked} = i\omega C \left(1 - k_{31}^2\right)$$

$$Z_{blocked} = \frac{1}{i\omega C}\left(1 - k_{31}^2\right)^{-1}$$

(3.41)

### 3.2.1.6 CONSTRAINED PWAS UNDER QUASI-STATIC CONDITIONS

In the case of a fully constrained piezoelectric wafer we have $k_{str} \to \infty$ and $r \to \infty$. Now, the fraction which contains $r$ at the denominator cancels out, and the admittance and impedance are

$$Y = i\omega C \left(1 - k_{31}^2 \frac{r}{1+r}\right)$$

$$Z = \frac{1}{i\omega C}\left(1 - k_{31}^2 \frac{r}{1+r}\right)^{-1}$$

(3.42)

### 3.2.1.7 DAMPING EFFECTS

The damping effects can be related either with the piezoelectric material or with the elastic constrained. The damping effects in the piezoelectric material are covered through the adoption of complex compliance and dielectric constant expressions

$$\overline{s}_{11} = s_{11}\left(1 - i\eta\right), \quad \overline{\varepsilon}_{33} = \varepsilon_{33}\left(1 - i\delta\right)$$

(3.43)

The values of $\eta$ and $\delta$ vary with the piezoceramic formulation but are usually small (< 5%).

The damping in the elastic constraint is similarly accounted for by assuming a complex stiffness expression, $\overline{k}_{str}$. The stiffness ratio will also take complex values, that is $\overline{r} = \dfrac{\overline{k}_{str}}{\overline{k}_{PWAS}}$. This frequency–dependent complex stiffness ratio reflects both the elastic

constraint damping and the sensor dissipation mechanisms. Therefore, the admittance

and impedance expressions of equation (3.38) take the complex notation form

$$\overline{Y} = i\omega\overline{C}\left(1 - \overline{k}_{31}^2\left(1 - \frac{1}{\overline{\varphi}\cos\overline{\varphi} + \overline{r}}\right)\right)$$

$$\overline{Z} = \frac{1}{i\omega\overline{C}}\left[1 - \overline{k}_{31}^2\left(1 - \frac{1}{\overline{\varphi}\cos\overline{\varphi} + \overline{r}}\right)\right]^{-1}$$

(3.44)

where

$\overline{k}_{13}^2 = d_{31}^2/\left(\overline{s}_{11}\overline{s}_{33}\right)$ is the complex coupling factor and $\overline{C} = (1 - i\delta)C$, and $\overline{\phi} = \phi\sqrt{1 - i\eta}$

$$\overline{k}_{str}(\omega) = \left[k(\omega) - \omega^2 m(\omega)\right] - i\omega c(\omega)$$

(3.45)

### 3.2.1.8 RESONANCE

To determine the resonances, we analyze the behavior of the determinant of the

system of equations (3.16).

$$\Delta = \begin{vmatrix} (\varphi\cos\varphi + r\sin\varphi) & -(\varphi\sin\varphi - r\cos\varphi) \\ (\varphi\cos\varphi + r\sin\varphi) & (\varphi\sin\varphi - r\cos\varphi) \end{vmatrix}$$

(3.46)

$$\Delta = 2(\varphi\cos\varphi + r\sin\varphi)(\varphi\sin\varphi - r\cos\varphi)$$

(3.47)

This determinant Δ is zero when either the first parenthesis or the second

parenthesis is zero. When the first parenthesis in Δ is zero, the denominator of equation

(3.34) disappears and the response of the system to electrical excitation increases. This

is a case that can be identified with an *electromechanical resonance*. When the second

parenthesis in Δ vanishes, the denominator of the equation (3.34) does not disappear,

and the electromechanical response does not increase. This is a case that can be

identified with a *mechanical resonance*, which cannot be excited electrically under the

constant–field distribution considered here. Thus, the next two resonance conditions are identified.

$$\varphi \cos \varphi + r \sin \varphi = 0$$
$$\varphi \sin \varphi + r \cos \varphi = 0 \tag{3.48}$$

The condition that Δ is zero can be re-written as

$$\Delta = \left(\phi \cos \phi + r \sin \phi\right)\left(\phi \sin \phi - r \cos \phi\right) = 0$$
$$\phi^2 \cos \phi \sin \phi + r\phi\left(\sin^2 \phi - \cos^2 \phi\right) - r^2 \sin \phi \cos \phi = 0$$
$$\left(\phi^2 - r^2\right)\sin 2\phi - r\phi \cos 2\phi = 0$$
$$\tan 2\phi = \frac{r\phi}{\phi^2 - r^2} \tag{3.49}$$

The solution of equation (3.49) provides all the mechanical resonances, including the electromechanical ones.

## 4. Literature Review of Laminated Composites Theory

A basic definition for a composite material is a combination of two or more materials on a macroscopic scale that can have properties derived from its constituents or different properties. The components of a composite material can have different forms or material compositions and are fundamentally insoluble in each other.

As per Jones (1999), there are four commonly accepted types of composite materials and namely: fibrous composite materials (fibers in a matrix), laminated composite materials (layers of various materials), particulate composite materials (particles in a matrix), and combinations of some or all of the first three types.

In recent years, composite materials are increasingly being used in many aerospace, automotive, navy, and military applications since they can provide several key technical advantages over metals. For example, they are light but can achieve high strength and stiffness, provide better resistance to environmental degradation, superior fatigue performance and are multi-functional. However composite material can be very costly compared to metals and unpredictable in terms of behavior due to their complex structure.

## *4.1* Isotropy, Orthotropy And Anisotropy

The laminated composites present three important properties that help us study

their behavior in different environments and applications. We summarize their features

as per Jones (1999) in Table 2.

*Table 2: Composite Properties*

| Property | Material properties | Orientation at a point in the body |
|---|---|---|
| Isotropic | Material properties that are the same in every direction at a point in the body. | Material properties are independent of orientation at a point in the body. |
| Orthotropic | Material properties that are different in three mutually perpendicular directions at a point in the body and, further, has three mutually perpendicular planes of material property symmetry. | Properties depend on the orientation at a point in the body. |
| Anisotropic | Material properties that are different in all directions at a point in the body and no planes of material property symmetry exist. | Properties depend on the orientation at a point in the body. |

Figure 47 shows the differences in the deformation of isotropic, orthotropic and

anisotropic materials subjected to uniaxial tension and pure shear stresses.

$$G = \frac{E}{2(1+\nu)}$$
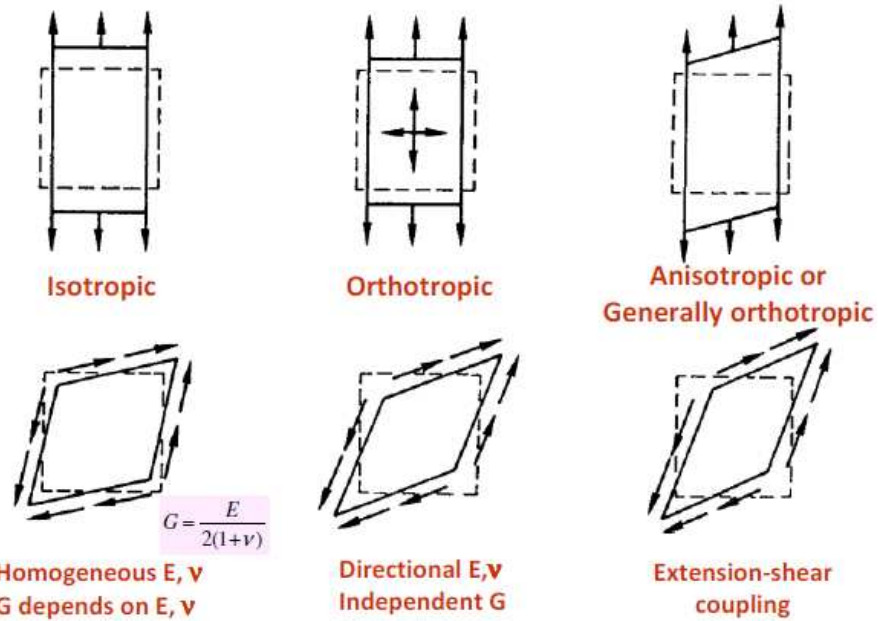
*Figure 47: Differences in the deformation of isotropic, orthotropic, and anisotropic materials subjected to uniaxial tension and pure shear stresses; Source: Jones (1999)*

## 4.2 REVIEW OF MECHANICS OF LAMINATED COMPOSITES

A laminate is constructed by stacking a number of laminas in the thickness direction (in Figure 48 in direction 3 of the coordinate system).
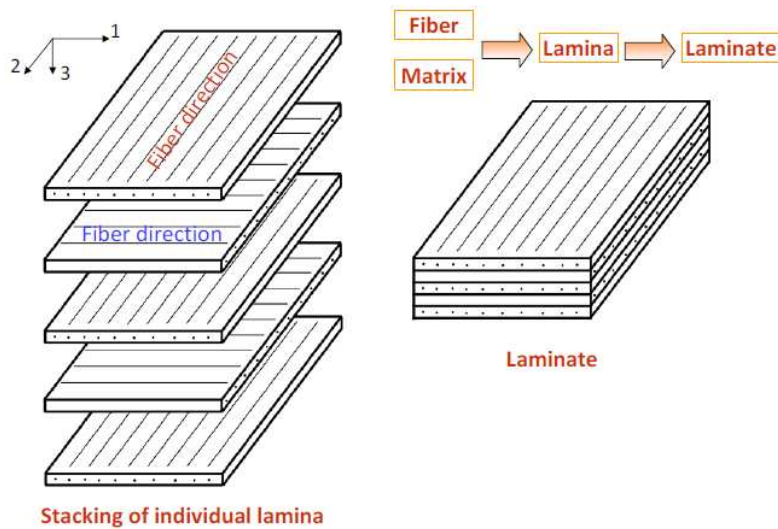


*Figure 48: Cross-ply laminate composite; Source: Majumdar (2009)*

The mechanics of the materials cover stresses, strains and deformations.

Conventional materials such as steel and aluminum have an isotropic endurance, while fiber reinforced composites are orthotropic which makes them more complex than metals.
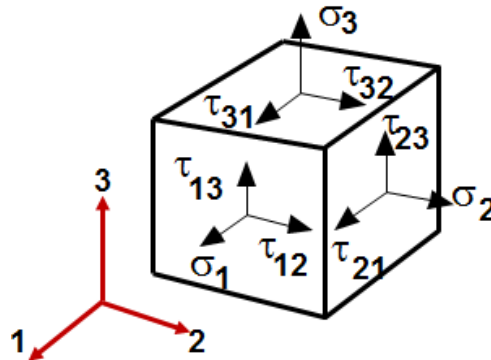


*Figure 49: General 3-D representation of strain and stress relations;*
*Source: Majumdar (2009)*

We will discuss the generalized stress-strain relations in laminate composite structures (Figure 49). Let us consider:

$E_{11}$ the longitudinal modulus in one direction of the coordinate system above

$E_{22}$ is the transversal modulus

$E_{33}$ is the vertical modulus

$v_{12}, v_{21}, v_{13}, v_{31}, v_{23}, v_{32}$ represent the Poisson's ratio $v_{13}, v_{31}, v_{23}, v_{32}$ are calculated using the same approach as for $v_{12}, v_{21}$

$\sigma_1, \sigma_2, \sigma_3$ are applied tensile stress

$\tau_{12}, \tau_{21}, \tau_{13}, \tau_{31}, \tau_{23}, \tau_{32}$ are shear stresses
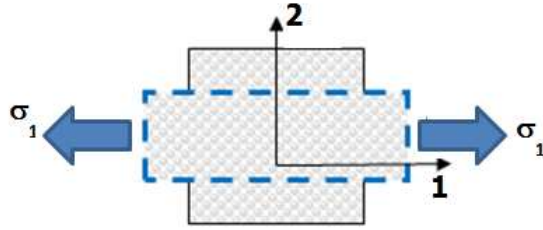
*Figure 50: Longitudinal tensile stress*

The Poisson ration when the tensile stress is longitudinal (Figure 50) is as follows:

$$V_{12} = -\frac{\varepsilon_2}{\varepsilon_1}$$

(4.1)
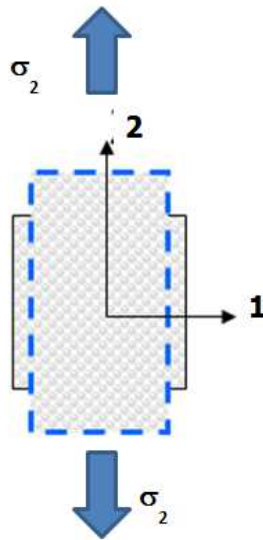


*Figure 51: Transversal tensile stress*

The Poisson ration when the tensile stress is transversal (Figure 51) is as follows:

$$V_{21} = -\frac{\varepsilon_1}{\varepsilon_2}$$

(4.2)

The equation for the engineering shear strain (Figure 52) is:

$$V_{21} = -\frac{\varepsilon_1}{\varepsilon_2}$$

(4.3)

And the equation for the tensor shear strain (Figure 52) is:

$$\varepsilon_{12} = \frac{1}{2}\left(\frac{\partial u_1}{\partial x_2} + \frac{\partial u_2}{\partial x_1}\right) = \varepsilon_{21}$$

(4.4)

70

The tensor shear strain is useful when we deal with transformation of coordinates. The Poisson ratios when the tensile stress is vertical are as follows:

$$v_{13} = -\frac{\varepsilon_3}{\varepsilon_1}; \quad v_{31} = -\frac{\varepsilon_1}{\varepsilon_3}$$

(4.5)

$$v_{23} = -\frac{\varepsilon_3}{\varepsilon_2}; \quad v_{31} = -\frac{\varepsilon_1}{\varepsilon_3}$$

(4.6)
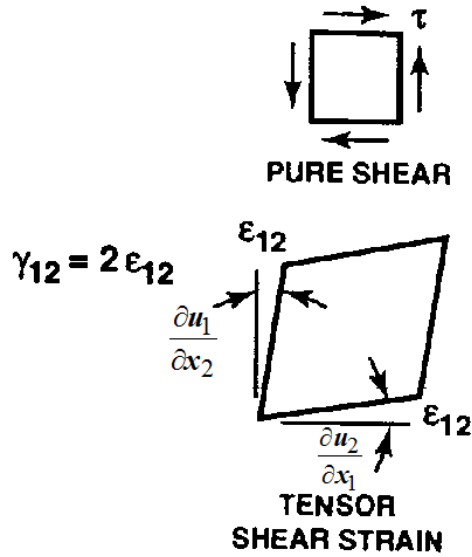


**Figure 52: Pure shear and tensor shear strain; Source: Jones (1999)**

In order to build a compliance matrix for the laminates, we have to go through different steps. First, we write the Generalized Hooke's law when stiffness and compliance matrices are not symmetric as:

$$[\varepsilon] = [S][\sigma]$$

(4.7)

$$[\sigma] = [C][\varepsilon]$$

(4.8)

$$[C] = [S]^{-1}$$

(4.9)

$$\begin{Bmatrix} \varepsilon_1 \\ \varepsilon_2 \\ \varepsilon_3 \\ \gamma_{23} \\ \gamma_{13} \\ \gamma_{12} \end{Bmatrix} = \begin{bmatrix} S_{11} & S_{12} & S_{13} & S_{14} & S_{15} & S_{16} \\ S_{21} & S_{22} & S_{23} & S_{24} & S_{25} & S_{26} \\ S_{31} & S_{32} & S_{33} & S_{34} & S_{35} & S_{36} \\ S_{41} & S_{42} & S_{43} & S_{44} & S_{45} & S_{46} \\ S_{51} & S_{52} & S_{53} & S_{54} & S_{55} & S_{56} \\ S_{61} & S_{62} & S_{63} & S_{64} & S_{65} & S_{66} \end{bmatrix} \begin{Bmatrix} \sigma_1 \\ \sigma_2 \\ \sigma_3 \\ \tau_{23} \\ \tau_{13} \\ \tau_{12} \end{Bmatrix}$$

(4.10)

$$\begin{Bmatrix} \sigma_1 \\ \sigma_2 \\ \sigma_3 \\ \tau_{23} \\ \tau_{13} \\ \tau_{12} \end{Bmatrix} = \begin{bmatrix} C_{11} & C_{12} & C_{13} & C_{14} & C_{15} & C_{16} \\ C_{21} & C_{22} & C_{23} & C_{24} & C_{25} & C_{26} \\ C_{31} & C_{32} & C_{33} & C_{34} & C_{35} & C_{36} \\ C_{41} & C_{42} & C_{43} & C_{44} & C_{45} & C_{46} \\ C_{51} & C_{52} & C_{53} & C_{54} & C_{55} & C_{56} \\ C_{61} & C_{62} & C_{63} & C_{64} & C_{65} & C_{66} \end{bmatrix} \begin{Bmatrix} \varepsilon_1 \\ \varepsilon_2 \\ \varepsilon_3 \\ \gamma_{23} \\ \gamma_{13} \\ \gamma_{12} \end{Bmatrix}$$

(4.11)

Where:

$[S]$ is called Compliance matrix

$[C]$ is called Stiffness matrix

When stiffness and compliance matrices are symmetric, we get:

$$S_{ij} = S_{ji} \quad for \quad i, j = 1, 2, 3 \cdots 6$$

(4.12)

$$C_{ij} = C_{ji} \quad for \quad i, j = 1, 2, 3 \cdots 6$$

(4.13)

$$\begin{Bmatrix} \varepsilon_1 \\ \varepsilon_2 \\ \varepsilon_3 \\ \gamma_{23} \\ \gamma_{13} \\ \gamma_{12} \end{Bmatrix} = \begin{bmatrix} S_{11} & S_{12} & S_{13} & S_{14} & S_{15} & S_{16} \\ S_{12} & S_{22} & S_{23} & S_{24} & S_{25} & S_{26} \\ S_{13} & S_{23} & S_{33} & S_{34} & S_{35} & S_{36} \\ S_{14} & S_{24} & S_{34} & S_{44} & S_{45} & S_{46} \\ S_{15} & S_{25} & S_{35} & S_{45} & S_{55} & S_{56} \\ S_{16} & S_{26} & S_{36} & S_{46} & S_{56} & S_{66} \end{bmatrix} \begin{Bmatrix} \sigma_1 \\ \sigma_2 \\ \sigma_3 \\ \tau_{23} \\ \tau_{13} \\ \tau_{12} \end{Bmatrix}$$

(4.14)

$$
\begin{Bmatrix} \sigma_1 \\ \sigma_2 \\ \sigma_3 \\ \tau_{23} \\ \tau_{13} \\ \tau_{12} \end{Bmatrix} = \begin{bmatrix} C_{11} & C_{12} & C_{13} & C_{14} & C_{15} & C_{16} \\ C_{12} & C_{22} & C_{23} & C_{24} & C_{25} & C_{26} \\ C_{13} & C_{23} & C_{33} & C_{34} & C_{35} & C_{36} \\ C_{14} & C_{24} & C_{34} & C_{44} & C_{45} & C_{46} \\ C_{15} & C_{25} & C_{35} & C_{45} & C_{55} & C_{56} \\ C_{16} & C_{26} & C_{36} & C_{46} & C_{56} & C_{66} \end{bmatrix} \begin{Bmatrix} \varepsilon_1 \\ \varepsilon_2 \\ \varepsilon_3 \\ \gamma_{23} \\ \gamma_{13} \\ \gamma_{12} \end{Bmatrix}
$$
(4.15)

If we split the cube figure in two identical parts, we obtain one plane of symmetry as shown in Figure 53.
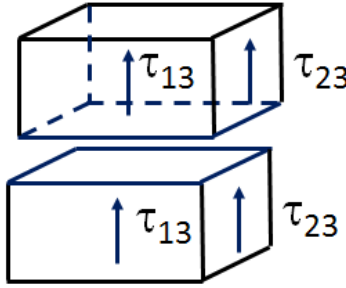


***Figure 53: One plane of symmetry***

In this case, if in one plane of symmetry, the direction 3 is normal to the plane of material symmetry, the stiffness and compliance matrices become:

$$
\begin{Bmatrix} \varepsilon_1 \\ \varepsilon_2 \\ \varepsilon_3 \\ \gamma_{23} \\ \gamma_{13} \\ \gamma_{12} \end{Bmatrix} = \begin{bmatrix} S_{11} & S_{12} & S_{13} & 0 & 0 & S_{16} \\ S_{12} & S_{22} & S_{23} & 0 & 0 & S_{26} \\ S_{13} & S_{23} & S_{33} & 0 & 0 & S_{36} \\ 0 & 0 & 0 & S_{44} & S_{45} & 0 \\ 0 & 0 & 0 & S_{45} & S_{55} & 0 \\ S_{16} & S_{26} & S_{36} & 0 & 0 & S_{66} \end{bmatrix} \begin{Bmatrix} \sigma_1 \\ \sigma_2 \\ \sigma_3 \\ \tau_{23} \\ \tau_{13} \\ \tau_{12} \end{Bmatrix}
$$
(4.16)

$$
\begin{Bmatrix} \sigma_1 \\ \sigma_2 \\ \sigma_3 \\ \tau_{23} \\ \tau_{13} \\ \tau_{12} \end{Bmatrix} = \begin{bmatrix} C_{11} & C_{12} & C_{13} & 0 & 0 & C_{16} \\ C_{12} & C_{22} & C_{23} & 0 & 0 & C_{26} \\ C_{13} & C_{23} & C_{33} & 0 & 0 & C_{36} \\ 0 & 0 & 0 & C_{44} & C_{45} & 0 \\ 0 & 0 & 0 & C_{45} & C_{55} & 0 \\ C_{16} & C_{26} & C_{36} & 0 & 0 & C_{66} \end{bmatrix} \begin{Bmatrix} \varepsilon_1 \\ \varepsilon_2 \\ \varepsilon_3 \\ \gamma_{23} \\ \gamma_{13} \\ \gamma_{12} \end{Bmatrix}
$$
(4.17)

For the case of orthotropic composite laminates, we have three mutually orthogonal planes of symmetry (Figure 54) and coordinates are aligned with principal material direction.
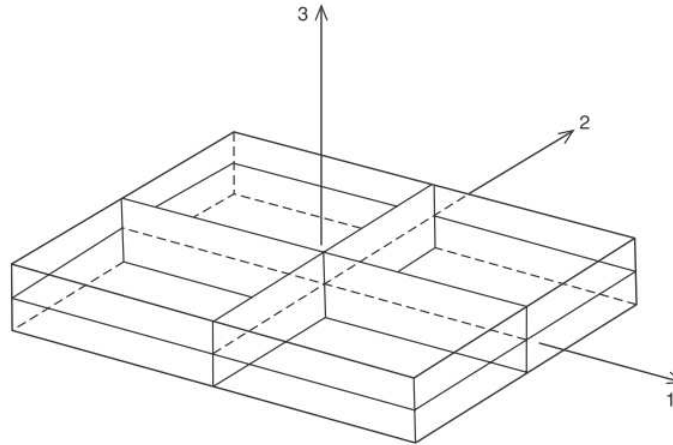


*Figure 54: Three symmetric planes; Source: Jones (1999)*

The stiffness and compliance matrices are:

$$\begin{Bmatrix} \varepsilon_1 \\ \varepsilon_2 \\ \varepsilon_3 \\ \gamma_{23} \\ \gamma_{13} \\ \gamma_{12} \end{Bmatrix} = \begin{bmatrix} S_{11} & S_{12} & S_{13} & 0 & 0 & 0 \\ S_{12} & S_{22} & S_{23} & 0 & 0 & 0 \\ S_{13} & S_{23} & S_{33} & 0 & 0 & 0 \\ 0 & 0 & 0 & S_{44} & 0 & 0 \\ 0 & 0 & 0 & 0 & S_{55} & 0 \\ 0 & 0 & 0 & 0 & 0 & S_{66} \end{bmatrix} \begin{Bmatrix} \sigma_1 \\ \sigma_2 \\ \sigma_3 \\ \tau_{23} \\ \tau_{13} \\ \tau_{12} \end{Bmatrix}$$

(4.18)

$$\begin{Bmatrix} \sigma_1 \\ \sigma_2 \\ \sigma_3 \\ \tau_{23} \\ \tau_{13} \\ \tau_{12} \end{Bmatrix} = \begin{bmatrix} C_{11} & C_{12} & C_{13} & 0 & 0 & 0 \\ C_{12} & C_{22} & C_{23} & 0 & 0 & 0 \\ C_{13} & C_{23} & C_{33} & 0 & 0 & 0 \\ 0 & 0 & 0 & C_{44} & 0 & 0 \\ 0 & 0 & 0 & 0 & C_{55} & 0 \\ 0 & 0 & 0 & 0 & 0 & C_{66} \end{bmatrix} \begin{Bmatrix} \varepsilon_1 \\ \varepsilon_2 \\ \varepsilon_3 \\ \gamma_{23} \\ \gamma_{13} \\ \gamma_{12} \end{Bmatrix}$$

(4.19)

It is important to note that for orthotropic materials, the extension shear is uncoupled and the shear modulus does not depend on the Young modulus.

In our next step we construct the components of the compliance matrix:

$$S_{11} = \frac{1}{E_{11}}; \quad S_{12} = -\frac{v_{21}}{E_{22}}; \quad S_{13} = -\frac{v_{31}}{E_{33}}$$

$$S_{11} = \frac{1}{E_{11}}; \quad S_{12} = -\frac{v_{21}}{E_{22}}; \quad S_{13} = -\frac{v_{31}}{E_{33}}$$

$$S_{21} = -\frac{v_{12}}{E_{11}}; \quad S_{22} = \frac{1}{E_{22}}; \quad S_{23} = -\frac{v_{32}}{E_{33}}$$

$$S_{31} = -\frac{v_{13}}{E_{11}}; \quad S_{32} = -\frac{v_{23}}{E_{22}}; \quad S_{33} = \frac{1}{E_{33}}$$

$$S_{44} = \frac{1}{G_{23}}; \quad S_{55} = \frac{1}{G_{13}}; \quad S_{66} = \frac{1}{G_{12}}$$

(4.20)

And the compliance matrix will take the following form:

$$\begin{Bmatrix} \varepsilon_1 \\ \varepsilon_2 \\ \varepsilon_3 \\ \gamma_{23} \\ \gamma_{13} \\ \gamma_{12} \end{Bmatrix} = \begin{bmatrix} S_{11} & S_{12} & S_{13} & 0 & 0 & 0 \\ S_{21} & S_{22} & S_{23} & 0 & 0 & 0 \\ S_{31} & S_{32} & S_{33} & 0 & 0 & 0 \\ 0 & 0 & 0 & S_{44} & 0 & 0 \\ 0 & 0 & 0 & 0 & S_{55} & 0 \\ 0 & 0 & 0 & 0 & 0 & S_{66} \end{bmatrix} \begin{Bmatrix} \sigma_1 \\ \sigma_2 \\ \sigma_3 \\ \tau_{23} \\ \tau_{13} \\ \tau_{12} \end{Bmatrix}$$

(4.21)

For orthotropic lamina, the strain-stress relation:

$$\begin{Bmatrix} \varepsilon_1 \\ \varepsilon_2 \\ \varepsilon_3 \\ \gamma_{23} \\ \gamma_{13} \\ \gamma_{12} \end{Bmatrix} = \begin{bmatrix} S_{11} & S_{12} & S_{13} & 0 & 0 & 0 \\ S_{12} & S_{22} & S_{23} & 0 & 0 & 0 \\ S_{13} & S_{23} & S_{33} & 0 & 0 & 0 \\ 0 & 0 & 0 & S_{44} & 0 & 0 \\ 0 & 0 & 0 & 0 & S_{55} & 0 \\ 0 & 0 & 0 & 0 & 0 & S_{66} \end{bmatrix} \begin{Bmatrix} \sigma_1 \\ \sigma_2 \\ \sigma_3 \\ \tau_{23} \\ \tau_{13} \\ \tau_{12} \end{Bmatrix}$$

(4.22)

Where:

$$S_{11} = \frac{1}{E_{11}}; \quad S_{12} = \frac{-v_{12}}{E_{11}}; \quad S_{13} = \frac{-v_{13}}{E_{11}}$$

$$S_{22} = \frac{1}{E_{22}}; \quad S_{23} = \frac{-v_{23}}{E_{22}}; \quad S_{33} = \frac{1}{E_{33}}$$

$$S_{44} = \frac{1}{G_{23}}; \quad S_{55} = \frac{1}{G_{13}}; \quad S_{66} = \frac{1}{G_{12}}$$

(4.23)

For the orthotropic lamina the stiffness matrix becomes:

$$
\begin{Bmatrix} \sigma_1 \\ \sigma_2 \\ \sigma_3 \\ \tau_{23} \\ \tau_{13} \\ \tau_{12} \end{Bmatrix} = \begin{bmatrix} C_{11} & C_{12} & C_{13} & 0 & 0 & 0 \\ C_{12} & C_{22} & C_{23} & 0 & 0 & 0 \\ C_{13} & C_{23} & C_{33} & 0 & 0 & 0 \\ 0 & 0 & 0 & C_{44} & 0 & 0 \\ 0 & 0 & 0 & 0 & C_{55} & 0 \\ 0 & 0 & 0 & 0 & 0 & C_{66} \end{bmatrix} \begin{Bmatrix} \varepsilon_1 \\ \varepsilon_2 \\ \varepsilon_3 \\ \gamma_{23} \\ \gamma_{13} \\ \gamma_{12} \end{Bmatrix}
$$

(4.24)

Where:

$$
C_{11} = \frac{S_{22}S_{33} - S_{23}S_{23}}{S} \qquad C_{12} = \frac{S_{13}S_{23} - S_{12}S_{33}}{S}
$$

$$
C_{22} = \frac{S_{33}S_{11} - S_{13}S_{13}}{S} \qquad C_{13} = \frac{S_{12}S_{23} - S_{13}S_{22}}{S}
$$

$$
C_{33} = \frac{S_{11}S_{22} - S_{12}S_{12}}{S} \qquad C_{23} = \frac{S_{12}S_{13} - S_{23}S_{11}}{S}
$$

$$
C_{44} = \frac{1}{S_{44}} \quad C_{55} = \frac{1}{S_{55}} \quad C_{66} = \frac{1}{S_{66}}
$$

(4.25)

$$
[\sigma] = [C][\varepsilon]
$$

(4.26)

$$
[C] = [S]^{-1}
$$

(4.27)

$$
S = S_{11}S_{22}S_{33} - S_{11}S_{23}S_{23} - S_{22}S_{13}S_{13} - S_{33}S_{12}S_{12} + 2S_{12}S_{23}S_{13}
$$

(4.28)

For the isotropic lamina, the properties are similar in every direction:

$$
E_{11} = E_{22} = E_{33} = E
$$

$$
V_{12} = V_{13} = V_{23}
$$

$$
G_{12} = G_{13} = G_{23} = G = \frac{E}{2(1+v)}
$$

(4.29)

$$
S_{11} = \frac{1}{E} \quad S_{12} = \frac{-v}{E} \quad S_{44} = \frac{1}{G} = \frac{2(1+v)}{E}
$$

(4.30)

$$
C_{11} = \frac{E}{(1+v)(1+2v)} \qquad C_{12} = \frac{(1-v)E}{(1+v)(1+2v)}
$$

$$
C_{44} = \frac{1}{G} = \frac{E}{2(1+v)}
$$

(4.31)

For this case, the compliance and stiffness matrix become:

$$[S] = \begin{bmatrix} S_{11} & S_{12} & S_{12} & 0 & 0 & 0 \\ S_{12} & S_{11} & S_{12} & 0 & 0 & 0 \\ S_{12} & S_{12} & S_{11} & 0 & 0 & 0 \\ 0 & 0 & 0 & S_{44} & 0 & 0 \\ 0 & 0 & 0 & 0 & S_{44} & 0 \\ 0 & 0 & 0 & 0 & 0 & S_{44} \end{bmatrix}$$

(4.32)

$$[C] = \begin{bmatrix} C_{11} & C_{12} & C_{12} & 0 & 0 & 0 \\ C_{12} & C_{11} & C_{12} & 0 & 0 & 0 \\ C_{12} & C_{12} & C_{12} & 0 & 0 & 0 \\ 0 & 0 & 0 & C_{44} & 0 & 0 \\ 0 & 0 & 0 & 0 & C_{44} & 0 \\ 0 & 0 & 0 & 0 & 0 & C_{44} \end{bmatrix}$$

(4.33)

Next, we consider the case when between the orthotropic material behavior and the isotropic material behavior there is transversely isotropic behavior where material is isotropic in one plane. If the 2-3 plane is considered as plane of transverse isotropy, then properties in the 2 and 3 directions are similar.

$$E_{22} = E_{33} \quad \nu_{12} = \nu_{13} \quad G_{12} = G_{13}$$

$$G_{23} = \frac{E_{22}}{2(1+\nu_{23})}$$

(4.34)

The components of the stiffness matrix are given by:

$$S_{11} = \frac{1}{E_{11}} \quad S_{12} = \frac{-\nu_{12}}{E_{11}} \quad S_{22} = \frac{1}{E_{22}}$$

$$S_{23} = \frac{-\nu_{23}}{E_{22}} \quad S_{33} = \frac{1}{E_{33}} \quad S_{55} = \frac{1}{G_{12}}$$

(4.35)

$$S_{44} = 2(S_{22} - S_{23}) = 2\left(\frac{1+\nu_{23}}{E_{22}}\right) = \frac{1}{G_{23}}$$

(4.36)

The compliance and stiffness matrices are as follows:

$$[S] = \begin{bmatrix} S_{11} & S_{12} & S_{12} & 0 & 0 & 0 \\ S_{12} & S_{22} & S_{23} & 0 & 0 & 0 \\ S_{12} & S_{23} & S_{22} & 0 & 0 & 0 \\ 0 & 0 & 0 & 2(S_{22}-S_{23}) & 0 & 0 \\ 0 & 0 & 0 & 0 & S_{55} & 0 \\ 0 & 0 & 0 & 0 & 0 & S_{55} \end{bmatrix}$$

(4.37)

$$[C] = \begin{bmatrix} C_{11} & C_{12} & C_{12} & 0 & 0 & 0 \\ C_{12} & C_{22} & C_{23} & 0 & 0 & 0 \\ C_{12} & C_{23} & C_{22} & 0 & 0 & 0 \\ 0 & 0 & 0 & 2(C_{22}-C_{23}) & 0 & 0 \\ 0 & 0 & 0 & 0 & C_{55} & 0 \\ 0 & 0 & 0 & 0 & 0 & C_{55} \end{bmatrix}$$

(4.38)

### 4.3 2D LAMINA PROPERTIES

The 3-D approach for the orthotropic material can be reduced to a 2-D approach by assuming a state of plane stress or plane strain. This is a convenient and reasonably accurate simplification. In this case, the height is much smaller compared to the length and the width which leads to the fact that the stress is much smaller in the height direction. If we make this assumption, the stress in the third direction is zero and as a result the 3-D stress is reduced to 2-D stress.

By assuming that the out-of-plane stresses are small relative to the in-plane stresses, we obtain the following reduced compliance matrix and stiffness matrix:

$$\begin{Bmatrix} \sigma_1 \\ \sigma_2 \\ \tau_{12} \end{Bmatrix} = \begin{bmatrix} Q_{11} & Q_{12} & 0 \\ Q_{12} & Q_{22} & 0 \\ 0 & 0 & Q_{66} \end{bmatrix} \begin{Bmatrix} \varepsilon_1 \\ \varepsilon_2 \\ \gamma_{12} \end{Bmatrix}$$

(4.39)

$$\begin{Bmatrix} \varepsilon_1 \\ \varepsilon_2 \\ \gamma_{12} \end{Bmatrix} = \begin{bmatrix} S_{11} & S_{12} & 0 \\ S_{12} & S_{22} & 0 \\ 0 & 0 & S_{66} \end{bmatrix} \begin{Bmatrix} \sigma_1 \\ \sigma_2 \\ \tau_{12} \end{Bmatrix}$$

(4.40)

Where:

$$Q_{11} = \frac{E_{11}}{1 - \nu_{12}\nu_{21}}, \qquad Q_{12} = \frac{E_2\nu_{12}}{1 - \nu_{12}\nu_{21}} = \frac{E_1\nu_{21}}{1 - \nu_{12}\nu_{21}}$$

$$Q_{22} = \frac{E_{22}}{1 - \nu_{12}\nu_{21}}, \qquad Q_{66} = G_{12}$$

(4.41)

and

$$S_{11} = \frac{1}{E_{11}}, \quad S_{12} = \frac{-\nu_{12}}{E_{11}} = \frac{-\nu_{21}}{E_2}$$

$$S_{22} = \frac{1}{E_{22}}, \quad S_{66} = \frac{1}{G_{12}}$$

(4.42)

In a global coordinate system, general laminates comprise of lamina of multiple orientations with each lamina having its own 3-D material coordinate system as per Figure 55:
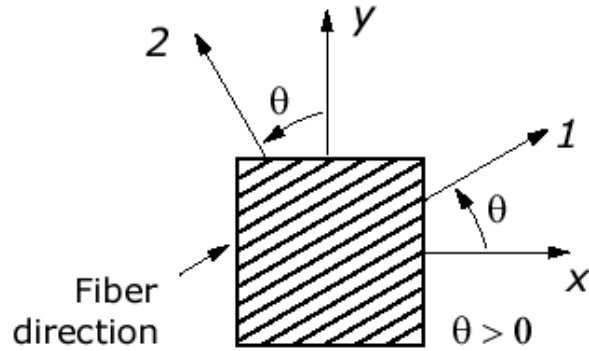


*Figure 55: Fiber orientation; Source: Jones (1999)*

In this case, we are building the transformation matrix (stress) as follows:

$$\begin{Bmatrix} \sigma_1 \\ \sigma_2 \\ \tau_{12} \end{Bmatrix} = \begin{bmatrix} \cos^2\theta & \sin^2\theta & 2\sin\theta\cos\theta \\ \sin^2\theta & \cos^2\theta & -2\sin\theta\cos\theta \\ -\sin\theta\cos\theta & \sin\theta\cos\theta & \cos^2\theta - \sin^2\theta \end{bmatrix} \begin{Bmatrix} \sigma_x \\ \sigma_y \\ \tau_{xy} \end{Bmatrix}$$

$$\begin{Bmatrix} \sigma_1 \\ \sigma_2 \\ \tau_{12} \end{Bmatrix} = \begin{bmatrix} m^2 & n^2 & 2mn \\ n^2 & m^2 & -2mn \\ -mn & mn & m^2 - n^2 \end{bmatrix} \begin{Bmatrix} \sigma_x \\ \sigma_y \\ \tau_{xy} \end{Bmatrix}$$

$$\begin{Bmatrix} \sigma_1 \\ \sigma_2 \\ \tau_{12} \end{Bmatrix} = [T] \begin{Bmatrix} \sigma_x \\ \sigma_y \\ \tau_{xy} \end{Bmatrix}$$

(4.43)

Where $m=\cos\theta$ $n=\sin\theta$ and the plane stress transformation matrix is of the form:

$$[T]=\begin{bmatrix} m^2 & n^2 & 2mn \\ n^2 & m^2 & -2mn \\ -mn & mn & m^2-n^2 \end{bmatrix}$$

(4.44)

Then, the inverse transformation matrix becomes:

$$\begin{Bmatrix} \sigma_x \\ \sigma_x \\ \tau_{xy} \end{Bmatrix} = \begin{bmatrix} \cos^2\theta & \sin^2\theta & -2\sin\theta\cos\theta \\ \sin^2\theta & \cos^2\theta & 2\sin\theta\cos\theta \\ \sin\theta\cos\theta & -\sin\theta\cos\theta & \cos^2\theta-\sin^2\theta \end{bmatrix}\begin{Bmatrix} \sigma_1 \\ \sigma_2 \\ \tau_{12} \end{Bmatrix}$$

$$\begin{Bmatrix} \sigma_x \\ \sigma_y \\ \tau_{xy} \end{Bmatrix} = \begin{bmatrix} m^2 & n^2 & -2mn \\ n^2 & m^2 & 2mn \\ mn & -mn & m^2-n^2 \end{bmatrix}\begin{Bmatrix} \sigma_1 \\ \sigma_2 \\ \tau_{12} \end{Bmatrix}$$

$$\begin{Bmatrix} \sigma_x \\ \sigma_y \\ \tau_{xy} \end{Bmatrix} = [T]^{-1}\begin{Bmatrix} \sigma_1 \\ \sigma_2 \\ \tau_{12} \end{Bmatrix}$$

(4.45)

Where

$$[T]^{-1}=\begin{bmatrix} m^2 & n^2 & -2mn \\ n^2 & m^2 & 2mn \\ mn & -mn & m^2-n^2 \end{bmatrix}$$

(4.46)

We can derive the transformed matrix (strain) as follows:

$$\begin{Bmatrix} \varepsilon_1 \\ \varepsilon_2 \\ \frac{1}{2}\gamma_{12} \end{Bmatrix} = \begin{bmatrix} m^2 & n^2 & 2mn \\ n^2 & m^2 & -2mn \\ -mn & mn & m^2-n^2 \end{bmatrix}\begin{Bmatrix} \varepsilon_x \\ \varepsilon_y \\ \frac{1}{2}\gamma_{xy} \end{Bmatrix}$$

(4.47)

Where

$$[T]=\begin{bmatrix} m^2 & n^2 & 2mn \\ n^2 & m^2 & -2mn \\ -mn & mn & m^2-n^2 \end{bmatrix}$$

(4.48)

We can derive the compliance matrix as follows:

$$\begin{Bmatrix} \varepsilon_1 \\ \varepsilon_2 \\ \frac{1}{2}\gamma_{12} \end{Bmatrix} = [T] \begin{Bmatrix} \varepsilon_x \\ \varepsilon_y \\ \frac{1}{2}\gamma_{xy} \end{Bmatrix}; \quad \begin{Bmatrix} \varepsilon_x \\ \varepsilon_y \\ \frac{1}{2}\gamma_{xy} \end{Bmatrix} = [T]^{-1} \begin{Bmatrix} \varepsilon_1 \\ \varepsilon_2 \\ \frac{1}{2}\gamma_{12} \end{Bmatrix} \quad (4.49)$$

$$\begin{Bmatrix} \varepsilon_1 \\ \varepsilon_2 \\ \gamma_{12} \end{Bmatrix} = \begin{bmatrix} S_{11} & S_{12} & 0 \\ S_{12} & S_{22} & 0 \\ 0 & 0 & S_{66} \end{bmatrix} \begin{Bmatrix} \sigma_{11} \\ \sigma_{22} \\ \sigma_{12} \end{Bmatrix} \quad (4.50)$$

Let's define the Reuter matrix:

$$[R] = \begin{bmatrix} 1 & 0 & 0 \\ 0 & 1 & 0 \\ 0 & 0 & 2 \end{bmatrix} \quad (4.51)$$

Where

$$\begin{Bmatrix} \varepsilon_1 \\ \varepsilon_2 \\ \gamma_{12} \end{Bmatrix} = [R] \begin{Bmatrix} \varepsilon_1 \\ \varepsilon_2 \\ \frac{1}{2}\gamma_{12} \end{Bmatrix}; \quad \begin{Bmatrix} \varepsilon_1 \\ \varepsilon_2 \\ \gamma_{xy} \end{Bmatrix} = [R] \begin{Bmatrix} \varepsilon_1 \\ \varepsilon_2 \\ \frac{1}{2}\gamma_{xy} \end{Bmatrix} \quad (4.52)$$

$$\begin{Bmatrix} \varepsilon_1 \\ \varepsilon_2 \\ \gamma_{12} \end{Bmatrix} = \begin{bmatrix} S_{11} & S_{12} & 0 \\ S_{12} & S_{22} & 0 \\ 0 & 0 & \bar{S}_{66} \end{bmatrix} \begin{Bmatrix} \varepsilon_{11} \\ \varepsilon_{22} \\ \tau_{12} \end{Bmatrix};$$

$$[R] \begin{Bmatrix} \varepsilon_1 \\ \varepsilon_2 \\ \dfrac{1}{2}\gamma_{12} \end{Bmatrix} = [R][T] \begin{Bmatrix} \varepsilon_x \\ \varepsilon_y \\ \dfrac{1}{2}\gamma_{xy} \end{Bmatrix} = [S][T] \begin{Bmatrix} \varepsilon_x \\ \varepsilon_y \\ \tau_{xy} \end{Bmatrix}$$

$$\begin{Bmatrix} \varepsilon_x \\ \varepsilon_y \\ \dfrac{1}{2}\gamma_{xy} \end{Bmatrix} = [T]^{-1}[R]^{-1}[S][T] \begin{Bmatrix} \varepsilon_x \\ \varepsilon_y \\ \tau_{xy} \end{Bmatrix};$$

$$[R]^{-1} \begin{Bmatrix} \varepsilon_x \\ \varepsilon_y \\ \gamma_{xy} \end{Bmatrix} = [T]^{-1}[R]^{-1}[S][T] \begin{Bmatrix} \varepsilon_x \\ \varepsilon_y \\ \tau_{xy} \end{Bmatrix} \tag{4.53}$$

Where

$$\begin{Bmatrix} \varepsilon_x \\ \varepsilon_y \\ \gamma_{xy} \end{Bmatrix} = [R][T]^{-1}[R]^{-1}[S][T] \begin{Bmatrix} \sigma_x \\ \sigma_y \\ \tau_{xy} \end{Bmatrix} = [T]^{T}[S][T] \begin{Bmatrix} \sigma_x \\ \sigma_y \\ \tau_{xy} \end{Bmatrix} = [\bar{S}] \begin{Bmatrix} \sigma_x \\ \sigma_y \\ \tau_{xy} \end{Bmatrix} \tag{4.54}$$

Note: $[T]^{T} = [R][T]^{-1}[R]^{-1}[S][T]$ and $[\bar{S}] = [T]^{T}[S][T]$

The transformed reduced compliance matrix is:

$$\begin{Bmatrix} \varepsilon_x \\ \varepsilon_y \\ \gamma_{xy} \end{Bmatrix} = \begin{bmatrix} \bar{S}_{11} & \bar{S}_{12} & \bar{S}_{16} \\ \bar{S}_{12} & \bar{S}_{22} & \bar{S}_{26} \\ \bar{S}_{16} & \bar{S}_{26} & \bar{S}_{66} \end{bmatrix} \begin{Bmatrix} \sigma_x \\ \sigma_y \\ \tau_{xy} \end{Bmatrix} \tag{4.55}$$

Where:

$$\{\bar{S}\} = [T]^{T}[S][T] \tag{4.56}$$

And

$$\left[ \bar{S} \right] = \bar{S}_{ij} \tag{4.57}$$

$$\bar{S}_{11} = S_{11}m^4 + \left(2S_{12} + S_{66}\right)n^2m^2 + S_{22}n^4$$

$$\bar{S}_{12} = \left(S_{11} + S_{22} - S_{66}\right)n^2m^2 + S_{12}\left(n^4 + m^4\right)$$

$$\bar{S}_{16} = \left(2S_{11} - 2S_{12} - S_{66}\right)nm^3 - \left(2S_{22} - 2S_{12} - S_{66}\right)n^3m$$

$$\bar{S}_{22} = S_{11}n^4 + \left(2S_{12} + S_{66}\right)n^2m^2 + S_{22}m^4$$

$$\bar{S}_{26} = \left(2S_{11} - 2S_{12} - S_{66}\right)n^3m - \left(2S_{22} - 2S_{12} - S_{66}\right)nm^3$$

$$\bar{S}_{66} = 2\left(2S_{11} + 2S_{22} - 4S_{12} - S_{66}\right)n^2m^2 + S_{66}\left(n^4 + m^4\right) \tag{4.58}$$

And the transformed reduced stiffness matrix is:

$$\begin{Bmatrix} \sigma_x \\ \sigma_y \\ \tau_{xy} \end{Bmatrix} = \begin{bmatrix} \bar{Q}_{11} & \bar{Q}_{12} & \bar{Q}_{16} \\ \bar{Q}_{12} & \bar{Q}_{22} & \bar{Q}_{26} \\ \bar{Q}_{16} & \bar{Q}_{26} & \bar{Q}_{66} \end{bmatrix} \begin{Bmatrix} \varepsilon_x \\ \varepsilon_y \\ \gamma_{xy} \end{Bmatrix} \tag{4.59}$$

Where

$$\left\{ \bar{Q} \right\} = [T]^{-1}[Q][T]^{-T} \tag{4.60}$$

$$\bar{Q}_{11} = Q_{11}m^4 + 2\left(Q_{12} + 2Q_{66}\right)n^2m^2 + Q_{22}n^4$$

$$\bar{Q}_{12} = \left(Q_{11} + Q_{22} - 4Q_{66}\right)n^2m^2 + Q_{12}\left(n^4 + m^4\right)$$

$$\bar{Q}_{16} = \left(Q_{11} - Q_{12} - 2Q_{66}\right)nm^3 + \left(Q_{12} - Q_{22} + 2Q_{66}\right)n^3m$$

$$\bar{Q}_{22} = Q_{11}n^4 + 2\left(Q_{12} + 2Q_{66}\right)n^2m^2 + Q_{22}m^4$$

$$\bar{Q}_{26} = \left(Q_{11} - Q_{12} - 2Q_{66}\right)n^3m - \left(Q_{12} - Q_{22} + 2Q_{66}\right)nm^3$$

$$\bar{Q}_{66} = \left(Q_{11} + Q_{22} - 2Q_{12} - 2Q_{66}\right)n^2m^2 + Q_{66}\left(n^4 + m^4\right) \tag{4.61}$$

### 4.4 LAMINATION THEORY

Following a 2-D plane stress analysis of a lamina and knowing the constitutive relations (stress-strain) we can determine the stress-strain relation at a point P on the reference plane (Figure 56) using Kirchhoff's hypothesis (normal line does not deform and it simply translates and rotates as a consequence of deformation of the reference surface).
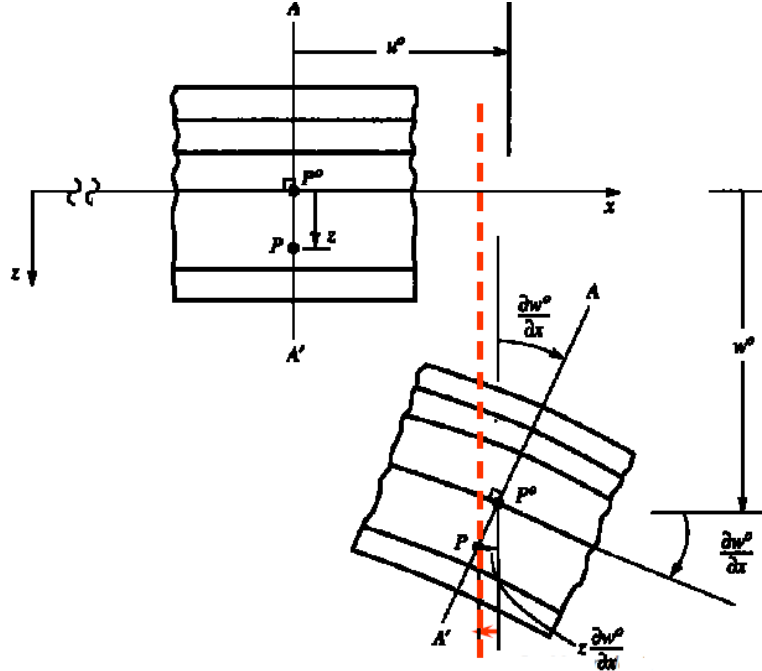
*Figure 56: Resulting Displacement; Source: Majumdar (2009)*

The mid-surface strains for the lamina are given by:

$$\varepsilon_x^0(x, y) = \frac{\partial u^0(x, y)}{\partial x}$$

$$\varepsilon_y^0(x, y) = \frac{\partial v^0(x, y)}{\partial y}$$

$$\gamma_{xy}^0(x, y) = \frac{\partial v^0(x, y)}{\partial x} + \frac{\partial u^0(x, y)}{\partial y}$$

(4.62)

And the mid-surface curvatures for the lamina are given by:

$$K_x^0(x, y) = \frac{\partial^2 w^0(x, y)}{\partial x^2}$$

$$K_y^0(x, y) = \frac{\partial^2 w^0(x, y)}{\partial y^2}$$

$$K_{xy}^0(x, y) = -2 \cdot \frac{\partial^2 w^0(x, y)}{\partial x \cdot \partial y}$$

(4.63)

The four keystones of the classical lamination theory consist of the kinematics,

constitutive, force and moment resultants and equilibrium equations.

Let's first consider the constitutive relations. We use the reduced transformed stiffness matrix (4.59) and the Kirchhoff strain relations(4.62), in order to determine the in plane stresses (4.63) in any ply and at any point within the $x, y$ plane defined by the reference surface.

$$\begin{Bmatrix} \sigma_x \\ \sigma_y \\ \tau_{xy} \end{Bmatrix} = \begin{bmatrix} \overline{Q}_{11} & \overline{Q}_{12} & \overline{Q}_{16} \\ \overline{Q}_{12} & \overline{Q}_{22} & \overline{Q}_{26} \\ \overline{Q}_{16} & \overline{Q}_{26} & \overline{Q}_{66} \end{bmatrix} \begin{Bmatrix} \varepsilon_x \\ \varepsilon_y \\ \gamma_{xy} \end{Bmatrix}$$

(4.64)

$$\varepsilon_x(x, y, z) = \varepsilon_x^0(x, y) + z \cdot \kappa_x^0(x, y)$$
$$\varepsilon_y(x, y, z) = \varepsilon_y^0(x, y) + z \cdot \kappa_y^0(x, y)$$
$$\gamma_{xy}(x, y, z) = \gamma_{xy}^0(x, y) + z \cdot \kappa_{xy}^0(x, y)$$

(4.65)

$$\begin{Bmatrix} \sigma_x \\ \sigma_y \\ \tau_{xy} \end{Bmatrix} = \begin{bmatrix} \overline{Q}_{11} & \overline{Q}_{12} & \overline{Q}_{16} \\ \overline{Q}_{12} & \overline{Q}_{22} & \overline{Q}_{26} \\ \overline{Q}_{16} & \overline{Q}_{26} & \overline{Q}_{66} \end{bmatrix} \begin{Bmatrix} \varepsilon_x^0 + z \cdot \kappa_x^0 \\ \varepsilon_y^0 + z \cdot \kappa_y^0 \\ \gamma_{xy}^0 + z \cdot \kappa_{xy}^0 \end{Bmatrix}$$

(4.66)

Before we proceed further, it is important to note several characteristics of the stress resultants and namely:

- Stress in each layer varies through the thickness.

- We can define stress in terms of equivalent forces at the middle surface.

- At the edge, stresses can be divided into increments and summed.

- The resulting integral is the stress resultant (force per length).

The stress resultant in X direction is represented in Figure 57:
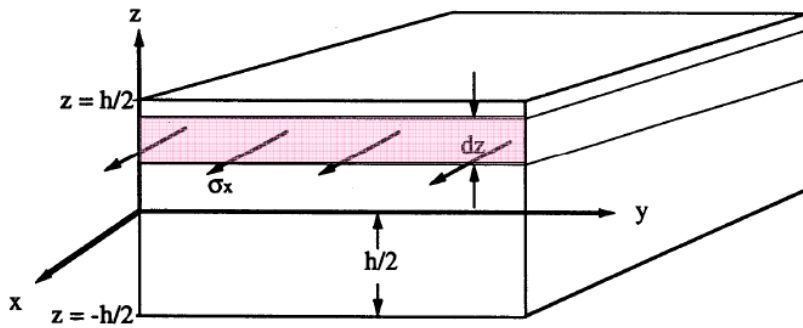
*Figure 57: Stress Resultant in X direction; Source: Majumdar (2009)*

Total force in $x$-direction = $\sum \sigma_x \cdot (dz) \cdot (y)$ and as $dz \to 0, \sum \sigma_x \cdot (dz) \cdot (y) = y \cdot \int\limits_{-h/2}^{h/2} \sigma_x \cdot dz$

As a result

$$N_x \equiv \int\limits_{-h/2}^{h/2} \sigma_x \cdot dz$$

(4.67)

If we consider all stress and moment resultants, they are as depicted in Figure 58:
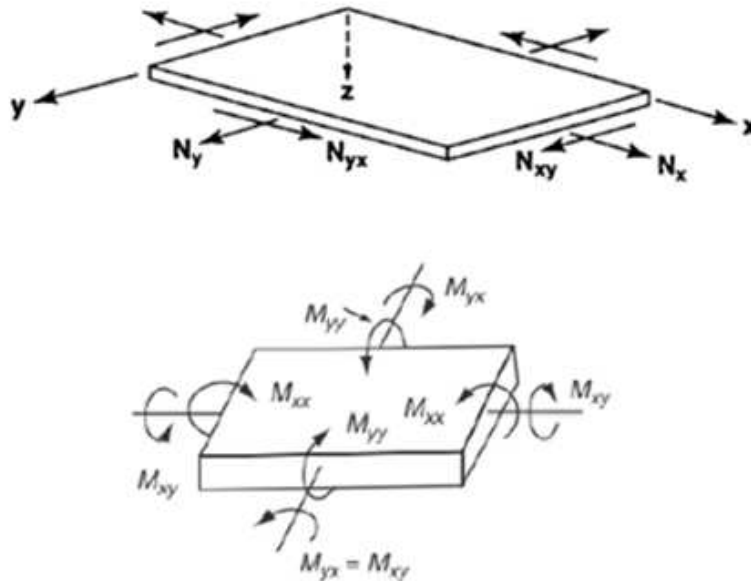


*Figure 58: Stress and Moment Resultants; Source: Jones (1999)*

After derivations, we obtain:

$$N_x = \int_{-h/2}^{h/2} \sigma_x \cdot dz$$

$$N_y = \int_{-h/2}^{h/2} \sigma_y \cdot dz$$

$$N_{xy} = \int_{-h/2}^{h/2} \sigma_{xy} \cdot dz$$

$$M_x = \int_{-h/2}^{h/2} \sigma_x \cdot z \cdot dz$$

$$M_y = \int_{-h/2}^{h/2} \sigma_y \cdot z \cdot dz$$

$$M_{xy} = \int_{-h/2}^{h/2} \tau_{xy} \cdot z \cdot dz$$

(4.68)

$$\begin{bmatrix} N_x \\ N_y \\ N_{xy} \end{bmatrix} = \sum_{k=0}^{n} \int_{h_{k-1}}^{h_k} \begin{bmatrix} \sigma_x \\ \sigma_y \\ \tau_{xy} \end{bmatrix}_k \cdot dz$$

$$\begin{bmatrix} M_x \\ M_y \\ M_{xy} \end{bmatrix} = \sum_{k=0}^{n} \int_{h_{k-1}}^{h_k} \begin{bmatrix} \sigma_x \\ \sigma_y \\ \tau_{xy} \end{bmatrix}_k \cdot z \cdot dz$$

(4.69)
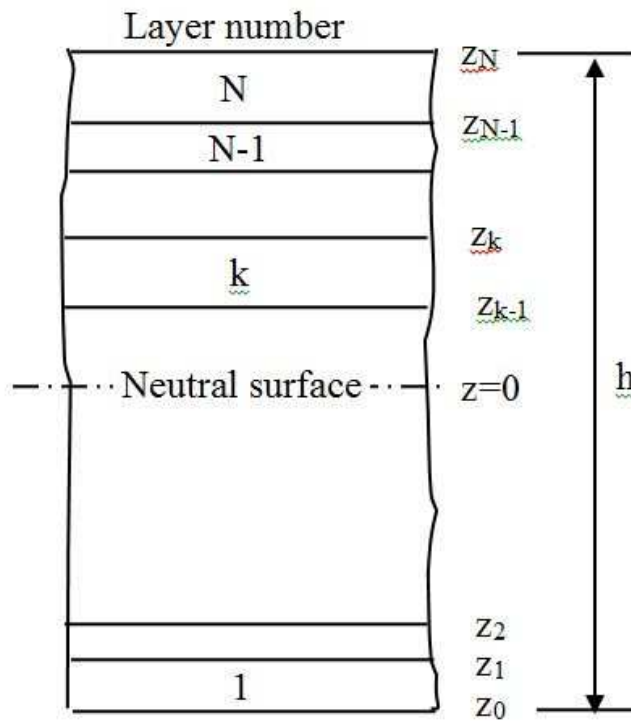
*Figure 59: Laminate cross-section with geometric mid-plane; Source: Giurgiutiu (2012)*

Figure 59 represents the cross-section of the laminate composite expressing the height of the layers from the mid-plane. When we relate stress to strain for the laminate composite we obtain:

$$
\begin{bmatrix} N_x \\ N_y \\ N_{xy} \end{bmatrix} =
$$

$$
\sum_{k=0}^{n} \left\{ \int_{h_{k-1}}^{h_k} \begin{bmatrix} \overline{Q}_{11} & \overline{Q}_{12} & \overline{Q}_{16} \\ \overline{Q}_{12} & \overline{Q}_{22} & \overline{Q}_{26} \\ \overline{Q}_{16} & \overline{Q}_{26} & \overline{Q}_{66} \end{bmatrix} \begin{bmatrix} \varepsilon_x^0 \\ \varepsilon_y^0 \\ \gamma_{xy}^0 \end{bmatrix} \cdot dz + \int_{h_{k-1}}^{h_k} \begin{bmatrix} \overline{Q}_{11} & \overline{Q}_{12} & \overline{Q}_{16} \\ \overline{Q}_{12} & \overline{Q}_{22} & \overline{Q}_{26} \\ \overline{Q}_{16} & \overline{Q}_{26} & \overline{Q}_{66} \end{bmatrix} \begin{bmatrix} K_x^0 \\ K_y^0 \\ K_{xy}^0 \end{bmatrix} \cdot z \cdot dz \right\}
$$

$$
\begin{bmatrix} M_x \\ M_y \\ M_{xy} \end{bmatrix} =
$$

$$
\sum_{k=0}^{n} \left\{ \int_{h_{k-1}}^{h_k} \begin{bmatrix} \overline{Q}_{11} & \overline{Q}_{12} & \overline{Q}_{16} \\ \overline{Q}_{12} & \overline{Q}_{22} & \overline{Q}_{26} \\ \overline{Q}_{16} & \overline{Q}_{26} & \overline{Q}_{66} \end{bmatrix} \begin{bmatrix} \varepsilon_x^0 \\ \varepsilon_y^0 \\ \gamma_{xy}^0 \end{bmatrix} \cdot z \cdot dz + \int_{h_{k-1}}^{h_k} \begin{bmatrix} \overline{Q}_{11} & \overline{Q}_{12} & \overline{Q}_{16} \\ \overline{Q}_{12} & \overline{Q}_{22} & \overline{Q}_{26} \\ \overline{Q}_{16} & \overline{Q}_{26} & \overline{Q}_{66} \end{bmatrix} \begin{bmatrix} K_x^0 \\ K_y^0 \\ K_{xy}^0 \end{bmatrix} \cdot z^2 \cdot dz \right\}
$$

(4.70)

Since the Stiffness $[\overline{Q}]$ is constant across the layer and since the mid-plane strains and

curvatures $\begin{bmatrix} \varepsilon_x^0 & \varepsilon_y^0 & \varepsilon_{xy}^0 \end{bmatrix}$, $\begin{bmatrix} k_x^0 & k_y^0 & k_{xy}^0 \end{bmatrix}$ are independent of $z$, Eq.(4.70) can be rearranged as

$$
\begin{bmatrix} N_x \\ N_y \\ N_{xy} \end{bmatrix} = \sum [Q] \begin{bmatrix} \varepsilon_x^0 \\ \varepsilon_y^0 \\ \varepsilon_{xy}^0 \end{bmatrix} \int_{h_{k-1}}^{h_k} dz
$$

$$
\begin{bmatrix} M_x \\ M_y \\ M_{xy} \end{bmatrix} = \sum [Q] \begin{bmatrix} k_x^0 \\ k_y^0 \\ k_{xy}^0 \end{bmatrix} \int_{h_{k-1}}^{h_k} z \, dz + \sum [Q] \begin{bmatrix} k_x^0 \\ k_y^0 \\ k_{xy}^0 \end{bmatrix} \int_{h_{k-1}}^{h_k} z^2 \, dz
$$

(4.71)

Note that

$$
\int_{h_{k-1}}^{h_k} dz = h_k - h_{k-1}
$$

$$
\int_{h_{k-1}}^{h_k} z \, dz = \frac{1}{2} z^2 \Big|_{h_{k-1}}^{h_k} = \frac{1}{2}\left( h_k^2 - h_{k-1}^2 \right)
$$

$$
\int_{h_{k-1}}^{h_k} z^2 \, dz = \frac{1}{3} z^3 \Big|_{h_{k-1}}^{h_k} = \frac{1}{3}\left( h_k^3 - h_{k-1}^3 \right)
$$

(4.72)

Substitution of Eq. (4.72)into (4.71) yields

$$
\begin{bmatrix} N_x \\ N_y \\ N_{xy} \end{bmatrix} =
$$

$$
\sum_{k=0}^{n} \left\{ \int_{h_{k-1}}^{h_k} \begin{bmatrix} \overline{Q}_{11} & \overline{Q}_{12} & \overline{Q}_{16} \\ \overline{Q}_{12} & \overline{Q}_{22} & \overline{Q}_{26} \\ \overline{Q}_{16} & \overline{Q}_{26} & \overline{Q}_{66} \end{bmatrix} \begin{bmatrix} \varepsilon_x^0 \\ \varepsilon_y^0 \\ \gamma_{xy}^0 \end{bmatrix} \cdot dz + \int_{h_{k-1}}^{h_k} \begin{bmatrix} \overline{Q}_{11} & \overline{Q}_{12} & \overline{Q}_{16} \\ \overline{Q}_{12} & \overline{Q}_{22} & \overline{Q}_{26} \\ \overline{Q}_{16} & \overline{Q}_{26} & \overline{Q}_{66} \end{bmatrix} \begin{bmatrix} K_x^0 \\ K_y^0 \\ K_{xy}^0 \end{bmatrix} \cdot z \cdot dz \right\}
$$

$$
\begin{bmatrix} M_x \\ M_y \\ M_{xy} \end{bmatrix} =
$$

$$
\sum_{k=0}^{n} \left\{ \int_{h_{k-1}}^{h_k} \begin{bmatrix} \overline{Q}_{11} & \overline{Q}_{12} & \overline{Q}_{16} \\ \overline{Q}_{12} & \overline{Q}_{22} & \overline{Q}_{26} \\ \overline{Q}_{16} & \overline{Q}_{26} & \overline{Q}_{66} \end{bmatrix} \begin{bmatrix} \varepsilon_x^0 \\ \varepsilon_y^0 \\ \gamma_{xy}^0 \end{bmatrix} \cdot z \cdot dz + \int_{h_{k-1}}^{h_k} \begin{bmatrix} \overline{Q}_{11} & \overline{Q}_{12} & \overline{Q}_{16} \\ \overline{Q}_{12} & \overline{Q}_{22} & \overline{Q}_{26} \\ \overline{Q}_{16} & \overline{Q}_{26} & \overline{Q}_{66} \end{bmatrix} \begin{bmatrix} K_x^0 \\ K_y^0 \\ K_{xy}^0 \end{bmatrix} \cdot z^2 \cdot dz \right\}
$$

(4.73)

Next, we define the laminate stiffness terms $ABD$ as follows:

$[A]$ is the extensional stiffness matric for the laminate

$[B]$ is the coupling stiffness matrix for the laminate

$[D]$ is the bending stiffness matrix for the laminate

$$
A_{ij} = \sum_{k=1}^{n} \int_{h_{k-1}}^{h_k} \left[ \overline{Q}_{ij} \right]_k (h_k - h_{k-1})
$$

$$
B_{ij} = \frac{1}{2} \sum_{k=1}^{n} \int_{h_{k-1}}^{h_k} \left[ \overline{Q}_{ij} \right]_k (h_k^2 - h_{k-1}^2)
$$

$$
D_{ij} = \frac{1}{3} \sum_{k=1}^{n} \int_{h_{k-1}}^{h_k} \left[ \overline{Q}_{ij} \right]_k (h_k^3 - h_{k-1}^3)
$$

(4.74)

The constitutive equations in matrix form are:

90

$$\begin{bmatrix} N_{xx} \\ N_{yy} \\ N_{xy} \end{bmatrix} = [A] \begin{bmatrix} \varepsilon^0_{xx} \\ \varepsilon^0_{yy} \\ \gamma^0_{xy} \end{bmatrix} + [B] \begin{bmatrix} \kappa_{xx} \\ \kappa_{yy} \\ \kappa_{xy} \end{bmatrix}$$

$$\begin{bmatrix} M_{xx} \\ M_{yy} \\ M_{xy} \end{bmatrix} = [B] \begin{bmatrix} \varepsilon^0_{xx} \\ \varepsilon^0_{yy} \\ \gamma^0_{xy} \end{bmatrix} + [D] \begin{bmatrix} \kappa_{xx} \\ \kappa_{yy} \\ \kappa_{xy} \end{bmatrix}$$

(4.75)

$$\begin{Bmatrix} N_x \\ N_y \\ N_{xy} \\ M_x \\ M_y \\ M_{xy} \end{Bmatrix} = \begin{bmatrix} A_{11} & A_{12} & A_{16} & B_{11} & B_{12} & B_{16} \\ A_{12} & A_{22} & A_{26} & B_{12} & B_{22} & B_{26} \\ A_{16} & A_{26} & A_{66} & B_{16} & B_{26} & B_{66} \\ B_{11} & B_{12} & B_{16} & D_{11} & D_{12} & D_{16} \\ B_{12} & B_{22} & B_{26} & D_{12} & D_{22} & D_{26} \\ B_{16} & B_{26} & B_{66} & D_{16} & D_{26} & D_{66} \end{bmatrix} \cdot \begin{Bmatrix} \varepsilon^o_x \\ \varepsilon^o_y \\ \gamma^o_{xy} \\ \kappa_x \\ \kappa_y \\ \kappa_{xy} \end{Bmatrix}$$

(4.76)

Next, we will cover the physical significance of the matrix in which we can observe the

shear, bending, and bend-twist couplings.

$$\begin{Bmatrix} N_x \\ N_y \\ N_{xy} \end{Bmatrix} = \begin{bmatrix} A_{11} & A_{12} & A_{16} \\ A_{12} & A_{22} & A_{26} \\ A_{16} & A_{26} & A_{66} \end{bmatrix} \begin{Bmatrix} \varepsilon^0_x \\ \varepsilon^0_y \\ \gamma^0_{xy} \end{Bmatrix} + \begin{bmatrix} B_{11} & B_{12} & B_{16} \\ B_{12} & B_{22} & B_{26} \\ B_{16} & B_{26} & B_{66} \end{bmatrix} \begin{Bmatrix} \kappa_x \\ \kappa_y \\ \kappa_{xy} \end{Bmatrix}$$

$$\begin{Bmatrix} M_x \\ M_y \\ M_{xy} \end{Bmatrix} = \begin{bmatrix} B_{11} & B_{12} & B_{16} \\ B_{12} & B_{22} & B_{26} \\ B_{16} & B_{26} & B_{66} \end{bmatrix} \begin{Bmatrix} \varepsilon^0_x \\ \varepsilon^0_y \\ \gamma^0_{xy} \end{Bmatrix} + \begin{bmatrix} D_{11} & D_{12} & D_{16} \\ D_{12} & D_{22} & D_{26} \\ D_{16} & D_{26} & D_{66} \end{bmatrix} \begin{Bmatrix} \kappa_x \\ \kappa_y \\ \kappa_{xy} \end{Bmatrix}$$

(4.77)

Where

$A_{16}$ and $A_{26}$ are the shear-extension coupling

$D_{16}$ and $D_{26}$ represents the bend-twist coupling

$B = \begin{bmatrix} B_{11} & B_{12} & B_{16} \\ B_{12} & B_{22} & B_{26} \\ B_{16} & B_{26} & B_{66} \end{bmatrix}$ represents the bending-extension coupling

Equation (4.77) can be written in compact form as:

$$\mathbf{N} = A\boldsymbol{\varepsilon} + B\boldsymbol{\kappa}$$
$$\mathbf{M} = B\boldsymbol{\varepsilon} + D\boldsymbol{\kappa} \qquad (4.78)$$

Where

$$\mathbf{N} = \begin{bmatrix} N_x \\ N_y \\ N_{xy} \end{bmatrix}, \quad \mathbf{M} = \begin{bmatrix} M_x \\ M_y \\ M_{xy} \end{bmatrix}, \quad \boldsymbol{\varepsilon} = \begin{bmatrix} \varepsilon_x^0 \\ \varepsilon_y^0 \\ \gamma_{xy}^0 \end{bmatrix}, \quad \boldsymbol{\kappa} = \begin{bmatrix} \kappa_x \\ \kappa_y \\ \kappa_{xy} \end{bmatrix} \qquad (4.79)$$

and

$$A = \begin{bmatrix} A_{11} & A_{12} & A_{16} \\ A_{12} & A_{22} & A_{26} \\ A_{16} & A_{26} & A_{66} \end{bmatrix}, \quad \boldsymbol{B} = \begin{bmatrix} B_{11} & B_{12} & B_{16} \\ B_{12} & B_{22} & B_{26} \\ B_{16} & B_{26} & B_{66} \end{bmatrix}, \quad \boldsymbol{D} = \begin{bmatrix} D_{11} & D_{12} & D_{16} \\ D_{12} & D_{22} & D_{26} \\ D_{16} & D_{26} & D_{66} \end{bmatrix} \qquad (4.80)$$

The ABD matrix can take different shapes, depending, on the fiber orientation. For example in the case of symmetric laminates as per Figure 60, for every layer to one side of the laminate reference surface with a specific thickness, material properties, and fiber orientation, there is another layer at an identical distance on the opposite side. In this case, all components of the $B$ matrix are zero and the 6x6 set of equations decouples into two 3x3 sets of equations.
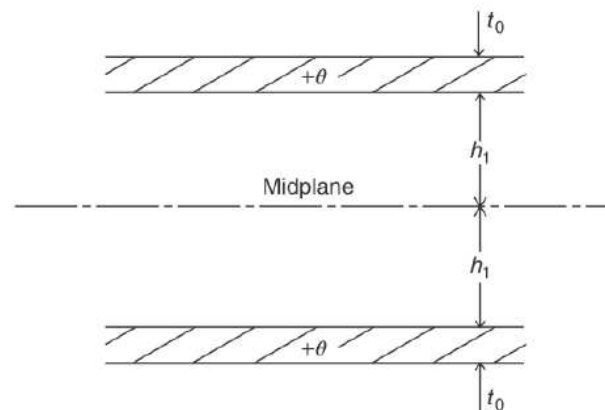


*Figure 60: Symmetric laminates: Source: Jones (1999)*

For the case of balanced laminates as per Figure 61 , for every layer with a specified thickness, material properties, and fiber orientation, there is another layer

with the identical thickness, material properties, but opposite fiber orientation somewhere in the laminate, That means that if the laminate is balanced, $A_{16}$ and $A_{26}$ are always zero and $\overline{Q}_{16}$ and $\overline{Q}_{26}$ from opposite orientation have opposite signs.
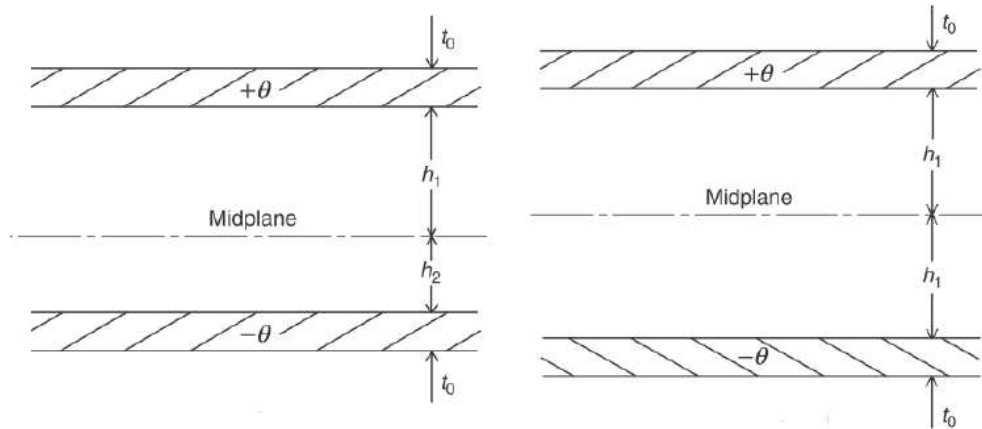


*Figure 61: Balanced laminates; Source: Jones (1999)*

Table 3  shows several examples of common laminate configurations.

*Table 3: Laminate Examples*

| Fiber Orientation (layers and angle) | Laminate Type |
|---|---|
| 0/90/90/0 | Symmetric |
| 0/90/0 | Symmetric |
| 0/90/0/90 | Non-symmetric-tension / bending coupling |
| 0/90/45/90/0 | Symmetric, non-balanced tension/ shear coupling |
| 0/90/45/-45/-45/45/90/0 | Balanced and symmetric |

## *4.5* STRENGTH OF COMPOSITES

The performance of a material is determined by its properties and behavior under tensile, compressive, shear and other static or dynamic loading (Figure 62), so we should take this into consideration when selecting the material in different applications. The material properties are determined by conducting mechanical and physical experiments.
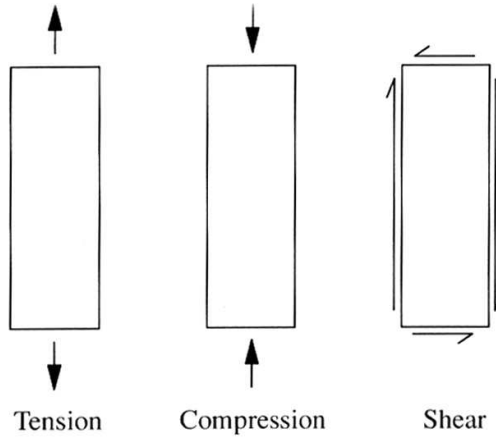
*Figure 62: Tension, Compression, and Shear; Source: Jones (1999)*

Another important aspect for the behavior of the anisotropic materials is the failure criteria. Test configurations can have a significant effect on the results of the tests (Figure 63), especially for thin sections, which are common for composite materials.
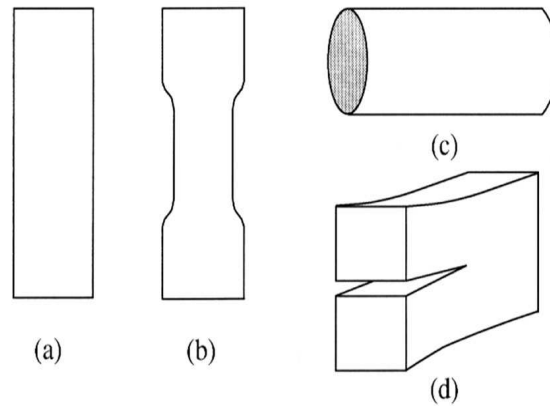


*Figure 63: Tensile test specimen configurations; Source: Jones (1999)*

Test results may be elastic, or elasto-plastic, or visco-elastic under various loading conditions (Figure 64).
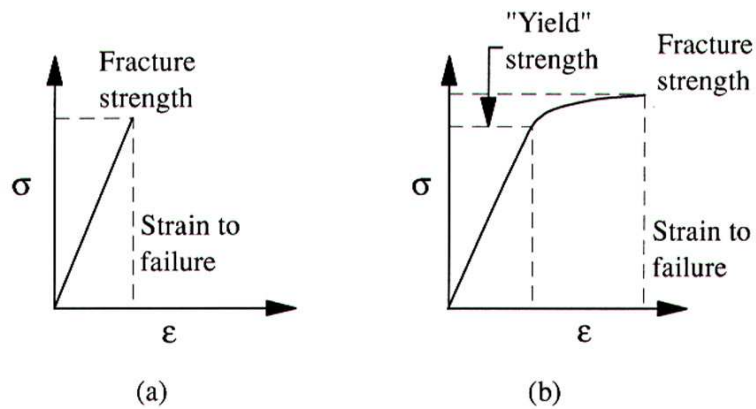
*Figure 64: Strength / Strain; Source: Jones (1999)*

The loading direction (Figure 65) relative to the fiber direction has a significant effect on the strength test.
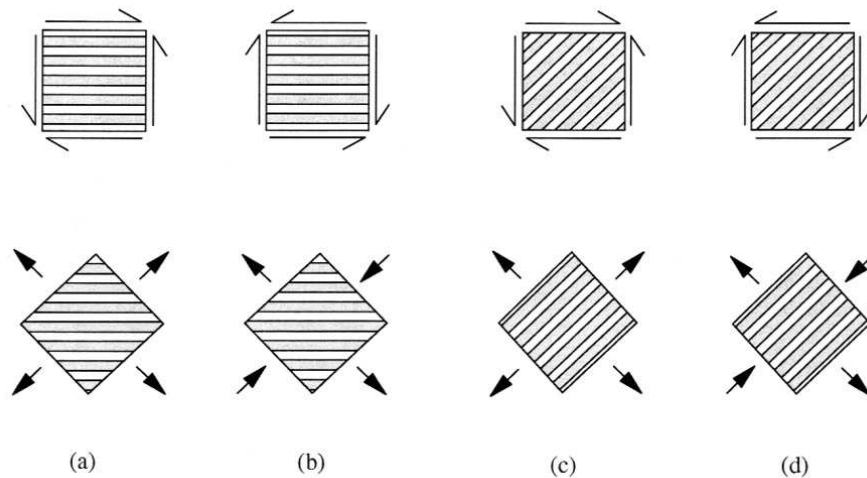


*Figure 65: Load distribution; Source: Jones (1999)*

For an anisotropic material, the failure criteria used are as follows:

- Maximum stress criterion entails that the material will fail when the maximum stress reaches the critical value which is called the strength of the material.

- Maximum shear stress entails that the material will fail when the maximum shear stress reaches the critical value (Tresca and Guest approach)

- Total strain energy entails that the material will fail when the total strain energy reaches the critical value (Beltrami approach) or when the distortional energy reaches a critical value (Huber, Von Mises and Hencky approach).

For the anisotropic, inhomogeneous composite materials, it is required that the failure criteria incorporate a sufficient number of material parameters to correctly represent the failure modes detected in the material under multi-axial applied stress states. In this sense, we can consider the formulation of Tsai and Wu (1971) and Tsai and Hahn (1980):

$$f(\sigma_{ij}) = F_{ij}\sigma_{ij} + F_{ijkl}\sigma_{ij}\sigma_{kl} + F_{ijklmn}\sigma_{ij}\sigma_{kl}\sigma_{mn} + etc \qquad (4.81)$$

The comparison of fiber stress of Tsai and Wu (1971) and Tsai and Hahn (1980) versus measured data is represented in Figure 66:
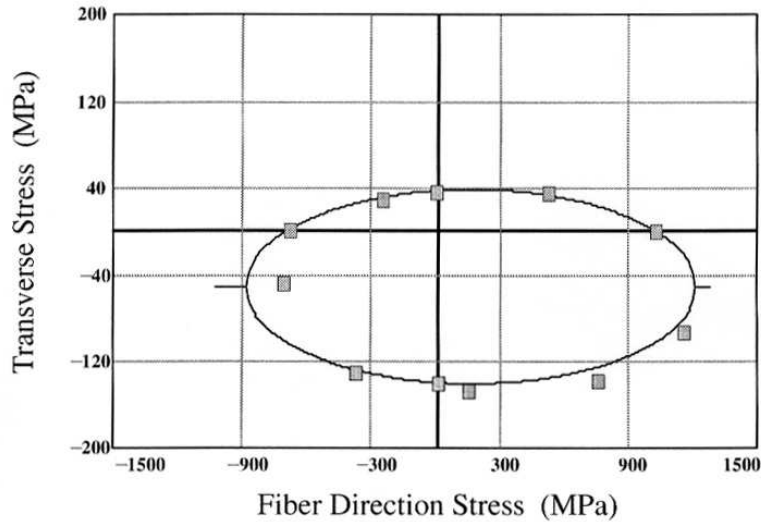


*Figure 66: Fiber Direction Stress; Source: Majumdar (2009)*

If we take a 2-D approach for a fiber-reinforced material, we get:

$$F_1\sigma_1 + F_2\sigma_2 + 2F_{12}\sigma_1\sigma_2 + F_{11}\sigma_1^2 + F_{22}\sigma_2^2 + F_{66}\sigma_6^2 = 1 \qquad (4.82)$$

Using the minimum value for F12 from Tsai and Hahn (1980), the resulting expression becomes:

$$\sigma_1(\frac{1}{X_t}-\frac{1}{Xc})+\sigma_2(\frac{1}{Y_t}-\frac{1}{Y_c})+\sigma_1^2\frac{1}{X_tX_c}+\sigma_2^2\frac{1}{Y_tY_c}-\sigma_1\sigma_2\frac{1}{\sqrt{X_tX_cY_tY_c}}=1$$

(4.83)

This general form of the equation is a comparison of stress in a given direction to strength in that direction. It is important to note that the anisotropic materials can be much stronger in one direction (fiber direction) than in another (the direction perpendicularly to the fiber), so that the stress required to cause failure can be much smaller in the first direction than in the second. That is why, criteria based only on effective stress, distortional energy, principal stress, and principal strain is intrinsically not suitable for the representation of the strength of anisotropic, inhomogeneous materials.

### *4.6* DAMAGE AND LIFE PREDICTION CONCEPTS

The modes of failure in composite laminates are tension, compression and shear. These three modes cause a progression of damage in an area of the structure before the failure occurs and although the progressive damage is not critical, it will eventually lead to failure.

According to Talreja (1981), when a composite laminate has a load applied to it as in Figure 67, the individual layers that make up the composite will have a normal stress in the fiber direction, a normal in-plane stress perpendicular to the fibers and a shear in-plane stress. When there is a tensile in-plane stress perpendicular to the fibers,

97

small cracks will develop in the composite. When dealing with cyclic loading conditions, these micro-cracks play a critical role in the expansion of subsequent damage.
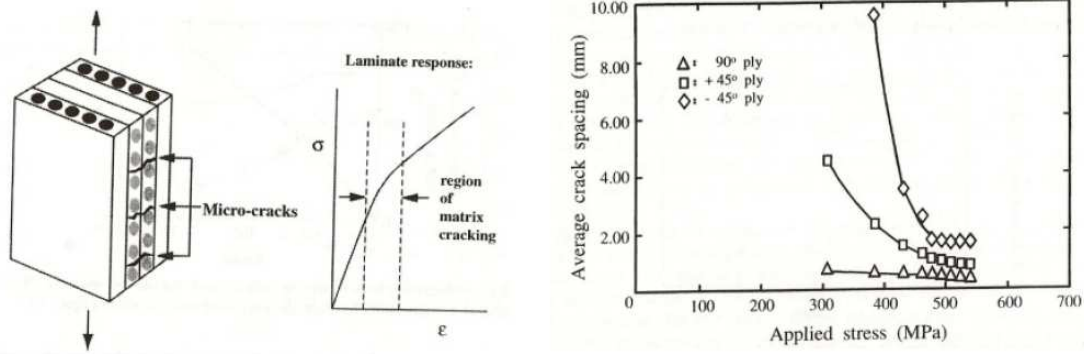


*Figure 67: Crack spacing in 900, 450 and 450 plies as function of global applied stress; Source: Jones (1999)*

The crack progresses until the point the matrix of the composite reaches its saturation or the fatigue limit is reached, point after which no future cracks form as the load is increased.

The saturation matrix crack spacing (before delamination) is the same for cyclic and fatigue loading. In general, fiber fractures develop near the matrix crack tips (Figure 68), while debonds occur near the broken fiber ends.
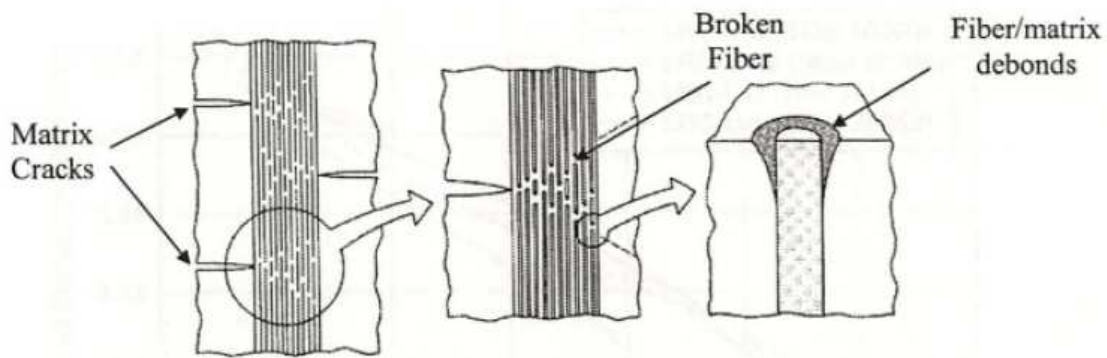


*Figure 68: Different defects; Source: Jones (1999)*

Due to the loads, a region of the laminated composite deforms differently generating a separation between layers (3-D Poisson effect) which is known as

delamination. Figure 69 shows the stages of damage development in the lifetime of a composite material.



**Controlling Damage Modes During Fatigue Life**

1—MATRIX CRACKING
3—DELAMINATION
5—FRACTURE

CDS

2—CRACK COUPLING—INTERFACIAL DEBONDING
4—FIBER BREAKING

DAMAGE

PERCENT OF LIFE          100

Local Failure Function

Damage Initiation

Damage Accumulation and Growth

Damage Interaction
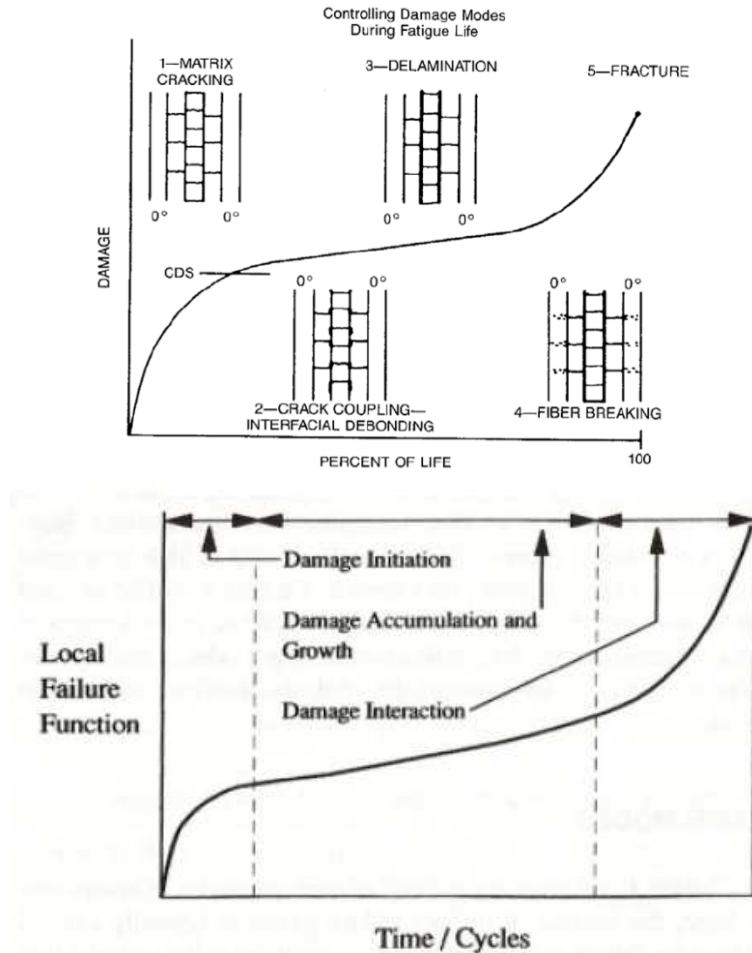
Time / Cycles

*Figure 69: Time cycle; Source: Talreja (1981)*

The delamination is the main damage in the laminated composite material. This damage can be either developed during the manufacturing stage (because of incomplete curing or foreign particles) or produced by impact damage, or result of inter-laminar stresses that generate discontinuities. The delamination grows under different loads, redistributes stresses in layers and can affect residual stiffness, strength and fatigue life. Figure 70 presents examples of partial and total edge delamination in a composite.
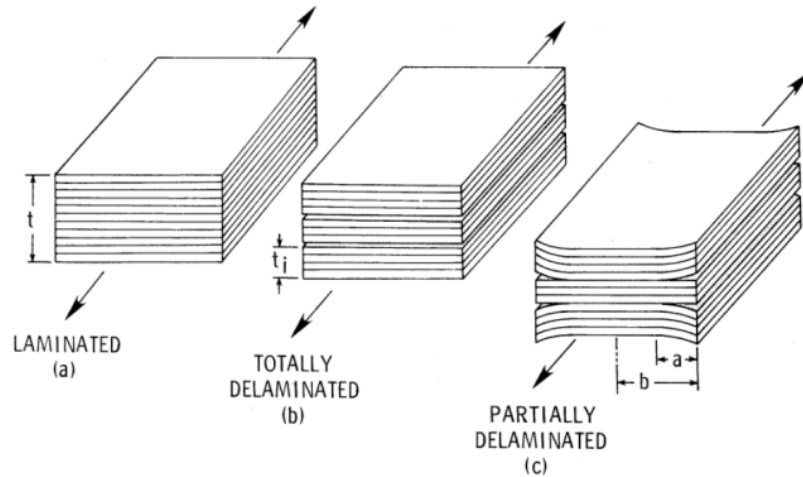
*Figure 70: Different stages of delamination; Source: Talreja (1981)*

The general case of damage progression in a composite laminate is as follows. First, the small micro-cracks develop in the matrix between fibers that are not parallel to the loading direction. Second, the micro-cracks grow and become macroscopic cracks as the cyclic loading carries on, at which point the material has reached the Characteristic Damage State (CDS). Then, the cracks spread through the ply and the stress concentrations cause micro-cracks to advance in the plies on each part. At this point, the stress concentrations between plies cause local delaminations and from this point on the damage in the composite material will grow rapidly and then cause failure. As a result, a composite structure has to be examined periodically to monitor the progression of damage (Figure 71).
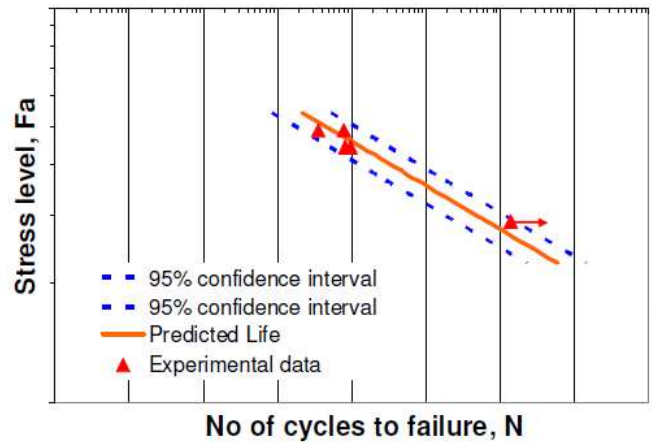
*Figure 71: Life predictions of a composite laminate; Source: Majumdar (2009)*

## 5. LITERATURE REVIEW OF TRANSFER MATRIX METHOD (TMM)

The transfer matrix method (TMM) is an analytical method for structural analysis which is an alternative to modal expansion. The transfer matrix method is a new way to determine the natural frequencies of a nonuniform beam. Pestel and Leckie introduced the TMM concept for beams in 1967.

The TMM principle is to break up the structure into smaller components across which one calculates the transfer of a state vector (displacements and forces). For example, if we have a beam with a PWAS bonded to the structure as per Figure 72(a), by applying TMM we will split the beam in segments with the same configuration (same height, width and same excitation) as per Figure 72(b). For each end of segment we show the relevant axial forces, flexural moments, shear forces and the moment generated by the PWAS.
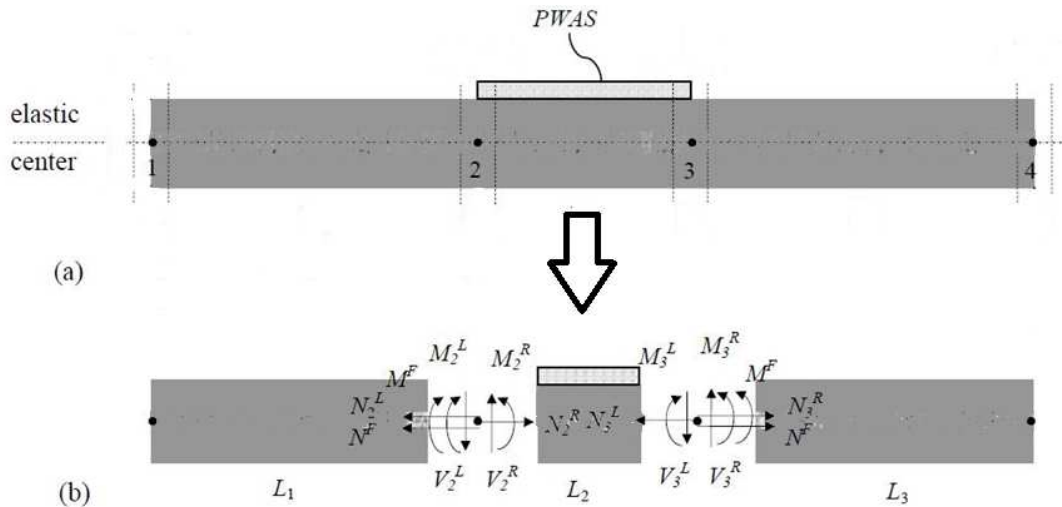
*Figure 72: Free vibration of a uniform beam:*
*(a) schematic of beam elements; (b) free-body diagram*

## *5.1* TRANSFER MATRIX METHOD DEVELOPED BY PESTEL AND LECKIE (1967)

Pestel and Leckie presented the transfer matrix method in their seminal 1967 textbook. The beam is divided in smaller segments, and for each segment the state vectors (displacements and internal forces) are calculated using the field transfer matrices and the point transfer matrices. Then, the state vectors and the frequency response function at any location on the beam are determined. Finally, the overall frequency response function is computed. Euler-Bernoulli beam theory is used; shear deformation and rotary inertia are disregarded. The field transfer matrices and point transfer matrices are used to determine the state vectors at different points in the structure and solve the eigenvalues and eigenvectors in MATLAB.

Figure 73 shows a uniform beam of length $l$ (which can be under both axial and flexural loads) and can be divided into $N$ segments.
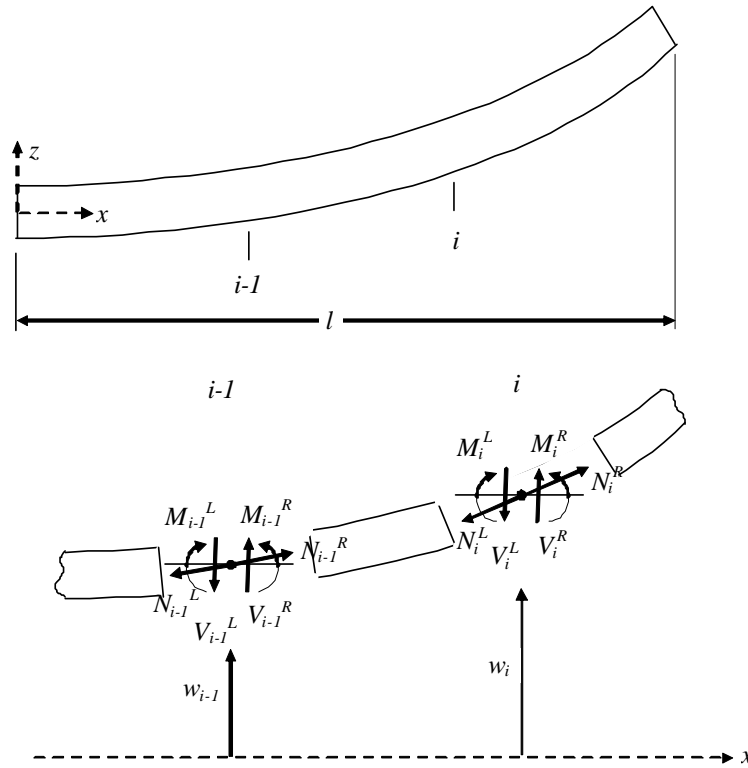
*Figure 73: Beam element with displacement and internal forces; Source: Cuc (2010)*

In order to proceed with the TMM, we have to build a state vector $\mathbf{z_i}$ comprising

the displacements and internal forces for each interval:

$$\mathbf{z}_i = \begin{bmatrix} u \\ w \\ \varphi \\ N \\ V \\ M \end{bmatrix}_i \tag{5.1}$$

**Displacements** are: $u$ - axial displacement; $w$ - flexural displacement; $\varphi = \dfrac{\partial w}{\partial x}$ -

rotation or slope

**Internal forces** are: $N$ = axial force; $V$ = shear force; $M$ = bending moment;

**Nodes index** is: $i = 0, 1, 2 \ldots N$

**Segments index** $(i+1)$ is: $j = 1, 2 \ldots N$ , $j = i+1$; $i < N$

104

Using the elastodynamic equations, we write the relation between two consecutive state vectors as

$$\mathbf{z}_i^L = \mathbf{F}_i \mathbf{z}_{i-1}^R$$

(5.2)

where superscript $L$ or $R$ represents left or right hand side of the beam segment (Figure 74).
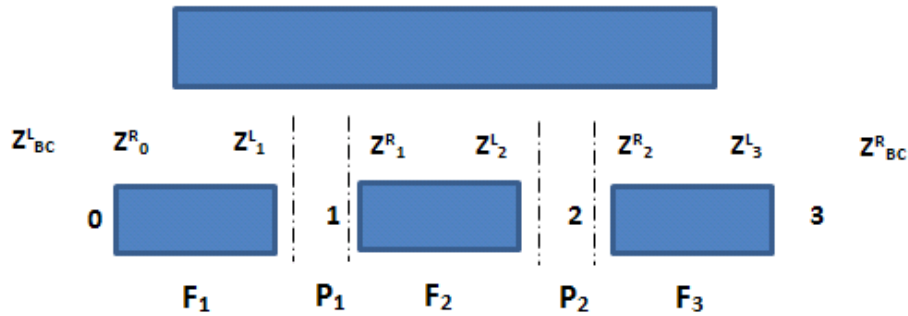


Figure 74: State vectors, field and point transformation matrices (three segment-case)

The matrix $\mathbf{F_i}$ is the field transfer matrix and connects the state vectors at the left and right end side of the i<sup>th</sup> segment. For each node, we express the state vector on the right side of the node given the left side one.

From the equilibrium equation and the continuity conditions for each node we have:

$$\mathbf{z}_i^R = \mathbf{P}_i \mathbf{z}_i^L$$

(5.3)

where matrix $\mathbf{P}_i$ is the point transfer matrix and connects two neighboring state vectors.

The matrix $\mathbf{P}_i$ can take into account changes of axes between one segment and the next.

Matrix $\mathbf{P}_i$ can be also extended to include external forces and moments applied at the nodes.

From equations (5.2) and (5.3) we get the relations between adjacent state vectors.

As an example, consider a beam split <u>into three segments</u> (Figure 74)

$$
\begin{aligned}
\mathbf{z}_0^R &= \mathbf{z}_{BC}^L \\
\mathbf{z}_1^L &= \mathbf{F}_1 \cdot \mathbf{z}_0^R = \mathbf{F}_1 \cdot \mathbf{z}_{BC}^L \\
\mathbf{z}_1^R &= \mathbf{P}_1 \cdot \mathbf{z}_1^L = \mathbf{P}_1 \cdot \mathbf{F}_1 \cdot \mathbf{z}_{BC}^L \\
\mathbf{z}_2^L &= \mathbf{F}_2 \cdot \mathbf{z}_1^R = \mathbf{F}_2 \cdot \mathbf{P}_1 \cdot \mathbf{F}_1 \cdot \mathbf{z}_{BC}^L \\
\mathbf{z}_2^R &= \mathbf{P}_2 \cdot \mathbf{z}_2^L = (\mathbf{P}_2 \cdot \mathbf{F}_2) \cdot (\mathbf{P}_1 \cdot \mathbf{F}_1) \cdot \mathbf{z}_{BC}^L \\
\mathbf{z}_{BC}^R &= \mathbf{z}_3^L = \mathbf{F}_3 \cdot \mathbf{z}_2^R = \mathbf{F}_3 \cdot (\mathbf{P}_2 \cdot \mathbf{F}_2) \cdot (\mathbf{P}_1 \cdot \mathbf{F}_1) \cdot \mathbf{z}_{BC}^L
\end{aligned}
\tag{5.4}
$$

The start and end state vectors of the beam connect through an overall transfer matrix

$\mathbf{U}$, defined as

$$
\mathbf{U} = \mathbf{F}_3 \cdot (\mathbf{P}_2 \cdot \mathbf{F}_2) \cdot (\mathbf{P}_1 \cdot \mathbf{F}_1)
\tag{5.5}
$$

Hence, equation (5.4) can be expressed as

$$
\mathbf{z}_{BC}^R = \mathbf{U}\mathbf{z}_{BC}^L
\tag{5.6}
$$

From equations (5.6), we get the displacements and forces at one end knowing the state

vector at the other end.

Let's consider the general case of Figure 75.
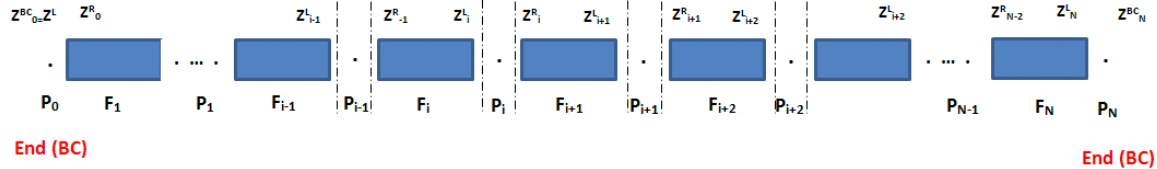


*Figure 75: General state vectors, field and point transfer matrices*

Using the same approach as in the three-segment case, we get the following relations

between adjacent state vectors and transfer matrix $\mathbf{U}$ so that:

$$
\begin{aligned}
\mathbf{z}_i^R &= \mathbf{P}_i \cdot \mathbf{z}_i^L \\
\mathbf{z}_{i+1}^L &= \mathbf{F}_{i+1} \cdot \mathbf{z}_i^R = (\mathbf{F}_{i+1} \cdot \mathbf{P}_i) \cdot \mathbf{z}_i^L \\
\mathbf{U} &= \mathbf{P}_N \cdot (\mathbf{F}_N \cdot \mathbf{P}_{N-1}) \cdot \ldots \cdot (\mathbf{F}_{i+1} \cdot \mathbf{P}_i) \cdot \ldots \cdot (\mathbf{F}_2 \cdot \mathbf{P}_1) \cdot (\mathbf{F}_1 \cdot \mathbf{P}_0) \\
\mathbf{z}_{BC}^R &= \mathbf{U}\mathbf{z}_{BC}^L
\end{aligned}
\tag{5.7}
$$

### 5.1.1 CALCULATION OF THE FIELD TRANSFER MATRIX $\mathbf{F}$

Consider a single element of length $l$. To calculate the field transfer matrix $\mathbf{F}$

consider a generic point $x$ inside the segment and write the state vector $\mathbf{z}(x)$ as a

matrix $\mathbf{B}(x)$ multiplied by a constant column $\mathbf{a}$, i.e.,

$$\mathbf{z}(x) = \mathbf{B}(x)\mathbf{a} \tag{5.8}$$

where $\mathbf{z} = \begin{bmatrix} u & w & \varphi & N & V & M \end{bmatrix}^T$, $\quad \mathbf{a} = \begin{bmatrix} A_1 & A_2 & A_3 & A_4 & A_5 & A_6 \end{bmatrix}^T$

To determine the expression of $\mathbf{B}(x)$, consider the general solutions for axial and

flexural vibration of a uniform beam, i.e.,

$$u(x) = A_1 g_1(x) + A_2 g_2(x) \tag{5.9}$$

$$w(x) = A_3 f_1(x) + A_4 f_2(x) + A_5 f_3(x) + A_6 f_4(x) \tag{5.10}$$

where

$$g_1(x,\omega) = \sin\left[\gamma_a(\omega)x\right]$$

$$g_2(x,\omega) = \cos\left[\gamma_a(\omega)x\right]$$

$$f_1(x,\omega) = \frac{1}{2}\left\{\cosh\left[\gamma_f(\omega)x\right] + \cos\left[\gamma_f(\omega)x\right]\right\}$$

$$f_2(x,\omega) = \frac{1}{2\gamma_f(\omega)}\left\{\sinh\left[\gamma_f(\omega)x\right] + \sin\left[\gamma_f(\omega)x\right]\right\}$$

$$f_3(x,\omega) = \frac{1}{2\gamma_f^2(\omega)}\left\{\cosh\left[\gamma_f(\omega)x\right] - \cos\left[\gamma_f(\omega)x\right]\right\}$$

$$f_4(x,\omega) = \frac{1}{2\gamma_f^3(\omega)}\left\{\sinh\left[\gamma_f(\omega)x\right] - \sin\left[\gamma_f(\omega)x\right]\right\} \tag{5.11}$$

The constants $\gamma_a$ and $\gamma_f$ are the wave numbers for axial and flexural vibration, i.e.,

$$\gamma_a(\omega) = \omega\sqrt{\frac{m}{EA}} = \frac{\omega}{c} \tag{5.12}$$

$$\gamma_f(\omega) = \left(\frac{m}{EI}\right)^{1/4} \sqrt{\omega} = \frac{\sqrt{\omega}}{a}$$

(5.13)

The axial force is defined as

$$N = EA \frac{\partial u}{\partial x}$$

(5.14)

The bending moment and shear force are defined as

$$M = EI \frac{\partial^2 w}{\partial x^2}, \quad V = -EI \frac{\partial^3 w}{\partial x^3}$$

(5.15)

Hence, the state vector becomes

$$\begin{bmatrix} u \\ w \\ \varphi \\ N \\ V \\ M \end{bmatrix} = \begin{bmatrix} u \\ w \\ \dfrac{\partial w}{\partial x} \\ EA \dfrac{\partial u}{\partial x} \\ -EI \dfrac{\partial^3 w}{\partial x^3} \\ EI \dfrac{\partial^2 w}{\partial x^2} \end{bmatrix}$$

(5.16)

Substitution of equations (5.9), (5.10),(5.11) into equation (5.16) yields

$$\begin{bmatrix} u \\ w \\ \varphi \\ N \\ V \\ M \end{bmatrix} = \begin{bmatrix} g_1 & g_2 & 0 & 0 & 0 & 0 \\ 0 & 0 & f_1 & f_2 & f_3 & f_4 \\ 0 & 0 & \dfrac{\partial f_1}{\partial x} & \dfrac{\partial f_2}{\partial x} & \dfrac{\partial f_3}{\partial x} & \dfrac{\partial f_4}{\partial x} \\ EA\dfrac{\partial g_1}{\partial x} & EA\dfrac{\partial g_2}{\partial x} & 0 & 0 & 0 & 0 \\ 0 & 0 & -EI\dfrac{\partial^3 f_1}{\partial x^3} & -EI\dfrac{\partial^3 f_2}{\partial x^3} & -EI\dfrac{\partial^3 f_3}{\partial x^3} & -EI\dfrac{\partial^3 f_4}{\partial x^3} \\ 0 & 0 & EI\dfrac{\partial^2 f_1}{\partial x^2} & EI\dfrac{\partial^2 f_2}{\partial x^2} & EI\dfrac{\partial^2 f_3}{\partial x^2} & \dfrac{\partial^2 f_4}{\partial x^2} \end{bmatrix} \begin{bmatrix} A_1 \\ A_2 \\ A_3 \\ A_4 \\ A_5 \\ A_6 \end{bmatrix}$$

(5.17)

If we define

$$\mathbf{B} = \begin{bmatrix} g_1 & g_2 & 0 & 0 & 0 & 0 \\ 0 & 0 & f_1 & f_2 & f_3 & f_4 \\ 0 & 0 & \dfrac{\partial f_1}{\partial x} & \dfrac{\partial f_2}{\partial x} & \dfrac{\partial f_3}{\partial x} & \dfrac{\partial f_4}{\partial x} \\ EA\dfrac{\partial g_1}{\partial x} & EA\dfrac{\partial g_2}{\partial x} & 0 & 0 & 0 & 0 \\ 0 & 0 & -EI\dfrac{\partial^3 f_1}{\partial x^3} & -EI\dfrac{\partial^3 f_2}{\partial x^3} & -EI\dfrac{\partial^3 f_3}{\partial x^3} & -EI\dfrac{\partial^3 f_4}{\partial x^3} \\ 0 & 0 & EI\dfrac{\partial^2 f_1}{\partial x^2} & EI\dfrac{\partial^2 f_2}{\partial x^2} & EI\dfrac{\partial^2 f_3}{\partial x^2} & \dfrac{\partial^2 f_4}{\partial x^2} \end{bmatrix}$$

$$(5.18)$$

Then, equation (5.17) can be expressed as

$$\mathbf{z} = \mathbf{B}\cdot\mathbf{a} \tag{5.19}$$

Note the matrix $\mathbf{B}$ depends on $x$ and $\omega$, i.e., $\mathbf{B}=\mathbf{B}(x,\omega)$, since the functions

$g_1, g_2, f_1, f_2, f_3, f_4$ of equation (5.11) depend on $x$ and $\omega$.

From equation (5.19), the state vector at the two ends of a segment of length $l_i$ can be

written as

$$\mathbf{z}(0) = \mathbf{B}(0)\mathbf{a} \tag{5.20}$$

$$\mathbf{z}(l) = \mathbf{B}(l)\mathbf{a} \tag{5.21}$$

The coefficients column vector $\mathbf{a}$ can be calculated as

$$\mathbf{a} = \mathbf{B}^{-1}(0)\mathbf{z}(0) \tag{5.22}$$

From (5.22) and (5.21) we get

$$\mathbf{z}(l) = \mathbf{B}(l)\mathbf{B}^{-1}(0)\mathbf{z}(0) \tag{5.23}$$

Equation (5.23) can be written as

$$\mathbf{z}(l) = \mathbf{F}\cdot\mathbf{z}(0) \tag{5.24}$$

Where $\mathbf{F}$ is the field transfer matrix defined as

$$\mathbf{F} = \mathbf{B}(l)\mathbf{B}^{-1}(0) \tag{5.25}$$

For the general case of $N$ segments, the field transfer matrix is calculated for each segment as

$$\mathbf{F}_i = \mathbf{B}_i(l_i)\mathbf{B}_i^{-1}(0), \quad i = 1, ..., N \tag{5.26}$$

### 5.1.2 CALCULATION OF THE POINT TRANSFER MATRIX $\mathbf{P}$

The point transfer matrix is used to apply forces and moments at the nodes. To calculate the point transfer matrix $\mathbf{P}$, we impose the compatibility conditions and apply the equilibrium equations at each node. Figure 76 shows a beam segment with forces applied at each end. At the left side and, i.e. at node $1$, the force $F$ is applied in the negative direction; at the right end, i.e. at node $2$, the force $F$ is applied in the positive direction. The forces $F$ induce axial loads $N_1^F, N_2^F$, and bending moments $M_1^F, M_2^F$ at the nodes $1$ and $2$, respectively.

The calculation of the point matrices $\mathbf{P}_1$ and $\mathbf{P}_2$ is illustrated next.
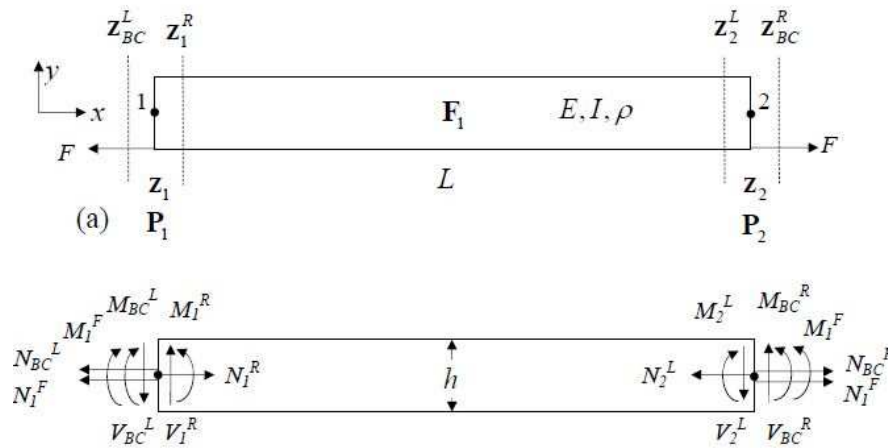


*Figure 76: One segment - Forced vibration of a uniform beam:*

@ node #1

Compatibility conditions:

$$u_1^R = u_{BC}^L$$
$$\varphi_1^R = \varphi_{BC}^L$$
$$w_1^R = w_{BC}^L \tag{5.27}$$

Equilibrium equations:

$$\sum F_x : \qquad\qquad N_1^R = N_{BC}^L + N_1^F \tag{5.28}$$

$$\sum F_y : \qquad\qquad V_1^R = V_{BC}^L \tag{5.29}$$

$$\sum M : \qquad\qquad M_1^R = M_{BC}^L + M_1^F \tag{5.30}$$

In matrix form Eqs. (5.27) through (5.29) can be written as

$$
\begin{bmatrix} u \\ w \\ \varphi \\ N \\ V \\ M \end{bmatrix}_1^R =
\begin{bmatrix}
1 & 0 & 0 & 0 & 0 & 0 \\
0 & 1 & 0 & 0 & 0 & 0 \\
0 & 0 & 1 & 0 & 0 & 0 \\
0 & 0 & 0 & 1 & 0 & 0 \\
0 & 0 & 0 & 0 & 1 & 0 \\
0 & 0 & 0 & 0 & 0 & 1
\end{bmatrix}
\cdot
\begin{bmatrix} u \\ w \\ \varphi \\ N \\ V \\ M \end{bmatrix}_{BC}^L +
\begin{bmatrix} 0 \\ 0 \\ 0 \\ N_1^F \\ 0 \\ M_1^F \end{bmatrix} \tag{5.31}
$$

$$\mathbf{z}_1^R = \mathbf{P}_1 \cdot \mathbf{z}_{BC}^L + \mathbf{P}_1^F \tag{5.32}$$

$$
\mathbf{P}_1^F =
\begin{bmatrix} 0 \\ 0 \\ 0 \\ N_1^F \\ 0 \\ M_1^F \end{bmatrix}
$$

where $\mathbf{P}_1 = \mathbf{I}$ and the forcing term $\mathbf{P}_1^F$ is

In a similar manner

@ node #2

Compatibility conditions

$$u_{BC}^R = u_2^L$$
$$\varphi_{BC}^R = \varphi_2^L$$
$$w_{BC}^R = w_2^L \tag{5.33}$$

Equilibrium equations

$$\sum F_x : \qquad\qquad N_{BC}^R = N_2^L - N_2^F \qquad\qquad (5.34)$$

$$\sum V_y : \qquad\qquad V_{BC}^R = V_2^L \qquad\qquad (5.35)$$

$$\sum M : \qquad\qquad M_{BC}^R = M_2^L - M_2^F \qquad\qquad (5.36)$$

Eqs. (5.33) through (5.35) can be written in matrix form as

$$\begin{bmatrix} u \\ w \\ \varphi \\ N \\ V \\ M \end{bmatrix}_2^{BC} = \begin{bmatrix} 1 & 0 & 0 & 0 & 0 & 0 \\ 0 & 1 & 0 & 0 & 0 & 0 \\ 0 & 0 & 1 & 0 & 0 & 0 \\ 0 & 0 & 0 & 1 & 0 & 0 \\ 0 & 0 & 0 & 0 & 1 & 0 \\ 0 & 0 & 0 & 0 & 0 & 1 \end{bmatrix} \cdot \begin{bmatrix} u \\ w \\ \varphi \\ N \\ V \\ M \end{bmatrix}_2^{L} + \begin{bmatrix} 0 \\ 0 \\ 0 \\ -N_1^F \\ 0 \\ -M_1^F \end{bmatrix} \qquad (5.37)$$

$$\mathbf{z}_{BC}^R = \mathbf{P}_2 \cdot \mathbf{z}_2^L + \mathbf{P}_2^F \qquad\qquad (5.38)$$

where $\mathbf{P}_2 = \mathbf{I}$ and the forcing term is

$$\mathbf{P}_2^F = \begin{bmatrix} 0 \\ 0 \\ 0 \\ -N_1^F \\ 0 \\ -M_1^F \end{bmatrix} \qquad\qquad (5.39)$$

For an uniform continuous isotropic beam, the point transfer matrix $\mathbf{P}$ is the unit matrix $\mathbf{I}$, that is,

$$\mathbf{P}_i = \mathbf{I} \qquad\qquad (5.40)$$

### 5.1.3 TMM FOR FREE VIBRATION ANALYSIS

Partition the state vector $\mathbf{z}$ into displacement and stress resultant components $\mathbf{u}$ and $\mathbf{p}$, respectively, i.e.,

$$\mathbf{z} = \begin{bmatrix} \mathbf{u} \\ \mathbf{p} \end{bmatrix}, \quad \mathbf{u} = \begin{bmatrix} u \\ \varphi \\ w \end{bmatrix}, \quad \mathbf{p} = \begin{bmatrix} N \\ V \\ M \end{bmatrix} \qquad (5.41)$$

112

Consider the free-free boundary conditions in the form

$$\mathbf{p}_{BC}^{L} = \begin{bmatrix} N \\ V \\ M \end{bmatrix} = 0; \quad \mathbf{p}_{BC}^{R} = \begin{bmatrix} N \\ V \\ M \end{bmatrix} = 0$$
(5.42)

In this case, the unknowns are the displacements, $\mathbf{u}_{BC}^{L}$ and $\mathbf{u}_{BC}^{R}$, i.e.,

$$\mathbf{u}_{BC}^{L} = \begin{bmatrix} u \\ \varphi \\ w \end{bmatrix}_{BC}^{L} ; \quad \mathbf{u}_{BC}^{R} = \begin{bmatrix} u \\ \varphi \\ w \end{bmatrix}_{BC}^{R}$$
(5.43)

Recall Eq. (5.7) and write the state vector at the right-end in terms of the state vector at the left –end as

$$\mathbf{z}_{BC}^{R} = \mathbf{U}\,\mathbf{z}_{BC}^{L}$$
(5.44)

Equation (5.44) can be rewritten in partitioned form as

$$\begin{bmatrix} \mathbf{u}_{BC}^{R} \\ \mathbf{p}_{BC}^{R} \end{bmatrix} = \begin{bmatrix} \mathbf{U}_{uu} & \mathbf{U}_{up} \\ \mathbf{U}_{pu} & \mathbf{U}_{pp} \end{bmatrix} \begin{bmatrix} \mathbf{u}_{BC}^{L} \\ \mathbf{p}_{BC}^{L} \end{bmatrix}$$
(5.45)

By expansion, equation (5.45) becomes

$$\mathbf{u}_{BC}^{R} = \mathbf{U}_{uu}\mathbf{u}_{BC}^{L} + \mathbf{U}_{up}\mathbf{p}_{BC}^{L}$$
$$\mathbf{p}_{BC}^{R} = \mathbf{U}_{pu}\mathbf{u}_{BC}^{L} + \mathbf{U}_{pp}\mathbf{p}_{BC}^{L}$$
(5.46)

Applying the free-free boundary conditions and rearranging, equations (5.46) become

$$\begin{cases} \mathbf{u}_{BC}^{R} = \mathbf{U}_{uu}\mathbf{u}_{BC}^{L} \\ 0 = \mathbf{U}_{pu}\mathbf{u}_{BC}^{L} \end{cases} \Leftrightarrow \begin{bmatrix} \mathbf{U}_{uu} & -I \\ \mathbf{U}_{pu} & 0 \end{bmatrix} \begin{bmatrix} \mathbf{u}_{BC}^{L} \\ \mathbf{u}_{BC}^{R} \end{bmatrix} = 0$$
(5.47)

We have a linear homogeneous system which has a unique non-trivial solution if its determinant is non-zero. The solutions of the homogeneous system yields the eigenvalues $\omega_i$.

To obtain the eigenvalue we perform a search for the roots of determinant, i.e.,

$$\left| \mathbf{U}_{pu}\left( \omega \right) \right| = 0$$

(5.48)

The eigenvalues are calculated using a frequency search algorithm. A search algorithm (e.g., bisection method, Newton-Raphson, etc.) can be used to scan a predetermined interval to extract all the $\omega$ roots, i.e. the natural frequencies of the beam.

For each natural frequency $\omega$, we use equation (5.47) to find $\mathbf{u}_{BC}^{R}$ and $\mathbf{u}_{BC}^{L}$. Thus, we can complete the left-end state vector as

$$\mathbf{z}_{BC}^{L} = \begin{bmatrix} \mathbf{u}_{BC}^{L} \\ 0 \end{bmatrix}$$

(5.49)

From $\mathbf{z}_{BC}^{R}$, we can use the transfer matrix process to find state vectors $\mathbf{z}_{i}^{R}$, $i = 0,1,...,N-1$ at the beginning of each segment. From the state vector $\mathbf{z}_{i}^{R}$ at the beginning of each segment we calculate the coefficients $\left\{ A_{1}^{i},...A_{6}^{i} \right\} = \mathbf{a}_{i}$ with the formula.

$$\mathbf{a}_{i} = \mathbf{B}_{i}^{-1}\left( 0,\omega \right) \cdot \mathbf{z}_{i}^{R} = \begin{bmatrix} A_{1}^{i} \\ A_{2}^{i} \\ A_{3}^{i} \\ A_{4}^{i} \\ A_{5}^{i} \\ A_{6}^{i} \end{bmatrix}$$

(5.50)

Knowing the coefficients $A_{1}^{i}, A_{2}^{i}, A_{3}^{i}, A_{4}^{i}, A_{5}^{i}, A_{6}^{i}$, we can calculate the mode shapes for axial and flexural vibrations inside the element as

$$u_{i}\left( x \right) = A_{1}^{i} g_{1}^{i}\left( x \right) + A_{2}^{i} g_{2}^{i}\left( x \right)$$
$$w_{i}\left( x \right) = A_{3}^{i} f_{1}^{i}\left( x \right) + A_{4}^{i} f_{2}^{i}\left( x \right) + A_{5}^{i} f_{3}^{i}\left( x \right) + A_{6}^{i} f_{4}^{i}\left( x \right)$$

(5.51)

Repeating this process for all the segments yields the modeshape over the whole beam.

### 5.1.4 TMM FOR FORCED VIBRATION ANALYSIS

Consider the boundary conditions generated by time harmonic external forces applied on the beam. E.g., for an external force $Fe^{i\omega t}$ applied as shown in Figure 76; the left and right boundary conditions in terms of stress resultants are

$$\mathbf{p}_{BC}^{L} = \begin{bmatrix} -N \\ 0 \\ M \end{bmatrix} e^{i\omega t}; \quad \mathbf{p}_{BC}^{R} = \begin{bmatrix} N \\ 0 \\ -M \end{bmatrix} e^{i\omega t} \tag{5.52}$$

The state vector at the right-end can be expressed in terms of the state vectors at the left using the overall transfer matrix $\mathbf{U}$, i.e.,

$$\mathbf{z}_{BC}^{R} = \mathbf{U}\,\mathbf{z}_{BC}^{L} \tag{5.53}$$

By applying the boundary conditions, the following relation between state vectors at the right –end and the left-end is obtained

$$\begin{bmatrix} \mathbf{u}_{BC}^{R} \\ \mathbf{p}_{BC}^{R} \end{bmatrix} = \begin{bmatrix} \mathbf{U}_{uu} & \mathbf{U}_{up} \\ \mathbf{U}_{pu} & \mathbf{U}_{pp} \end{bmatrix} \begin{bmatrix} \mathbf{u}_{BC}^{L} \\ \mathbf{p}_{BC}^{L} \end{bmatrix} \tag{5.54}$$

By expansion of equation (5.54) we get

$$\mathbf{u}_{BC}^{R} = \mathbf{U}_{uu}\mathbf{u}_{BC}^{L} + \mathbf{U}_{up}\mathbf{p}_{BC}^{L} \tag{5.55}$$

$$\mathbf{p}_{BC}^{R} = \mathbf{U}_{pu}\mathbf{u}_{BC}^{L} + \mathbf{U}_{pp}\mathbf{p}_{BC}^{L} \tag{5.56}$$

We can rearrange equation (5.56) to get

$$\mathbf{U}_{pu}\mathbf{u}_{BC}^{L} = \left(\mathbf{p}_{BC}^{R} - \mathbf{U}_{pp}\mathbf{u}_{BC}^{L}\right) \tag{5.57}$$

We use equation (5.57) to find $\mathbf{u}_{BC}^{L}$

$$\mathbf{u}_{BC}^{L} = \mathbf{U}_{pu}^{-1}\left(\mathbf{u}_{BC}^{R} - \mathbf{U}_{pp}\mathbf{p}_{BC}^{L}\right) \tag{5.58}$$

From (5.58) and (5.55) we calculate $\mathbf{u}_{BC}^{R}$

$$\mathbf{u}_{BC}^{R} = \mathbf{U}_{uu}\mathbf{U}_{pu}^{-1}\left(\mathbf{p}_{BC}^{R} - \mathbf{U}_{pp}\mathbf{p}_{BC}^{L}\right) + \mathbf{U}_{up}\mathbf{p}_{BC}^{L} \tag{5.59}$$

Equations (5.58), (5.59) give the displacements $\mathbf{u}_{BC}^{L}$, $\mathbf{u}_{BC}^{R}$. Knowing the displacements we can build the frequency response function FRF.

For frequencies outside resonance range, the response is given by equation (5.59). This assumes that the invers of matrix $\mathbf{U}_{pu}$ exists, i.e. the matrix is not singular, i.e. $\left|\mathbf{U}_{pu}\right| \neq 0$.

At resonance, the matrix $\mathbf{U}_{pu}$ becomes singular, i.e. $\left|\mathbf{U}_{pu}\right| = 0$. In this case, the response $\mathbf{u}_{BC}^{R}$ given by equation (5.59) become infinite and the structure oscillates in a natural mode of vibration.

### 5.1.5 PROBLEMS WITH TMM

The main problem of TMM is the numerical instability at high frequencies. This aspect will be presented in detail in the next sections.

### 5.2 TMM DEVELOPMENTS

Vibration analysis of complexly shaped structures using the transfer matrix method has been the focus of many researchers. Ritchie et. al. (1975) integrated the transfer matrix method into a simple FEM to calculate the spectrum of flexural and torsional resonant frequencies of specimens of material of orthotropic symmetry.

Authors considered the torsion-flexure coupling and utilized the Timoshenko beam corrections for flexure. They stated that the transfer matrix technique can be used to predict the free-free resonant frequencies for composite material beams of orthotropic symmetry and that the coupling torsion-flexure produces measurable perturbations of the resonant frequencies and distortion of the vibration shapes.

116

Giurgiutiu and Stafford (1977) used TMM to calculate the vibration of helicopter blades modeled as rotating Timoshenko beams. Subrahmanyam and Garg (1997) used TMM to determine the frequencies and mode shapes for uncoupled flexural vibrations of straight beams for different types of boundary conditions. Authors considered in their method the shear deformation effects, rotary inertia and variable axial loading and utilized a beam of length L = 1 m divided into 100 equal segments. The mass and mass moments of inertia were lumped at the centroid of each segment. They used the Timoshenko beam theory in order to derive the exact solution for the pinned-sliding case and used the Euler-Bernoulli theory to compare the results. Authors showed that there was a match between their TMM method solutions and the exact analytical solutions.

Lee (2000) presented a general approach to the spectral transfer matrix method (STMM) by merging the features of the spectral element method (i.e., high accuracy) with the features of the TMM (i.e., high analysis efficiency) and used this method for solving vibration problems of large periodic lattice structures. He used a plane lattice structure with four beam-like lattice substructures and one single lattice cell, united at the center. He applied the STMM method to both a simple Euler-Bernoulli beam a large plane lattice structure and was able predict the dynamic response for each structure. Ellakany et. al. (2004) used a mix between the TMM and the analog beam method (TMABM) in order to study the vibration of a composite beam (composed of an upper slab and a lower beam, connected at the interface by shear transmitting studs). TMABM provides the coupling between the bending and torsional modes of deformation. As part

of their method, authors replace the real beam by an equivalent beam where all the shear deformation is concentrated in a thin horizontal layer called the shear layer. Several assumptions are made: (a) each sub-beam behaves as a simple Euler-Bernoulli beam (no shear effects); (b) the vertical displacements of the sub-beams are the same (the shear layer is transversely rigid). Authors used the method to calculate the natural frequencies of a simple supported beam with uniformly distribute mass and compared the results against the classical solution for simple supported beams. They found that the TMABM method and the classical method converge.

Bilello and Bergman (2004) used TMM to solve the eigenvalue problem for a one-dimensional system with non-uniform mechanical properties (the vibration of a damaged beam under a moving mass). The beam was divided into N segments of constant linear mass density, flexural stiffness, and length and the cracked beam was modeled using the "rotational spring model" which considers the damage by using the local compliance, which assesses the relation between the load and the strain in the proximity of the crack. Authors used the modal expansion method to obtain the dynamic response and they found that the analytical and experimental results converge. In addition, the presence of damage produced larger perturbation to the dynamic response of a moving load.

The use of TMM to analyze the detection of delamination with PWAS transducers and the electromechanical impedance method was recently been attempted by Bois et.al. (2004, 2007) and Cuc (2010). These developments are detailed in the next sections.

### 5.3 TMM METHOD DEVELOPED BY BOIS ET. AL. (2004, 2007) FOR DELAMINATION DETECTION IN COMPOSITE BEAMS

Bois, Herzog, and Hochard (2004, 2007) used the theory of piezoelectric laminates to extend TMM to composite beams. They focus on building a monitoring system that can predict the damage in a quasi-isotropic laminate. The analysis of Bois et al. (2004, 2007) has the following steps:

1. Analysis of a composite laminated plate with piezoelectric layers and simplification to the case of a composite beam.

2. Transfer matrix modeling of a beam with a localized delamination and a piezoelectric wafer located away from the delamination.

3. Determination of the electric current resulting from an electric a.c. voltage applied to the piezo wafer at various frequencies. The a.c. voltage induces the vibrations of the composite beam through piezoelectric transduction; hence, the resulting current varies strongly around the beam resonances. This is shown in the plot of admittance $(Y(\omega) = I(\omega)/V(\omega))$ and of equivalent capacitance $C(\omega)$.

The next sections present details of this method using the notations of Bois et al. (2004, 2007).

### 5.3.1 ANALYSIS OF THE LAMINATED COMPOSITE BEAM

In order to proceed with this method, let us consider a 2-D approach and define a stress vector $\sigma$ and a strain vector $\varepsilon$.

$$\boldsymbol{\sigma} = \begin{bmatrix} \sigma_{11} \\ \sigma_{22} \\ \sigma_{12} \end{bmatrix}; \quad \boldsymbol{\varepsilon} = \begin{bmatrix} \varepsilon_{11} \\ \varepsilon_{22} \\ 2\varepsilon_{12} \end{bmatrix} \tag{5.60}$$

The constitutive law first shown in equation (4.6) can be expressed as follows (where $\mathbf{S}$ is the compliance tensor):

$$\boldsymbol{\varepsilon} = \mathbf{S}\,\boldsymbol{\sigma} \tag{5.61}$$

For an orthotropic material, $\mathbf{S}$ becomes:

$$\mathbf{S} = \begin{pmatrix} \dfrac{1}{E_1} & -\dfrac{\upsilon_{21}}{E_2} & 0 \\[2mm] -\dfrac{\upsilon_{21}}{E_2} & \dfrac{1}{E_2} & 0 \\[2mm] 0 & 0 & \dfrac{1}{G_{12}} \end{pmatrix} \tag{5.62}$$

where:

$E_1$ is the longitudinal Young's modulus

$E_2$ is the transversal Young's modulus

$G_{12}$ is the shear modulus

$\upsilon_{21}$ is the Poisson's ratio.

Let us then consider a piezoelectric material approach and considering equations (3.1) and (3.2) for the mechanical strain $\varepsilon_{ij}$, and respectively the displacement, $D_j$, we can write:

$$\boldsymbol{\varepsilon_{ij}} = \mathbf{S}^E \boldsymbol{\sigma} + \mathbf{d} \cdot E_3 \tag{5.63}$$

$$D_3 = \mathbf{d}^T \boldsymbol{\sigma} + \varepsilon_{33}^{\sigma} E_3 \tag{5.64}$$

where:

$\varepsilon_{33}^{\sigma}$ is the dielectric tensor at constant stress field

$\mathbf{S}^{E}$ is the compliance tensor at constant electrical field

$\mathbf{d}$ is the corresponding piezoelectric coupling tensor

$$\mathbf{d} = \begin{bmatrix} d_{113} \\ d_{223} \\ d_{123} \end{bmatrix} \qquad (5.65)$$

and $\mathbf{d}^{T}$ is the transposed of $\mathbf{d}$.

We can rewrite equation (5.63) as follows:

$$\boldsymbol{\sigma} = (\mathbf{S}^{E})^{-1}(\boldsymbol{\varepsilon} - \mathbf{d} \cdot E_{3}) \qquad (5.66)$$

And by replacing $\boldsymbol{\sigma}$ into (5.64) we obtain

$$D_{3} = \mathbf{d}^{T}(\mathbf{S}^{E})^{-1}\boldsymbol{\varepsilon} + [\varepsilon_{33}^{\sigma} - \mathbf{d}^{T}(\mathbf{S}^{E})^{-1}\mathbf{d}]E_{3} \qquad (5.67)$$

(5.66) and (5.67) are the constitutive laws and $\boldsymbol{\varepsilon}$ and $E_{3}$ are independent variables.
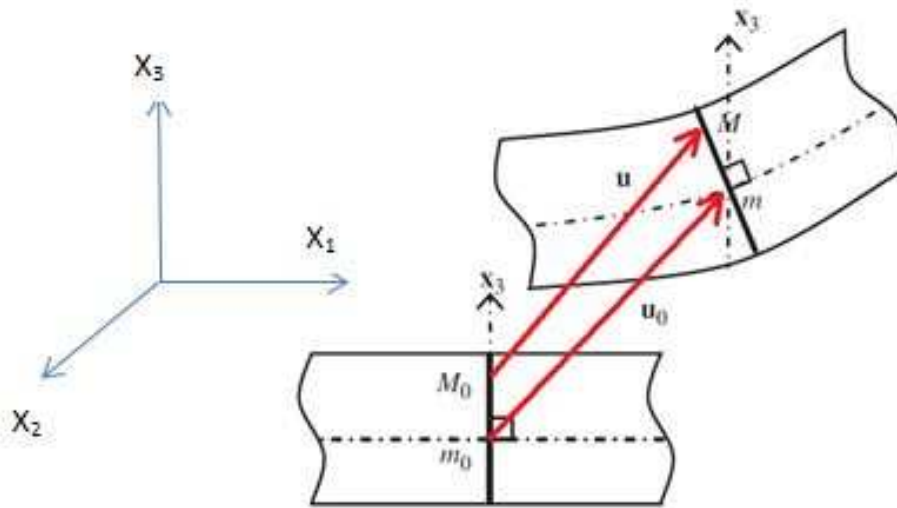


*Figure 77: Kirchhoff-Love's displacement field (Bois et al., 2007) Fig. modified*

For simplicity, let us consider equations (4.62) and (4.63) but follow the coordinate system shown in Figure 77. Following Kirchhoff Love's displacement field, we have:

$$u = u^0 - x_3 grad(u_3^0)$$

(5.68)

where $u^0$ is the displacement of the point $m^0$.

Following this approach, we can rewrite (5.60) as follows:

$$\varepsilon = \varepsilon^0 + x_3 \mathbf{K}$$

(5.69)

$$\varepsilon^0 = \begin{bmatrix} u_{1,1}^0 \\ u_{2,2}^0 \\ u_{1,2}^0 + u_{2,1}^0 \end{bmatrix}, \quad \mathbf{K} = \begin{bmatrix} -u_{3,11}^0 \\ -u_{3,22}^0 \\ -2u_{3,12}^0 \end{bmatrix}$$

(5.70)

We can calculate the dynamic bending equations for piezoelectric laminates taking into consideration all assumptions above. Figure 78 shows the layers for a laminate composite, with height being defined from the center.
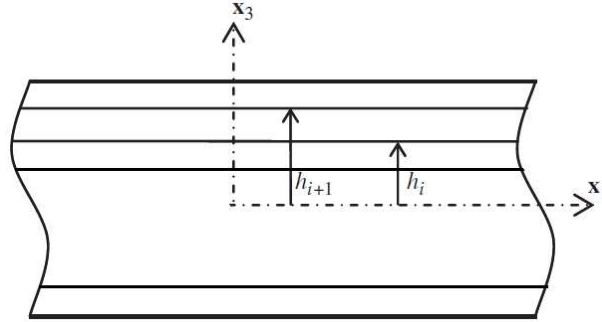


*Figure 78: Layers for Laminate Composite (Bois el al., 2007) Fig. modified*

As a first step, we calculate the axial forces and the moments:

$$\mathbf{N} = \int_{h_1}^{h_{n+1}} \sigma dx_3 = \sum_{i=1}^{n} \left( \int_{h_i}^{h_{i+1}} \sigma dx_3 \right)$$

$$\mathbf{M} = \int_{h_1}^{h_{n+1}} \sigma x_3 dx_3 = \sum_{i=1}^{n} \left( \int_{h_i}^{h_{i+1}} \sigma x_3 dx_3 \right)$$

(5.71)

Using equation (5.66) and (5.71), we can express the system of equations as follows:

$$\mathbf{N} = \int_{h_1}^{h_{n+1}} (\mathbf{S}^E)^{-1} \varepsilon dx_3 - \int_{h_1}^{h_{n+1}} (\mathbf{S}^E)^{-1} \mathbf{d} \cdot E_3 dx_3$$

$$\mathbf{M} = \int_{h_1}^{h_{n+1}} (\mathbf{S}^E)^{-1} \varepsilon x_3 dx_3 - \int_{h_1}^{h_{n+1}} (\mathbf{S}^E)^{-1} \mathbf{d} \cdot E_3 x_3 dx_3$$

(5.72)

122

Using equations (5.69) through (5.72), the system becomes:

$$\mathbf{N} = \mathbf{A}\boldsymbol{\varepsilon}^0 + \mathbf{B}\mathbf{K} - \mathbf{F}E_3$$
$$\mathbf{M} = \mathbf{B}\boldsymbol{\varepsilon}^0 + \mathbf{D}\mathbf{K} - \mathbf{G}E_3$$

(5.73)

Where:

$$\mathbf{A} = \sum_{i=1}^{n} (\mathbf{S}_i^E)^{-1}(h_{i+1} - h_i)$$

$$\mathbf{B} = \sum_{i=1}^{n} \left( (\mathbf{S}_i^E)^{-1} \frac{h_{i+1}^2 - h_i^2}{2} \right)$$

$$\mathbf{D} = \sum_{i=1}^{n} \left( (\mathbf{S}_i^E)^{-1} \frac{h_{i+1}^3 - h_i^3}{3} \right)$$

(5.74)

$$\mathbf{F} = (h_{i+1} - h_i) \, (\mathbf{S}_i^E)^{-1}\mathbf{d}$$

$$\mathbf{G} = \frac{(h_{(i+1)}^2 - h_i^2)}{2}(\mathbf{S}_i^E)^{-1}\mathbf{d}$$

And $i$ represents the layer index in the equations above.

Following the same approach presented above, we can rewrite equation (5.67) as:

$$D_3 = \mathbf{d}^T \left( \mathbf{S}_i^E \right)^{-1} \left( \boldsymbol{\varepsilon}^0 + x_3 \mathbf{K} \right) + \left[ \varepsilon_{33}^\sigma - \mathbf{d}^T \left( \mathbf{S}_i^E \right)^{-1} \mathbf{d} \right] E_3$$

(5.75)

Our initial assumption was that $D_3$ is independent of $x_3$, however as per

equation (5.36), this is not the case and $D_3$ is strictly related to $x_3$. Because the PWAS is

very thin though, we do not take into consideration this relation, but we can take an

approximation on the average displacement of the electrical charge in the $x_3$ direction

and rewrite (5.75) as follows:

$$D_3 = \mathbf{d}^T \left( \mathbf{S}_i^E \right)^{-1} \left( \boldsymbol{\varepsilon}^0 + \frac{h_{i+1}^2 - h_i^2}{2} \mathbf{K} \right) + \left[ \varepsilon_{33}^\sigma - \mathbf{d}^T \left( \mathbf{S}_i^E \right)^{-1} \mathbf{d} \right] E_3$$

(5.76)

We study the bending moments of the beam in the 2-D plane $(x_1, x_3)$ and we are looking only at solutions where only the forces in the $x_1$ direction is not equal to zero, which leads to:

$$N_{22} = 0; \quad M_{22} = 0; \quad N_{12} = 0; \quad M_{12} = 0 \tag{5.77}$$

The conditions given by equation (5.67) and (5.73) allow us to determine the stresses in terms of $\varepsilon_{11}^0, K_{11}, D_3$. We are only left now with solving the equation:

$$A_{22}\varepsilon_{22}^0 + B_{22}K_{22} + A_{23}\varepsilon_{12}^0 + B_{23}K_{12} = -A_{12}\varepsilon_{11}^0 - B_{12}K_{11} + F_2E_3$$
$$B_{22}\varepsilon_{22}^0 + D_{22}K_{22} + B_{23}\varepsilon_{12}^0 + D_{23}K_{12} = -B_{12}\varepsilon_{11}^0 - D_{12}K_{11} + G_2E_3$$
$$A_{32}\varepsilon_{22}^0 + B_{32}K_{22} + A_{33}\varepsilon_{12}^0 + B_{33}K_{12} = -A_{13}\varepsilon_{11}^0 - B_{13}K_{11} + F_3E_3$$
$$B_{32}\varepsilon_{22}^0 + D_{32}K_{22} + B_{33}\varepsilon_{12}^0 + D_{33}K_{12} = -B_{13}\varepsilon_{11}^0 - D_{13}K_{11} + G_3E_3 \tag{5.78}$$

This can be expressed in a matrix format

$$\begin{bmatrix} A_{22} & B_{22} & A_{23} & B_{23} \\ B_{22} & D_{22} & B_{23} & D_{23} \\ A_{32} & B_{32} & A_{33} & B_{33} \\ B_{32} & D_{32} & B_{33} & D_{33} \end{bmatrix} \begin{bmatrix} \varepsilon_{22}^0 \\ K_{22} \\ \varepsilon_{12}^0 \\ K_{12} \end{bmatrix} = \begin{bmatrix} -A_{12}\varepsilon_{11}^0 - B_{12}K_{11} + F_2E_3 \\ -B_{12}\varepsilon_{11}^0 - D_{12}K_{11} + G_2E_3 \\ -A_{13}\varepsilon_{11}^0 - B_{13}K_{11} + F_3E_3 \\ -B_{13}\varepsilon_{11}^0 - D_{13}K_{11} + G_3E_3 \end{bmatrix} \tag{5.79}$$

We then determine $N_{11}$ and $M_{11}$ as a function of $\varepsilon_{11}^0, K_{11}$ and $E_3$ as

$$N_{11} = A^N \varepsilon_{11}^0 + B^N K_{11} - F^N E_3$$
$$M_{11} = B^M \varepsilon_{11}^0 + D^M K_{11} - G^M E_3 \tag{5.80}$$

Similarly, we solve (5.76)

$$D_3 = P^D \varepsilon_{11}^0 + Q^D K_{11} + J^D E_3 \tag{5.81}$$

All the coefficients above $A^N, B^N, F^N, G^M, B^M, D^M, P^D, Q^D, J^D$ are numerically calculated. Then, we apply Kirchhoff Love's plate theory and obtain the dynamical

equilibrium equations, (we ignore the inertial forces in directions $x_1$ and $x_2$ due to the bending mode which is much lower than the first axial mode):

$$N_{11,1} + N_{12,2} = 0$$
$$N_{22,2} + N_{12,1} = 0$$
$$M_{11,11} + M_{22,22} + M_{12,12} + \lambda \omega^2 u_3^0 = 0$$
(5.82)

where $\lambda$ is the area density.

From equations (5.77) and (5.82) we obtain:

$$N_{11,1} = 0$$
$$M_{11,11} + \lambda \omega^2 u_3^0 = 0$$
(5.83)

From equations (5.80) and (5.83) and also considering the fact that $E_3$ does not depend on $x_1$, we obtain:

$$\begin{cases} A^N u_{1,11}^0 - B^N u_{3,111}^0 - F^N E_{3,1} = 0 \\ B^M u_{1,111}^0 - D^M u_{3,1111}^0 - G^M E_{3,11} + \lambda \omega^2 u_3^0 = 0 \end{cases}$$
(5.84)

Knowing that $E_3$ is independent of $x_1$, we obtain:

$$\begin{cases} A^N u_{1,11}^0 - B^N u_{3,111}^0 = 0 \\ B^M u_{1,111}^0 - D^M u_{3,1111}^0 + \lambda \omega^2 u_3^0 = 0 \end{cases}$$
(5.85)

The terms $B^N$ and $B^M$ will be zero due to the laminate symmetry and only on the delaminated zone we will have asymmetry. To decouple the system of equations in (5.85), and use the first equation as follows:

$$u_{1,11}^0 = \frac{B^N}{A^N} u_{3,111}^0$$
(5.86)

The derivative gives

$$u_{1,111}^0 = \frac{B^N}{A^N} u_{3,1111}^0$$
(5.87)

Replacing into the second equation of the system we obtain:

$$Ru^0_{3,1111} - \lambda\omega^2 u^0_3 = 0 \tag{5.88}$$

Where

$$R = D^M - \frac{B^N B^M}{A^N} \tag{5.89}$$

The solutions for equation (5.88) are given by:

$$u^0_3(x_1) = a_1 cos(\gamma x_1) + a_2 sin(\gamma x_1) + a_3 cosh(\gamma x_1) + a_4 sinh(\gamma x_1) \tag{5.90}$$

Where

$$\gamma = \sqrt{\frac{\lambda\omega^2}{R}} \tag{5.91}$$

and the solutions for equation (5.86) are given by:

$$u^0_1(x_1) = \frac{\gamma B^N}{A^N}\left[-a_1 \sin(\gamma x_1) + a_2 \cos(\gamma x_1) + a_3 \sinh(\gamma x_1) + a_4 \cosh(\gamma x_1)\right] \tag{5.92}$$
$$+a_5 x_1 + a_6$$

$a_1, a_2, a_3, a_4, a_5, a_6$ are constants determined from the initial strain and stress conditions.

Following the transfer matrix method approach, the beam is split into several segments and then we write the kinematical and dynamical conditions between each of adjacent pairs of the segments. We use expressions (5.90) and (5.92) for each pair shown in Figure 79 to build the whole beam.
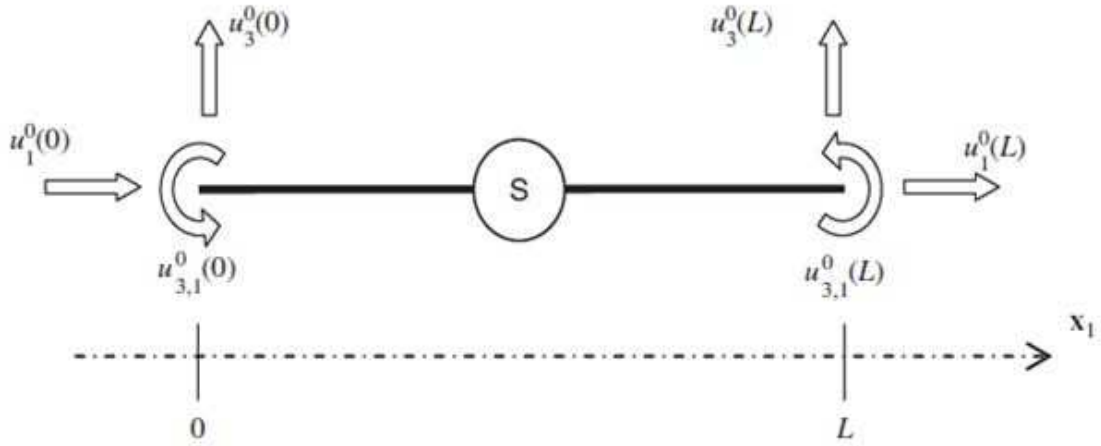
*Figure 79: Kinematical node variables; Source: Bois, Herzog, and Hochard (2007)*

The displacement $u_1^0(x_1)$ is:

$$
u_1^0(x_1) = \begin{bmatrix} u_1^0(0) \\ u_1^0(L) \\ u_{1,1}^0(0) \\ u_{1,1}^0(L) \\ u_1^0(0) \\ u_1^0(L) \end{bmatrix}^T CL_1^T \begin{bmatrix} \cos(\gamma x_1) \\ \sin(\gamma x_1) \\ \cosh(\gamma x_1) \\ \sinh(\gamma x_1) \\ x_1 \\ 1 \end{bmatrix}
\tag{5.93}
$$

The displacement $u_3^0(x_1)$ is:

$$
u_3^0(x_1) = \begin{bmatrix} u_3^0(0) \\ u_3^0(L) \\ u_{3,1}^0(0) \\ u_{3,1}^0(L) \\ u_3^0(0) \\ u_3^0(L) \end{bmatrix}^T CL_3^T \begin{bmatrix} \cos(\gamma x_1) \\ \sin(\gamma x_1) \\ \cosh(\gamma x_1) \\ \sinh(\gamma x_1) \\ x_1 \\ 1 \end{bmatrix}
\tag{5.94}
$$

where:

$$CL_1^T = \begin{bmatrix} -\dfrac{X\gamma}{Y}(ChSi+CoSh) & -\dfrac{X\gamma}{Y}(Si+Sh) & \dfrac{X}{Y}(CoSh+SiSh-1) & \dfrac{X}{Y}(Ch-Co) & 0 & 0 \\[2mm] \dfrac{X\gamma}{Y}(SiSh-CoSh+1) & \dfrac{X\gamma}{Y}(Co-Ch) & \dfrac{X}{Y}(ChSi-CoSh) & \dfrac{X}{Y}(Sh-Si) & 0 & 0 \\[2mm] -\dfrac{X\gamma}{Y}(ChSi+CoSh) & \dfrac{X\gamma}{Y}(Si+Sh) & \dfrac{X}{Y}(CoCh-SiSh-1) & \dfrac{X}{Y}(Co-Ch) & 0 & 0 \\[2mm] \dfrac{X\gamma}{Y}(CoSh+SiSh-1) & -\dfrac{X\gamma}{Y}(Co-Ch) & \dfrac{X}{Y}(ChSi-CoSh) & \dfrac{X}{Y}(Sh-Si) & 0 & 0 \\[2mm] 0 & 0 & \dfrac{X}{L} & -\dfrac{X}{L} & -\dfrac{1}{L} & \dfrac{1}{L} \\[2mm] 0 & 0 & -X & 0 & 0 & 0 \end{bmatrix} \tag{5.95}$$

$$CL_3^T = \begin{bmatrix} \gamma(CoCh-SiSh-1) & \gamma(Ch-Co) & CoSh-ChSi & Si-Sh & 0 & 0 \\ \gamma(ChSi+CoSh) & -\gamma(Si+Sh) & CoCh+SiSh-1 & Ch-Co_2 & 0 & 0 \\ \gamma(CoCh+SiSh-1) & \gamma(Co-Ch) & ChSi-CoSh & Sh-Si & 0 & 0 \\ -\gamma(ChSi+CoSh) & \gamma(Si+Sh) & CoCh-SiSh-1 & Co-Ch & 0 & 0 \\ 0 & 0 & 0 & 0 & 0 & 0 \\ 0 & 0 & 0 & 0 & 0 & 0 \end{bmatrix} \tag{5.96}$$

and

$$Co = \cos(\gamma L); \ Si = \sin(\gamma L); \ Ch = \cosh(\gamma L); \ Sh = \sinh(\gamma L)$$
$$X = \frac{B^N}{A^N}; \quad Y = 2(CoCh-1) \tag{5.97}$$

Then, we can write the dynamic equilibrium for each node. By solving the system of equations, we can calculate the displacement field depending on the electric potential.

### 5.3.2 Determination of the E/M Impedance of the Laminated Composite

We describe now the mathematical algorithm for the E/M impedance method for composite materials following Bois, Herzog and Hochard (2007) approach.

Let us consider that the transducer admittance is

$$Y = \frac{\dot{I}}{V^+} \tag{5.98}$$

From the electric charge displacement, we obtain the electrical current I as follows:

$$I = \int\limits_{+ter\min al} D_3 ds = jw \int\limits_{+ter\min al} D_3 ds = jwb \int_{n_i}^{n_{i+1}} D_3 dx_1 \qquad (5.99)$$

$n_i, n_{i+1}$ are the nodes at the transducer ends.

We then use (5.99) to express $I$ depending on the displacement field and the electrical field:

$$I = jwb \int_{n_i}^{n_{i+1}} \left( P^N u_{1,1}^0 - Q^N u_{3,11}^0 + J^N E_3 \right) dx_1 \qquad (5.100)$$

$$I = jwbV^+ \left( P^N \Delta u_1^0 - Q^N \Delta u_{3,11}^0 + J^D \frac{L_i}{h_i} \right) \qquad (5.101)$$

where $L_p$ is the length of the transducer

$$P^N = d^T (S_i^E)^{-1}$$
$$Q^N = d^T (S_i^E)^{-1} \left[ \frac{h_{i+1}^2 - h_i^2}{2} \right] \qquad (5.102)$$
$$J^N = \varepsilon_{33}^\sigma - d^T (S_i^E)^{-1} d$$

And $\Delta u_1^0$ and $\Delta u_{3,1}^0$ are:

$$\Delta u_1^0 = \frac{u_1^0(n_{i+1}) - u_1^0(n_i)}{V^+} \qquad (5.103)$$

$$\Delta u_{3,1}^0 = \frac{[u_{3,1}^0(n_{i+1}) - u_{3,1}^0(n_i)]}{V^+[u_1^0(n_{i+1}) - u_1^0(n_i)]} \qquad (5.104)$$

Admittance becomes:

$$Y = jw \left[ b(P^N \Delta u_1^0 - Q^N \Delta u_{3,11}^0) + J^D \frac{L_i}{h_i} \right] \qquad (5.105)$$

And total capacitance is:

$$C_T = b(P^N \Delta u_1^0 - Q^N \Delta u_{3,11}^0) + J^D \left( \frac{L_i}{h_i} \right) \qquad (5.106)$$

### 5.3.3 Damage Detection with the Bois et al. (2004, 2007) Method

Bois et al. (2004,2007) used the piezoelectric impedance method as a local detection technique to provide information on the size and the position of the delamination inside the beam's structure and concluded that there is a phase shift in the impedance measurement and the resonance peaks are smaller in experimental results than in the simulation (error rate =15%). When looking at the influence of relative position between sensor and damage, they found that the excitation position does not modify the mode frequency, but influences their amplitude. The simulations were used to study more closely the influence of damage (Figure 80) and sensor size in order to consider the insertion of thinner sensors in composite materials to generate bending modes. They found that resonance frequency increases with delamination depth and that only resonances of modes located near the sensor (on the delamination) are shifted when the thickness or the length changes as shown in Figure 81 and Figure 82.
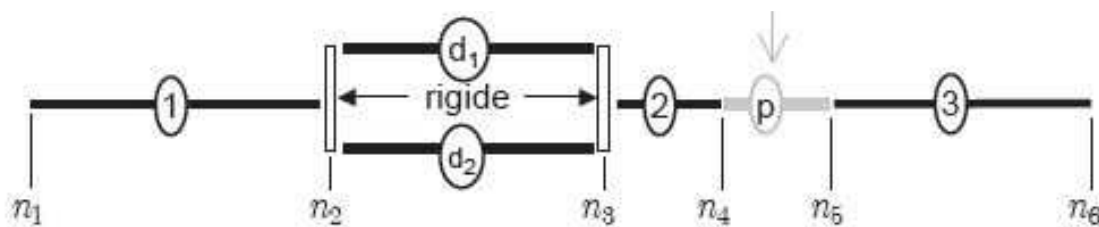


*Figure 80: TMM model of a delaminated composite beam with a segment having a piezoelectric wafer (Bois et al.,2007)*

130
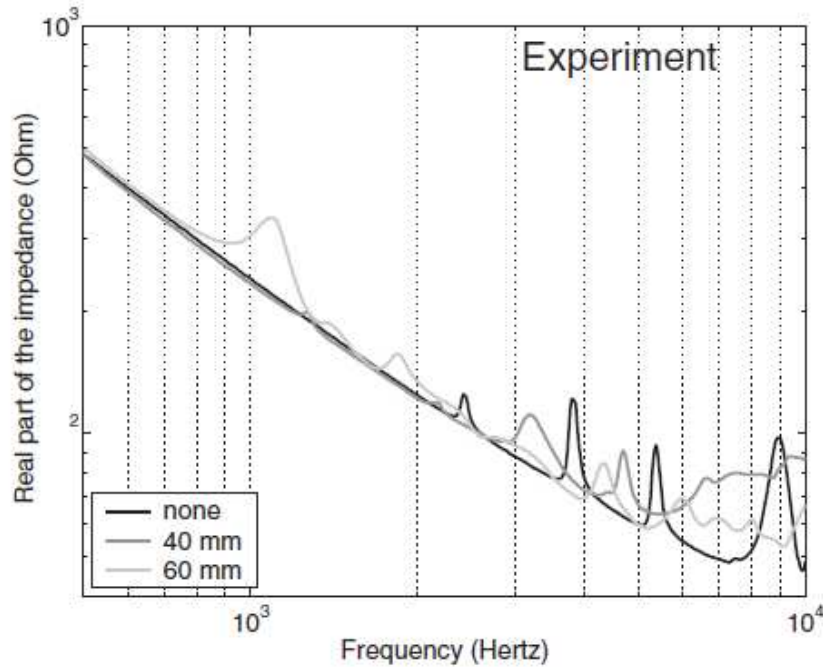
*Figure 81: Influence of delamination length – Experiment L=180mm (length), $L_d$=40mm (delamination), $L_1$=20mm, and $L_2$=23mm ($L_1$, $L_2$ - delamination located inside the beam) Source: Bois et. al. (2004)*
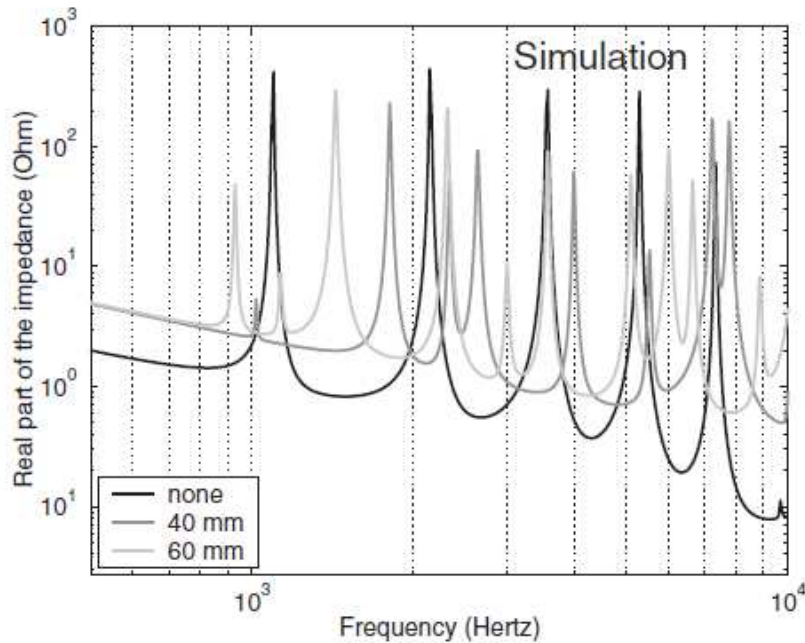


*Figure 82:  Carbon/epoxy- Influence of delamination length – Simulation L=180mm (length), $L_d$=40mm (delamination), $L_1$=20mm, and $L_2$=23mm ($L_1$, $L_2$ - delamination located inside the beam) Source: Bois et. al. (2004)*

Bois et. al. (2007) extends the analysis in Bois et. al. (2004) and calculate the

frequency response of a composite beam with delaminations. The analytical model also

considered the 3D constitutive laws for the PWAS and expressed them in terms of the plane stress terms with uniaxial electric field and instead of measuring the admittance they measure the capacitance of the PWAS (Figure 83).
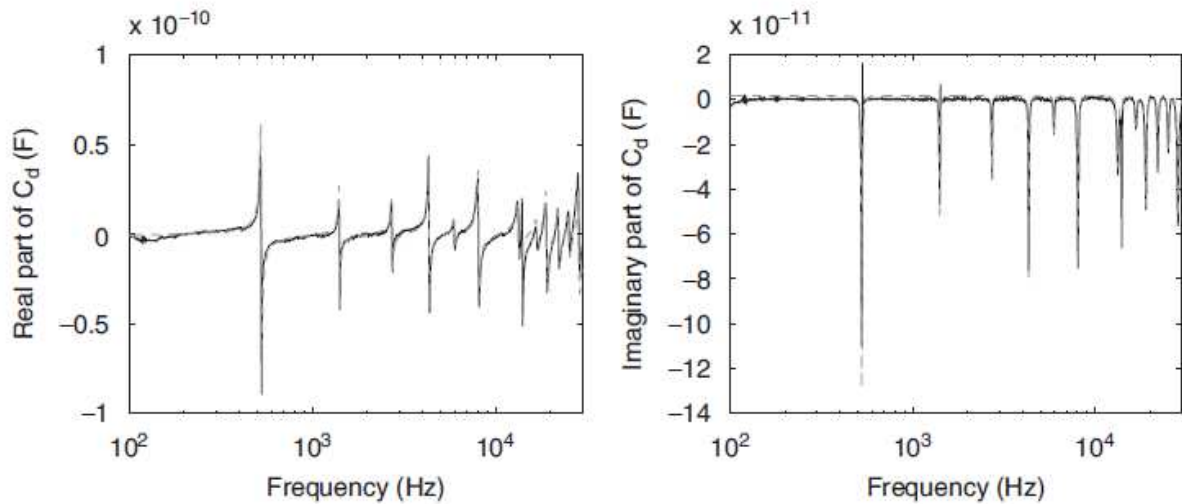


*Figure 83: Delamination at one end - Real part and imaginary part of the equivalent capacitor*
*Source: Bois et al. (2007)*

Authors derived the expressions for the electric charge displacement, longitudinal displacement and transversal displacement and divided the beam into several segments (the kinematic and continuity conditions were applied for each segment). They obtained an $3n$ linear system of equation where In is the number of nodes and by solving the system they obtain the displacement fields in terms of the electric potential $V+$. Then, from the displacement fields, the current I was calculated and the electrical admittance $Y$.

Experimentally, they considered a laminate consisted of 16 unidirectional carbon/epoxy plies; six piezoelectric transducers were bonded on the beam. Two cases of delaminations were considered: 1) when delamination is at one end of the beam and 2) when delamination is located inside the beam (Figure 84). The frequency range

considered was 0.1 kHz-30 kHz. For the first delamination case, authors considered two influence parameters, length, and depth and they concluded that their simulated delamination was underestimated by 10% compared to experimental results. For the second delamination case, authors used three parameters, length, position and depth and they concluded that their simulated delamination was underestimated by 15% compared to experimental results.
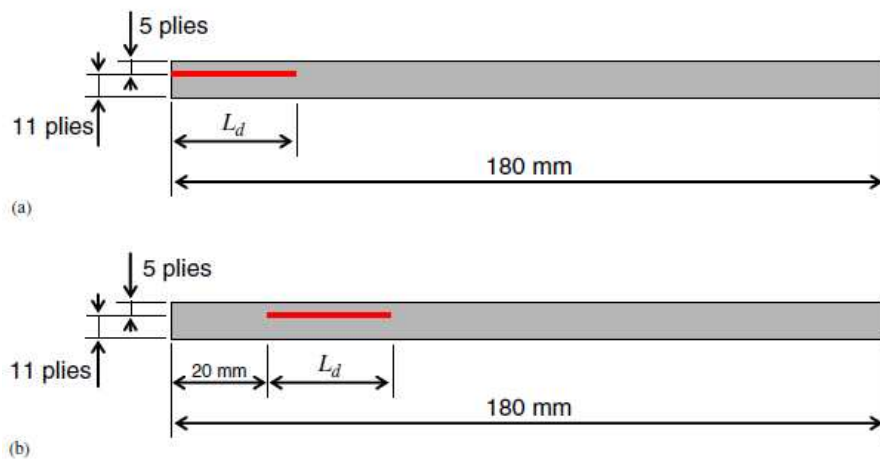


*Figure 84: Configurations of studied delamination.*
*(a) Delamination at one end of the beam. (b) Delamination located inside the beam*
*Source: Bois et. al. (2007)*

### 5.3.4 NUMERICAL RESULTS WITH BOIS ET AL. (2004, 2007) METHOD

In order to understand this theory, we start with a simple case: one single composite beam segment (10 unidirectional epoxy plies). Having one segment means we have 2 nodes: one at the beginning and one at the end of the segment. For each node, we will have 3 unknowns: the displacement on $x_1$ (horizontal) axis, the displacement on $x_3$ (vertical) axis and the bending moment $M$. Hence, for one segment, we have a total of 6 unknowns. The link between the two nodes is the shape functions given by Equations (5.95) and (5.96).

133

Following the transfer matrix method approach, the beam is split into several segments and then we write the kinematical and dynamical conditions between each of adjacent pairs of the segments. Using the same approach, we write the dynamic equilibrium for each node and by solving the system of equations, and then we calculate the displacement field depending on the electric potential.

*Table 4: Material & PWAS Properties*

| MATERIAL | | PWAS |
|---|---|---|
| **Material Properties** | **Unidirectional glass-epoxy Composite** | **APC-850** |
| **Elastic properties** | E1/E2/G12/v12/v21 | E1/E2/v12/v21 |
| **Gpa** | 32/30/4/0.26/0.26 | 64.5/64.5/0.3/0.3 |
| **Damping Coefficient** | $\xi 1/\xi 2/\xi 12$ | $\xi 1/\xi 2/\xi 12$ |
| **Elastic Properties with Damping** | 0.001/0.01/0.01 | 0.001/0.01/0.01 |
| **Mass Density** | 1900 | 7500 |
| **Permittivity** | - | $1750*8.85*10^{-12}$ |
| **Coupling Terms: d33, and d31** | - | $400*10^{-12}$ / $-175*10^{-12}$ |
| **Layers ( No. & Hight)** | 10 layers;   h=2mm;   200µm/layer | Dimensions   8x8x0.2 mm |
| **Stacking Sequence** | $(0^0)_{10}$ | - |

| **Segment dimensions:** | **one segment  - beam length = PWAS** | **two segmments - PWAS + segment** |
|---|---|---|
| **Length** | 60 mm | (100 + 8) mm |
| **Hight** | 2 mm | 2 mm |
| **Width** | 8 mm | 8 mm |

The material and PWAS properties for this case are presented in Table 4.
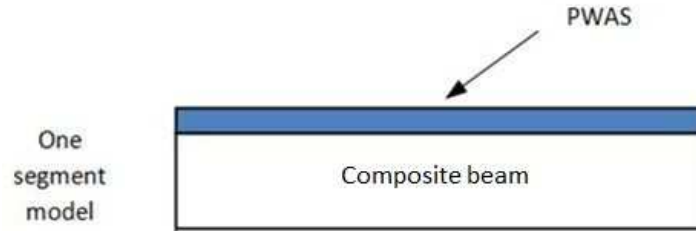
*Figure 85: One – segment model with PWAS*

Figure 86 and Figure 87 represent the real and imaginary parts of the total

capacitance of the PWAS for one single segment when using the TMM method. The

simulation was done in MATLAB in the range 0.1-30 kHz.
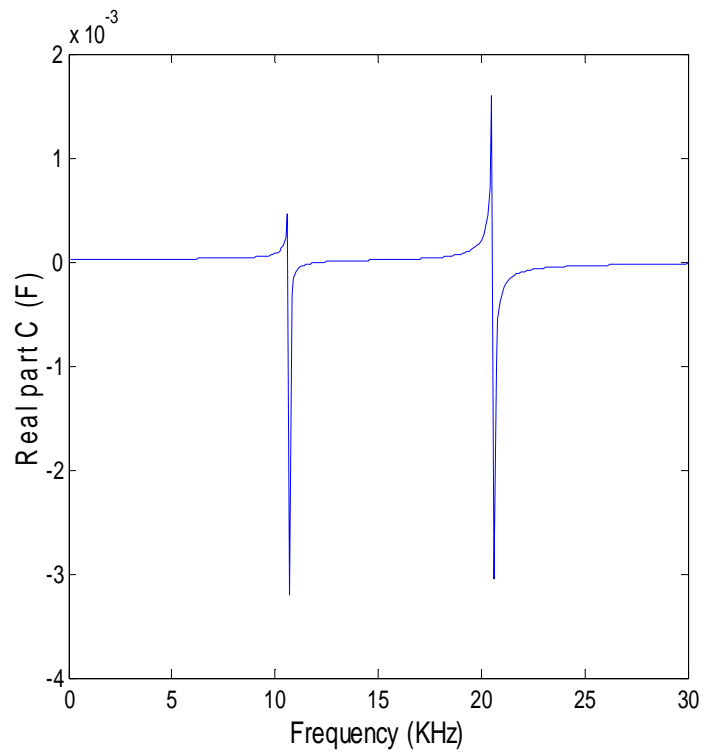


*Figure 86: One – segment model - The real part of the capacitance*
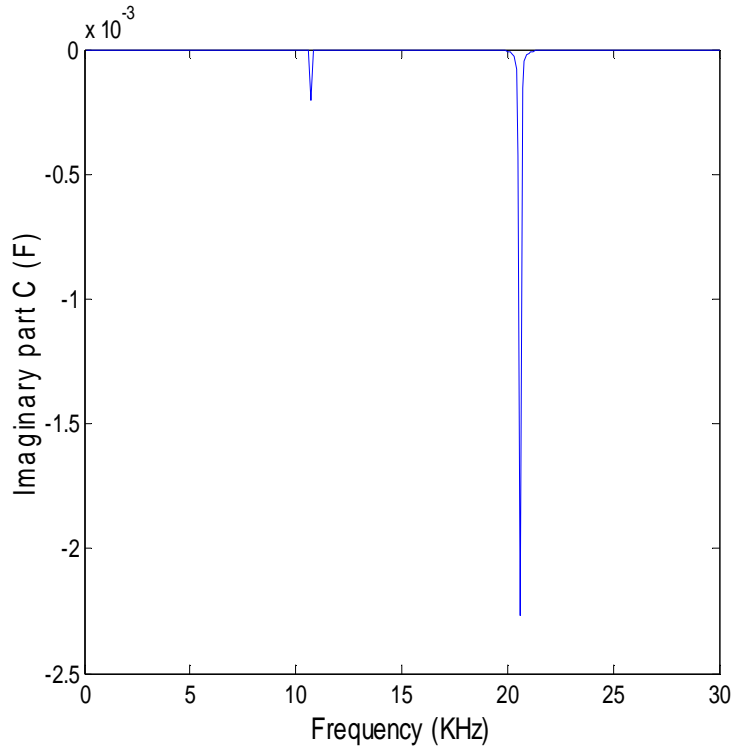
*Figure 87: One – segment model - The imaginary part of the capacitance*

Figure 88 and Figure 89 show the real part and the imaginary part of the admittance.
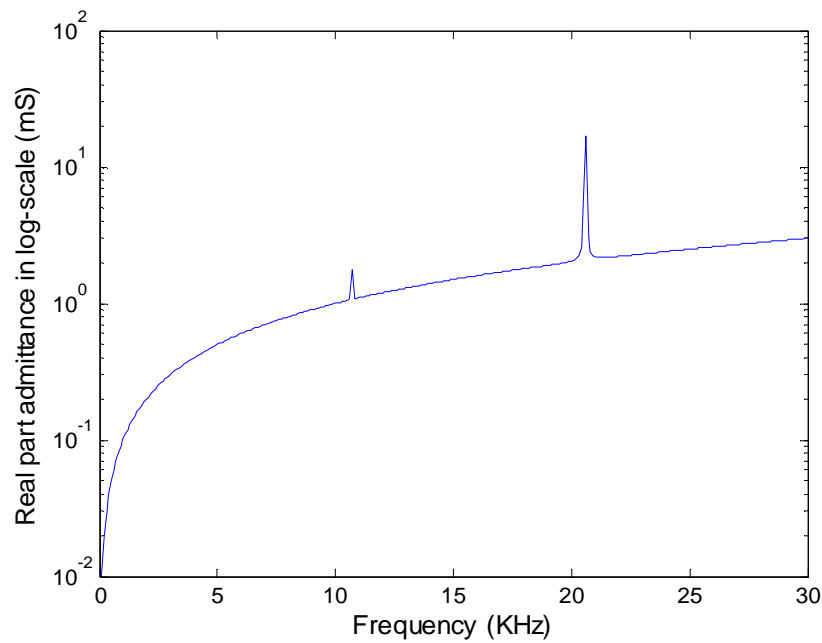


*Figure 88: One – segment model - The real part of admittance (Re Y)*

136
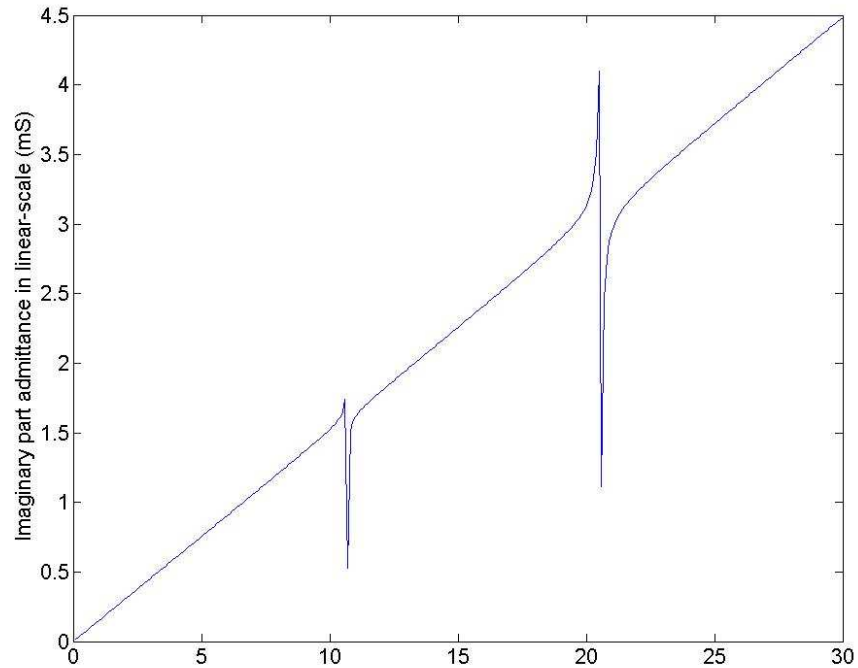
*Figure 89: One – segment model - The imaginary part of admittance (Imag Y)*

We then redo the analysis for 2 segments which represent 3 nodes (Figure 90).

For each node, we have the $x_1$ displacement, $x_3$ displacement and the bending moment. We can express the dynamic equilibrium at the middle node following the approach described above. Applying the continuity laws and the displacement fields, we were able to express the dynamic equilibrium equations according the kinematical node variables, obtaining a matrix 18 x 9. Starting from the left hand side, we can write the link between the middle node and the first one by the shape functions, $CL_1^T$ and $CL_3^T$. The starting point of the second segment will be equal with the end point of the first segment, so these two points are only one. The displacements of the end of point of the second segment will be determined using the same shape function but all the results for the second segment will be linked to the first segment by the middle point.
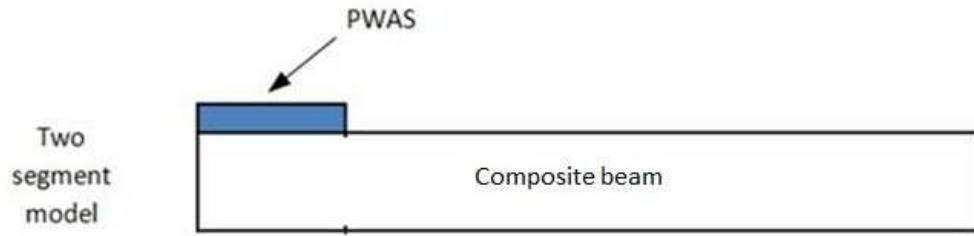
*Figure 90: Two segments with PWAS*

Figure 91 and Figure 92 represent the real and imaginary parts of the total capacitance of the PWAS for two segments when using the TMM method. The simulation was done in MATLAB in the range 1-30 kHz.
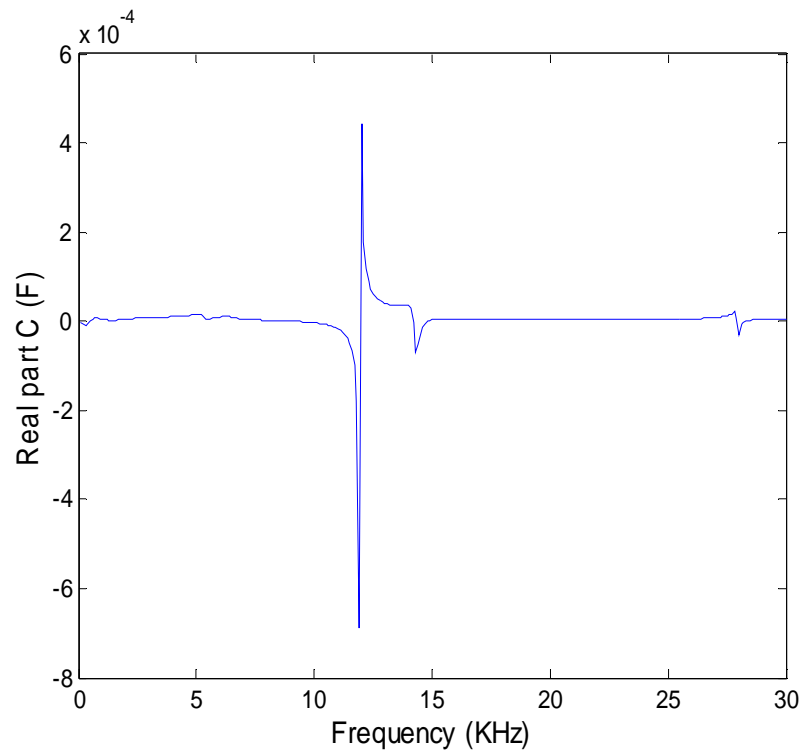


*Figure 91: Two - segment model - The real part of the capacitance*
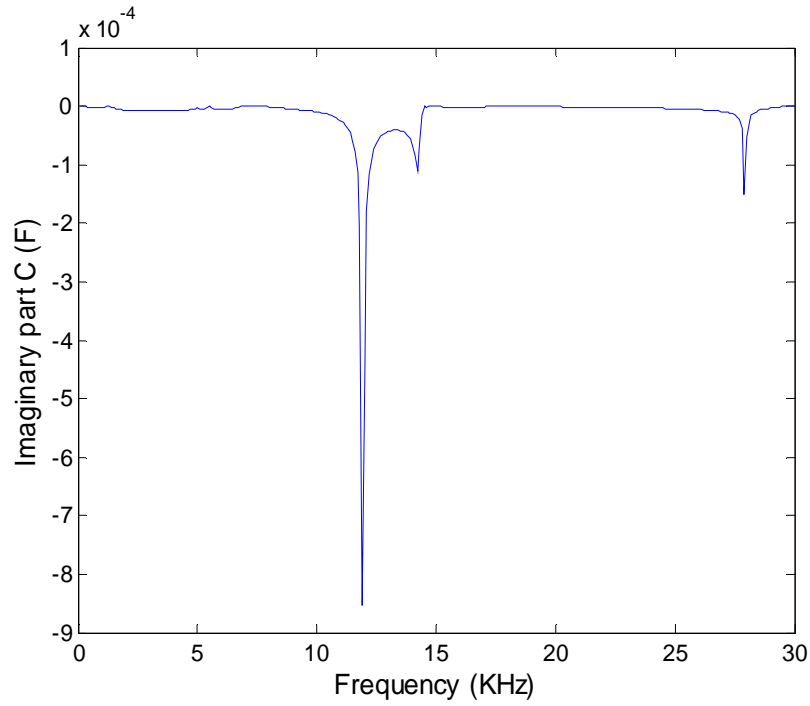
*Figure 92: Two - segment model - The imaginary part of the capacitance*

Figure 93 and Figure 94 show the real part and the imaginary part of the admittance.
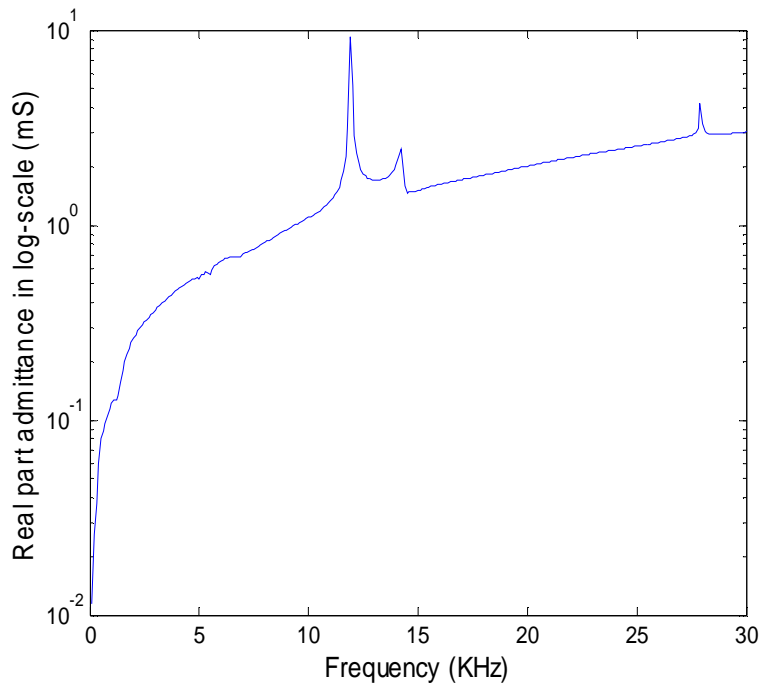


*Figure 93: Two - segment model -The real part of the admitance (Re Y)*

139
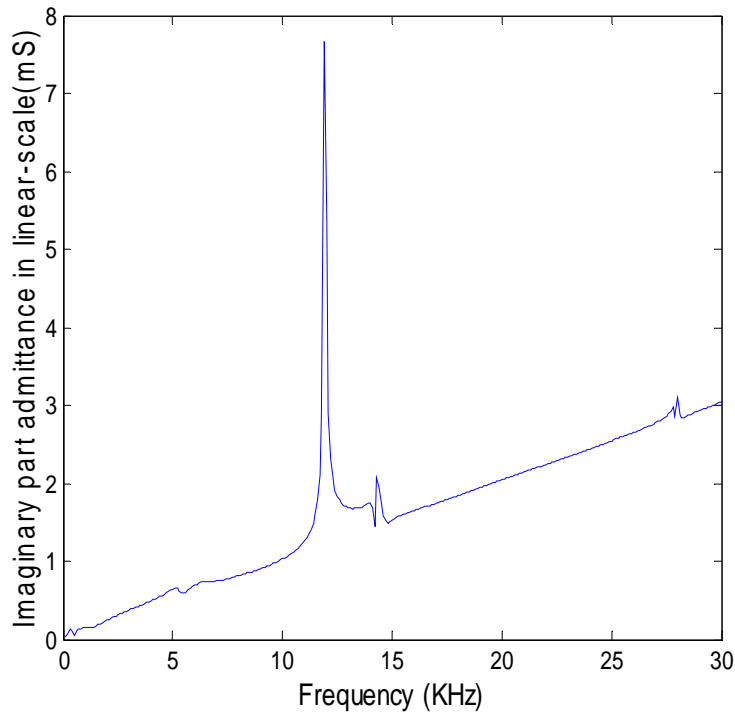
*Figure 94: Two - segment model -The imaginary part of the admittance (Imag Y)*

### 5.3.5  CRITIQUE OF THE BOIS ET AL. (2004, 2007) METHOD

The numerical tests presented above have shown how this method works, but have also highlighted its limitations:

1.  The method was applied by Bois et al. (2004, 2007) only to low frequencies ($\leq 30$ kHz). For these frequencies, the changes in the vibration behavior due to a small delamination were small and hence difficult to detect.

2.  In our tests shown above, we took the method to 30 kHz, but could not go further up because the method had a breakdown. This is due to numerical instability in the TMM algorithm, a fact that has been also reported elsewhere.

### *5.4* TMM DEVELOPED BY CUC (2010) FOR DISBOND DETECTION

Cuc (2010) used TMM to develop the analytical model for a uniform beam using the Euller-Bernoulli beam theory (shear deformation and rotary inertia were not considered) and expanded the method to the case of a multi-layer adhesively bonded beam (Figure 95). The length of the beam was divided in smaller segments, and for each segment he calculated the state vectors (displacements and internal forces) using the field transfer matrices and the point transfer matrices. If damage (disbond) was present in the structure, then the beam was divided in branches and for each branch, the mathematical formulation for the equivalent material properties, field and point transfer matrices were developed. As a final step, he calculated the state vectors, and the frequency response function at any location on the beam as well as the electromechanical impedance using the frequency response function. Cuc (2010) also performed FEM analysis in which a harmonic force was applied at the nodes to simulate the two ends of the PWAS. A coupled-field FEM was performed and he compared both analytical and FEM results with the experimental results from two simple beam specimens: one pristine and one damaged with artificially simulated disbond. In addition, a set of damage indices were developed to detect the presence of disbond damage in the structure. From the results, it was shown that by using only one damage index it may be difficult to have positive damage detection and different damage indices respond in different ways to changes in the impedance spectrum. Author also concluded that analytical and experimental results are in agreement (Figure 98) and that a small

change in the location of one sensor produced a significant change in the impedance

response.
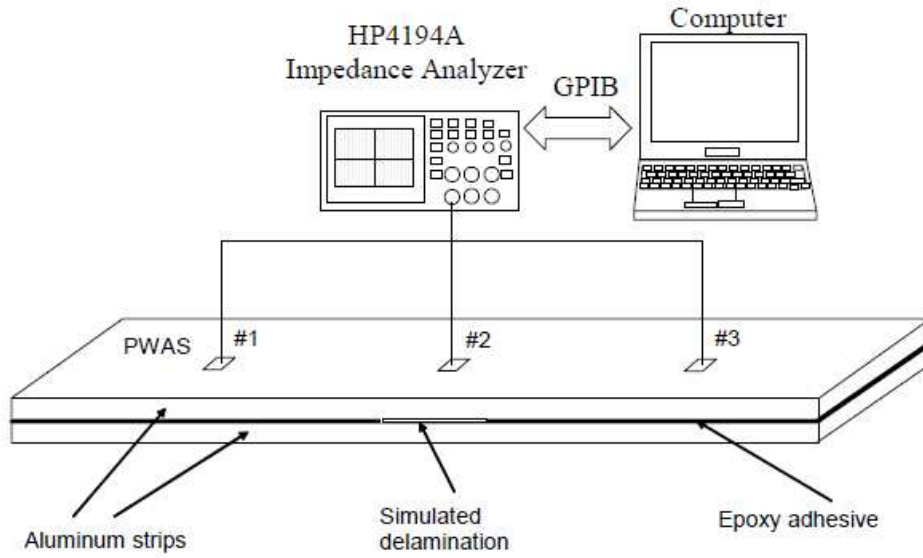


*Figure 95: Instrumentation set-up*
*Source: Cuc (2010)*
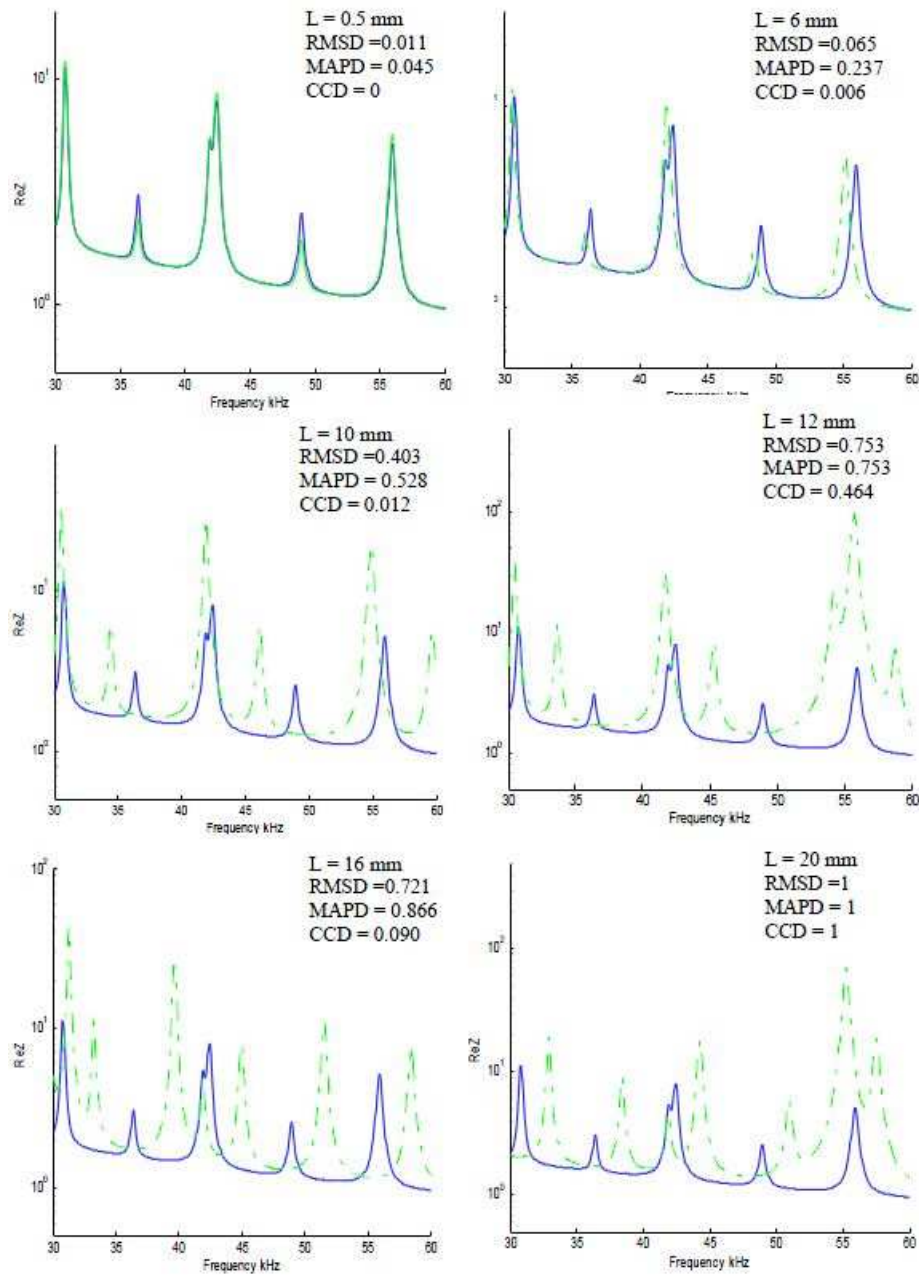
***Figure 96: Changes in the damage indices and the real part of the electromechanical impedance for different damage lengths (dotted line is the damaged case; solid line is the pristine case).Source: Cuc (2010)***

Cuc (2010) plotted the analytical electromechanical impedance results for a narrower frequency interval of 30 kHz to 60 kHz to the changes in the impedance spectra due to increased damage. (Figure 96). The electromechanical impedance spectra

display amplified frequency response changes as the damage increases. Moreover, author found the following changes due to damage growth: peak shifts, usually to the left, indicative of increased structural stiffness, peak splitting or coalescence, increase in peak heights and appearance of new peaks.
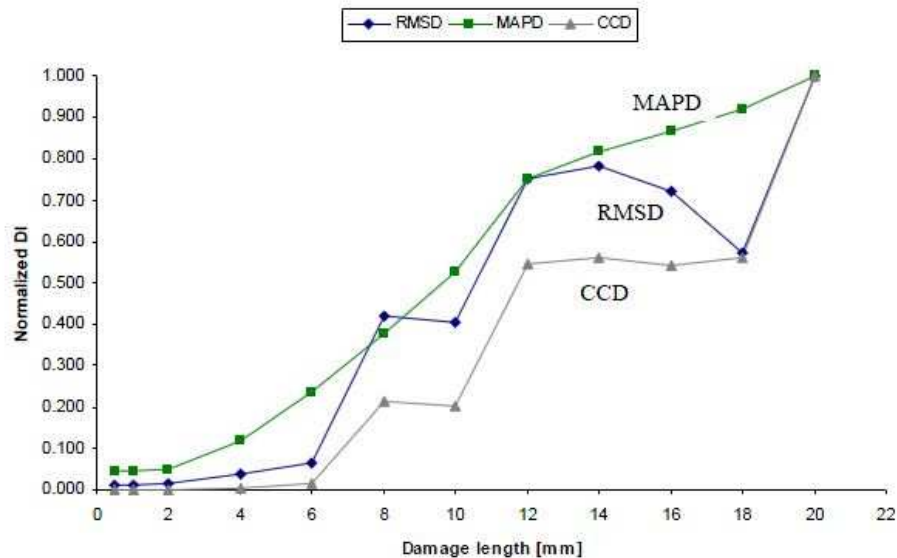


*Figure 97: DI comparison for different damage lengths. Source: Cuc (2010)*

In addition, Cuc (2010) finds that the values of the damage indices are also varying with the change in the damage size. A comparison of all three DI's in Cuc(2010) is presented in Figure 97 indicates that all three damage indices modify with the increase in damage length. However, each of the DI curves has a different shape. The only DI that shows steady increase with the damage length is the mean absolute percentage deviation (MAPD). The other two, RMSD and CCD, are not monotonic with damage length; this result is credited to the fact that they are not as sensitive to the small unceasing variations in the electromechanical impedance range but only to the more sudden ones.

144
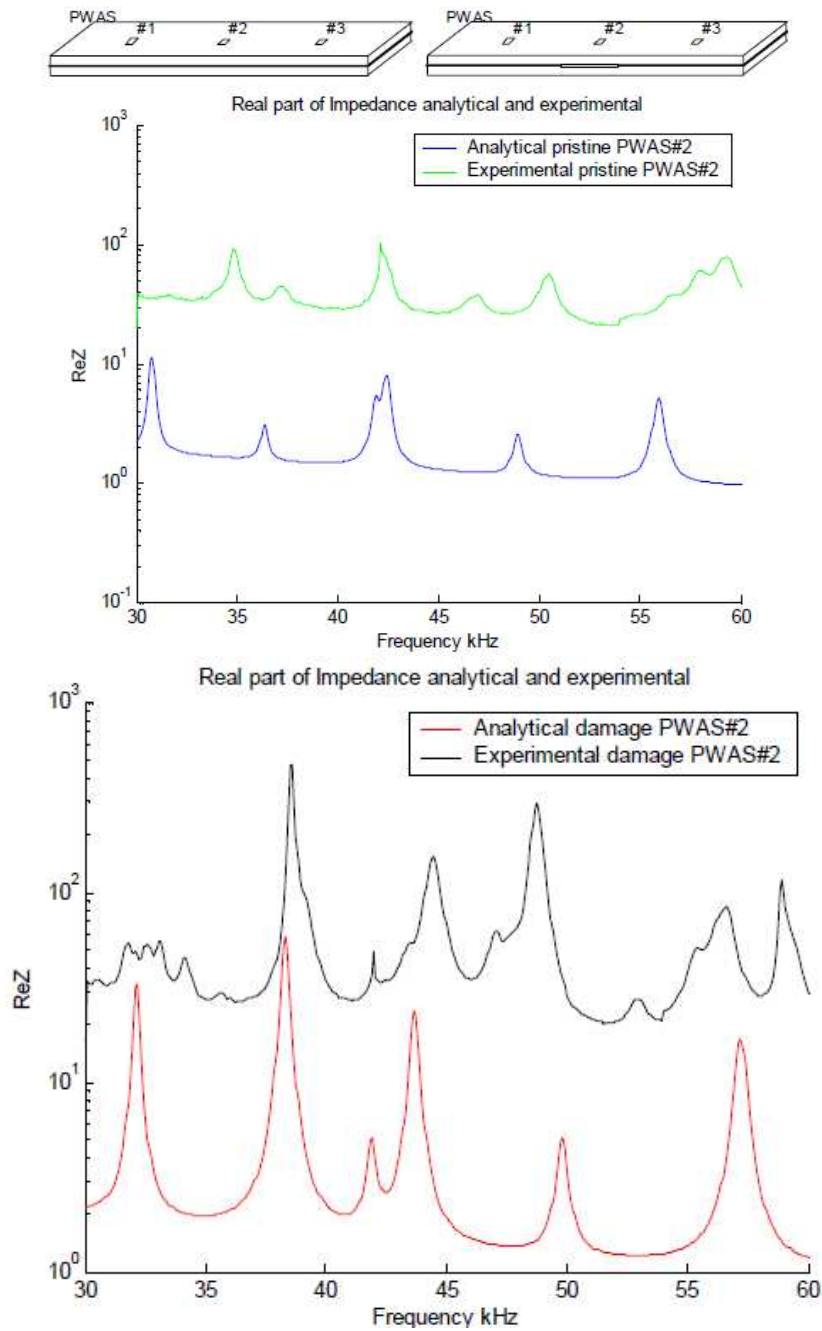
*Figure 98: Comparison between the analytical and experimental electro-mechanical impedance spectrum for PWAS #2: (top) pristine specimen; (bottom) damaged specimen Source: Cuc (2010)*

# 6. Literature Review of Fiber Optic Bragg Grating Sensors (FBG)

Fiber optic is one predominant damage detection technique for composite structures. Kuang (2003) states that optical fiber sensors are flexible, small and thus can be integrated into composite materials for damage detection. Among the various types of optical fiber sensors, the fiber Bragg gratings (FBG) are the primary method used to monitor structures for damage.

## 6.1 Features of Fiber Bragg Gratings

The fiber brag grating sensors (FBGS) are becoming more and more utilized in the field of experimental stress analysis because they are well suited for composites. Kreuzer (2007) provides a review of the FBG sensors and discusses their special strengths and weaknesses compared to alternative methods (e.g. strain gage). He also provides details on measuring FBG and strain gages at the same time. Kreutzer (2007) mentions that the main superior advantage of FBG is the fact that they are immune to electro-magnetic interference, even lighting interference and thus they are adequate for special applications in the aerospace and navy industry. Besides, Kreutzer (2007) and other authors mention other important strengths of FBG such as: FBG match well with the new composite materials (carbon and fiber glass), can measure very high strain, are of small size and light, intrinsically passive, and no electrical power needed. Also, they are not distance dependent, can provide long-term stability, low magnetic field

interference, and are easy to install. Special FBG versions also present good corrosion and resistance to extreme temperatures.

Since FBGs are used by monitoring shifts in optical wavelength, Guemes et al. (2010) and Ciang (2009) find that FBG does not suffer problems typical for plague electrical strain gages, such as signal attenuation, background noise, electrical interference, and power surges.

Some drawbacks though to using FBG are the fact that they present high temperature dependency, cannot provide self-compensation of apparent strain, show high sensitivity to lateral forces or pressure, and are expensive.

## 6.2 FBG Sensors Functional Principle

The FBG consists of a very small inner core (which has a high reflection index caused by germanium dopping) and an outer part of pure glass. The glass fiber is coated with acrylate, polyimide, or ORMOCER (organic modulated ceramic) to protect it against the water. In order to measure the strain, the sensor should be securely bonded to the specimen. Each individual fringe reflects a very small part of the incoming wavelength.

The FBG presents multiplexing aptitude and can sense strain in only one small region of the fiber, characteristics that permit strain mapping over the entire area on which the fibers are placed. FBGs are formed by using UV light to generate multiple mirrors over the length of the fiber which reflects only a slim part of a broadband light source transmitted through the fiber. Figure 99 shows the schematic of a fiber bragg grating and Figure 100 presents the functioning principle of a FBG.
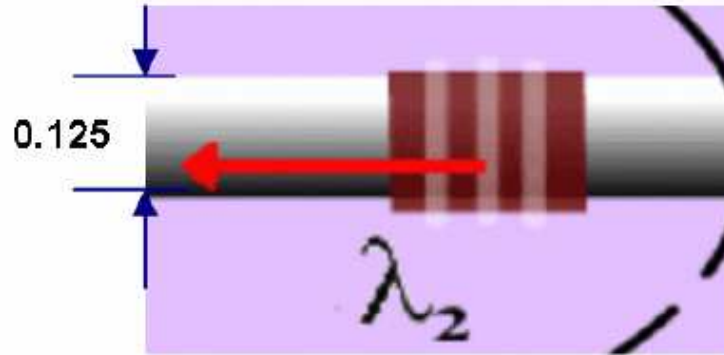
*Figure 99: Fiber Bragg Grating Schematic*
*Source: Kreuzer (2007)*
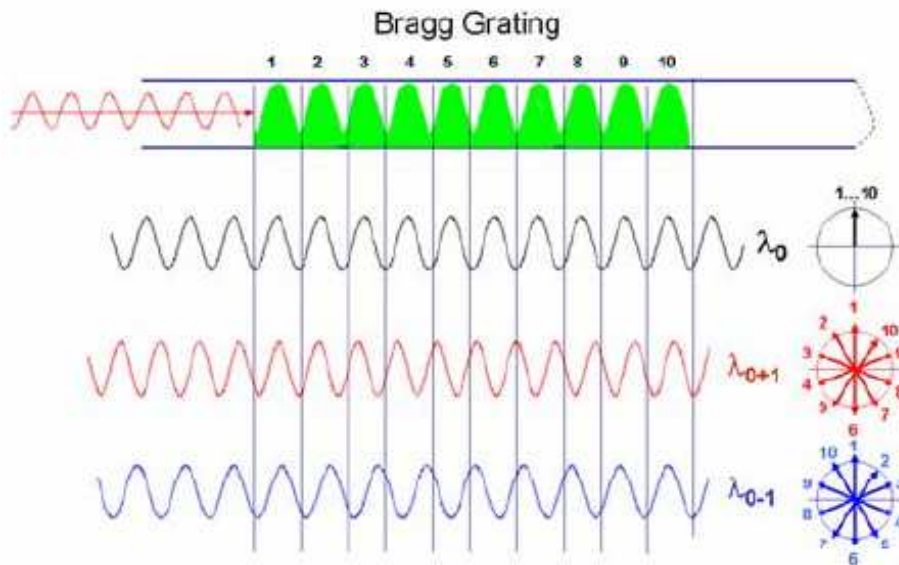


*Figure 100: Functioning Principle of Fiber Bragg Grating*
*Source: Kreuzer (2007)*

## 6.3 METHODS TO INDUCE FIBER OPTIC BRAGG GRATINGS

In order to induce the fiber optic bragg gratings, a Excimer laser is used and the interference can be generated via the phase mask or by slitting laser beams.

### 6.3.1 BRAGG GRATING INDUCED BY A LASER AND A PHASE MASK

In the case of the bragg grating induced by a laser and a phase mask, Kreuzer (2007) states that "the standard procedure to produce high reflections is to dismantle a standard telecom fiber (remove the acrylate and polyimide coating), expose to the fiber

148

to UV interference pattern and then embed it again in the suited coating" (see Figure 101). It is important to mention that when measuring strain with FBG, it is best to use polyimide coating, rather than acrylate since acrylate is too soft and cannot transfer very well the strain from specimen to fiber, in particular when having high temperature.
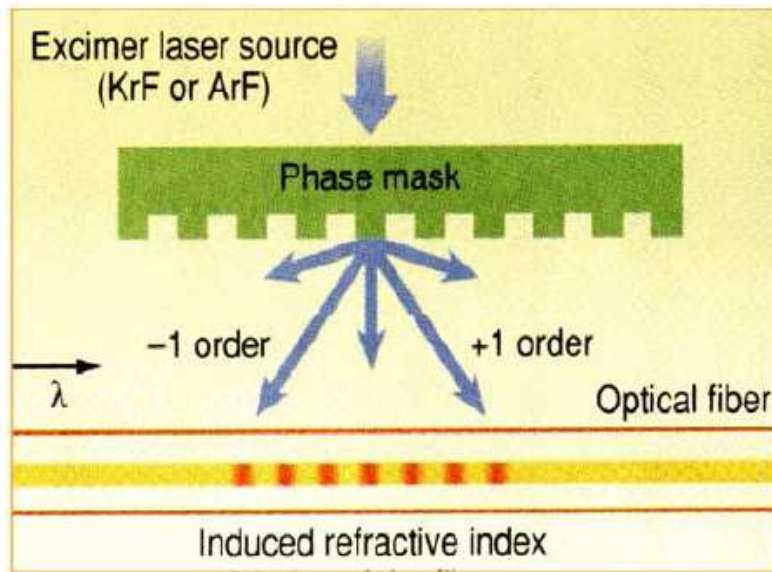


*Figure 101: Bragg grating induced by a laser and a phase mask*
*Source: Kreuzer (2007)*

Due to the energy to which the FBG is exposed by using this method, a 0.01-0.1 change in the reflection index will occur. In order to avoid this problem, a second method was developed, the FBG gratings produced on the fly.

### 6.3.2 FBG GRATINGS PRODUCED ON THE FLY

Using the FBG grating produced on the fly method, the inscription occurs on the fly during the fiber pulling process (Figure 102) and after the fiber is inserted into the coating. For this method, no additional dismantling process is needed.
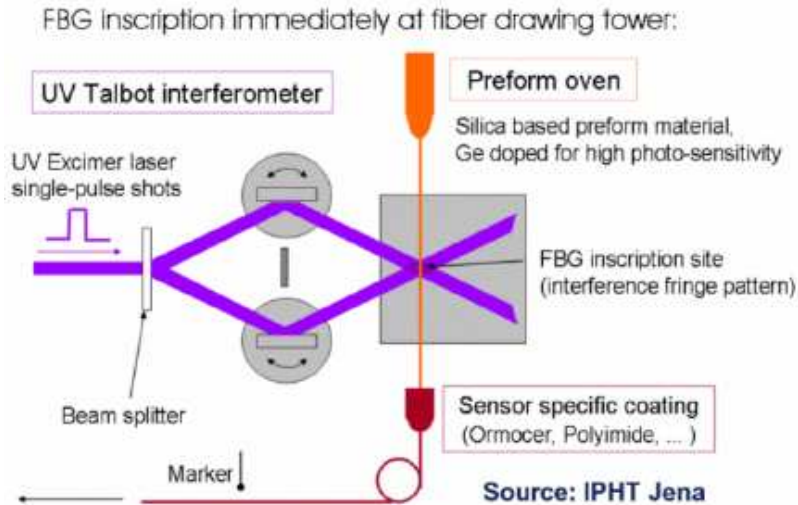
*Figure 102: FBG grating produced on the fly*
*Source: Kreuzer (2007)*

This technique implies that only one inscription UV laser flash is triggered for each bragg grating uses ORMOCER (organic modulated ceramic) as primary coating material due to the fact that its Young's modulus is high.

## 6.4 MEASURING SYSTEM FOR FBG SENSORS

There are two main approaches to read the strain from the fiber. In the first approach, the mirrors (grating) can be produced in such a way so as each grating reflects a different frequency of the incoming light and thus the strain measurements for each grating can be done individually. In the second approach, all gratings are generated so that they reflect the same frequency. Figure 103 show a strain field produced using this second approach.
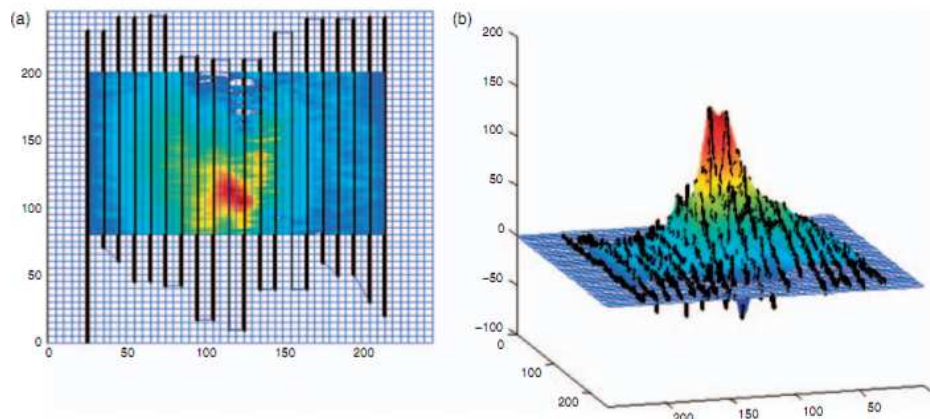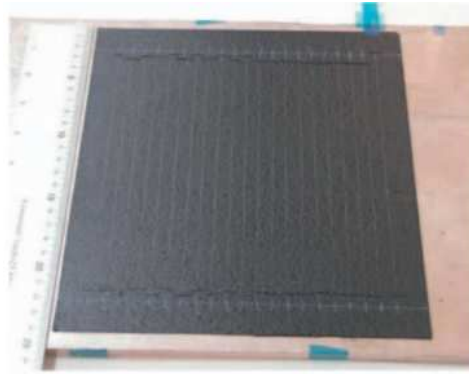
*Figure 103: Network created by one fiber to map the strain on the surface of the composite plate Guemes et al. (2010)*

FBG is designed to work with minimal instrumentation, which makes them very useful in health monitoring of composite structure. For example, they are good at detecting delaminations and impact damage as shown in Figure 104 from Guemes et al. (2010).

Also, due to the optical nature of these sensors, the strain readings are not predisposed to drift during a long-term test. Recent research in the field focuses on the use of FBGs for real time impact detection and acoustic emission detection.
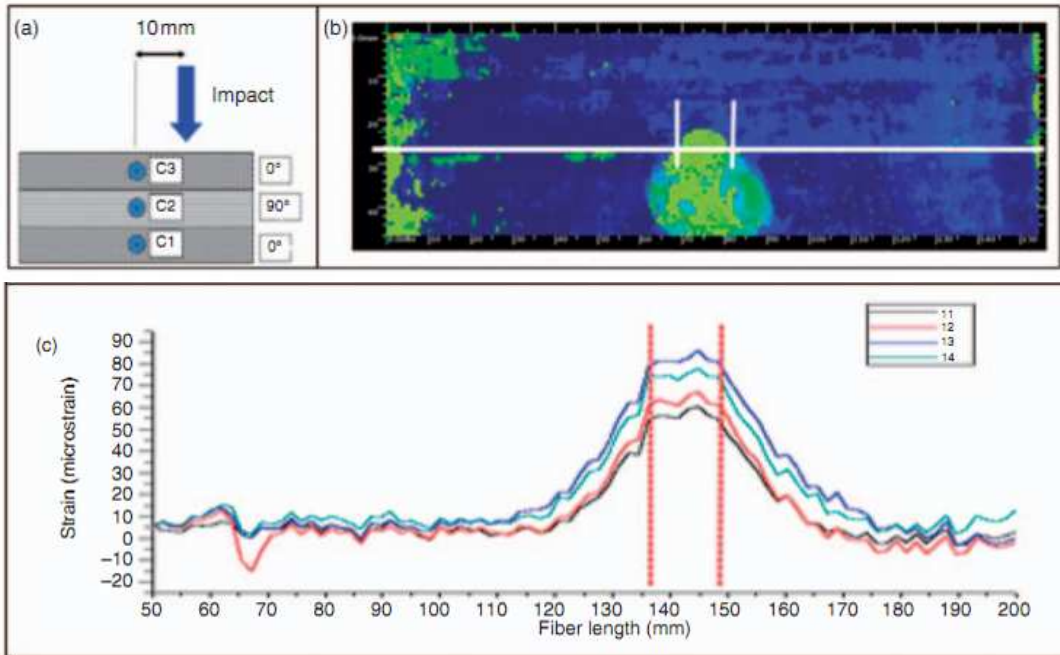
*Figure 104: (a) Ultrasonic C-scan of an impacted area. (b) Strain increase in the impacted area measured by a FBG sensor; Source: Guemes et al. (2010)*

## 7. Admittance and Impedance Calculation Based on the Dynamic Structural Stiffness

According to Giurgiutiu (2008, page 283), the electrical admittance for a constrained PWAS is

$$Y = i\omega C \left[ 1 - \kappa_{31}^2 \left( 1 - \frac{1}{\varphi \cot \varphi + r} \right) \right]$$

(7.1)

The electrical impedance at the PWAS terminals is

$$Z = \frac{1}{Y} = \frac{1}{i\omega C} \left[ 1 - \kappa_{31}^2 \left( 1 - \frac{1}{\varphi \cot \varphi + r} \right) \right]^{-1}$$

(7.2)

Where $\varphi = \dfrac{\gamma_p l_p}{2}, \quad \gamma_p = \omega \rho_p s_{11}^E$

Following Giurgiutiu (2008, page 280) the frequency-dependent stiffness ratio is

$$r(\omega) = \frac{k_{str}(\omega)}{k_{PWAS}}$$

(7.3)

where $k_{str}$ is the frequency dependent dynamic stiffness of the structure and $k_{PWAS}$ is the PWAS static stiffness determined as

$$k_{PWAS} = \frac{A_p}{s_{11}^E l_p}$$

(7.4)
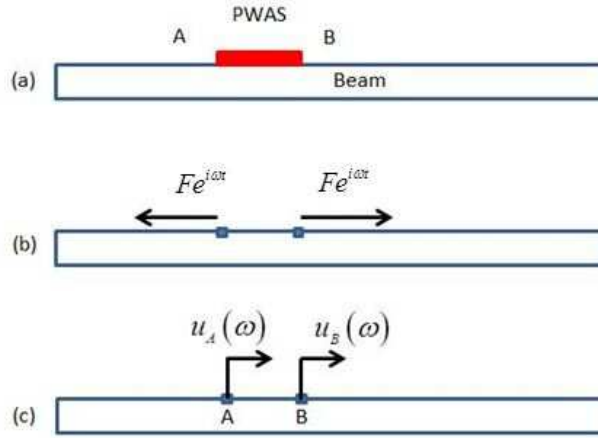
***Figure 105: (a)*** $PWAS$ ***attached to a beam;. (b) pin-end forces*** $F$ ***acting on the beam at PWAS ends; (c) displacement*** $u_A$ ***and*** $u_B$ ***used to calculate*** $PWAS$ ***expansion***

$$u_{PWAS} = u_B - u_A$$

For a $PWAS$ attached to a beam as shown in Figure 105 the structural stiffness $k_{str(\omega)}$ is calculated by taking the ratio between the applied force $F$ and the frequency dependent response $u_{PWAS(\omega)}$. First, we calculate the frequency response function, $FRF$, i.e.,

$$FRF(\omega) = \frac{u_{PWAS}(\omega)}{F} \tag{7.5}$$

where

$$u_{PWAS}(\omega) = u_B(\omega) - u_A(\omega) \tag{7.6}$$

Next we calculate the dynamic structural stiffness $k_{str}(\omega)$ as the inverse of $FRF$, i.e.,

$$k_{str}(\omega) = \frac{F}{u_{PWAS}(\omega)} = FRF^{-1}(\omega) \tag{7.7}$$

The $FRF(\omega)$ can be calculated in various ways. One way to calculate the $FRF(\omega)$ uses the modal expansion. Another way to calculate the $FRF(\omega)$ uses the TMM approach.

In the following sections, we will exemplify these methods and will give numerical results for the test beam presented in Table 5. As a benchmark, we perform a set of experiments on a steel beam instrumented with a PWAS as described in the next section.

**Table 5: Test beam for numerical trials**

| MATERIAL | | PWAS |
|---|---|---|
| Material Properties | SS 304 | APC-850 |
| Elastic properties | E/v | E1/E2/v12/v21 |
| Gpa | 200/0.3 | 64.5/64.5/0.3/0.3 |
| Damping Coefficient | $\xi$ | $\xi 1/\xi 2/\xi 12$ |
| Elastic Properties with Damping | 0.01 | 0.001/0.01/0.01 |
| Mass Density | 7750 | $p_p = 7500$ |
| Permittivity | - | $S_{11}^{E} = 1750*8.85*10^{-12}$ |
| Coupling Terms: d33 and d31 | - | $400*10^{-12}/ -175*10^{-12}$ |
| Dimensions (Length, Height, Width) | L = 100 mm;   h = 2.035 mm;   b = 8 mm | $l_p = 8$mm; $h_p = 0.2$mm |

| | |
|---|---|
| PWAS location | 60 mm from o side of the beam |

## *7.1* BENCHMARK E/M ADMITTANCE EXPERIMENTS ON A STEEL BEAM

In this section, we conduct the experiment that serves as benchmark for all theoretical methods. We machined a stainless steel (SS) 304 beam specimen (Figure 107), having a length of 100 mm, width of 8 mm and height of 2.035 mm and we keep precision around 0.1 mm for dimensions, flatness, and parallelism (the minimum chamfer possible). We bonded a PWAS (7x7x0.2 mm) from one side of the beam at 60 mm and then excite it between 10 to 100 kHz. We collected the impedance and

admittance using a HP spectrum / impedance analyzer and imported results into MATLAB for comparison with the modal expansion, FEM and TMM results.

As part of the experiment, a small beam specimen was machined out of 304 stainless steel (100mx8x2.035 mm3) and a PWAS was bonded to the beam and the frequency testing range was 10 to 100 kHz. In Figure 106 and Figure 107 we have the experimental setup and the beam specimen with bonded PWAS.
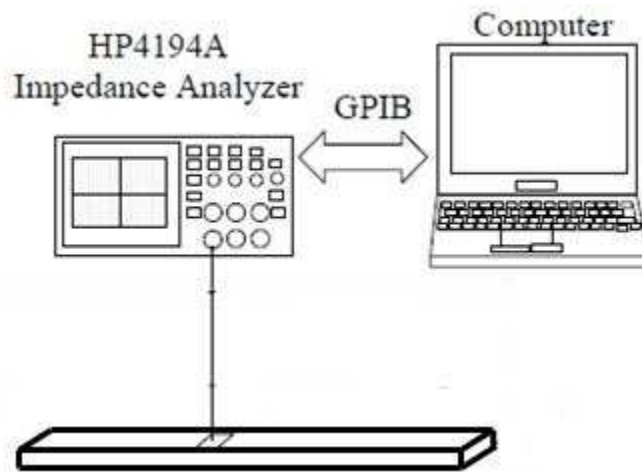


*Figure 106: Instrumentation set-up*
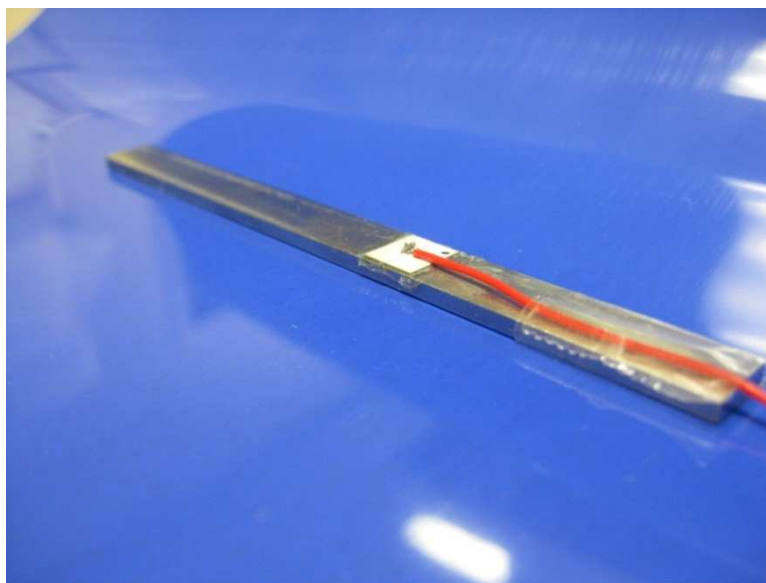


*Figure 107: Beam Specimen with bonded PWAS*

In Figure 108, we show a graph plotting the admittance results from the HP spectrum / impedance analyzer (Re Y). As shown, we obtain 13 values for the natural frequencies between 10 and 100 kHz, which includes both flexural and axial resonance frequencies.
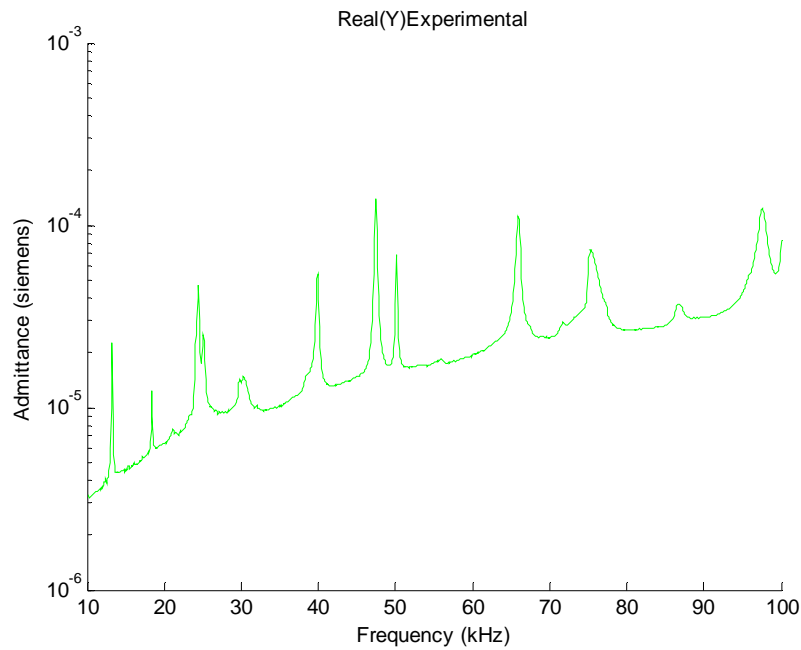


**Figure 108: Experiment –Admittance (Re Y)**

## 7.2 ADMITTANCE CALCULATION VIA MODAL EXPANSION

The $PWAS$ excitation of Figure 109 induces both axial vibration $u$ and flexural vibration $w$ in the beam.
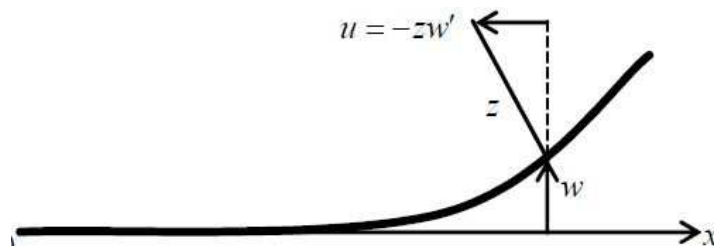


**Figure 109: Horizontal displacement induced by flexure**
**Source: Giurgiutiu (2008)**

In order to proceed with the computation of the frequency response function, $FRF(\omega)$, we find the total in-plane displacement $u_T$ on the top of the beam where the PWAS is located. The total displacement on the top of the beam is the superposition of the axial displacement $u$ and the rotation $w'$.

$$u_T = u + \frac{h}{2}w'$$
(7.8)

For a PWAS attached to a beam, the differential displacement between two points $A$ and $B$ representing the terminals of the PWAS is

$$u_{PWAS}(x) = u_B(x) - u_A(x) = u_B(x_2) - u_A(x_1)$$
(7.9)

From (7.8), (7.9) becomes

$$u_{PWAS} = u(x_2) - u(x_1) - \frac{h}{2}\left[w'(x_2) - w'(x_1)\right]$$
(7.10)

Using (1.29) and (7.10), we can get the axial displacement u and the rotation $w'$ at the two locations x1 and x2. We substitute these values into Equation (7.10) and get

$$
u_{PWAS} = \frac{\hat{N}_P}{\rho A}\left[\sum_j \frac{U_j(x_2) - U_j(x_1)}{(1+ig)\omega_j^2 - \omega^2}U_j(x_2) - \sum_j \frac{U_j(x_2) - U_j(x_1)}{(1+ig)\omega_j^2 - \omega^2}U_j(x_1)\right]e^{i\omega t}
$$
$$
+ \frac{h}{2}\frac{\hat{M}_P}{\rho A}\left[\sum_j \frac{W_j'(x_2) - W_j'(x_1)}{(1+ig)\omega_j^2 - \omega^2}W_j(x_2) - \sum_j \frac{W_j'(x_2) - W_j'(x_1)}{(1+ig)\omega_j^2 - \omega^2}W_j(x_1)\right]e^{i\omega t}
$$
(7.11)

By calculations and simplifications, the total axial displacement is

$$
u_{PWAS} = \frac{F_P}{\rho A}\left\{\sum_j \frac{\left[U_j(x_2) - U_j(x_1)\right]^2}{(1+ig)\omega_j^2 - \omega^2} + \left(\frac{h}{2}\right)^2 \sum_j \frac{\left[W_j'(x_2) - W_j'(x_1)\right]^2}{(1+ig)\omega_j^2 - \omega^2}\right\}
$$
(7.12)

The frequency response function $FRF(\omega)$ is

$$FRF(\omega) = \frac{1}{\rho A}\left\{\sum_j \frac{\left[U_j(x_2)-U_j(x_1)\right]^2}{(1+ig)\omega_j^2-\omega^2} + \left(\frac{h}{2}\right)^2 \sum_j \frac{\left[W_j'(x_2)-W_j'(x_1)\right]^2}{(1+ig)\omega_j^2-\omega^2}\right\}^{-1}$$

(7.13)

For the test beam of Table 5,we combine the axial and flexural vibrations and we obtain in MATLAB the frequency function response as per Figure 110. Next, we use the FRF results to calculate the admittance.
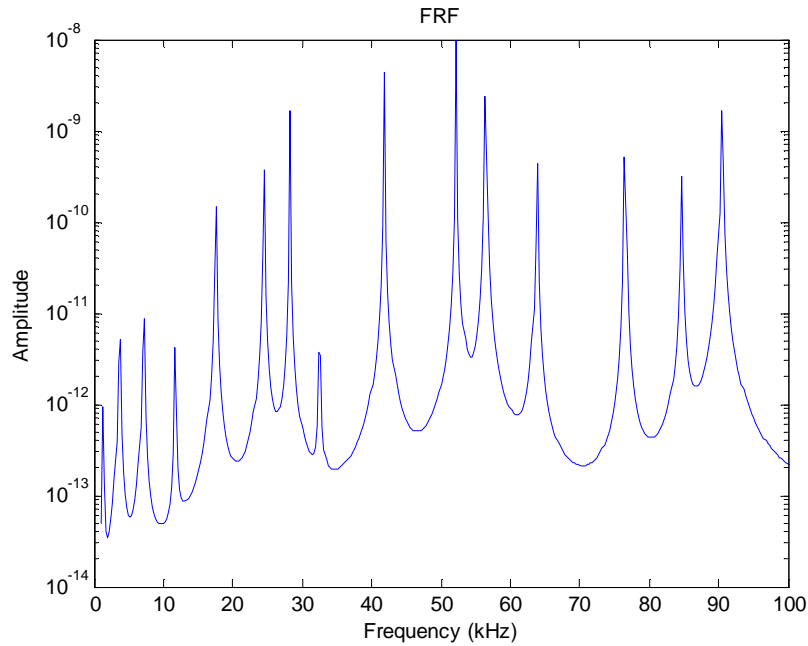


**Figure 110: Frequency Response Function,** $\left|FRF(\omega)\right|$

Based on the results, we obtain for the frequency range 10 and 100 kHz a total of 13 frequencies, out of which 3 are axial and 10 are flexural natural frequencies. By comparing these with the experimental results, we can conclude that there is a very good match in terms of accuracy with the experimental values (13 frequencies).

The dynamic stiffness of the structure is $k_{str}=1/FRF$.

$$k_{str}(\omega) = \frac{F_{PWAS}}{u_{PWAS}(\omega)} =$$

$$= \rho A \left\{ \sum_j \frac{\left[ U_j(x_2) - U_j(x_1) \right]^2}{(1+ig)\omega_j^2 - \omega^2} + \left( \frac{h}{2} \right)^2 \sum_j \frac{\left[ W_j'(x_2) - W_j'(x_1) \right]^2}{(1+ig)\omega_j^2 - \omega^2} \right\}^{-1} \quad (7.14)$$

Since we now know the frequency response function of the structure, we can relate the mechanical impedance of the structure to the electrical impedance of the sensor.

Using the frequency function response, we calculate the admittance (Re Y) in MATLAB as shown in Figure 111.
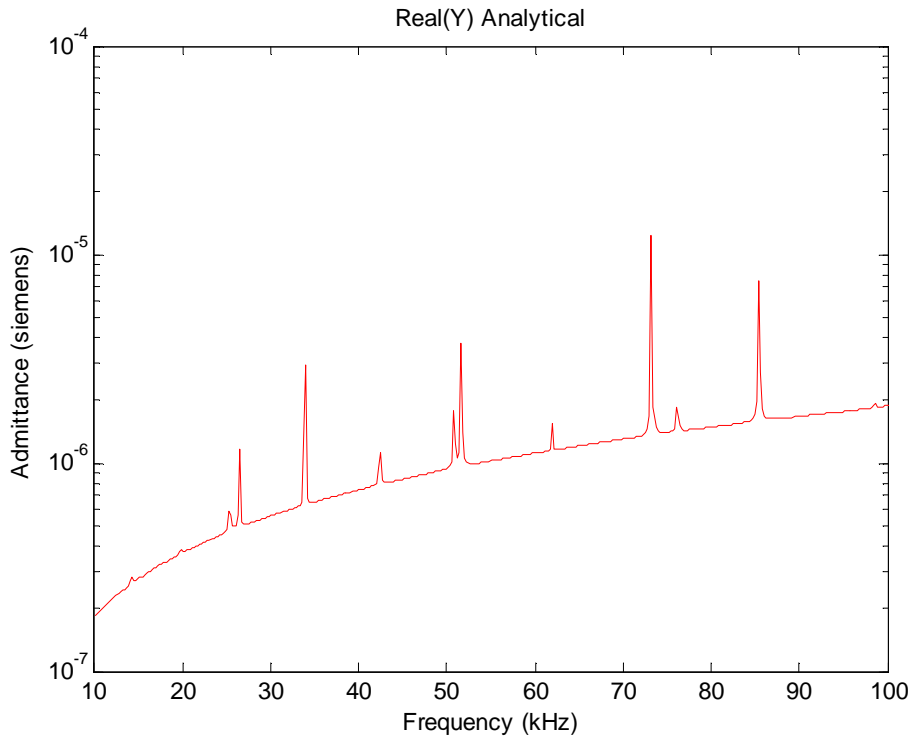


*Figure 111: Modal Expansion Solution – Admittance (Re Y)*

## 7.3 ADMITTANCE CALCULATION VIA TRANSFER MATRIX METHOD

In this part we calculate electromechanical admittance for a uniform beam via the transfer matrix method approach. On top of the beam, we attach a PWAS transducer which will apply a force $F_P$ on the structure as shown in Figure 112. The field transfer matrices are calculated as shown in Section 4.1.1.
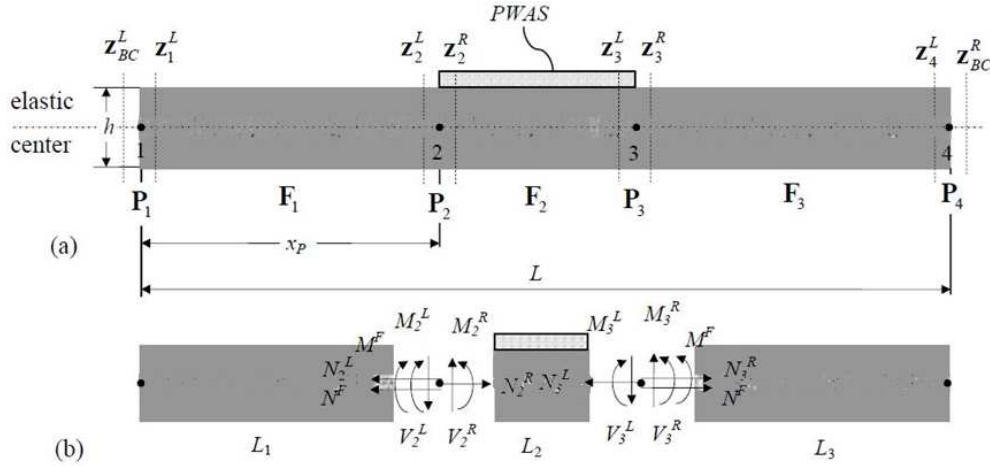


**Figure 112: Uniform beam under PWAS excitation:**
**(a) schematic of beam elements, (b) free-body diagram**

In order to determine the point transfer matrices we apply the compatibility conditions and the equilibrium equations to each node.

Thus, for node #1 we have

Compatibility conditions

$$u_1^R = u_{BC}^L$$
$$\varphi_1^R = \varphi_{BC}^L \qquad\qquad (7.15)$$
$$w_1^R = w_{BC}^L$$

Equilibrium equations

$$\sum F_x : \quad N_1^R = N_{BC}^L \qquad\qquad (7.16)$$

$$\sum V_y : \quad V_1^R = V_{BC}^L \qquad\qquad (7.17)$$

161

$$\sum M: \quad M_1^R = M_{BC}^L \qquad (7.18)$$

Equations (7.15) through (7.17) can be written as

$$\begin{bmatrix} u \\ w \\ \varphi \\ N \\ V \\ M \end{bmatrix}_1^R = \begin{bmatrix} 1 & 0 & 0 & 0 & 0 & 0 \\ 0 & 1 & 0 & 0 & 0 & 0 \\ 0 & 0 & 1 & 0 & 0 & 0 \\ 0 & 0 & 0 & 1 & 0 & 0 \\ 0 & 0 & 0 & 0 & 1 & 0 \\ 0 & 0 & 0 & 0 & 0 & 1 \end{bmatrix} \cdot \begin{bmatrix} u \\ w \\ \varphi \\ N \\ V \\ M \end{bmatrix}_{BC}^L \qquad (7.19)$$

$$\mathbf{z}_1^R = \mathbf{P}_1 \cdot \mathbf{z}_{BC}^L, \text{ where } \mathbf{P}_1 = \mathbf{I} \qquad (7.20)$$

Now for node #2 we have

Compatibility conditions

$$\begin{aligned} u_2^R &= u_2^L \\ \varphi_2^R &= \varphi_2^L \\ w_2^R &= w_2^L \end{aligned} \qquad (7.21)$$

Equilibrium equations

$$\sum F_x: \quad N_2^R = N_2^L + N^F \qquad (7.22)$$

$$\sum V_y: \quad V_2^R = V_2^L \qquad (7.23)$$

$$\sum M: \quad M_2^R = M_2^L + M^F \qquad (7.24)$$

Equations (7.21) through (7.23) can be written as

$$\begin{bmatrix} u \\ w \\ \varphi \\ N \\ V \\ M \end{bmatrix}_2^R = \begin{bmatrix} 1 & 0 & 0 & 0 & 0 & 0 \\ 0 & 1 & 0 & 0 & 0 & 0 \\ 0 & 0 & 1 & 0 & 0 & 0 \\ 0 & 0 & 0 & 1 & 0 & 0 \\ 0 & 0 & 0 & 0 & 1 & 0 \\ 0 & 0 & 0 & 0 & 0 & 1 \end{bmatrix} \cdot \begin{bmatrix} u \\ w \\ \varphi \\ N \\ V \\ M \end{bmatrix}_2^L + \begin{bmatrix} 0 \\ 0 \\ 0 \\ N^F \\ M^F \\ 0 \end{bmatrix} \qquad (7.25)$$

$$\mathbf{z}_2^R = \mathbf{P}_2 \cdot \mathbf{z}_2^L + \mathbf{P}_1^F \qquad (7.26)$$

$$\mathbf{P}_1^F = \begin{bmatrix} 0 \\ 0 \\ 0 \\ N^F \\ 0 \\ M^F \end{bmatrix}$$

where $\mathbf{P}_2 = \mathbf{I}$ and the forcing term $\mathbf{P}_1^F$ is

Then for node#3 we have

Compatibility conditions

$$u_3^R = u_3^L$$
$$\varphi_3^R = \varphi_3^L \qquad (7.27)$$
$$w_3^R = w_3^L$$

Equilibrium equations

$$\sum F_x : \quad N_3^R = N_3^L - N^F \qquad (7.28)$$

$$\sum V_y : \quad V_3^R = V_3^L \qquad (7.29)$$

$$\sum M : \quad M_3^R = M_3^L - M^F \qquad (7.30)$$

Equations (7.26) through (7.29) can be written as

$$\begin{bmatrix} u \\ w \\ \varphi \\ N \\ V \\ M \end{bmatrix}_3^R = \begin{bmatrix} 1 & 0 & 0 & 0 & 0 & 0 \\ 0 & 1 & 0 & 0 & 0 & 0 \\ 0 & 0 & 1 & 0 & 0 & 0 \\ 0 & 0 & 0 & 1 & 0 & 0 \\ 0 & 0 & 0 & 0 & 1 & 0 \\ 0 & 0 & 0 & 0 & 0 & 1 \end{bmatrix} \cdot \begin{bmatrix} u \\ w \\ \varphi \\ N \\ M \\ V \end{bmatrix}_3^L + \begin{bmatrix} 0 \\ 0 \\ 0 \\ -N^F \\ 0 \\ -M^F \end{bmatrix} \qquad (7.31)$$

$$\mathbf{z}_3^R = \mathbf{P}_3 \cdot \mathbf{z}_3^L + \mathbf{P}_2^F \qquad (7.32)$$

$$\mathbf{P}_2^F = \begin{bmatrix} 0 \\ 0 \\ 0 \\ -N^F \\ 0 \\ -M^F \end{bmatrix}$$

where $\mathbf{P}_3 = \mathbf{I}$ and the forcing term is

163

Then for node#4 we have

Compatibility conditions

$$
\begin{aligned}
u_{BC}^{R} &= u_{4}^{L} \\
\varphi_{BC}^{R} &= \varphi_{4}^{L} \\
w_{BC}^{R} &= w_{4}^{L}
\end{aligned}
\tag{7.33}
$$

Equilibrium equations

$$\sum F_x: \quad N_{BC}^{R} = N_{4}^{L} \tag{7.34}$$

$$\sum V_y: \quad V_{BC}^{R} = V_{4}^{L} \tag{7.35}$$

$$\sum M: \quad M_{BC}^{R} = M_{4}^{L} \tag{7.36}$$

Equations (7.33) through (7.36) can be written as

$$
\begin{bmatrix} u \\ w \\ \varphi \\ N \\ V \\ M \end{bmatrix}_{BC}^{R}
=
\begin{bmatrix}
1 & 0 & 0 & 0 & 0 & 0 \\
0 & 1 & 0 & 0 & 0 & 0 \\
0 & 0 & 1 & 0 & 0 & 0 \\
0 & 0 & 0 & 1 & 0 & 0 \\
0 & 0 & 0 & 0 & 1 & 0 \\
0 & 0 & 0 & 0 & 0 & 1
\end{bmatrix}
\cdot
\begin{bmatrix} u \\ w \\ \varphi \\ N \\ V \\ M \end{bmatrix}_{4}^{L}
\tag{7.37}
$$

$$\mathbf{z}_{BC}^{R} = \mathbf{P}_4 \cdot \mathbf{z}_{4}^{L} \quad where \quad \mathbf{P}_4 = \mathbf{I} \tag{7.38}$$

In order to calculate the frequency response function we determine the unknown state

vectors: $\mathbf{z}_{BC}^{L}$, $\mathbf{z}_{1}^{R}$, $\mathbf{z}_{2}^{R}$, $\mathbf{z}_{3}^{R}$ and $\mathbf{z}_{BC}^{R}$.

Then we apply the free-free boundary conditions:

$$\text{at } x = 0: \ N_{BC}^{L} = M_{BC}^{L} = V_{BC}^{L} = 0 \ \Rightarrow \ \mathbf{p}_{BC}^{L} = \mathbf{0} \tag{7.39}$$

$$\text{at } x = L: \ N_{BC}^{R} = M_{BC}^{R} = V_{BC}^{R} = 0 \ \Rightarrow \ \mathbf{p}_{BC}^{R} = \mathbf{0} \tag{7.40}$$

After considering the free-free boundary conditions, the corresponding unknown

displacements and internal forces vectors are: $\mathbf{d}_{BC}^{L}$, $\mathbf{d}_{1}^{R}$, $\mathbf{p}_{1}^{R}$, $\mathbf{d}_{2}^{R}$, $\mathbf{p}_{2}^{R}$, $\mathbf{d}_{3}^{R}$, $\mathbf{p}_{3}^{R}$, $\mathbf{d}_{BC}^{R}$.

From (7.20), $\mathbf{p}_1^R = \mathbf{p}_{BC}^L = \mathbf{0}$ and hence we will have seven unknowns $\mathbf{d}_{BC}^L$, $\mathbf{d}_1^R$, $\mathbf{d}_2^R$, $\mathbf{p}_2^R$, $\mathbf{d}_3^R$,

$\mathbf{p}_3^R$, $\mathbf{d}_{BC}^R$ which requires seven equations in order to solve for the unknowns.

Since all the point transfer matrices P are equal with the unity matrix I we will drop them from the future calculations. From the equations (7.14),(7.16), (7.22), and (7.28) we get:

$$\begin{cases} \mathbf{z}_1^R = \mathbf{z}_{BC}^L \\ \mathbf{z}_2^R = \mathbf{z}_2^L + \mathbf{P}_1^F \\ \mathbf{z}_3^R = \mathbf{z}_3^L + \mathbf{P}_2^F \\ \mathbf{z}_{BC}^R = \mathbf{z}_4^L \end{cases}$$
(7.41)

which is expanded into

$$\begin{cases} -\mathbf{d}_{BC}^L + \mathbf{d}_1^R = \mathbf{0} \\ \mathbf{F}_3^{dd} \cdot \mathbf{d}_3^R + \mathbf{F}_3^{dd} \cdot \mathbf{p}_3^R - \mathbf{d}_{BC}^R = \mathbf{0} \\ \mathbf{F}_3^{pd} \cdot \mathbf{d}_3^R + \mathbf{F}_3^{pp} \cdot \mathbf{p}_3^R = \mathbf{0} \\ \mathbf{F}_1^{dd} \cdot \mathbf{d}_1^R - \mathbf{d}_2^R = \mathbf{0} \\ \mathbf{F}_1^{pd} \cdot \mathbf{d}_1^R - \mathbf{p}_2^R = -\mathbf{p}_1^F \\ \mathbf{F}_2^{dd} \cdot \mathbf{d}_2^R + \mathbf{F}_2^{dp} \cdot \mathbf{p}_2^R - \mathbf{d}_3^R = \mathbf{0} \\ \mathbf{F}_2^{pd} \cdot \mathbf{d}_2^R + \mathbf{F}_2^{pp} \cdot \mathbf{p}_2^R - \mathbf{p}_3^R = -\mathbf{p}_2^F \end{cases}$$
(7.42)

(7.42) is a non-homogeneous system of equations and can be written in a matrix form as

$$\mathbf{M} \cdot \mathbf{X} = \mathbf{N}$$
(7.43)

and the unknown column vector $\mathbf{X}$ is

$$\mathbf{X} = \begin{bmatrix} \mathbf{d}_{BC}^L & \mathbf{d}_1^R & \mathbf{d}_2^R & \mathbf{p}_2^R & \mathbf{d}_3^R & \mathbf{p}_3^R & \mathbf{d}_{BC}^R \end{bmatrix}^T$$
(7.44)

From (7.43), the unknown column vector of displacements and internal forces can be solved as

$$\mathbf{X} = \mathbf{M}^{-1} \cdot \mathbf{N}$$
(7.45)

Now that we have the axial and flexural displacements u and w and the rotation $w'$, the total displacement between the two ends of a PWAS attached to the beam at the distances x1 and x2 from LHS end can be calculated as

$$u_{PWAS} = u(x_2) - u(x_1) - \frac{h}{2}\left[w'(x_2) - w'(x_1)\right] \quad or \quad u_{PWAS} = \left(u_3^L - u_2^R\right) - \frac{h}{2}\left(\varphi_3^L - \varphi_2^R\right) \quad (7.46)$$

We divide (7.46) by the excitation force $F$ and we get the frequency response function $FRF(\omega)$:

$$\frac{u_{PWAS}}{F} = \frac{\left(u_3^L - u_2^R\right)}{F} - \frac{\frac{h}{2}\left(\varphi_3^L - \varphi_2^R\right)}{F} \quad (7.47)$$

$$FRF(\omega) = FRF_u(\omega) - FRF_w(\omega) \quad (7.48)$$

Where

$$FRF_u(\omega) = \frac{\left(u_3^L - u_2^R\right)}{F}; \quad and \quad FRF_w(\omega) = \frac{h\left(\varphi_3^L - \varphi_2^R\right)}{2F}. \quad (7.49)$$

The dynamic structural stiffness of the beam can be calculated as

$$k_{str}(\omega) = \frac{1}{FRF(\omega)} \quad (7.50)$$

Given the material properties and the dimensions of the PWAS, the electromechanical impedance is $Z$, while $Y = 1/Z$ represents the admittance.

$$Z = \frac{1}{Y} = \frac{1}{i\omega C}\left[1 - \kappa_{31}^2\left(1 - \frac{1}{\varphi\cot\varphi + r}\right)\right]^{-1} \quad (7.51)$$

where $\varphi = \frac{\gamma_p l_p}{2}, \quad \gamma_p = \omega\rho_p s_{11}^E.$

Using the above procedure and the data shown in Table 5, we obtain the admittance $(\mathrm{Re}\,Y)$ plot shown in Figure 113.

Real(Y) Transfer Matrix
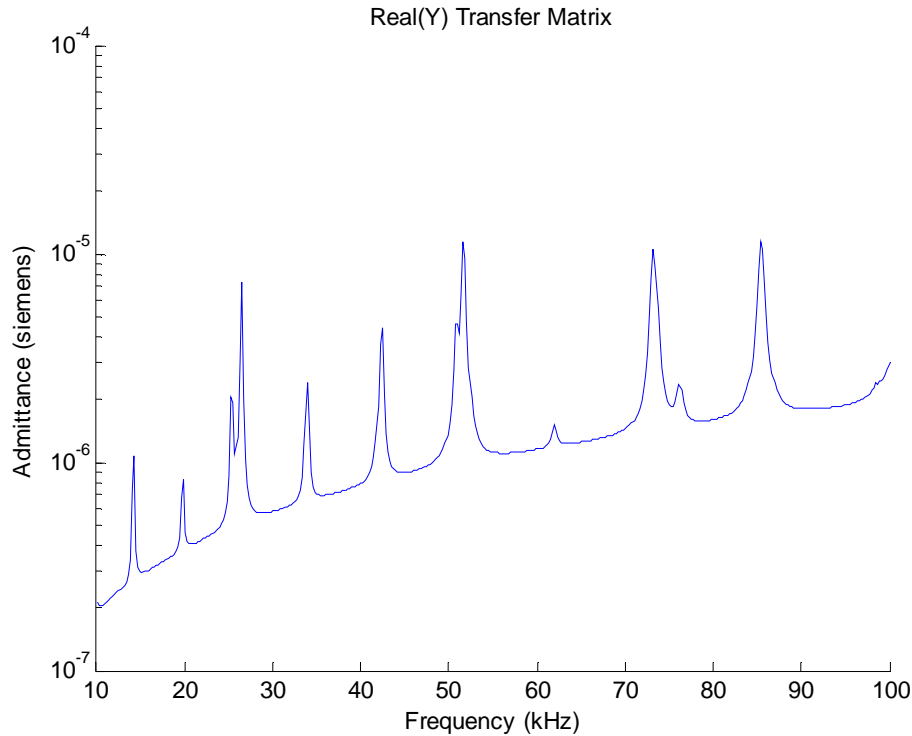
*Figure 113: TMM – Admittance (Re Y)*

As per results shown in Figure 113, we obtain 13 natural frequencies that match

the experimental results and also match the modal expansion solution.

## 7.4 ADMITTANCE CALCULATION VIA FINITE ELEMENT METHOD (FEM)

The FEM approach involves mathematical approximations associated with the

displacement function of a particular element and geometric approximations to the

component shape. A key advantage of FEM is that it can be used to analyze virtually any

structural problem in a routine manner - hence non homogeneous material can be

accommodated as the assembly of elements with different properties is

straightforward. However, it might require increased computational time, large storage

capabilities, and memory limitations.

167

We use the FEM approach (2D and 3D) to calculate the electromechanical admittance. In order to do this, we use the coupled-field FEM where the electromechanical admittance is obtained directly from the coupling between the structure's stress field and the PWAS electrical field. Here, the electrical field of the PWAS is coupled with the mechanical stress field of the structure and a change in one field will generate a change in the other field based on the piezoelectric principles. In 3D, we used 20-node multiphysics SOLID226 element for the PWAS and 20-node SOLID95 element for the beam (Figure 116). A voltage is applied to the two PWAS electrodes. The voltage applied is of unity amplitude. After that, a harmonic analysis is performed and the change with frequency of the electrical charge on the two PWAS electrodes is recorded. In order to be able to use the voltage DOF, the PWAS was modeled using a PLANE13 four nodes element with up to four DOF per node. The beam is modeled using a four node PLANE42 element with two degrees of freedom at each node.

We carry out the harmonic analysis in the frequency range of 10 kHz to 100 kHz and apply a constant damping factor of 0.005 during the simulation. Figure 115 and Figure 117 present the admittance results for the FEM 2D and 3D.
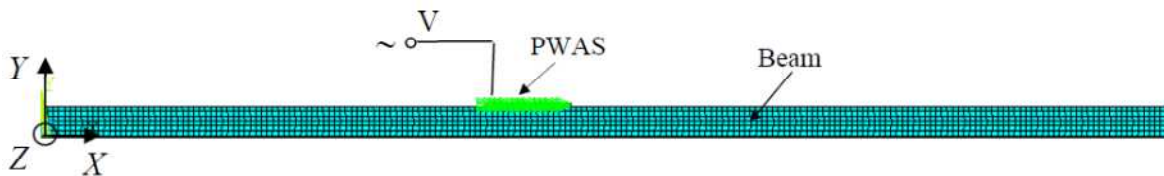


*Figure 114: FEM 2D Approach - Mesh / voltage charge of the PWAS*
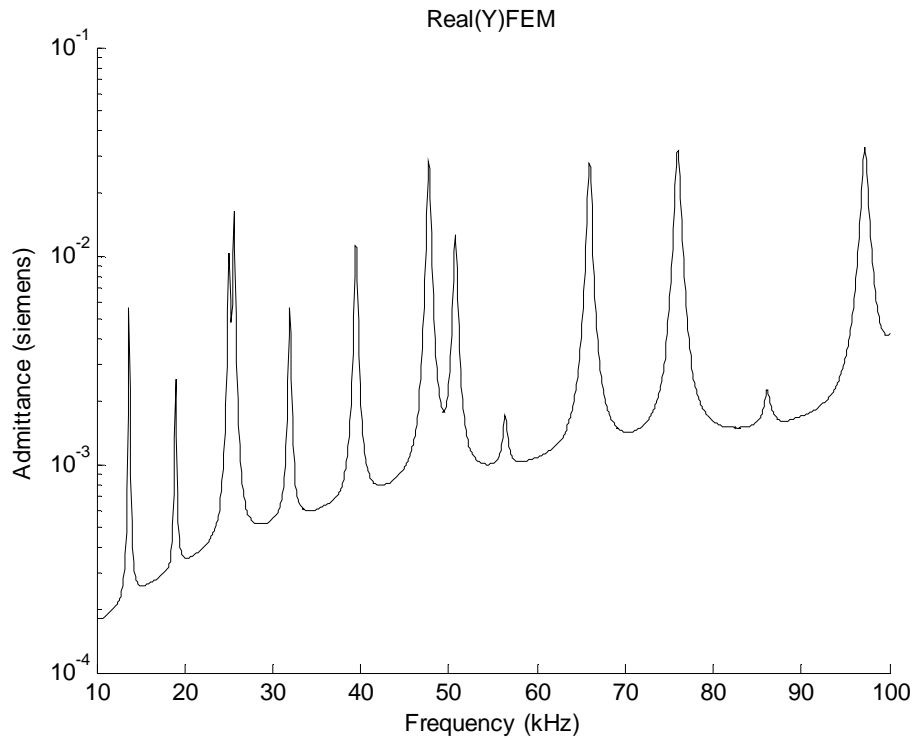
*Figure 115: FEM 2D Admittance (Re Y)*

As can be seen from Figure 115, the FEM 2D approach shows 13 resonance frequencies between 10-100 kHz. Even when increasing the meshing, we obtain the same resonance frequencies and, most importantly, they match the experimental results.
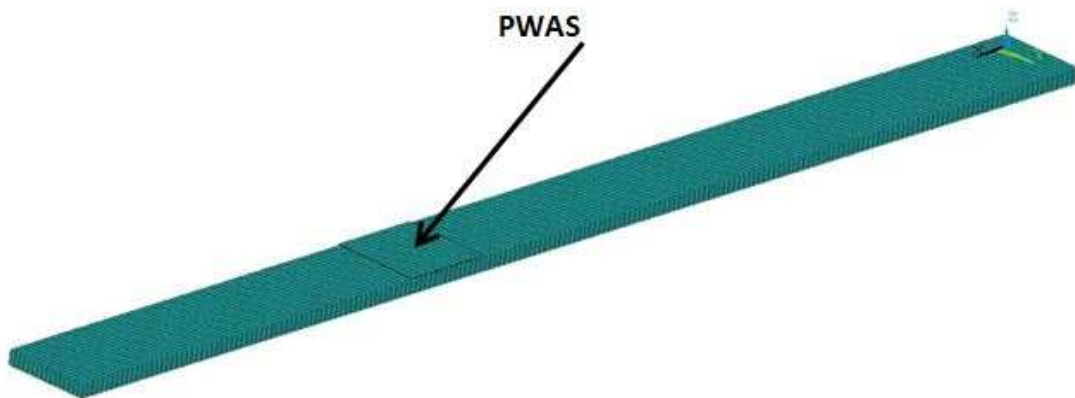


*Figure 116: FEM 3D Approach - Mesh / voltage charge of the PWAS*
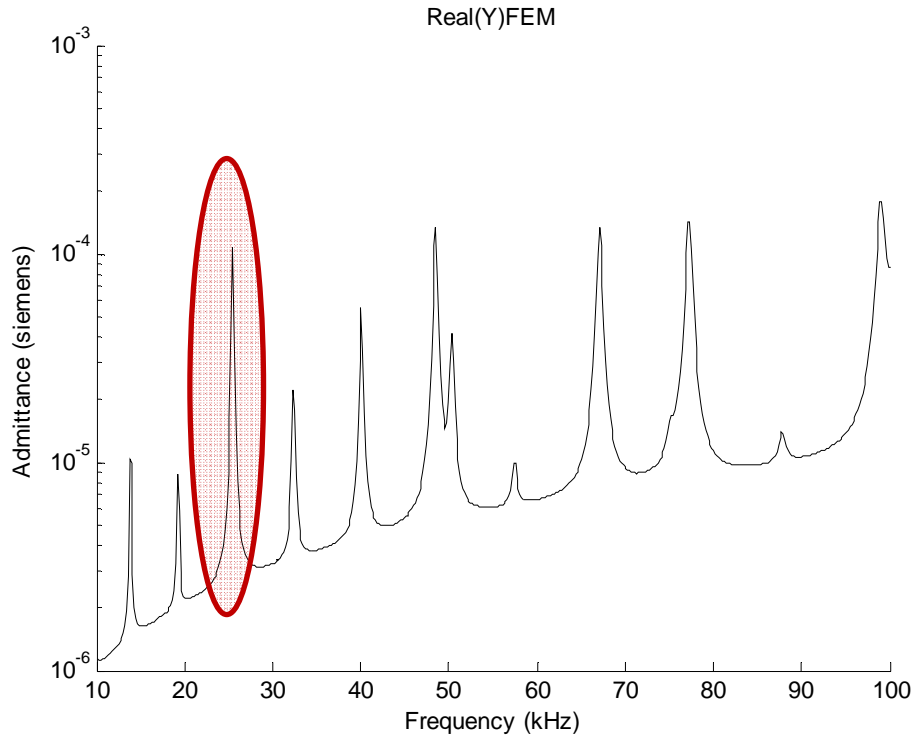
**Figure 117: FEM 3D Admittance (Re Y)**

As can be seen from Figure 117, the 3D approach matches the experimental results, except that it is missing one frequency between 20 and 30 kHz. We increase the meshing and number of points in this area and we run the FEM again and the results are still missing that frequency.

### 7.5 COMPARISON OF ANALYTICAL, TRANSFER MATRIX, FEM AND EXPERIMENTAL RESULTS

Giurgiutiu et al. (2011) focus on modeling the interaction between piezoelectric wafer active sensors (PWAS) and structural waves and vibration. The TMM approach was used to predict the E/M impedance response of a PWAS attached to a free-free beam. Authors compared all methods, the modal expansion method, TMM, FEM, and experimental results and concluded that they all concord (Figure 118), however in the case of E/M impedance modeling, the MP-FEM approach (2D) was found to be closer to

the measurements than the analytical methods (modal expansion and TMM). In addition, it was observed that the 3D MP-FEM gave much better prediction of the vertical position of the dereverberated baseline, but missed the splitting of the peak at ~26 kHz.
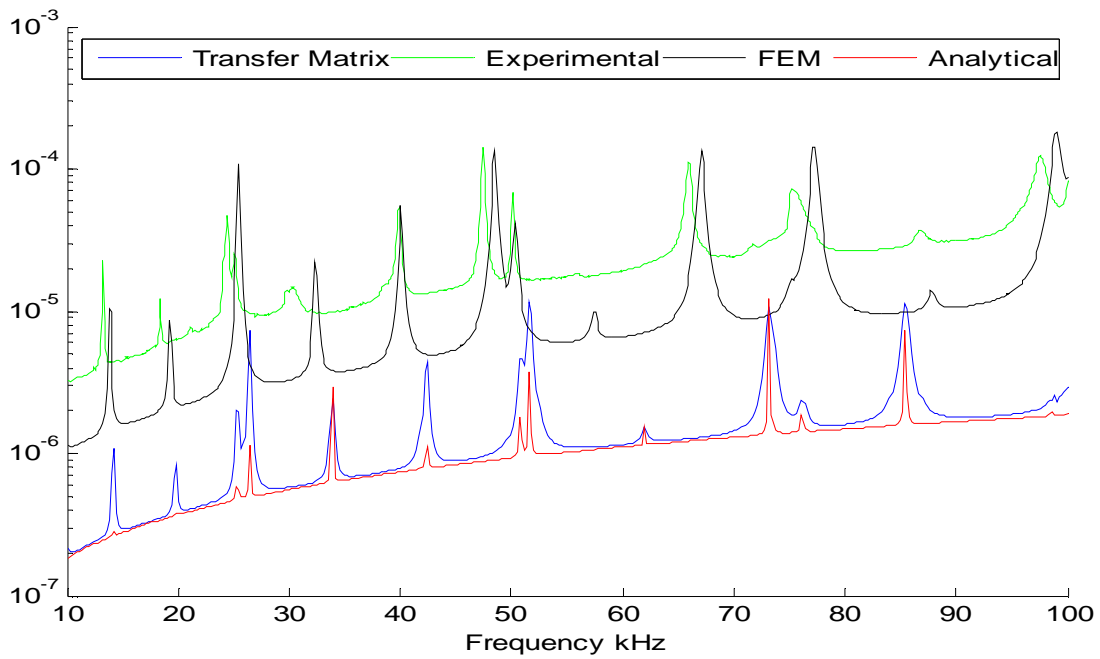


*Figure 118: Experimental admittance compared with predictions by analytical modal analysis, analytical TMM, and 3D MP-FEM; Source: Giurgiutiu et al. (2011)*

## 8. CRITIQUE OF GLOBAL MATRIX METHOD (GMM) PERFORMANCE IN THE CALCULATION OF ELECTROMECHANICAL IMPEDANCE AND ADMITTANCE

This section uses the global matrix method approach (GMM) of Cuc (2010) which uses the electromechanical impedance method to calculate the frequency resonances of a uniform beam. Our focus is on determining the high-frequency behavior of this method in order to identify its limitations. More precisely, we expand the results from a uniform beam in the range of 1-30 kHz from Cuc (2010) to a higher frequency range of 10-100 kHz and beyond, when possible. Cuc (2010) calculated the natural frequencies using a 100 mm length beam.

When extending the frequency range, we notice some limitations due to MATLAB mathematical approximations of the dynamic transformation matrix $\mathbf{B}$. Matrix $\mathbf{B}$ uses hyperbolic 'sin' and 'cos' functions in its calculation and length and frequency are implicit part of the 'sin' and 'cos' functions. In order to check the limitations of GMM using MATLAB, we conduct several tests on the two terms that are part of the $\mathbf{B}$ matrix: the beam length and the frequencies.

### 8.1 CRITIQUE OF SPECTRAL BEHAVIOR AT HIGH FREQUENCIES

First, we look at several beam lengths to see what the maximum frequency that can be calculated is. Using a beam of 100 mm length, we are able to excite it until 112 kHz and obtain all natural frequencies without any MATLAB errors (Figure 119).

172

However, whenever we reach 113 kHz (Figure 120), the errors generated by the functions 'sin' and 'cos' are visible and affect our results.
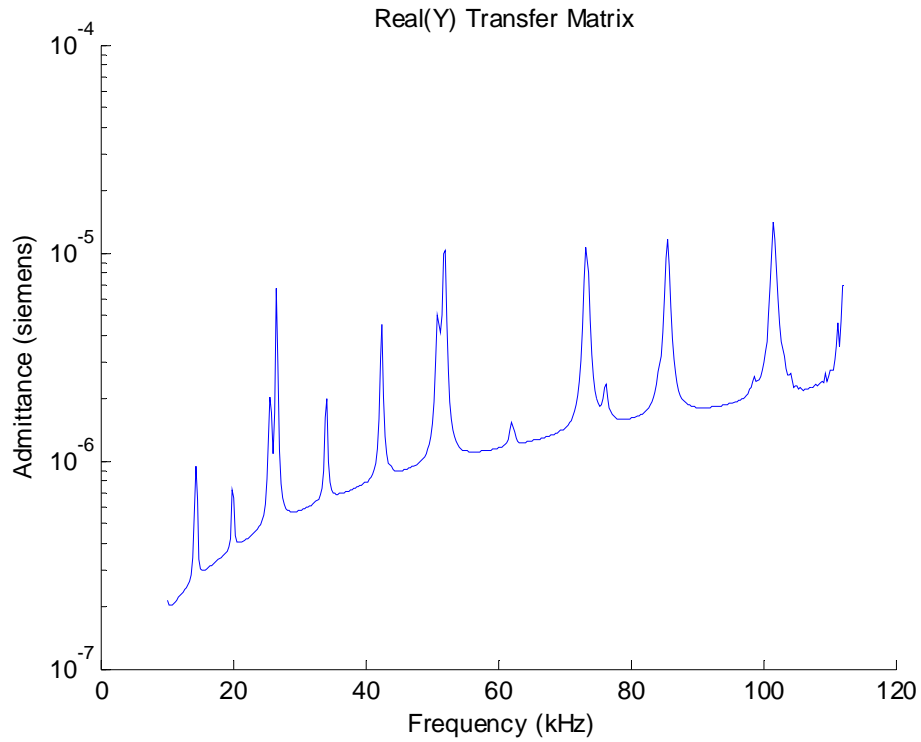


*Figure 119: Adequate numerical behavior for 100 mm 3-segment beam: maximum frequency attained without error is 112 kHz*
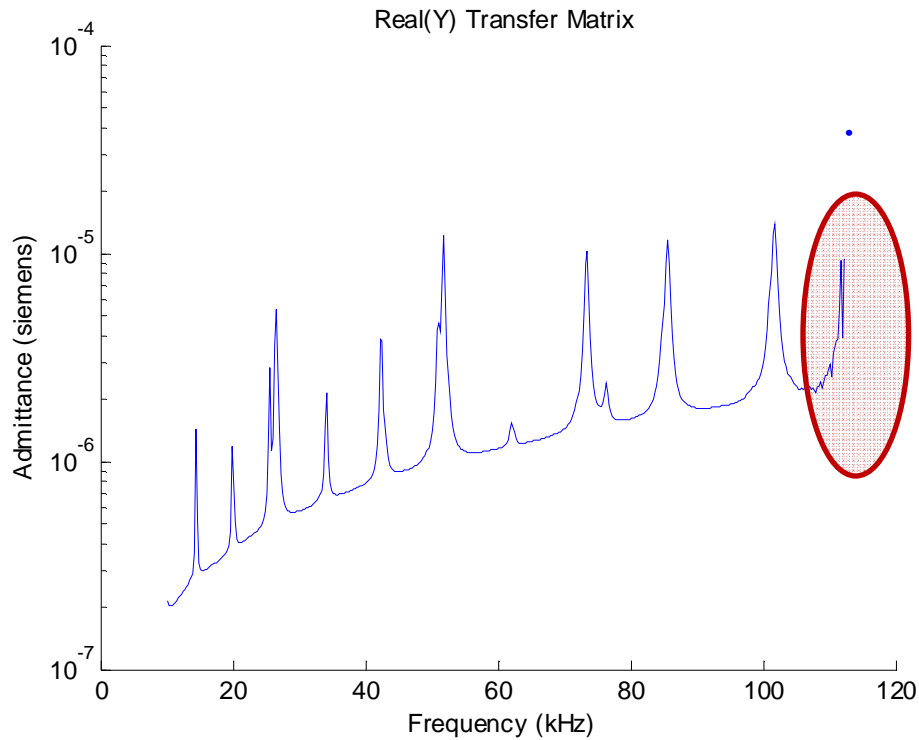
***Figure 120: Inadequate numerical behavior: for 100 mm 3-segment beam: numerical errors start to appear beyond 113 kHz***

Then, we do another test with a beam of 200mm length and we are able to excite it until 18 kHz without any MATLAB errors only until 17 kHz (Figure 121). The errors generated by the functions 'sin' and 'cos' are visible and affect our results (Figure 122).
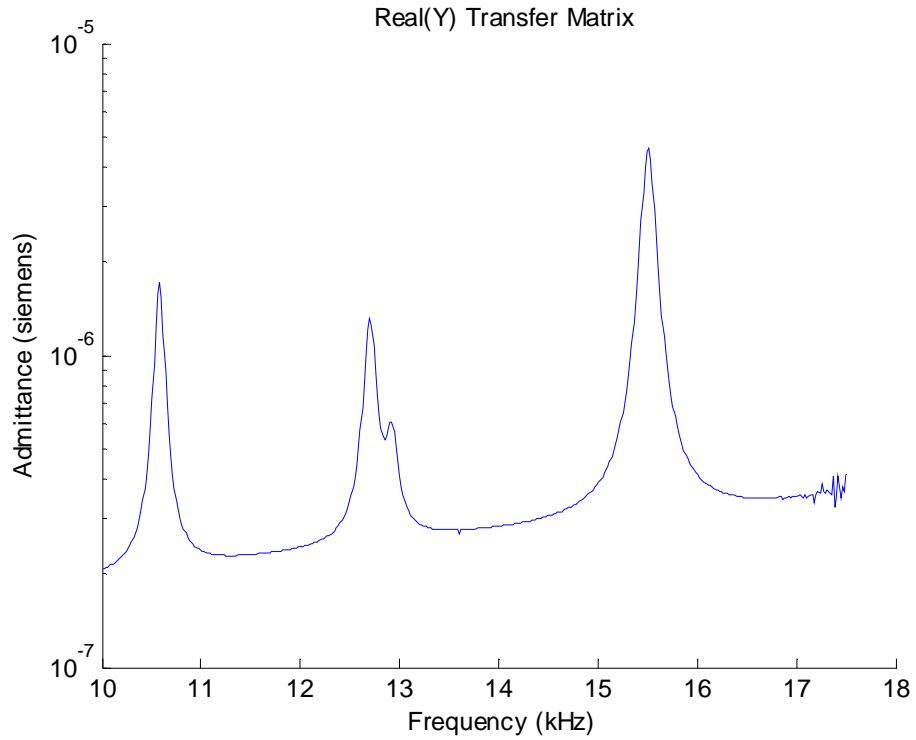
*Figure 121: Adequate numerical behavior for 200 mm 3-segment beam: maximum frequency attained without error is 17 kHz*
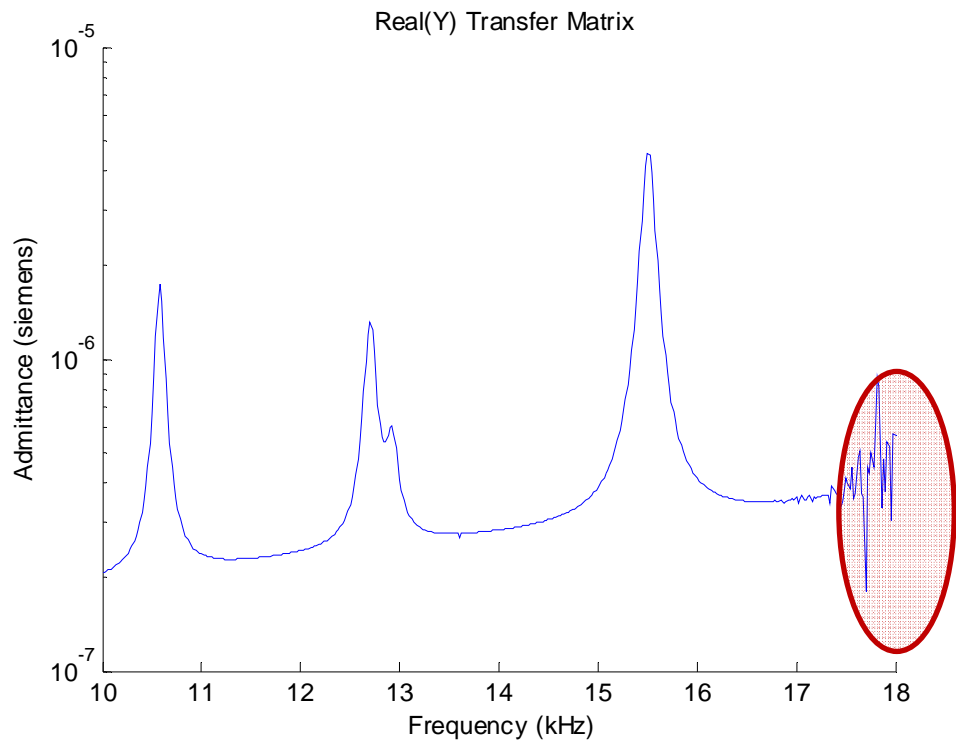


*Figure 122: Inadequate numerical behavior for 200 mm 3-segment beam: maximum frequency attained without error is 18 kHz*

175

Finally, we do another test with a beam of 50mm length and we are able to excite it until 393 kHz without any MATLAB errors (Figure 123). But when we reach 394 kHz, the errors generated by the functions 'sin' and 'cos' are visible and affect our results (Figure 124).
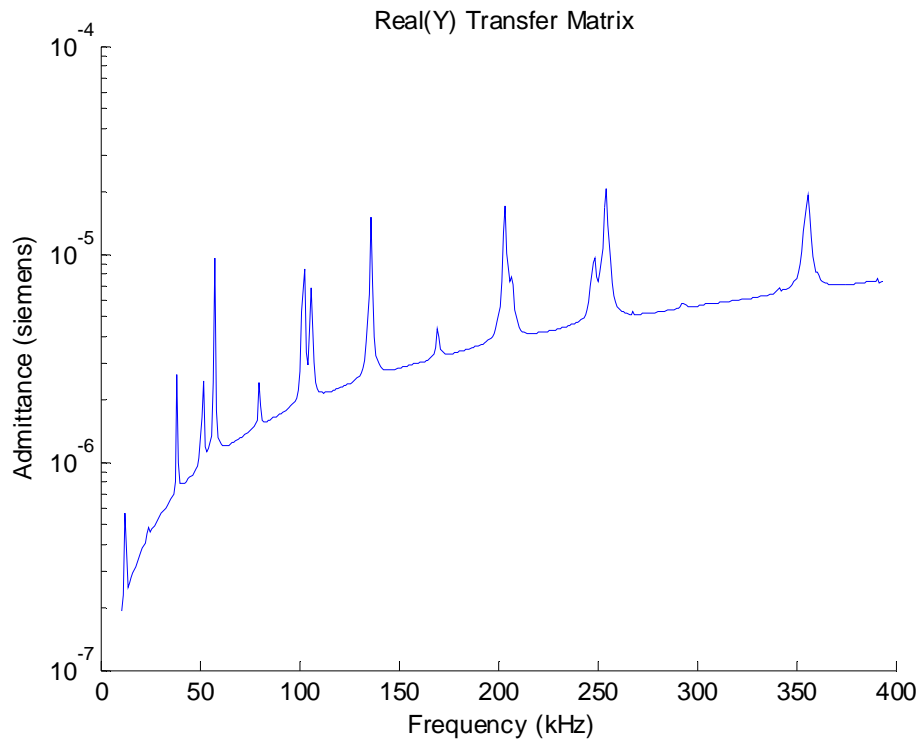


*Figure 123: Adequate numerical behavior for 50 mm 3-segment beam: maximum frequency attained without error is 393 kHz*
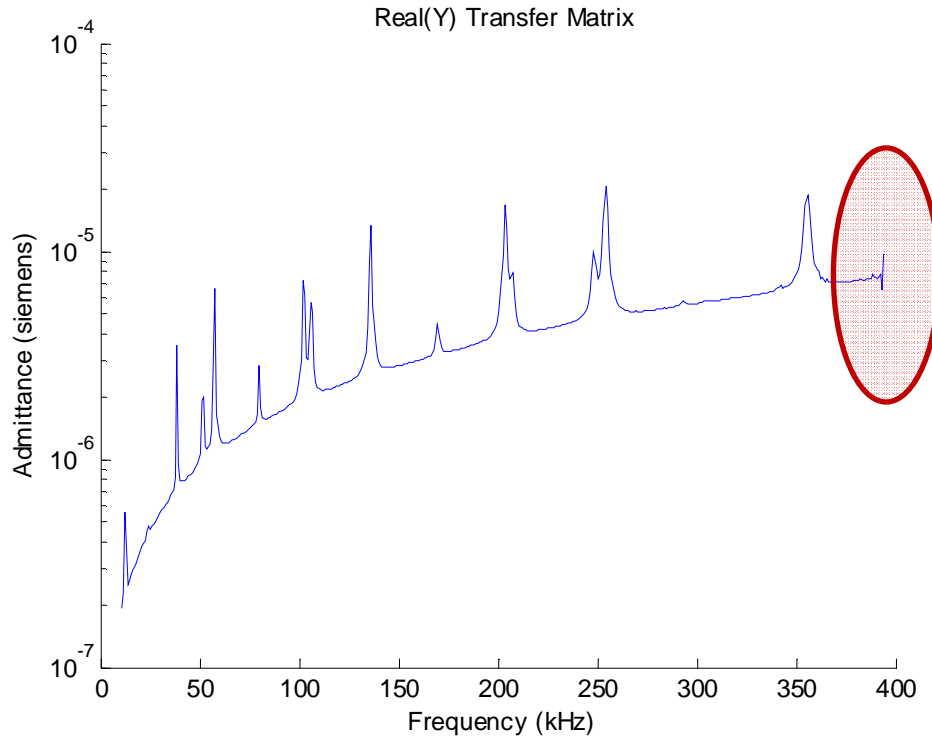
***Figure 124: Inadequate numerical behavior for 50 mm 3-segment beam: maximum frequency attained without error is 394 kHz***

As can be seen from the tests so far, the frequency and the length are inversely related, so the frequency variation gives opposite results than the length variation, that is, whenever we increase the frequency we should decrease the length in order to avoid numerical errors.

A solution to avoid these issues whenever the beam is long is to split the beam into more segments so that the errors that come from the 'sin' and 'cos' from the MATLAB code will not exceed the admissible limits so that we can calculate the natural frequencies without any errors. However, a possible aspect to be considered is that by adding more segments, the matrix becomes larger and more complex; nevertheless we are able to improve the accuracy for a large beam with a high frequency. In order to attain this solution, the 100 mm beam is split in 7 segments and we are able to excite

the beam and to obtain the natural frequencies until 324 kHz without errors as shown in

Figure 125. When we reach 324 kHz, the errors generated by the functions 'sin' and 'cos'

are visible and affect our results (Figure 126).
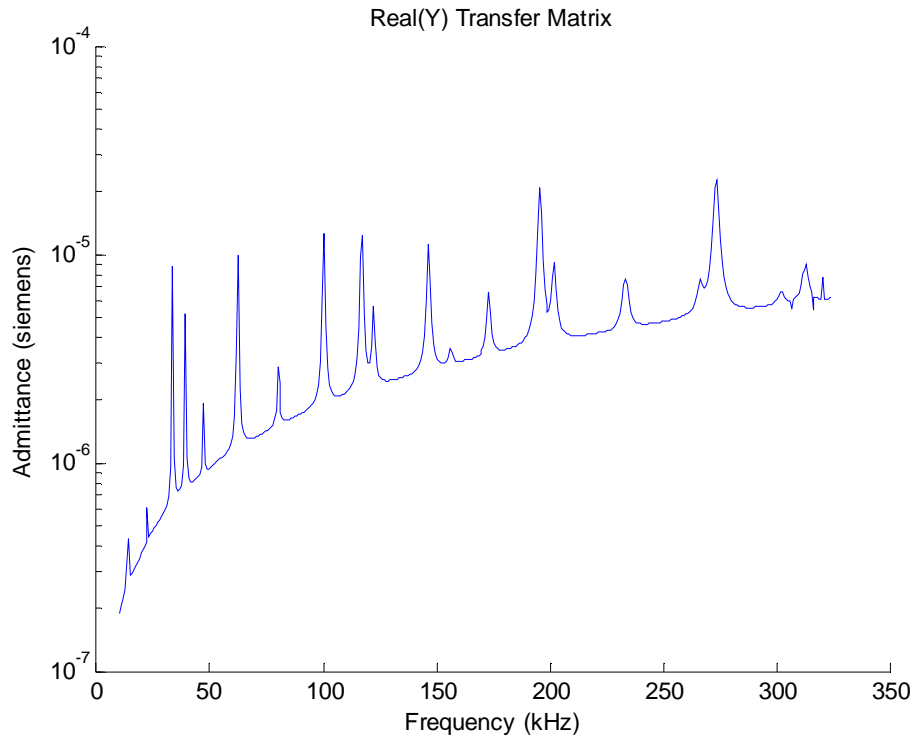


*Figure 125: Adequate numerical behavior for 100 mm 7-segment beam: maximum frequency attained without error is 323 kHz*
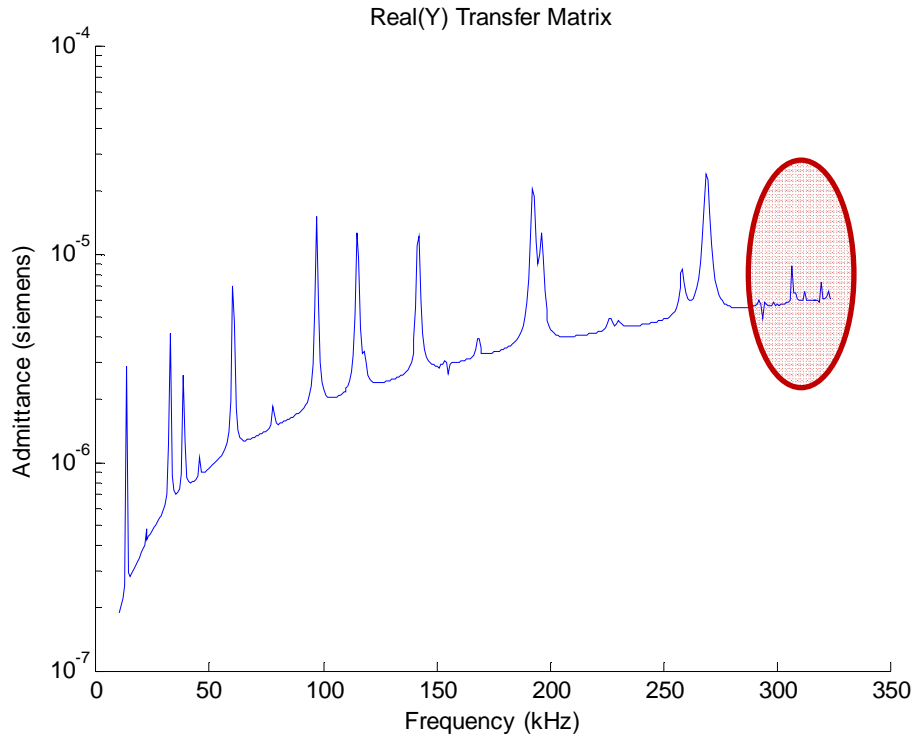
*Figure 126: Inadequate numerical behavior for 100 mm 7-segment beam: maximum frequency attained without error is 324 kHz*

## 8.2 CRITIQUE OF MODESHAPES BEHAVIOR AT HIGH FREQUENCIES

We used the modal analysis equations of Chapter 1 to calculate frequencies and mode shapes for a steel specimen with length $L$ = 100mm, width $W$ = 8mm and height $h$ =2.035 mm. The calculations were done in MATLAB. We calculate all axial natural frequencies between 10 and 100 kHz as in the experiment. The axial modes obtained are plotted in Figure 127 where $fU$ represents axial frequency.

179
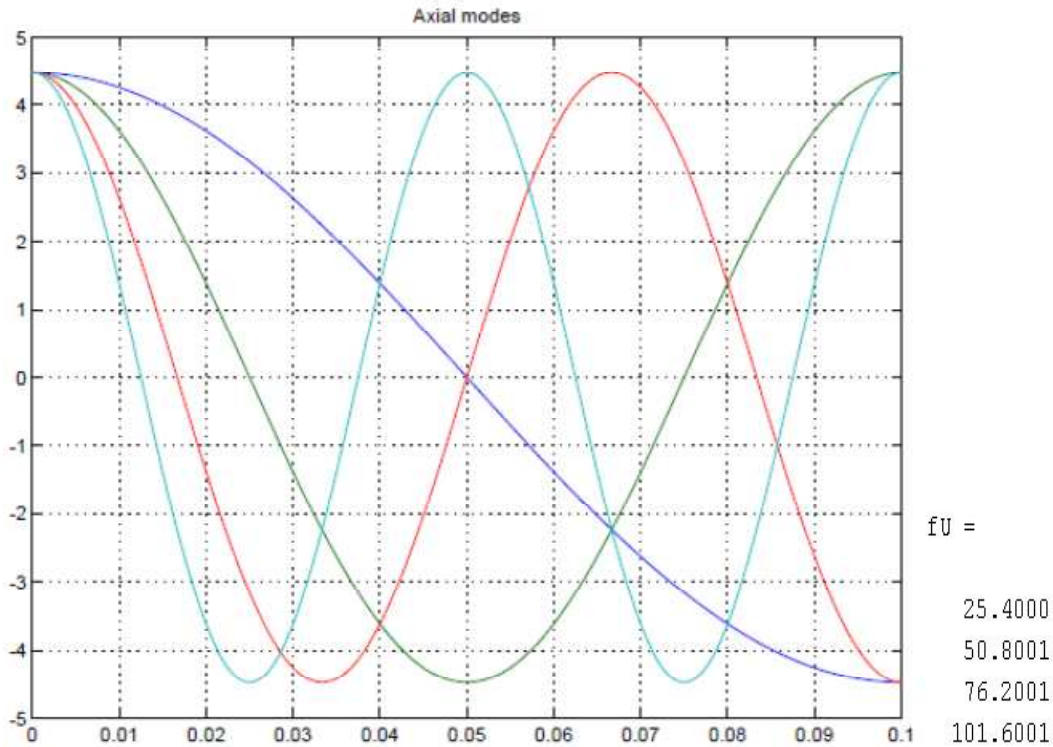
*Figure 127: Axial Modes (between 10 and 100 kHz); fU = Axial Frequency*

After calculating also the flexural frequencies in the next part, we will combine them and compare with the experimental results. What we can conclude so far is that between 10 and 100 kHz we have three axial frequencies.

We also calculate all flexural natural frequencies between 10 and 100 kHz as in the experiment. The flexural modes obtained are plotted in Figure 128 where $fW$ represents flexural frequency.

180
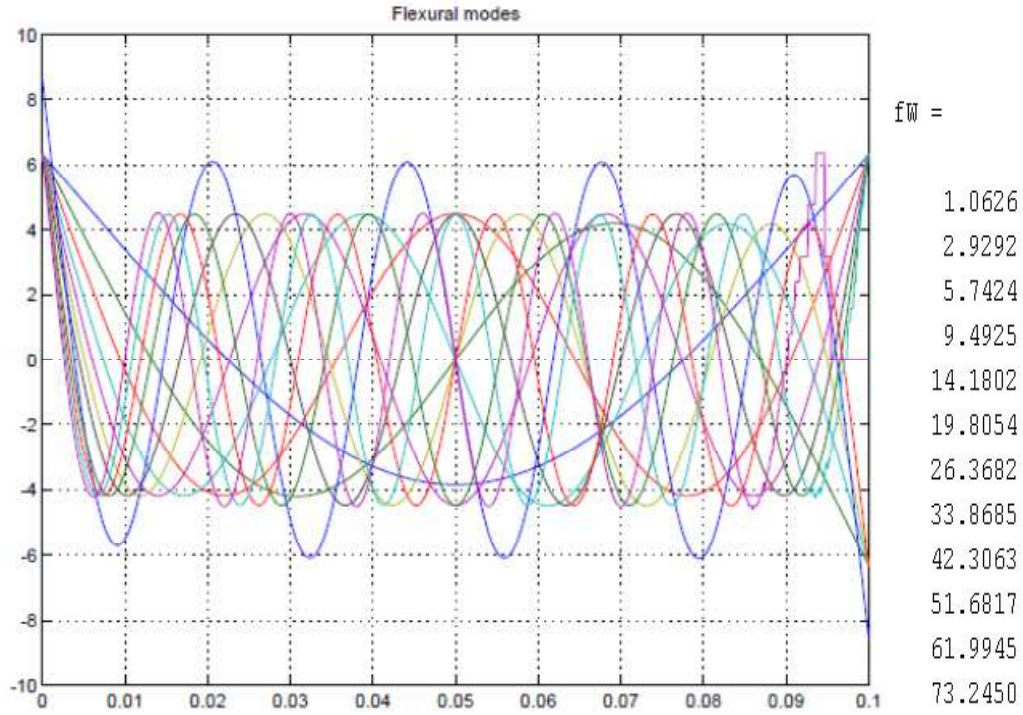
*Figure 128: Flexural Modes (between 10 and 100 kHz); fW = Flexural Frequency*

Knowing the axial and flexural modes, we are now able to calculate the frequency response function for the uniform beam between 10 and 100 kHz.
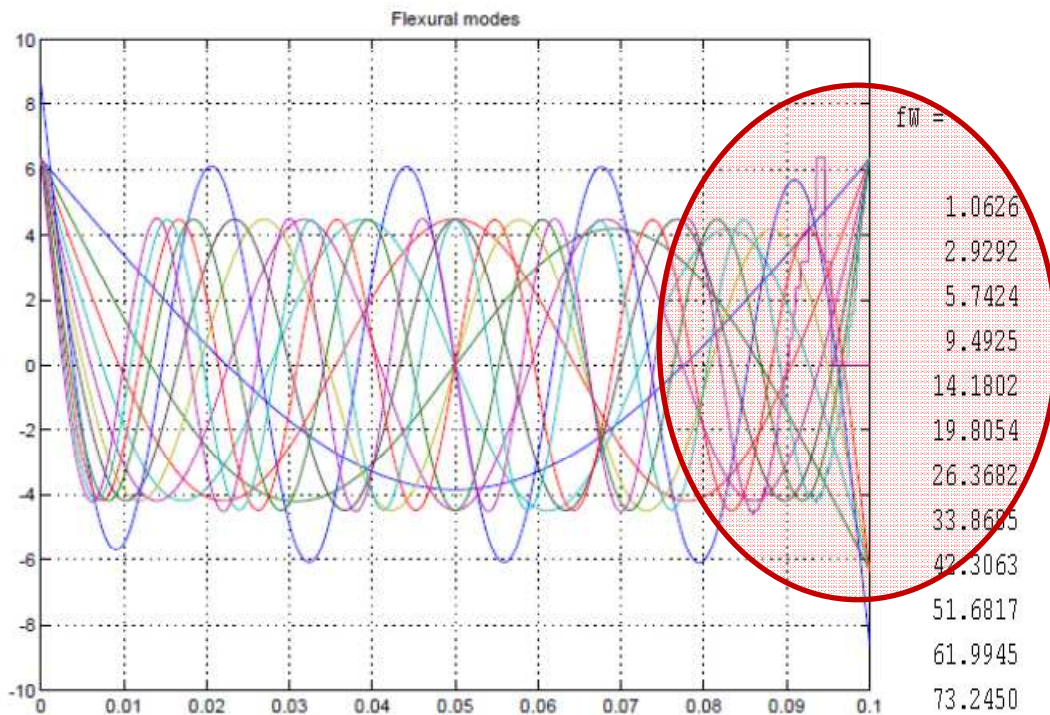


*Figure 129: Flexural Modes (between 10 and 100 kHz)*

Also, as per results obtained, we would like to point out some limitations of MATLAB. As can be seen in Figure 129 on flexural modes, the last frequencies come with some errors due to MATLAB approximation for 'sin' and 'cos' functions. Since the errors only appear for the last part of the mode shapes, a solution to avoid these errors (Lin, 2010) is to calculate only the first half of the flexural modes and the other half to be mirrored matching the symmetric or asymmetric shapes.
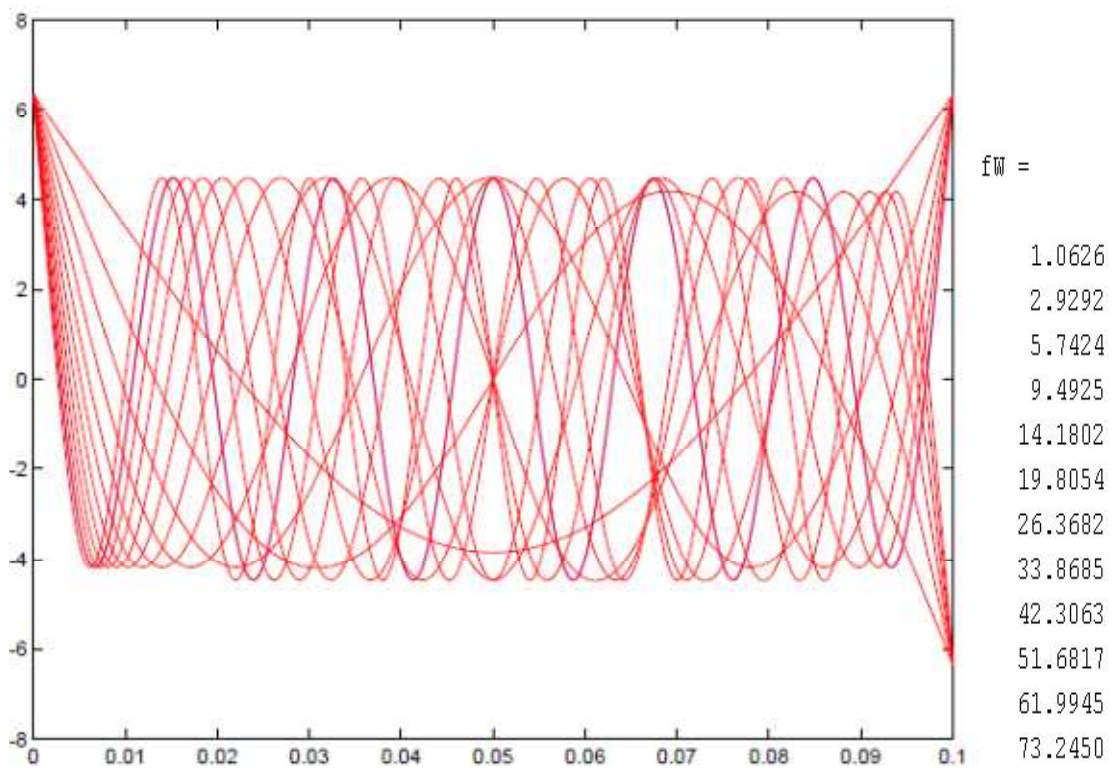


Figure 130: Flexural Modes (between 10 and 100 kHz) with proposed solution

As per Figure 130, after implementing the above mentioned solutions, there are no more errors.

# PART II – PERFORMED WORK

The present research proposes a new approach (STMM) to the nondestructive evaluation on composite laminates using small piezoelectric active sensors permanently fixed on the surface of the structure and develops a novel acousto-ultrasonic sensor that can detect ultrasonic waves for acoustic emission (AE) events using optical FBG sensing. In order to accomplish this, we will pursue the following tasks:

- Task #1 – Analytical Model for Vibration of Laminated Composite Beams

- Task #2 – The STMM Method

- Task #3 - Validation of the STMM Mathematical Model by Comparison with FEM and Experiment

- Task #4 - Sensitivity Studies of STMM E/M Impedance for Delamination Detection in Composite Beams

- Task #5 - Develop a novel acousto-ultrasonic sensor: the FBG ring sensor

# 9. Task #1: Analytical Model for Vibration of Laminated Composite Beams

In this task, the transfer matrix method was used to model the dynamic response of a composite laminate beam. The principle behind this method is to break down a long structure into small components that can be expressed in a matrix form. In this way, it can be easily solved and can be integrated into the Matlab program. In order to emphasize this method, we have to go through several steps and take into consideration some assumptions.

The new method which is called Stiffness Transfer Matrix Method (STMM) will incorporate concepts from the theory of laminate composites combined with the transfer matrix method concept.

## 9.1 Vibration Equations for Composite Beams

This subsection provides the fundamental concepts of composite beam vibration, which covers the first step in STMM. Figure 131 shows the stress nomenclature.
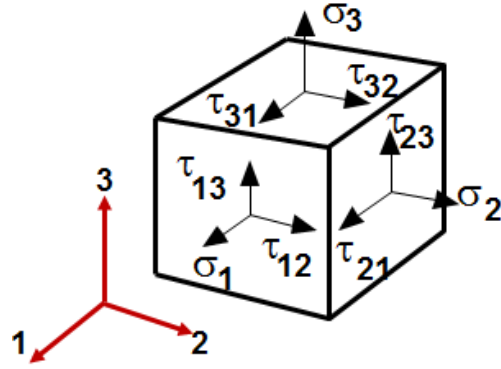
*Figure 131: Stress Nomenclature on body in deformed state*
*Source: Majumdar (2009)*

It is important to note that given that we have six strain equations and three unknown displacements, we do not obtain a unique solution or a continuous one unless certain conditions are fulfilled as shown later in this section.

### 9.1.1 EQUATIONS OF MOTION

Following Whitney (1987) pg. 3, the nonlinear strain displacement relations are given by

$$\varepsilon_{11} = \frac{\partial u_1}{\partial x_1} + \frac{1}{2}\left[\left(\frac{\partial u_1}{\partial x_1}\right)^2 + \left(\frac{\partial u_2}{\partial x_1}\right)^2 + \left(\frac{\partial u_3}{\partial x_1}\right)^2\right]$$

$$\varepsilon_{22} = \frac{\partial u_2}{\partial x_2} + \frac{1}{2}\left[\left(\frac{\partial u_1}{\partial x_2}\right)^2 + \left(\frac{\partial u_2}{\partial x_2}\right)^2 + \left(\frac{\partial u_3}{\partial x_2}\right)^2\right]$$

$$\varepsilon_{33} = \frac{\partial u_3}{\partial x_3} + \frac{1}{2}\left[\left(\frac{\partial u_1}{\partial x_3}\right)^2 + \left(\frac{\partial u_2}{\partial x_3}\right)^2 + \left(\frac{\partial u_3}{\partial x_3}\right)^2\right]$$

$$\varepsilon_{23} = \frac{1}{2}\left(\frac{\partial u_3}{\partial x_2} + \frac{\partial u_2}{\partial x_3} + \frac{\partial u_1}{\partial x_2}\frac{\partial u_1}{\partial x_3} + \frac{\partial u_2}{\partial x_2}\frac{\partial u_2}{\partial x_3} + \frac{\partial u_3}{\partial x_2}\frac{\partial u_3}{\partial x_3}\right)$$

$$\varepsilon_{13} = \frac{1}{2}\left(\frac{\partial u_3}{\partial x_1} + \frac{\partial u_1}{\partial x_3} + \frac{\partial u_1}{\partial x_1}\frac{\partial u_1}{\partial x_3} + \frac{\partial u_2}{\partial x_1}\frac{\partial u_2}{\partial x_3} + \frac{\partial u_3}{\partial x_1}\frac{\partial u_3}{\partial x_3}\right)$$

$$\varepsilon_{12} = \frac{1}{2}\left(\frac{\partial u_2}{\partial x_1} + \frac{\partial u_1}{\partial x_2} + \frac{\partial u_1}{\partial x_1}\frac{\partial u_1}{\partial x_2} + \frac{\partial u_2}{\partial x_1}\frac{\partial u_2}{\partial x_2} + \frac{\partial u_3}{\partial x_1}\frac{\partial u_3}{\partial x_2}\right)$$

(9.1)

where $\varepsilon_{ij}$ are strains and $u_i$ are displacements.

185

From the theory of elasticity, we have the following compatibility relations (Whitney, 1987)

$$\frac{\partial^2 \varepsilon_{12}}{\partial x_1 \partial x_2} = \frac{\partial^2 \varepsilon_{11}}{\partial x_2^2} + \frac{\partial^2 \varepsilon_{22}}{\partial x_1^2}$$

$$\frac{\partial^2 \varepsilon_{23}}{\partial x_2 \partial x_3} = \frac{\partial^2 \varepsilon_{22}}{\partial x_3^2} + \frac{\partial^2 \varepsilon_{33}}{\partial x_2^2}$$

$$\frac{\partial^2 \varepsilon_{13}}{\partial x_1 \partial x_3} = \frac{\partial^2 \varepsilon_{11}}{\partial x_3^2} + \frac{\partial^2 \varepsilon_{33}}{\partial x_1^2}$$

$$\frac{\partial^2 \varepsilon_{11}}{\partial x_2 \partial x_3} = \frac{\partial}{\partial x_1} \left( -\frac{\partial \varepsilon_{23}}{\partial x_1} + \frac{\partial \varepsilon_{13}}{\partial x_2} + \frac{\partial \varepsilon_{12}}{\partial x_3} \right)$$

$$\frac{\partial^2 \varepsilon_{22}}{\partial x_1 \partial x_3} = \frac{\partial}{\partial x_2} \left( \frac{\partial \varepsilon_{23}}{\partial x_1} - \frac{\partial \varepsilon_{13}}{\partial x_2} + \frac{\partial \varepsilon_{12}}{\partial x_3} \right)$$

$$\frac{\partial^2 \varepsilon_{33}}{\partial x_1 \partial x_2} = \frac{\partial}{\partial x_3} \left( \frac{\partial \varepsilon_{23}}{\partial x_1} - \frac{\partial \varepsilon_{13}}{\partial x_2} - \frac{\partial \varepsilon_{12}}{\partial x_3} \right)$$

(9.2)

For small displacements, equations (9.1) become

$$\varepsilon_{11} = \frac{\partial u_1}{\partial x_1}; \qquad \varepsilon_{23} = \frac{1}{2}\left( \frac{\partial u_3}{\partial x_2} + \frac{\partial u_2}{\partial x_3} \right); \qquad \gamma_{23} = \frac{\partial u_3}{\partial x_2} + \frac{\partial u_2}{\partial x_3}$$

$$\varepsilon_{22} = \frac{\partial u_2}{\partial x_2}; \qquad \varepsilon_{13} = \frac{1}{2}\left( \frac{\partial u_3}{\partial x_1} + \frac{\partial u_1}{\partial x_3} \right); \qquad \gamma_{13} = \frac{\partial u_3}{\partial x_1} + \frac{\partial u_1}{\partial x_3}$$

$$\varepsilon_{33} = \frac{\partial u_3}{\partial x_3}; \qquad \varepsilon_{12} = \frac{1}{2}\left( \frac{\partial u_2}{\partial x_1} + \frac{\partial u_1}{\partial x_2} \right); \qquad \gamma_{12} = \frac{\partial u_2}{\partial x_1} + \frac{\partial u_1}{\partial x_2}$$

(9.3)

The nonlinear equations of motion are (Whitney, 1987)

$$\frac{\partial}{\partial x_1}\left[\sigma_{11}\left(1+\frac{\partial u_1}{\partial x_1}\right)+\sigma_{12}\frac{\partial u_1}{\partial x_2}+\sigma_{13}\frac{\partial u_1}{\partial x_3}\right]+\frac{\partial}{\partial x_2}\left[\sigma_{12}\left(1+\frac{\partial u_1}{\partial x_1}\right)+\sigma_{22}\frac{\partial u_1}{\partial x_2}+\sigma_{23}\frac{\partial u_1}{\partial x_3}\right]+$$

$$+\frac{\partial}{\partial x_3}\left[\sigma_{13}\left(1+\frac{\partial u_1}{\partial x_1}\right)+\sigma_{23}\frac{\partial u_1}{\partial x_2}+\sigma_{33}\frac{\partial u_1}{\partial x_3}\right]+X_1=\rho_0\frac{\partial^2 u_1}{\partial t^2}$$

$$\frac{\partial}{\partial x_1}\left[\sigma_{11}\frac{\partial u_2}{\partial x_1}+\sigma_{12}\left(1+\frac{\partial u_2}{\partial x_2}\right)+\sigma_{13}\frac{\partial u_2}{\partial x_3}\right]+\frac{\partial}{\partial x_2}\left[\sigma_{12}\frac{\partial u_2}{\partial x_1}+\sigma_{22}\left(1+\frac{\partial u_2}{\partial x_2}\right)+\sigma_{23}\frac{\partial u_2}{\partial x_3}\right]+$$

$$+\frac{\partial}{\partial x_3}\left[\sigma_{13}\frac{\partial u_2}{\partial x_1}+\sigma_{23}\left(1+\frac{\partial u_2}{\partial x_2}\right)+\sigma_{33}\frac{\partial u_2}{\partial x_3}\right]+X_2=\rho_0\frac{\partial^2 u_2}{\partial t^2}$$

$$\frac{\partial}{\partial x_1}\left[\sigma_{11}\frac{\partial u_3}{\partial x_1}+\sigma_{12}\frac{\partial u_3}{\partial x_2}+\sigma_{13}\left(1+\frac{\partial u_2}{\partial x_3}\right)\right]+\frac{\partial}{\partial x_2}\left[\sigma_{12}\frac{\partial u_3}{\partial x_1}+\sigma_{22}\frac{\partial u_3}{\partial x_2}+\sigma_{23}\left(1+\frac{\partial u_3}{\partial x_3}\right)\right]+$$

$$+\frac{\partial}{\partial x_3}\left[\sigma_{13}\frac{\partial u_3}{\partial x_1}+\sigma_{23}\frac{\partial u_3}{\partial x_2}+\sigma_{33}\left(1+\frac{\partial u_3}{\partial x_3}\right)\right]+X_3=\rho_0\frac{\partial^2 u_3}{\partial t^2}$$

$$(9.4)$$

where $t$ is time, $\rho_0$ is the density and $X_i$ are body forces.

For small linear deformation, equations (9.4) become

$$\frac{\partial\sigma_{11}}{\partial x_1}+\frac{\partial\sigma_{12}}{\partial x_2}+\frac{\partial\sigma_{13}}{\partial x_3}+X_1=\rho_0\frac{\partial^2 u_1}{\partial t^2}$$

$$\frac{\partial\sigma_{12}}{\partial x_1}+\frac{\partial\sigma_{22}}{\partial x_2}+\frac{\partial\sigma_{23}}{\partial x_3}+X_2=\rho_0\frac{\partial^2 u_2}{\partial t^2}$$

$$\frac{\partial\sigma_{13}}{\partial x_1}+\frac{\partial\sigma_{23}}{\partial x_2}+\frac{\partial\sigma_{33}}{\partial x_3}+X_3=\rho_0\frac{\partial^2 u_3}{\partial t^2}$$

$$(9.5)$$

By integrating equation (9.3), we can calculate the displacements.

Please note the following change of notations

$$x=x_1 \qquad y=x_2 \qquad z=x_3$$

$$\sigma_x=\sigma_{11} \qquad \sigma_y=\sigma_{22} \qquad \sigma_z=\sigma_{33}$$

$$\sigma_{xy}=\sigma_{12} \qquad \sigma_{yz}=\sigma_{23} \qquad \sigma_{xz}=\sigma_{13}$$

$$(9.6)$$

### 9.1.2 BASIC ASSUMPTIONS

In order to proceed for laminated plates and beams, it is important to make several basic assumptions

1. The beam consists of several orthotropic layers bonded together

2. The thickness edge is much smaller than all the other dimensions

3. $u, v, w$ are small displacements compared to the plate thickness

4. in-plane strains $\varepsilon_x, \varepsilon_y, \varepsilon_{xy}$ are small compared to unity

5. For in-plane stress effects, the nonlinear terms in the motion relations that comprise of products of stresses and plates slope are retained

6. transverse shear strains $\varepsilon_{xz}, \varepsilon_{yz}$ are negligible

7. Displacements $u, v$ are linear functions of the z direction

8. the transverse normal strain $\varepsilon_z$ is negligible

9. Each layer follows Hooke's Law

10. The plate or beam thickness is constant

11. Rotary inertia terms are negligible

12. There are no body forces

13. $\sigma_{xz}, \sigma_{yz}$ vanish on the surfaces $z = \pm \dfrac{h}{2}$

14. $\sigma_z$ is negligible ($\sigma_z = 0$).

Recall the lamination theory of Section 3 and the definition of the stress resultants Figure 132 and Figure 134
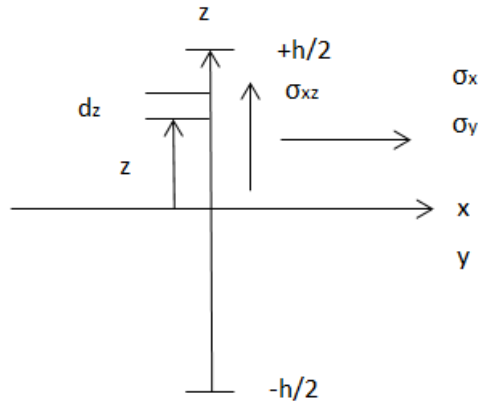
Figure 132: Definition of cross-section stresses $\sigma_x, \sigma_y, \sigma_{xy}$.
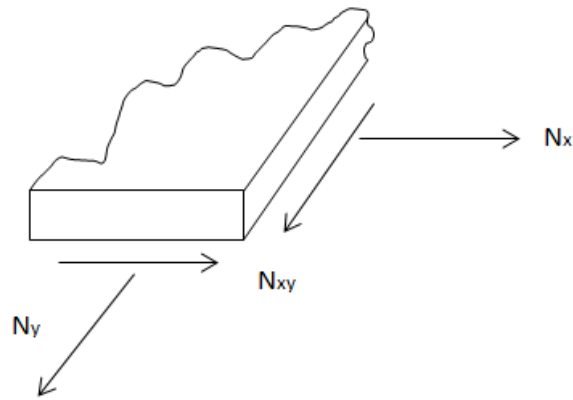


Figure 133: In-plane stress resultants $N_x, N_y, N_{xy}$.
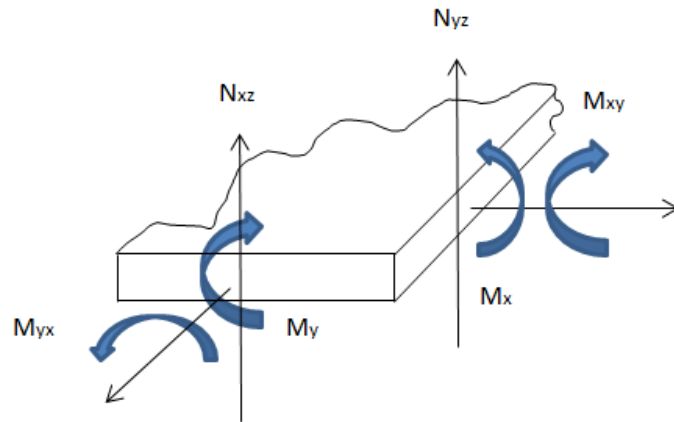


Figure 134: Out-of-plane stress resultants (moments and transverse shears) $M_x, M_y, M_{xy}, N_{xz}, N_{yz}$.

189
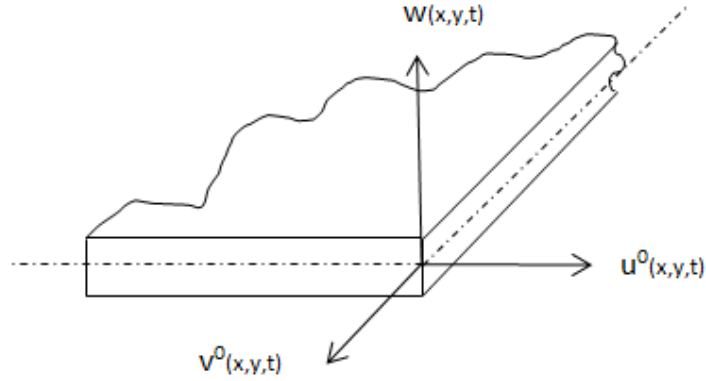
*Figure 135: Mid-plane displacements* $u^0, v^0, w.$

## 9.1.2.1 Simplification of the Nonlinear Equations of Motion

Recall the strain displacement equations (3.54) and (3.55) defining the mid-surface strains Figure 135

$$\varepsilon_x^0 = \frac{\partial u^0}{\partial x}; \quad \varepsilon_y^0 = \frac{\partial v^0}{\partial y}; \quad \varepsilon_{xy}^0 = \frac{\partial u^0}{\partial y} + \frac{\partial v^0}{\partial x}$$

$$\kappa_x = -\frac{\partial^2 w}{\partial x^2}; \quad \kappa_y = -\frac{\partial^2 w}{\partial y^2}; \quad \kappa_{xy} = -2\frac{\partial^2 w}{\partial x \partial y}$$

$$(9.7)$$

Retaining only the nonlinear terms in the equations of motion(9.4) that involve products of stress and plate slopes (and recalling the assumption $\sigma_z = 0$), we get the following relations for the kth layer of laminates

$$\frac{\partial \sigma_x^{(k)}}{\partial x} + \frac{\partial \sigma_{xy}^{(k)}}{\partial y} + \frac{\partial \sigma_{xz}^{(k)}}{\partial z} = \rho_0^{(k)} \frac{\partial^2 u^0}{\partial t^2}$$

$$\frac{\partial \sigma_{xy}^{(k)}}{\partial x} + \frac{\partial \sigma_y^{(k)}}{\partial y} + \frac{\partial \sigma_{yz}^{(k)}}{\partial z} = \rho_0^{(k)} \frac{\partial^2 v^0}{\partial t^2}$$

$$\frac{\partial}{\partial x}\left(\sigma_{xz}^{(k)} + \sigma_x^{(k)} \frac{\partial w}{\partial x} + \sigma_{xy}^{(k)} \frac{\partial w}{\partial y}\right) + \frac{\partial}{\partial y}\left(\sigma_{yz}^{(k)} + \sigma_{xy}^{(k)} \frac{\partial w}{\partial x} + \sigma_y^{(k)} \frac{\partial w}{\partial y}\right) +$$

$$+ \frac{\partial}{\partial z}\left(\sigma_{xz}^{(k)} \frac{\partial w}{\partial x} + \sigma_{yz}^{(k)} \frac{\partial w}{\partial y}\right) = \rho_0^{(k)} \frac{\partial^2 w}{\partial t^2}$$

$$(9.8)$$

190

### 9.1.2.2 Integration of the Nonlinear Equations of Motion

Recall the stress resultants defined by equations (4.68),i.e.,

$$N_x = \int_{-h/2}^{h/2} \sigma_x dz$$

$$N_y = \int_{-h/2}^{h/2} \sigma_y dz$$

$$N_{xy} = \int_{-h/2}^{h/2} \sigma_{xy} dz$$

$$N_{xz} = \int_{-h/2}^{h/2} \sigma_{xz} dz$$

$$N_{yz} = \int_{-h/2}^{h/2} \sigma_{yz} dz$$

$$M_x = \int_{-h/2}^{h/2} \sigma_x z dz$$

$$M_y = \int_{-h/2}^{h/2} \sigma_y z dz$$

$$M_{xy} = \int_{-h/2}^{h/2} \sigma_{xy} z dz \qquad (9.9)$$

Integrating the first of equations (9.8) with respect to $z$ and interchanging the order of differentiation and integration, we get

$$\int_{-\frac{h}{2}}^{\frac{h}{2}} \left[ \frac{\partial \sigma_x}{\partial x} + \frac{\partial \sigma_{xy}}{\partial y} + \frac{\partial \sigma_{xz}}{\partial z} = \rho_0 \frac{\partial^2 u^0}{\partial t^2} \right] dz \qquad (9.10)$$

Note that

$$\int \frac{\partial \sigma_x}{\partial x} dz + \int \frac{\partial \sigma_{xy}}{\partial y} dz = \frac{\partial}{\partial x} \int \sigma_x dz + \frac{\partial}{\partial y} \int \sigma_{xy} dz = \frac{\partial N_x}{\partial x} + \frac{\partial N_{xy}}{\partial y} \qquad (9.11)$$

Define the equivalent mass per unit area (area mass density)

$$\rho = \int_{-h/2}^{h/2} \rho_0(z) dz \qquad (9.12)$$

Hence, equation (9.10) becomes

$$\boxed{\frac{\partial N_x}{\partial x} + \frac{\partial N_{xy}}{\partial y} = \rho \frac{\partial^2 u^0}{\partial t^2}} \qquad (9.13)$$

In a similar manner, integrating the second of equations (9.8) with respect to $z$ and interchanging the order of differentiation and integration yields

191

$$\int_{-\frac{h}{2}}^{\frac{h}{2}} \left[ \frac{\partial \sigma_{xy}}{\partial x} + \frac{\partial \sigma_y}{\partial y} + \frac{\partial \sigma_{yz}}{\partial z} = \rho \frac{\partial^2 v^0}{\partial t^2} \right] dz$$

(9.14)

$$\int \frac{\partial \sigma_{xy}}{\partial x} dz + \int \frac{\partial \sigma_y}{\partial y} dz = \frac{\partial}{\partial x} \int \sigma_{xy} dz + \frac{\partial}{\partial y} \int \sigma_y dz$$

(9.15)

$$\boxed{\frac{\partial N_{xy}}{\partial x} + \frac{\partial N_y}{\partial y} = \rho \frac{\partial^2 v^0}{\partial t^2}}$$

(9.16)

For integrating the third of equations (9.8) with respect to z and interchanging the order

of differentiation and integration we proceed as follows

$$\int_{-\frac{h}{2}}^{\frac{h}{2}} \left[ \begin{array}{l} \frac{\partial}{\partial x}\left( \sigma_{xz} + \sigma_x \frac{\partial w}{\partial x} + \sigma_{xy} \frac{\partial w}{\partial y} \right) + \frac{\partial}{\partial y}\left( \sigma_{yz} + \sigma_{xy} \frac{\partial w}{\partial x} + \sigma_y \frac{\partial w}{\partial y} \right) + \\ + \frac{\partial}{\partial z}\left( \sigma_{xz} \frac{\partial w}{\partial x} + \sigma_{yz} \frac{\partial w}{\partial y} \right) = \rho \frac{\partial^2 w}{\partial t^2} \end{array} \right] dz$$

(9.17)

We note that:

$$\int \frac{\partial \sigma_{xz}}{\partial x} dz = \frac{\partial}{\partial x} \int \sigma_{xz} dz = \frac{\partial}{\partial x} N_{xz}$$

(9.18)

$$\int \left( \frac{\partial \sigma_x}{\partial x} \frac{\partial w}{\partial x} + \sigma_x \frac{\partial^2 w}{\partial x^2} \right) dz = \frac{\partial w}{\partial x} \frac{\partial}{\partial x} \int \sigma_x dz + \frac{\partial^2 w}{\partial x^2} \int \sigma_x dz$$

(9.19)

$$= \frac{\partial w}{\partial x} \frac{\partial N_x}{\partial x} + \frac{\partial^2 w}{\partial x^2} N_x$$

(9.20)

$$\int \left( \frac{\partial \sigma_{xy}}{\partial x} \frac{\partial w}{\partial y} + \sigma_{xy} \frac{\partial^2 w}{\partial x \partial y} \right) dz = \frac{\partial w}{\partial y} \frac{\partial}{\partial x} \int \sigma_{xy} dz + \frac{\partial^2 w}{\partial x \partial y} \int \sigma_{xy} dz$$

(9.21)

$$= \frac{\partial w}{\partial y} \frac{\partial N_{xy}}{\partial x} + \frac{\partial^2 w}{\partial x \partial y} N_{xy}$$

(9.22)

$$\frac{\partial}{\partial y} \int \sigma_{yz} dz = \frac{\partial}{\partial y} N_{yz}$$

(9.23)

$$\int \left( \frac{\partial \sigma_{xy}}{\partial y} \frac{\partial w}{\partial x} + \sigma_{xy} \frac{\partial^2 w}{\partial y \partial x} \right) dz = \frac{\partial w}{\partial x} \frac{\partial}{\partial y} \int \sigma_{xy} dz + \frac{\partial^2 w}{\partial y \partial x} \int \sigma_{xy} dz$$

(9.24)

$$= \frac{\partial w}{\partial x} \frac{\partial N_{xy}}{\partial y} + \frac{\partial^2 w}{\partial y \partial x} N_{xy}$$

(9.25)

192

$$\int \left( \frac{\partial \sigma_y}{\partial y} \frac{\partial w}{\partial x} + \sigma_y \frac{\partial^2 w}{\partial y^2} \right) dz = \frac{\partial w}{\partial x} \frac{\partial}{\partial y} \int \sigma_y dz + \frac{\partial^2 w}{\partial y^2} \int \sigma_y dz$$

(9.26)

$$= \frac{\partial w}{\partial x} \frac{\partial N_y}{\partial y} + \frac{\partial^2 w}{\partial y^2}$$

(9.27)

Recall that

$$\int_a^b \frac{\partial}{\partial z} (f) dz = f(b) - f(a)$$

(9.28)

Hence

$$\int_{-\frac{h}{2}}^{\frac{h}{2}} \frac{\partial}{\partial z} \left( \sigma_{xz} \frac{\partial w}{\partial x} + \sigma_{yz} \frac{\partial w}{\partial y} \right) dz = \rightarrow$$

$$\sigma_{xz}\left(\frac{h}{2}\right) \frac{\partial w}{\partial x} + \sigma_{yz}\left(\frac{h}{2}\right) \frac{\partial w}{\partial y} - \sigma_{xz}\left(-\frac{h}{2}\right) \frac{\partial w}{\partial x} - \sigma_{yz}\left(-\frac{h}{2}\right) \frac{\partial w}{\partial y} = 0$$

(9.29)

Substituting equation (9.18) through (9.29) into equation(9.17), we get

$$\frac{\partial}{\partial x} N_{xz} + \frac{\partial w}{\partial x} \frac{\partial N_x}{\partial x} + \frac{\partial^2 w}{\partial x^2} N_x + \frac{\partial w}{\partial y} \frac{\partial N_{xy}}{\partial x} + \frac{\partial^2 w}{\partial x \partial y} N_{xy} +$$

$$+ \frac{\partial}{\partial y} N_{yz} + \frac{\partial w}{\partial x} \frac{\partial N_{xy}}{\partial y} + \frac{\partial^2 w}{\partial y \partial x} N_{xy} + \frac{\partial w}{\partial x} \frac{\partial N_y}{\partial y} + \frac{\partial^2 w}{\partial y^2} = \rho \frac{\partial^2 w}{\partial t^2}$$

(9.30)

Upon rearrangement, equations (9.30) becomes

$$\boxed{N_x \frac{\partial^2 w}{\partial x^2} + 2N_{xy} \frac{\partial^2 w}{\partial x \partial y} + N_y \frac{\partial^2 w}{\partial y^2} + \frac{\partial N_{xz}}{\partial x} + \frac{\partial N_{yz}}{\partial y} = \rho \frac{\partial^2 w}{\partial t^2}}$$

(9.31)

Equations (9.13), (9.16), (9.31) are the equations of motion in terms of stress resultants, further simplification may be achieved by eliminating the stress resultants associated with out –of-plane shears, $N_{xz}, N_{yz}$. To achieve this, we first establish the relations between moments $M_x, M_y, M_{xy}$ and out of plane shear resultants $N_{xz}, N_{yz}$ and then use these relations to eliminate $N_{xz}, N_{yz}$ in equation (9.31). These steps are achieved in the next section.

## 9.1.2.3 Eliminations of out-of-Plane Shear Resultants $N_{xz}, N_{yz}$

Multiplying the first of equations (9.8) by z and integrating with respect to z over the plate thickness yields

$$\int_{-h/2}^{h/2} \frac{\partial \sigma_x}{\partial x} z dz + \int_{-h/2}^{h/2} \frac{\partial \sigma_{xy}}{\partial y} z dz + \int_{-h/2}^{h/2} \frac{\partial \sigma_{xz}}{\partial z} z dz = \int_{-h/2}^{h/2} \rho \frac{\partial^2 u}{\partial t^2} z dz$$

(9.32)

$$\frac{\partial}{\partial x} \int_{-h/2}^{h/2} \sigma_x z dz + \frac{\partial}{\partial y} \int_{-h/2}^{h/2} \sigma_{xy} z dz + \int_{-h/2}^{h/2} \frac{\sigma_{xz}}{\partial z} z dz = \int_{-h/2}^{h/2} \rho \frac{\partial^2 u}{\partial t^2} z dz$$

(9.33)

$$\frac{\partial M_x}{\partial x} + \frac{\partial M_{xy}}{\partial y} + \int_{-h/2}^{h/2} \frac{\partial \sigma_{xz}}{\partial z} z dz = \int_{-h/2}^{h/2} \rho \frac{\partial^2 u}{\partial t^2} z dz$$

(9.34)

Note

$$\frac{\partial (z \sigma_{xz})}{\partial z} = \frac{\partial z}{\partial z} \sigma_{xz} + z \frac{\partial \sigma_{xz}}{\partial_z}$$

(9.35)

Hence

$$z \frac{\partial \sigma_{xz}}{\partial z} = \frac{\partial (z \sigma_{xz})}{\partial z} - \sigma_{xz}$$

(9.36)

Also note

$$\int_{-h/2}^{h/2} \rho \frac{\partial^2 u}{\partial t^2} z dz = \frac{\partial^2 u}{\partial t^2} \int_{-h/2}^{h/2} \rho z dz = 0 \qquad \text{(assumption 11)}$$

(9.37)

Substituting equations (9.36) and (9.37) into equation (9.34) yields

$$\frac{\partial M_x}{\partial x} + \frac{\partial M_{xy}}{\partial y} + \int_{-h/2}^{h/2} \left[ \frac{\partial (z \sigma_{xz})}{\partial z} - \sigma_{xz} \right] dz = 0$$

(9.38)

Note

$$\int_{-h/2}^{h/2} \frac{\partial (z \sigma_{xz})}{\partial z} dz = z \sigma_{xz} \Big|_{-h/2}^{h/2} = 0 \qquad \text{(assumption 13)}$$

(9.39)

and

$$\int_{-h/2}^{h/2} \sigma_{xz} dz = N_{xz}$$

(9.40)

194

Hence, equation (9.38) becomes

$$\boxed{\frac{\partial M_x}{\partial x} + \frac{\partial M_{xy}}{\partial y} - N_{xz} = 0}$$

(9.41)

In a similar way, multiplying the second of equations (9.8) by z and integrating with respect to z over the plate thickness yields

$$\int_{-h/2}^{h/2} \frac{\partial \sigma_{xy}}{\partial x} z \, dz + \int_{-h/2}^{h/2} \frac{\partial \sigma_y}{\partial y} z \, dz + \int_{-h/2}^{h/2} \frac{\partial \sigma_{yz}}{\partial z} z \, dz = \int_{-h/2}^{h/2} \rho \frac{\partial^2 v}{\partial t^2} z \, dz$$

(9.42)

$$\frac{\partial}{\partial x} \int_{-h/2}^{h/2} \sigma_{xy} z \, dz + \frac{\partial}{\partial y} \int_{-h/2}^{h/2} \sigma_y z \, dz + \int_{-h/2}^{h/2} \frac{\sigma_{yz}}{\partial z} z \, dz = \int_{-h/2}^{h/2} \rho \frac{\partial^2 v}{\partial t^2}$$

(9.43)

$$\frac{\partial M_{xy}}{\partial x} + \frac{\partial M_y}{\partial y} + \int_{-h/2}^{h/2} \frac{\partial \sigma_{yz}}{\partial z} z \, dz = \int_{-h/2}^{h/2} \rho \frac{\partial^2 v}{\partial t^2} z \, dz$$

(9.44)

Note

$$\frac{\partial \left( z \sigma_{yz} \right)}{\partial z} = \frac{\partial z}{\partial z} \sigma_{yz} + z \frac{\partial \sigma_{yz}}{\partial_z}$$

(9.45)

Hence

$$z \frac{\partial \sigma_{yz}}{\partial z} = \frac{\partial \left( z \sigma_{yz} \right)}{\partial z} - \sigma_{yz}$$

(9.46)

Also note

$$\int_{-h/2}^{h/2} \rho \frac{\partial^2 v}{\partial t^2} z \, dz = \frac{\partial^2 v}{\partial t^2} \int_{-h/2}^{h/2} \rho z \, dz = 0 \quad \text{(assumption 11)}$$

(9.47)

Substituting equations (9.46) and (9.45) into equation (9.44) yields

$$\frac{\partial M_{xy}}{\partial x} + \frac{\partial M_y}{\partial y} + \int_{-h/2}^{h/2} \left[ \frac{\partial \left( z \sigma_{yz} \right)}{\partial z} - \sigma_{yz} \right] dz = 0$$

(9.48)

Note

$$\int_{-h/2}^{h/2} \frac{\partial \left( z \sigma_{yz} \right)}{\partial z} dz = z \sigma_{yz} \Big|_{-h/2}^{h/2} = 0 \quad \text{(assumption 13)}$$

(9.49)

and

$$\int_{-h/2}^{h/2} \sigma_{yz} dz = N_{yz} \tag{9.50}$$

Hence, equation (9.48) becomes

$$\boxed{\frac{\partial M_{xy}}{\partial x} + \frac{\partial M_y}{\partial y} - N_{yz} = 0} \tag{9.51}$$

Differentiating equations (9.41) & (9.51) with respect to x and y, respectively, yields

$$\frac{\partial N_{xz}}{\partial x} = \frac{\partial^2 M_x}{\partial x^2} + \frac{\partial^2 M_{xy}}{\partial x \partial y}$$

$$\frac{\partial N_{yz}}{\partial y} = \frac{\partial^2 M_{xy}}{\partial x \partial y} + \frac{\partial^2 M_y}{\partial y^2} \tag{9.52}$$

Substituting equations (9.52) into (9.31) yields

$$N_x \frac{\partial^2 w}{\partial x^2} + 2N_{xy} \frac{\partial^2 w}{\partial x \partial y} + N_y \frac{\partial^2 w}{\partial y^2} + \frac{\partial^2 M_x}{\partial x^2} + \frac{\partial^2 M_{xy}}{\partial x \partial y} + \frac{\partial^2 M_{xy}}{\partial x \partial y} + \frac{\partial^2 M_y}{\partial y^2} = \rho \frac{\partial^2 w}{\partial t^2} \tag{9.53}$$

Upon rearrangement, equation (9.53) becomes

$$\boxed{\frac{\partial^2 M_x}{\partial x^2} + 2\frac{\partial^2 M_{xy}}{\partial x \partial y} + \frac{\partial^2 M_y}{\partial y^2} + N_x \frac{\partial^2 w}{\partial x^2} + 2N_{xy} \frac{\partial^2 w}{\partial x \partial y} + N_y \frac{\partial^2 w}{\partial y^2} = \rho \frac{\partial^2 w}{\partial t^2}} \tag{9.54}$$

### 9.1.2.4 Displacement Equations of Motion for Composite Plates

Recall the constitutive relations for the plate, equations (3.65), Chapter 3, i.e.

$$\begin{Bmatrix} N_x \\ N_y \\ N_{xy} \\ M_x \\ M_y \\ M_{xy} \end{Bmatrix} = \begin{bmatrix} A_{11} & A_{12} & A_{16} & B_{11} & B_{12} & B_{16} \\ A_{12} & A_{22} & A_{26} & B_{12} & B_{22} & B_{26} \\ A_{16} & A_{26} & A_{66} & B_{16} & B_{26} & B_{66} \\ B_{11} & B_{12} & B_{16} & D_{11} & D_{12} & D_{16} \\ B_{12} & B_{22} & B_{26} & D_{12} & D_{22} & D_{26} \\ B_{16} & B_{26} & B_{66} & D_{16} & D_{26} & D_{66} \end{bmatrix} \cdot \begin{Bmatrix} \varepsilon_x^o \\ \varepsilon_y^o \\ \gamma_{xy}^o \\ \kappa_x \\ \kappa_y \\ \kappa_{xy} \end{Bmatrix} \tag{9.55}$$

Recall equation (9.7)

$$\varepsilon_x^0 = \frac{\partial u^0}{\partial x}; \quad \varepsilon_y^0 = \frac{\partial v^0}{\partial y}; \quad \varepsilon_{xy}^0 = \frac{\partial u^0}{\partial y} + \frac{\partial v^0}{\partial x}$$

$$\kappa_x = -\frac{\partial^2 w}{\partial x^2}; \quad \kappa_y = -\frac{\partial^2 w}{\partial y^2}; \quad \kappa_{xy} = -2\frac{\partial^2 w}{\partial x \partial y} \tag{9.56}$$

Substitute equation (9.56) into equation (9.55) to get

$$\begin{Bmatrix} N_x \\ N_y \\ N_{xy} \\ M_x \\ M_y \\ M_{xy} \end{Bmatrix} = \begin{bmatrix} A_{11} & A_{12} & A_{16} & B_{11} & B_{12} & B_{16} \\ A_{12} & A_{22} & A_{26} & B_{12} & B_{22} & B_{26} \\ A_{16} & A_{26} & A_{66} & B_{16} & B_{26} & B_{66} \\ B_{11} & B_{12} & B_{16} & D_{11} & D_{12} & D_{16} \\ B_{12} & B_{22} & B_{26} & D_{12} & D_{22} & D_{26} \\ B_{16} & B_{26} & B_{66} & D_{16} & D_{26} & D_{66} \end{bmatrix} \cdot \begin{Bmatrix} \dfrac{\partial u^0}{\partial x} \\[2mm] \dfrac{\partial v^0}{\partial y} \\[2mm] \dfrac{\partial u^0}{\partial y} + \dfrac{\partial v^0}{\partial x} \\[2mm] -\dfrac{\partial^2 w}{\partial x^2} \\[2mm] -\dfrac{\partial^2 w}{\partial y^2} \\[2mm] -2\dfrac{\partial^2 w}{\partial x \partial y} \end{Bmatrix} \tag{9.57}$$

$$N_x = A_{11}\left(\frac{\partial u^0}{\partial x}\right) + A_{12}\left(\frac{\partial v^0}{\partial y}\right) + A_{16}\left(\frac{\partial u^0}{\partial y} + \frac{\partial v^0}{\partial x}\right) + B_{11}\left(-\frac{\partial^2 w}{\partial x^2}\right) + B_{12}\left(-\frac{\partial^2 w}{\partial y^2}\right) + B_{16}\left(-2\frac{\partial^2 w}{\partial x \partial y}\right)$$

$$N_y = A_{12}\left(\frac{\partial u^0}{\partial x}\right) + A_{22}\left(\frac{\partial v^0}{\partial y}\right) + A_{26}\left(\frac{\partial u^0}{\partial y} + \frac{\partial v^0}{\partial x}\right) + B_{12}\left(-\frac{\partial^2 w}{\partial x^2}\right) + B_{22}\left(-\frac{\partial^2 w}{\partial y^2}\right) + B_{26}\left(-2\frac{\partial^2 w}{\partial x \partial y}\right)$$

$$N_{xy} = A_{16}\left(\frac{\partial u^0}{\partial x}\right) + A_{26}\left(\frac{\partial v^0}{\partial y}\right) + A_{66}\left(\frac{\partial u^0}{\partial y} + \frac{\partial v^0}{\partial x}\right) + B_{16}\left(-\frac{\partial^2 w}{\partial x^2}\right) + B_{26}\left(-\frac{\partial^2 w}{\partial y^2}\right) + B_{66}\left(-2\frac{\partial^2 w}{\partial x \partial y}\right)$$

$$M_x = B_{11}\left(\frac{\partial u^0}{\partial x}\right) + B_{12}\left(\frac{\partial v^0}{\partial y}\right) + B_{16}\left(\frac{\partial u^0}{\partial y} + \frac{\partial v^0}{\partial x}\right) + D_{11}\left(-\frac{\partial^2 w}{\partial x^2}\right) + D_{12}\left(-\frac{\partial^2 w}{\partial y^2}\right) + D_{16}\left(-2\frac{\partial^2 w}{\partial x \partial y}\right)$$

$$M_y = B_{12}\left(\frac{\partial u^0}{\partial x}\right) + B_{22}\left(\frac{\partial v^0}{\partial y}\right) + B_{26}\left(\frac{\partial u^0}{\partial y} + \frac{\partial v^0}{\partial x}\right) + D_{12}\left(-\frac{\partial^2 w}{\partial x^2}\right) + D_{22}\left(-\frac{\partial^2 w}{\partial y^2}\right) + D_{26}\left(-2\frac{\partial^2 w}{\partial x \partial y}\right)$$

$$M_{xy} = B_{16}\left(\frac{\partial u^0}{\partial x}\right) + B_{26}\left(\frac{\partial v^0}{\partial y}\right) + B_{66}\left(\frac{\partial u^0}{\partial y} + \frac{\partial v^0}{\partial x}\right) + D_{16}\left(-\frac{\partial^2 w}{\partial x^2}\right) + D_{26}\left(-\frac{\partial^2 w}{\partial y^2}\right) + D_{66}\left(-2\frac{\partial^2 w}{\partial x \partial y}\right) \tag{9.58}$$

In order to substitute equation (9.58) into equation(9.13), calculate

$$\frac{\partial N_x}{\partial x} = A_{11}\left(\frac{\partial^2 u^0}{\partial x^2}\right) + A_{12}\left(\frac{\partial^2 v^0}{\partial x \partial y}\right) + A_{16}\left(\frac{\partial^2 u^0}{\partial x \partial y} + \frac{\partial^2 v^0}{\partial x^2}\right) +$$

$$+ B_{11}\left(-\frac{\partial^3 w}{\partial x^3}\right) + B_{12}\left(-\frac{\partial^3 w}{\partial x \partial y^2}\right) + B_{16}\left(-2\frac{\partial^3 w}{\partial x^2 \partial y}\right)$$

$$(9.59)$$

$$\frac{\partial N_{xy}}{\partial y} = A_{16}\left(\frac{\partial^2 u^0}{\partial y \partial x}\right) + A_{26}\left(\frac{\partial^2 v^0}{\partial y^2}\right) + A_{66}\left(\frac{\partial^2 u^0}{\partial y^2} + \frac{\partial^2 v^0}{\partial y \partial x}\right) +$$

$$+ B_{16}\left(-\frac{\partial^3 w}{\partial y \partial x^2}\right) + B_{26}\left(-\frac{\partial^3 w}{\partial y^3}\right) + B_{66}\left(-2\frac{\partial^3 w}{\partial x \partial y^2}\right)$$

$$(9.60)$$

Adding equations (9.59) and (9.60), and substituting into equation (9.13) yields the x equation of motion

$$A_{11}\left(\frac{\partial^2 u^0}{\partial x^2}\right) + 2A_{16}\left(\frac{\partial^2 u^0}{\partial x \partial y}\right) + A_{66}\left(\frac{\partial^2 u^0}{\partial y^2}\right) + A_{16}\left(\frac{\partial^2 v^0}{\partial x^2}\right) + \left(A_{12} + A_{16}\right)\left(\frac{\partial^2 v^0}{\partial x \partial y}\right) + A_{26}\left(\frac{\partial^2 v^0}{\partial y^2}\right) -$$

$$- B_{11}\left(\frac{\partial^3 w}{\partial x^3}\right) - 3B_{16}\left(\frac{\partial^2 w}{\partial x^2 \partial y}\right) - \left(B_{12} + 2B_{66}\right)\left(\frac{\partial^3 w}{\partial x \partial y^2}\right) - B_{26}\left(\frac{\partial^3 w}{\partial y^3}\right) = \rho\left(\frac{\partial^2 u^0}{\partial t^2}\right)$$

$$(9.61)$$

In order to substitute equation (9.58) into equation (9.16) calculate

$$\frac{\partial N_{xy}}{\partial x} = A_{16}\left(\frac{\partial^2 u^0}{\partial x^2}\right) + A_{26}\left(\frac{\partial^2 v^0}{\partial x \partial y}\right) + A_{66}\left(\frac{\partial^2 u^0}{\partial x \partial y} + \frac{\partial^2 v^0}{\partial x^2}\right) +$$

$$+ B_{16}\left(-\frac{\partial^3 w}{\partial x^3}\right) + B_{26}\left(-\frac{\partial_3 w}{\partial x \partial y^2}\right) + B_{66}\left(-2\frac{\partial^3 w}{\partial x^2 \partial y}\right)$$

$$(9.62)$$

$$\frac{\partial N_y}{\partial y} = A_{12}\left(\frac{\partial^2 u^0}{\partial y \partial x}\right) + A_{22}\left(\frac{\partial^2 v^0}{\partial y^2}\right) + A_{26}\left(\frac{\partial^2 u^0}{\partial y^2} + \frac{\partial v^0}{\partial y \partial x}\right) +$$

$$+ B_{12}\left(-\frac{\partial^3 w}{\partial y \partial x^2}\right) + B_{22}\left(-\frac{\partial^3 w}{\partial y^3}\right) + B_{26}\left(-2\frac{\partial^3 w}{\partial x \partial y^2}\right)$$

$$(9.63)$$

Adding equations (9.62) and (9.63), and substituting into equation (9.16) yields the y equation of motion

$$A_{16}\left(\frac{\partial^2 u^0}{\partial x^2}\right)+\left(A_{12}+A_{66}\right)\left(\frac{\partial^2 u^0}{\partial x\partial y}\right)+A_{26}\left(\frac{\partial^2 u^0}{\partial y^2}\right)+A_{66}\left(\frac{\partial^2 v^0}{\partial x^2}\right)+2A_{26}\left(\frac{\partial^2 v^0}{\partial x\partial y}\right)+A_{22}\left(\frac{\partial^2 v^0}{\partial y^2}\right)-$$

$$-B_{16}\left(\frac{\partial^3 w}{\partial x^3}\right)-\left(B_{12}+2B_{66}\right)\left(\frac{\partial^3 w}{\partial x^2\partial y}\right)-3B_{26}\left(\frac{\partial^3 w}{\partial x\partial y^2}\right)-B_{22}\left(\frac{\partial^3 w}{\partial y^3}\right)=\rho\left(\frac{\partial^2 v^0}{\partial t^2}\right)$$

$$(9.64)$$

In order to substitute equation (9.58) into equation(9.54), calculate

$$\frac{\partial^2 M_x}{\partial x^2}=B_{11}\left(\frac{\partial^3 u^0}{\partial x^3}\right)+B_{12}\left(\frac{\partial^3 v^0}{\partial x^2\partial y}\right)+B_{16}\left(\frac{\partial^3 u^0}{\partial x^2\partial y}+\frac{\partial^3 v^0}{\partial x^3}\right)+$$

$$+D_{11}\left(-\frac{\partial^4 w}{\partial x^4}\right)+D_{12}\left(-\frac{\partial^4 w}{\partial x^2\partial y^2}\right)+D_{16}\left(-2\frac{\partial^4 w}{\partial x^3\partial y}\right)$$

$$(9.65)$$

$$2\frac{\partial^2 M_{xy}}{\partial x\partial y}=2\left[\begin{array}{l}B_{16}\left(\frac{\partial^3 u^0}{\partial x^2\partial y}\right)+B_{26}\left(\frac{\partial^3 v^0}{\partial x\partial y^2}\right)+B_{66}\left(\frac{\partial^3 u^0}{\partial x\partial y}+\frac{\partial^3 v^0}{\partial x^2\partial y}\right)+\\[2mm]+D_{16}\left(-\frac{\partial^4 w}{\partial x^3\partial y}\right)+D_{26}\left(-\frac{\partial^4 w}{\partial x\partial y^3}\right)+D_{66}\left(-2\frac{\partial^4 w}{\partial x^2\partial y^2}\right)\end{array}\right]$$

$$(9.66)$$

$$\frac{\partial^2 M_y}{\partial y^2}=B_{12}\left(\frac{\partial^3 u^0}{\partial y^2\partial x}\right)+B_{22}\left(\frac{\partial^3 v^0}{\partial y^3}\right)+B_{26}\left(\frac{\partial^3 u^0}{\partial y^3}+\frac{\partial^3 v^0}{\partial y^2\partial x}\right)+$$

$$+D_{12}\left(-\frac{\partial^4 w}{\partial y^2\partial x^2}\right)+D_{22}\left(-\frac{\partial^4 w}{\partial y^4}\right)+D_{26}\left(-2\frac{\partial^4 w}{\partial x\partial y^3}\right)$$

$$(9.67)$$

$$N_x\frac{\partial^2 w}{\partial x^2}=\left[\begin{array}{l}A_{11}\left(\frac{\partial u^0}{\partial x}\right)+A_{12}\left(\frac{\partial v^0}{\partial y}\right)+A_{16}\left(\frac{\partial u^0}{\partial y}+\frac{\partial v^0}{\partial x}\right)+\\[2mm]+B_{11}\left(-\frac{\partial^2 w}{\partial x^2}\right)+B_{12}\left(-\frac{\partial^2 w}{\partial y^2}\right)+B_{16}\left(-2\frac{\partial^2 w}{\partial x\partial y}\right)\end{array}\right]\left(\frac{\partial^2 w}{\partial x^2}\right)$$

$$(9.68)$$

$$2N_{xy}\frac{\partial^2 w}{\partial x\partial y}=2\left[\begin{array}{l}A_{16}\left(\frac{\partial u^0}{\partial x}\right)+A_{26}\left(\frac{\partial v^0}{\partial y}\right)+A_{66}\left(\frac{\partial u^0}{\partial y}+\frac{\partial v^0}{\partial x}\right)+\\[2mm]+B_{16}\left(-\frac{\partial^2 w}{\partial x^2}\right)+B_{26}\left(-\frac{\partial^2 w}{\partial y^2}\right)+B_{66}\left(-2\frac{\partial^2 w}{\partial x\partial y}\right)\end{array}\right]\left(\frac{\partial^2 w}{\partial x\partial y}\right)$$

$$(9.69)$$

$$N_y\frac{\partial^2 w}{\partial y^2}=\left[\begin{array}{l}A_{12}\left(\frac{\partial u^0}{\partial x}\right)+A_{22}\left(\frac{\partial v^0}{\partial y}\right)+A_{26}\left(\frac{\partial u^0}{\partial y}+\frac{\partial v^0}{\partial x}\right)+\\[2mm]+B_{12}\left(-\frac{\partial^2 w}{\partial x^2}\right)+B_{22}\left(-\frac{\partial^2 w}{\partial y^2}\right)+B_{26}\left(-2\frac{\partial^2 w}{\partial x\partial y}\right)\end{array}\right]\left(\frac{\partial^2 w}{\partial y^2}\right)$$

$$(9.70)$$

Adding equations (9.65) through (9.70) and substituting into equation (9.54) yields the z

equation of motion

$$D_{11}\left(\frac{\partial^4 w}{\partial x^4}\right) + 4D_{16}\left(\frac{\partial^4 w}{\partial x^3 \partial y}\right) + 2\left(D_{12} + 2D_{66}\right)\left(\frac{\partial^4 w}{\partial x^2 \partial y^2}\right) + 4D_{26}\left(\frac{\partial^4 w}{\partial x \partial y^3}\right) + D_{22}\left(\frac{\partial^4 w}{\partial y^4}\right)$$

$$-B_{11}\left(\frac{\partial^3 u^0}{\partial x^3}\right) - 3B_{16}\left(\frac{\partial^3 u^0}{\partial x^2 \partial y}\right) - \left(B_{12} + 2B_{66}\right)\left(\frac{\partial^3 u^0}{\partial x \partial y^2}\right) - B_{26}\left(\frac{\partial^3 u^0}{\partial y^3}\right) - B_{16}\left(\frac{\partial^2 v^0}{\partial x_3}\right)$$

$$-\left(B_{12} + B_{66}\right)\left(\frac{\partial^3 v^0}{\partial x^2 \partial y}\right) - 3B_{26}\left(\frac{\partial^3 v^0}{\partial x \partial y^2}\right) - B_{22}\left(\frac{\partial^3 v^0}{\partial y^3}\right) = -\rho\left(\frac{\partial^2 w}{\partial t^2}\right) \tag{9.71}$$

Equations (9.61), (9.64), (9.71) are the equations of motion in term of displacements for

the composite plate. Upon rearrangement, we get

$$\boxed{\begin{aligned} A_{11}\frac{\partial^2 u^0}{\partial x^2} + 2A_{16}\frac{\partial^2 u^0}{\partial x \partial y} + A_{66}\frac{\partial^2 u^0}{\partial y^2} + A_{16}\frac{\partial^2 v^0}{\partial x^2} + \left(A_{12} + A_{66}\right)\frac{\partial^2 v^0}{\partial x \partial y} + A_{26}\frac{\partial^2 v^0}{\partial y^2} - B_{11}\frac{\partial^3 w}{\partial x^3} - \\ 3B_{16}\frac{\partial^3 w}{\partial x^2 \partial y} - \left(B_{12} + 2B_{66}\right)\frac{\partial^3 w}{\partial x \partial y^2} - B_{26}\frac{\partial^3 w}{\partial y^3} - \rho\frac{\partial^2 u^0}{\partial t^2} = 0 \end{aligned}} \tag{9.72}$$

$$\boxed{\begin{aligned} A_{16}\frac{\partial^2 u^0}{\partial x^2} + \left(A_{22} + A_{66}\right)\frac{\partial^2 u^0}{\partial x \partial y} + A_{26}\frac{\partial^2 u^0}{\partial y^2} + A_{66}\frac{\partial^2 v^0}{\partial x^2} + 2A_{26}\frac{\partial^2 v^0}{\partial x \partial y} + A_{22}\frac{\partial^2 v^0}{\partial y^2} - \\ B_{16}\frac{\partial^3 w}{\partial x^3} - \left(B_{12} - 2B_{66}\right)\frac{\partial^3 w}{\partial x^2 \partial y} - 3B_{26}\frac{\partial^3 w}{\partial x \partial y^2} - B_{22}\frac{\partial^3 w}{\partial y^3} - \rho\frac{\partial^2 v^0}{\partial t^2} = 0 \end{aligned}} \tag{9.73}$$

$$\boxed{\begin{aligned} D_{11}\frac{\partial^4 w}{\partial x^4} + 4D_{16}\frac{\partial^4 w}{\partial x^3 \partial y} + 2\left(D_{12} + 2D_{66}\right)\frac{\partial^4 w}{\partial x^2 \partial y^2} + 4D_{26}\frac{\partial^4 w}{\partial x \partial y^3} + D_{22}\frac{\partial^4 w}{\partial y^4} \\ -B_{11}\frac{\partial^3 u^0}{\partial x^3} - 3B_{16}\frac{\partial^3 u^0}{\partial x^2 \partial y} - \left(B_{12} + 2B_{66}\right)\frac{\partial^3 u^0}{\partial x \partial y^2} - B_{26}\frac{\partial^3 u^0}{\partial y^3} - B_{16}\frac{\partial^3 v^0}{\partial x^3} \\ -\left(B_{12} + 2B_{66}\right)\frac{\partial^3 v^0}{\partial x^2 \partial y} - 3B_{26}\frac{\partial^3 v^0}{\partial x \partial y^2} - B_{22}\frac{\partial^3 v^0}{\partial y^3} + \rho\frac{\partial^2 w}{\partial t^2} = 0 \end{aligned}} \tag{9.74}$$

**9.1.2.5 Equations of Motion for Symmetric laminates**

For symmetric laminates $B_{ij} = 0$; in this case, equations (9.72) through (9.74)

become

$$A_{11}\frac{\partial^2 u^0}{\partial x^2}+2A_{16}\frac{\partial^2 u^0}{\partial x\partial y}+A_{66}\frac{\partial^2 u^0}{\partial y^2}+A_{16}\frac{\partial^2 v^0}{\partial x^2}+\left(A_{12}+A_{66}\right)\frac{\partial^2 v^0}{\partial x\partial y}+A_{26}\frac{\partial^2 v^0}{\partial y^2}-\rho\frac{\partial^2 u^0}{\partial t^2}=0$$

$$A_{16}\frac{\partial^2 u^0}{\partial x^2}+\left(A_{22}+A_{66}\right)\frac{\partial^2 u^0}{\partial x\partial y}+A_{26}\frac{\partial^2 u^0}{\partial y^2}+A_{66}\frac{\partial^2 v^0}{\partial x^2}+2A_{26}\frac{\partial^2 v^0}{\partial x\partial y}+A_{22}\frac{\partial^2 v^0}{\partial y^2}-\rho\frac{\partial^2 v^0}{\partial t^2}=0$$

$$D_{11}\frac{\partial^4 w}{\partial x^4}+4D_{16}\frac{\partial^4 w}{\partial x^3\partial y}+2\left(D_{12}+2D_{66}\right)\frac{\partial^4 w}{\partial x^2\partial y^2}+4D_{26}\frac{\partial^4 w}{\partial x\partial y^3}+D_{22}\frac{\partial^4 w}{\partial y^4}+\rho\frac{\partial^2 w}{\partial t^2}=0$$

(9.75)

Equations (9.75) are the equations of motion for couplet in plane ($u^0, v^0$) and out of plane ($w$) vibration of a laminated composite plate with symmetric layup.

### 9.1.2.6 Equations of Motion for Composite Beams

For laminated composite beams, we assume the y displacement to be identically zero, $v^0 \equiv 0$; hence its derivatives are also identically zero, i.e., $\dfrac{\partial^2 v}{\partial x^2}, \dfrac{\partial^2 v}{\partial x\partial y}, \dfrac{\partial^2 v}{\partial y^2}, \dfrac{\partial^2 v}{\partial t^2} \equiv 0.$

We also assume $y$ invariance, i.e., $\dfrac{\partial}{\partial y}, \dfrac{\partial^2}{\partial x\partial y}, \dfrac{\partial^2}{\partial y^2}, \dfrac{\partial^4}{\partial x\partial y^3}, \dfrac{\partial^4}{\partial y^4} = 0$. Hence, equations (9.75) become

$$A_{11}\frac{\partial^2 u^0}{\partial x^2}+2A_{16}\cancel{\frac{\partial^2 u^0}{\partial x\partial y}}+A_{66}\cancel{\frac{\partial^2 u^0}{\partial y^2}}-\rho\frac{\partial^2 u^0}{\partial t^2}=0$$

$$D_{11}\frac{\partial^4 w}{\partial x^4}+4D_{16}\cancel{\frac{\partial^4 w}{\partial x^3\partial y}}+2\left(D_{12}+2D_{66}\right)\cancel{\frac{\partial^4 w}{\partial x^2\partial y^2}}+4D_{26}\cancel{\frac{\partial^4 w}{\partial x\partial y^3}}+D_{22}\cancel{\frac{\partial^4 w}{\partial y^4}}+\rho\frac{\partial^2 w}{\partial t^2}=0$$

(9.76)

i.e.,

$$A_{11}\frac{\partial^2 u^0}{\partial x^2}-\rho\frac{\partial^2 u^0}{\partial t^2}=0$$

(9.77)

$$D_{11}\frac{\partial^4 w}{\partial x^4}+\rho\frac{\partial^2 w}{\partial t^2}=0$$

(9.78)

Equation (9.77) can be related to the axial vibration equation (1.8) of Section 1.1, whereas equation (9.78) can be related with the flexural vibration equation (1.34) of Section 1.2.

201

For axial vibration, define

$$c^2 = A_{11} / \rho$$

(9.79)

Substitution of equation (9.79) into equation (9.80) yields

$$\boxed{c^2 \frac{\partial^2 u^0}{\partial x^2} - \frac{\partial^2 u^0}{\partial t^2} = 0}$$

(9.80)

Equation (9.80) is now of the same form as equation (1.8a); hence, the same solution

procedure applies as described in Section 1

For flexural vibration, define

$$a^4 = D_{11} / \rho$$

(9.81)

Substitution of equation (9.81) into equation (9.78) yields

$$\boxed{a^4 \frac{\partial^4 w}{\partial x^4} + \frac{\partial^2 w}{\partial t^2} = 0}$$

(9.82)

Equation (9.82) is now of the same form as equation (1.34a); hence, the same solution

procedure applies, as described in Section 1.

### 9.1.2.7 Equivalence with Isotropic Beam Model

In order to seek the general solution for axial and flexural vibration of a uniform

beam, we have to link the composite theory with the isotropic model. To proceed, recall

the decoupled equations of motion for the vibration of an elastic beam Figure 136 as

described in Section 1.
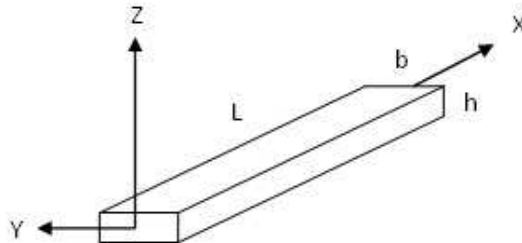


*Figure 136: Isotropic beam geometry, axes, and dimensions*

$$c^2 \frac{\partial^2 u}{\partial x^2} - \frac{\partial^2 u}{\partial t^2} = 0, \quad c^2 = \frac{EA}{m}$$

(9.83)

$$a^4 \frac{\partial^4 w}{\partial x^4} + \frac{\partial^2 w}{\partial t^2} = 0, \quad a^4 = \frac{EI}{m}$$

(9.84)

where $m$ is the mass per unit length of the beam,

$$m = \rho_0 bh$$

(9.85)

Recall Eq. (3.66) of Chapter 3 defining the $[A], [B], [D]$ matrix for a composite plate, i.e.,

$$[A] = \sum_{k=1}^{n} [\bar{Q}]_k (h_k - h_{k-1})$$

$$[B] = \frac{1}{2} \sum_{k=1}^{n} [\bar{Q}]_k (h_k^2 - h_{k-1}^2)$$

$$[D] = \frac{1}{3} \sum_{k=1}^{n} [\bar{Q}]_k (h_k^3 - h_{k-1}^3)$$

(9.86)

where $[\bar{Q}]_k$ is defined by equation (3.52) of Chapter 3 as

$$[\bar{Q}] = [T]^{-1} [Q][T]$$

(9.87)

Where $[T]$ is the rotation matrix and $[Q]$ is the stiffness matrix in the local coordinates

of the ply (layer) as given by equation (3.39), i.e.,

$$[Q]_k = \begin{bmatrix} \dfrac{E_{11}}{1-\upsilon_{12}\upsilon_{21}} & \dfrac{E_{11}\upsilon_{12}}{1-\upsilon_{12}\upsilon_{21}} & 0 \\[3mm] \dfrac{E_{11}\upsilon_{21}}{1-\upsilon_{12}\upsilon_{21}} & \dfrac{E_{22}}{1-\upsilon_{12}\upsilon_{21}} & 0 \\[3mm] 0 & 0 & G_{12} \end{bmatrix}$$

(9.88)

Assuming the beam to be made up of isotropic layers of same properties,

$$E_1 = E_2 = E, \quad \upsilon_{12} = \upsilon_{21} = \upsilon, \quad G_{12} = G = \frac{E}{2(1+\upsilon)}, \text{ we get}$$

$$[Q]_k = \begin{bmatrix} \dfrac{E}{1-v^2} & \dfrac{Ev}{1-v^2} & 0 \\[2mm] \dfrac{Ev}{1-v^2} & \dfrac{E}{1-v^2} & 0 \\[2mm] 0 & 0 & G \end{bmatrix} = [Q], \quad k = 1,\ldots,n$$

(9.89)

Hence, the new constant matrix $[Q]_k = [Q]$ can be factor out of Eq.(9.86) to get

$$[A] = \bar{Q}_k \sum_{k=1}^{n} (h_k - h_{k-1})$$

$$[B] = \frac{1}{2}\bar{Q}_k \sum (h_k^2 - h_{k-1}^2)$$

$$[D] = \frac{1}{3}\bar{Q}_k \sum (h_k^3 - h_{k-1}^3)$$

(9.90)

Mutual cancelation inside the summation (e.g. $\cancel{h_1} - h_0 + h_2 - \cancel{h_1} = h_2 - h_0$, etc.) yields

$$\sum_{k=1}^{n} (h_k - h_{k-1}) = h_n - h_0 = h$$

$$\frac{1}{2}\sum (h_k^2 - h_{k-1}^2) = \frac{1}{2}(h_n^2 - h_0^2) = \frac{1}{2}\left[\left(\frac{h}{2}\right)^2 - \left(-\frac{h}{2}\right)^2\right] = 0$$

$$\frac{1}{3}\sum (h_k^3 - h_{k-1}^3) = \frac{1}{3}(h_n^3 - h_0^3) = \frac{1}{3}\left[\left(\frac{h}{2}\right)^3 - \left(-\frac{h}{2}\right)^3\right]$$

$$= \frac{1}{3}\left(\frac{h^3}{8} + \frac{h^3}{8}\right) = \frac{1}{3}\cdot\frac{2}{8}h^3 = \frac{h^3}{12}$$

(9.91)

Substitution of Eq.(9.91) into Eq.(9.90) gives

$$[A] = [Q]h$$
$$[B] = [0]$$
$$[D] = [Q]\frac{h^3}{12}$$

(9.92)

Substitution of Eq.(9.89) into Eq.(9.92) yields

$$[A] = \begin{bmatrix} \dfrac{E}{1-\upsilon^2}h & \dfrac{E\upsilon}{1-\upsilon^2}h & 0 \\[3mm] \dfrac{E\upsilon}{1-\upsilon^2}h & \dfrac{E}{1-\upsilon^2}h & 0 \\[3mm] 0 & 0 & Gh \end{bmatrix} \rightarrow A_{11} = \dfrac{E}{1-\upsilon^2}h$$

(9.93)

$$[D] = \begin{bmatrix} \dfrac{E}{1-\upsilon^2}\dfrac{h^3}{12} & \dfrac{E\upsilon}{1-\upsilon^2}\dfrac{h^3}{12} & 0 \\[3mm] \dfrac{E\upsilon}{1-\upsilon^2}\dfrac{h^3}{12} & \dfrac{E}{1-\upsilon^2}\dfrac{h^3}{12} & 0 \\[3mm] 0 & 0 & Gh \end{bmatrix} \rightarrow D_{11} = \dfrac{E}{1-\upsilon^2}\dfrac{h^3}{12}$$

(9.94)

Recall now Eq.(9.12) defining the equivalent mass per unit area, i.e.

$$\rho = \int_{-h/2}^{h/2} \rho_0(z)\,dz$$

(9.95)

In our case of isotropic layers of same properties, we have $\rho_0(z) = \rho_0 = const.$ Hence,

Eq.(9.95) becomes

$$\rho = \rho_0 h$$

(9.96)

Substitution of Eq.(9.93) and (9.96) into Eq.(9.79) yields

$$c^2 = \frac{A_{11}}{\rho} = \frac{E}{1-\upsilon^2}h\frac{1}{\rho} = \left(\frac{E}{1-\upsilon^2}\right)\frac{h}{\rho_0 h} = \frac{E}{1-\upsilon^2}\cdot\frac{hb}{\rho_0 hb} = \left(\frac{E}{1-\upsilon^2}\right)\frac{A}{m}$$

(9.97)

Comparison of Eq. (9.97) and (9.83) indicates that agreement is achieved by using the

plane-strain correction

$$\boxed{E^* = \frac{E}{\left(1-\upsilon^2\right)}}$$

(9.98)

Similarly, multiplication of Eq. (9.94) by the width $b$ yields

$$b \cdot D_{11} = \frac{E}{1-\upsilon^2}\frac{bh^3}{12} = \frac{E}{1-\upsilon^2}I$$

(9.99)

or

$$D_{11} = \frac{E}{1-\upsilon^2} \frac{I}{b}$$

(9.100)

Substitution of Eq. (9.100) into Eq. (9.81) and use of Eq. (9.85) yields

$$a^4 = \frac{D_{11}}{\rho} = \frac{E}{1-\upsilon^2} \cdot \frac{I}{b\rho} = \frac{E}{1-\upsilon^2} \cdot \frac{I}{\rho_0 bh} = \frac{E}{1-\upsilon^2} \cdot \frac{I}{m} = E^* \frac{I}{m}$$

(9.101)

Comparison of Eq. (9.101) and (9.84) indicates that agreement is achieved by using the

plane-strain correction of Eq. (9.98)

# 10.     TASK #2: THE STMM METHOD

Rokhlin et al (2002) resolve the numerical instability of the TMM by introducing the layer stiffness matrix and use an efficient recursive algorithm to calculate the global stiffness matrix for an arbitrary anisotropic layered structure. In this latter method, a layer stiffness matrix substitutes the layer transfer matrix. It is important to note that the stiffness matrix transmits the stresses at the top and bottom of the layer with the displacements at the top and bottom layer. The terms in the matrix have exponentially decomposing terms and the matrix has the same dimension and easiness to solve as the transfer matrix. Overall, the stiffness matrix method is unconditionally stable and is more computationally efficient than the TMM method. We combine both GMM and STMM approaches and apply the new simplifications to the composite materials theory described in Chapter 8. This novel approach builds a new direction for the STMM method.

1. Beam is divided into segments as needed to introduce external loading

2. Segments are subdivided into subsegments to improve numerical convergence at high frequencies as shown in Figure 137.
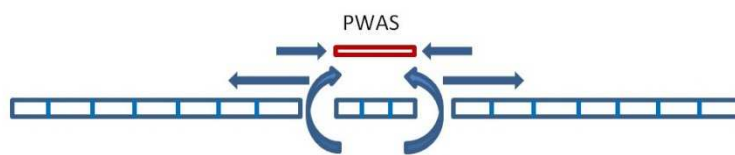


*Figure 137: Beam Segmentation*

207

3. Global matrix method (GMM) is applied to the beam segments

4. Stiffness transfer matrix method (STMM) is used in the subsegments

From the steps presented, the main advantages of combining the STMM and GMM approaches for composite materials are:

1. Numerical stability is achieved through subsegmentation using STMM

2. The number of variables is maintained low even at high frequencies (unlike GMM where high frequencies could only be attained through an expansion of the size of the global matrix

3. Subsegmentation is achieved without the need to modify the global system of equations. This can be easily automated using convergence criteria.

Unlike TMM method which can only handle a very short range of resonance frequencies without errors (~ 50 kHz as shown in Section 4), the STMM method brings a great improvement, allowing us to determine a long range of resonance frequencies without errors. (~500 kHz as will be shown in the new mathematical model in the current subsection).

The general principle behind the STMM method is similar to TMM, in the sense that it breaks up a complicated structure into several smaller segments which then can be expressed in a matrix format. However, the mathematical approach is different. Namely, the instability problem in TMM is solved by introducing the compliance matrix and using a recursive algorithm to calculate the global stiffness matrix.

Recalling the general solutions for axial and flexural vibrations of the uniform beam as described in Section 4.

$$u(x) = A_1 g_1(x) + A_2 g_2(x) \tag{10.1}$$

$$w(x) = A_3 f_1(x) + A_4 f_2(x) + A_5 f_3(x) + A_6 f_4(x) \tag{10.2}$$

$$g_1(x,\omega) = \sin\left[\gamma_a(\omega)x\right]$$

$$g_2(x,\omega) = \cos\left[\gamma_a(\omega)x\right]$$

$$f_1(x,\omega) = \frac{1}{2}\left\{\cosh\left[\gamma_f(\omega)x\right] + \cos\left[\gamma_f(\omega)x\right]\right\}$$

$$f_2(x,\omega) = \frac{1}{2\gamma_f(\omega)}\left\{\sinh\left[\gamma_f(\omega)x\right] + \sin\left[\gamma_f(\omega)x\right]\right\}$$

$$f_3(x,\omega) = \frac{1}{2\gamma_f^2(\omega)}\left\{\cosh\left[\gamma_f(\omega)x\right] - \cos\left[\gamma_f(\omega)x\right]\right\}$$

$$f_4(x,\omega) = \frac{1}{2\gamma_f^2(\omega)}\left\{\sinh\left[\gamma_f(\omega)x\right] - \sin\left[\gamma_f(\omega)x\right]\right\} \tag{10.3}$$

The quantities $\gamma_a$ and $\gamma_f$ are the wave numbers for the axial and flexural vibration, i.e.,

$$\gamma_a = \omega\sqrt{\frac{m}{EA}} \tag{10.4}$$

$$\gamma_f = \sqrt{\omega\sqrt{\frac{m}{EI}}} \tag{10.5}$$

Recall the matrix $\mathbf{B} = \mathbf{B}(x,\omega)$

$$[\mathbf{B}] = \begin{bmatrix} g_1 & g_2 & 0 & 0 & 0 & 0 \\ 0 & 0 & f_1 & f_2 & f_3 & f_4 \\ 0 & 0 & \dfrac{\partial f_1}{\partial x} & \dfrac{\partial f_2}{\partial x} & \dfrac{\partial f_3}{\partial x} & \dfrac{\partial f_4}{\partial x} \\ EA\dfrac{\partial g_1}{\partial x} & EA\dfrac{\partial g_2}{\mathrm{d}x} & 0 & 0 & 0 & 0 \\ 0 & 0 & EI\dfrac{\partial^2 f_1}{\partial x^2} & EI\dfrac{\partial^2 f_2}{\partial x^2} & EI\dfrac{\partial^2 f_3}{\partial x^2} & \dfrac{\partial^2 f_4}{\partial x^2} \\ 0 & 0 & EI\dfrac{\partial^3 f_1}{\partial x^3} & EI\dfrac{\partial^3 f_2}{\partial x^3} & EI\dfrac{\partial^3 f_3}{\partial x^3} & EI\dfrac{\partial^3 f_4}{\partial x^3} \end{bmatrix} \tag{10.6}$$

Introduce displacement vector, coefficient vector and the relation

$$[u] = [B][A] \tag{10.7}$$

209

Where constant column vector $A$ is:

$$[A] = \begin{bmatrix} A_1 \\ A_2 \\ A_3 \\ A_4 \\ A_5 \\ A_6 \end{bmatrix}$$

(10.8)

And vector $u$ :

$$[u] = \begin{bmatrix} u \\ w \\ \varphi \\ N \\ V \\ M \end{bmatrix}$$

(10.9)

## 10.1 *FREE VIBRATION OF THE UNIFORM COMPOSITE BEAM*

### 10.1.1 STMM FOR ONE SEGMENT BEAM

Before we develop the analytical model using the STMM for the composite beam, we start with a much simpler case: one segment having length L.



*Figure 138: One Segment*

Let us consider $u$ for displacements which will cover $w$ the flexural displacement and $\varphi$ the rotation on the slope and $p$ for forces which will cover $V$ the shear force and $M$ the bending moment. Let us express the state vector $z$ for the start point of the beam, $0$, as

$$z_0 = \begin{bmatrix} u_0 \\ p_0 \end{bmatrix}$$

(10.10)

210

according to the transfer matrix theory. Next, we rewrite the state vector $z$ as the product of matrix $B$ and a constant column vector $A$ as follows:

$$\begin{cases} z_0 = \begin{bmatrix} u_0 \\ p_0 \end{bmatrix} = \left[B(0)\right]\left[A\right] \\ u_0 = B_u(0) \cdot A \\ p_0 = B_p(0) \cdot A \end{cases}$$

$$(10.11)$$

Similarly, we do for the other end of the beam as follows:

$$\begin{cases} z_L = \begin{bmatrix} u_L \\ p_L \end{bmatrix} = \left[B(L)\right]\left[A\right] \\ u_L = B_u(L) \cdot A \\ p_L = B_p(L) \cdot A \end{cases}$$

$$(10.12)$$

By rearranging the displacements from the beginning and the end of the beam in one matrix and similarly for the forces, we obtain

$$\begin{bmatrix} u(0) \\ u(L) \end{bmatrix} = \begin{bmatrix} B_u(0) \\ B_p(L) \end{bmatrix} \cdot \left[A\right]$$

$$(10.13)$$

$$\begin{bmatrix} p(0) \\ p(L) \end{bmatrix} = \begin{bmatrix} B_p(0) \\ B_p(L) \end{bmatrix} \cdot \left[A\right]$$

$$(10.14)$$

By solving for matrix $A$ in the equation(10.13) in and replacing it into from the equation(10.14), we get the stiffness matrix $K$.

$$\begin{bmatrix} p(0) \\ p(L) \end{bmatrix} = \begin{bmatrix} B_p(0) \\ B_p(L) \end{bmatrix}\left[A\right] = \begin{bmatrix} B_p(0) \\ B_p(L) \end{bmatrix}\begin{bmatrix} B_u(0) \\ B_u(L) \end{bmatrix}^{-1}\begin{bmatrix} u(0) \\ u(L) \end{bmatrix} = [K]\begin{bmatrix} u(0) \\ u(L) \end{bmatrix} \Rightarrow$$

$$\begin{bmatrix} p(0) \\ p(L) \end{bmatrix} = \begin{bmatrix} B_p \\ B_u \end{bmatrix}\begin{bmatrix} u(0) \\ u(L) \end{bmatrix}; K = \frac{B_p}{B_u}$$

$$(10.15)$$

In a similar manner, by solving for matrix $A$ in equation (10.14) and replacing it into equation (10.13), we get the compliance matrix $S$.

$$\begin{bmatrix} u(0) \\ u(L) \end{bmatrix} = \begin{bmatrix} B_u(0) \\ B_u(L) \end{bmatrix}[A] = \begin{bmatrix} B_u(0) \\ B_u(L) \end{bmatrix}\begin{bmatrix} B_p(0) \\ B_p(L) \end{bmatrix}^{-1}\begin{bmatrix} p(0) \\ p(L) \end{bmatrix} = [S]\begin{bmatrix} p(0) \\ p(L) \end{bmatrix} \Rightarrow$$

$$\begin{bmatrix} u(0) \\ u(L) \end{bmatrix} = \begin{bmatrix} B_u \\ B_p \end{bmatrix}\begin{bmatrix} p(0) \\ p(L) \end{bmatrix}; \quad S = \frac{B_u}{B_p}$$

(10.16)

With the axial and flexural displacements calculated, the total displacement between the ends of a PWAS $x_1$ and $x_2$ are calculated

$$u_P = u_{(x_2)} - u_{(x_1)} - \frac{h}{2}\left[w'(x_2) - w'(x_1)\right]$$

(10.17)

The frequency response function FRF $(\omega)$ can be expressed by dividing by the excitation force F:

$$\frac{u_P}{F} = \frac{u_{(x_2)} - u_{(x_1)}}{F} - \frac{\frac{h}{2}\left[w'(x_2) - w'(x_1)\right]}{F}$$

(10.18)

$$FRF(\omega) = FRF_u(\omega) - FRF_w(\omega)$$

(10.19)

Where:

$$FRF_u(\omega) = \frac{u_{(x_2)} - u_{(x_1)}}{F}; \quad FRF_w(\omega) = \frac{\frac{h}{2}\left[w'(x_2) - w'(x_1)\right]}{F}$$

(10.20)

The dynamic structural stiffness of the composite beam is calculated as:

$$k_{str}(\omega) = \frac{1}{FRF(\omega)}$$

(10.21)

The electromechanical impedance of the PWAS can be expressed as:

$$Z = \frac{1}{Y} = \frac{1}{i\omega C}\left[1 - k_{31}^2\left(1 - \frac{1}{\varphi \cot \varphi + r}\right)\right]^{-1}$$

(10.22)

Where:

$$\varphi = \frac{\gamma_p l_p}{2}; \quad \gamma_p = \omega \rho_p s_{11}^E \tag{10.23}$$

Where piezoelectric properties of PWAS material (Giurgiutiu, 2008) are presented in

Table 6

*Table 6: PWAS Material Properties*

| Property | Symbol | Value |
|---|---|---|
| Compliance, in plane | $s_{11}^E$ | 15.3e-12 $Pa^{-1}$ |
| Compliance, thickness wise | $s_{33}^E$ | 17.3e-12 $Pa^{-1}$ |
| Dielectric constant | $s_{33}^T$ | 1750 $\varepsilon_0$ ; $\varepsilon_0$ =8.85e-12 F/m |
| Thickness wise induced strain coefficient | $d_{33}$ | 400e-12 m/V |
| In plane induced strain coefficient | $d_{31}$ | -175e-12 m/V |
| Coupling factor, parallel to electric field | $k_{33}$ | 0.72 |
| Coupling factor, transverse to electric field | $k_{31}$ | 0.36 |
| Poisson ratio | $v$ | 0.35 |
| Density | $\rho$ | 7700 $Kg/m^3$ |

Using STMM method, we look at the maximum resonance frequencies (stability) that

can be calculated using one segment beam of 100mm length, as described in Section 4

for TMM method. We are able to excite it until 500 kHz and obtain all natural

frequencies without any MATLAB errors (Figure 139). However, whenever we reach 525

kHz (Figure 140), the errors generated by the functions 'sin' and 'cos' are visible and
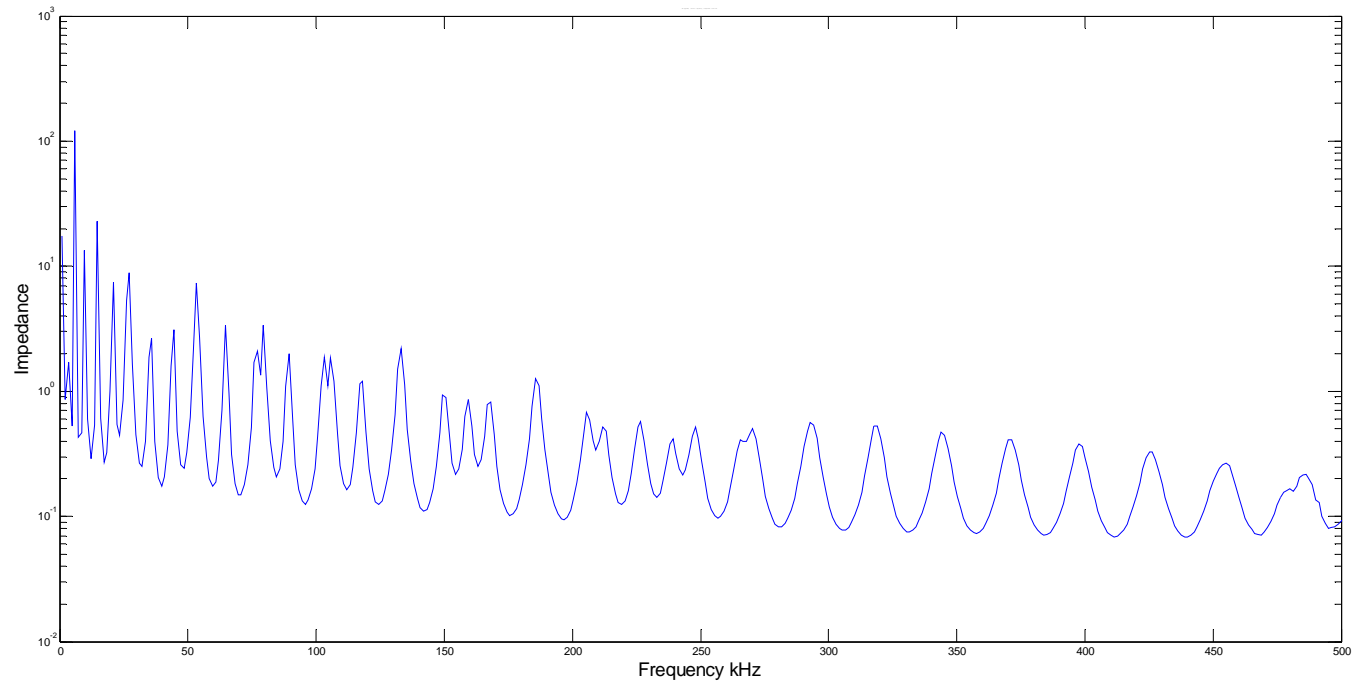
affect our results.

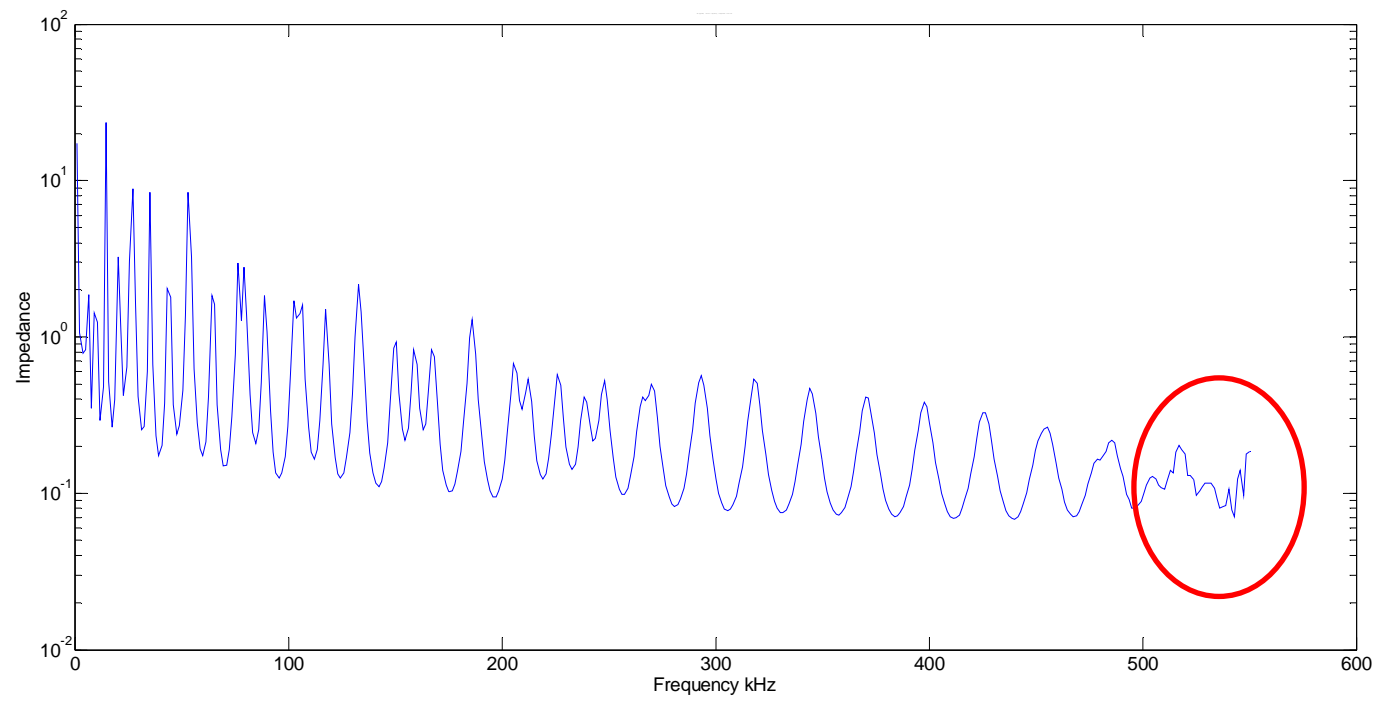*Figure 139: Maximum frequency 500 kHz without error - for 100 mm 1-segment beam*

*Figure 140: Frequency 525 kHz with error for 100 mm 1-segment beam*

215

We are able to improve the accuracy for a large beam with a high frequency with the new method STMM

### 10.1.2 STMM MULTI-SEGMENT BEAM

We now continue with a multi-segment case. As we can see in Figure 141, for a two-segment $(1,2)$ case, we have three nodes $(1,2,3)$. In a general case (multi-segment), we have the segments $(j, j+1)$ and nodes $(j, j+1, j+2)$.
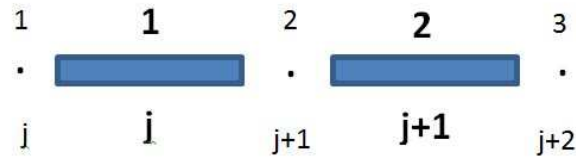


*Figure 141: Multi-segment concept*

Let us apply the same technique described for one segment for a two-segment case. This can be then extended to for the general case ( $j+1$ segments).

$$seg\ \#1 \Rightarrow \quad \{u\}_1 = [S]_1 \{p\}_1 \Rightarrow \quad \begin{bmatrix} u_1 \\ u_2 \end{bmatrix} = \begin{bmatrix} S1_{11} & S1_{12} \\ S1_{21} & S1_{22} \end{bmatrix} \begin{bmatrix} p_1 \\ p_2 \end{bmatrix}$$

$$seg\ \#2 \Rightarrow \quad \{u\}_2 = [S]_2 \{p\}_2 \Rightarrow \quad \begin{bmatrix} u_2 \\ u_3 \end{bmatrix} = \begin{bmatrix} S2_{22} & S2_{23} \\ S2_{32} & S2_{33} \end{bmatrix} \begin{bmatrix} p_2 \\ p_3 \end{bmatrix}$$

(10.24)

Let us rewrite the equation (10.24) in an expanded way as follows:

$$u_1 = S1_{11} p_1 + S1_{12} p_2$$

(10.25)

$$u_2 = S1_{21} p_1 + S1_{22} p_2$$

(10.26)

$$u_2 = S2_{22} p_2 + S2_{23} p_3$$

(10.27)

$$u_3 = S2_{32} p_2 + S2_{33} p_3$$

(10.28)

From (10.26) and (10.27), by eliminating $u_2$ from the first segment and replacing it into the second segment, we will be able to calculate $p_2$.

216

$$\left(S2_{22} - S1_{22}\right)p_2 - S1_{21}\,p_1 + S2_{23}\,p_3 = 0$$

$$p_2 = \left(S2_{22} - S1_{22}\right)^{-1} S1_{21}\,p_1 - \left(S2_{22} - S1_{22}\right)^{-1} S2_{23}\,p_3$$

$$p_2 = IS \cdot S1_{21}\,p_1 - IS \cdot S2_{23}\,p_3 \tag{10.29}$$

Where:

$$IS = \left(S2_{22} - S1_{22}\right)^{-1} \tag{10.30}$$

$$u_1 = S1_{11} \cdot p_1 + S1_{22} \cdot IS \cdot S1_{21} \cdot p_1 - S1_{12} \cdot IS \cdot S2_{23} \cdot p_3 =$$

$$\left(S1_{11} + S1_{12} \cdot IS \cdot S1_{21}\right)p_1 - \left(S1_{12} \cdot IS \cdot S2_{23}\right)p_3 \tag{10.31}$$

Where:

$$S_{11} = S1_{11} + S1_{12} \cdot IS \cdot S1_{21}$$

$$S_{13} = S1_{12} \cdot IS \cdot S2_{23} \tag{10.32}$$

In a similar manner we obtain $u_3$:

$$u_3 = S2_{32} \cdot IS \cdot S1_{21} \cdot p_1 - S2_{32} \cdot IS \cdot S2_{23} \cdot p_3 + S2_{33} \cdot p_3 =$$

$$\left(S2_{32} \cdot IS \cdot S1_{21}\right)p_1 + \left(S2_{23} - S2_{32} \cdot IS \cdot S2_{23}\right)p_3 \tag{10.33}$$

Where:

$$S_{31} = S2_{32} \cdot IS \cdot S1_{21}$$

$$S_{33} = S2_{33} - S2_{32} \cdot IS \cdot S2_{23} \tag{10.34}$$

Briefly, this is equivalent to:

$$IS = \frac{1}{\left(S2_{22} - S1_{22}\right)}$$

$$\{u\}_{13} = [S]_{13}\,\{p\}_{13}$$

$$\begin{bmatrix} u_1 \\ u_3 \end{bmatrix} = \begin{bmatrix} S_{11} & S_{13} \\ S_{31} & S_{33} \end{bmatrix} \begin{bmatrix} p_1 \\ p_3 \end{bmatrix}$$

$$S_{11} = S1_{11} + S1_{12} \cdot IS \cdot S1_{21}$$

$$S_{13} = -S1_{12} \cdot IS \cdot S2_{23}$$

$$S_{31} = S2_{32} \cdot IS \cdot S1_{21}$$

$$S_{33} = S2_{33} - S2_{32} \cdot IS \cdot S2_{23} \tag{10.35}$$

## 10.2    ADDING EXTERNAL LOADS

External loads (forces and moments) are introduced at the nodes between segments.

### 10.2.1 SIMPLE CASE: OFFSET AXIAL LOAD APPLIED TO A SINGLE SEGMENT

For illustration, we will consider the excitation $F$ to be a horizontal force applied to node 2 as shown in Figure 142. For simplicity, we represent the forces with a superscript $1$ or $2$ to denote the left or the right side of the node. $F$ is a generalized

$$F = \begin{bmatrix} N \\ V \\ M \end{bmatrix}$$

force containing forces and moments $\begin{bmatrix} N \\ V \\ M \end{bmatrix}$ up to case study.(In this case we will consider $F = N$ )
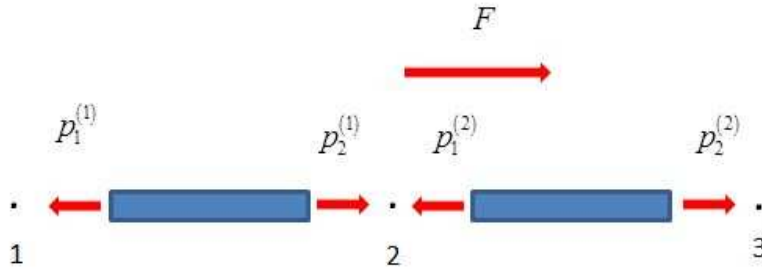


**Figure 142: Forced vibration of a uniform beam**

Now we rewrite all equations for a two-segment case and, in addition, we add the excitation force $p_2^e$:

$$\begin{bmatrix} u_1 \\ u_2 \end{bmatrix} = \begin{bmatrix} S1_{11} & S1_{12} \\ S1_{21} & S1_{22} \end{bmatrix} \begin{bmatrix} p_1^R \\ p_2^L \end{bmatrix}$$

$$\begin{bmatrix} u_2 \\ u_3 \end{bmatrix} = \begin{bmatrix} S2_{22} & S2_{23} \\ S2_{32} & S2_{33} \end{bmatrix} \begin{bmatrix} p_2^R \\ p_3^L \end{bmatrix}$$

(10.36)

This is equivalent to the following expanded form:

$$u_1 = S1_{11} p_1^R + S1_{12} p_2^L \tag{10.37}$$

$$u_2 = S1_{21} p_1^R + S1_{22} p_2^L \tag{10.38}$$

$$u_2 = S2_{22} p_2^R + S2_{23} p_3^L \tag{10.39}$$

$$u_3 = S2_{32} p_2^R + S2_{33} p_3^L \tag{10.40}$$

We then introduce the excitation force and using the free body diagram in Figure 142 ,

we write the equilibrium equation for node two as follows:

$$p_2^R = p_2^L + p_2^e \tag{10.41}$$

From equations (10.38), (10.39) and (10.41), we determine $p_2^L$ :

$$
\begin{aligned}
S1_{21} p_1^R + S1_{22} p_2^L &= S2_{22} p_2^R + S2_{23} p_3^L = \\
S2_{22} p_2^L + S2_{22} p_2^e &+ S2_{23} p_3^L \quad \Rightarrow \\
\left( S2_{22} - S1_{22} \right) p_2^L &= S1_{21} p_1^R - S2_{23} p_3^L - S2_{22} p_2^e
\end{aligned}
\tag{10.42}
$$

Where:

$$IS = \left( S2_{22} - S1_{22} \right)^{-1} \tag{10.43}$$

By rearranging the equation(10.42), $p_2^L$ became:

$$p_2^L = IS \cdot S1_{21} \cdot p_1^R - IS \cdot S2_{23} \cdot p_3^L - IS \cdot S2_{22} \cdot p_2^e \tag{10.44}$$

From (10.44) and (10.37), we can calculate the displacements on node 1:

$$u_1 = \left( S1_{11} + S1_{12} \cdot IS \cdot S1_{21} \right) p_1^R - \left( S1_{12} \cdot IS \cdot S2_{23} \right) p_3^L - \left( S1_{12} \cdot IS \cdot S2_{22} \right) p_2^e \tag{10.45}$$

From (10.44) and (10.40), we can calculate the displacements on node 3:

$$u_3 = \left( S2_{32} \cdot IS \cdot S1_{21} \right) p_1^R + \left( S2_{33} - S2_{32} \cdot IS \cdot S2_{23} \right) p_3^L + \left( S2_{32} - S2_{32} \cdot IS \cdot S2_{22} \right) p_2^e \tag{10.46}$$

Rewriting (10.45) and (10.46) in matrix form, we obtain:

$$
\begin{bmatrix} u_1 \\ u_2 \end{bmatrix} =
\begin{bmatrix} S13_{11} & S13_{13} \\ S13_{31} & S13_{33} \end{bmatrix}
\begin{bmatrix} p_1^R \\ p_3^L \end{bmatrix} +
\begin{bmatrix} 0 & S13_{e1} \\ 0 & S13_{e2} \end{bmatrix}
\begin{bmatrix} 0 \\ p_2^e \end{bmatrix}
\tag{10.47}
$$

Where

$$IS = \frac{I}{(S2_{22} - S1_{22})}$$

$$S13_{11} = S1_{11} + S1_{12} \cdot IS \cdot S1_{21}$$

$$S13_{13} = -S1_{12} \cdot IS \cdot S2_{23}$$

$$S13_{31} = S2_{32} \cdot IS \cdot S1_{21}$$

$$S13_{33} = S2_{33} - S2_{32} \cdot IS \cdot S2_{23}$$

$$S13_{e1} = -S1_{12} \cdot IS \cdot S2_{22}$$

$$S13_{e2} = S2_{32} - S2_{32} \cdot IS \cdot S2_{22} \tag{10.48}$$

Having all the equations for all three nodes, we can write the compliance matrix S:

$$
\begin{bmatrix} u_1^{(1)} \\ u_2^{(1)} \\ u_1^{(2)} \\ u_2^{(2)} \\ u_1^{(3)} \\ u_2^{(3)} \end{bmatrix} = 
\begin{bmatrix} S^{(1)} & & \\ & S^{(2)} & \\ & & S^{(3)} \end{bmatrix}
\begin{bmatrix} p_1^{(1)} \\ p_2^{(1)} \\ p_1^{(2)} \\ p_2^{(2)} \\ p_1^{(3)} \\ p_2^{(3)} \end{bmatrix} \tag{10.49}
$$

Where $S^{(1)}, S^{(2)}, S^{(3)}$ are $2x2$ matrices. The general form is:

$$u = S \cdot p \tag{10.50}$$

Where

$$[S] = \begin{bmatrix} S^{(1)} & & \\ & S^{(2)} & \\ & & S^{(3)} \end{bmatrix} \tag{10.51}$$

We then apply the external moment to the beam as shown in Figure 143. (In this case
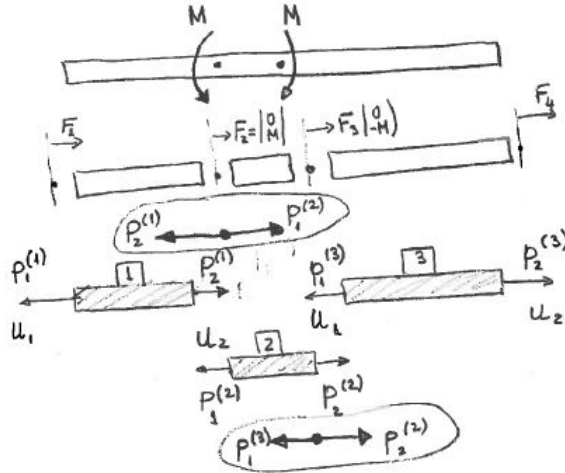
we will consider $F = M$ )

*Figure 143: Moment vibration of a uniform beam*

Let us build a general case equation for the compliance matrix:

$$\begin{bmatrix} u_1 \\ u_2 \end{bmatrix}_j = [S]_j \begin{bmatrix} p_1 \\ p_2 \end{bmatrix}_j$$

(10.52)

Where $j$ is a positive integer number. In the current case, $j = 3$.

We then write the node equilibrium equation

$$\begin{cases} p_1^{(1)} = -F_1 \\ p_1^{(2)} = p_2^{(1)} - F_2 \\ p_1^{(3)} = p_2^{(2)} - F_3 \\ p_2^{(3)} = F_4 \end{cases} \Rightarrow \begin{cases} p_1^{(1)} = -F_1 \\ -p_2^{(1)} + p_1^{(2)} = -F_2 \\ -p_2^{(2)} + p_1^{(3)} = -F_3 \\ -p_2^{(3)} = -F_4 \end{cases}$$

(10.53)

This is equivalent to matrix form:

$$\begin{bmatrix} I & 0 & 0 & 0 & 0 & 0 \\ 0 & -I & I & 0 & 0 & 0 \\ 0 & 0 & 0 & -I & I & 0 \\ 0 & 0 & 0 & 0 & 0 & I \end{bmatrix} \begin{bmatrix} p_1^{(1)} \\ p_2^{(1)} \\ p_1^{(2)} \\ p_2^{(2)} \\ p_1^{(3)} \\ p_2^{(3)} \end{bmatrix} = \begin{bmatrix} F_1 \\ F_2 \\ F_3 \\ F_4 \end{bmatrix}$$

(10.54)

Where $I$ is the identity matrix and for simplicity we denote

$$[A] = \begin{bmatrix} I & 0 & 0 & 0 & 0 & 0 \\ 0 & -I & I & 0 & 0 & 0 \\ 0 & 0 & 0 & -I & I & 0 \\ 0 & 0 & 0 & 0 & 0 & I \end{bmatrix}$$

(10.55)

The displacement compatibility equations are

$$\begin{cases} u_1^{(2)} = u_2^{(1)} \\ u_1^{(3)} = u_2^{(2)} \end{cases} \Rightarrow \begin{cases} u_1^{(2)} - u_2^{(1)} = 0 \\ u_1^{(3)} - u_2^{(2)} = 0 \end{cases}$$

(10.56)

This is equivalent to

$$\begin{bmatrix} 0 & -I & I & 0 & 0 & 0 \\ 0 & 0 & 0 & -I & I & 0 \end{bmatrix} \begin{bmatrix} u_1^{(1)} \\ u_2^{(1)} \\ u_1^{(2)} \\ u_2^{(2)} \\ u_1^{(3)} \\ u_2^{(3)} \end{bmatrix} = 0$$

(10.57)

Where

$$[B] = \begin{bmatrix} 0 & -I & I & 0 & 0 & 0 \\ 0 & 0 & 0 & -I & I & 0 \end{bmatrix}$$

(10.58)

We thus have 12 unknowns and 12 equations, which should be solvable using the global matrix approach, which is numerically stable. The numerical instability can be solved by subsegmenting.

We build a global matrix

$$[M] \cdot [X] = [N]$$

(10.59)

Where

$$\{X\} = \left\{ \begin{array}{c} \{u\} \\ \{p\} \end{array} \right\}$$

$$[I \quad -S]\begin{bmatrix} u \\ p \end{bmatrix} = [0]$$

$$[0 \quad A]\begin{bmatrix} u \\ p \end{bmatrix} = [F]$$

$$[B \quad 0]\begin{bmatrix} u \\ p \end{bmatrix} = [0]$$

(10.60)

$$\begin{bmatrix} I & -S \\ 0 & A \\ B & 0 \end{bmatrix}\begin{bmatrix} u \\ p \end{bmatrix}_{12} = \begin{bmatrix} 0 \\ F \\ 0 \end{bmatrix}$$

$$[M] = \begin{bmatrix} I & -S \\ 0 & A \\ B & 0 \end{bmatrix}; \quad [X] = \begin{bmatrix} u \\ p \end{bmatrix}_{12}; \quad [N] = \begin{bmatrix} 0 \\ F \\ 0 \end{bmatrix}$$

(10.61)

The expanded form of the global matrix is

$$\begin{bmatrix} I & & & & & & -S^{(1)} & & & & & \\ & I & & & & & & & & & & \\ & & I & & & & & -S^{(2)} & & & & \\ & & & I & & & & & & & & \\ & & & & I & & & & & -S^{(3)} & & \\ & & & & & I & & & & & & \\ & & 0 & & & & -I & 0 & 0 & 0 & 0 & 0 \\ & & & & & & 0 & I & -I & 0 & 0 & 0 \\ & & 0 & & & & 0 & 0 & 0 & I & -I & 0 \\ & & & & & & 0 & 0 & 0 & 0 & 0 & I \\ 0 & -I & I & 0 & 0 & 0 & & & & 0 & & \\ 0 & 0 & 0 & -I & I & 0 & & & & & & \end{bmatrix}\begin{bmatrix} u \\ p \end{bmatrix} = \begin{bmatrix} 0 \\ 0 \\ 0 \\ 0 \\ 0 \\ 0 \\ F1 \\ F2 \\ F3 \\ F4 \\ 0 \\ 0 \end{bmatrix}$$

(10.62)

Each $u$ and $p$ contains two components

$$u = \begin{bmatrix} w \\ p \end{bmatrix}; \quad p = \begin{bmatrix} V \\ M \end{bmatrix}$$

(10.63)

Hence the sizes of the matrices double

$$\begin{bmatrix} I_{12} & -S_{12x12} \\ O_{8x12} & A_{8x12} \\ B_{4x12} & O_{4x12} \end{bmatrix}_{24x24} \begin{bmatrix} u \\ p \end{bmatrix}_{24x1} = \begin{bmatrix} O_{12x1} \\ F_{8x1} \\ O_{4x1} \end{bmatrix}_{24x1} \tag{10.64}$$

Where:

$$[A]_{8x12} = \begin{bmatrix} -I_2 & O_2 & O_2 & O_2 & O_2 & O_2 \\ O_2 & I_2 & -I_2 & O_2 & O_2 & O_2 \\ O_2 & O_2 & O_2 & I_2 & -I_2 & O_2 \\ O_2 & O_2 & O_2 & O_2 & O_2 & I_2 \end{bmatrix}_{2x2xN_{seg}}$$

$$[B]_{4x12} = \begin{bmatrix} O_2 & -I_2 & I_2 & O_2 & O_2 & O_2 \\ O_2 & O_2 & O_2 & -I_2 & I_2 & O_2 \end{bmatrix}_{2x2xN_{seg}}$$

$$[S]_{12x12} = \begin{bmatrix} S^{(1)} & & \\ & S^{(2)} & \\ & & S^{(3)} \end{bmatrix} \tag{10.65}$$

Having the global matrix $M \cdot X = N$, we can solve for $X$ as $X = M / N$.

We start the analysis of force vibrations of the uniform composite beam by assuming a value for $\omega$ and calculating the displacement based on STMM approach.

### 10.2.2 EXTERNAL FORCES AND MOMENTS

Figure 144 shows the schematic of the beam with both force and moment excitation. We denote by $u$ displacements that cover $u$ the axial displacement, $w$ the flexural displacement and $\varphi$ the rotation on the slope. We denote by $p$ forces that cover $N$ the axial force, $V$ the shear force and $M$ the bending moment.

224
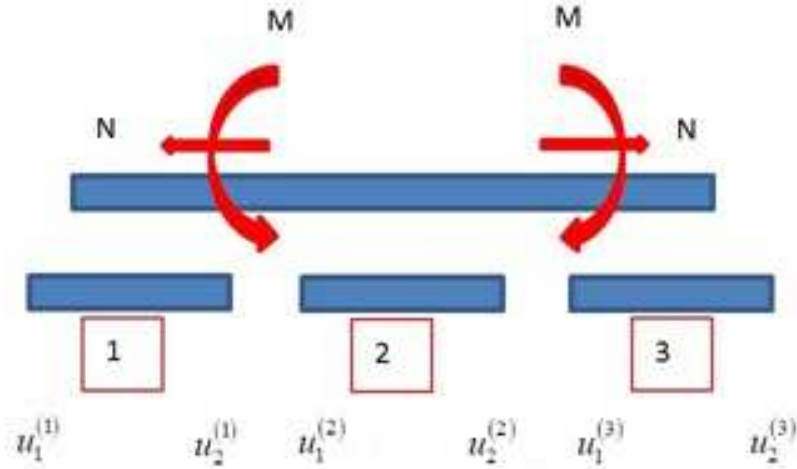
**Figure 144: External Force and Moment**

The compliance matrix will take the following form for a three-segment case:

$$\begin{bmatrix} u_1 \\ u_2 \end{bmatrix}_6 = [S]_{6x6} \begin{bmatrix} p_1 \\ p_2 \end{bmatrix}_6$$

(10.66)

We build a global matrix

$$[M] \cdot [X] = [N]$$

(10.67)

Where:

$$\begin{bmatrix} I_{18} & -S_{18x18} \\ O_{12x18} & A_{12x18} \\ B_{6x18} & O_{6x18} \end{bmatrix}_{36x36} \begin{bmatrix} u \\ p \end{bmatrix}_{36x1} = \begin{bmatrix} O_{18x1} \\ F_{12x1} \\ O_{6x1} \end{bmatrix}_{36x1}$$

$$[M] = \begin{bmatrix} I_{18} & -S_{18x18} \\ O_{12x18} & A_{12x18} \\ B_{6x18} & O_{6x18} \end{bmatrix}_{36x36} \quad ; \quad [X] = \begin{bmatrix} u \\ p \end{bmatrix}_{36x1} \quad ; \quad [N] = \begin{bmatrix} O_{18x1} \\ F_{12x1} \\ O_{6x1} \end{bmatrix}_{36x1}$$

(10.68)

and,

$$[A]_{12x18} = \begin{bmatrix} -I_3 & O_3 & O_3 & O_3 & O_3 & O_3 \\ O_3 & I_3 & -I_3 & O_3 & O_3 & O_3 \\ O_3 & O_3 & O_3 & I_3 & -I_3 & O_3 \\ O_3 & O_3 & O_3 & O_3 & O_3 & I_3 \end{bmatrix}_{2x2xN_{seg}}$$

$$[B]_{6x18} = \begin{bmatrix} O_3 & -I_3 & I_3 & O_3 & O_3 & O_3 \\ O_3 & O_3 & O_3 & -I_3 & I_3 & O_3 \end{bmatrix}_{2x2xN_{seg}}$$

$$[S]_{18x18} = \begin{bmatrix} S_{6x6}^{(1)} & O_6 & O_6 \\ O_6 & S_{6x6}^{(2)} & O_6 \\ O_6 & O_6 & S_{6x6}^{(3)} \end{bmatrix}$$

(10.69)

The complete expanded form of the global matrix can be seen in Figure 145.
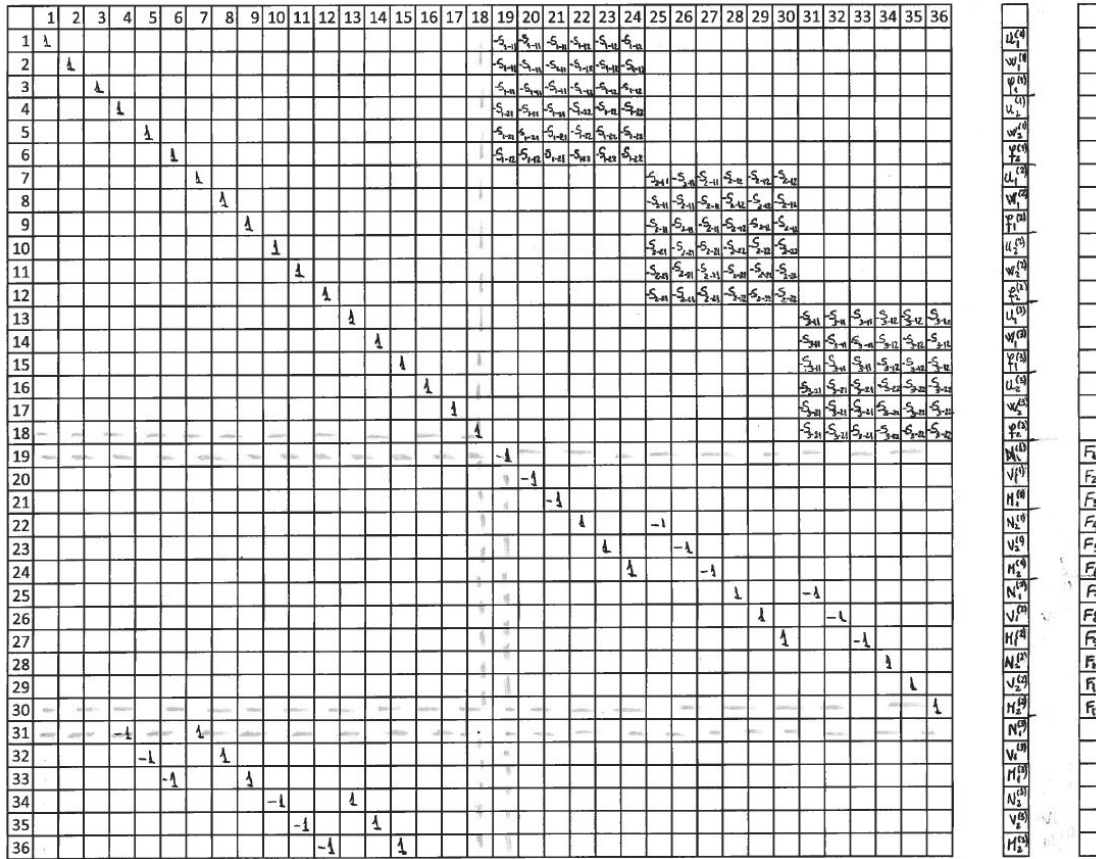


**Figure 145: Global matrix with all elements**

Having the global matrix $M \cdot X = N$, we can solve for $X$ as $X = M / N$.

## 10.3 MODELING OF A DELAMINATED COMPOSITE BEAM

The methodology to model a delaminated composite beam is almost the same as previously demonstrated with the difference that we have to divide the beam in several segments. The delamination will create a discontinuity in the composite material which will split the beam in two branches as illustrated in Figure 146.
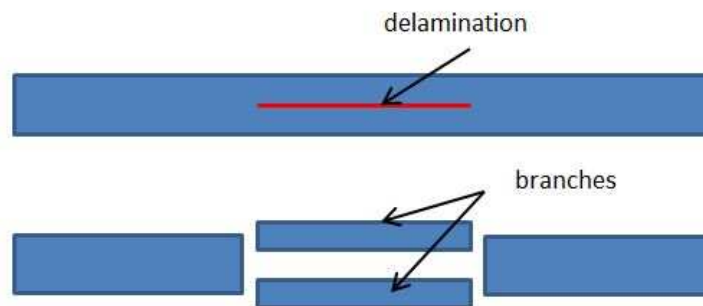


*Figure 146: Schematic of delaminate composite beam*

In this section, we develop a mathematical model which integrates the delamination into STMM. In order to do this, the first step is to find the location of the neutral axis for a composite multi-layer beam. Once the location of the neutral axis is determined, all the multi-layer beam material properties will be expressed with respect to the elastic center.

### 10.3.1 NEUTRAL AXIS SHIFT

For a better understanding of this concept, we will study neutral axis for an isotropic bar of arbitrary cross-section (Figure 147). By definition, neutral axis is such that the axial and flexural effects are decoupled.
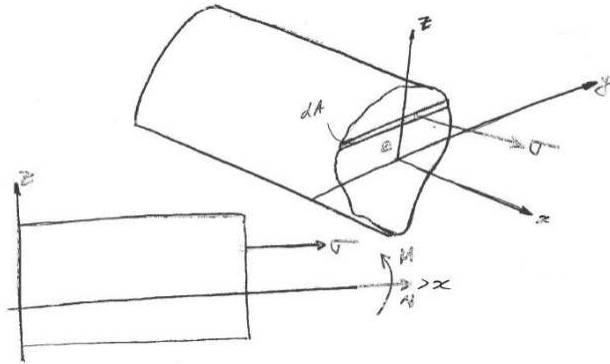
*Figure 147: Neutral axis –Arbitrary cross section*

Where:

$$E = const.$$

$$\varepsilon = \varepsilon_0 + zk_x$$

$$k_x = -\frac{\partial^2 \omega_0}{\partial x^2}$$

$$\sigma = E\varepsilon_0 + Ek_x z \qquad (10.70)$$

$$N = \int_A \sigma dA = \int_A \left( E\varepsilon_0 + Ek_x z \right) dA = EA\varepsilon_0 + Ek_x \int_A zdA \qquad (10.71)$$

$$-M = \int_A \sigma zdA = \int_A \left( E\varepsilon_0 + Ek_x z \right) zdA = E\varepsilon_0 \int_A zdA + EIk_x \qquad (10.72)$$

To decouple axial and flexural effects, we need the first moment of area to be zero, i.e.

$$\int_A zdA = 0 \qquad (10.73)$$

Consider a generic system of axis $0\bar{x}Z$ (Figure 148).
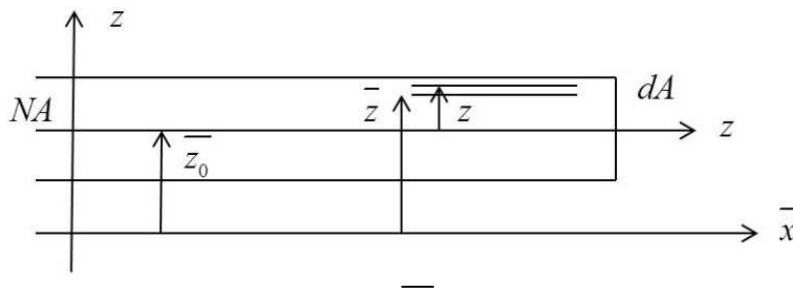


*Figure 148: Position $\bar{z}_0$ of the neutral axis*

228

We want to find the position $\overline{z}_0$ of the neutral axis. The solution is to calculate first moment of area about the neutral axis and make it zero.

$$\int z dA = \int \left(\overline{z} - \overline{z}_0\right) dA = \int \overline{z} dA - \overline{z}_0 \int dA = 0$$

(10.74)

$$\overline{z}_0 = \frac{\int_A \overline{z} dA}{\int_A dA} = \frac{1}{A}\int_A \overline{z} dA$$

(10.75)

Neutral axis for a composite laminate by definition is such that the axial and flexural effects are decoupled. Difference from isotropic bar:

$$E \neq const; \quad E = E(z)$$
$$\rho \neq const; \quad \rho = \rho(z)$$

(10.76)

From equation (10.76), (10.71)and (10.72) we got:

$$N = \int_A \sigma dA = \int_A \left(E\varepsilon_0\right) dA = \int_A Ek_x z dA$$
$$-M = \int_A \sigma z dA = \int_A E\varepsilon_0 z dA + \int_A Ek_x z^2 dA$$

(10.77)

Define equivalent elastic properties:

$$EA = \int_A E dA; \quad EI = \int_A Ez^2 dA; \quad m = \int_A \rho dA$$

(10.78)

From equations (10.78) and(10.76):

$$N = EA\varepsilon_0 + k_x \cancel{\int_A Ez dA}$$
$$-M = \varepsilon_0 \cancel{\int_A Ez dA} + EIk_x$$

(10.79)

Need to make zero the integral (modulus-weighted first moment of area)

$$\int_A Ez dA = 0$$

(10.80)

To find position of neutral axis, we modify equation (10.75) such that:

229

$$\overline{z}_0 = \frac{\int_A E \overline{z} dA}{\int_A E dA}$$

(10.81)

For a laminated composite, the properties $E(z), \rho(z)$ are piece wise constant inside a

lamina and integrate become summations, i.e.,( per unit width b=1)

$$EA = \int_A E dA = \sum_{k=1}^{N} \int_{z_{k-1}}^{z_k} E_k dz = \sum_{k=1}^{N} E_k \left( z_k - z_{k-1} \right)$$

$$EI = \int_A E z^2 dA = \frac{1}{3} \sum_{k=1}^{N} E_k \left( z_k^3 - z_{k-1}^3 \right)$$

$$m = \int_A \rho dA = \sum_{k=1}^{N} \rho_k \left( z_k - z_{k-1} \right)$$

$$\overline{z}_0 = \frac{\dfrac{1}{2} \sum_{k=1}^{N} E_k \left( z_k^2 - z_{k-1}^2 \right)}{\sum_{k=1}^{N} E_k \left( z_k - z_{k-1} \right)}$$

(10.82)
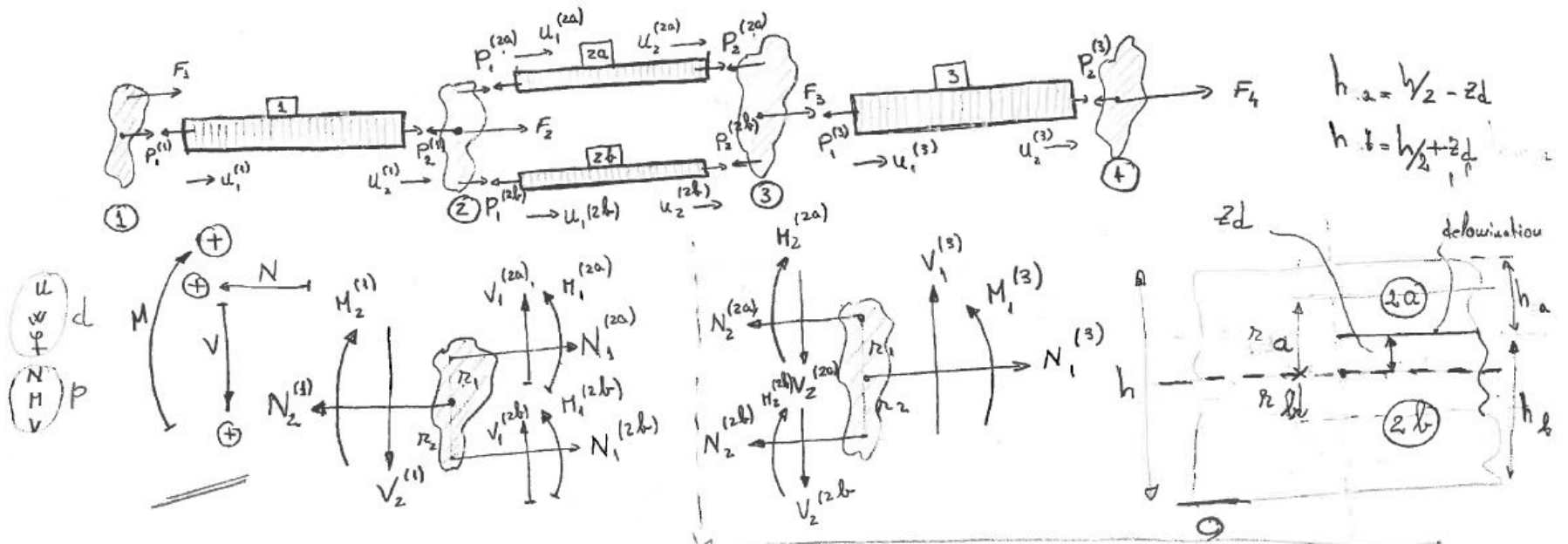
*Figure 149: STMM delamination - free body diagram*

231

### 10.3.2 NODE EQUILIBRIUM AND COMPATIBILITY EQUATIONS FOR TRANSFER INTO THE DELAMINATED REGION

We write the node equilibrium equations for the left hand side (node 2) and right hand side (node 3) of the delamination shown in Figure 149. In this case, segment $2$, which contains the delamination, will be split into two segments: the upper part denoted $2a$ and the bottom part denoted $2b$. In order to link those two new segments with the previous segment (segment $1$), we have to define the distance between the center of the first segment and the center of the new upper segment $2a$ and respectively the lower segment $2b$. We denote by $r_a$ the distance between the center of segment $1$ and the center of the segment $2a$ and $r_b$ the distance between the center of segment $1$ and the center of the segment $2b$.

$$
\begin{cases}
N_2^{(1)} - N_1^{(2a)} - N_1^{(2b)} = 0 \\
V_2^{(1)} - V_1^{(2a)} - V_1^{(2b)} = 0 \\
M_2^{(1)} + r_a N_1^{(2a)} - M_1^{(2a)} - r_b N_1^{(2b)} - M_1^{(2b)} = 0
\end{cases}
$$

$$
\begin{cases}
-N_1^{(3)} + N_2^{(2a)} + N_2^{(2b)} = 0 \\
-V_1^{(3)} + V_2^{(2a)} + V_2^{(2b)} = 0 \\
-M_1^{(3)} - r_a N_2^{(2a)} + M_2^{(2a)} + r_b N_2^{(2b)} + M_2^{(2b)} = 0
\end{cases}
$$

$$(10.83)$$

We can rewrite the moment equations in a matrix form as follow:

$$
\begin{bmatrix} 0 & 0 & 1 \end{bmatrix}\begin{bmatrix} N_2^{(1)} \\ V_2^{(1)} \\ M_2^{(1)} \end{bmatrix} + \begin{bmatrix} r_a & 0 & -1 \end{bmatrix}\begin{bmatrix} N_1^{(2a)} \\ V_1^{(2a)} \\ M_1^{(2a)} \end{bmatrix} + \begin{bmatrix} -r_b & 0 & -1 \end{bmatrix}\begin{bmatrix} N_1^{(2b)} \\ V_1^{(2b)} \\ M_1^{(2b)} \end{bmatrix} = 0
$$

$$
\begin{bmatrix} 0 & 0 & -1 \end{bmatrix}\begin{bmatrix} N_1^{(3)} \\ V_1^{(3)} \\ M_1^{(3)} \end{bmatrix} + \begin{bmatrix} -r_a & 0 & 1 \end{bmatrix}\begin{bmatrix} N_2^{(2a)} \\ V_2^{(2a)} \\ M_2^{(2a)} \end{bmatrix} + \begin{bmatrix} r_b & 0 & 1 \end{bmatrix}\begin{bmatrix} N_2^{(2b)} \\ V_2^{(2b)} \\ M_2^{(2b)} \end{bmatrix} = 0
$$

(10.84)

By rearranging:

$$
\begin{bmatrix} \begin{bmatrix} 0 & 0 & 1 \end{bmatrix} & \begin{bmatrix} r_a & 0 & -1 \end{bmatrix} & \begin{bmatrix} -r_b & 0 & -1 \end{bmatrix} \end{bmatrix}\begin{bmatrix} N_2^{(1)} \\ V_2^{(1)} \\ M_2^{(1)} \\ N_1^{(2a)} \\ V_1^{(2a)} \\ M_1^{(2a)} \\ N_1^{(2b)} \\ V_1^{(2b)} \\ M_1^{(2b)} \end{bmatrix} = 0
$$

(10.85)

$$
\begin{bmatrix} \begin{bmatrix} 0 & 0 & -1 \end{bmatrix} & \begin{bmatrix} -r_a & 0 & 1 \end{bmatrix} & \begin{bmatrix} r_b & 0 & 1 \end{bmatrix} \end{bmatrix}\begin{bmatrix} N_1^{(3)} \\ V_1^{(3)} \\ M_1^{(3)} \\ N_2^{(2a)} \\ V_2^{(2a)} \\ M_2^{(2a)} \\ N_2^{(2b)} \\ V_2^{(2b)} \\ M_2^{(2b)} \end{bmatrix} = 0
$$

(10.86)

or:

$$\begin{bmatrix} 1 & 0 & 0 & -1 & 0 & 0 & -1 & 0 & 0 \\ 0 & 1 & 0 & 0 & -1 & 0 & 0 & -1 & 0 \\ 0 & 0 & 1 & r_a & 0 & -1 & -r_b & 0 & 1 \end{bmatrix} \begin{bmatrix} N_2^{(1)} \\ V_2^{(1)} \\ M_2^{(1)} \\ N_1^{(2a)} \\ V_1^{(2a)} \\ M_1^{(2a)} \\ N_1^{(2b)} \\ V_1^{(2b)} \\ M_1^{(2b)} \end{bmatrix} = 0$$

$$\Rightarrow \begin{bmatrix} I & -T_1^{2a} & -T_1^{2b} \end{bmatrix} \begin{bmatrix} p_2^{(1)} \\ p_1^{(2a)} \\ p_1^{(2b)} \end{bmatrix}$$

$$\begin{bmatrix} T_1^{2a} \end{bmatrix} = \begin{bmatrix} 1 & 0 & 0 \\ 0 & 1 & 0 \\ -r_a & 0 & 1 \end{bmatrix}; \quad \begin{bmatrix} T_1^{2b} \end{bmatrix} = \begin{bmatrix} 1 & 0 & 0 \\ 0 & 1 & 0 \\ r_b & 0 & 1 \end{bmatrix};$$

(10.87)

$$\begin{bmatrix} -1 & 0 & 0 & 1 & 0 & 0 & 1 & 0 & 0 \\ 0 & -1 & 0 & 0 & 1 & 0 & 0 & 1 & 0 \\ 0 & 0 & -1 & -r_a & 0 & 1 & r_b & 0 & 1 \end{bmatrix} \begin{bmatrix} N_1^{(3)} \\ V_1^{(3)} \\ M_1^{(3)} \\ N_2^{(2a)} \\ V_2^{(2a)} \\ M_2^{(2a)} \\ N_2^{(2b)} \\ V_2^{(2b)} \\ M_2^{(2b)} \end{bmatrix} = 0$$

$$\Rightarrow \begin{bmatrix} -I & +T_1^{2a} & +T_1^{2b} \end{bmatrix} \begin{bmatrix} p_1^{(3)} \\ p_2^{(2a)} \\ p_2^{(2b)} \end{bmatrix}$$

$$\left[ T_2^{2a} \right] = \begin{bmatrix} 1 & 0 & 0 \\ 0 & 1 & 0 \\ -r_a & 0 & 1 \end{bmatrix}; \quad \left[ T_2^{2b} \right] = \begin{bmatrix} 1 & 0 & 0 \\ 0 & 1 & 0 \\ r_b & 0 & 1 \end{bmatrix}$$

(10.88)

We write the node equilibrium equations for the entire beam

$$\begin{cases} -p_1^{(1)} = F_1 \\ p_2^{(1)} - T_1^{(2a)} p_1^{(2a)} - T_1^{(2b)} p_1^{(2b)} = F_2 \\ T_2^{(2a)} p_2^{(2a)} + T_2^{(2b)} p_2^{b} - p_1^{(3)} = \\ p_2^{(3)} = F_4 \end{cases}$$

(10.89)

This is equivalent to the matrix format:

$$
\begin{bmatrix}
-I & 0 & 0 & 0 & 0 & 0 & 0 & 0 \\
0 & I & -T_1^{2a} & 0 & -T_1^{2b} & 0 & 0 & 0 \\
0 & 0 & 0 & T_2^{2a} & 0 & T_2^{2b} & -I & 0 \\
0 & 0 & 0 & 0 & 0 & 0 & 0 & I
\end{bmatrix}
\begin{bmatrix}
N_2^{(1)} \\
V_2^{(1)} \\
M_2^{(1)} \\
N_1^{(2a)} \\
V_1^{(2a)} \\
M_1^{(2a)} \\
N_1^{(2b)} \\
V_1^{(2b)} \\
M_1^{(2b)}
\end{bmatrix}
=
\begin{bmatrix}
F_1 \\
F_2 \\
F_3 \\
F_4
\end{bmatrix}
$$

$$[A][P]=[F]$$

$$
[A]=
\begin{bmatrix}
-I & 0 & 0 & 0 & 0 & 0 & 0 & 0 \\
0 & I & -T_1^{2a} & 0 & -T_1^{2b} & 0 & 0 & 0 \\
0 & 0 & 0 & T_2^{2a} & 0 & T_2^{2b} & -I & 0 \\
0 & 0 & 0 & 0 & 0 & 0 & 0 & I
\end{bmatrix};
$$

$$
[P]=
\begin{bmatrix}
N_2^{(1)} \\
V_2^{(1)} \\
M_2^{(1)} \\
N_1^{(2a)} \\
V_1^{(2a)} \\
M_1^{(2a)} \\
N_1^{(2b)} \\
V_1^{(2b)} \\
M_1^{(2b)}
\end{bmatrix};
\quad
[F]=
\begin{bmatrix}
F_1 \\
F_2 \\
F_3 \\
F_4
\end{bmatrix}
$$

(10.90)

We write the displacement compatibility equations:

$$
\begin{cases}
u_2^{(1)} - u_1^{(2a)} = 0 \\
u_2^{(1)} - u_1^{(2b)} = 0 \\
u_2^{(2a)} - u_1^{(3)} = 0 \\
u_2^{(2b)} - u_1^{(3)} = 0
\end{cases}
$$

(10.91)

This is equivalent to the matrix format:

$$\begin{bmatrix} 0 & I & -I & 0 & 0 & 0 & 0 & 0 \\ 0 & I & 0 & 0 & -I & 0 & 0 & 0 \\ 0 & 0 & 0 & I & 0 & 0 & -I & 0 \\ 0 & 0 & 0 & 0 & 0 & I & -I & 0 \end{bmatrix} \begin{bmatrix} u_1^{(1)} \\ u_2^{(1)} \\ u_1^{(2a)} \\ u_2^{(2a)} \\ u_1^{(2b)} \\ u_2^{(2b)} \\ u_1^{(3)} \\ u_2^{(3)} \end{bmatrix} = 0$$

$$[B][u] = 0$$

$$[B] = \begin{bmatrix} 0 & I & -I & 0 & 0 & 0 & 0 & 0 \\ 0 & I & 0 & 0 & -I & 0 & 0 & 0 \\ 0 & 0 & 0 & I & 0 & 0 & -I & 0 \\ 0 & 0 & 0 & 0 & 0 & I & -I & 0 \end{bmatrix}; \quad [u] = \begin{bmatrix} u_1^{(1)} \\ u_2^{(1)} \\ u_1^{(2a)} \\ u_2^{(2a)} \\ u_1^{(2b)} \\ u_2^{(2b)} \\ u_1^{(3)} \\ u_2^{(3)} \end{bmatrix}$$

(10.92)

### 10.3.3 Global Matrix Formation for Applying PWAS Loads to Delaminated Composite Beam

We build a global matrix

$$[M][X] = [N]$$

(10.93)

Where:

$$\begin{bmatrix} I_{24} & -S_{24x24} \\ O_{12x24} & A_{12x24} \\ B_{12x24} & O_{12x24} \end{bmatrix}_{48x48} \begin{bmatrix} u \\ p \end{bmatrix}_{48x1} = \begin{bmatrix} O_{24x1} \\ F_{12x1} \\ O_{12x1} \end{bmatrix}_{48x1}$$

$$[M] = \begin{bmatrix} I_{24} & -S_{24x24} \\ O_{12x24} & A_{12x24} \\ B_{12x24} & O_{12x24} \end{bmatrix}_{48x48} \quad ; \quad [X] = \begin{bmatrix} u \\ p \end{bmatrix}_{48x1} \quad ; \quad [N] = \begin{bmatrix} O_{24x1} \\ F_{12x1} \\ O_{12x1} \end{bmatrix}_{48x1}$$

(10.94)

The expanded form of the global matrix is

$$\begin{bmatrix} I & & & & & & & & -S^{(1)} & & & \\ & I & & & & & & & & -S^{(2)} & & \\ & & I & & & & & & & & & \\ & & & I & & & & & -S^{(2)} & & & \\ & & & & I & & & & & -S^{(3)} & & \\ & & & & & I & & & & & & \\ & & & & & & I & & & -S^{(4)} & & \\ & & & & & & & I & & & & \\ & & & & & & & & -I & 0 & 0 & 0 & 0 & 0 & 0 & 0 \\ & & & & & & & & 0 & I & -T_1^{2a} & 0 & -T_1^{2b} & 0 & 0 & 0 \\ & & & & & & & & 0 & 0 & 0 & T_2^{2a} & 0 & T_2^{2b} & -I & 0 \\ & & & & & & & & 0 & 0 & 0 & 0 & 0 & 0 & 0 & I \\ 0 & I & -I & 0 & 0 & 0 & 0 & 0 & & & 0 & & & & & \\ 0 & I & 0 & 0 & -I & 0 & 0 & 0 & & & & & & & & \\ 0 & 0 & 0 & I & 0 & 0 & -I & 0 & & & 0 & & & & & \\ 0 & 0 & 0 & 0 & 0 & I & -I & 0 & & & & & & & & \end{bmatrix} \begin{bmatrix} u \\ p \end{bmatrix} = \begin{bmatrix} 0 \\ 0 \\ 0 \\ 0 \\ 0 \\ 0 \\ 0 \\ 0 \\ 0 \\ F_1 \\ F_2 \\ F_3 \\ F_4 \\ 0 \\ 0 \\ 0 \\ 0 \end{bmatrix}$$

$$(10.95)$$

After developing the mathematical approach to integrate a delamination into STMM, let us apply the theory to two different situations which are detailed in next subsections.

### 10.3.4 DELAMINATION OUTSIDE THE PWAS ZONE

Let us consider a composite beam with a PWAS attached on top and a delamination between the pre-specified layers (non-overlapping). Figure 150 is a graphical representation of the case under study.



*Figure 150: Location of the PWAS different from the delamination*

We build the free body diagram for the current case study as shown in Figure 151. We have six segments and six nodes.
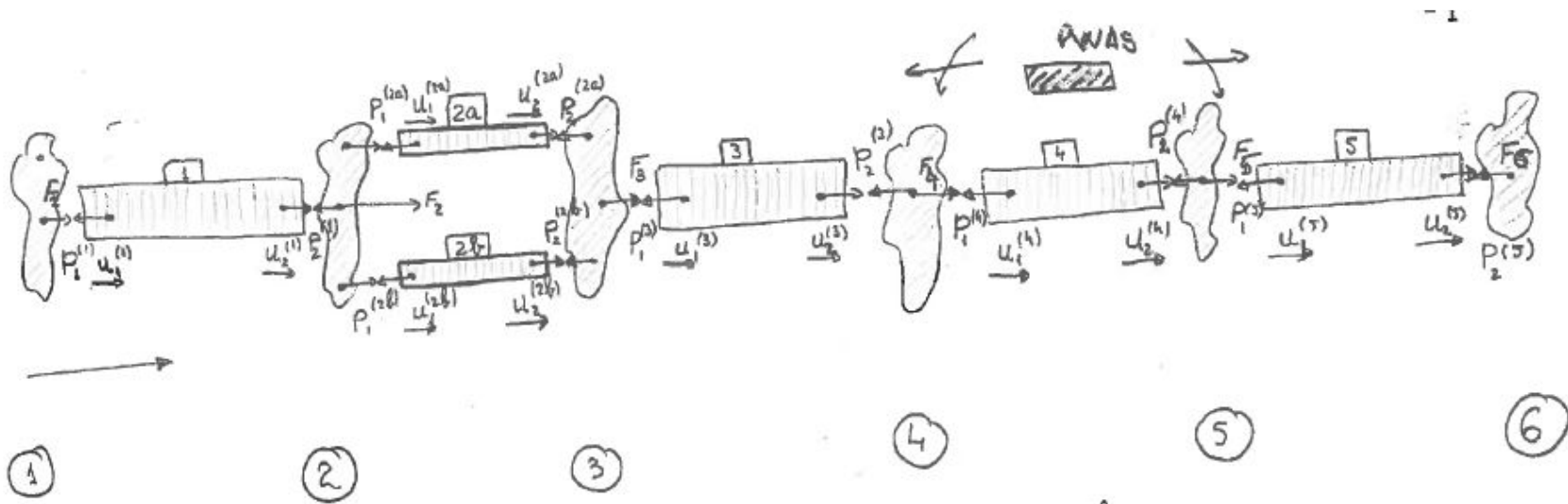
*Figure 151: Free body diagram*

As a first step, we write the equilibrium equation following the free body diagram:

$$\begin{cases} -p_1^{(1)} = F_1 \\ p_2^{(1)} - T_1^{(2a)} p_1^{(2a)} - T_1^{(2b)} p_1^{(2b)} = F_2 \\ T_2^{(2a)} p_2^{(2a)} + T_2^{(2b)} p_2^{(2b)} - p_1^{(3)} = F_3 \\ p_2^{(3)} - p_1^{(4)} = F_4 \\ p_2^{(4)} - p_1^{(5)} = F_5 \\ p_2^{(5)} = F_6 \end{cases}$$

(10.96)

We can rearrange them in a matrix form as follows:

$$\begin{bmatrix} -I & 0 & 0 & 0 & 0 & 0 & 0 & 0 & 0 & 0 & 0 & 0 \\ 0 & I & -T_1^{2a} & 0 & -T_1^{2b} & 0 & 0 & 0 & 0 & 0 & 0 & 0 \\ 0 & 0 & 0 & T_2^{2a} & 0 & T_2^{2b} & -I & 0 & 0 & 0 & 0 & 0 \\ 0 & 0 & 0 & 0 & 0 & 0 & 0 & I & -I & 0 & 0 & 0 \\ 0 & 0 & 0 & 0 & 0 & 0 & 0 & 0 & 0 & I & -I & 0 \\ 0 & 0 & 0 & 0 & 0 & 0 & 0 & 0 & 0 & 0 & 0 & I \end{bmatrix} \begin{bmatrix} p_1^{(1)} \\ p_2^{(1)} \\ p_1^{(2a)} \\ p_2^{(2a)} \\ p_1^{(2b)} \\ p_2^{(2b)} \\ p_1^{(3)} \\ p_2^{(3)} \\ p_1^{(4)} \\ p_2^{(4)} \\ p_1^{(5)} \\ p_2^{(5)} \end{bmatrix} = \begin{bmatrix} F_1 \\ F_2 \\ F_3 \\ F_4 \\ F_5 \\ F_6 \end{bmatrix}$$

(10.97)

$$[A] \cdot [p] = [F]$$

(10.98)

$$[A] = \begin{bmatrix} -I & 0 & 0 & 0 & 0 & 0 & 0 & 0 & 0 & 0 & 0 & 0 \\ 0 & I & -T_1^{2a} & 0 & -T_1^{2b} & 0 & 0 & 0 & 0 & 0 & 0 & 0 \\ 0 & 0 & 0 & T_2^{2a} & 0 & T_2^{2b} & -I & 0 & 0 & 0 & 0 & 0 \\ 0 & 0 & 0 & 0 & 0 & 0 & 0 & I & -I & 0 & 0 & 0 \\ 0 & 0 & 0 & 0 & 0 & 0 & 0 & 0 & 0 & I & -I & 0 \\ 0 & 0 & 0 & 0 & 0 & 0 & 0 & 0 & 0 & 0 & 0 & I \end{bmatrix}$$

(10.99)

$$[p] = \begin{bmatrix} p_1^{(1)} \\ p_2^{(1)} \\ p_1^{(2a)} \\ p_2^{(2a)} \\ p_1^{(2b)} \\ p_2^{(2b)} \\ p_1^{(3)} \\ p_2^{(3)} \\ p_1^{(4)} \\ p_2^{(4)} \\ p_1^{(5)} \\ p_2^{(5)} \end{bmatrix}; \quad [F] = \begin{bmatrix} F_1 \\ F_2 \\ F_3 \\ F_4 \\ F_5 \\ F_6 \end{bmatrix}$$

(10.100)

Where:

$$\left[-T_1^{2a}\right] = \begin{bmatrix} 1 & 0 & 0 \\ 0 & 1 & 0 \\ -r_a & 0 & 1 \end{bmatrix}; \quad \left[-T_1^{2b}\right] = \begin{bmatrix} 1 & 0 & 0 \\ 0 & 1 & 0 \\ r_b & 0 & 1 \end{bmatrix};$$

$$\left[T_2^{2a}\right] = \begin{bmatrix} 1 & 0 & 0 \\ 0 & 1 & 0 \\ -r_a & 0 & 1 \end{bmatrix}; \quad \left[T_2^{2b}\right] = \begin{bmatrix} 1 & 0 & 0 \\ 0 & 1 & 0 \\ r_b & 0 & 1 \end{bmatrix}$$

(10.101)

The displacement compatibility equations are:

$$\begin{cases} u_2^{(1)} - u_1^{(2a)} = 0 \\ u_2^{(1)} - u_1^{(2b)} = 0 \\ u_2^{(2a)} - u_1^{(3)} = 0 \\ u_2^{(2b)} - u_1^{(3)} = 0 \\ -u_1^{(4)} + u_2^{(3)} = 0 \\ -u_1^{(5)} + u_2^{(4)} = 0 \end{cases}$$

(10.102)

This is equivalent to the matrix form:

$$\begin{bmatrix} 0 & I & -I & 0 & 0 & 0 & 0 & 0 & 0 & 0 & 0 & 0 \\ 0 & I & 0 & 0 & -I & 0 & 0 & 0 & 0 & 0 & 0 & 0 \\ 0 & 0 & 0 & I & 0 & 0 & -I & 0 & 0 & 0 & 0 & 0 \\ 0 & 0 & 0 & 0 & 0 & I & -I & 0 & 0 & 0 & 0 & 0 \\ 0 & 0 & 0 & 0 & 0 & 0 & 0 & I & -I & 0 & 0 & 0 \\ 0 & 0 & 0 & 0 & 0 & 0 & 0 & 0 & 0 & I & -I & 0 \end{bmatrix} \begin{bmatrix} u_1^{(1)} \\ u_2^{(1)} \\ u_1^{(2a)} \\ u_2^{(2a)} \\ u_1^{(2b)} \\ u_2^{(2b)} \\ u_1^{(3)} \\ u_2^{(3)} \\ u_1^{(4)} \\ u_2^{(4)} \\ u_1^{(5)} \\ u_2^{(5)} \end{bmatrix} = 0$$

(10.103)

$$[B][u] = 0$$

(10.104)

$$[B] = \begin{bmatrix} 0 & I & -I & 0 & 0 & 0 & 0 & 0 & 0 & 0 & 0 & 0 \\ 0 & I & 0 & 0 & -I & 0 & 0 & 0 & 0 & 0 & 0 & 0 \\ 0 & 0 & 0 & I & 0 & 0 & -I & 0 & 0 & 0 & 0 & 0 \\ 0 & 0 & 0 & 0 & 0 & I & -I & 0 & 0 & 0 & 0 & 0 \\ 0 & 0 & 0 & 0 & 0 & 0 & 0 & I & -I & 0 & 0 & 0 \\ 0 & 0 & 0 & 0 & 0 & 0 & 0 & 0 & 0 & I & -I & 0 \end{bmatrix}$$

(10.105)

$$[u] = \begin{bmatrix} u_1^{(1)} \\ u_2^{(1)} \\ u_1^{(2a)} \\ u_2^{(2a)} \\ u_1^{(2b)} \\ u_2^{(2b)} \\ u_1^{(3)} \\ u_2^{(3)} \\ u_1^{(4)} \\ u_2^{(4)} \\ u_1^{(5)} \\ u_2^{(5)} \end{bmatrix}$$

(10.106)

We build a global matrix

$$[M] \cdot [X] = [N]$$

(10.107)

Where:

$$\begin{bmatrix} I_{36} & -S_{36x36} \\ O_{18x36} & A_{18x36} \\ B_{18x36} & O_{18x36} \end{bmatrix}_{72x72} \begin{bmatrix} u \\ p \end{bmatrix}_{72x1} = \begin{bmatrix} O_{36x1} \\ F_{18x1} \\ O_{18x1} \end{bmatrix}_{72x1}$$

$$[M] = \begin{bmatrix} I_{36} & -S_{36x36} \\ O_{18x36} & A_{18x36} \\ B_{18x36} & O_{18x36} \end{bmatrix}_{72x72} \quad ; \quad [X] = \begin{bmatrix} u \\ p \end{bmatrix}_{72x1} \quad ; \quad [N] = \begin{bmatrix} O_{36x1} \\ F_{18x1} \\ O_{18x1} \end{bmatrix}_{72x1}$$

(10.108)

The expanded form of the global matrix is

$$
\begin{bmatrix}
I & & & & & & & & & & & & -S^{(1)} \\
 & I & & & & & & & & & & & \\
 & & I & & & & & & & & & -S^{(2a)} & \\
 & & & I & & & & & & & & & \\
 & & & & I & & & & & & -S^{(2b)} & & \\
 & & & & & I & & & & & & & \\
 & & & & & & I & & & -S^{(3)} & & & \\
 & & & & & & & I & & & & & \\
 & & & & & & & & I & & -S^{(4)} & & \\
 & & & & & & & & & I & & & \\
 & & & & & & & & & & -S^{(5)} & & \\
 & & & & & & & & & I & & & \\
 & & & 0 & & & & & & & A & & \\
 & & & B & & & & & & & 0 & &
\end{bmatrix}
\begin{bmatrix} u \\ p \end{bmatrix}
=
\begin{bmatrix}
0 \\ 0 \\ 0 \\ 0 \\ 0 \\ 0 \\ 0 \\ 0 \\ 0 \\ 0 \\ 0 \\ 0 \\ 0 \\ 0 \\ 0 \\ F_1 \\ F_2 \\ F_3 \\ F_4 \\ F_5 \\ F_6 \\ 0 \\ 0 \\ 0 \\ 0 \\ 0 \\ 0
\end{bmatrix}
\tag{10.109}
$$

## 10.3.5 DELAMINATION INSIDE THE PWAS ZONE

Let us consider a composite beam with a PWAS attached on top and a delamination located under it. Figure 152 is a graphical representation of this case.



*Figure 152: Location of the delamination is under the PWAS*

We build the free body diagram for the current case study as shown in Figure 153. We now have eight segments and eight nodes.

*Figure 153: Free body diagram*

246

Following the same approach as in the previous case, the equilibrium equations become:

$$
\begin{cases}
-p_1^{(1)} = F_1 \\
p_2^{(1)} - T_1^{(2a)} p_1^{(2a)} - T_1^{(2b)} p_1^{(2b)} = F_2 \\
p_2^{(2a)} - p_1^{(3)} = F_3 \\
p_2^{(2b)} - p_1^{(3b)} = F_3 \\
p_2^{(3a)} - p_1^{(4a)} = F_4 \\
p_2^{(3b)} - p_1^{(4b)} = F_4 \\
T_2^{(4a)} p_2^{(4a)} + T_2^{(4b)} p_2^{(4b)} - p_1^{(5)} = F_5 \\
p_2^{(5)} = F_6
\end{cases}
$$

(10.110)

This can be written in matrix format as follows:

$$
\begin{bmatrix}
-I & 0 & 0 & 0 & 0 & 0 & 0 & 0 & 0 & 0 & 0 & 0 & 0 & 0 & 0 & 0 \\
0 & I & -T_1^{2a} & 0 & T_1^{2b} & 0 & 0 & 0 & 0 & 0 & 0 & 0 & 0 & 0 & 0 & 0 \\
0 & 0 & 0 & I & 0 & 0 & -I & 0 & 0 & 0 & 0 & 0 & 0 & 0 & 0 & 0 \\
0 & 0 & 0 & 0 & 0 & I & 0 & 0 & -I & 0 & 0 & 0 & 0 & 0 & 0 & 0 \\
0 & 0 & 0 & 0 & 0 & 0 & 0 & I & 0 & 0 & -I & 0 & 0 & 0 & 0 & 0 \\
0 & 0 & 0 & 0 & 0 & 0 & 0 & 0 & 0 & I & 0 & 0 & -I & 0 & 0 & 0 \\
0 & 0 & 0 & 0 & 0 & 0 & 0 & 0 & 0 & 0 & 0 & T_2^{4a} & 0 & T_2^{4b} & -I & 0 \\
0 & 0 & 0 & 0 & 0 & 0 & 0 & 0 & 0 & 0 & 0 & 0 & 0 & 0 & 0 & I
\end{bmatrix}
\begin{bmatrix}
p_1^{(1)} \\
p_2^{(1)} \\
p_1^{(2a)} \\
p_2^{(2a)} \\
p_1^{(2b)} \\
p_2^{(2b)} \\
p_2^{(3a)} \\
p_1^{(3a)} \\
p_2^{(3b)} \\
p_1^{(3b)} \\
p_2^{(4a)} \\
p_1^{(4a)} \\
p_2^{(4b)} \\
p_1^{(4b)} \\
p_1^{(5)} \\
p_2^{(6)}
\end{bmatrix}
=
\begin{bmatrix}
F_1 \\
F_2 \\
F_{3a} \\
F_{3b} \\
F_{4a} \\
F_{4b} \\
F_5 \\
F_6
\end{bmatrix}
$$

(10.111)

Where

$$[A]\cdot[p]=[F]$$

$$[A]=\begin{bmatrix} -I & 0 & 0 & 0 & 0 & 0 & 0 & 0 & 0 & 0 & 0 & 0 & 0 & 0 & 0 & 0 \\ 0 & I & -T_1^{2a} & 0 & T_1^{2b} & 0 & 0 & 0 & 0 & 0 & 0 & 0 & 0 & 0 & 0 & 0 \\ 0 & 0 & 0 & I & 0 & 0 & -I & 0 & 0 & 0 & 0 & 0 & 0 & 0 & 0 & 0 \\ 0 & 0 & 0 & 0 & 0 & I & 0 & 0 & -I & 0 & 0 & 0 & 0 & 0 & 0 & 0 \\ 0 & 0 & 0 & 0 & 0 & 0 & 0 & I & 0 & 0 & -I & 0 & 0 & 0 & 0 & 0 \\ 0 & 0 & 0 & 0 & 0 & 0 & 0 & 0 & 0 & I & 0 & 0 & -I & 0 & 0 & 0 \\ 0 & 0 & 0 & 0 & 0 & 0 & 0 & 0 & 0 & 0 & 0 & T_2^{4a} & 0 & T_2^{4b} & -I & 0 \\ 0 & 0 & 0 & 0 & 0 & 0 & 0 & 0 & 0 & 0 & 0 & 0 & 0 & 0 & 0 & I \end{bmatrix}$$

(10.112)

$$[p]=\begin{bmatrix} p_1^{(1)} \\ p_2^{(1)} \\ p_1^{(2a)} \\ p_2^{(2a)} \\ p_1^{(2b)} \\ p_2^{(2b)} \\ p_2^{(3a)} \\ p_1^{(3a)} \\ p_2^{(3b)} \\ p_1^{(3b)} \\ p_2^{(4a)} \\ p_1^{(4a)} \\ p_2^{(4b)} \\ p_1^{(4b)} \\ p_1^{(5)} \\ p_2^{(6)} \end{bmatrix}; \quad [F]=\begin{bmatrix} F_1 \\ F_2 \\ F_{3a} \\ F_{3b} \\ F_{4a} \\ F_{4b} \\ F_5 \\ F_6 \end{bmatrix}$$

(10.113)

and

$$\left[-T_1^{2a}\right]=\begin{bmatrix} 1 & 0 & 0 \\ 0 & 1 & 0 \\ -r_a & 0 & 1 \end{bmatrix}; \quad \left[-T_1^{2b}\right]=\begin{bmatrix} 1 & 0 & 0 \\ 0 & 1 & 0 \\ r_b & 0 & 1 \end{bmatrix};$$

$$\left[T_2^{4a}\right]=\begin{bmatrix} 1 & 0 & 0 \\ 0 & 1 & 0 \\ -r_a & 0 & 1 \end{bmatrix}; \quad \left[T_2^{4b}\right]=\begin{bmatrix} 1 & 0 & 0 \\ 0 & 1 & 0 \\ r_b & 0 & 1 \end{bmatrix}$$

(10.114)

The displacement compatibility equations are:

$$\begin{cases} u_2^{(1)} - u_1^{(2a)} = 0 \\ u_2^{(1)} - u_1^{(2b)} = 0 \\ u_2^{(2a)} - u_1^{(3a)} = 0 \\ u_2^{(2b)} - u_1^{(3b)} = 0 \\ u_2^{(3a)} - u_1^{(4a)} = 0 \\ u_2^{(3b)} - u_1^{(4b)} = 0 \\ -u_2^{(4a)} - u_1^{(5)} = 0 \\ -u_2^{(4b)} - u_1^{(5)} = 0 \end{cases} \tag{10.115}$$

$$\begin{bmatrix} 0 & I & -I & 0 & 0 & 0 & 0 & 0 & 0 & 0 & 0 & 0 & 0 & 0 & 0 & 0 \\ 0 & I & 0 & 0 & -I & 0 & 0 & 0 & 0 & 0 & 0 & 0 & 0 & 0 & 0 & 0 \\ 0 & 0 & 0 & I & 0 & 0 & -I & 0 & 0 & 0 & 0 & 0 & 0 & 0 & 0 & 0 \\ 0 & 0 & 0 & 0 & 0 & I & 0 & 0 & -I & 0 & 0 & 0 & 0 & 0 & 0 & 0 \\ 0 & 0 & 0 & 0 & 0 & 0 & 0 & I & 0 & 0 & -I & 0 & 0 & 0 & 0 & 0 \\ 0 & 0 & 0 & 0 & 0 & 0 & 0 & 0 & 0 & I & 0 & 0 & -I & 0 & 0 & 0 \\ 0 & 0 & 0 & 0 & 0 & 0 & 0 & 0 & 0 & 0 & 0 & I & 0 & 0 & -I & 0 \\ 0 & 0 & 0 & 0 & 0 & 0 & 0 & 0 & 0 & 0 & 0 & 0 & 0 & I & -I & 0 \end{bmatrix} \begin{bmatrix} u_1^{(1)} \\ u_2^{(1)} \\ u_1^{(2a)} \\ u_2^{(2a)} \\ u_1^{(2b)} \\ u_2^{(2b)} \\ u_1^{(3a)} \\ u_2^{(3a)} \\ u_1^{(3b)} \\ u_2^{(3b)} \\ u_1^{(4a)} \\ u_2^{(4a)} \\ u_1^{(4b)} \\ u_2^{(4b)} \\ u_1^{(5)} \\ u_2^{(5)} \end{bmatrix} = 0 \tag{10.116}$$

Where:

$$[B] \cdot [u] = 0 \tag{10.117}$$

$$[B]=\begin{bmatrix} 0 & I & -I & 0 & 0 & 0 & 0 & 0 & 0 & 0 & 0 & 0 & 0 & 0 & 0 & 0 \\ 0 & I & 0 & 0 & -I & 0 & 0 & 0 & 0 & 0 & 0 & 0 & 0 & 0 & 0 & 0 \\ 0 & 0 & 0 & I & 0 & 0 & -I & 0 & 0 & 0 & 0 & 0 & 0 & 0 & 0 & 0 \\ 0 & 0 & 0 & 0 & 0 & I & 0 & 0 & -I & 0 & 0 & 0 & 0 & 0 & 0 & 0 \\ 0 & 0 & 0 & 0 & 0 & 0 & 0 & I & 0 & 0 & -I & 0 & 0 & 0 & 0 & 0 \\ 0 & 0 & 0 & 0 & 0 & 0 & 0 & 0 & 0 & I & 0 & 0 & -I & 0 & 0 & 0 \\ 0 & 0 & 0 & 0 & 0 & 0 & 0 & 0 & 0 & 0 & 0 & I & 0 & 0 & -I & 0 \\ 0 & 0 & 0 & 0 & 0 & 0 & 0 & 0 & 0 & 0 & 0 & 0 & 0 & I & -I & 0 \end{bmatrix}; \quad [u]=\begin{bmatrix} u_1^{(1)} \\ u_2^{(1)} \\ u_1^{(2a)} \\ u_2^{(2a)} \\ u_1^{(2b)} \\ u_2^{(2b)} \\ u_1^{(3a)} \\ u_2^{(3a)} \\ u_1^{(3b)} \\ u_2^{(3b)} \\ u_1^{(4a)} \\ u_2^{(4a)} \\ u_1^{(4b)} \\ u_2^{(4b)} \\ u_1^{(5)} \\ u_2^{(5)} \end{bmatrix} \quad (10.118)$$

We build a global matrix

$$[M]\cdot[X]=[N] \tag{10.119}$$

Where:

$$\begin{bmatrix} I_{48} & -S_{48x48} \\ O_{24x48} & A_{24x48} \\ B_{24x48} & O_{24x48} \end{bmatrix}_{96x96} \begin{bmatrix} u \\ p \end{bmatrix}_{96x1} = \begin{bmatrix} O_{48x1} \\ F_{24x1} \\ O_{24x1} \end{bmatrix}_{96x1}$$

$$[M]=\begin{bmatrix} I_{48} & -S_{48x48} \\ O_{24x48} & A_{24x48} \\ B_{24x48} & O_{24x48} \end{bmatrix}_{96x96} \quad ; \quad [X]=\begin{bmatrix} u \\ p \end{bmatrix}_{96x1} \quad ; \quad [N]=\begin{bmatrix} O_{48x1} \\ F_{24x1} \\ O_{24x1} \end{bmatrix}_{96x1} \tag{10.120}$$

The expanded form of the global matrix is

$$
\begin{bmatrix}
I & & & & & & & & & & & -S^{(1)} & & & \\
& I & & & & & & & & & & & -S^{(2a)} & & \\
& & I & & & & & & & & & & & -S^{(2b)} & \\
& & & I & & & & & & & & & & & \\
& & & & I & & & & & & & & & -S^{(3a)} & \\
& & & & & I & & & & & & & & & -S^{(3b)} \\
& & & & & & I & & & & & & & & \\
& & & & & & & I & & & & & & -S^{(4a)} & \\
& & & & & & & & I & & & & & & -S^{(4b)} \\
& & & & & & & & & I & & & & & \\
& & & & & & & & & & I & & & & -S^{(5)} \\
& & & & & & & & & I & & & & & \\
& & 0 & & & & & & & & & & A & & \\
& & B & & & & & & & & & & 0 & &
\end{bmatrix}
\begin{bmatrix} u \\ p \end{bmatrix}
=
\begin{bmatrix}
0 \\ 0 \\ 0 \\ 0 \\ 0 \\ 0 \\ 0 \\ 0 \\ 0 \\ 0 \\ 0 \\ 0 \\ 0 \\ 0 \\ F_1 \\ F_2 \\ F_3 \\ 0 \\ F_4 \\ F_5 \\ F_6 \\ 0 \\ 0 \\ 0 \\ 0 \\ 0 \\ 0 \\ 0 \\ 0
\end{bmatrix}
\tag{10.121}
$$

Having the analytical approach of the STMM expanded, we next plan to integrate this algorithm in Matlab. STMM is intended to require less mathematical calculation and to give accurate predictions as FEM in a shorter period of time. Having this in mind, the next steps will be to validate this mathematical algorithm.

# 11. TASK #3: VALIDATION OF THE STMM MATHEMATICAL MODEL BY COMPARISON WITH FEM AND EXPERIMENTS

In this chapter, we validate the STMM mathematical model by comparison with FEM and experiments. In addition, we compare the results obtained for the pristine and damaged specimens.

We will go step-by-step through this process, where properties for the three composite materials under study are shown in Table 7.

*Table 7: Material Properties*

| | COMPOSITE MATERIALS | | | PWAS |
|---|---|---|---|---|
| **Material Properties** | **Unidirectional CFRP Composite** | **T300/5208 Quasi-Isotropic** | **Woven Glass-epoxy Composite** | **APC-850** |
| **Elastic properties** | E1/E2/G12/v12/v21 | E1/E2/G12/v12/v21 | E1/E2/G12/v12/v21 | E1/E2/v12/v21 |
| **Gpa** | 32/10.5/5.65/0.24/0.2 | 132/10.8/5.65/0.24/0.24 | 32/30/4/0.26/0.26 | 64.5/64.5/0.3/0.3 |
| **Damping Coefficient** | $\xi_1/\xi_2/\xi_{12}$ | $\xi_1/\xi_2/\xi_{12}$ | $\xi_1/\xi_2/\xi_{12}$ | $\xi_1/\xi_2/\xi_{12}$ |
| **Elastic Properties with Damping** | 0.001/0.01/0.01 | 0.001/0.01/0.01 | 0.001/0.01/0.01 | 0.001/0.01/0.01 |
| **Mass Density** | 1540 | 1540 | 1900 | 7500 |
| **Permittivity** | - | - | - | $1750*8.85*10^{-12}$ |
| **Coupling Terms: d11, d22 and d12** | - | - | - | $1750*8.85*10^{-12}/$ $-175*10^{-12}/$ $400*10^{-12}$ |
| **Layers ( No. & Hight)** | 12 layers h=1.500mm 125µm/layer | 16 layers h=2.24mm 140µm/layer | 10 layers h=3.2mm 320µm/layer | - |
| **Stacking Sequence** | $(0^0)_{12}$ | $(0^0/45^0/90^0/-45^0)_{2S}$ <br> 0 <br> 45 <br> 90 <br> -45 <br> -45 <br> 90 <br> 45 <br> 0 | $(0^0/90^0)_{10}$ | - |

## 11.1    CALCULATION OF STMM RESULTS FOR COMPARISON WITH FEM AND EXPERIMENTS

To validate the analytical method STMM, we calculate two sets of results to compare with FEM and experiments. We considered two composite beam specimens: one pristine and one damaged ($180mm\ x\ 10mm\ x\ 1.5mm$).The chosen material is unidirectional CFRP as per Table 7. The impedance response in the range 0-100 kHz was simulated for each case.

We start with the pristine case. We first consider the case when the sensor is located at $60mm$ distance from one side and the impedance response for the pristine specimen in this case can be seen in Figure 154.

By looking at the frequency response function, we are able to differentiate how many axial and flexural frequency response functions we have between 0 and 100 kHz. As per Figure 155 and Figure 156, we have 4 axial frequencies and 30 flexural frequencies, respectively.

Then, we consider the case where the PWAS is located 100mm from one side and we are looking for the impedance response in the same range 0-100 kHz and to see the sensitivity of the PWAS location. The impedance response for the new location can be seen in Figure 157.

Let us overlap those two impedance response functions for those two different locations for the PWAS. This can be seen in Figure 158. What we can conclude from this figure is that the analytical method (STMM) is sensitive to the PWAS location, thus registering a decrease in the impedance amplitude.

We now consider the damaged case and we take the more complex situation when the delamination is under the PWAS. More specifically, the sensor is located at $60mm$ distance from one side and the delamination is 10mm long and located between layers 3 and 4 under the PWAS as can be seen in Figure 159.

We next analyze whether STMM is sensitive to the delamination by overlapping the impedance response of the pristine specimen with the impedance response of the delamination specimen. As can be seen from Figure 160, there are shifts and impedance amplitude changes which implies that the presence of the damage will significantly change the impedance spectrum.
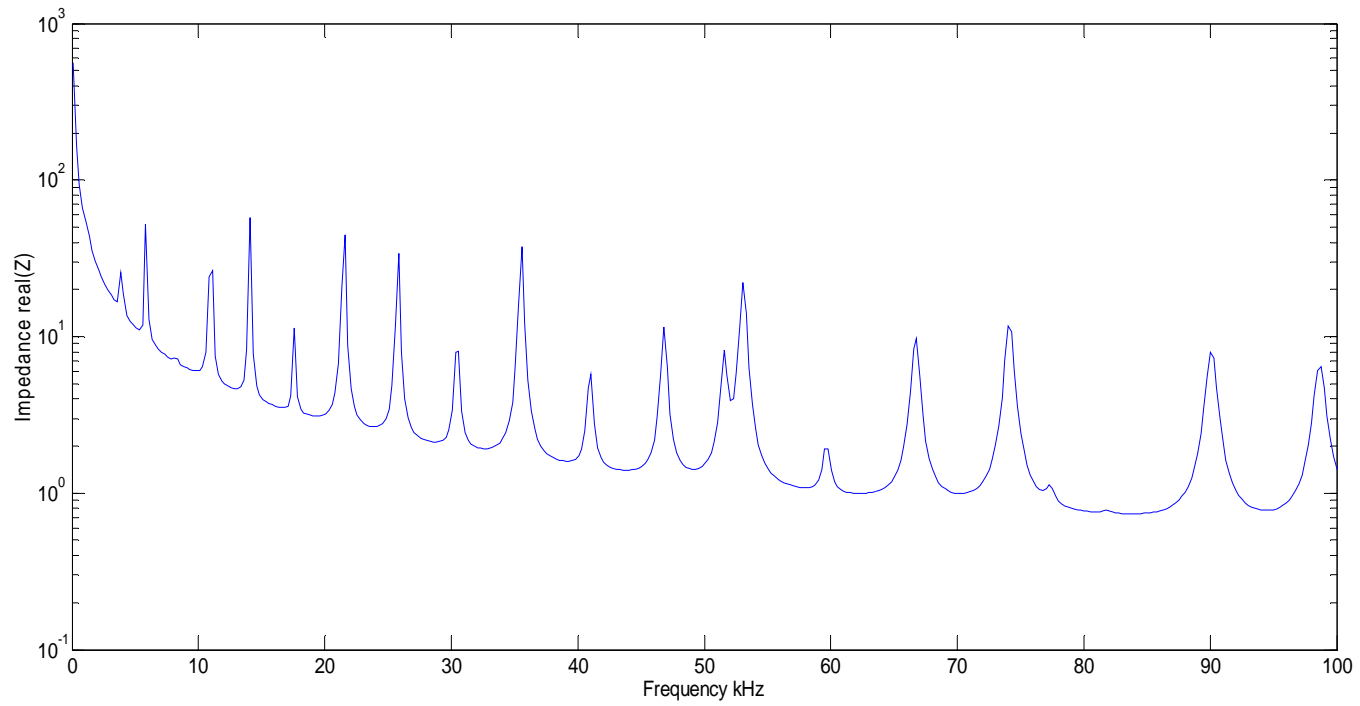
*Figure 154: STMM impedance spectrum for pristine specimen*
*(PWAS 60 mm distance from one side)*
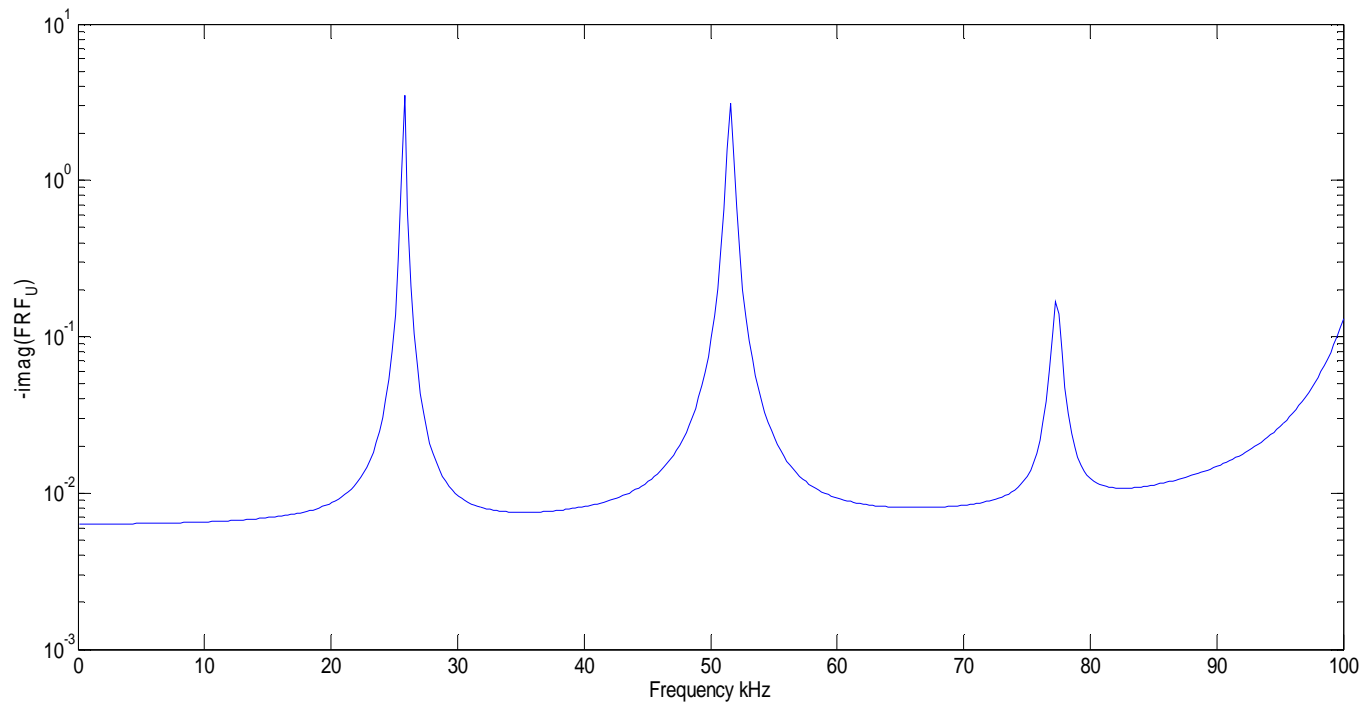
***Figure 155: Axial Frequency Response Function for pristine specimen (PWAS 60 mm distance from one side)***
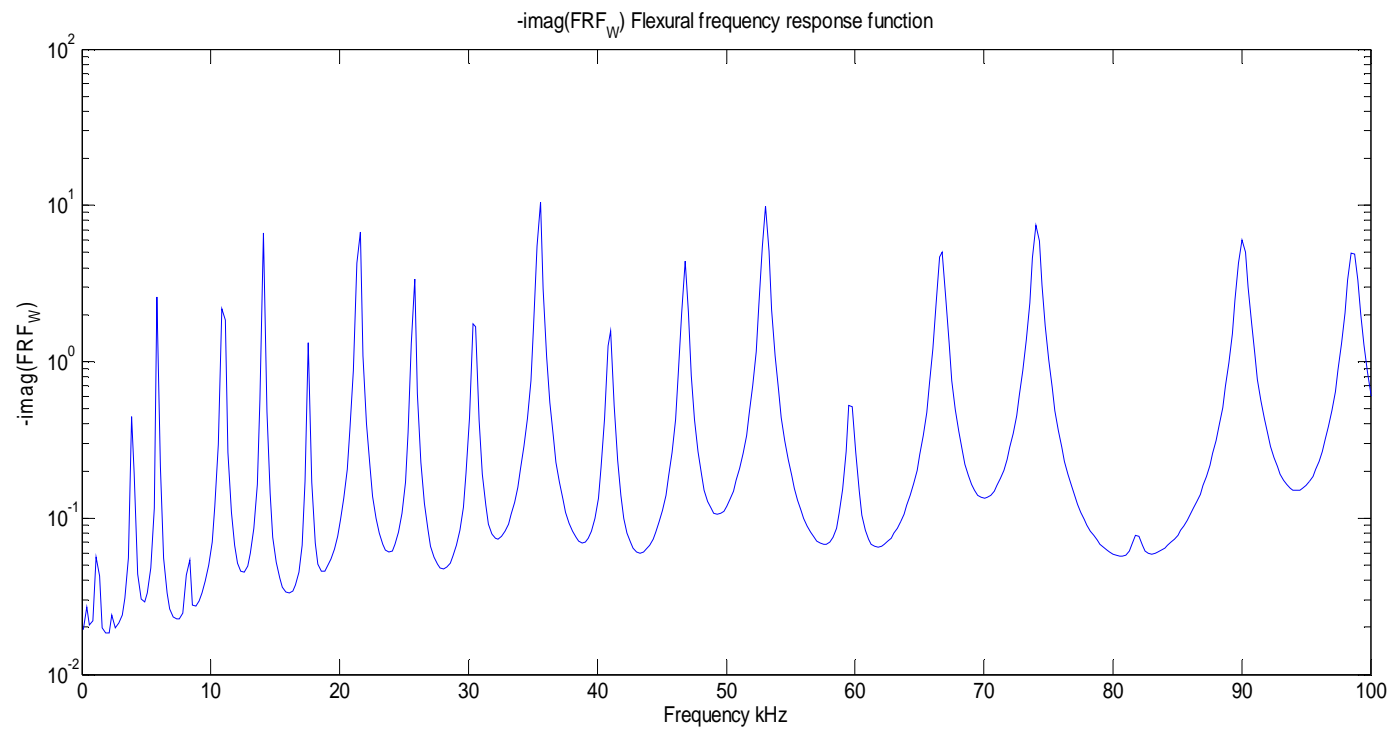
***Figure 156: Flexural Frequency Response Function for pristine specimen***
***(PWAS 60 mm distance from one side)***
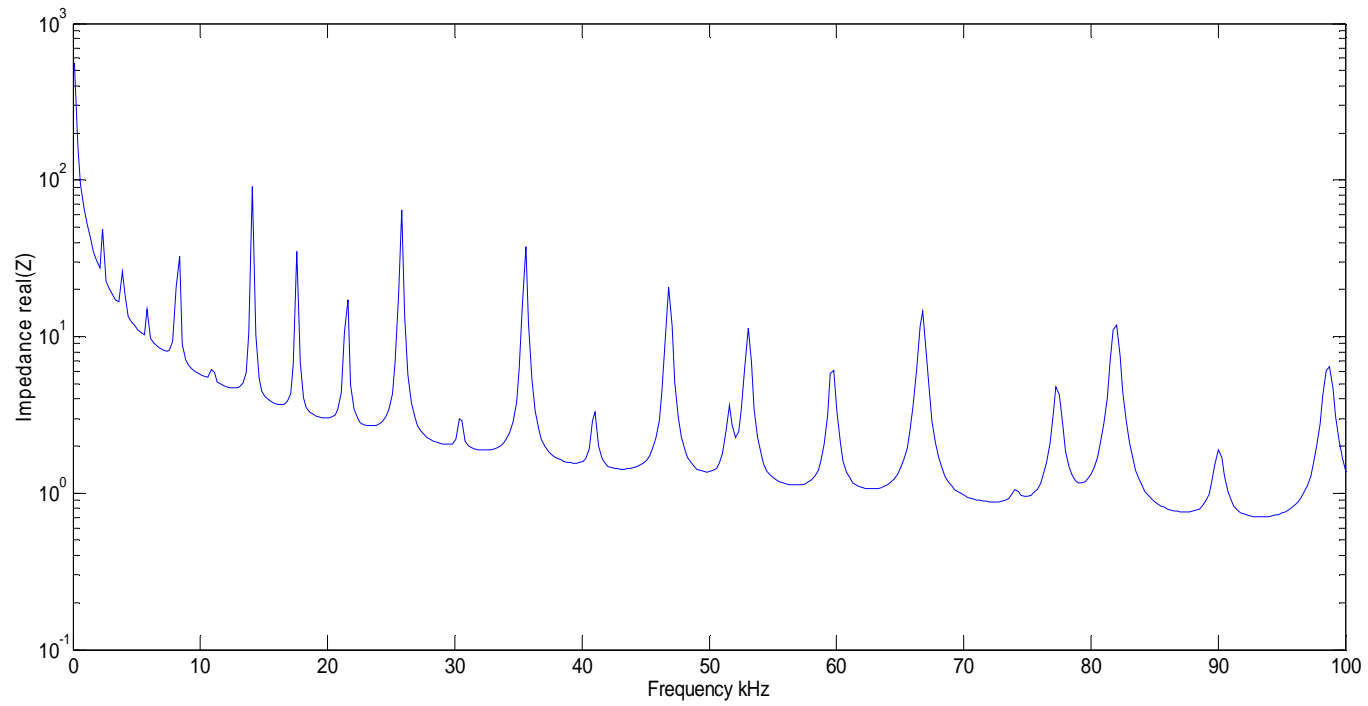
*Figure 157: STMM impedance spectrum for pristine specimen*
*(PWAS 100 mm distance from one side)*
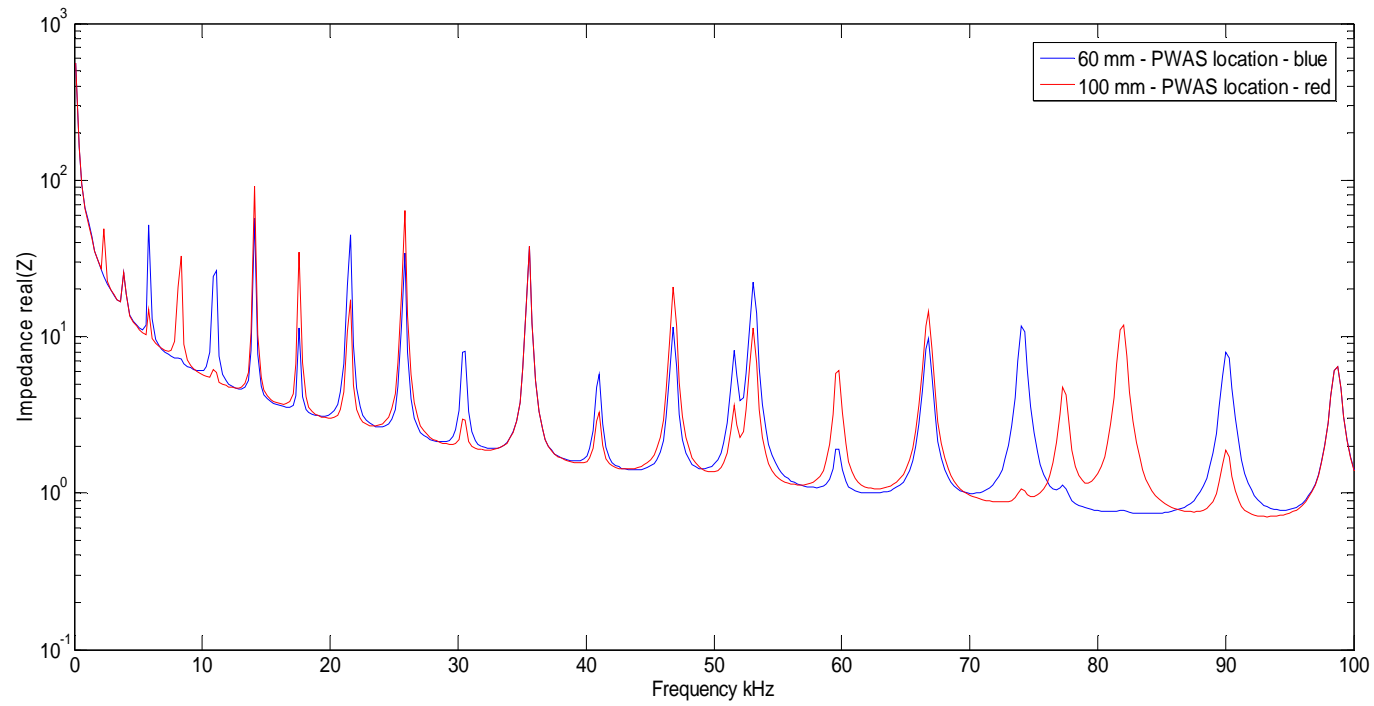
*Figure 158: Impedance Response for 60 and 100mm PWAS location*
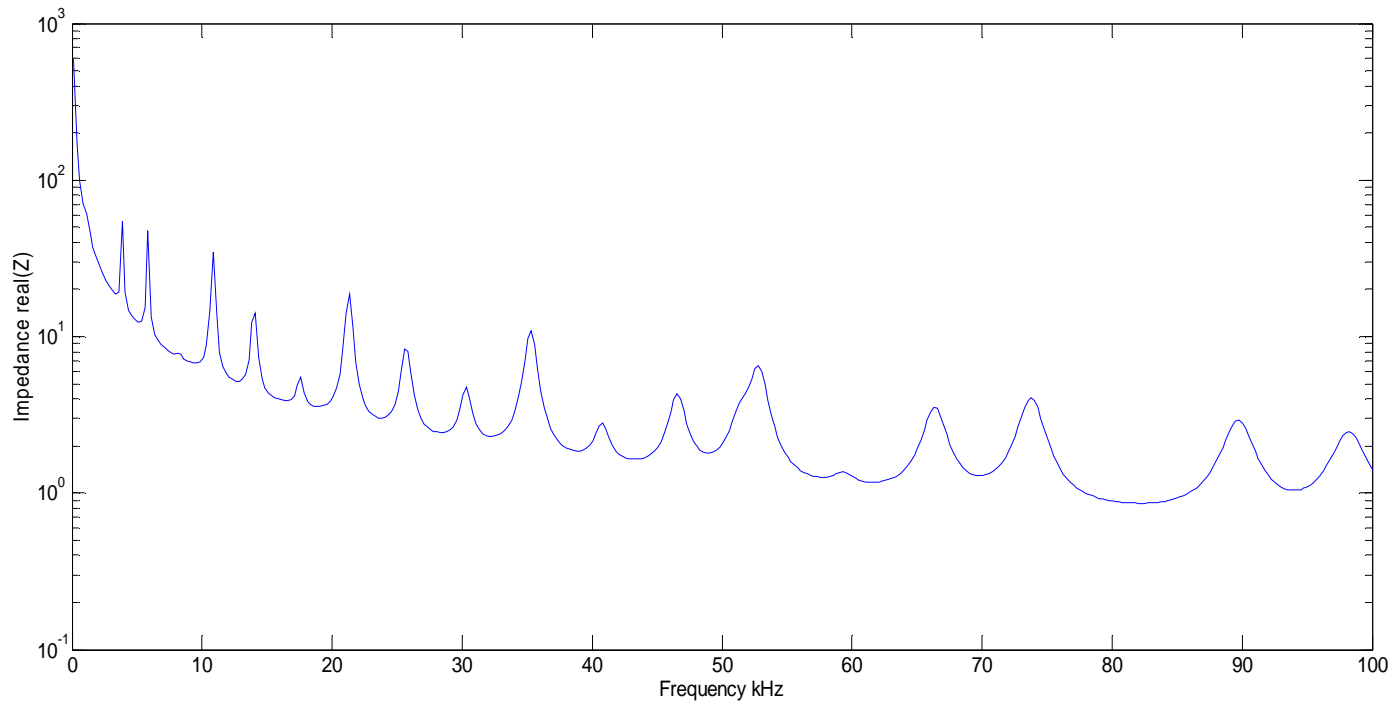
*Figure 159: Impedance Response for Delamination Specimen*

*(PWAS location is at 60mm from one side; delamination between layers 3 and 4)*

260
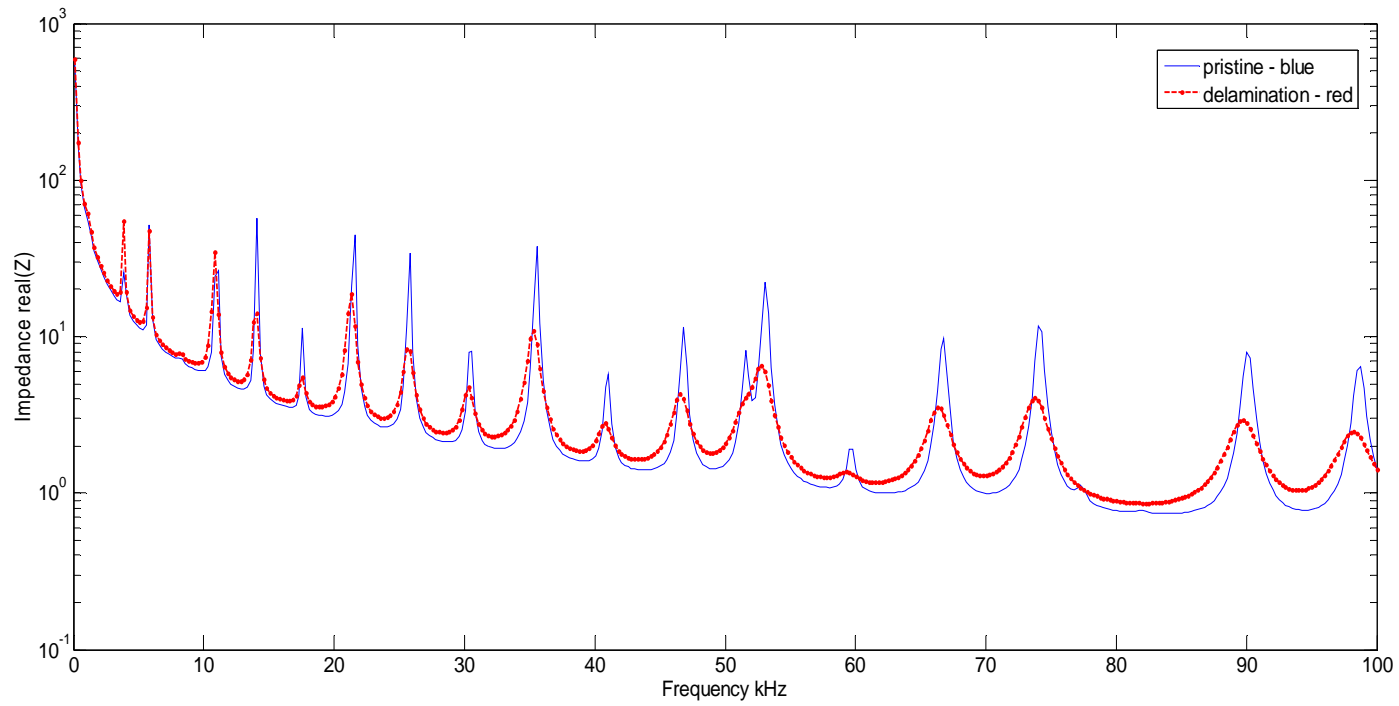
*Figure 160: STMM Impedance Response for Pristine and Delamination Specimens*

## 11.2 VALIDATION WITH FINITE ELEMENT METHOD

Another approach to calculate the impedance is the finite element method (FEM), which is broadly used in engineering. Its key advantages are a good accuracy of the results, predicting relatively well the reality. However, it also has some limitations: it can increase the computation time, has large storage requirements and memory limitations.

We use this method to calculate the electro-mechanical impedance. In order to do this, we use a 2D ANSYS FEM (multi-physics) and 3D FEM (Workbench) analysis. Following FEM calculation procedure presented in Giurgiutiu et al. (2011), we determine the impedance of the pristine and delaminated composite beams.

We first show the results for the 2D FEM analysis as shown in Figure 161 (pristine) and Figure 162 (delamination).Next, we overlap the pristine and delamination impedance 2D results as shown in Figure 163. We find that there are shifts and impedance amplitude changes which imply that the presence of the damage will significantly change the impedance spectrum same as in the STMM approach presented in previous section.

Then, we calculate resonant frequencies using the modal analysis from ANSYS WB (3D).This type of analysis allows us to better understand and distinguish between axial and flexural frequencies and modeshapes. It also highlights the effects of delamination (Figure 191) on modeshapes. The results for the pristine specimen are shown in Figure 164 to Figure 190. The results for the delaminated specimen are shown in Figure 192 and Figure 216.

It is very important to stop on some situations which seem to be very complex; the main factor is the arrangement of the laminate layers of the composite material with respect to the delaminations position. As you can see in Figure 217, Figure 218, Figure 219, the delamination creates a local resonance which seems to be decoupled from the whole beam.
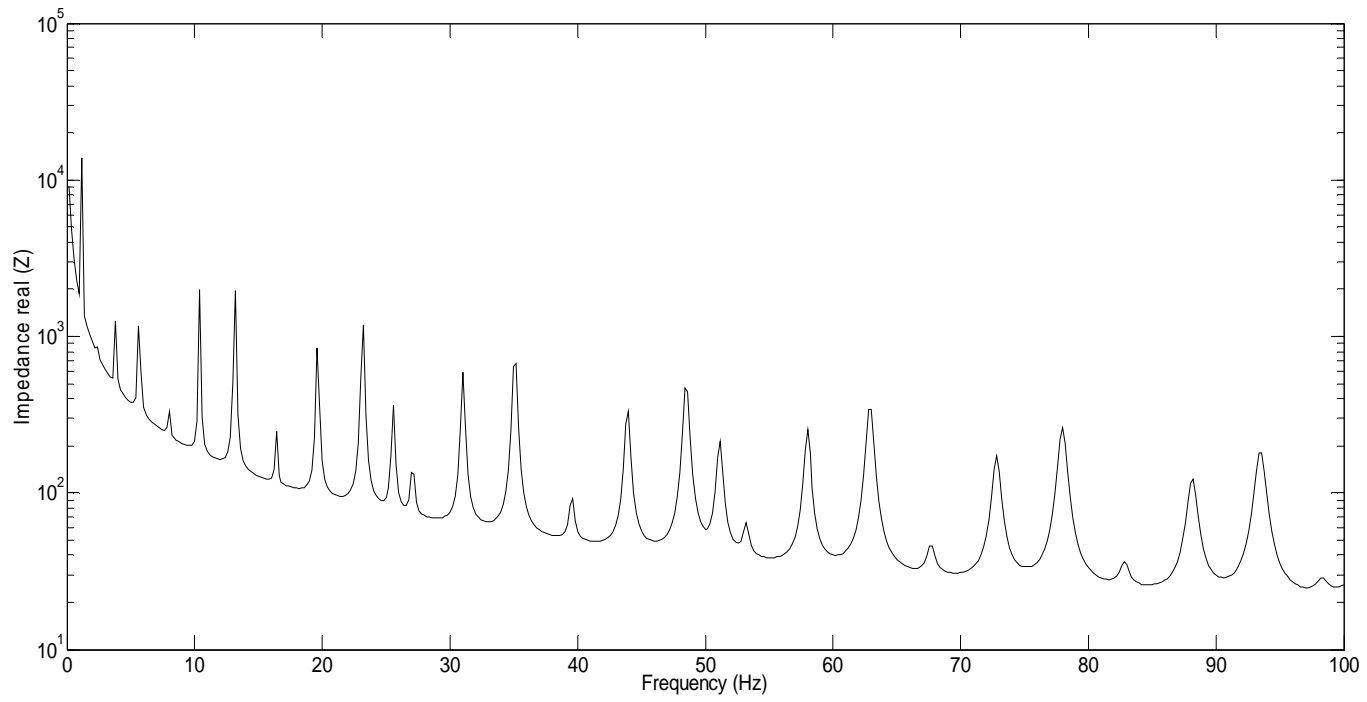
*Figure 161: Impedance ANSYS 2D Analysis (Pristine Specimen)*

264
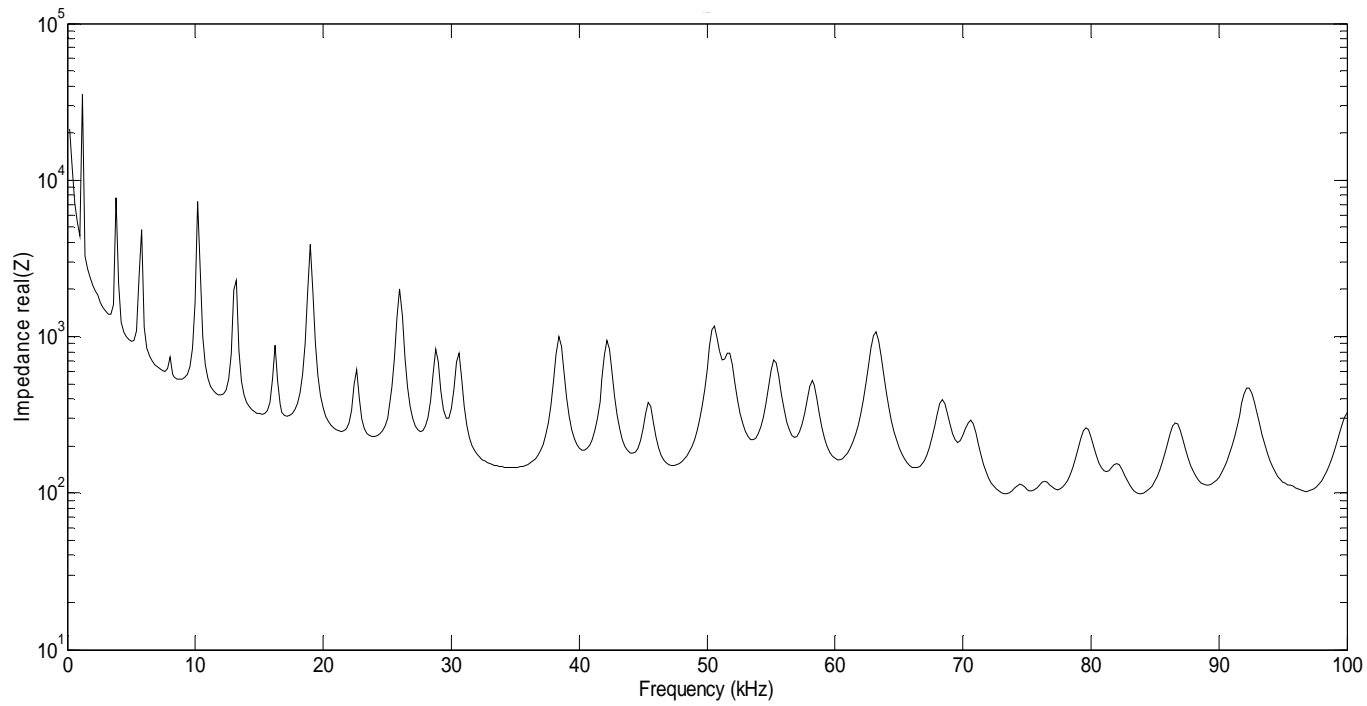
***Figure 162: Impedance ANSYS 2D Analysis***
***(Delamination Specimen, layers 3 and 4,10mm delamination)***
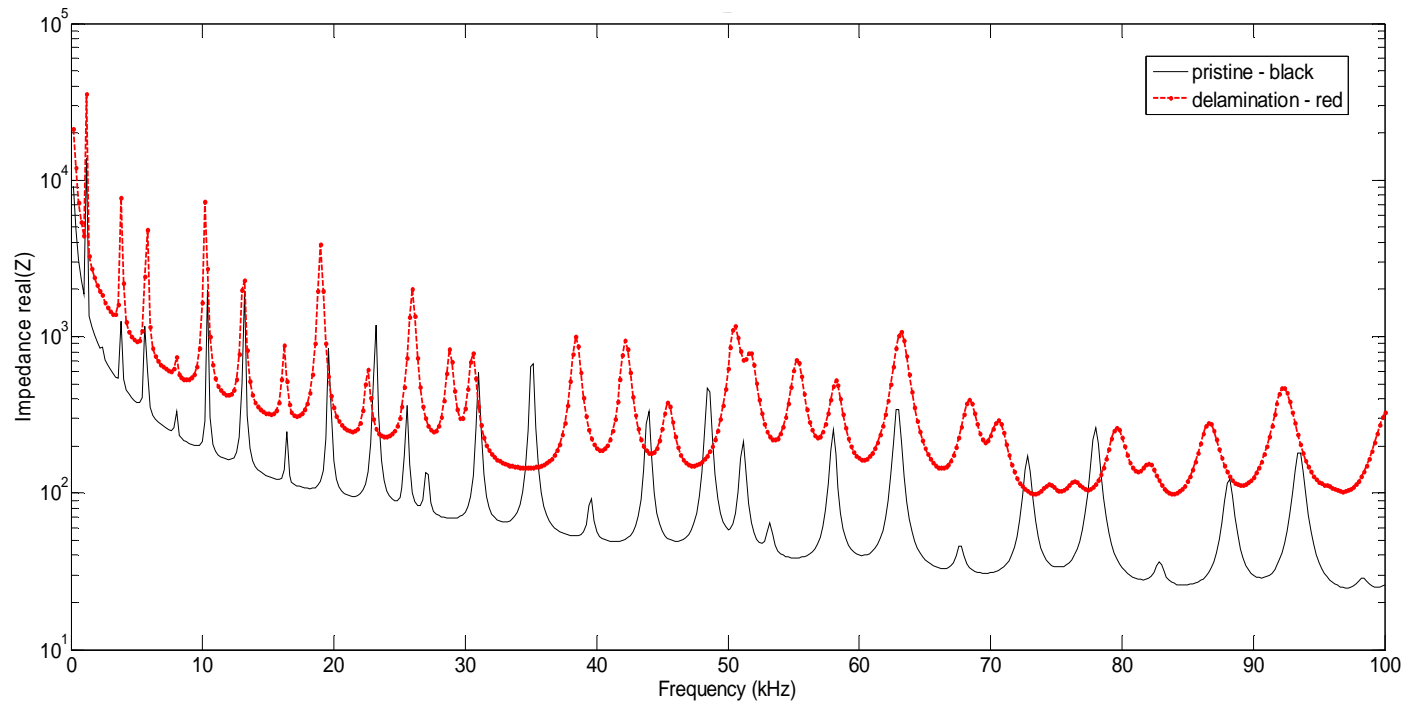
*Figure 163: FEM Impedance Response for Pristine and Delamination Specimen*

266
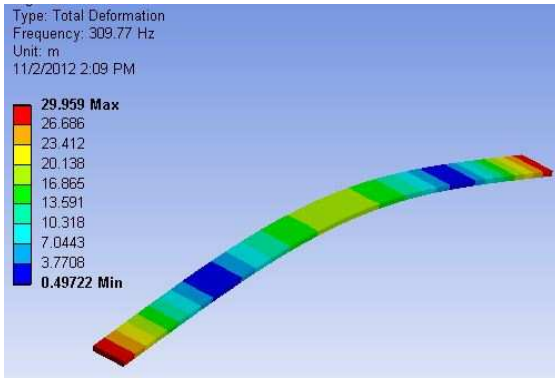
*Figure 164: Flexural (0.3 kHz)*
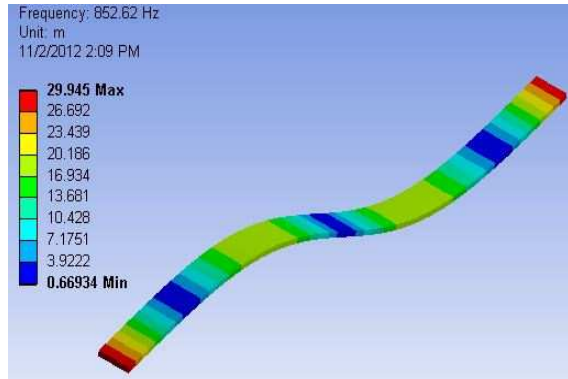


*Figure 165: Flexural (0.8 kHz)*



*Figure 166: Flexural (1.6 kHz)*



*Figure 167: Flexural (2.7 kHz)*
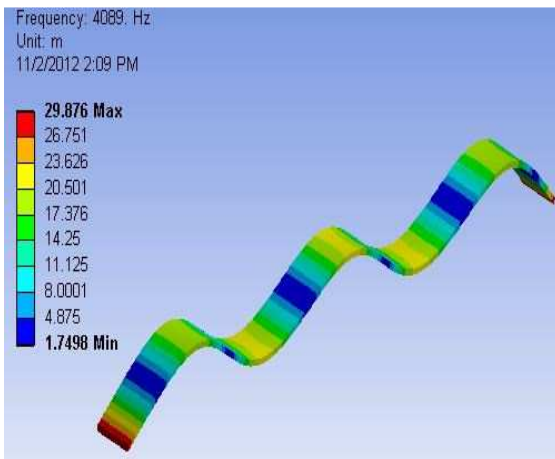


*Figure 168: Flexural (4.1 kHz)*
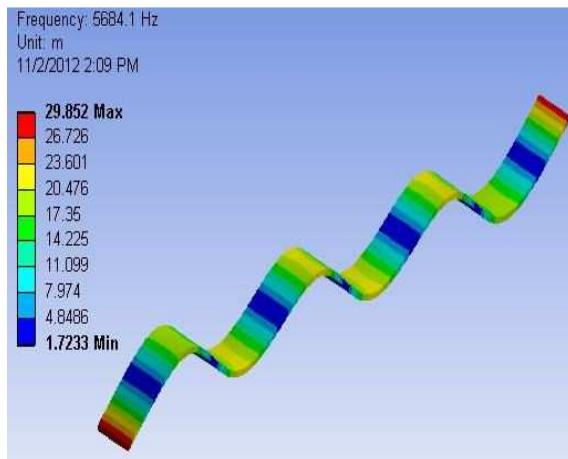


*Figure 169: Flexural (5.7 kHz)*

267

Frequency: 7526.1 Hz
Unit: m
11/2/2012 2:09 PM

29.831 Max
26.735
23.638
20.542
17.446
14.349
11.253
8.1568
5.0606
1.9643 Min
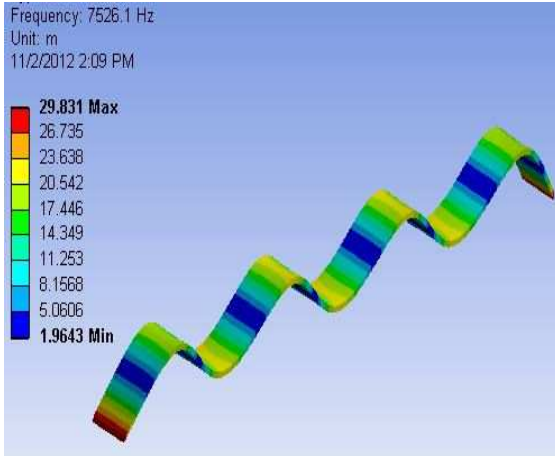
*Figure 170: Flexural (7.5 kHz)*



Frequency: 9606.5 Hz
Unit: m
11/2/2012 2:09 PM

29.817 Max
26.744
23.671
20.597
17.524
14.451
11.378
8.3043
5.231
2.1578 Min
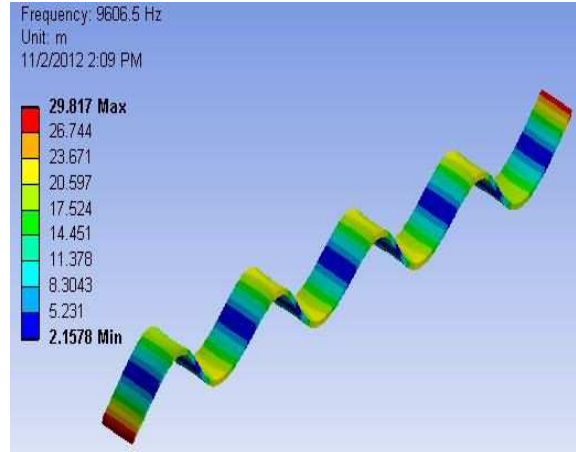
*Figure 171: Flexural (9.6 kHz)*



Frequency: 11916 Hz
Unit: m
11/2/2012 2:09 PM

29.815 Max
26.771
23.726
20.682
17.638
14.593
11.549
8.5043
5.4599
2.4154 Min
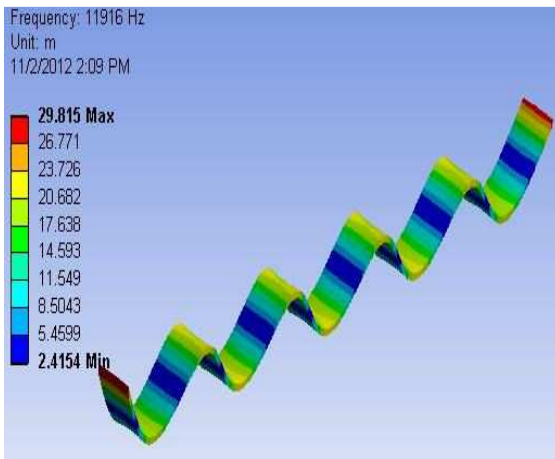
*Figure 172: Flexural (11.9 kHz)*



Type: Total Deformation
Frequency: 14446 Hz
Unit: m
11/2/2012 2:09 PM

29.832 Max
26.807
23.783
20.758
17.734
14.709
11.685
8.6603
5.6358
2.6113 Min
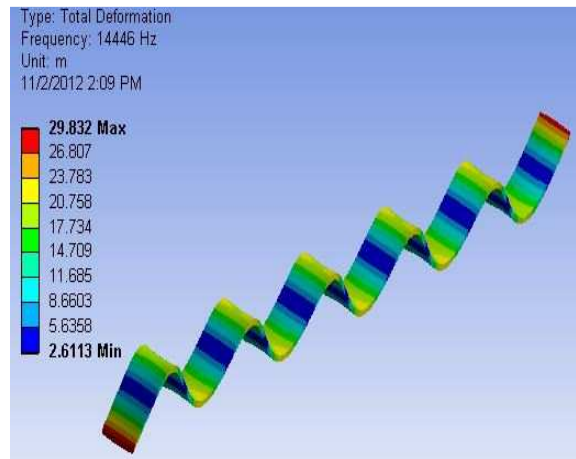
*Figure 173: Flexural (14.4 kHz)*



Type: Total Deformation
Frequency: 17185 Hz
Unit: m
11/2/2012 2:09 PM

29.877 Max
26.872
23.867
20.861
17.856
14.85
11.845
8.8392
5.8337
2.8282 Min
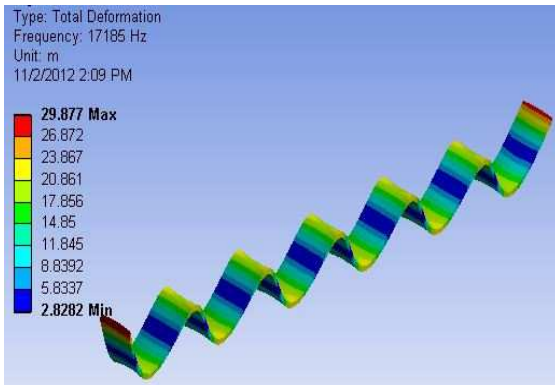
*Figure 174: Flexural (17.85 kHz)*



Frequency: 18091 Hz
Unit: m
11/2/2012 2:09 PM

21.194 Max
18.845
16.497
14.148
11.8
9.4512
7.1027
4.7541
2.4056
0.057056 Min
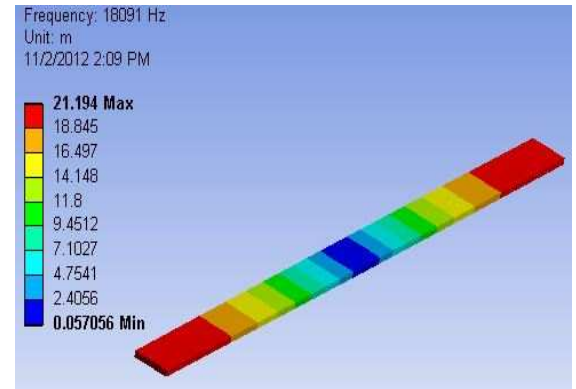
*Figure 175: Axial (18.1 kHz)*

268
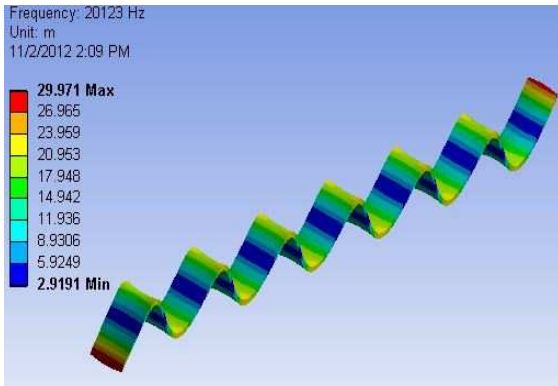
**Figure 176: Flexural (20.1 kHz)**
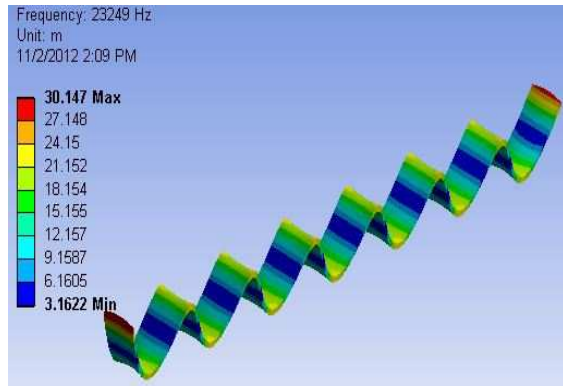


**Figure 177: Flexural (23.25 kHz)**
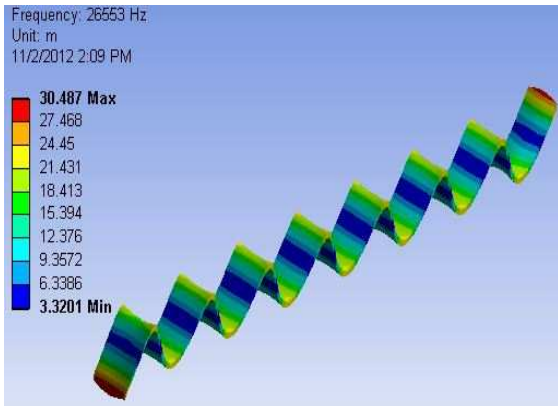


**Figure 178: Flexural (26.55 kHz)**
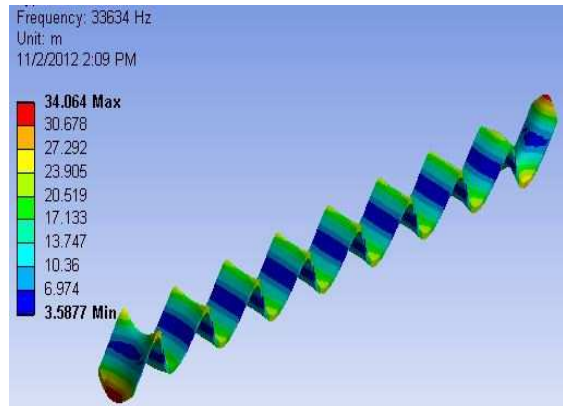


**Figure 179: Flexural (33.63 kHz)**
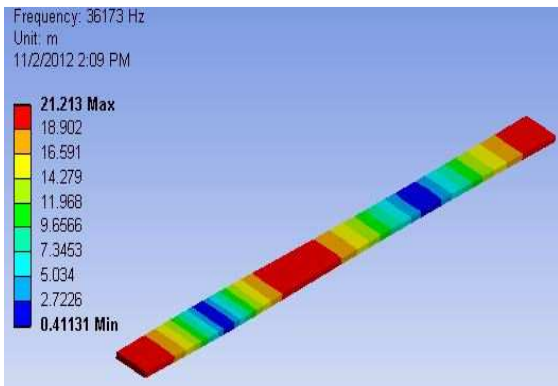


**Figure 180: Axial (36.17 kHz)**
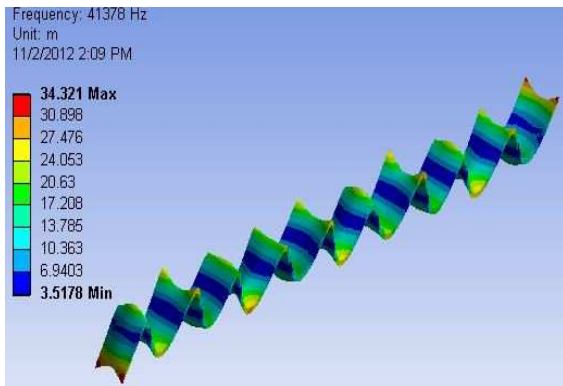


**Figure 181: Flexural (41.37 kHz)**

269
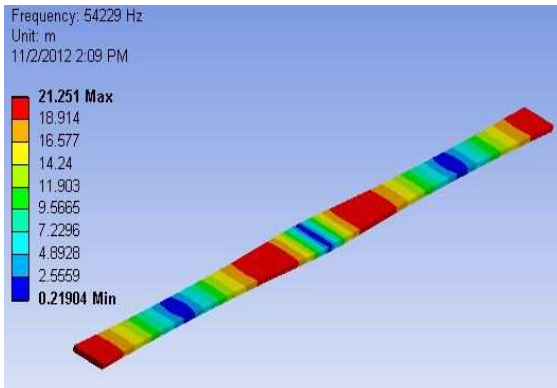
*Figure 182: Axial (54.22 kHz)*
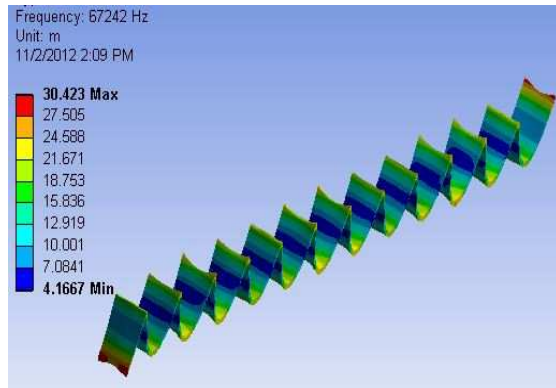


*Figure 183: Flexural (67.24 kHz)*
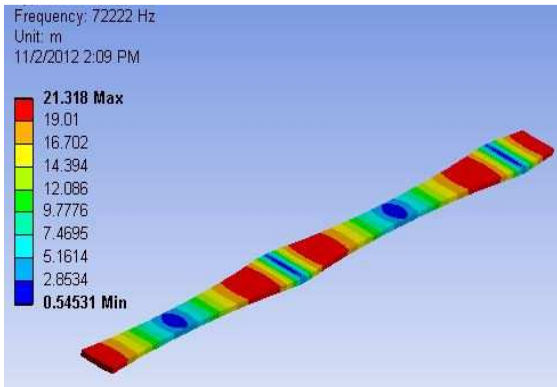


*Figure 184: Axial (72.22 kHz)*
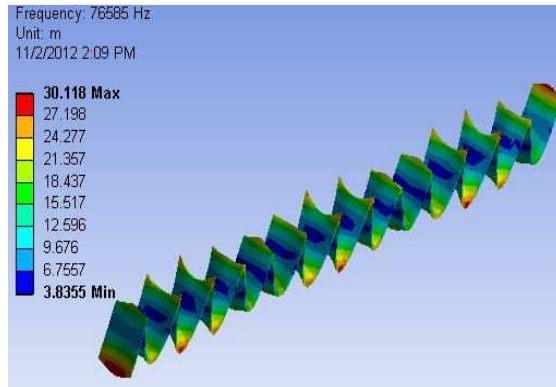


*Figure 185: Flexural (76.58 kHz)*
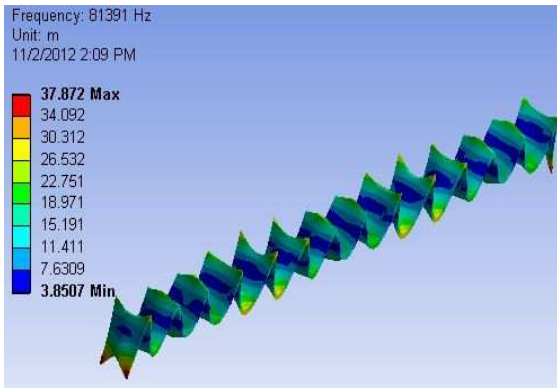


*Figure 186: Flexural (81.39 kHz)*
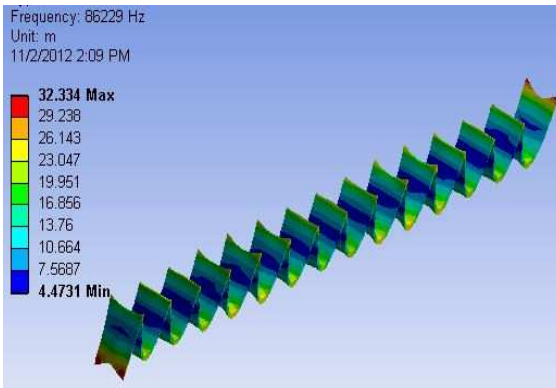


*Figure 187: Flexural (86.22 kHz)*

270
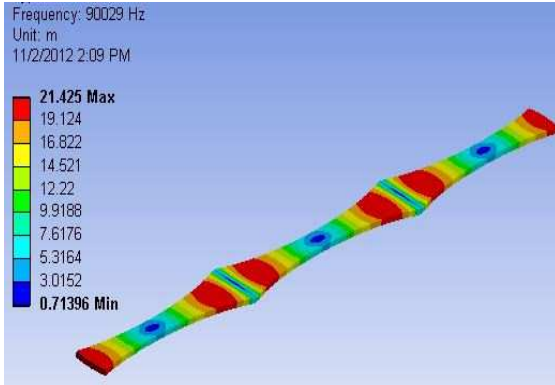
*Figure 188: Axial (90 kHz)*
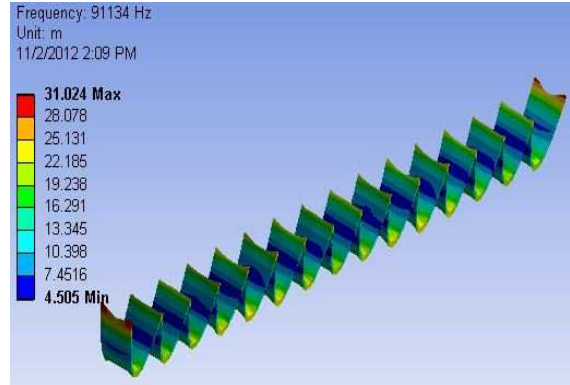


*Figure 189: Flexural (91.13 kHz)*
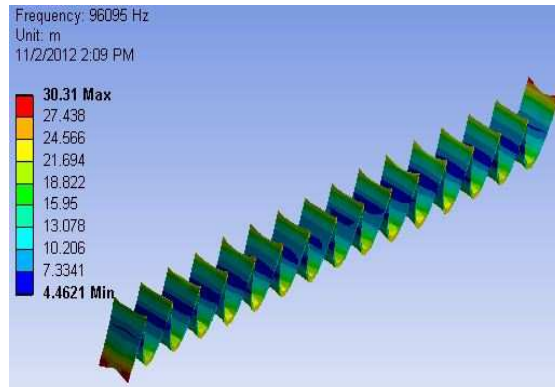


*Figure 190: Flexural (96.1 kHz)*
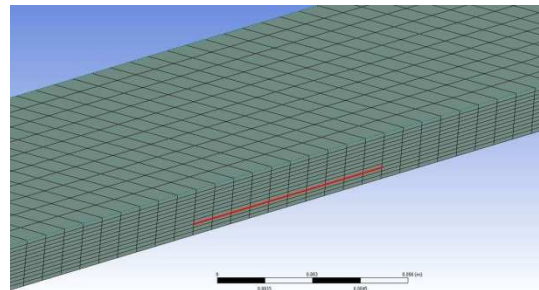


*Figure 191: Beam with delamination*
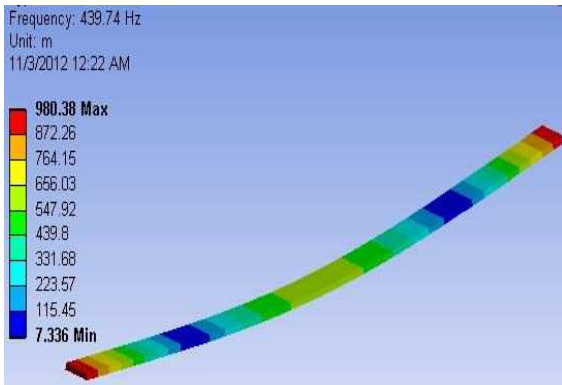


*Figure 192: Flexural (0.44 kHz)*
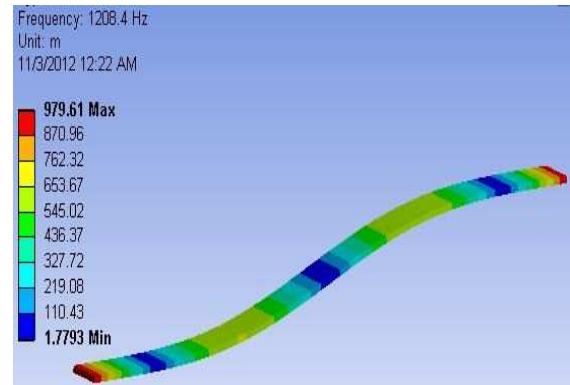


*Figure 193: Flexural (1.2 kHz)*

271
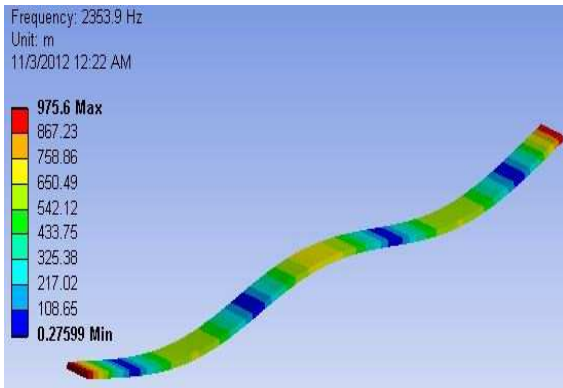
Figure 194: Flexural (2.35 kHz)
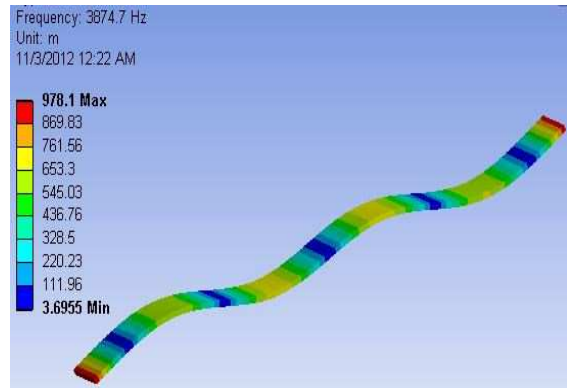

Figure 195: Flexural (3.87 kHz)
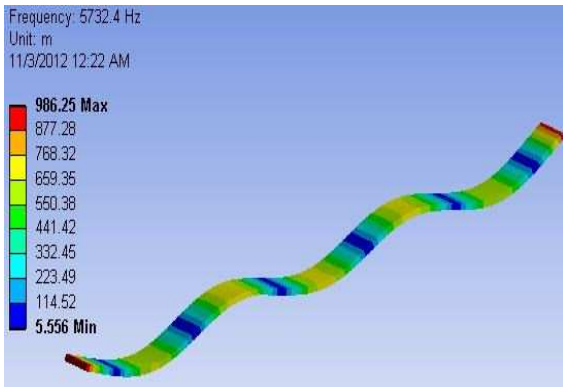

Figure 196: Flexural (5.73 kHz)
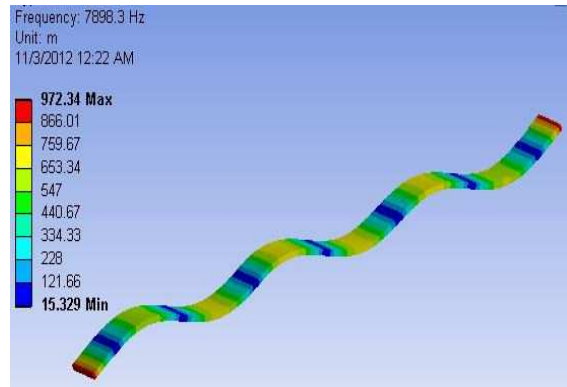

Figure 197: Flexural (7.8 kHz)
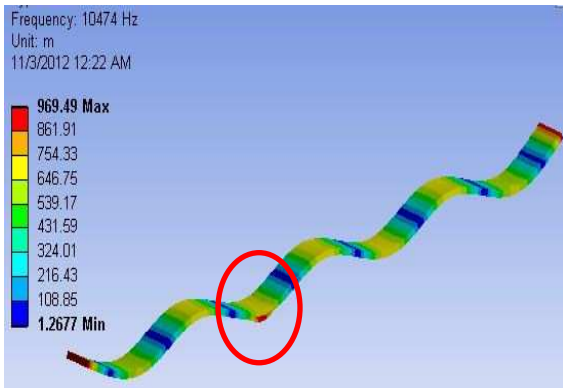

Figure 198: Flexural (10.47 kHz)
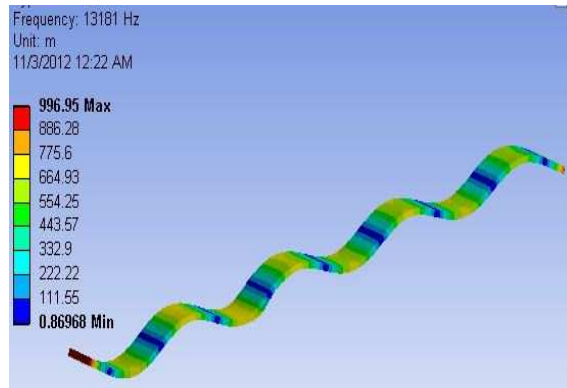

Figure 199: Flexural (13.18 kHz)

272

Frequency: 16228 Hz
Unit: m
11/3/2012 12:22 AM

977.85 Max
869.89
761.93
653.96
546
438.04
330.08
222.11
114.15
6.187 Min
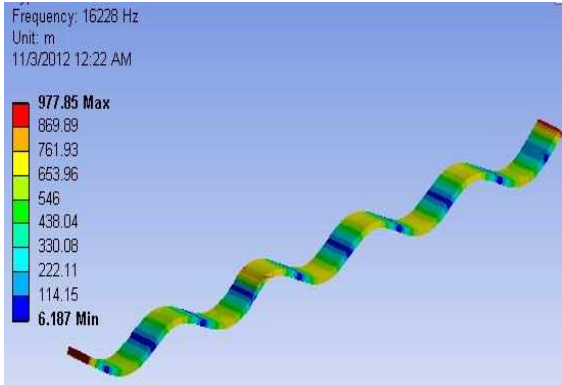
*Figure 200: Flexural (16.22 kHz)*



Frequency: 19591 Hz
Unit: m
11/3/2012 12:22 AM

1774.3 Max
1577.7
1381.1
1184.5
987.96
791.38
594.8
398.21
201.63
5.0501 Min
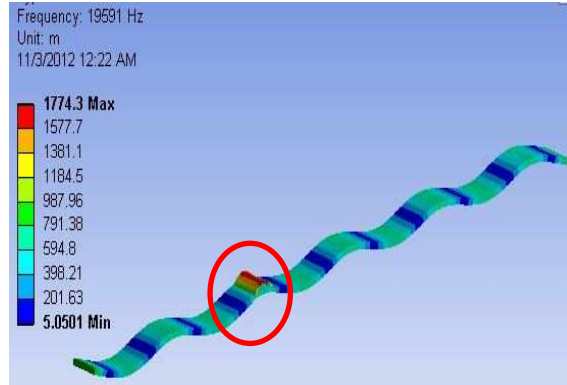
*Figure 201: Flexural (19.59 kHz*



Frequency: 22944 Hz
Unit: m
11/3/2012 12:22 AM

1029.5 Max
915.96
802.46
688.95
575.44
461.93
348.43
234.92
121.41
7.9016 Min
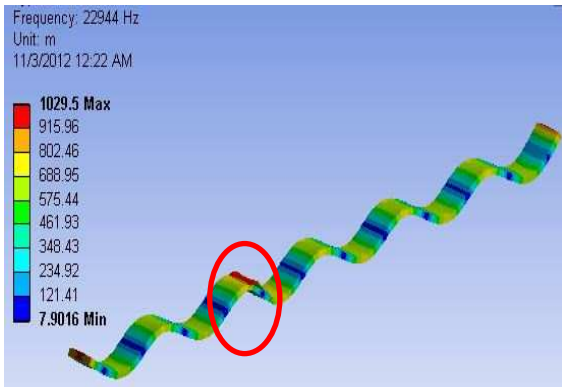
*Figure 202: Flexural (22.94 kHz)*



Frequency: 31998 Hz
Unit: m
11/3/2012 12:22 AM

1736.5 Max
1544.1
1351.8
1159.4
967.05
774.69
582.33
389.98
197.62
5.2676 Min
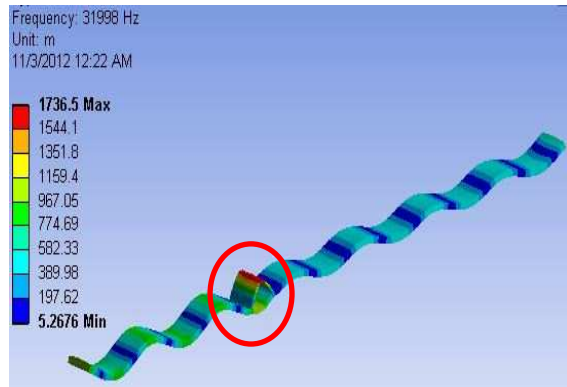
*Figure 203: Flexural (31.99 kHz)*



Frequency: 34665 Hz
Unit: m
11/3/2012 12:22 AM

1011.3 Max
898.97
786.68
674.38
562.09
449.79
337.5
225.2
112.91
0.61143 Min
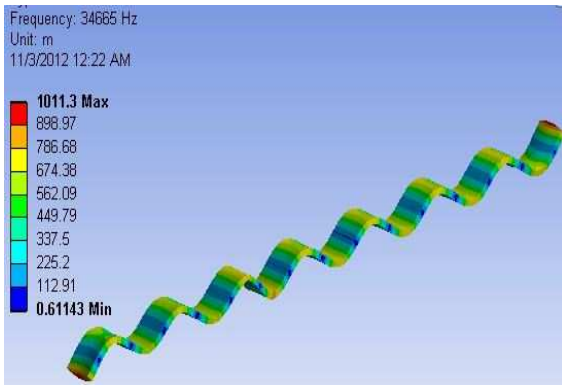
*Figure 204: Flexural (34.66 kHz)*



Frequency: 44293 Hz
Unit: m
11/3/2012 12:22 AM

1553 Max
1380.7
1208.4
1036.1
863.76
691.44
519.12
346.79
174.47
2.1512 Min
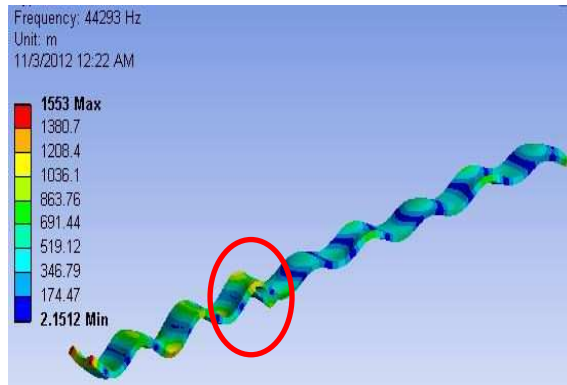
*Figure 205: Flexural (44.29 kHz)*

273
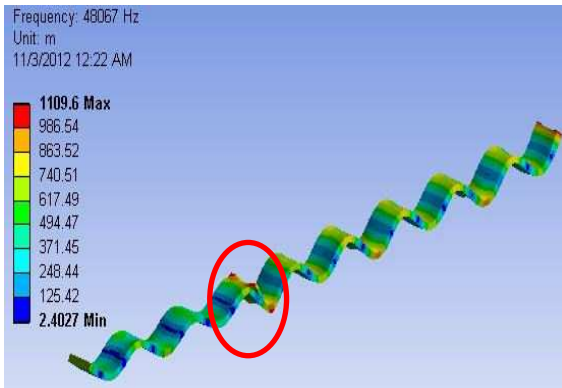
*Figure 206: Flexural (48 kHz)*
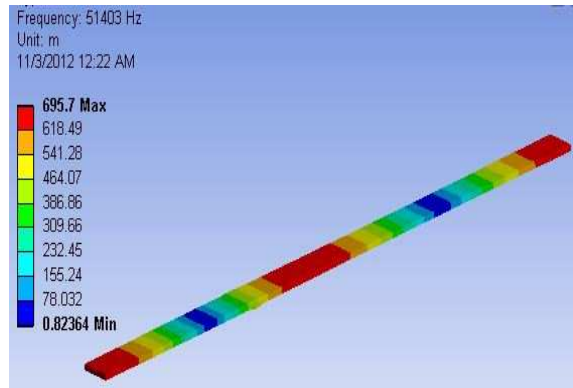


*Figure 207: Axial (51.4 kHz)*
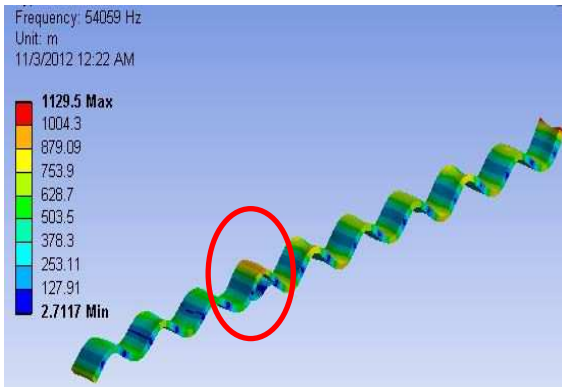


*Figure 208: Flexural (54.06kHz)*
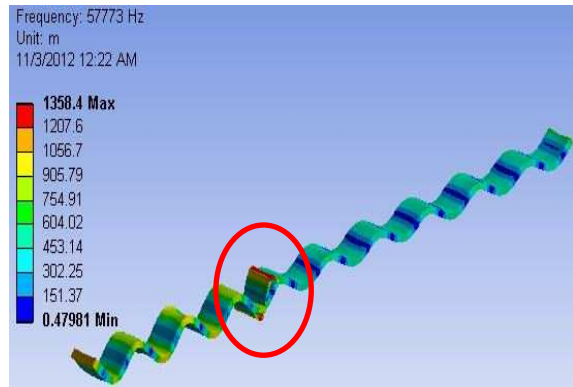


*Figure 209: Flexural (57.77 kHz)*
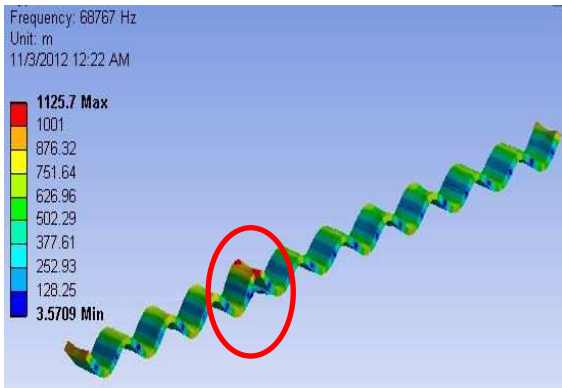


*Figure 210: Flexural (68.76 kHz)*
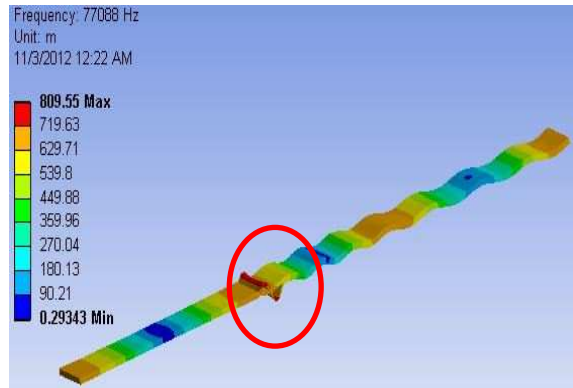


*Figure 211: Axial (77.08 kHz)*
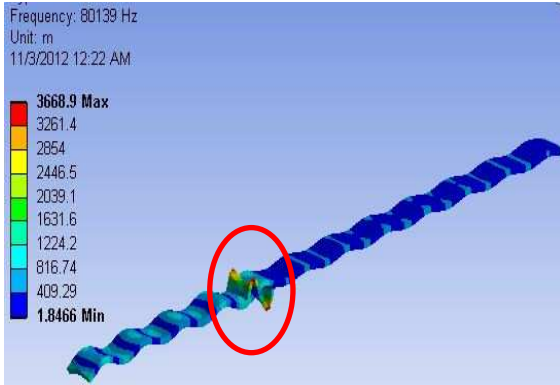
Figure 212: Flexural (80.14 kHz)
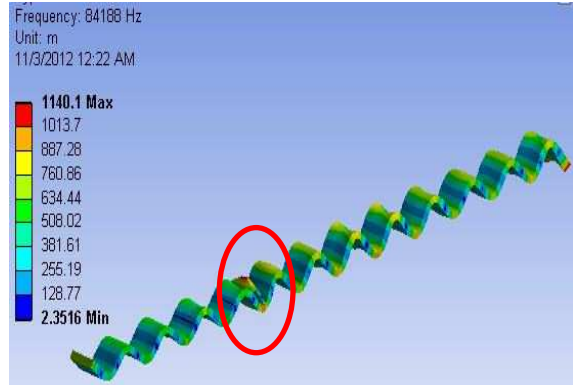

Figure 213: Flexural (84.18 kHz)
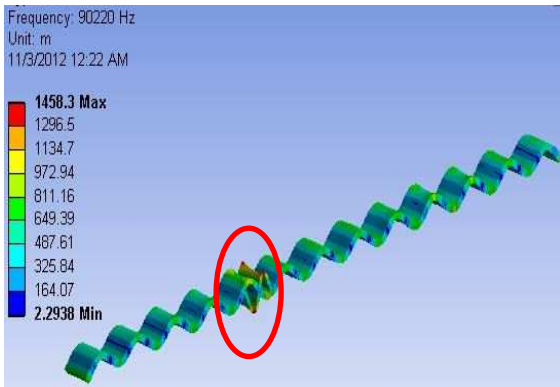

Figure 214: Flexural (90.22 kHz)
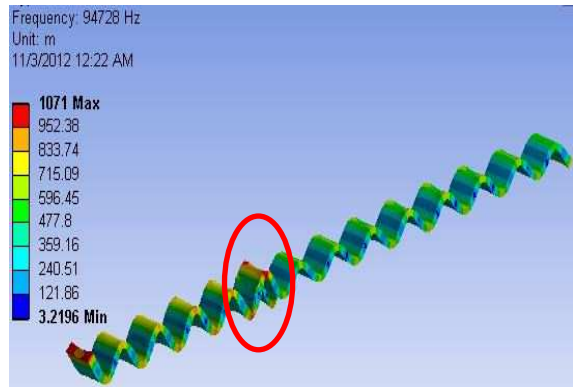

Figure 215: Flexural (94.72 kHz)
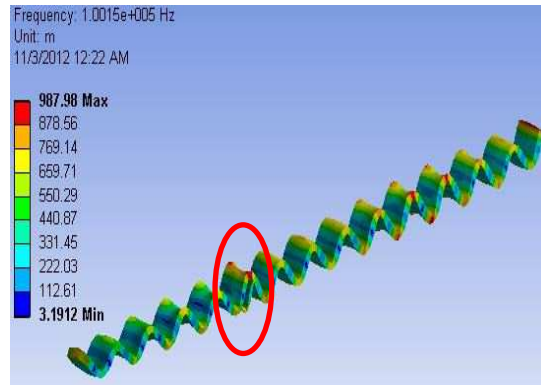

Figure 216: Flexural (100 kHz).

275
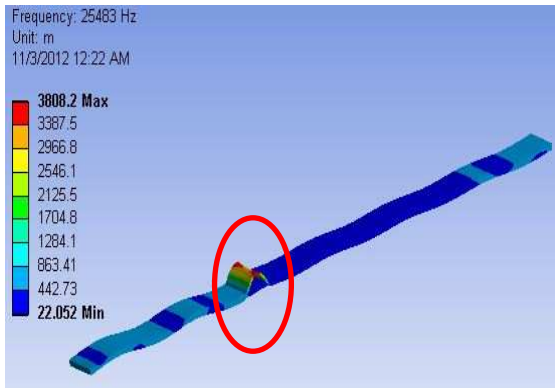
**Figure 217: Flexural (25.48 kHz)**
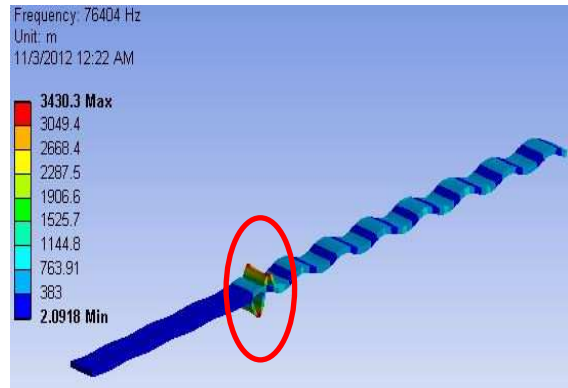


**Figure 218: Flexural (76.4 kHz)**
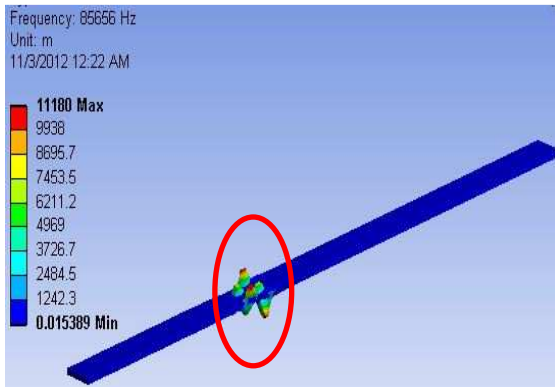


**Figure 219: Local torsional (95.65 kHz)**

## 11.3    VALIDATION WITH EXPERIMENTS

In order to perform the experiments (pristine and delamination beam), we take a unidirectional CFRP composite beam and mount a PWAS at different locations (e.g. 60mm, 80mm, 100mm, 120mm, 140mm and 160mm distance) from one side as per Figure 220. In order to be consistent, we use the 60mm PWAS location as above. The experimental setap for E/M impedance measurements was as described in Section 7.1, Figure 107.
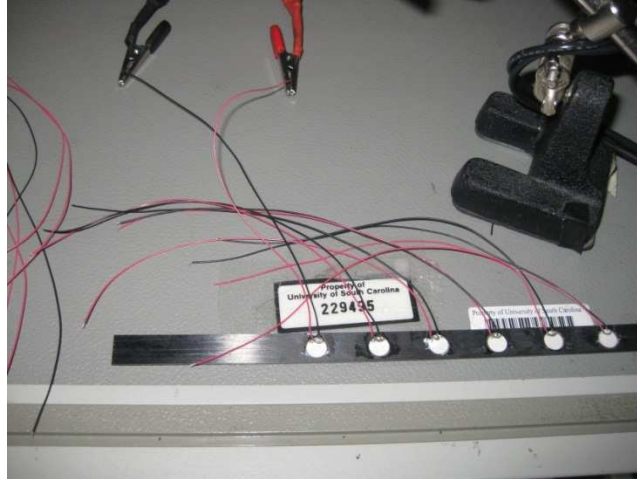
*Figure 220: Pristine Beam Experiment*

Using the HP Impedance Analyzer, we take the measurements in order to validate the experiment. For the first PWAS located at 60mm, the impedance response can be seen in Figure 221 and for the PWAS located at 100mm; the impedance response can be seen in Figure 222.

We then overlap the impedance results for the two experiments and effects are shown in Figure 223. For delamination, the results are presented in Figure 224 and the overlap of the two cases (pristine and delamination), the results are shown in Figure 225.
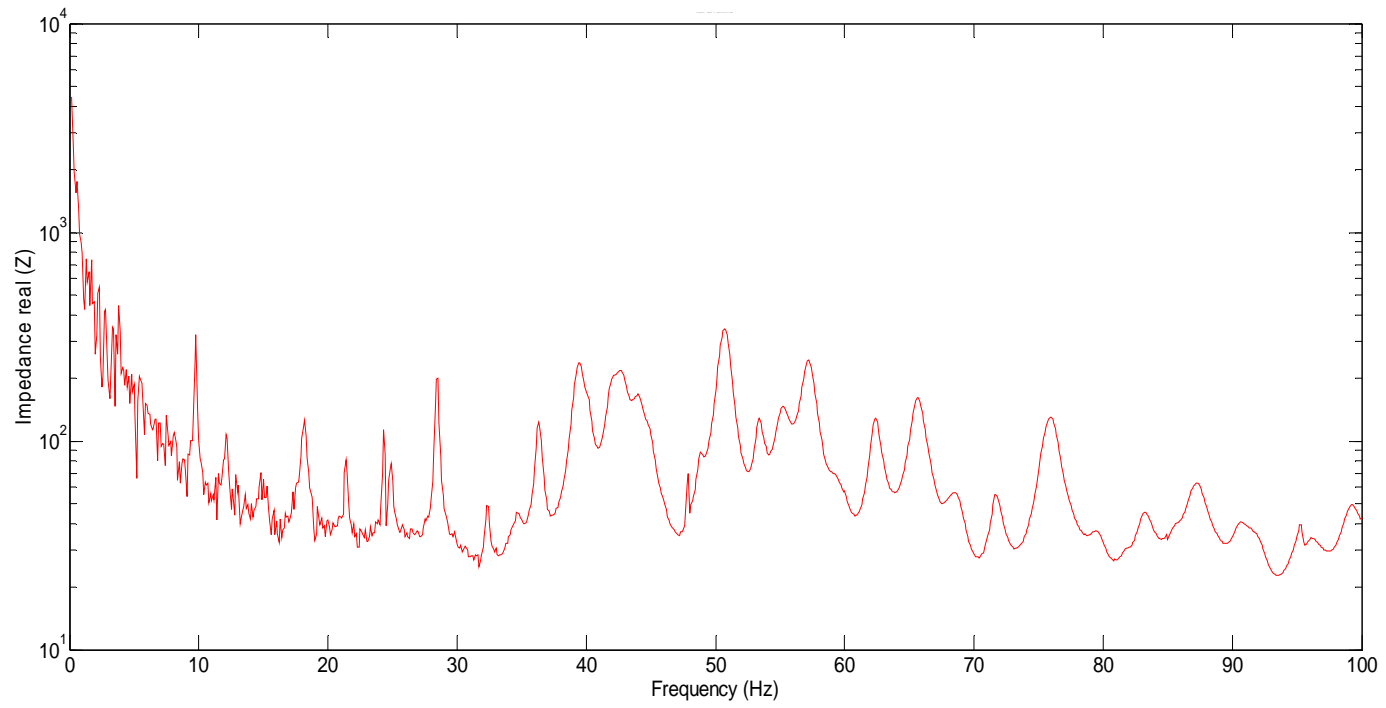
*Figure 221: Experimental Pristine Beam Impedance (60mm location PWAS)*
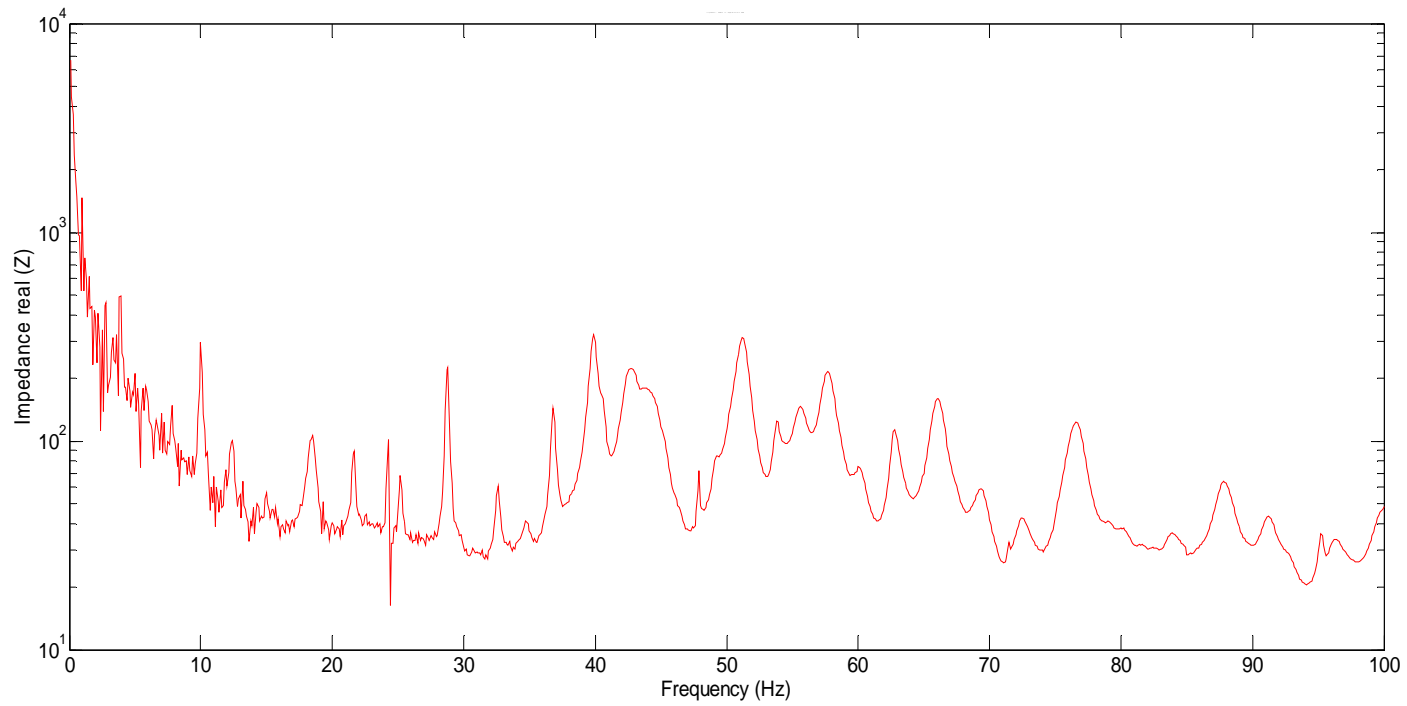
*Figure 222: Experimental Pristine Beam Impedance (100mm location PWAS)*
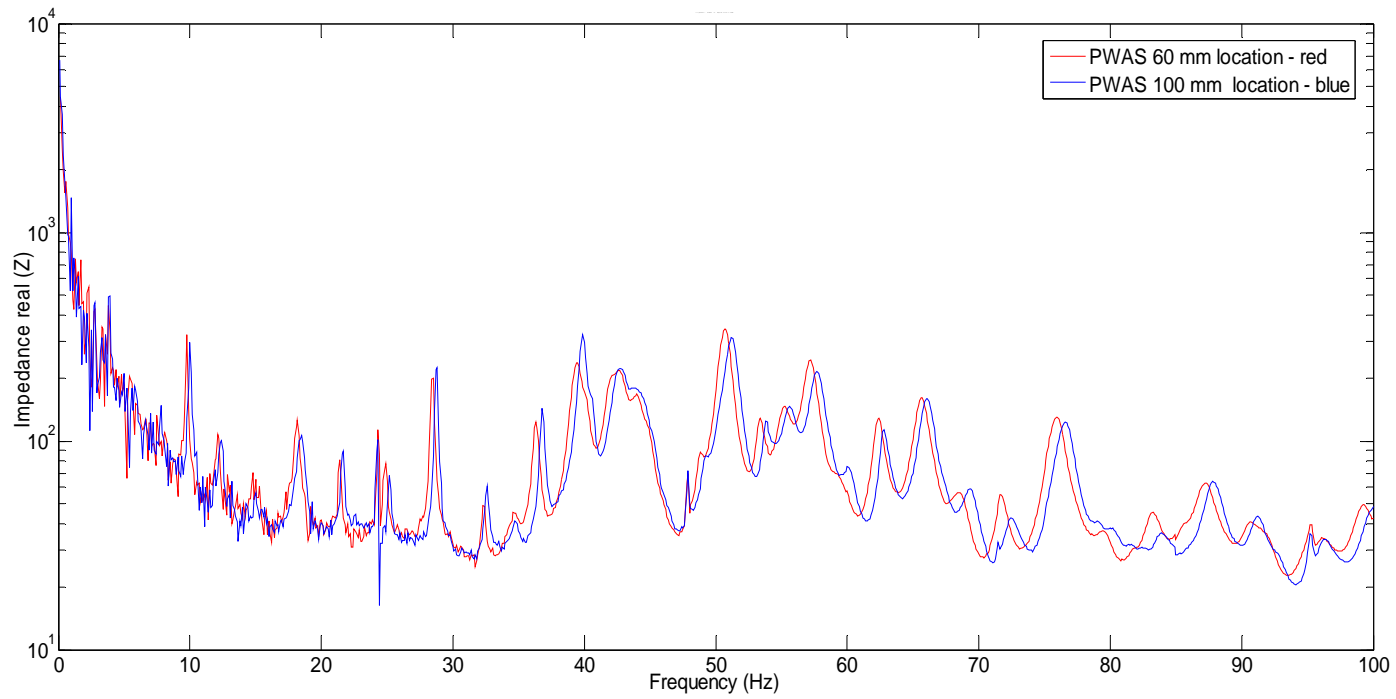
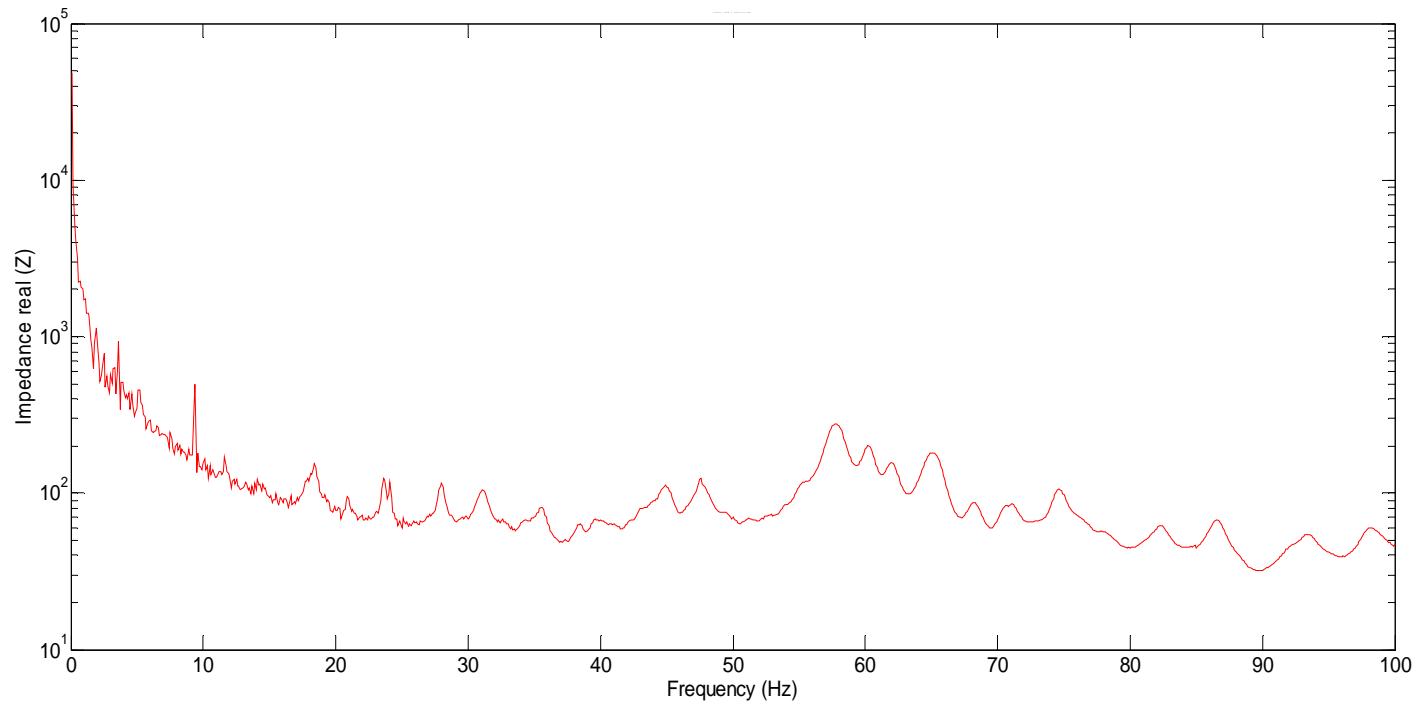*Figure 223: Experimental Impedance Response for Pristine and Delamination Specimen*

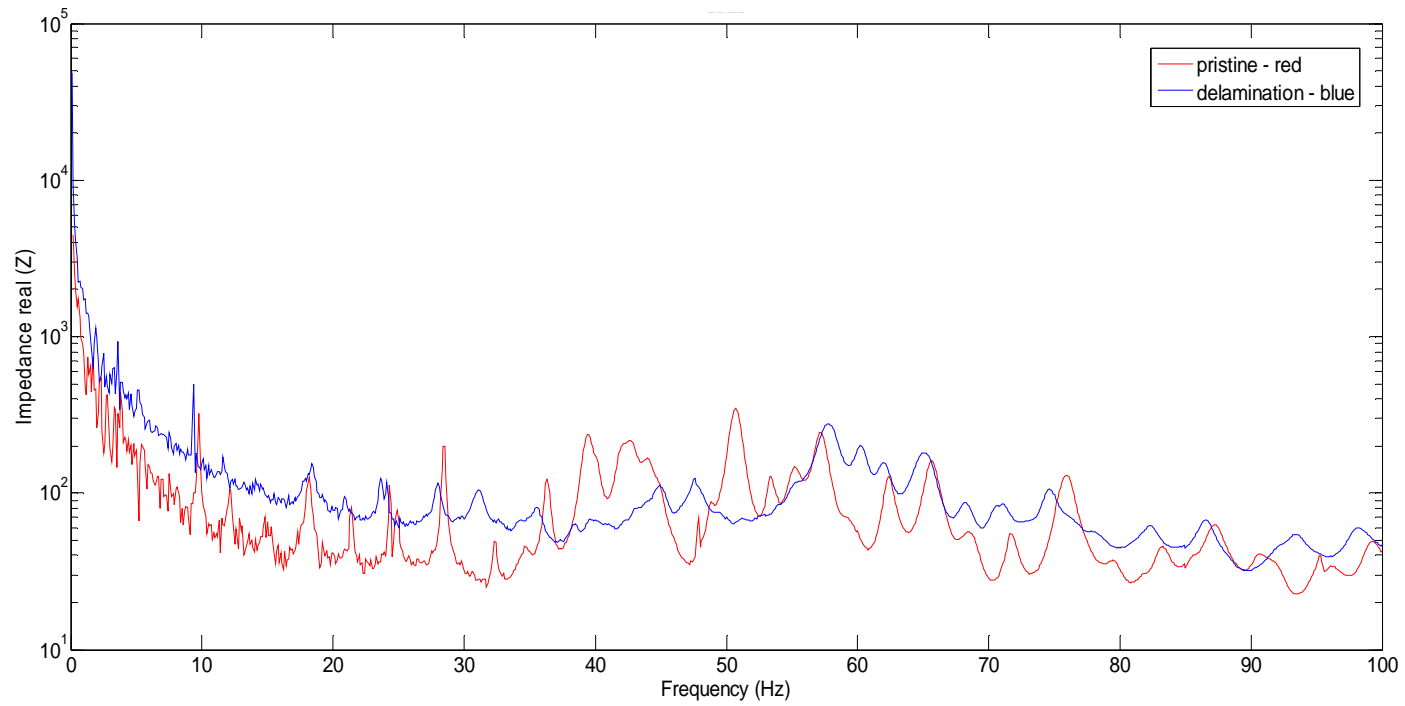*Figure 224: Experimental Delamination Impedance (60mm location PWAS)*

*Figure 225: Experimental Pristine and Delamination Beam Impedance (60mm location PWAS)*

## 11.4 Comparison of STMM, FEM and Experiments for Pristine and Delamination Beams

Before starting to compare the results from all three methods, it is very important to take into consideration a few aspects which can have some influence on our experimental results. Location of the delamination (position) and the length of the delamination are very hard to be checked on the physical model as well difficult to generate the delamination.

The thickness of the non-uniformity of the beam (manufacturing) is another important aspect. The theoretical model is running under perfect conditions, which in reality is impossible to match. Having all those factors in our analysis, we seek to compare the results.

We compare the three possible approaches (STMM, FEM and Experiments) to understand similarities differences among the methods in terms of the resonant frequencies.

Figure 226 and Table 8 presents the pristine beam case. Figure 226 shows the impedance spectrum and the resonance peaks. In Table 8, we can see the resonance frequencies calculated using the three methods.

Figure 227 and Table 9 presents the pristine beam case. Figure 227 shows the impedance spectrum and the resonance peaks. In Table 9, we can see the resonance frequencies calculated using the three methods.

By looking at Table 8 and Table 9, with few exceptions, we see a good correlation between all the methods. The analytical numerical results are in accordance with the

experiment results. This proves that our method reached the goal. The main advantage of our method is the short time required to calculate the impedance spectrum.

Using ANSYS WB, we have the possibility to observe the predicted modeshape of the beam at a certain resonance frequency. Figure 217, Figure 218, Figure 219, which are related to the resonance of the delamination, seem to be very complex, which raise some questions. Let's assume the PWAS to be bounded, close to one of the sides in the experiment case. The question is what this sensor will read, because on one side we have a very strong flexural mode and on the other side a very weak flexural mode. Definitely, our PWAS will read a different resonance frequency depending on its location.

Another case is when the PWAS is bonded on the top of the delamination. By looking at Figure 219 from ANSYS WB, the sensor will see a flexural mode in that particular area but the whole beam is in the axial mode.These cases can explain some of the differences presented in Table 8 and Table 9.

4From all these observations, the laminate theory seems to be very complex and hard to predict, which leaves room for further research in this area to better understand the behavior of laminates under different conditions as well as develop ways to control its behavior and make it more predictable so it can be used in industrial applications.

***Table 8: Comparison of resonant frequencies:***
***STMM vs. FEM vs. Experiment – pristine case study***

| type | CFRP - \<kHz\> | | | |
|---|---|---|---|---|
| | STMM | FEM 2D | FEM 3D | experiment |
| F | 0.35 | 0.4 | 0.3 | 0.3 |
| F | ? | ? | 0.85 | ? |
| F | 1.1 | 1.2 | 1.66 | 1.3 |
| F | 2.35 | 2.4 | 2.75 | 2.3 |
| F | 3.85 | 3.8 | 4.1 | 3.8 |
| F | 5.85 | 5.6 | 5.7 | 5.4 |
| F | 8.1 | 8 | 7.52 | 7.5 |
| F | 10.84 | 10.4 | 9.6 | 9.8 |
| F | 11.09 | ? | 11.09 | 12.1 |
| F | 14.09 | 13.2 | 14.44 | 14.8 |
| F | 17.58 | 16.4 | 17.85 | 18.2 |
| A | 21.58 | 19.6 | 23.25 | 21.4 |
| F | 25.82 | 25.6 | 26.55 | 24.3 |
| F | 30.32 | 27 | 26.55 | 24.9 |
| F | 30.57 | 31 | 30 | 28.5 |
| F | 35.56 | 35.2 | 33.63 | 32.3 |
| F | 41.06 | 39.6 | 36.17 | 36.3 |
| F | 46.8 | 44 | 41.37 | 39.4 |
| F | 51.55 | 48.4 | 49.57 | 42.7 |
| F | 53.05 | 51.2 | 53.83 | 50.7 |
| A | 59.54 | 53.2 | 54.22 | 53.4 |
| F | ? | ? | ? | 55.3 |
| F | 59.79 | 58 | 58.23 | 57.2 |
| F | 66.53 | 62.8 | 62.68 | 62.4 |
| F | 66.78 | 67.8 | 67.24 | 65.6 |
| F | 74.03 | ? | ? | 68.6 |
| A | 74.28 | 72.8 | 72.22 | 71.7 |
| F | 77.27 | 78 | 76.58 | 76.1 |
| F | 81.77 | 82.8 | 81.39 | 83.2 |
| F | 90.01 | 88.2 | 86.22 | 87.2 |
| A | 90.26 | ? | 90 | 90.6 |
| F | ? | 93.6 | ? | 95.3 |
| F | 98.75 | 98.4 | 96.09 | 99.3 |
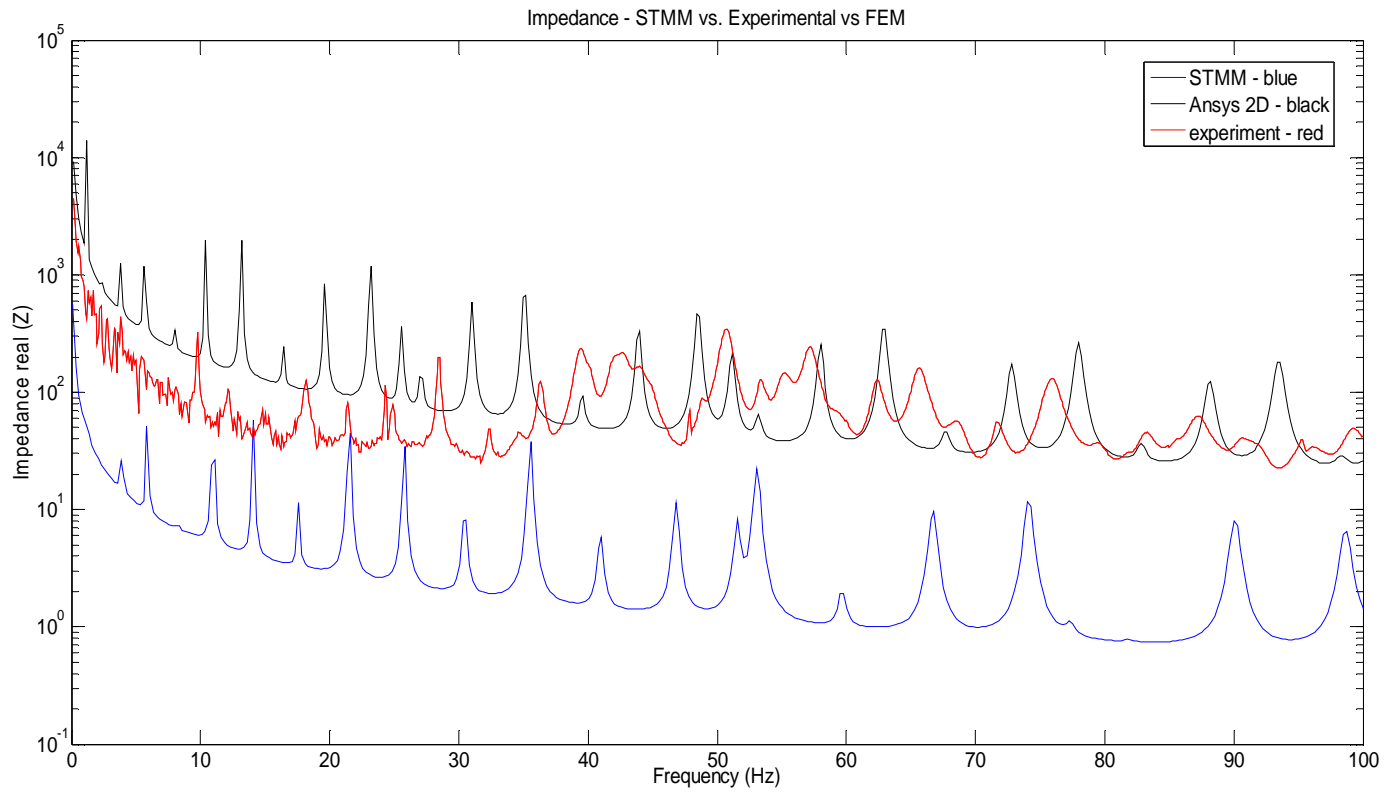
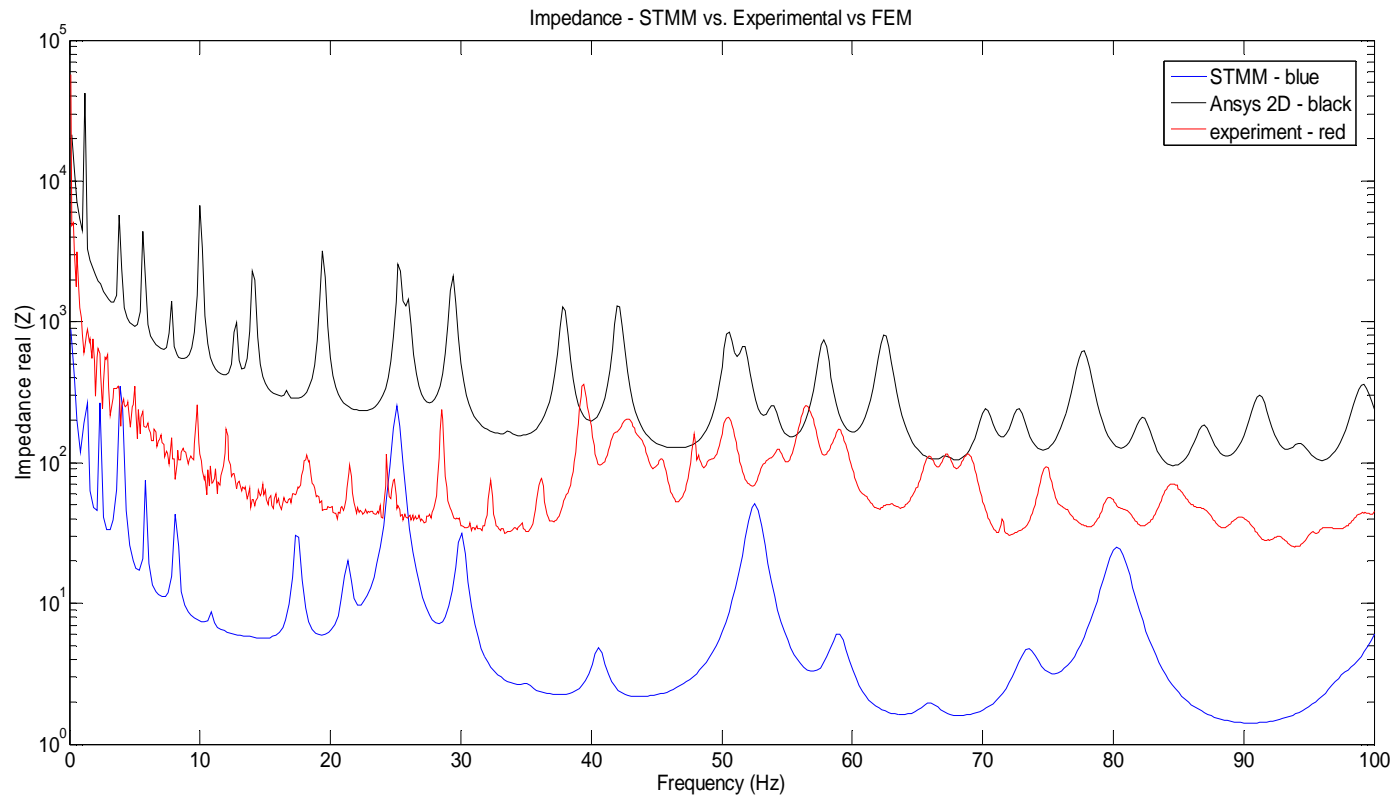*Figure 226: unidirectional CFRP Impedance – STMM vs. FEM vs. Experiment – pristine case*

*Figure 227: unidirectional CFRP Impedance – STMM vs. FEM vs. Experiment – delamination case*

***Table 9: Comparison of resonant frequencies:***
***STMM vs. Fem vs. Experiment – delamination case study***

| type | CFRP <kHz> | | | |
|---|---|---|---|---|
| | STMM | FEM 2D | FEM 3D | experiment |
| F | ? | ? | 0.44 | ? |
| F | 1.1 | 1.2 | 1.2 | 1.4 |
| F | ? | ? | 2.35 | ? |
| F | 3.8 | 3.8 | 3.87 | 3.6 |
| F | 5.8 | 5.8 | 5.73 | 5.2 |
| F | 8.1 | 8 | 7.89 | 7.5 |
| F | ? | ? | 10.47 | 11.6 |
| F | 14.1 | 13.2 | 13.18 | 14.1 |
| F | 17.5 | 16.2 | 16.22 | 15.5 |
| F | ? | 19 | 19.59 | 18.3 |
| F | 21.33 | 22.6 | 22.94 | 20.9 |
| F | 25.57 | 26 | ? | 24.2 |
| F | ? | 28.8 | ? | 28.1 |
| F | 30.32 | 30.6 | 31.99 | 31.1 |
| F | 35.1 | ? | 34.66 | 35.7 |
| F | 40.81 | 38.4 | ? | 39.6 |
| F | 40.81 | 42.4 | 44.29 | 43.3 |
| F | 46.55 | 45.4 | 48 | 45.1 |
| A | 51.3 | 50.6 | 51.4 | 47.6 |
| F | 52.8 | 55.2 | 54.06 | 55.3 |
| F | 54.8 | 55.2 | 57.77 | 55.3 |
| F | ? | ? | ? | 60.2 |
| F | 59.29 | 63.2 | ? | 62 |
| F | ? | ? | ? | 65.2 |
| F | 66.28 | 68.4 | 68.76 | 38.4 |
| F | 72.3 | 70.6 | 71 | 71.1 |
| F | 74.03 | 74 | ? | 74.6 |
| F | ? | 79.6 | 80.14 | ? |
| F | ? | 82.6 | 84.18 | 82.2 |
| F | 89.26 | 86.6 | 90.22 | 86.8 |
| F | ? | 92.4 | 94.72 | 93.4 |
| F | 98.25 | 99.8 | 100 | 98.1 |

## 12. TASK #4: SENSITIVITY STUDIES OF STMM E/M IMPEDANCE FOR DELAMINATION DETECTION IN COMPOSITE BEAMS

We conducted experiments and simulations with different sensor positions on the damaged beam in order to determine the influence of the bonded PWAS and we will look for their modes frequencies and their amplitude.

A very important aspect will be played by the position of the sensor of the PWAS (60mm location from the left side of the beam) given the damaged zone of the beam. We will look at several configurations:

1) Delamination is 10mm length between layers 3 and 4 and it is located at 30mm from the left side of the beam

2) Delamination is 10mm length between layers 2 and 3 and it is located at 30mm from the left side of the beam

3) Delamination is 15mm length between layers 3 and 4 and it is located at 30mm from the left side of the beam

4) Delamination is 10mm length between layers 3 and 4 and it is located at 25mm from the left side of the beam

5) Delamination is 10mm length between layers 3 and 4 and it is located at 60mm from the left side of the beam (delamination under the PWAS)

We looked for different phase shifts in the impedance measurements. We will ran more experiments for each case and determine the average error rate, standard

deviation of the error, skewness etc. in order to draw conclusions about the best accuracy that can be obtained in each case.

We studied these aspects for three different materials: unidirectional CFRP composite, woven-glass epoxy composite and T300/5208 Quasi-Isotropic as per Table 7. The experimental setap for E/M impedance measurements was as described in Section 7.1, Figure 107.

## 12.1    CASE1: UNIDIRECTIONAL CFRP COMPOSITE

Figure 228 shows all five configurations under study for CFRP. We use all three methods (STMM, ANSYS and Experiment) to look for the resonance frequencies and to measure the impedance.
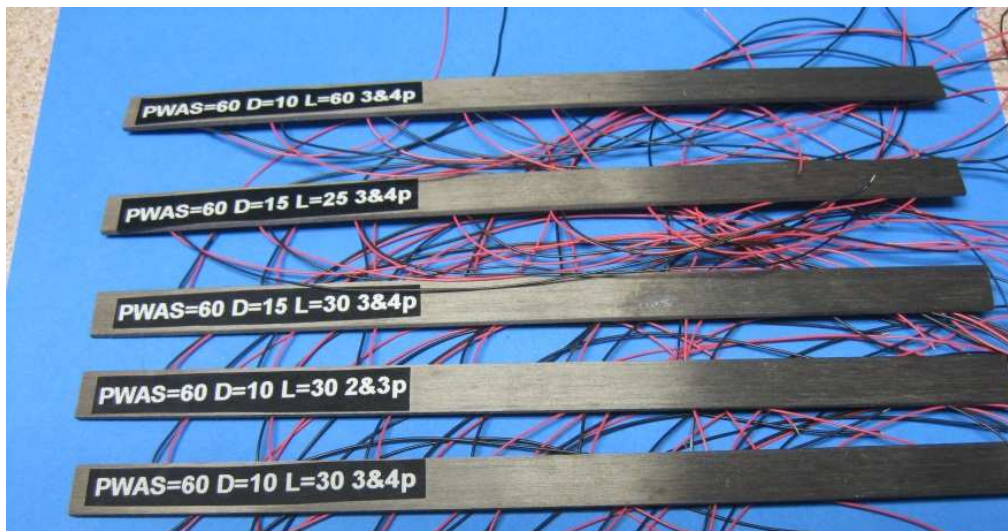


*Figure 228: CFRP: 5 Configurations*

First, let us consider a CFRP beam (180x10x1.5mm) where the delamination is 10mm length between layers 3 and 4and it is located at 30mm from the left side. The PWAS is bonded at 60 mm from the left side. In Figure 229, we can see the results for all three methods.

Second, we change the location of the delamination and consider a CFRP beam (180x10x1.5mm) where the delamination is 10mm length between layers 2 and 3 and it is located at 30mm from the left side. Results are shown in Figure 230.

Third, we increase the delamination size and consider a CFRP beam (180x10x1.5mm) where the delamination is 15mm length between layers 3 and 4 and it is located at 30mm from the left side. Results are shown in Figure 231.

Fourth, we modify the delamination location and consider a CFRP beam (180x10x1.5mm) where the delamination is 10mm length between layers 3 and 4 and it is located at 25mm from the left side. Results are shown in Figure 232.

Fifth, we modify the delamination location and consider a CFRP beam (180x10x1.5mm) where the delamination is 10mm length between layers 3 and 4 and it is located at 60mm from the left side (delamination  is under the PWAS). Results are shown in Figure 233.
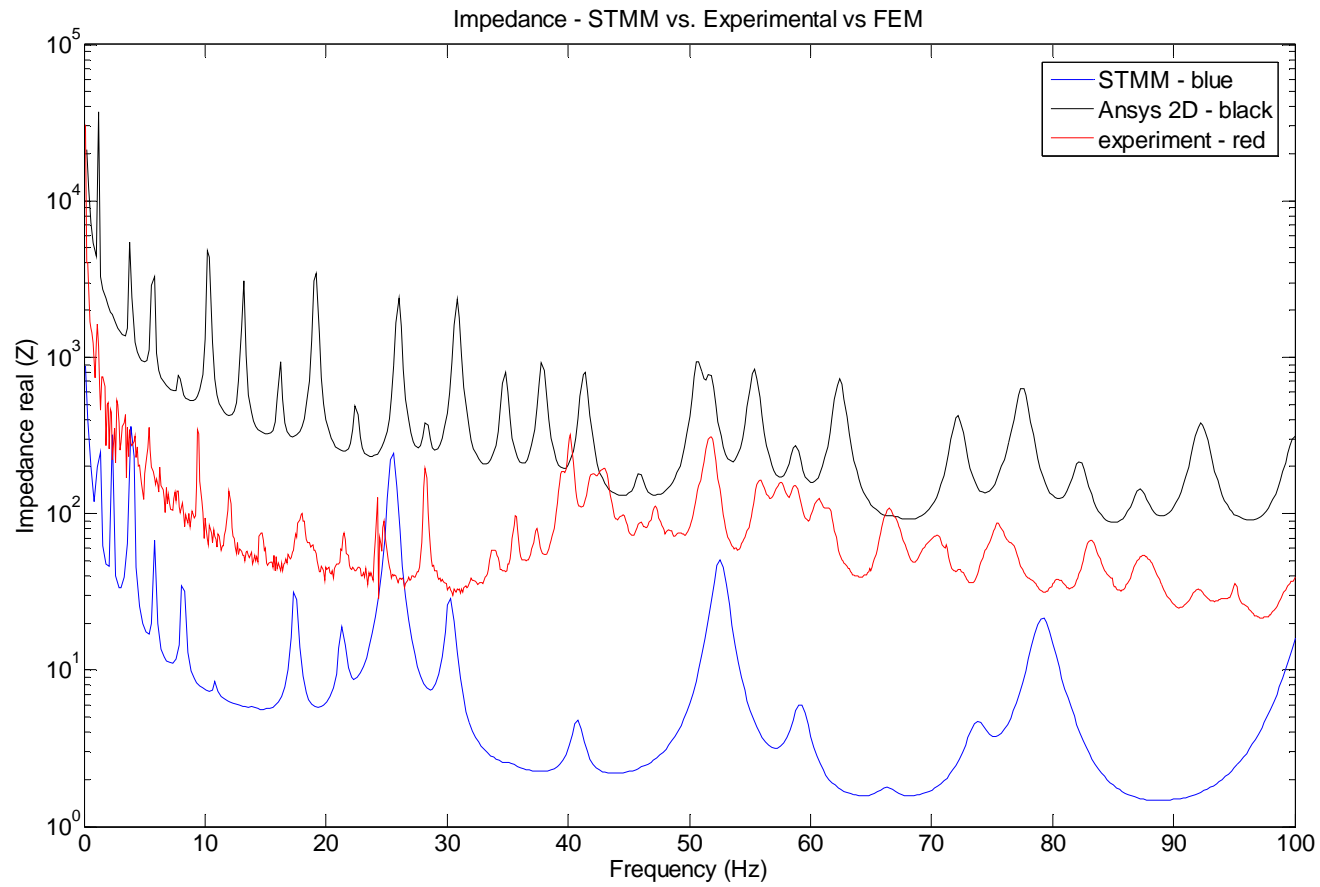
**Figure 229: CFRP: PWAS=60mm & D=10 mm Loc =30mm for D (layers 3 & 4)**
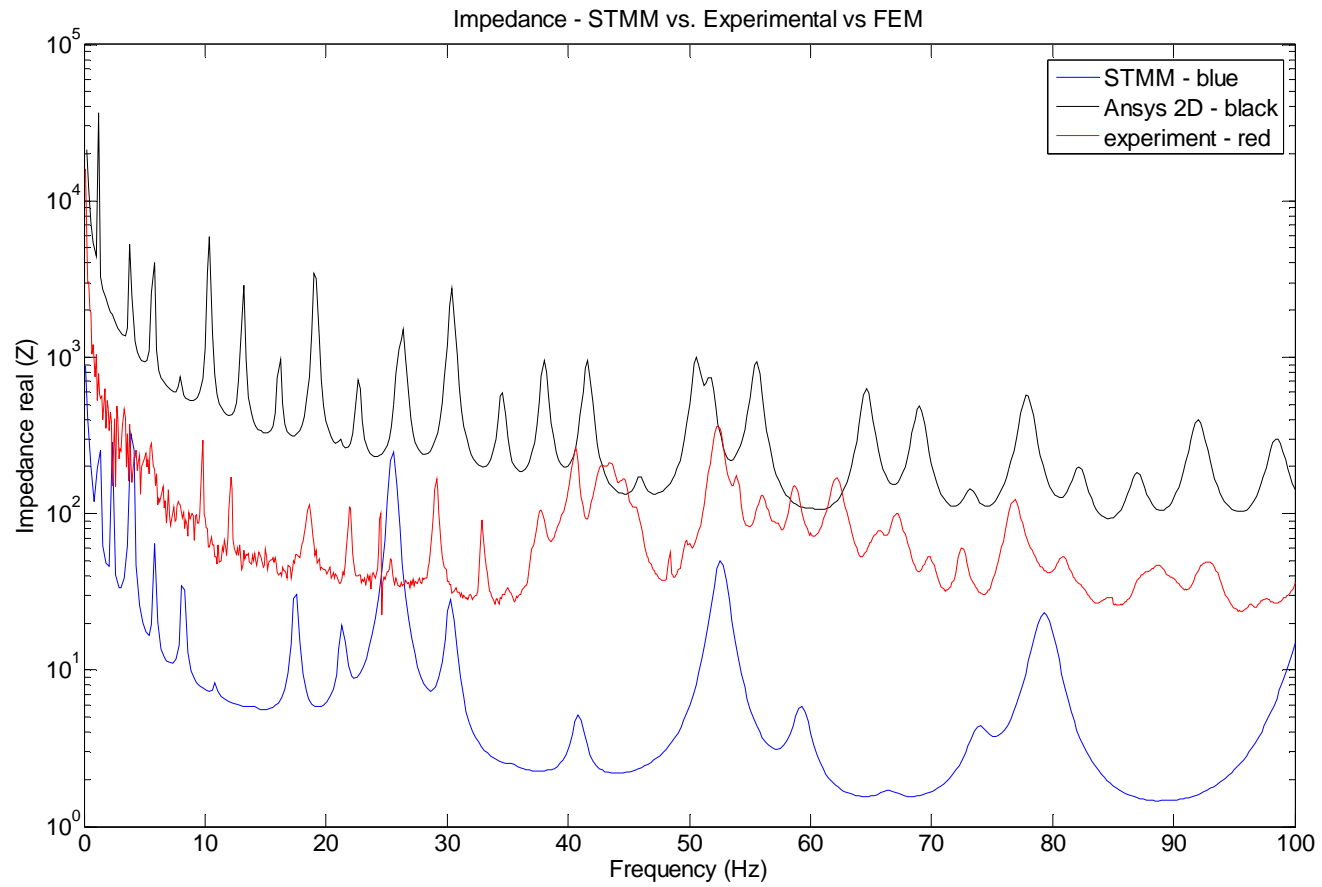
**Figure 230: CFRP: PWAS=60mm & D=10 mm Loc =30mm for D (layers 2 & 3)**
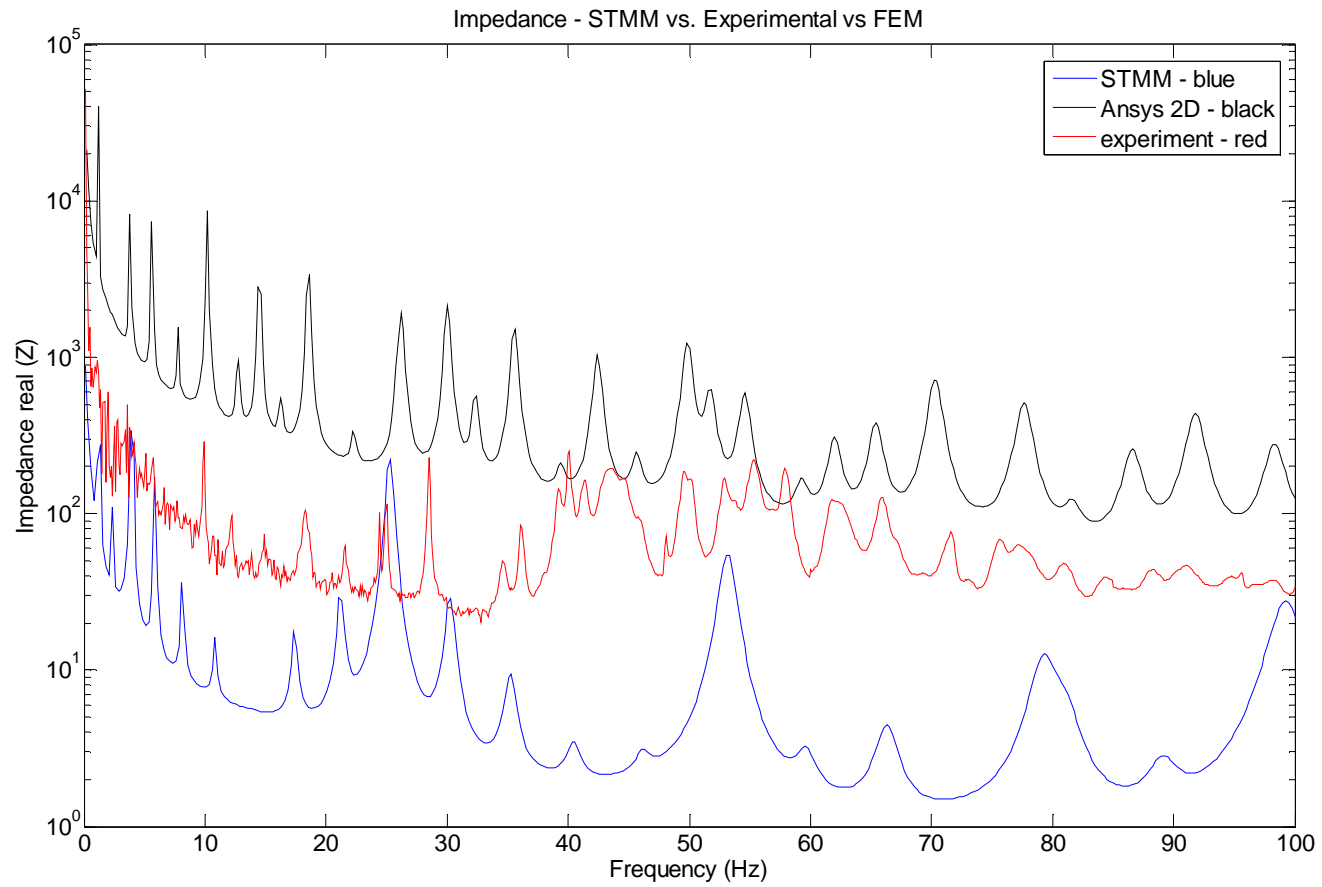
*Figure 231: CFRP: PWAS=60mm & D=15 mm Loc =30mm for D (layers 3 & 4)*
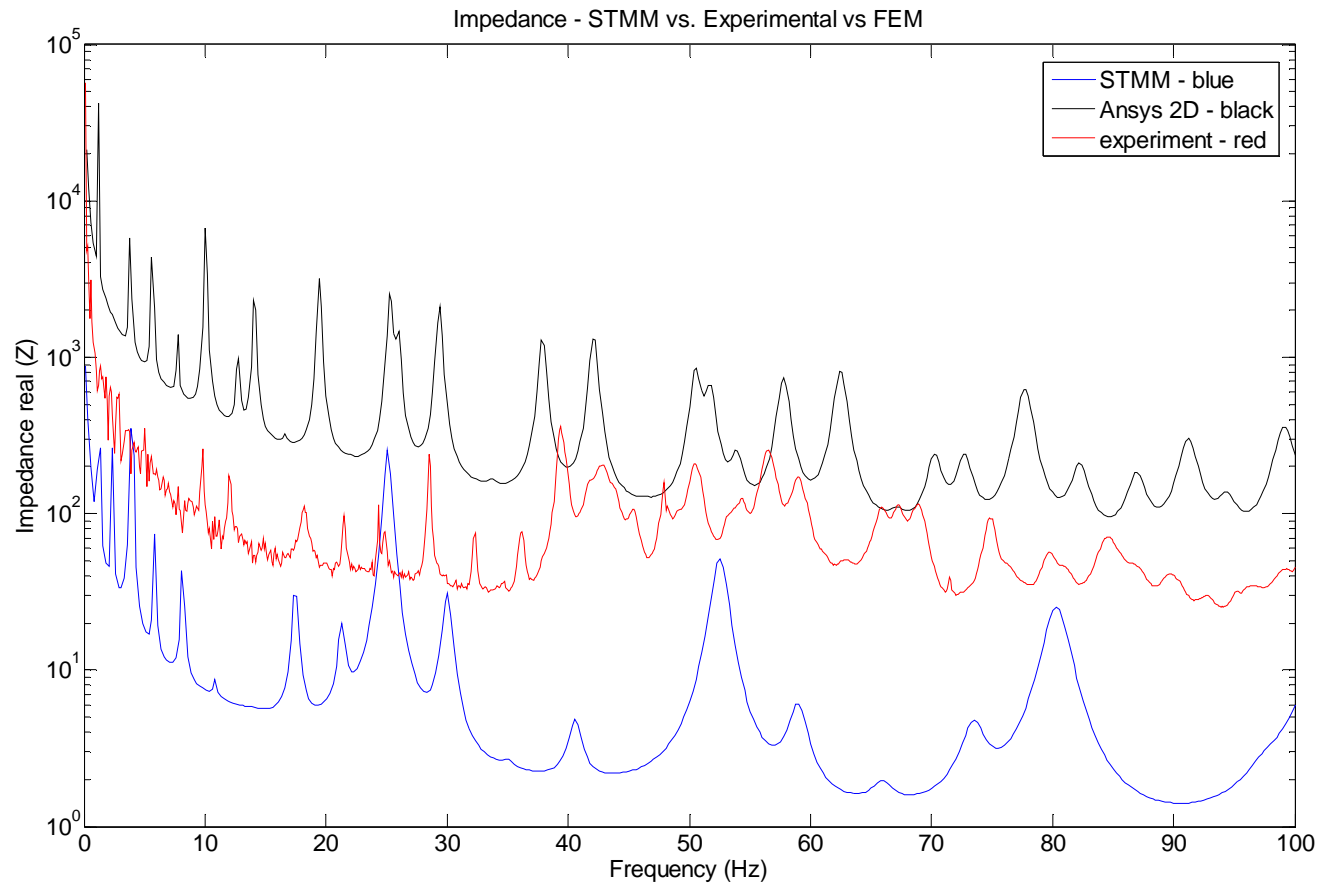
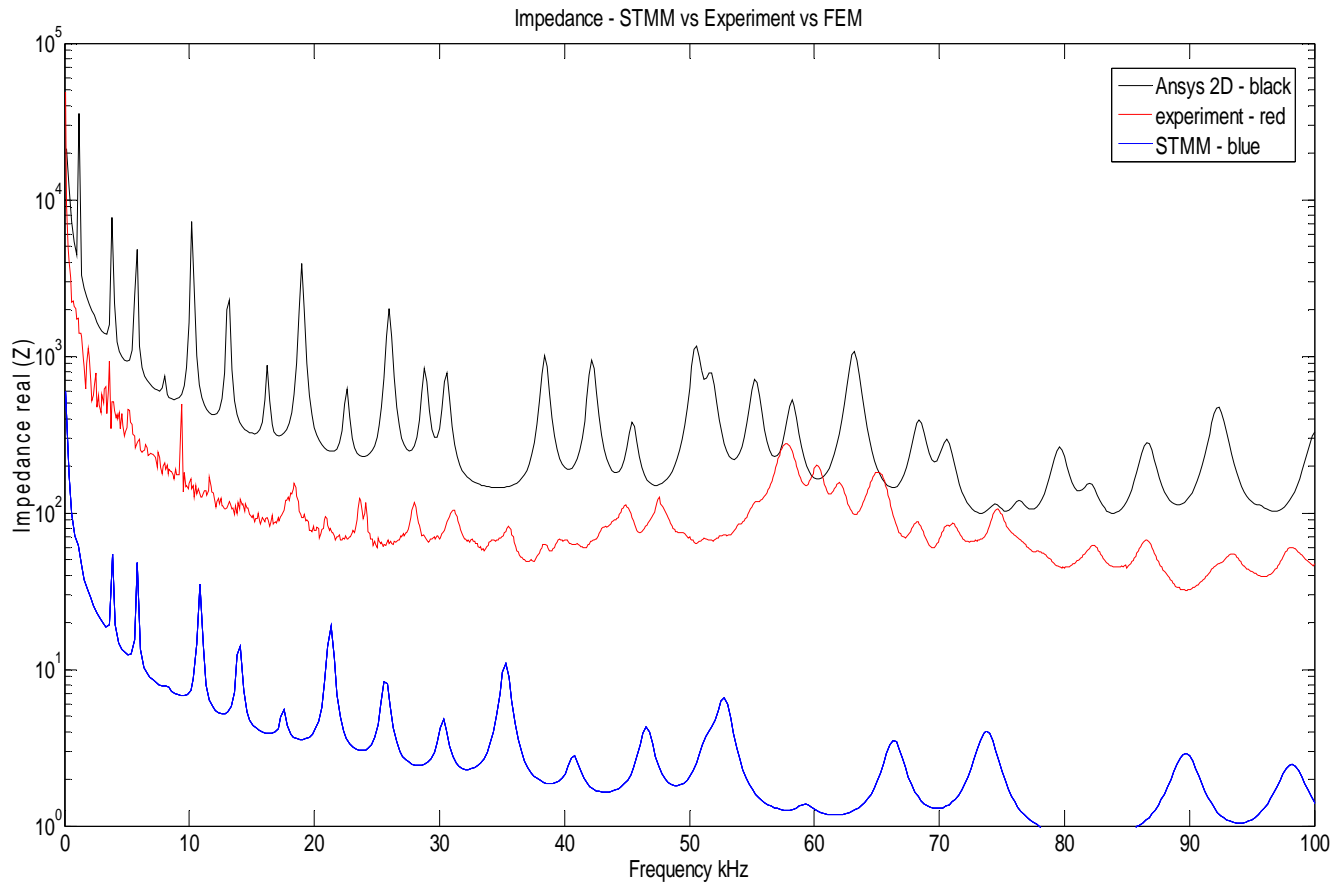**Figure 232: CFRP: PWAS=60mm & D=15 mm Loc =25mm for D (layers 3 & 4)**

*Figure 233: CFRP: PWAS=60mm & D=15 mm Loc =60mm for D (layers 3 & 4)*

## 12.2    CASE2: WOVEN GLASS-EPOXY COMPOSITE

Figure 234 shows all five configurations under study for woven glass epoxy composite.

We use two methods (STMM and Experiment) to look for the resonance frequencies and to measure the impedance for delamination cases. Figure 236 shows the impedance spectrum and the resonance peaks for pristine case. The experimental setap for E/M impedance measurements was as described in Section 7.1, Figure 107.
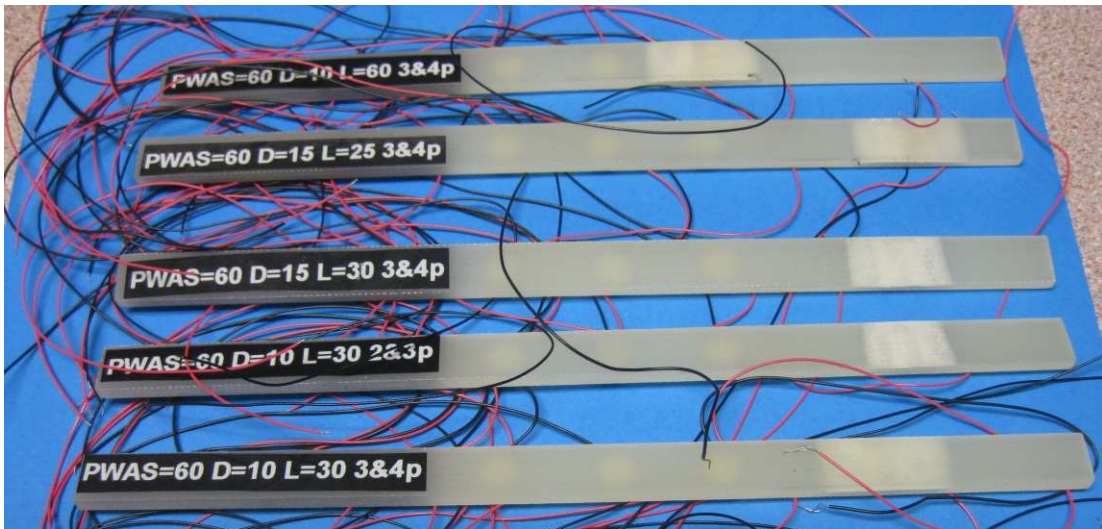


*Figure 234: Woven Glass-Epoxy: 5 Configurations*

First, we considered a woven glass-epoxy beam (180x10x1.5mm) where the delamination is 10mm length between layers 3 and 4and it is located at 30mm from the left side. The PWAS is bounded at 60 mm from the left side. In Figure 236, we can see the results for all experiments.

Second, we change the location of the delamination and consider a woven glass-epoxy beam (180x10x1.5mm) where the delamination is 10mm length between layers 2 and 3 and it is located at 30mm from the left side. Results are shown in Figure 237.

Third, we increase the delamination size and consider a woven glass-epoxy beam (180x10x1.5mm) where the delamination is 15mm length between layers 3 and 4 and it is located at 30mm from the left side. Results are shown in Figure 238.

Fourth, we modify the delamination location and consider a woven glass-epoxy beam (180x10x1.5mm) where the delamination is 10mm length between layers 3 and 4 and it is located at 25mm from the left side. Results are shown in Figure 239.

Fifth, we modify the delamination location and consider a woven glass-epoxy beam (180x10x1.5mm) where the delamination is 10mm length between layers 3 and 4 and it is located at 60mm from the left side (delamination is under the PWAS). Results are shown in Figure 240.
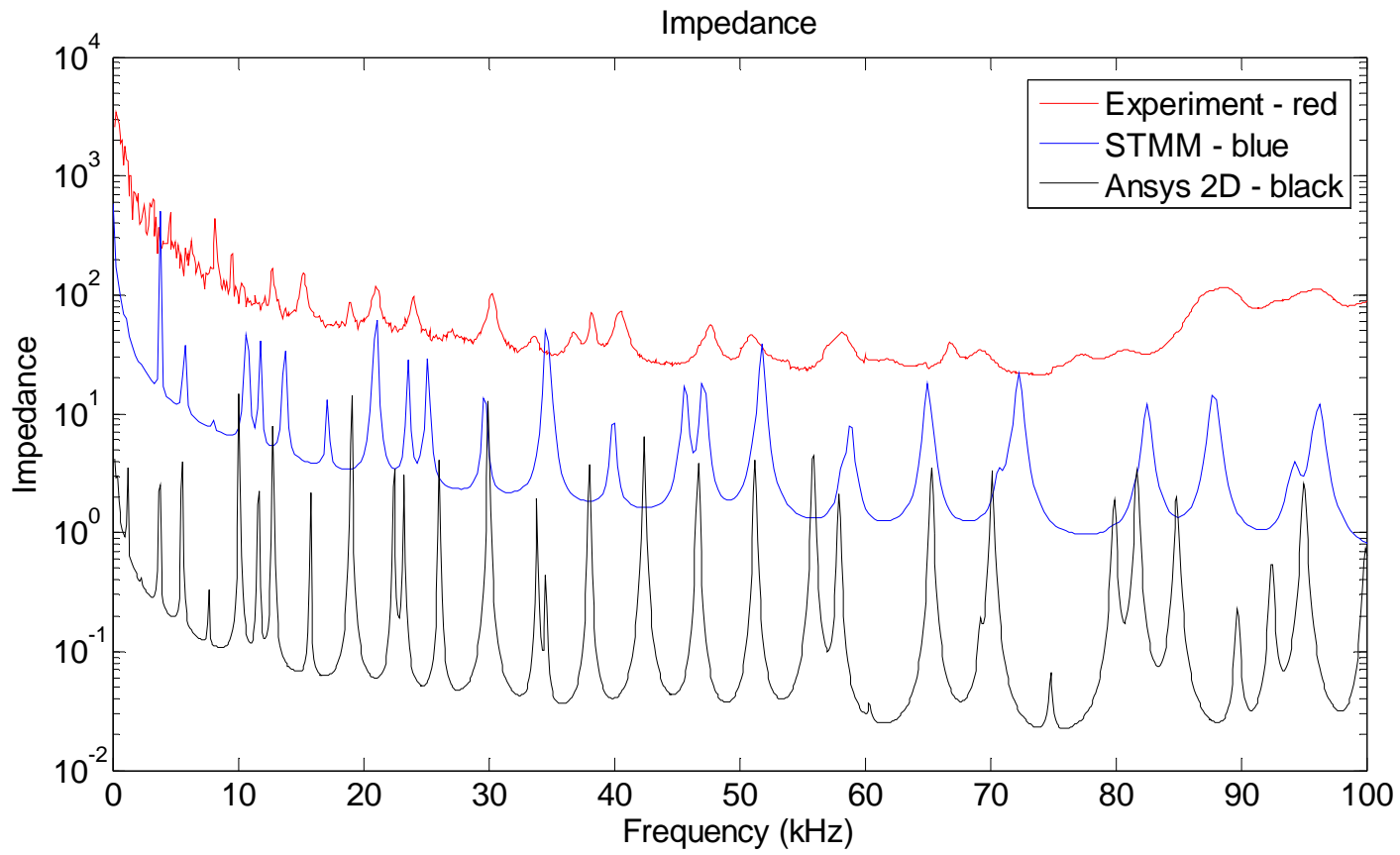
*Figure 235: Woven Glass-Epoxy: PWAS=60mm - pristine*
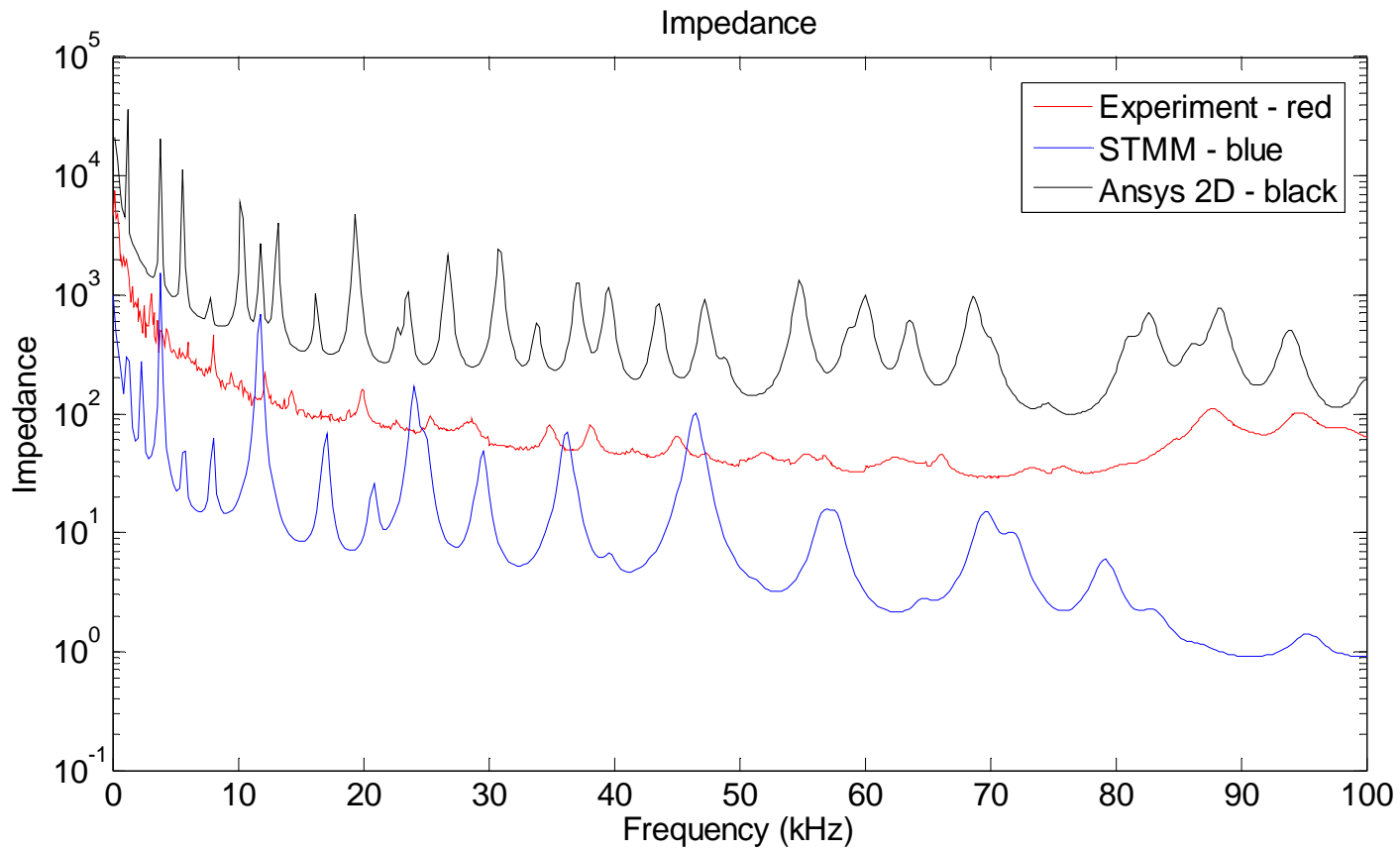
*Figure 236: Woven Glass-Epoxy: PWAS=60mm & D=10 mm Loc =30mm for D (layers 3 & 4)*
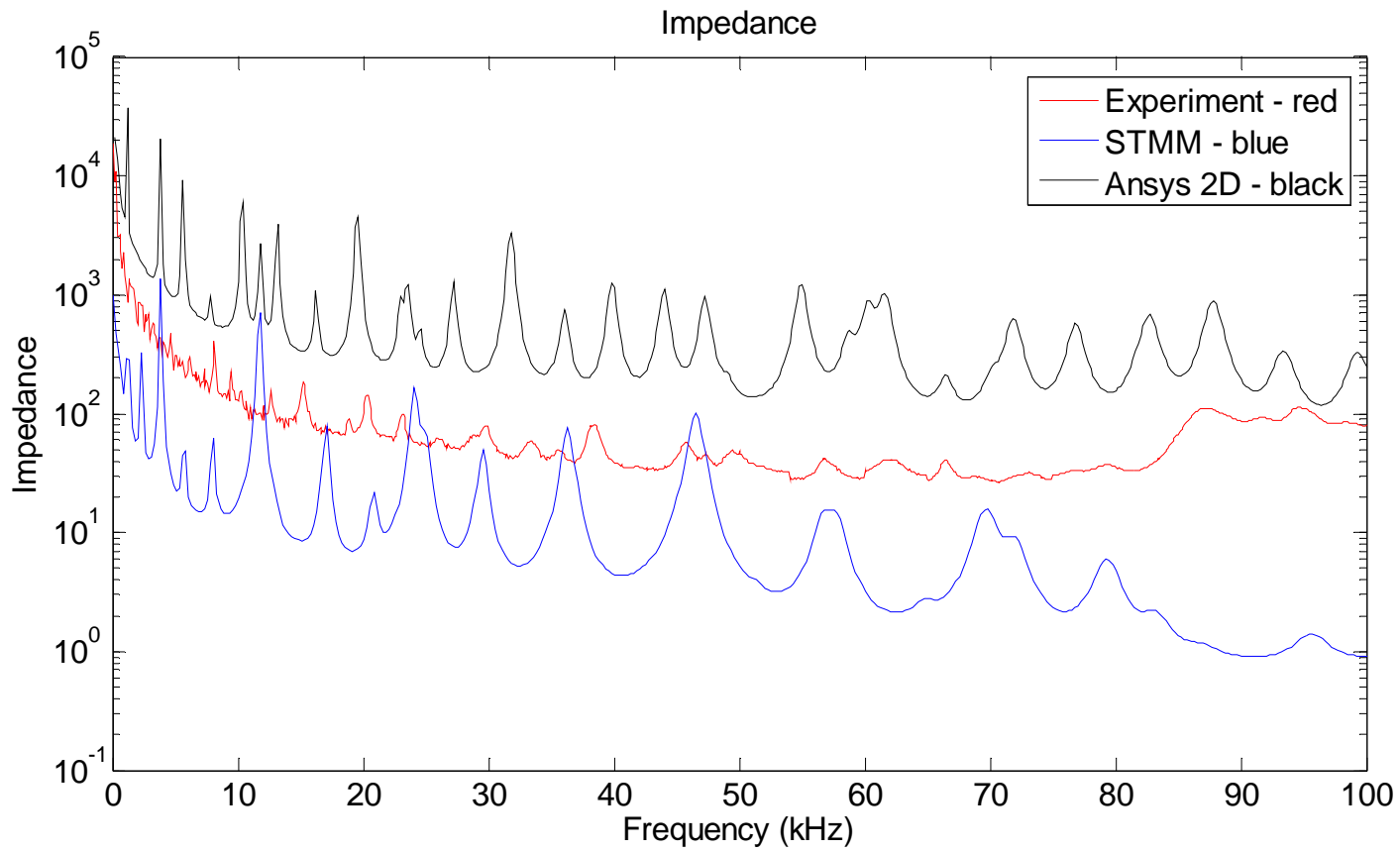
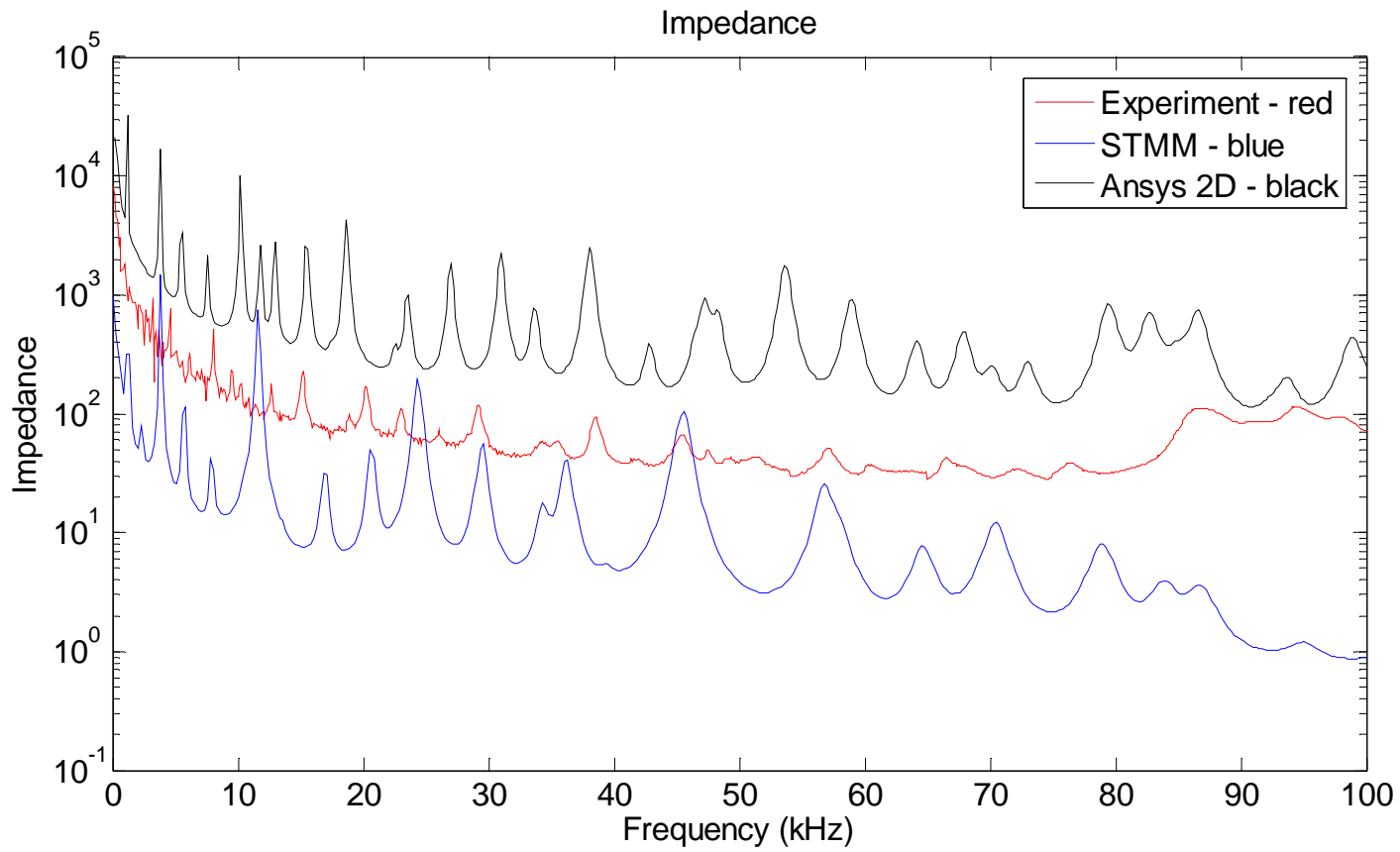**Figure 237: Woven Glass-Epoxy: PWAS=60mm & D=10 mm Loc =30mm for D (layers 2 & 3)**

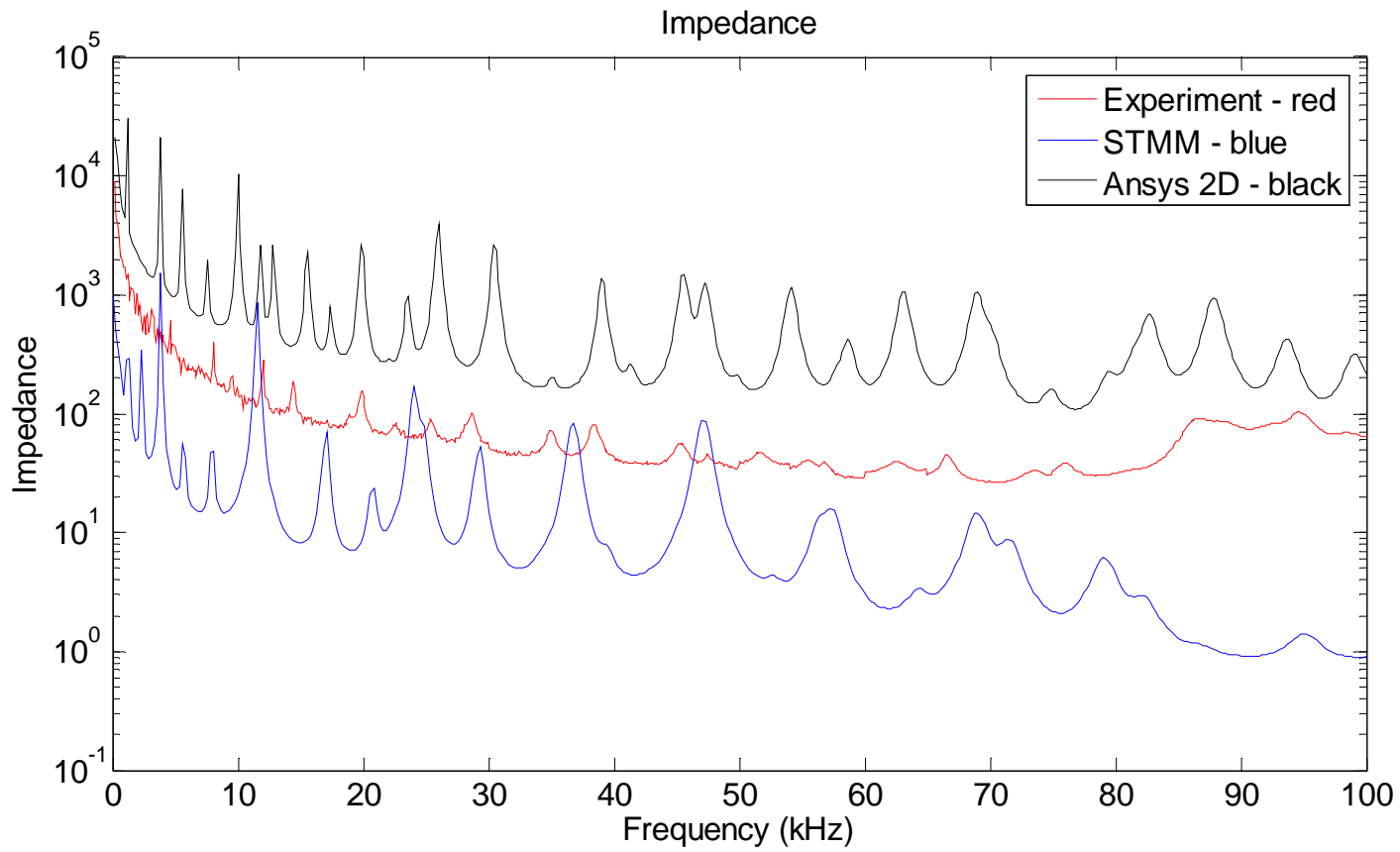*Figure 238: Woven Glass-Epoxy: PWAS=60mm & D=15 mm Loc =30mm for D (layers 3 & 4)*

*Figure 239: Woven Glass-Epoxy: PWAS=60mm & D=15 mm Loc =25mm for D (layers 3 & 4)*
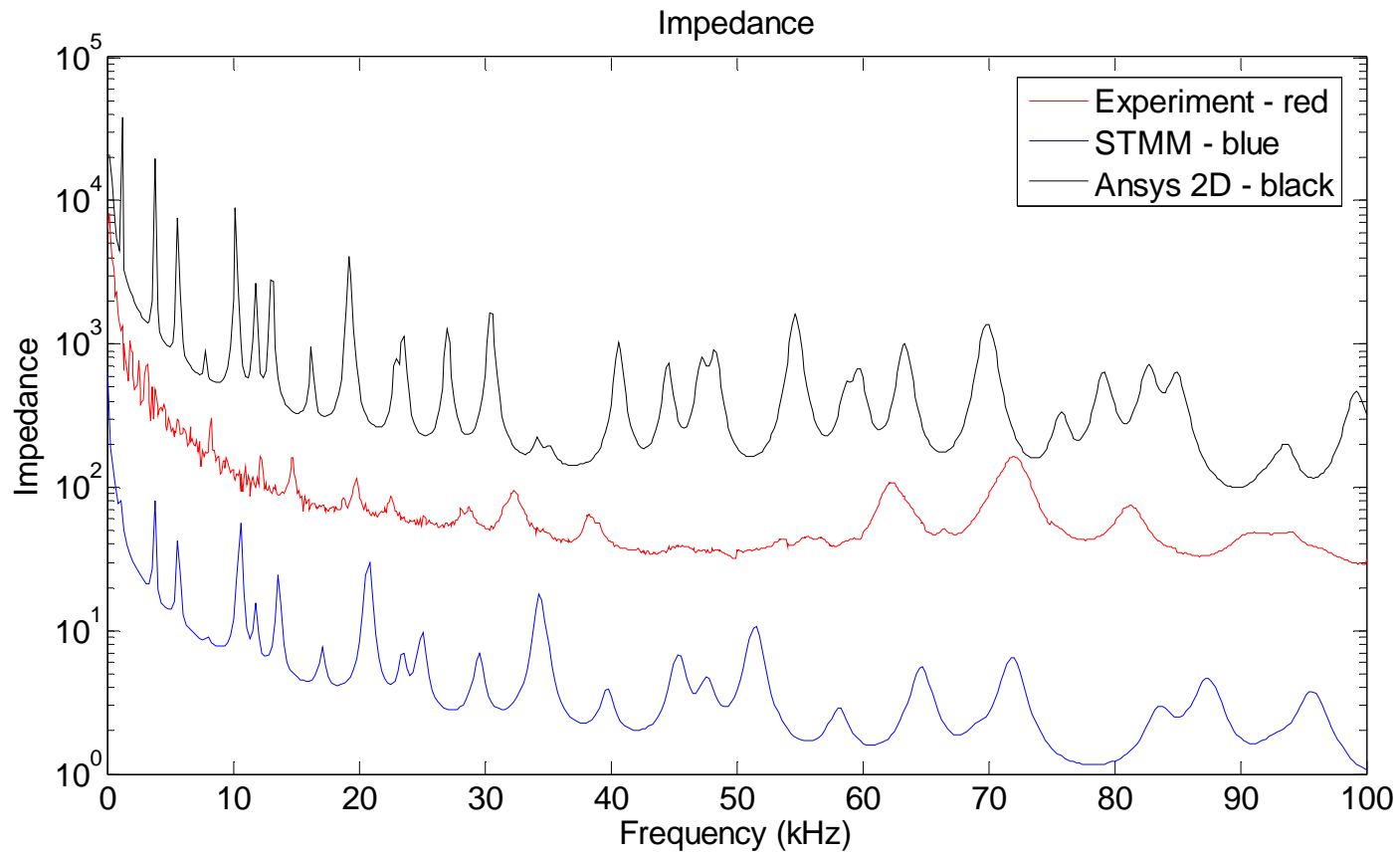
*Figure 240: Woven Glass-Epoxy: PWAS=60mm & D=15 mm Loc =60mm for D (layers 3 & 4)*

## *12.3* CASE3: T300/5208 QUASI-ISOTROPIC COMPOSITE

Figure 241 shows all five configurations under study for T300/5208 quasi-isotropic composite. We use two methods (STMM and Experiment) to look for the resonance frequencies and to measure the impedance for delamination cases. Figure 242 shows the impedance spectrum and the resonance peaks for pristine case.
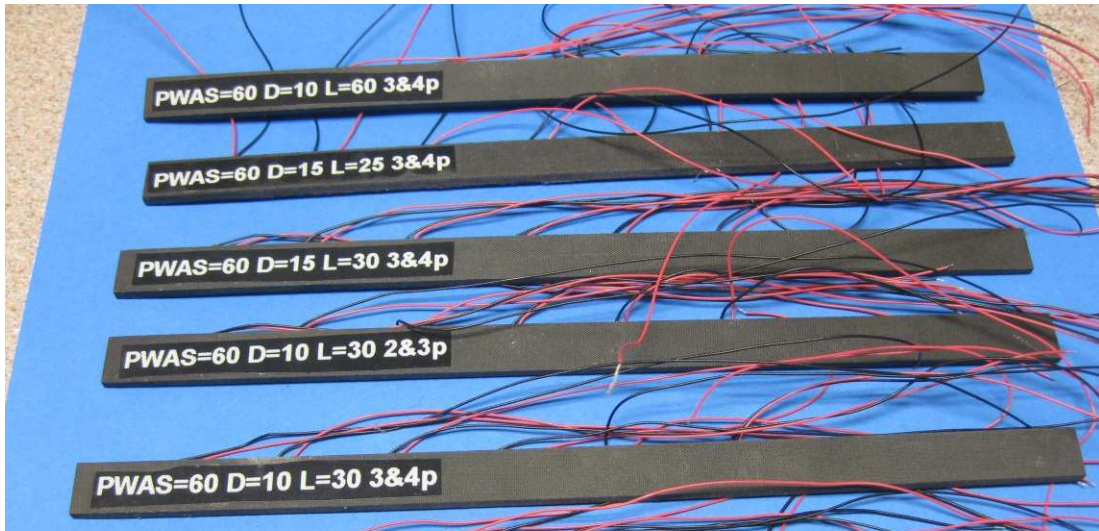


*Figure 241: T300/5208 Quasi-Isotropic: 5 Configurations*

First, let us consider a T300/5208 quasi-isotropic composite beam (180x10x1.5mm) where the delamination is 10mm length between layers 3 and 4and it is located at 30mm from the left side. The PWAS is bounded at 60 mm from the left side. In Figure 243, we can see the results for all experiments.

Second, we change the location of the delamination and consider a T300/5208 quasi-isotropic composite beam (180x10x1.5mm) where the delamination is 10mm length between layers 2 and 3 and it is located at 30mm from the left side. Results are shown in Figure 244.

Third, we increase the delamination size and consider a T300/5208 quasi-isotropic composite beam (180x10x1.5mm) where the delamination is 15mm length

between layers 3 and 4 and it is located at 30mm from the left side. Results are shown in Figure 245.

Fourth, we modify the delamination location and consider a T300/5208 quasi-isotropic composite beam (180x10x1.5mm) where the delamination is 10mm length between layers 3 and 4 and it is located at 25mm from the left side. Results are shown in Figure 246.

Fifth, we modify the delamination location and consider a T300/5208 quasi-isotropic composite beam (180x10x1.5mm) where the delamination is 10mm length between layers 3 and 4 and it is located at 60mm from the left side (delamination is under the PWAS). Results are shown in Figure 247.
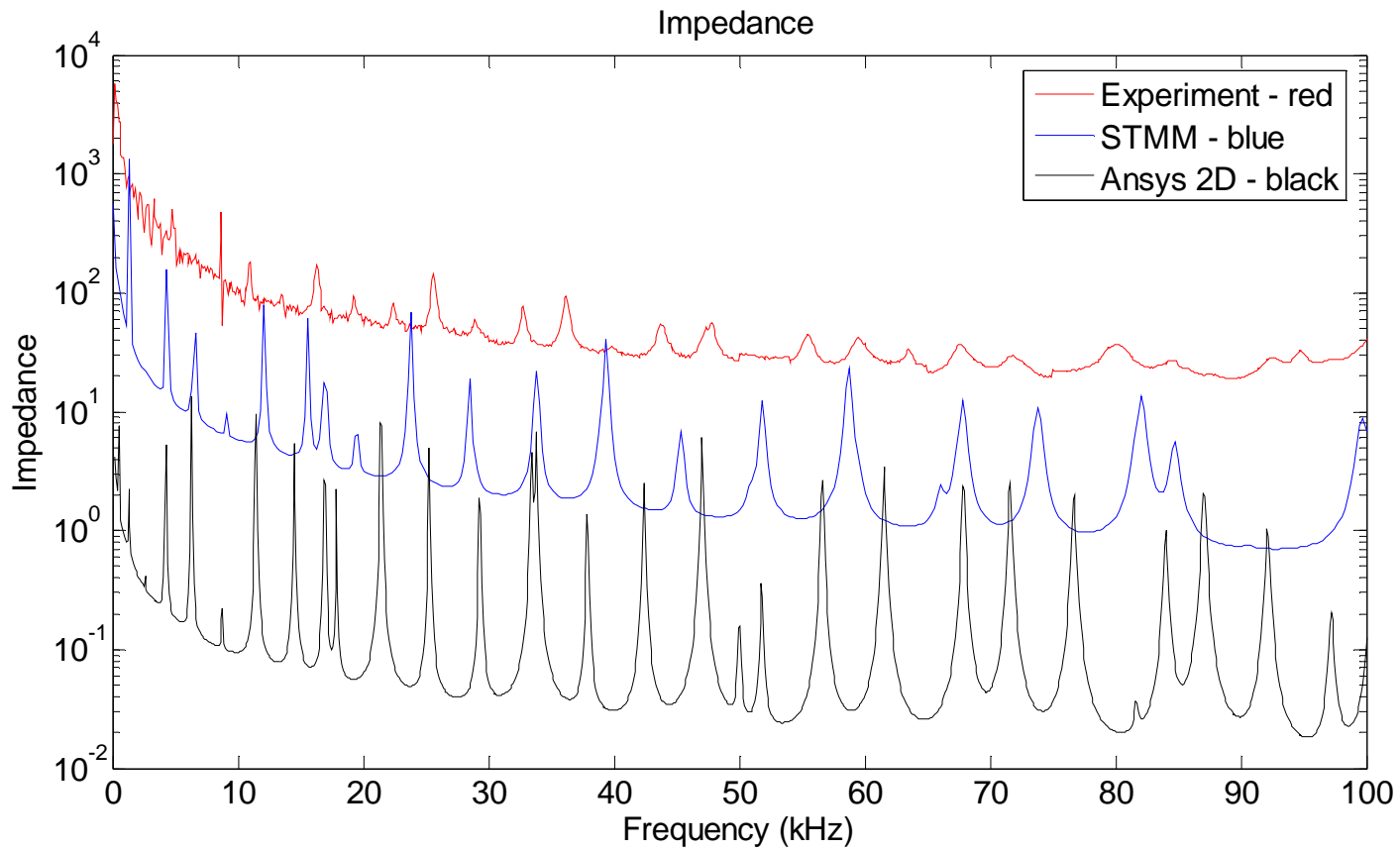
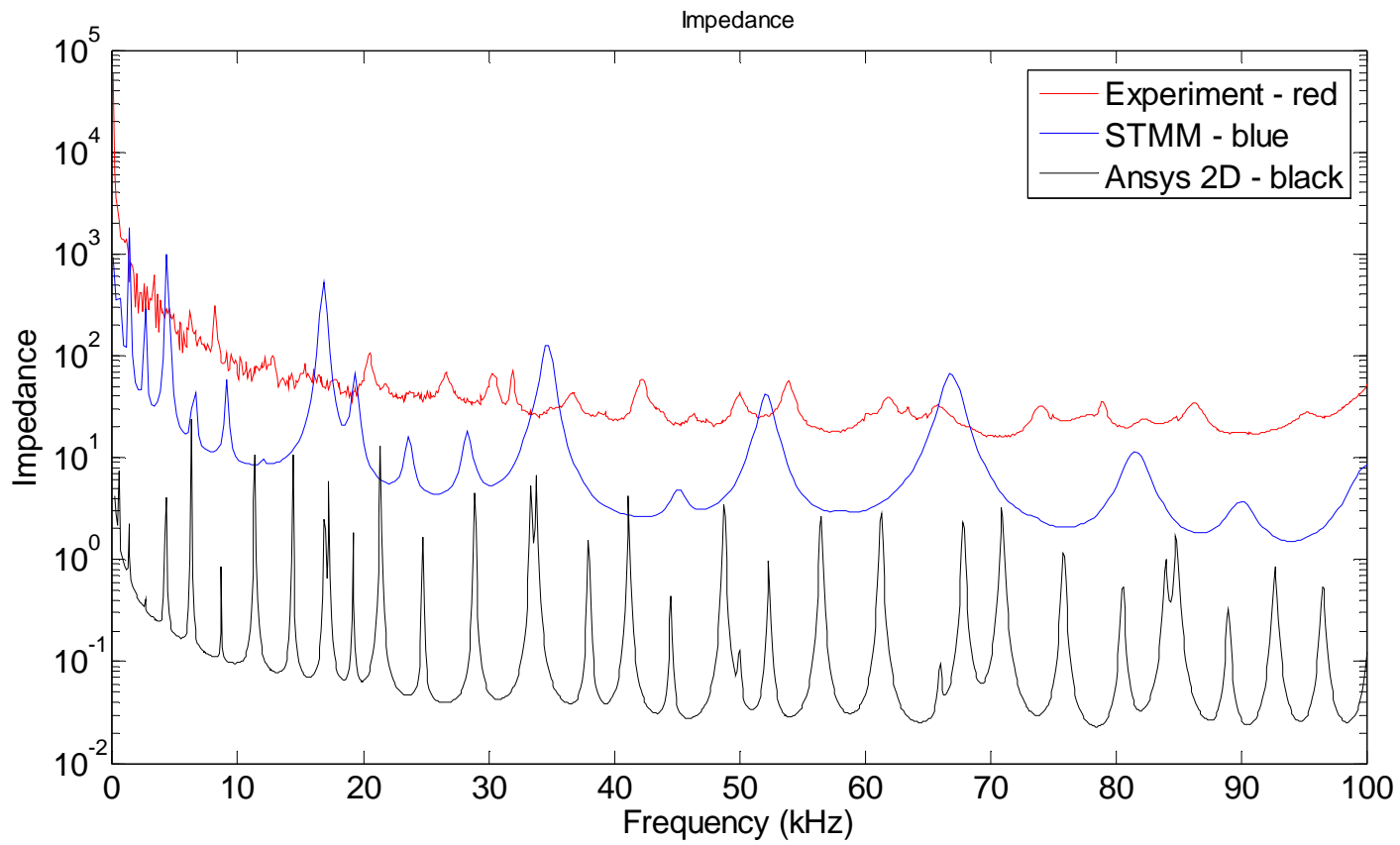*Figure 242: T300/5208 Quasi-Isotropic: PWAS=60mm - pristine*

***Figure 243: T300/5208 Quasi-Isotropic: PWAS=60mm &
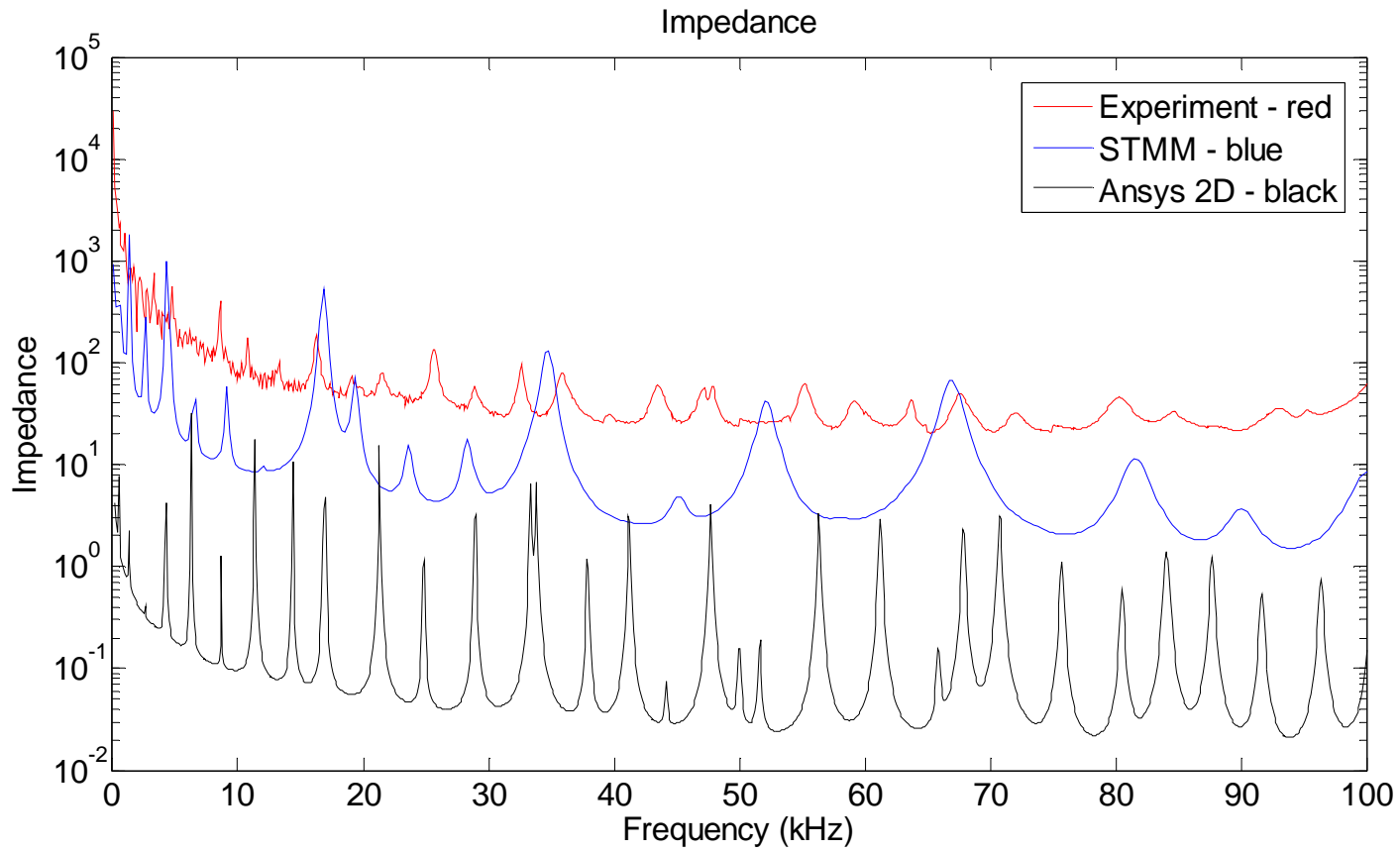D=10 mm Loc =30mm for D (layers 3 & 4)***

***Figure 244: T300/5208 Quasi-Isotropic: PWAS=60mm &
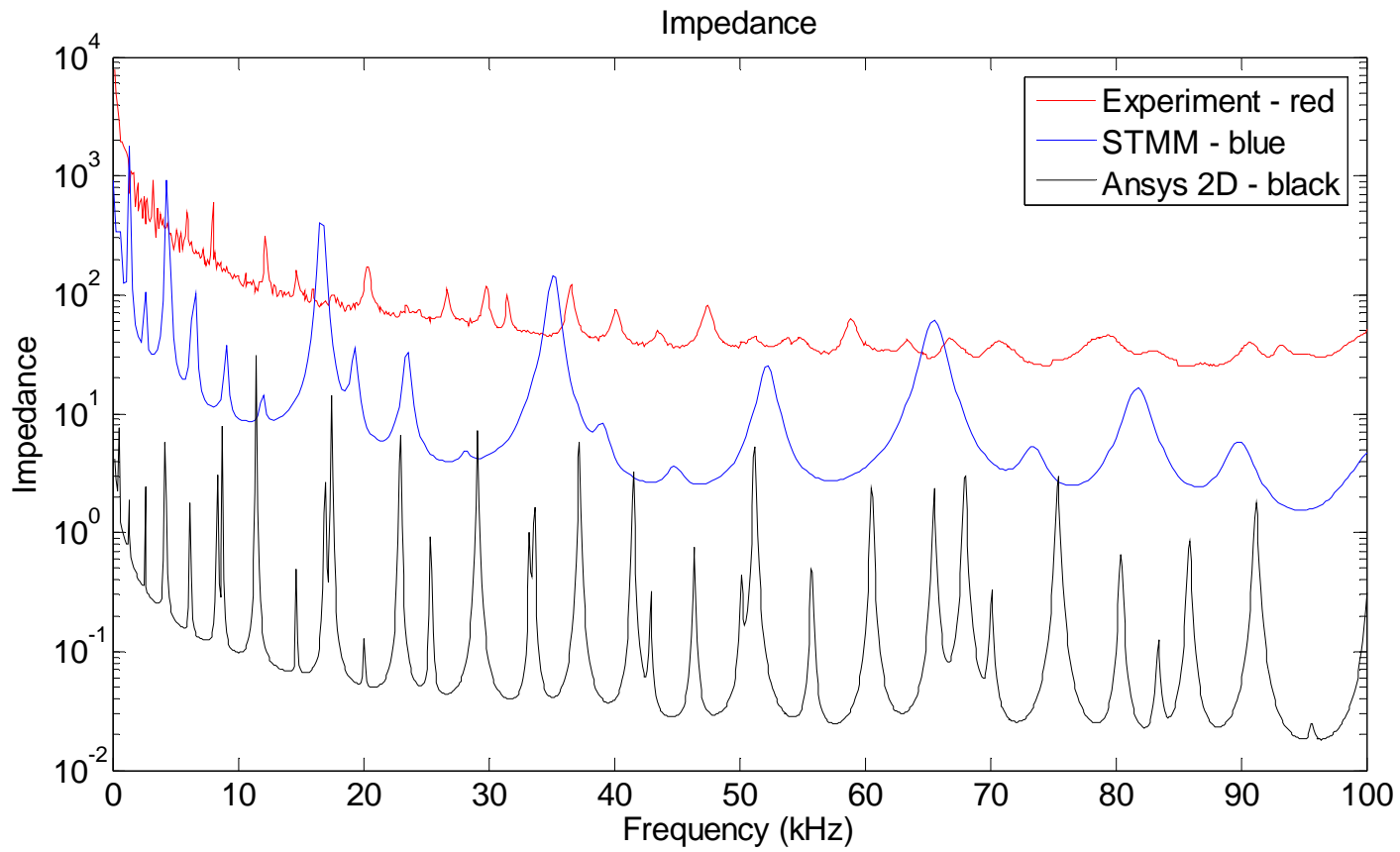D=10 mm Loc =30mm for D (layers 2 & 3)***

**Figure 245: T300/5208 Quasi-Isotropic: PWAS=60mm &**
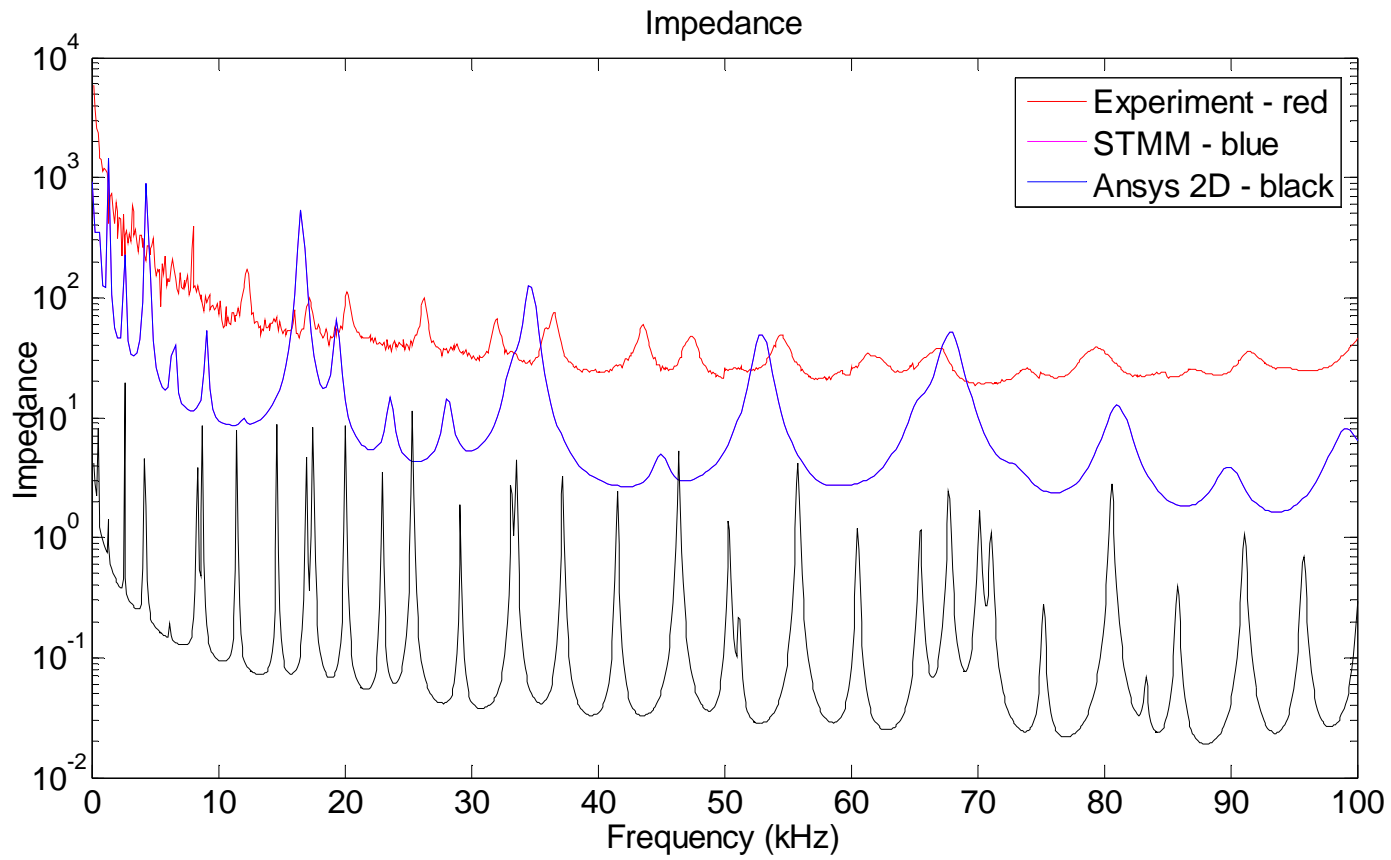**D=15 mm Loc =30mm for D (layers 3 & 4)**

**Figure 246: T300/5208 Quasi-Isotropic: PWAS=60mm &
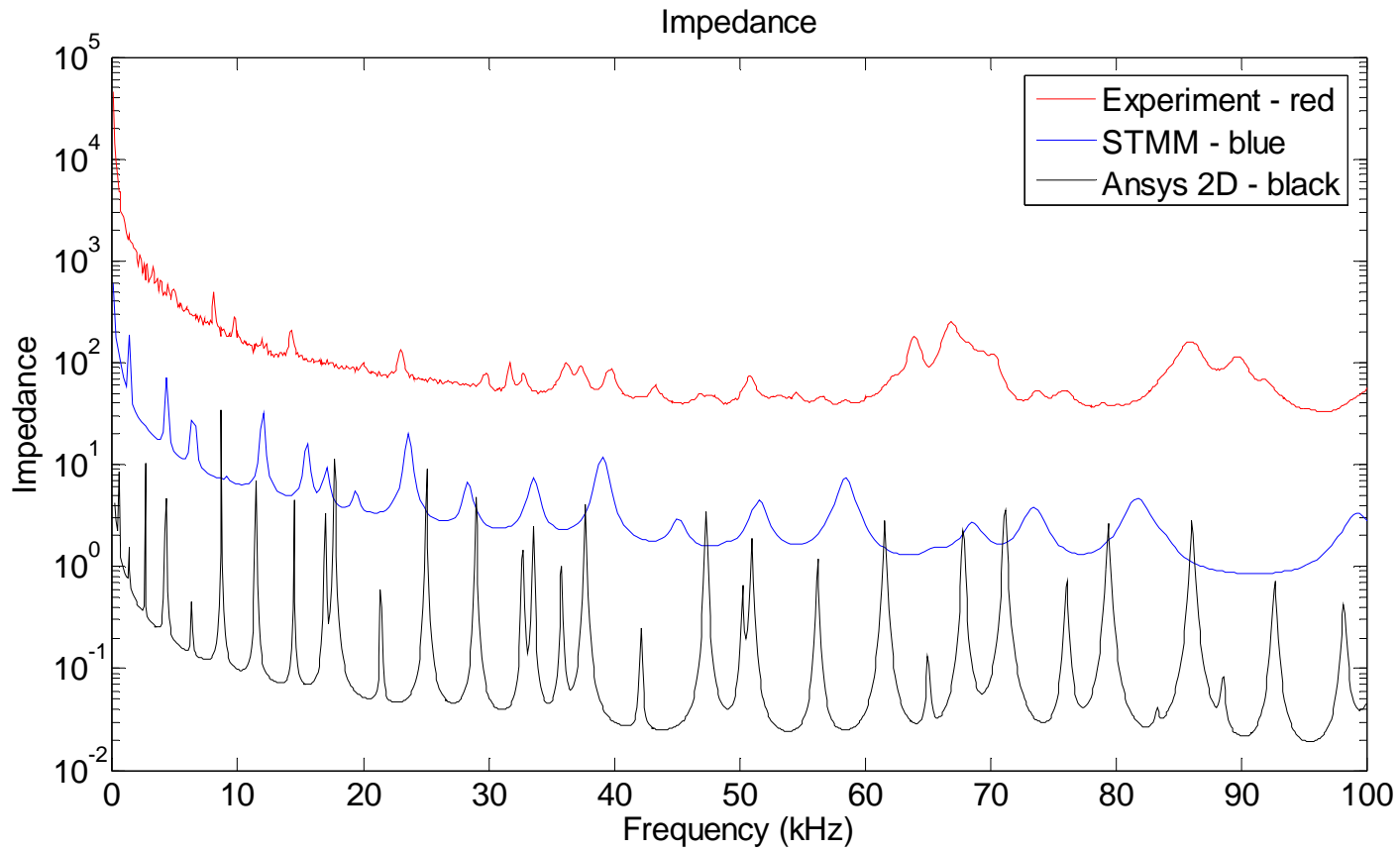D=15 mm Loc =25mm for D (layers 3 & 4)**

*Figure 247: T300/5208 Quasi-Isotropic: PWAS=60mm &*
*D=15 mm Loc =60mm for D (layers 3 & 4)*

## *12.4* SENSITIVITY OF STMM TO DELAMINATION SIZE AND LOCATION

As can be seen from all cases described above, the STMM method gives a good agreement with the experiments. The range 0-30 kHz gives a reasonably good correlation between all the methods. The range 30-100 kHz shows some more differences. This aspect was also observed and discussed in Section 11.4.

Now, let us look at the sensitivity of the STMM regarding delamination. By overlapping the pristine case with the other five delamination cases, described in this section, as shown in Figure 248, Figure 249 and Figure 250 , we have a clearer view about STMM sensitivity for the unidirectional CFRP, woven glass epoxy and T300/5308 quasi-isotropic materials.

STMM sensitivity:

1. Presence of the delamination can be seen as a shift in the impedance and a change in the amplitude

2. By increasing the side of the delamination, the impedance shift and the change in amplitude become very clear, leading to new peaks (new resonance frequencies)

3. The location of the delamination seems to be very important, resulting in new peaks

4. PWAS reads different resonance frequencies depending on its location.

5. Delamination location between layers seems to have some effect, but not so strong when compared to all the other factors described.

It is very important to notice the sensitivity of the method to the dimensions of the beam, the location of the sensor and the delamination. Even a small chance in the location of the PWAS will produce a change in the impedance respond.
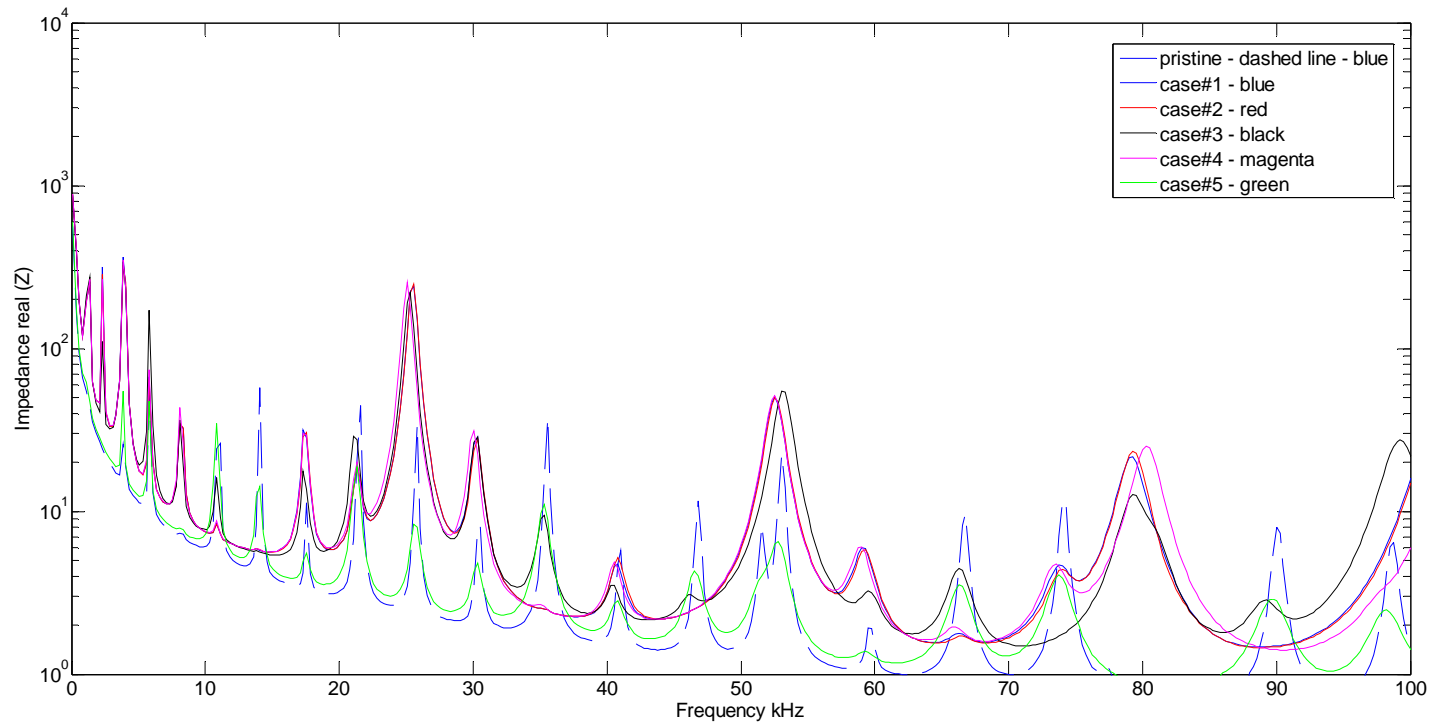
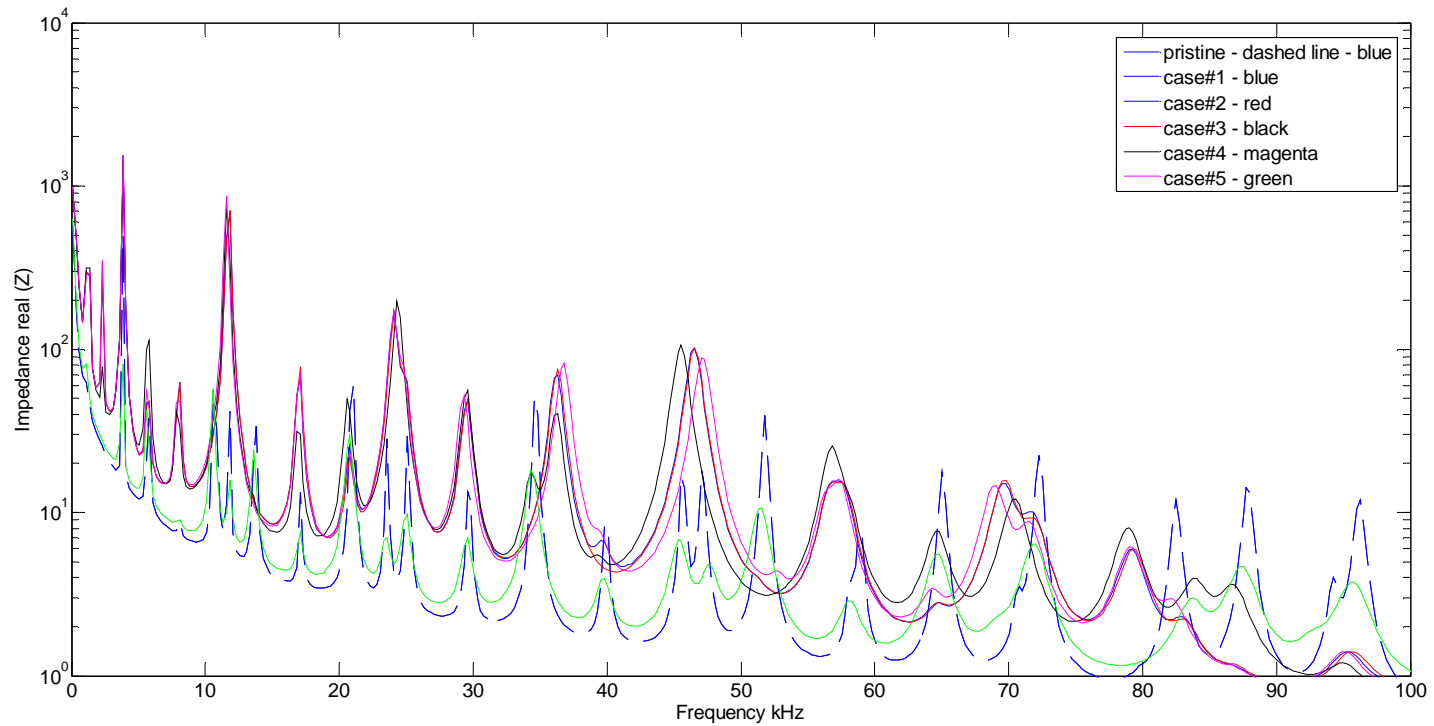*Figure 248: Unidirectional CFRP: STMM Sensitivity*

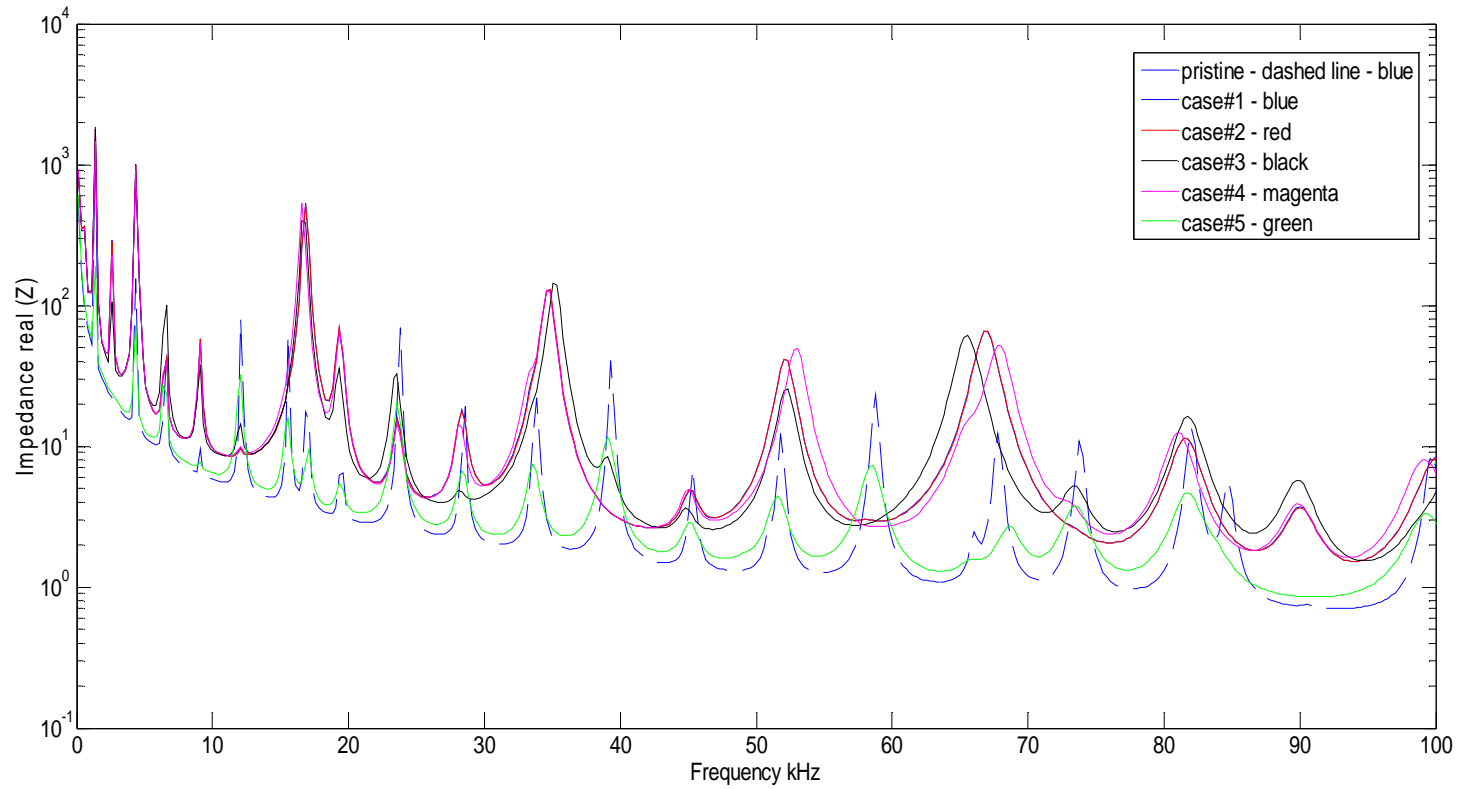*Figure 249: Woven Glass-Epoxy : STMM Sensitivity*

*Figure 250: T300/5208 Quasi-Isotropic: STMM Sensitivity*

# 13.    TASK #5: DEVELOPMENT OF A NOVEL ACOUSTO-ULTRASONIC SENSOR: THE FBG RING SENSOR

The aim of this task is to develop a novel acousto-ultrasonic sensor that can detect the ultrasonic waves from acoustic emission $AE$ events using optical FBG sensing combined with mechanical resonance amplification principles.

The method consists of a sensor that can detect the ultrasonic out of plane motion with preference for a certain frequency ($f_{cr} = 300kHz$). The mechanical amplification would produce a strain of around 5000 micro-strain in the FBG.

In order to design such a sensor, we proceed to solve using two different methods: 1) analytical methods (2-D) and 2) numerical methods (FEM).

## 13.1    FIRST CONCEPT: FBG D-SHAPE SENSOR

### 13.1.1 ANALYTICAL APPROACH

As per Figure 251, we consider the 2-D approach. In order to proceed with this method, we make the following three assumptions:

a)  disregard the undulations of the two arms

b)  consider the FBG fiber attached to a spring with constant $K$

c)  small displacement approximation: $\Delta X, \Delta Y$ much smaller than $L$ and $h$.
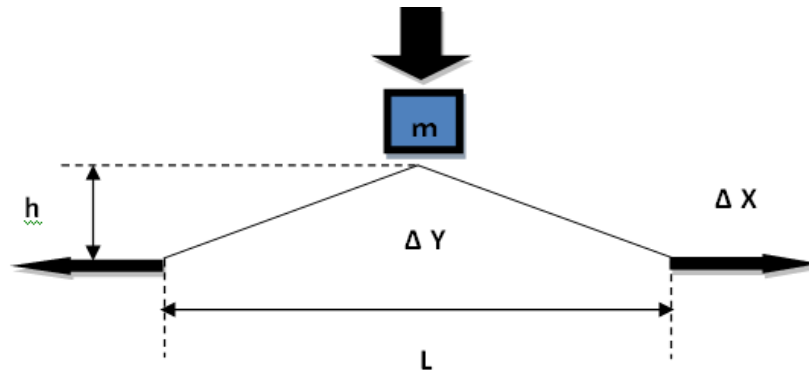
318

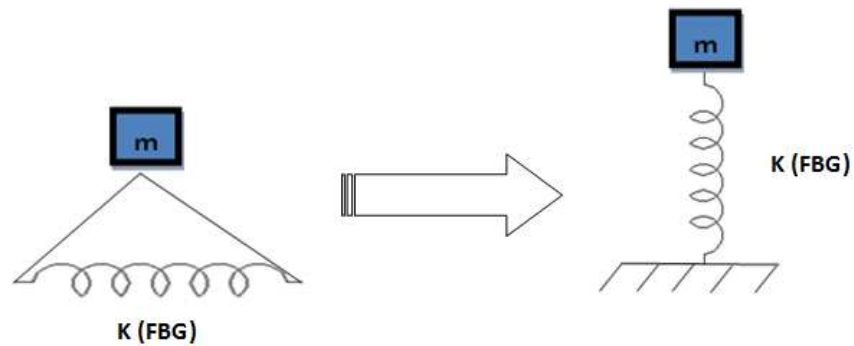*Figure 251: Schematic representation of the sensor concept*



*Figure 252: Simplification of the sensor concept*

Where:

$K$ is the elastic constant of the spring to which the FBG optical sensing element is attached

$m$ is the effective mass of the sensor

$\Delta X$ is the displacement on the $X$ axis

$\Delta Y$ is the displacement on the $Y$ axis

$h$ is the height of the sensor

$L$ is the length of the sensor

We choose the design values for $h, m$ and $L$ such that the system can reach 300

kHz resonance subject to maximizing the ratio $r = \dfrac{\Delta X}{\Delta Y}$ where $r > 1$. In order to build a

319

2-D model and to simplify the approach, we disregard the vibrational undulations of the two arms (i.e. we assume them to be massless and infinitely stiff). By building the free-body diagram (FBD) and kinematics, we find the equation of motion in the form of 1 degree of freedom.

$$\ddot{y} - \frac{k}{m} \cdot y = 0$$

(13.1)

In order to calculate the optimum dimensions for the sensor to reach 300 kHz, we looked at the connection between the displacement in the $x$ and y directions and we obtain:

$$\Delta Y = \frac{1}{2} \cdot \frac{\frac{L}{2}}{h} \cdot \Delta X = \frac{L}{h} \cdot \Delta X$$

(13.2)

Then we obtain an equation that contains all three adjustable parameters. By optimizing the configuration of the three parameters, $L, h$ and $m$, we seek to reach 300 kHz for the frequency as follows:

$$E \cdot A = \pi^2 \cdot m \cdot f^2 \cdot \left[ \frac{(L/2)^3}{h^2} \right]$$

(13.3)

Using the OptimTool in MATLAB, we were able to come up with an optimum range for the parameters. We find that m should be between 0.014 - 0.056 kg, $L$ should be 0.02 m and $h$ should be between 0.05 – 0.10m. We choose the minimum allowable configuration: $m$ = 0.014 kg, $L$ = 0.02 m and $h$ = 0.05 m in order to obtain 300 kHz for the frequency.

### 13.1.2 NUMERICAL APPROACH (FEM)

For this approach, we use the commercial FEM software ANSYS Workbench and more precisely the analysis system Modal. We model a 3-D sensor using the dimensions predicted by the analytical method dimensions. We apply the boundary conditions and calculate the natural frequencies as per Figure 253.
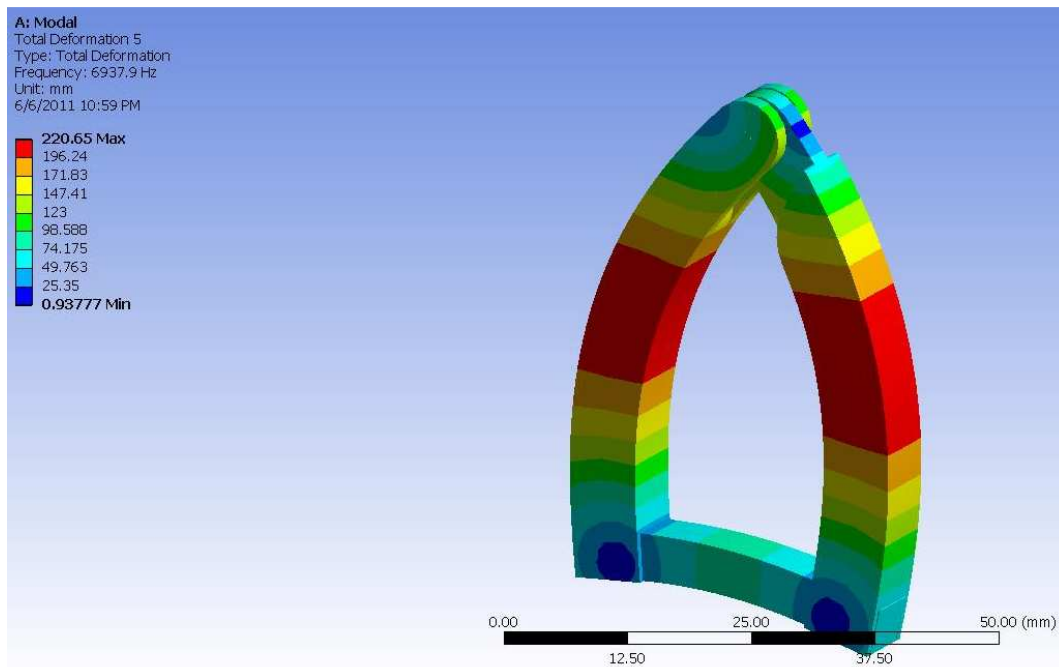


*Figure 253: D-shape sensor where the straight part (FBG fiber) vibrates in flexure*

Material: SS 300 series;

Geometry: L = 0.020 m; H = 0.050 m; FBG (cross-section) =0.006 X 0.006 m.

Frequency:

Analytical: 300 kHz;

FEM: 6.93 kHz;

Vibration mode for FBG: Flexural

We obtain 6.93 kHz, instead of the 300 kHz predicted analytically. This is a big difference, so we try different adjustments in order to reach 300 kHz (Figure 254 and

Figure 255). First, we try to increase the depth of the side arms in order to stop the flexure as per Figure 254.
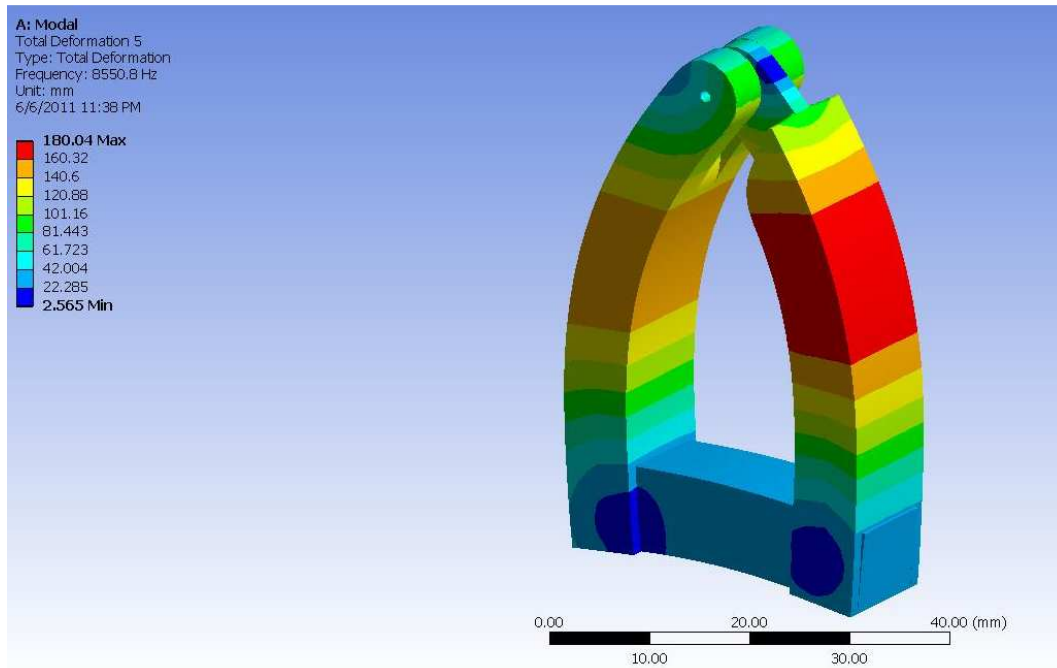


*Figure 254: D-shape when we increase the depth to stop the flexure*

Material: SS 300 series;

Geometry: L = 0.020 m; H = 0.050 m; FBG (cross-section) =0.010 X 0.010 m.

Frequency:

Analytical: 325 kHz;

FEM: 8.55 kHz;

Vibration mode for FBG: Flexural

Then by increasing the depth even further (Figure 255), we find that the frequency remains at almost the same level when using FEM.
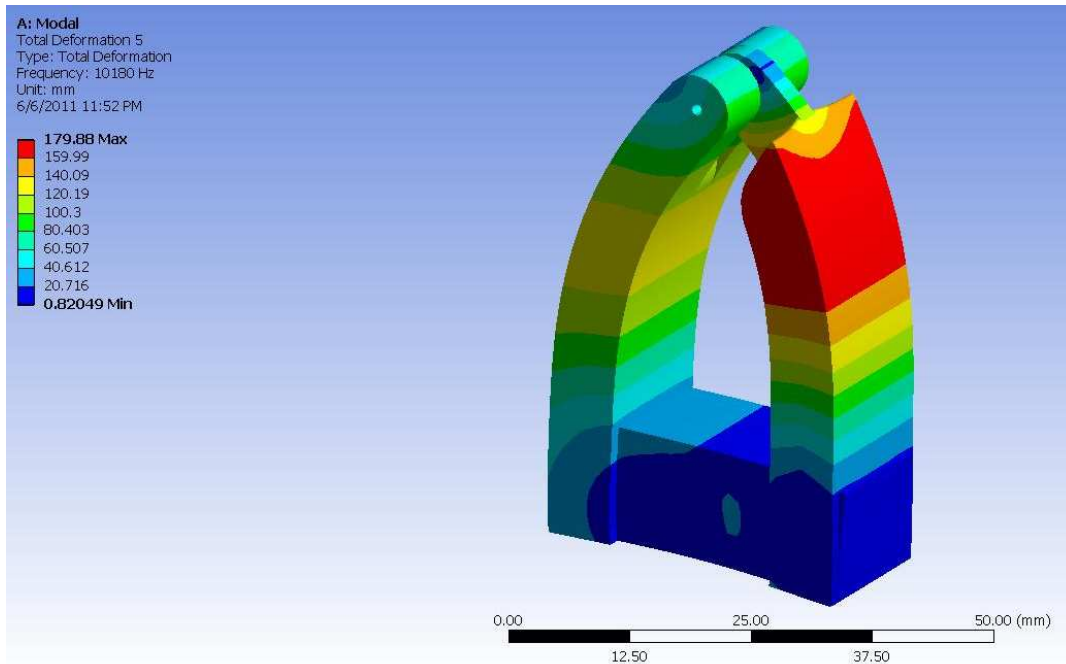
*Figure 255: D-shape when we increase the depth to stop the flexure but ended up with undulations of the wall*

Material: SS 300 series;

Geometry: L = 0.020 m; H = 0.050 m; FBG (cross-section) =0.0127 X 0.0127 m.

Frequency:

Analytical: 350 kHz;

FEM: 10.18 kHz;

Vibration mode for FBG: Flexural

### 13.1.3 FIRST CONCEPT CONCLUSIONS

As per the numerical method FEM results presented above, we conclude that the simplifying of assumptions in the analytical approach is not correct. More precisely, we are referring here to assumption a) which states that we disregard the undulations of the two arms. This assumption was made in order to simplify the calculations; however

323

the two arms will add their own deflections which can be significant and thus reduce the natural frequency by more than an order of magnitude.

Besides using both the analytical and FEM methods, it is always the case that the flexural resonance occurs first and the axial resonance occurs second for the beams. However, in the present case, the first resonant frequency needs to be 300 kHz and should be axial for FBG to work properly.

Considering these aspects we conclude that the D-shape sensor approach is not suitable to reach an axial resonance of 300 kHz. Based on these results, we look at different sensor shapes that are able to reach 300 kHz and we decide to study rings. The modes of vibration of the rings can be of four different types as follows:

a) Extensional  which are longitudinal elongations and contractions of the ring along its own axis

b) Torsional  when ring twists around its own axis

c) In-plane flexural which are inextensional vibrations in the plane of the ring

d) Out-of-plane flexural which are inextensional vibrations out of the plane of the ring.

From all these modes, only the flexural are of practical importance because the natural frequencies of the first two modes, extensional and respectively torsional, are much higher than the fundamental natural frequencies of the flexural modes.

Given that the D-shape did not fit our purpose for the 300 kHz frequency and since theoretically the ring shape seems promising, we redo the analysis using both approaches, analytical and numerical, and a ring shape for the sensor.

## *13.2* SECOND CONCEPT: FBG RING SENSOR

In order to design such a sensor, we proceed as before to solve using two different methods: 1) analytical methods (2-D) and 2) numerical methods (FEM).

### 13.2.1 ANALYTICAL APPROACH

We calculate the mode shape for a ring sensor (Figure 256) following Blevins (1979) approximation formula:

$$f_i = \frac{i\left(i^2 - 1\right)}{\sqrt{2\pi R^2 \left(i^2 + 1\right)}} \sqrt{\frac{EI}{m}}$$

(13.4)

Where: $i$ is the mode number

$R$ is the radius of the midline of the ring

$E$ is the modulus of elasticity

$I$ is the moments of inertia

$m$ is the mass per unit length of the ring

$f_i$ represents the natural frequencies

Running this formula with $ID$ = 0.058 m, $OD$ = 0.072 m and $H$ = 0.006 m, we obtain 109 kHz for the first mode. We also run the FEM with these dimensions to see from the beginning what is the difference between the two methods. We find that the analytical results given an approximately 25% greater frequency FEM. Knowing this aspect, as well the fact that Blevins' formula is an approximation, we proceed the reverse way since we assume the FEM approach would give us more precise solutions than the analytical approach case.
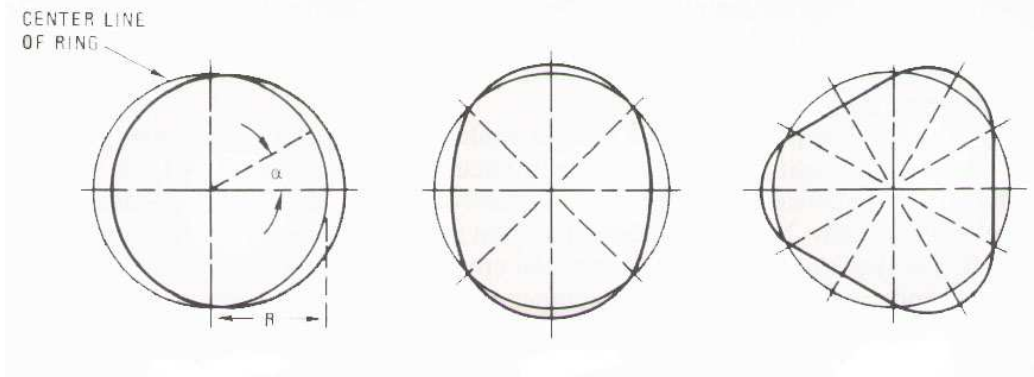
*Figure 256: In-plane flexural modes of the ring, Blevins (1979)*

Using dimensions $ID$ = 0.0016 m; $OD$ = 0.0048 m; $H$ = 0.0032 m and $E$ = 200 GPa and Blevin's formula (13.4), we obtain a flexural frequency of 391.4 kHz and using dimensions $ID$ = 0.0029 m; $OD$ = 0.0087 m; $H$ = 0.0058 m and $E$ = 133 GPa we obtain a flexural frequency of 387.5 kHz.

### 13.2.2 NUMERICAL APPROACH (FEM)

As before, we use the commercial software ANSYS WB (Modal Analysis). We model a 3-D sensor using the analytical method dimensions. We apply the boundary conditions and calculate the natural frequencies as per Figure 257, Figure 258 and Figure 259. Figure 257 shows a thin ring at low frequency and it is found that the FEM results are in accord with the analytical ones but we are not able to reach the 300 kHz that we require for the application. In the next steps we make more changes to dimensions until we reach the desired frequency using SS 300 series material. Figure 258 shows a new shape for the ring which is able to reach 300 KHZ on FEM
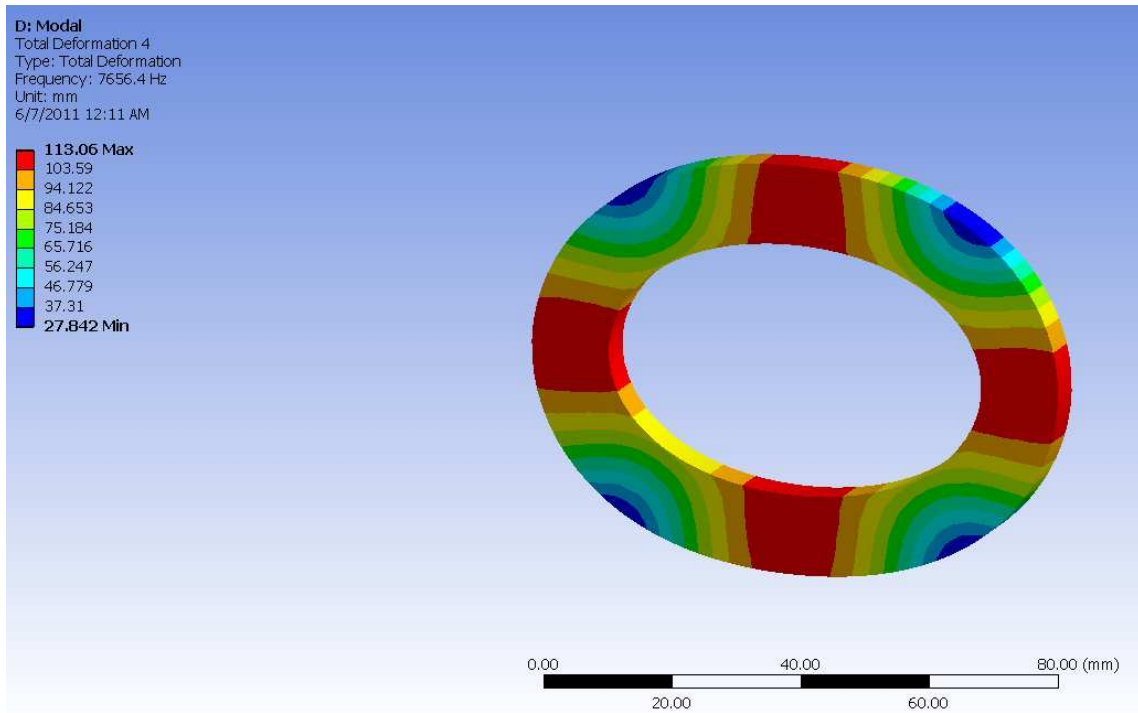
*Figure 257: Thin steel ring - low frequency*

Material: SS 300 series;

Geometry: ID = 0.058 m; OD = 0.072 m; H = 0.006 m.

Frequency:

Analytical: 109 kHz; (Blevins formula)

FEM: 76.56 kHz;
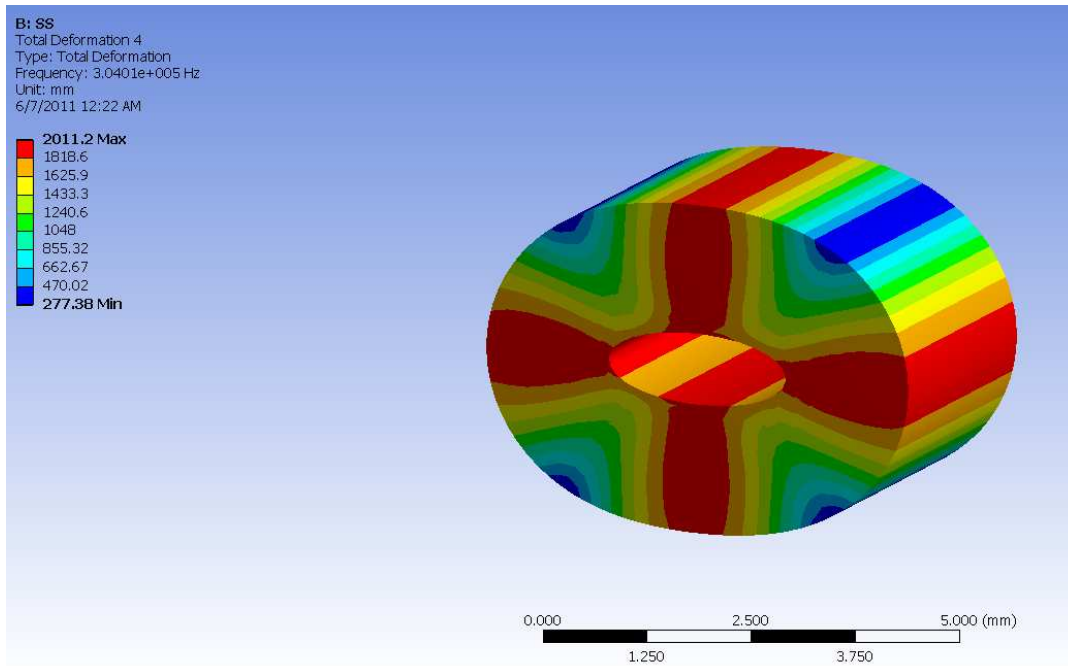
Vibration mode for FBG: Axial

*Figure 258: Thick steel ring with f=304 kHz*

Material: SS 300 series;

Geometry: ID = 0.0016 m; OD = 0.0048 m; H = 0.0032 m.

Frequency:

Analytical: 391.4 kHz; (Blevins formula)

FEM: 304 kHz;

Vibration mode for FBG: Axial

Finally, we are interested in reaching a frequency of 300 kHz by composite material instead of SS material. Due to the material properties of the composites and the fiber orientation in the ring, configuration in Figure 258 is not suitable, so we make further modifications to the ring dimensions. After multiple trials, we o in obtain the configuration in Figure 259, which allows us to reach the desired frequency of 300 kHz.
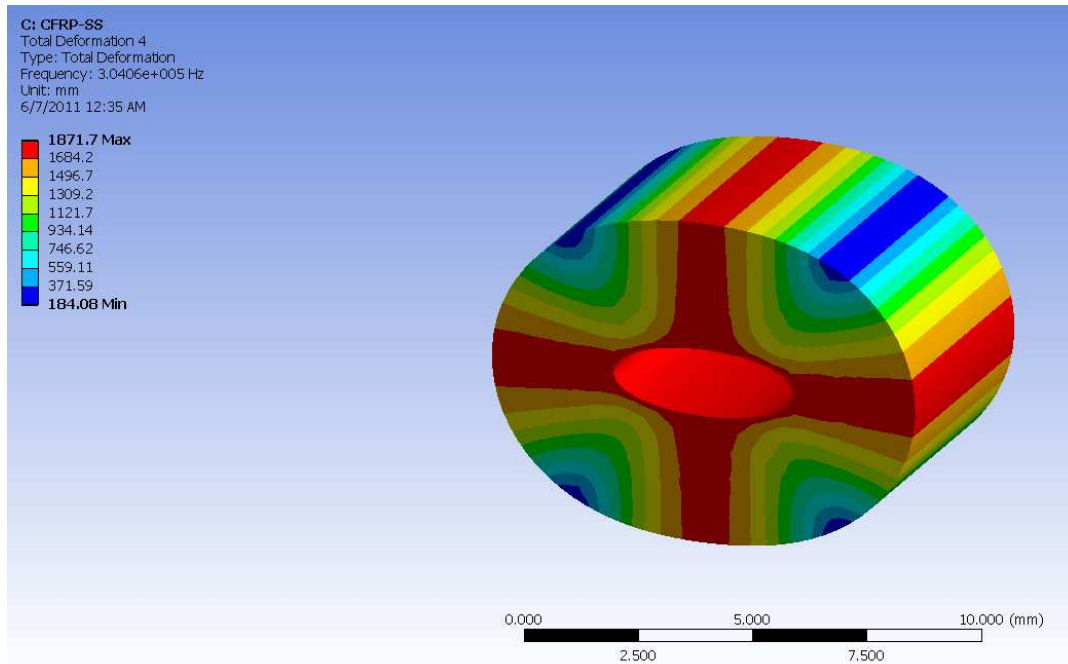
*Figure 259: Thick composite ring with f=304 kHz*

Material: CFRP;

Geometry: ID = 0.0029 m; OD = 0.0087 m; H = 0.0058 m.

Frequency:

Analytical: 387.5 kHz; (Blevins formula)

FEM: 304 kHz;

Vibration mode for FBG: Axial

### 13.2.3 PROOF OF CONCEPT - EXPERIMENTS

Following the mechanical design of the FBG ring sensor, we look for an inexpensive and very fast way to test the concept. The idea behind this is to have a ring-like shape which by excitation can reach the vibration mode around 300 kHz. Conveniently, we found for this purpose a steel hex ¼"-20 nut (Figure 260). The most appropriate way to excite the nut at high frequencies was using a PWAS.
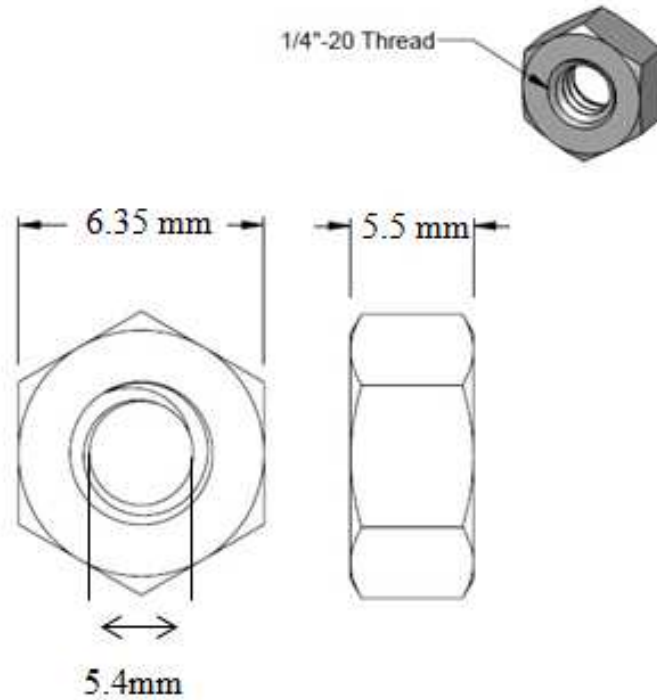
***Figure 260: Steel hex nut - 1/4"-20***

In order to understand better the behavior of the nut under the problem constraints, we run several simulations in ANSYS WB (Figure 261) and we find that the first resonant frequency appears at 89 kHz. We decide this is an appropriate concept and we decide to use it forward. Table 10 shows the relevant resonance frequencies up to 300 kHz.
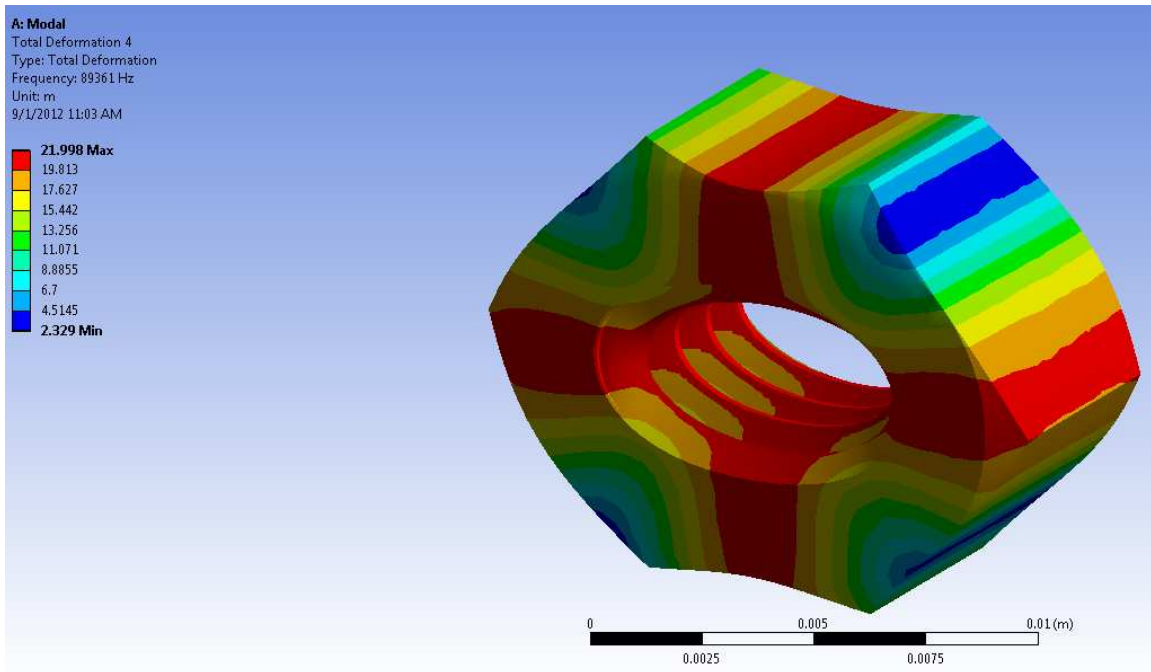
*Figure 261: ANSYS WB - Nut Simulation*

| Nut with thread | | Nut without thread | |
|---|---|---|---|
| ANSYS WB | EMIS Exp. | ANSYS WB | EMIS Exp. |
| 89 kHz | 78 kHz | 72 kHz | 69 kHz |
| 108 kHz | 83 kHz | 157 kHz | 169 kHz |
| 201 kHz | 186 kHz | 177 kHz | 185 kHz |
| 251 kHz | 234 kHz | 243 kHz | 239 kHz |
| 331 kHz | 294 kHz | 311 kHz | 281 kHz |

*Table 10: Resonance frequencies for Nut with/without thread*

### 13.2.3.1 EMIS EXPERIMENTS

We performed electromechanical impedance spectroscopy (EMIS) experiments on the nut specimens, one with thread, and the other with no thread (the thread was simply drilled out).

As part of the experiment, we bound the PWAS to one of the sides of the steel hex nut 1/4"-20 as per the experimental setup in Figure 262
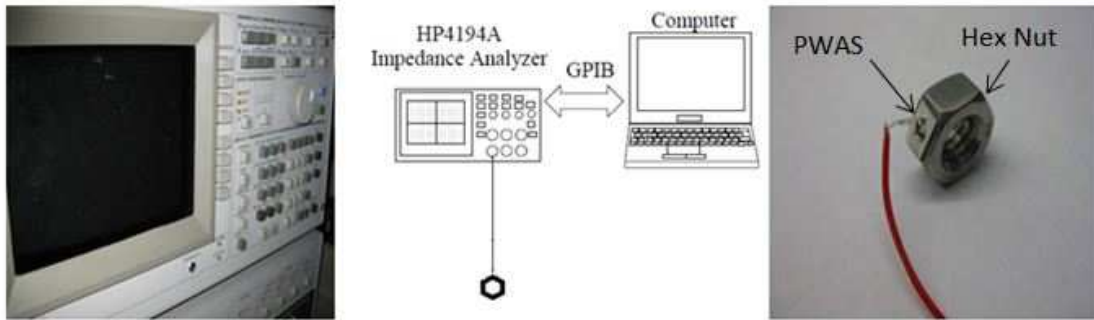
*Figure 262: Experimental Setup*

We bonded a PWAS on one side of the nut, excited the nut at the frequency range between 0 to 350 kHz and we collected the impedance results using a HP Analyzer. The resonant frequencies can be seen electromechanical impedance spectrum (EMIS) shown in Figure 263. The first frequency is around 75 kHz, which is an important step in proving our concept.
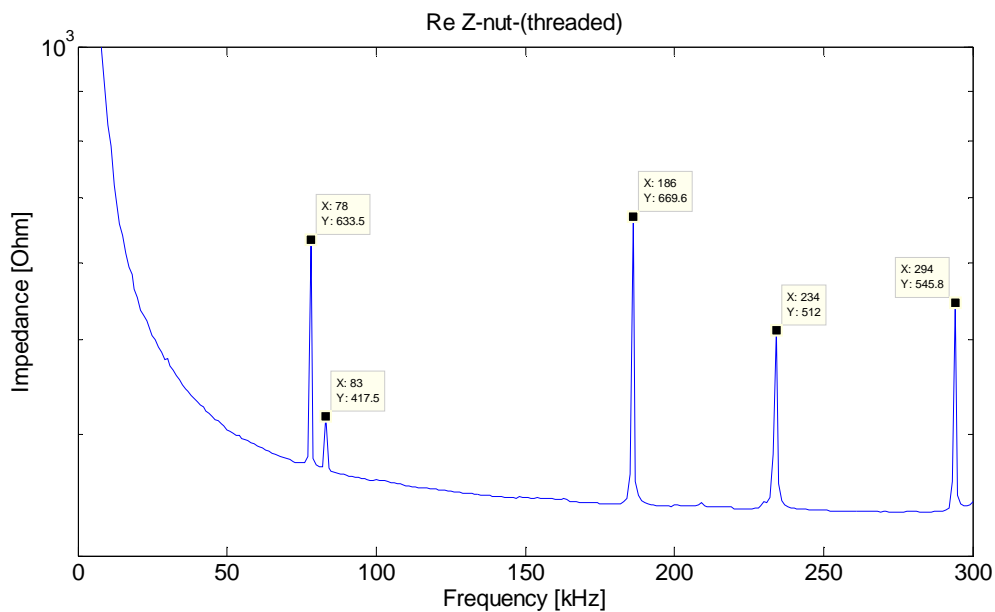


*Figure 263: EMIS of the nut with thread*

In the next step, we took the same nut and we machined the thread to see if we observe a shift in the resonant frequencies. As per Figure 264, the resonant frequency declined to 68 kHz.
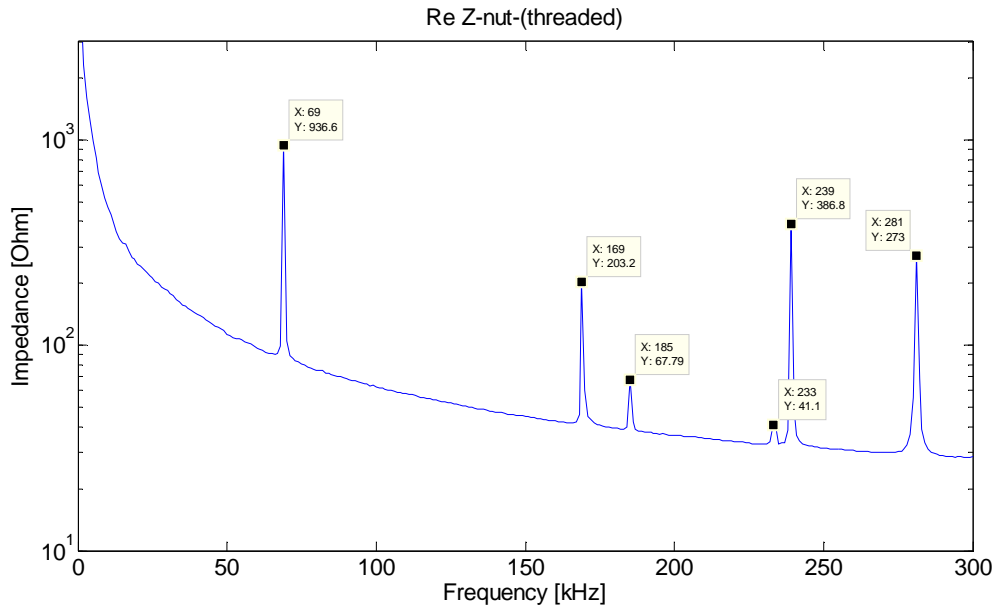
332

*Figure 264: EMIS of the nut without thread*

It is important to note that we see a difference between the ANSYS WB simulation and the experimental results. This is due to the fact that, in ANSYS WB, we model the nut with a sharp edge and in reality the nut has chamfers all over its edges and probably the beginning of the thread does not coincide perfectly; however this is not a concern.

### 13.2.3.2 LASER VIBROMETRY - MEASUREMENTS OF THE STEEL HEX NUT

Laser vibrometry is a non-contact technology based on the Doppler effect, which is able to sense the frequency shift of back scattered laser light from a moving surface. The main advantage of a laser vibrometer compared to other alternative methods is the fact that this technology allows the accurate measurement of vibrations without contact at frequencies up to 1.2 GHz. Scanning laser vibrometers have been used extensively and successfully in the last years for characterizing small and large amplitude ultrasonic vibrations in solid surfaces.

In this section, we use a laser vibrometry tool (PSV-400-3D from Polytec as shown in Figure 265) to study the mode shapes of the sensor ring under different resonance frequencies and we explore the range around 300 kHz in order to understand the behavior of the composite or stainless steel ring in the frequency bound of interest.
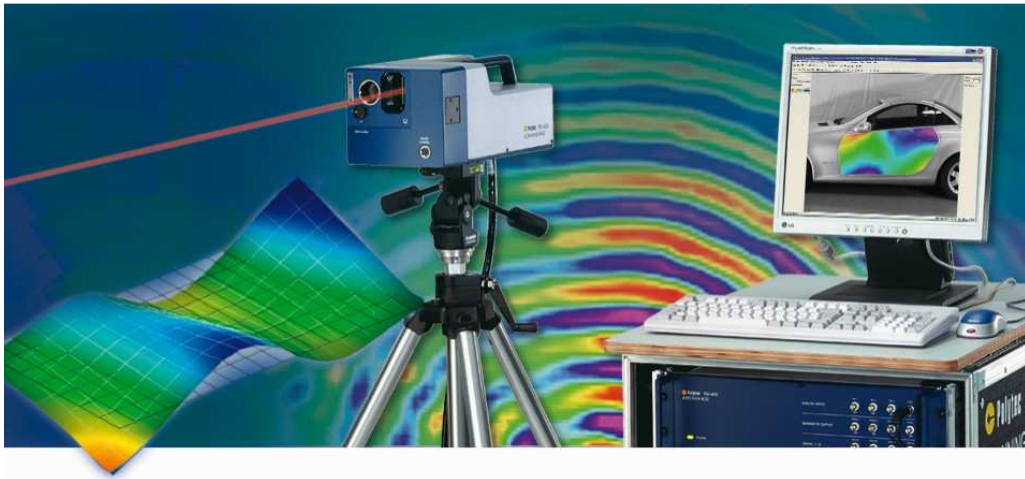


*Figure 265: PSV-400-3D from Polytec*

We then compare these results and shapes with the FEM predictions (ANSYS WB) for the stress and strain distributions.

The scanning vibrometer measures the strain at each point on a non-contact predefined grid using the laser probe. The non-contact measurement technique consists of a three lasers simultaneously measuring one grid point and each laser measures the vibration along its incident direction. Then the strain is calculated from the displacements. As a last step, the results of the strain from the laser vibrometer are compared with those from the FBG to understand which one is more accurate.

After we obtain the final FBG ring sensor, we bind a PWAS to the ring sensor. We excite the sensor at a range of 300 kHz and we take the resonance frequency measurements in order to validate the concept and to prove this design is working.

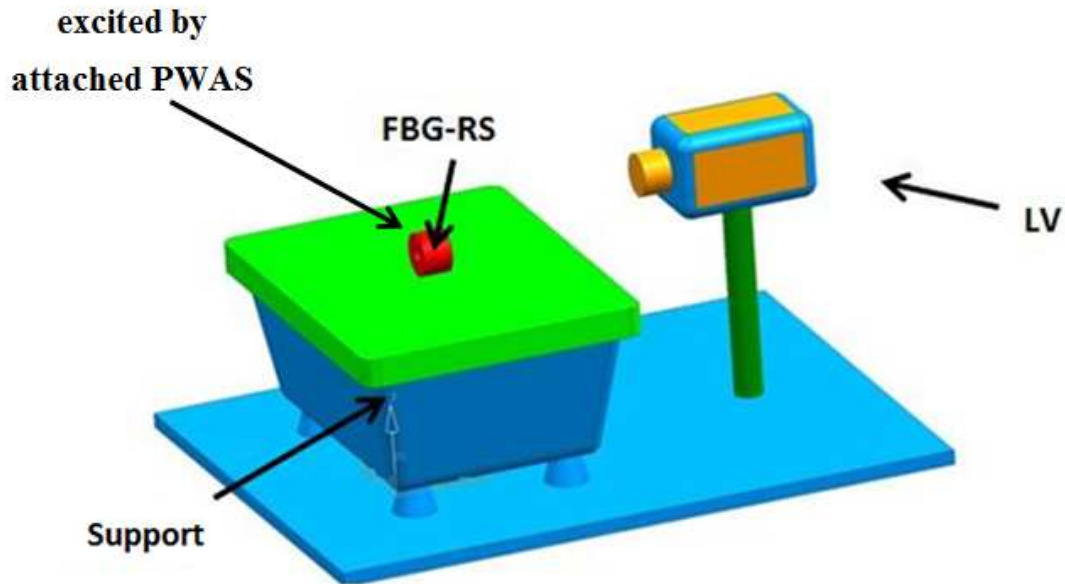Using the set-up (laser vibrometer) in Figure 266 we will conduct tests for the FBG ring sensor for 300 kHz.



*Figure 266: Conceptual instrumentation set-up for the FBG ring sensor laser vibrometer measurement*

Due to functionality limitations of the vibrometer available for the tests (one head), we are only able to conduct 1D measurements, which means, we are still able to measure out-of-plane displacement however not the in-plane displacement. To develop the laser measuring technique, we decide to use the nut (hexagonal) and measure the displacements out-of-plane on each lateral side. We take a variable-angle drill-press vise and mount the nut in the center using a double-sided tape in order to have a good control of the location of all six sides of the nut. Then, we spray paint the nut to reflect better the vibrometer laser beam. The final set-up is shown in Figure 267.
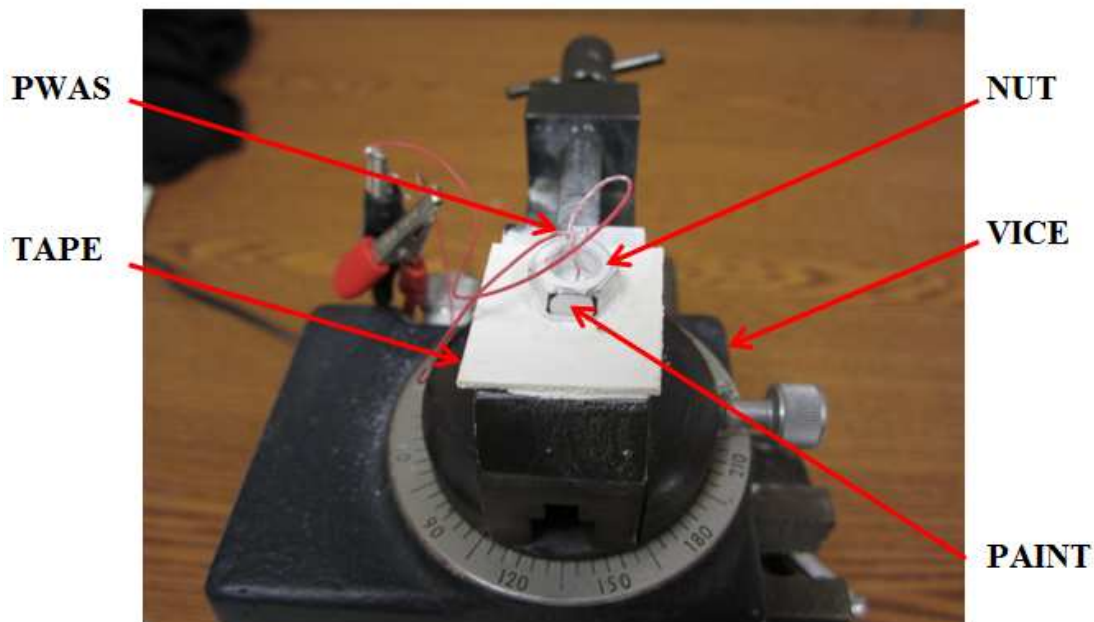
*Figure 267: Nut Set-up for Laser Vibrometer*

We use an amplifier to amplify the 3.5 V (Figure 268) a periodic chirp excitation

signal (one of the standard vibrometer excitation signals) by a factor of 10 (Figure 269).
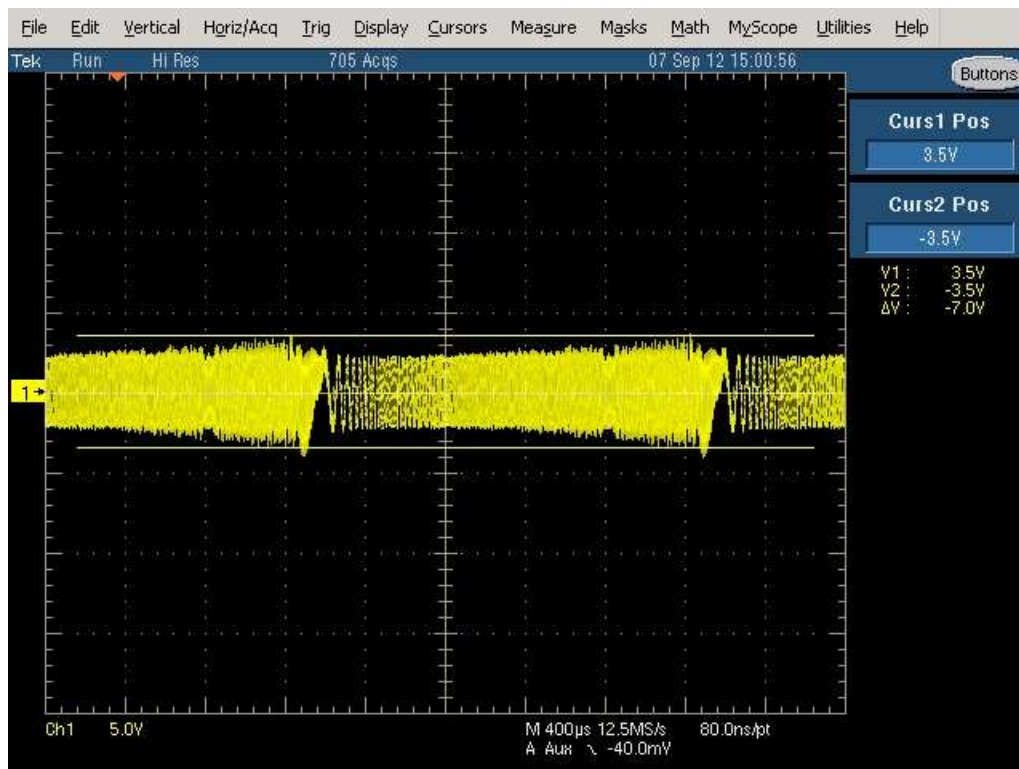


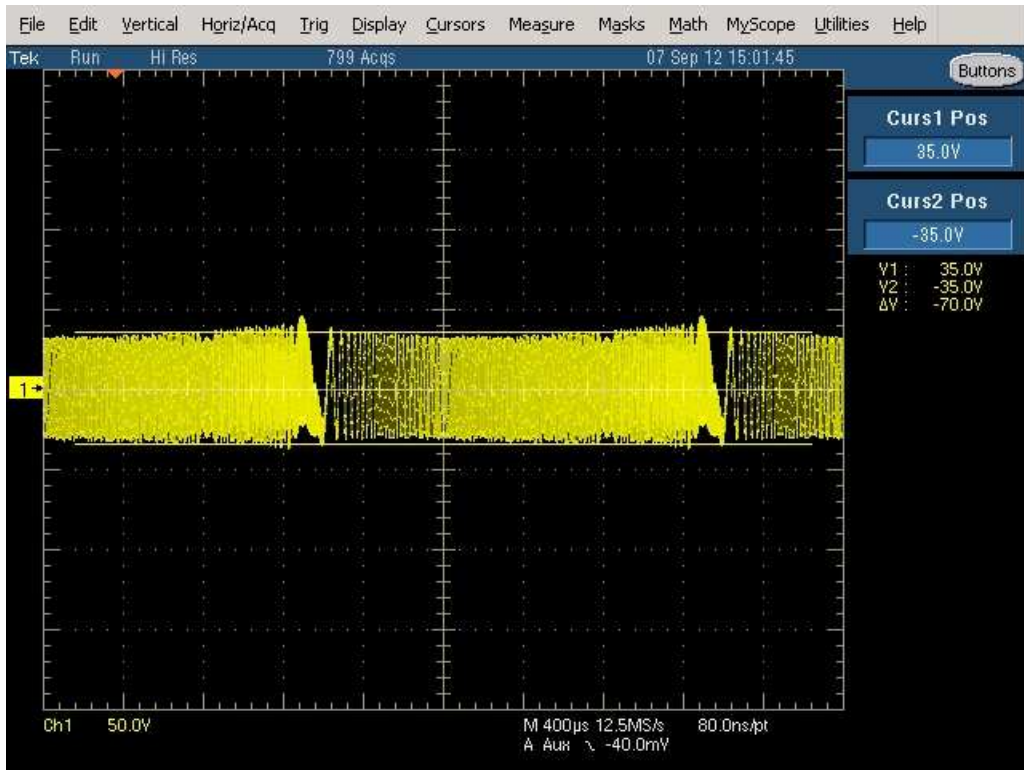*Figure 268: 3.5 V Periodic Chirp Excitation Signal (original – vibrometer)*

*Figure 269: Periodic Chirp Excitation Signal (X10 - amplifier)*

This type of signal allows long time samples such as are necessary for zoom FFT
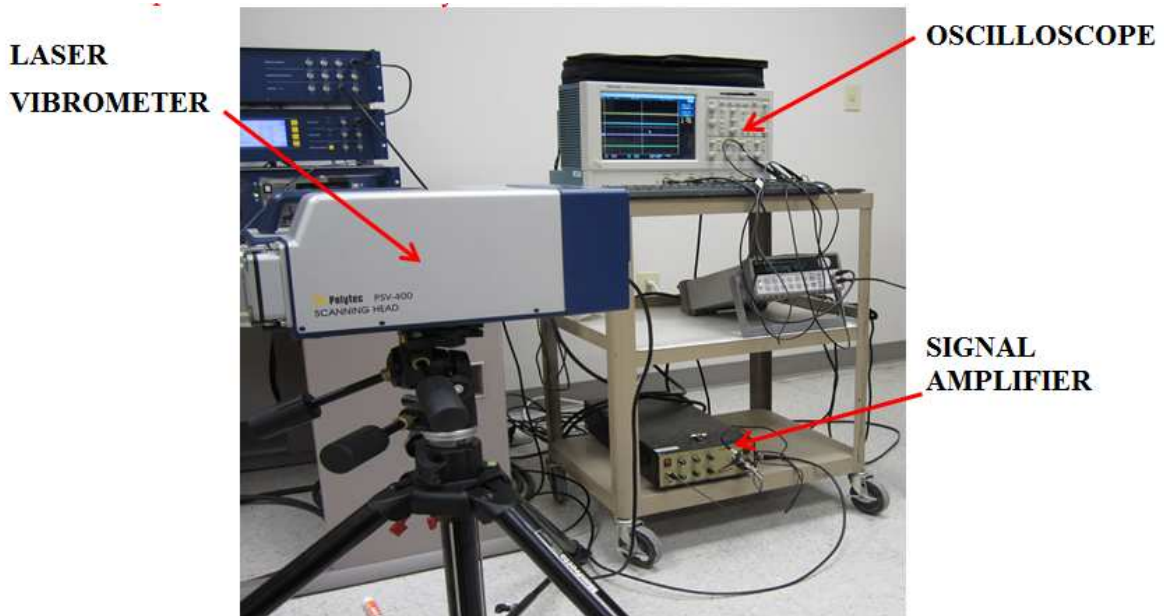
or other signal analysis methods.



*Figure 270: Laser Vibrometer Setup*

337

After doing all the alignments and set-up for the laser vibrometer (Figure 270), we are able to take the measurements (displacements out-of-plane) for all six sides of the nut and look for the resonance frequencies. The nut is then excited using the PWAS bound on one side as presented in Figure 271.
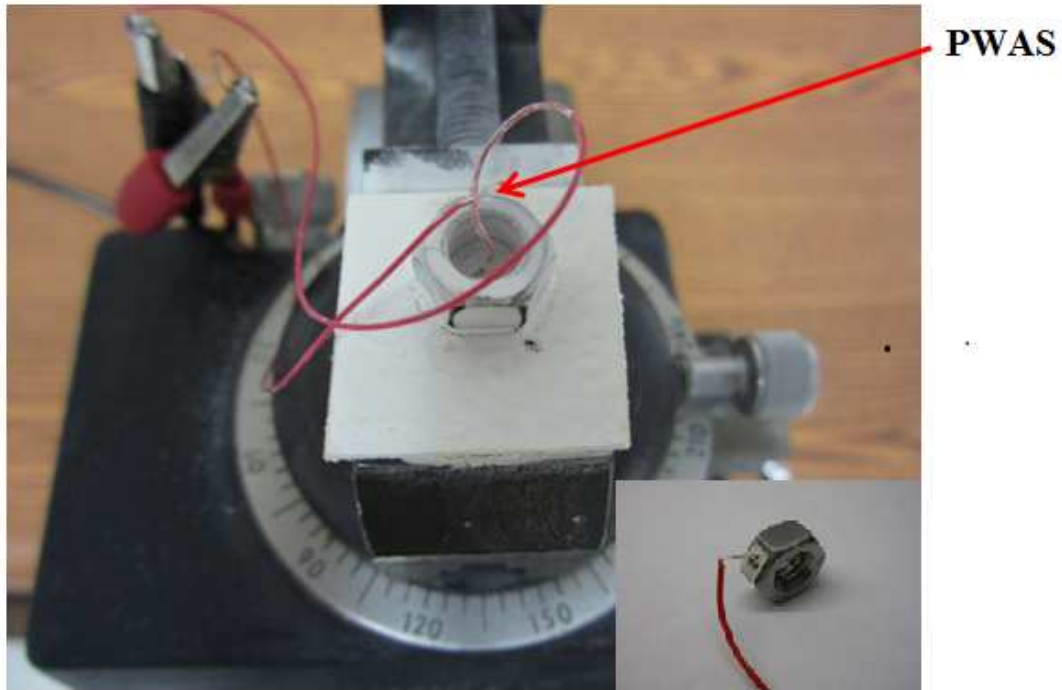


*Figure 271: PWAS Location*

We look at the vibrometer results for one side of the nut for the first resonance frequency which is at 69 kHz. We apply the same technique for all remaining sides of the nut and we notice that the resonance frequencies tend to appear at the same ranges as for the first side which is what we want as shown in Figure 272, Figure 273, Figure 274, Figure 275, Figure 276 and Figure 277. For reference, we observe the following frequencies 69, 167, 184 and 237 kHz.

*Figure 272: Vibrometer Results – side 1 – 69 kHz*



*Figure 273: Vibrometer Results – side 2 – 68 kHz*

*Figure 274: Vibrometer Results – side 3 – 68 kHz*



*Figure 275: Vibrometer Results – side 4 – 68 kHz*

*Figure 276: Vibrometer Results – side 5 – 69 kHz*
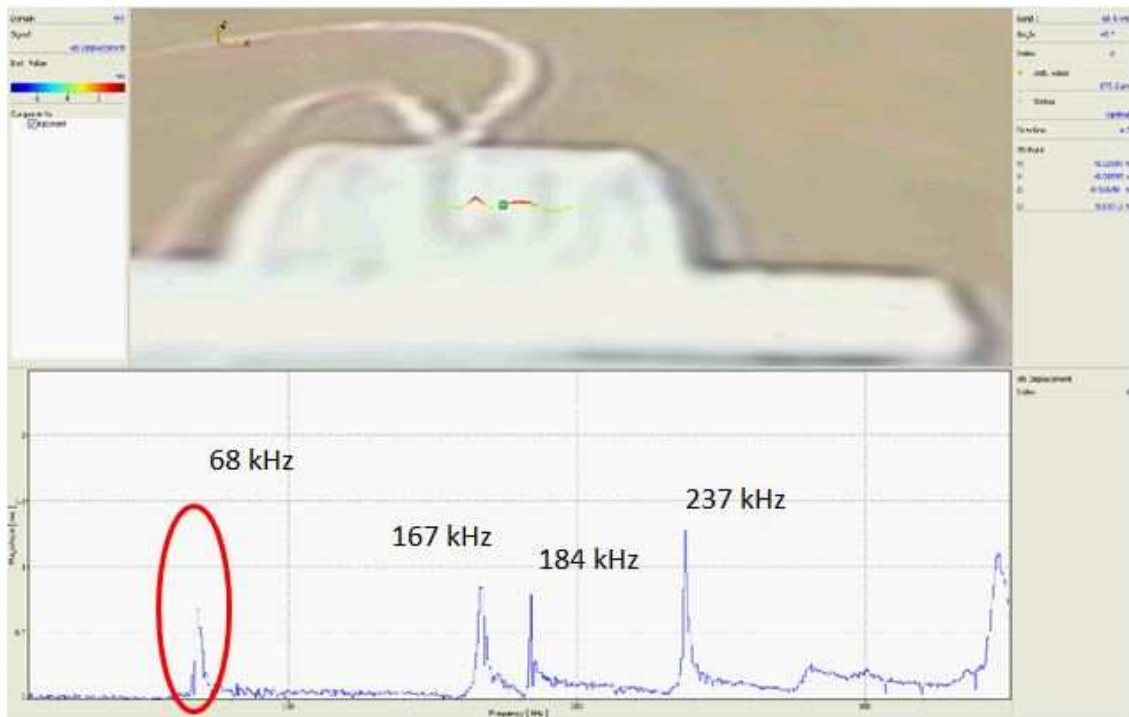


*Figure 277: Vibrometer Results – side 6 – 68 kHz*

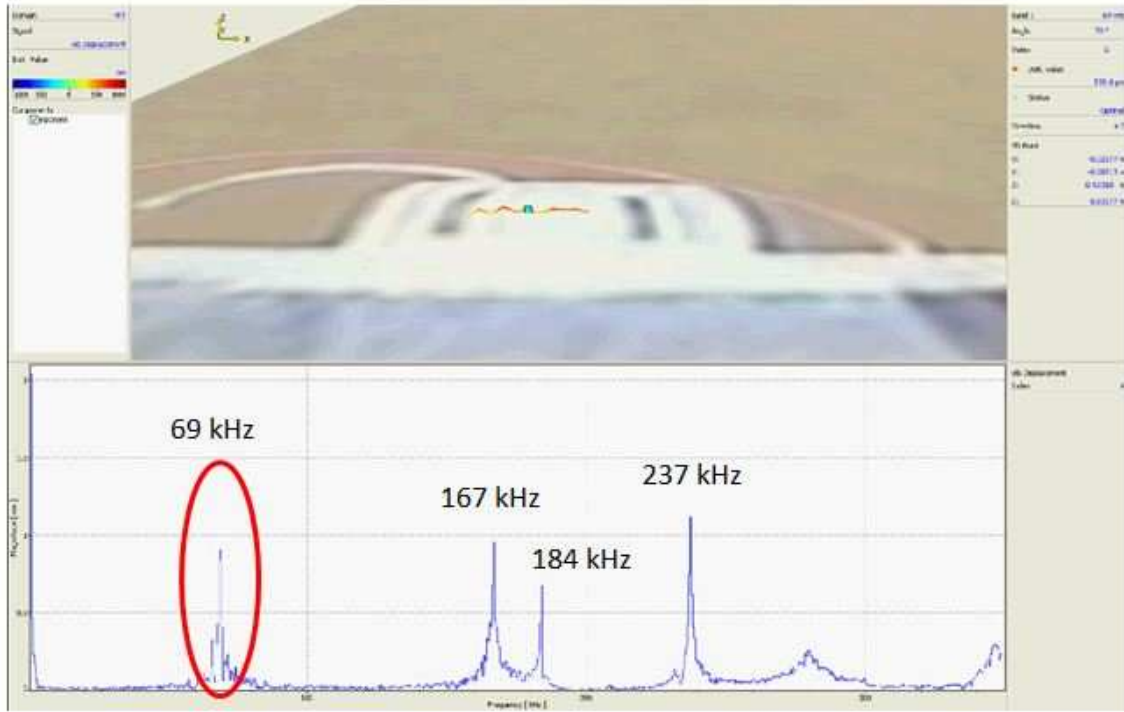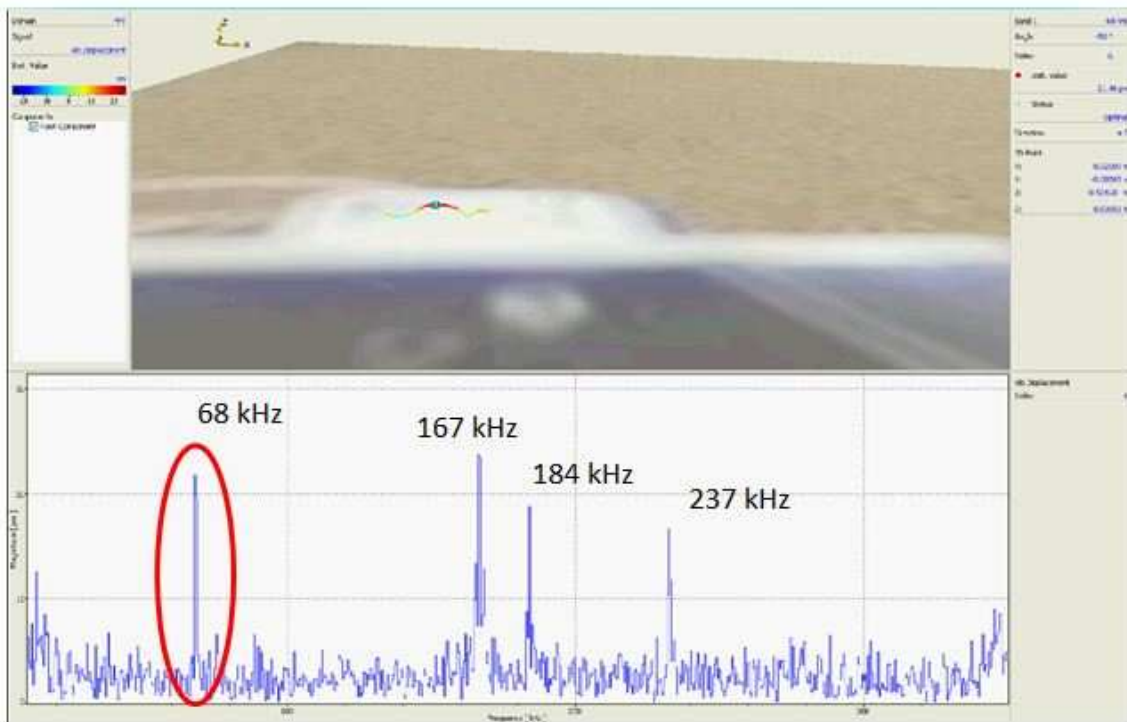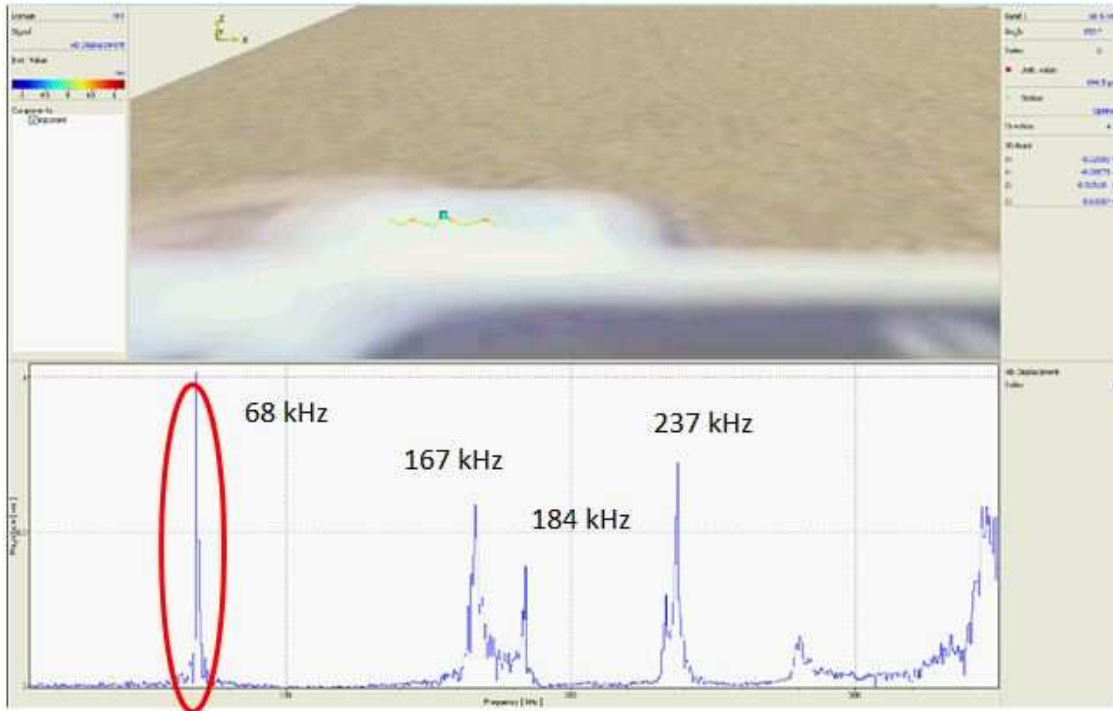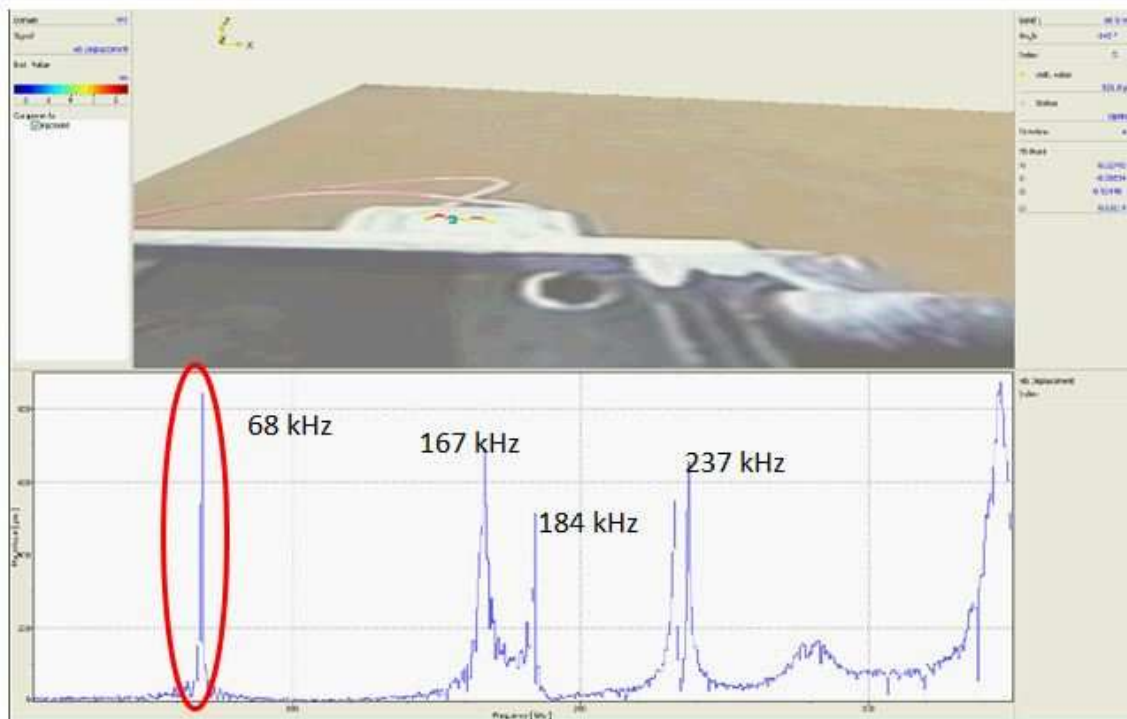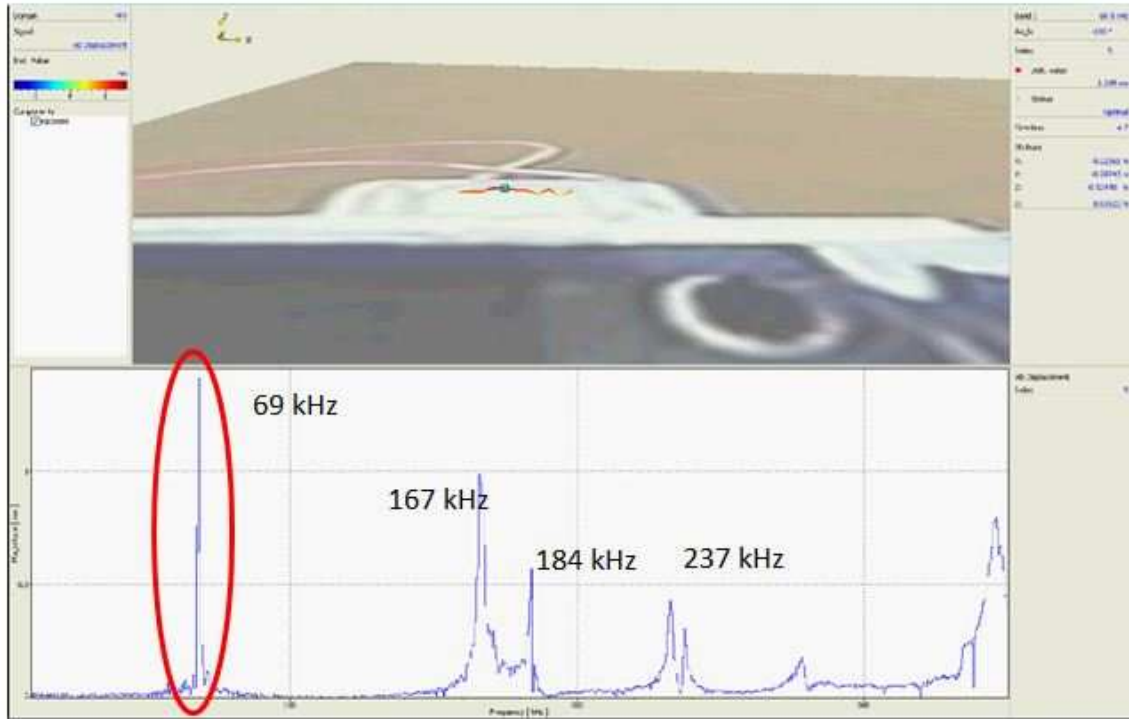Next, we compare the resonance Table 11 frequencies predicted by FEM, the impedance analyzer and vibrometer to see whether all these three methods agree or there are any differences. This is a screening step before we test the real FBG ring sensor. Our goal is to have a sensor that can reach the first resonance frequency at the desired range. Since all methods agree, we met our goal and the concept is working properly.

| FEM | Impedance | Laser vib. measurement |
|---|---|---|
| 75 kHz | 70 kHz | 69 kHz (side #1) |
| 75 kHz | 70 kHz | 68 kHz (side #2) |
| 75 kHz | 70 kHz | 68 kHz (side #3) |
| 75 kHz | 70 kHz | 68 kHz (side #4) |
| 75 kHz | 70 kHz | 69 kHz (side #5) |
| 75 kHz | 70 kHz | 68 kHz (side #6) |

*Table 11: Comparison of FEM, impedance, laser vibrometer measurement of nut resonances*

### 13.2.4 SECOND CONCEPT CONCLUSIONS

As per results obtained above, we can see that we have a 25% difference between the analytical and the FEM results, which is important to remember for future estimation.

We also notice the improvement of this design (ring shape) compared to the first design (D-shape). Knowing that the analytical results come with an approximation, we will use the FEM results as a benchmark until we will have experimental results.

We obtain this frequency 304 kHz using two different materials:

- Stainless steel ($E$ = 200 GPa and $\rho$ = 7750 Kg/m3) with dimensions: $ID$ = 0.0016 m; $OD$ = 0.0048 m; $H$ = 0.0032 m.

- CFRP ($E$ = 133 GPa and $\rho$ = 1600 Kg/m3 with dimensions: $ID$ = 0.0029 m; $OD$ = 0.0087 m; $H$ = 0.0058 m.

It is very important to mention here that for CFRP, we will wrap the fibers around the cylinder; hence this provides the stiffness properties in the direction we want. By using this ring approach, we conclude that we are able to reach 300 kHz and have an axial vibration into the FBG fiber.

After we performed the experiments with the stainless steel nut, using the EMIS method and the laser vibrometer, we conclude that the nut can reach the first resonance frequency in the form of axial displacement (2D plane). Those experiments emphasize the concept via the ring sensor. The sensitivity of the ring can be observed in tests where we have the stainless steel nut both with and without thread. By machining the thread, we can see a decrease in the first resonance frequency. This leads us to the idea that a very small ring can reach the first resonance frequency at a very high level.

Taking these into consideration, we conclude that this design can reach our goal of reaching the first resonance frequency at 300 kHz (axial displacement).

### 13.3    THIRD CONCEPT: REFINED FBG RING SENSOR

#### 13.3.1 IMPROVEMENTS OF THE FBG RING SENSOR DESIGN

Given all of the above about our concept, it's time to finalize the concept for our FBG ring sensor. There are a three more concerns to address to ensure correct functionality of our concept.

- First, we need to consider that, by solely looking at the ring sensor, it's quite difficult to predict that the in-plane displacement will be always in the

appropriate direction to stretch the fiber. Therefore, we should do something about this. One solution found to address this concern was to use an elliptical center instead of the round one; this, we force the in-plane displacement in one preferred direction all the time.

- Second issue at hand is the mounting of the ring sensor on the structure; the exterior is a circular cylinder and the contact to a flat surface is just a line, i.e., it cannot be mounted on the structure. In order to address this, we came up with the idea of machining flatness on the top and bottom of ring in locations corresponding to the longer sides of the interior ellipse. This helps both with the mounting and to forcing the displacement to be on the same direction all the time.

- Third concern is that, the fiber needs to be mounted in the direction of the longer part of the ellipse in such a way so that the in-plane displacements will stretch the fiber and enable us to measure the resonance frequency. In order to make this possible, we drill a hole from one side to the other and bind the fiber inside it with adhesive.

This design seems to be feasible from the concept standpoint, so we test the concept in ANSYS WB. Practically, by using this concept and changing the dimensions, we can design a FBG ring sensor for any desired frequency.

As a next step, we choose 3 frequencies for testing and proving our design: 100, 200 and 300 kHz. We choose 304 Stainless Steel as the material for all rings; the

dimensions are shown in Table 12. The final concept with these enhancements is shown in Figure 278 Figure 279 and Figure 280

The ANSYS WB results shown in Figure 278 Figure 279 and Figure 280 confirm that the predicted resonance is an in-plane mode and matches the desired frequency. By placing the FBG fiber inside the ring (in the direction of the ring deflection), we will be able to have axial displacements on the fiber. This ring will reach the natural frequencies predicted by the FEM analysis (100, 200, 300 kHz), exciting axially the FBG fiber as per the project request.

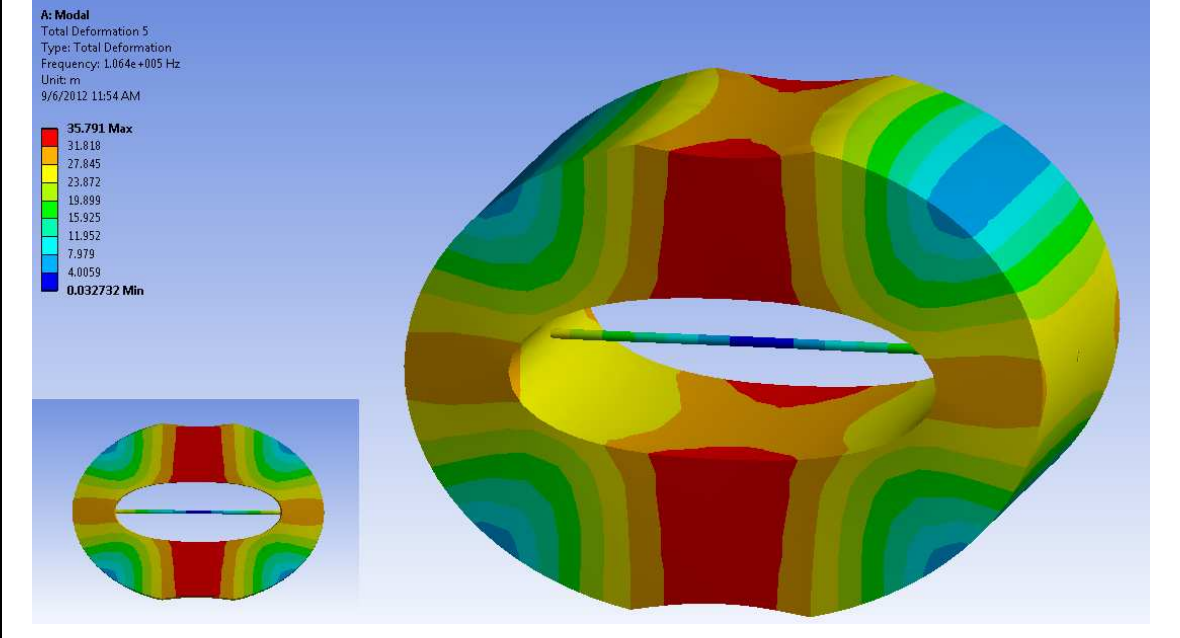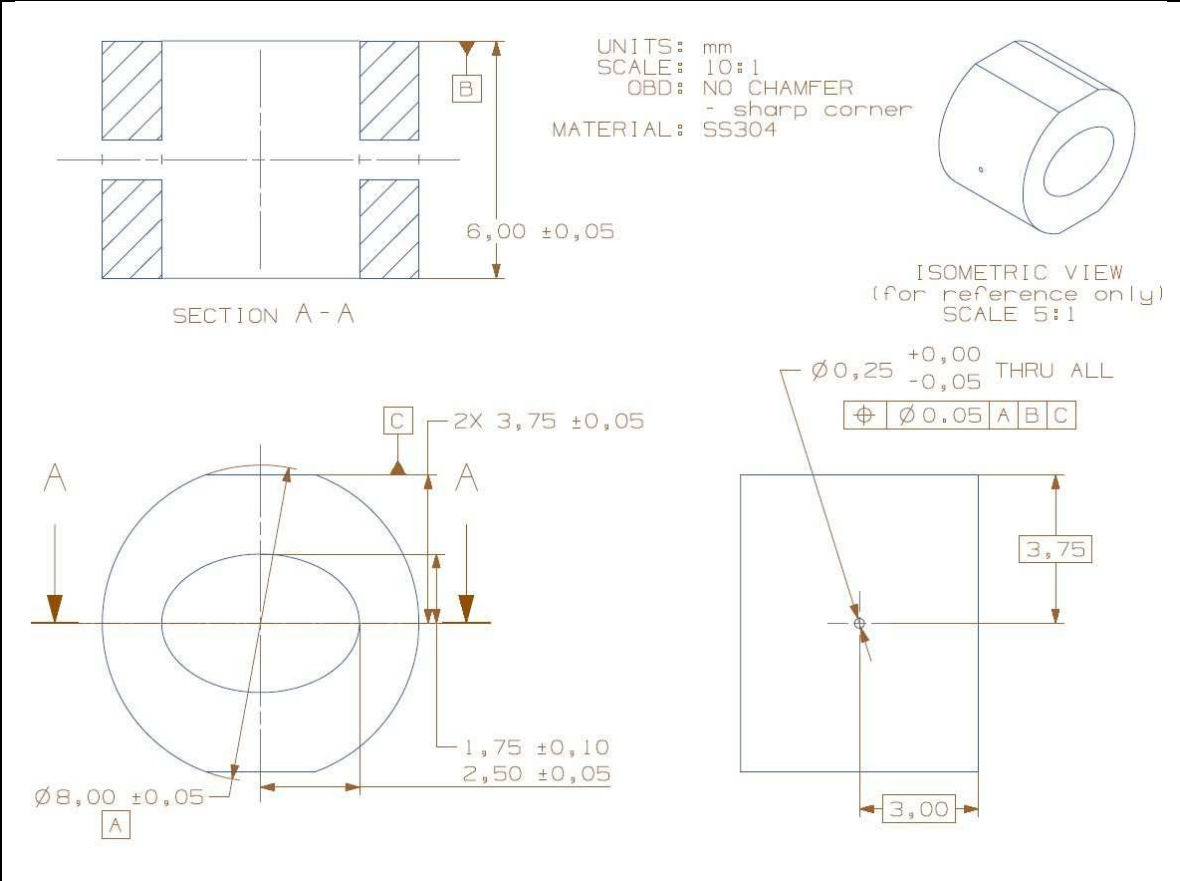| Resonance Frequency | OD | r1 | r2 | Depth |
|---|---|---|---|---|
| 100 kHz | 8.00 mm | 2.50 mm | 1.75 mm | 6.00 mm |
| 200 kHz | 6.00 mm | 1.45 mm | 0.95 mm | 5.00 mm |
| 300 kHz | 4.35 mm | 1.00 mm | 0.60 mm | 4.00 mm |

*Table 12: Dimension for Rings*

*Figure 278: Final concept - FBG ring sensor 100 kHz prototype*
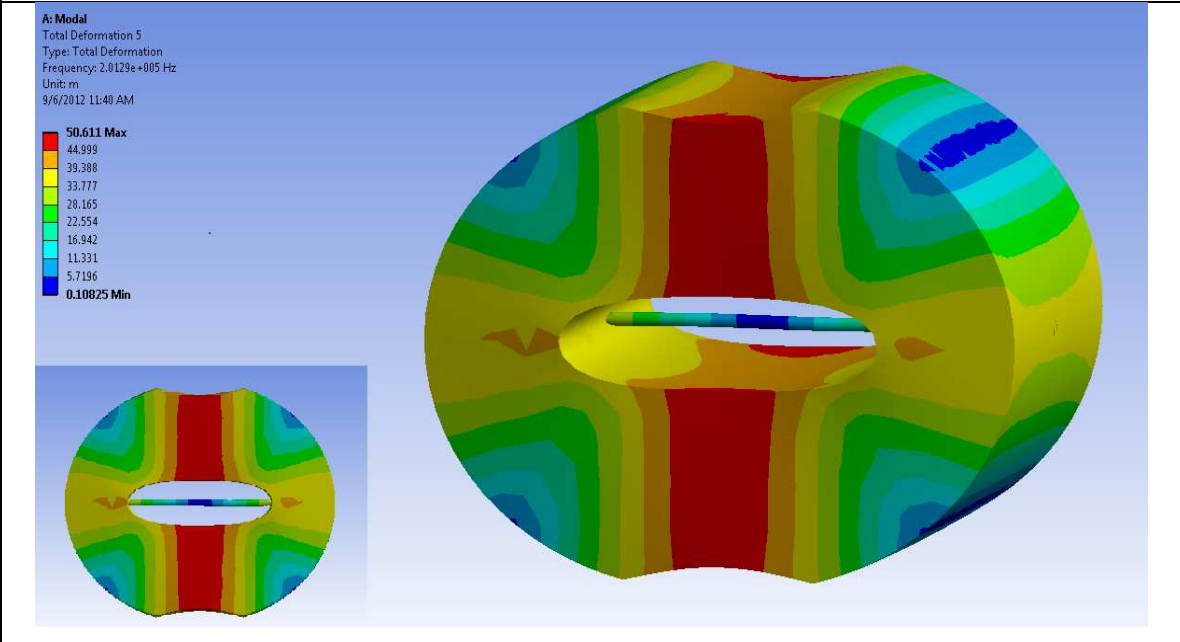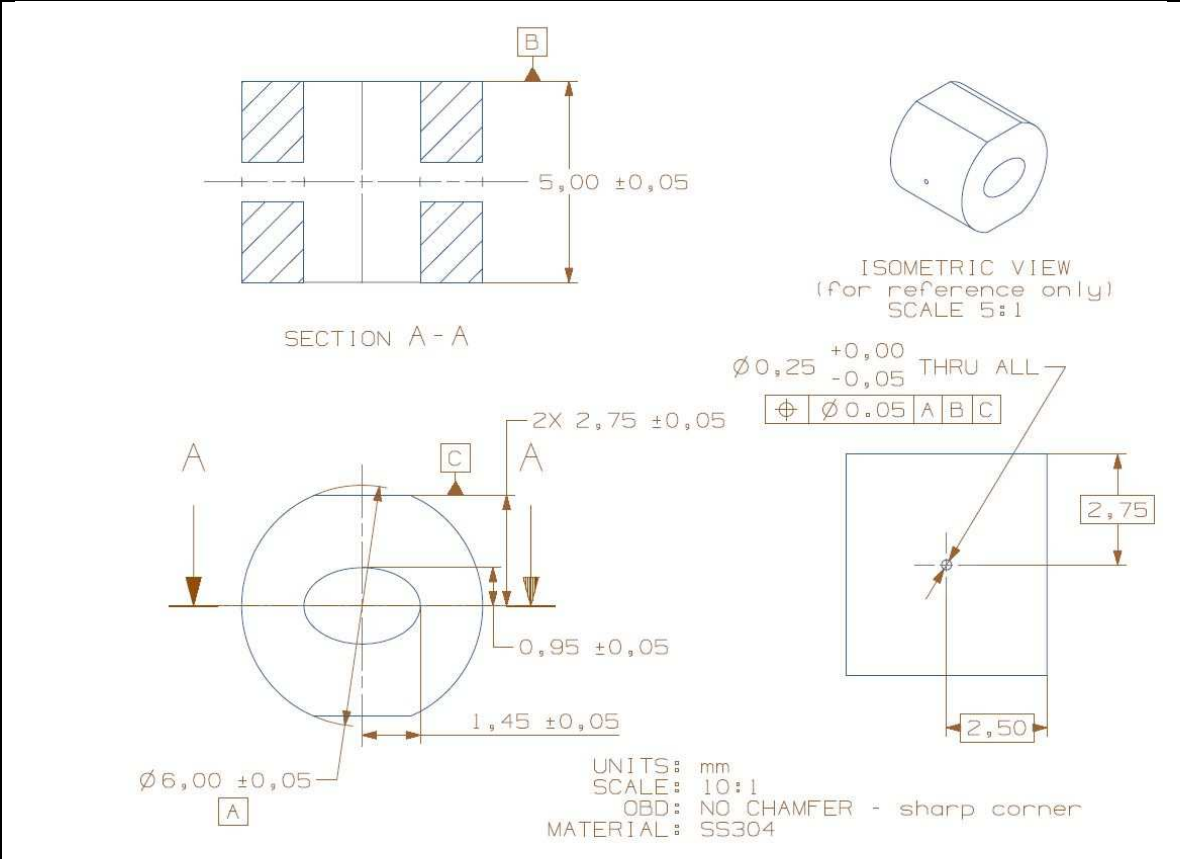
*Figure 279: Final concept - FBG ring sensor 200 kHz prototype*
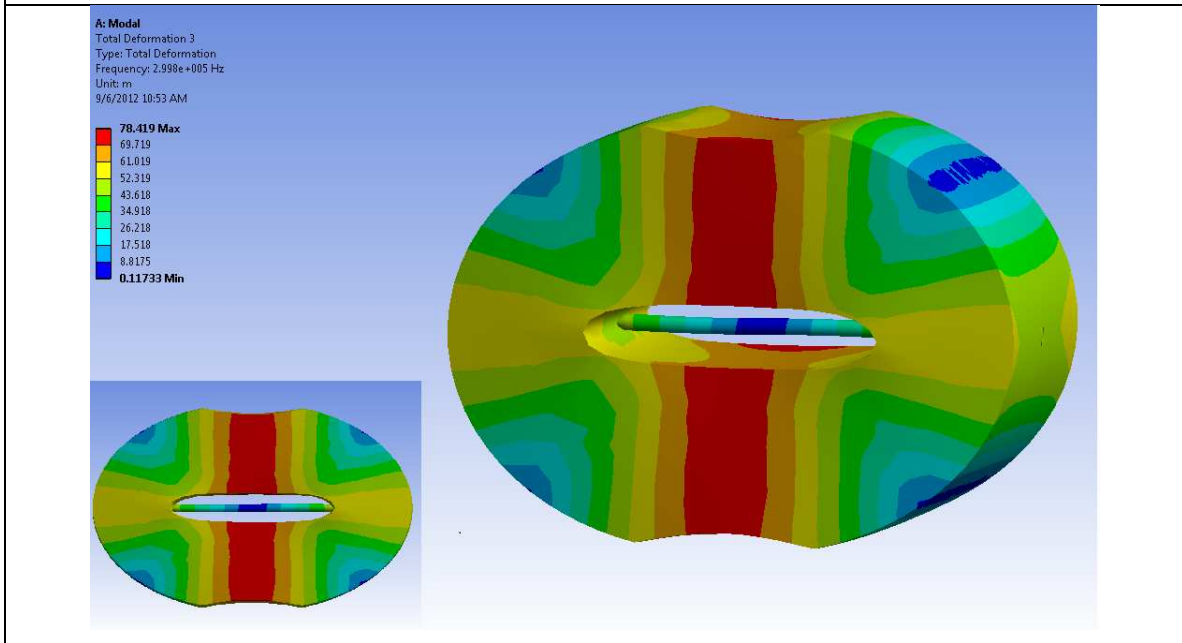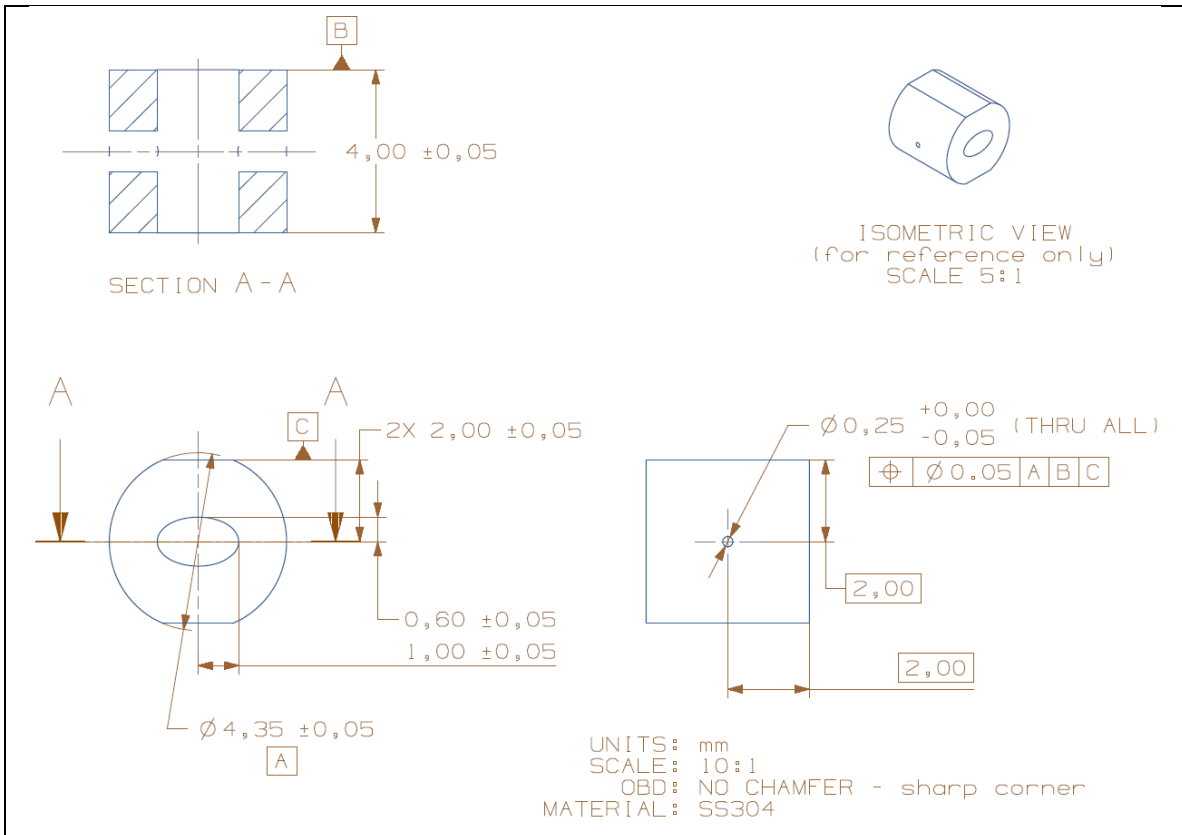
*Figure 280: Final concept - FBG ring sensor 300 kHz prototype*

### 13.3.2 MANUFACTURING OF FBG RING SENSOR PROTOTYPES

As a next step we found a vendor that could manufacture this ring using the above mentioned specifications. A hole had to be also drilled along the diameter of the ring from one side to the other and the FBG sensor was bound to it as per Figure 281.
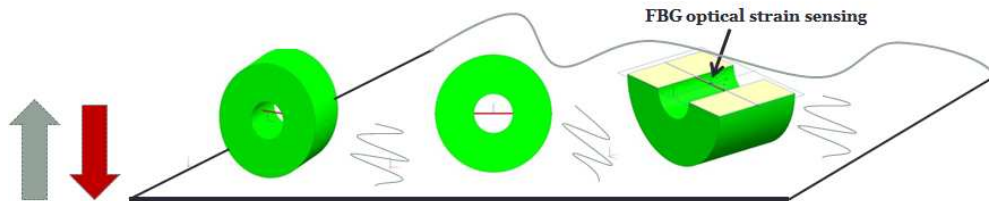


*Figure 281: FBG Ring Sensor*

Having the final design shape for the FBG ring sensor, we machine two prototypes: one for 100 kHz and the other one for 300 kHz.

#### 13.3.2.1 MANUFACTURING OF THE 100 kHz PROTOTYPE

The 100 kHz FBG ring sensor had manageable dimensions, and thus we were able to manufacture in the USC machine shop. We took a pipe, bent it to match the elliptical shape size and we cut it to match the necessary height. Then, we milled the flat sides. The final product seems to be approximately in our dimensions range and can be seen in Figure 282.
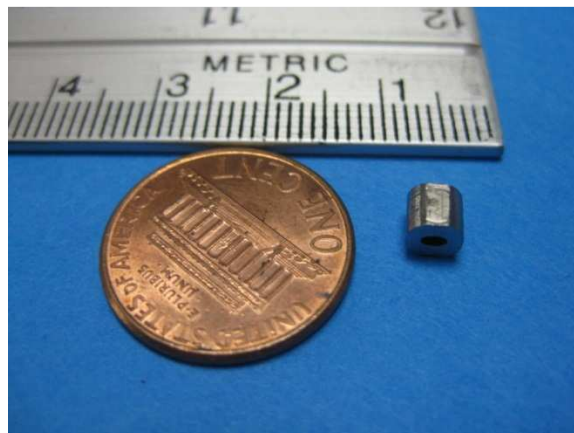


*Figure 282: 100 kHz FBG ring sensor*

The 300 kHz FBG ring sensor prototype could not be machined at USC due to the very small dimensions, so we sent it out to a vendor (Alpha Manufacturing CO INC, 100 Old Barnwell RD West Columbia SC 29171) which made the prototype for us using the EDM technology.

The manufacturing process seems to be very challenging due to the tiny size and very high tolerance. The most difficult step in this process of machining the rings is the hole and the alignment of the flat faces with the ellipse major axis. We can see in Figure 283 the 300 kHz FBG ring sensor prototype.
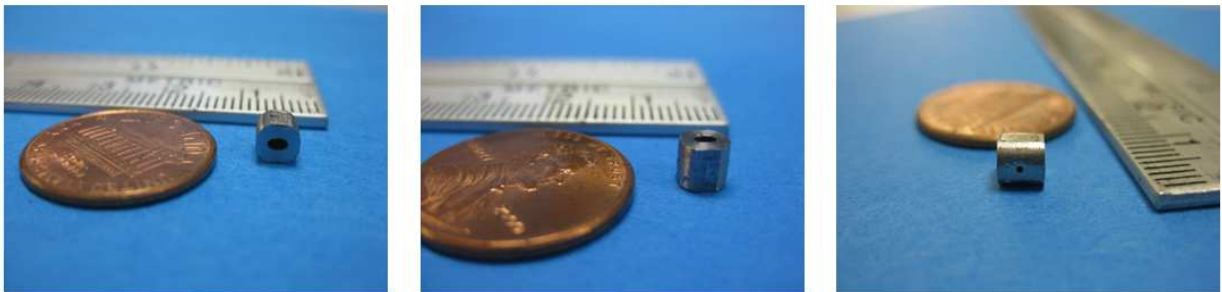


*Figure 283: 300 kHz FBG ring sensor (various views)*

**13.3.3 TESTING OF THE FBG RING SENSOR PROTOTYPES**

The FBG ring sensor prototypes were tested to determine their resonance frequencies and their response to vibration excitation in the high kHz range as described next.

### 13.3.3.1 TESTING OF THE 100 kHz PROTOTYPE

### 13.3.3.1.1 EMIS TESTING

The next step is to see if the first resonant frequency of the structure is around 100 kHz. In order to do this, we bound a PWAS on the flat service in order to excite the ring (Figure 284) and applied the EMIS method.
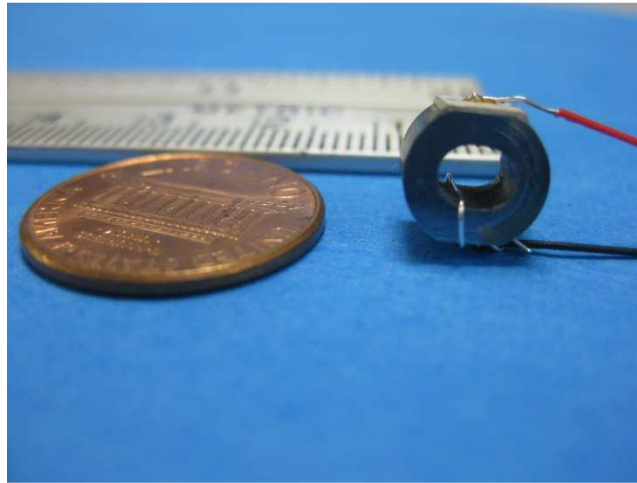


*Figure 284: 100 kHz ring sensor with PWAS attached to the top and wired*

The setup configuration and the result for 100 kHz FBG ring sensor is shown in Figure 285 and Figure 286, respectively. It is apparent from Figure 286 that the first resonance occurs at 114 kHz, while higher resonances appear beyond 250 kHz.
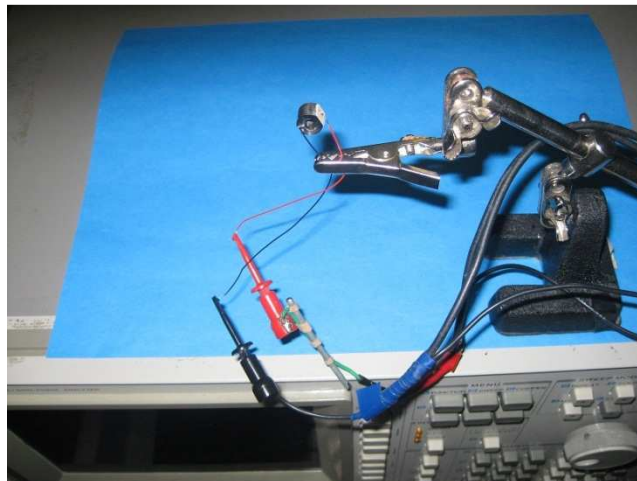


*Figure 285: 100 kHz FBG ring sensor experiment setup*
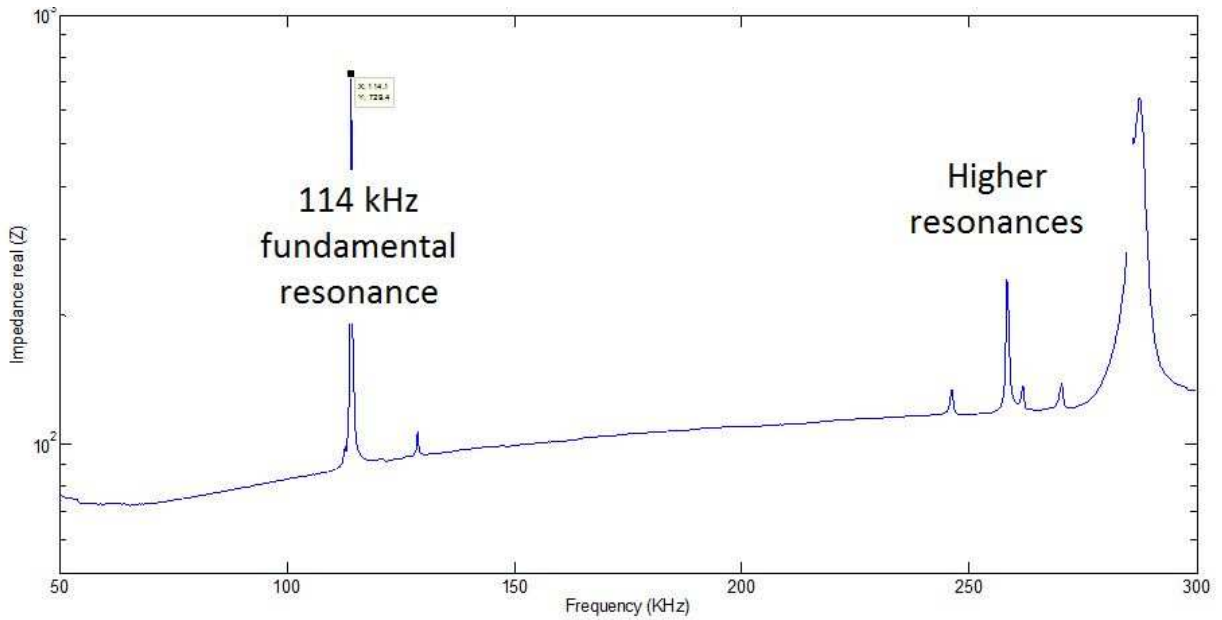
*Figure 286: Resonance frequency for 100 kHz FBG ring sensor*

### 13.3.3.1.2 FREQUENCY RESPONSE TESTING

In order to better understand and study the sensitivity of the FBG ring sensor for our desired resonance frequency, we apply the frequency response method and we look for the natural resonance frequencies. In order to do this, we bound an additional PWAS on the other side of the ring as shown in Figure 287.
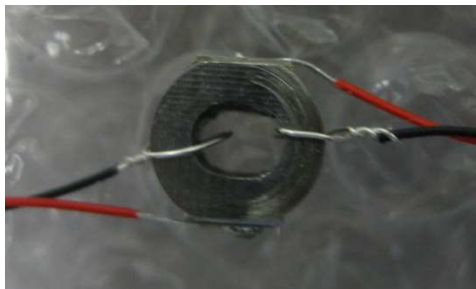


*Figure 287: FBG ring sensor with 2 PWAS*

Now, we have two PWAS, where one excites the specimen and the other measures its vibration response. This process takes place in the time domain. We use a function generator HP 33120A and apply a chirp signal excitation in the 0-250 kHz range for one second. We measured the response with a digital oscilloscope Tektronix

352

TDS5034B After each cycle, we notice a phase shift in the new starting position. Our HP 33120A does not have the "hold function". We notice this issue due to the fact that after we apply fast Fourier transform (FFT), we find a different resonance frequency for the ring than expected when computed with the impedance method. A FFT is an algorithm used to calculate the discrete Fourier transform (DFT) and its inverse. The DFT is obtained by breaking down a sequence of values into components of different frequencies.

In order to have the same starting position all the time for our chirp signal, we connect the front "output" port to the "modulation in" socket in the back of the HP 33120A with a cable so that we can synchronize and eliminate the phase shift.

A chirp signal is a sinusoid with a frequency that changes continuously over a certain band $(\Omega:\omega_1 \leq \omega \leq \omega_2)$ and a certain time period $(0 \leq t \leq M)$. We use the following signal:

$$u(t) = A\cos(\omega_1 t) + (\omega_2 - \omega_1)\frac{t^2}{2M}$$

(13.5)

Where:

$A$ is the amplitude, $t$ is time and $\omega$ is the angular frequency, $\omega = 2\pi f$

The instantaneous frequency in this signal is obtained by differentiating the argument with respect to time $t$:

$$\omega_i = \omega_1 + \frac{t}{M}(\omega_2 - \omega_1)$$

(13.6)

The instantaneous frequency rises from the lower bound of the frequency band to the higher. When applying the signal to a system, it provides good control over the excited frequency band and is thus often used for system identification.

The results obtained in the time domain Figure 288 from the receiver PWAS are then saved and converted into FFT using Matlab (Figure 289). Figure 288 indicates that during the chirp excitation experiment a strong resonance occur around ~456 ms, which corresponds to ~114 kHz.

This is identical to the resonance frequency obtained using the HP impedance analyzer. We can conclude that the "pitch-catch" method is a very good approach even for this type of applications and the FFT conversion from time domain to frequency domain works as predicted with high accuracy.

*Figure 288: Time domain testing:*
*(a) linear chirp characteristics between 0 to 250 kHz over a 1-sec duration;*
*(b) time domain signal showing a resonance at ~456 ms corresponding to ~ 114 kHz*

355
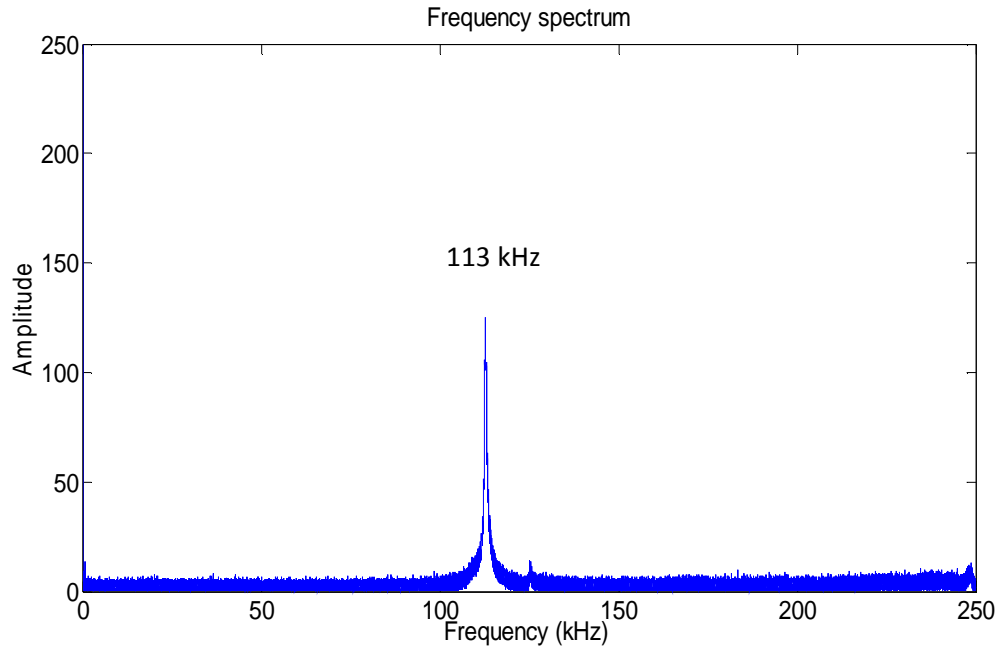
Figure 289: Frequency domain signal for 100 kHz prototype

### 13.3.3.2 TESTING OF THE 300 KHZ PROTOTYPE

### 13.3.3.2.1 EMIS TESTING

Following the same procedure described for 100 kHz ring sensor, we bound a PWAS on the flat surface of the 300 kHz (Figure 290).The setup configuration and the result for 300 kHz FBG ring sensor is shown in Figure 291 and Figure 292.
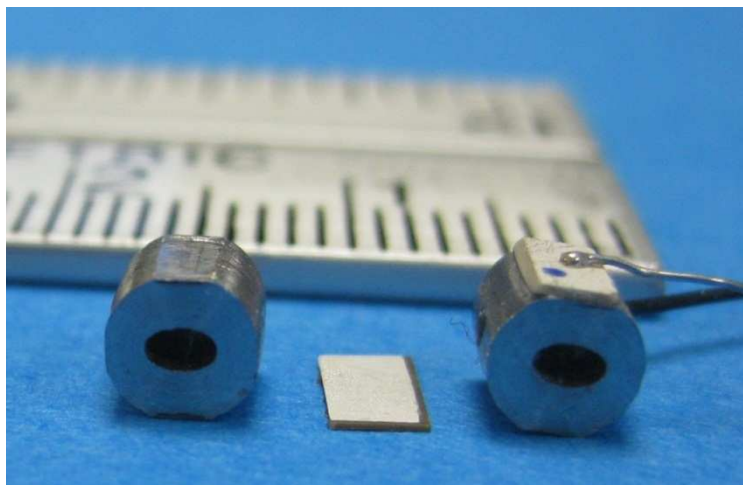


Figure 290: 300 kHz FBG ring sensor - setup configuration

356

*Figure 291: 300 kHz FBG ring sensor - setup configuration*

For the FBG ring sensor (300 kHz theoretical resonance frequency), the experimental result in Figure 292 shows that the resonance frequency is at 277 kHz in the ReZ spectrum.
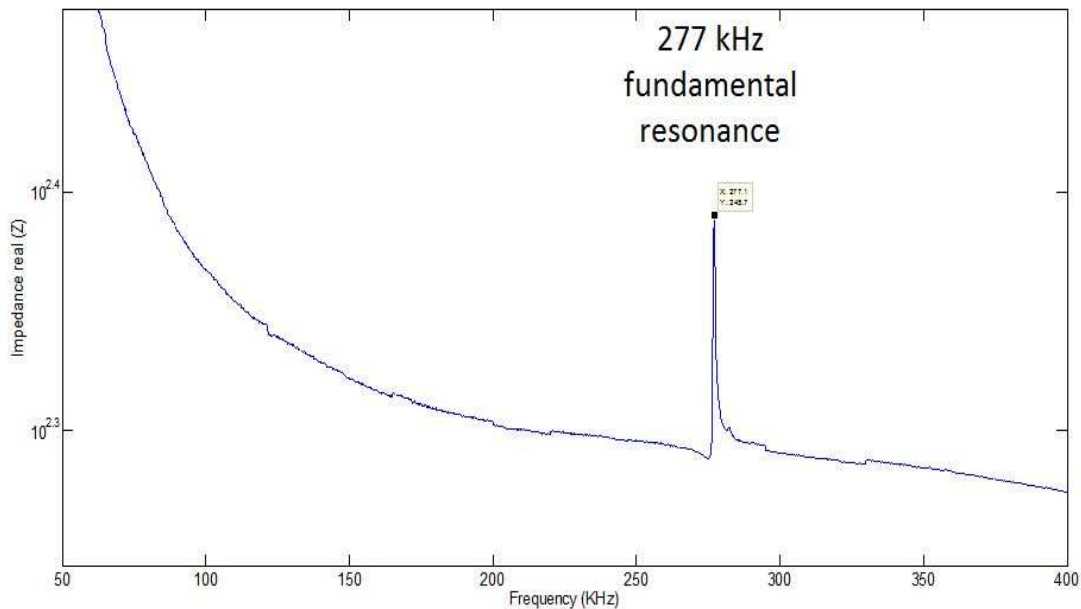


*Figure 292: Resonance frequency at 300 kHz FBG ring sensor*

### 13.3.3.2.2 FREQUENCY RESPONSE TESTING

Following the same procedure described for 100 kHz ring sensor, we obtain the results in time domain and convert them into FFT using Matlab for the 300 kHz ring sensor.
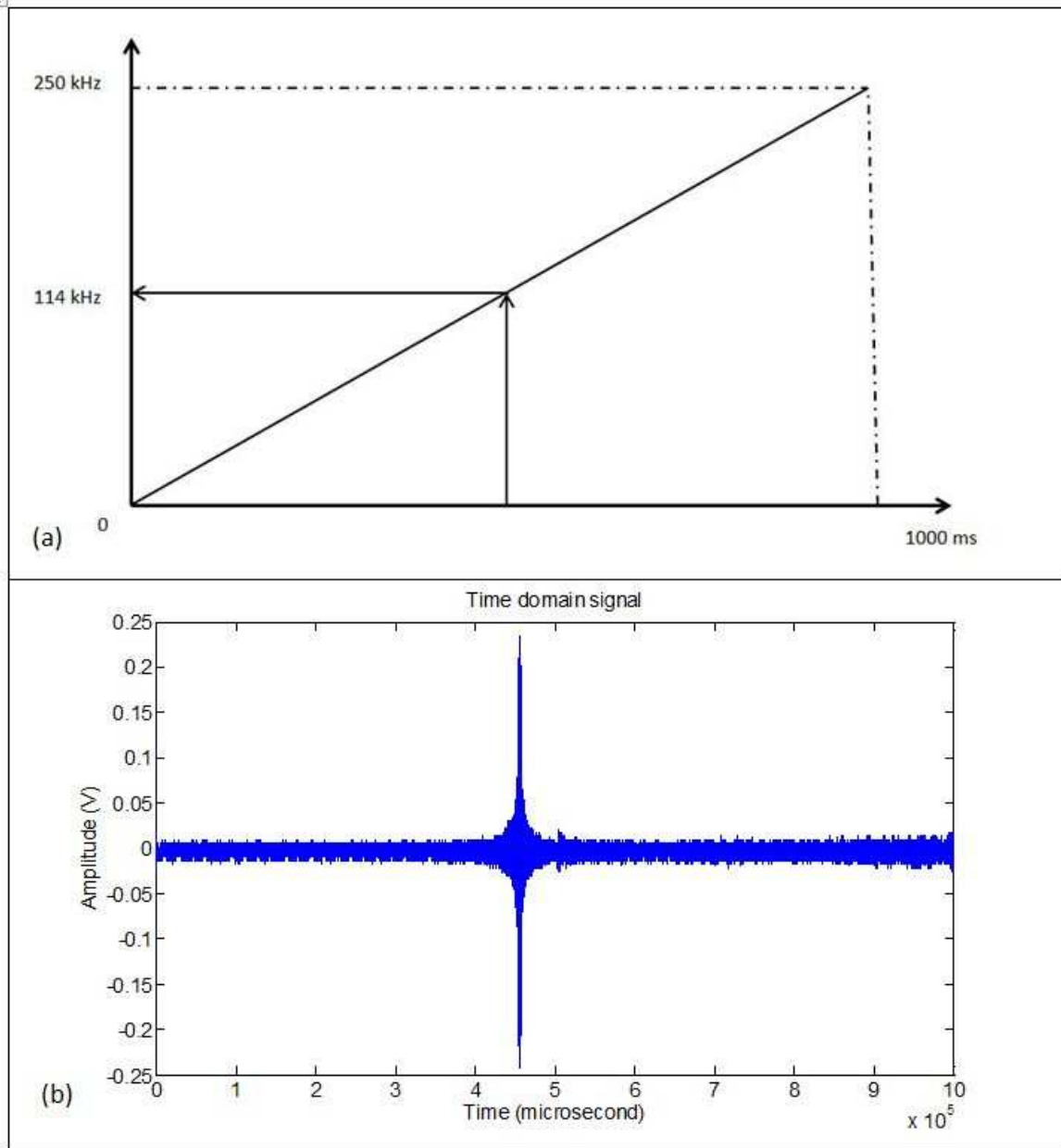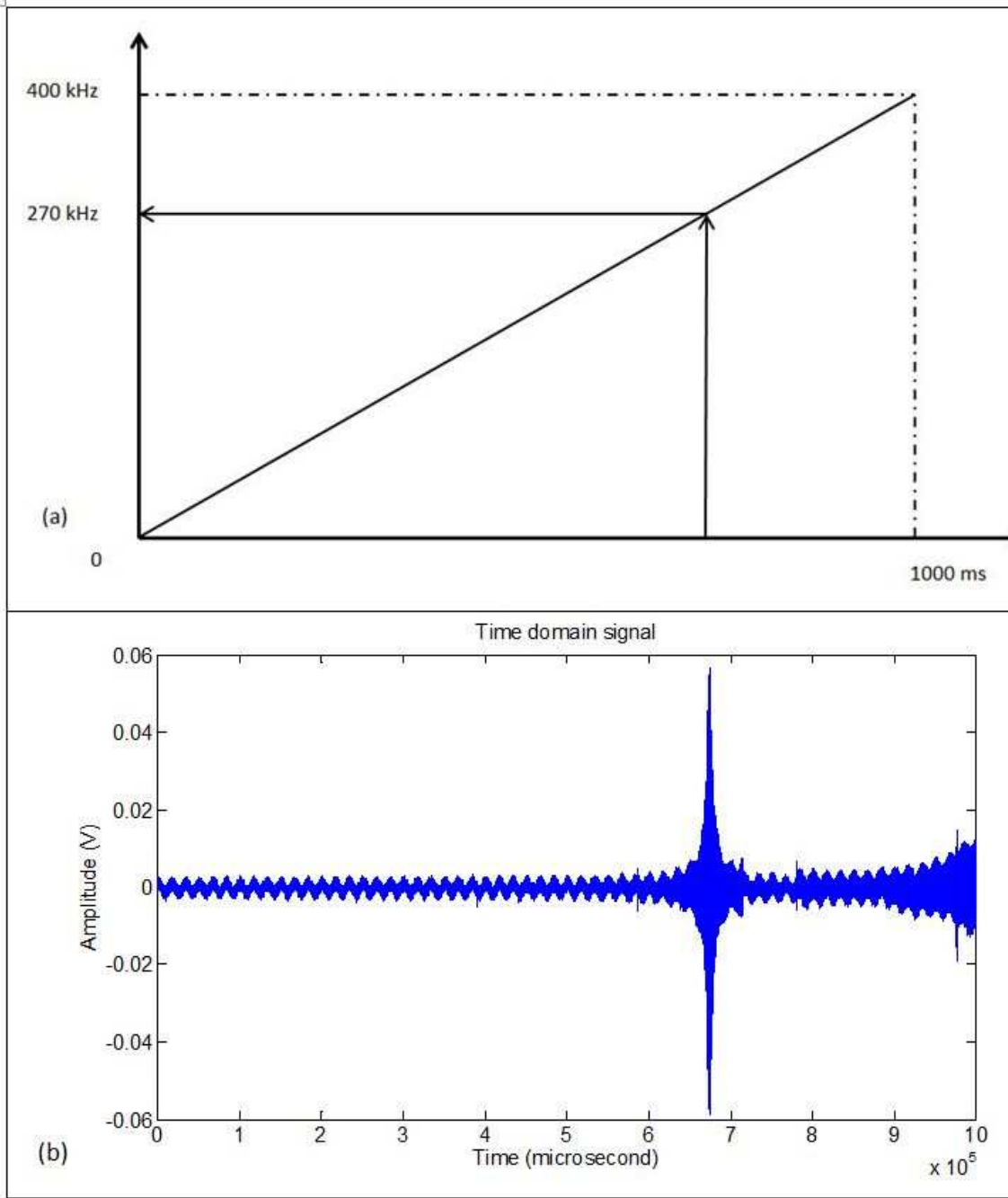
**Figure 293: Time domain testing:**
**(a) linear chirp characteristics between 0 to 400 kHz over a 1-sec duration;**
**(b) time domain signal showing a resonance at ~657 ms corresponding to ~ 270 kHz**
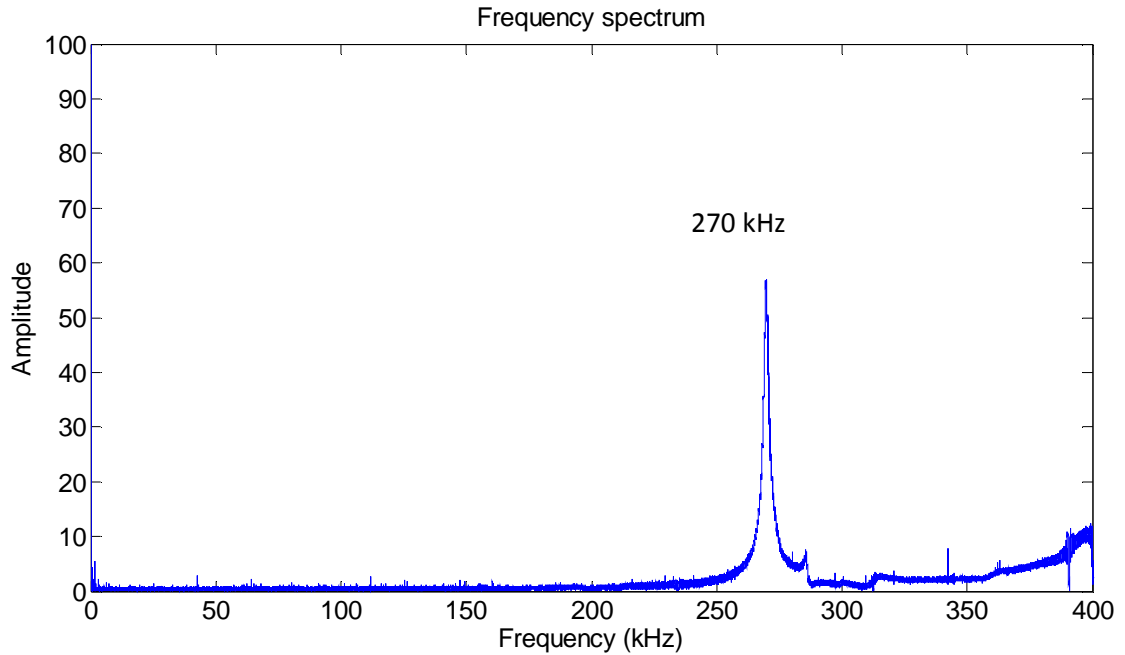
*Figure 294: Frequency domain signal for 300 kHz prototype*

### 13.3.4 FINAL DESIGN CONCLUSIONS

From the experimental results, we can see that we have a very good agreement with the predicted resonance frequencies. The first resonance frequency for both rings falls in the predicted area. In this case, the first resonance frequency is an axial one, which has the aim to stretch the fiber in order to get measurements with the FBG. In sum, our experiments proved that the concept is working and we can build such a ring sensor that can reach the first resonance frequency at any desired frequency.

# 14. CONCLUSION AND SUGGESTIONS FOR FUTURE WORK

## 14.1 CONCLUSIONS

The purpose of this dissertation has been to investigate the possibility of using small, permanently attached, low-cost piezoelectric wafer active sensors (PWAS) for structural health monitoring (SHM) of composite materials and detection of delamination. We direct our research towards the electromechanical impedance method for delamination detection.

The electromechanical impedance (EMI) method was studied comprehensively with analytical and finite element method; we compared the theoretical predictions results with experiments on geometrically controllable specimens.

The necessity for an analytical model to predict the behavior of composite materials guided us towards developing a new analytical model, which should reach higher frequencies, more stability and can precisely predict the vibration response under PWAS excitation.

Giurgiutiu (2008) implements the high-frequency vibration modal analysis method using PWAS transducers for calculating the electromechanical impedance. This constitutes the starting point in developing a new method to calculate resonance frequencies.

New consideration was given to the transfer matrix method (TMM) introduced by Pestel and Leckie (1963) for studying the vibration of mechanical systems. Giurgiutiu and Stafford (1977) used the TMM of Pestel and Leckie (1967) to calculate the vibration of helicopter blades modeled as rotating Timoshenko beams. Bois, Herzog, and Hochard (2004, 2007) used the theory of piezoelectric laminates to extend TMM to composite beams. They focus on building a monitoring system that can predict the damage in a quasi-isotropic laminate. Cuc (2010) used TMM to develop the analytical model for a uniform beam using the Euller-Bernoulli beam theory (shear deformation and rotary inertia were not considered) and expanded the method to the case of a multi-layer adhesively bonded beam. Due to the fact that all analytical methods so far are only able to run at very low frequencies and this aspect is very important for delamination detection studies, we develop a new method, Stiffness Transfer Matrix Method (STMM), which resolves some of the deficiencies in TMM (e.g. can run at high frequencies).The general principle behind the STMM is similar to TMM, in the sense that it breaks up a complicated structure into several smaller segments which then can be expressed in a matrix format. However, the mathematical approach is different. Namely, the instability problem in TMM is solved by introducing the compliance matrix and using a recursive algorithm to calculate the global stiffness matrix.

In our new method (STMM), the first step is to develop the analytical model for the simpler case of composite beams. Then, we expand the method to address delaminations in composite material beams. In the case of delamination, the mathematical model becomes complex and the beam is divided into branches. The idea

behind high frequencies is the fact that the part where the delamination is present behaves totally different from the part where delamination is not present. This latter aspect was emphasized in detail in this research by using ANSYS WB which gives us the possibility to visualize this feature. Practically, it seems to exist a "decouple" between the delamination zone and the pristine zone (one is in axial and the other one is in flexural resonance). This can be particularly seen at very high frequencies and seems to be diminished at low frequencies and much more difficult to detect.

Our current research is most closely related to Bois, Herzog, and Hochard (2004, 2007) however their method uses TMM and has some limitations that we are able to address using s new method: Bois et al. (2004, 2007) only use TMM for composites to low frequencies ($\leq$30 kHz). For these frequencies, the changes in the vibration behavior due to a small delamination were small and hence difficult to detect. In our tests, we took the method to 30 kHz, but could not go further up because the method had a breakdown. This is due to numerical instability in the TMM algorithm; a fact that has been also reported elsewhere.

In order to validate the analytical results, we use finite element analysis (FEA): ANSYS Multiphysics (2D) and ANSYS WB (3D). For ANSYS MUltiphysics, we calculate the impedance, by applying a voltage to the top and bottom electrodes of the PWAS and measuring the electrical charge. The electrical charge stored on the surface electrodes of the PWAS is directly linked with the changes in the mechanical stiffness of the beam.

The electrical charge is then used to calculate the current and he electromechanical impedance as the ratio between the applied voltage and the current.

For ANSYS WB, we were able to calculate only the resonance frequencies and the 3D visual results help us understand the behavior of the delamination.

We conduct experiments for both composite pristine beam specimen with PWAS transducers attached and damaged specimens and we utilize different materials and different PWAS locations given the delamination location. For the pristine composite beam case, we find a very agreement among all the methods. For the delamination, we find relatively good results among all the methods, even if the location and the size of the delamination are very hard to control. Overall, the impedance results are very sensitive to the PWAS location and some discrepancies can show up due to the fact that composite materials are not uniform (e.g. dimensions).

The last part of this research aimed to develop a novel acousto-ultrasonic sensor that can detect the ultrasonic waves from acoustic emission events using optical FBG sensing combined with mechanical resonance amplification principles. The method consists of a sensor that can detect the ultrasonic out of plane motion with preference for a certain frequency. We find a very good agreement with the predicted resonance frequencies. The first resonance frequency for the ring falls in the predicted area. In this case, the first resonance frequency is an axial one, which has the aim to stretch the fiber in order to get measurements with the FBG. In sum, our experiments proved that the concept is working and we built and successfully tested a ring sensor that can reach the first resonance at any desired frequency. This work was finalized with an invention disclosure for a novel acousto-ultrasonic FBG ring sensor (Disclosure ID No. 00937).

## *14.2* SUGGESTIONS FOR FUTURE WORK

The research in this dissertation emphasizes the need for more work to understand and develop an accurate predictive model for damage detection in composite materials using PWAS transducers. This is essential for the development and implementation of an embedded SHM system able to detect and assess the magnitude of various damages that could emerge and reach intolerable levels. The following directions are recommended for future research:

1. Extend current STMM method with new features to increase the stability for delamination cases

2.  Extend the analytical method to plates and shells using the plate theory

3. Extend the transfer matrix method to wave propagation theory in order to predict the wave propagation in composite materials.

4. Develop a graphical user interface (GUI) in MATLAB for an easier and friendlier way of entering analysis parameters.

5. Perform additional experimental tests with an increased number of specimens and with various features of damages.

6. Further develop suitable damage indices (DI) for better detection competences using the modal features of the EMI spectrum.

7. Perform additional FEA to compare the results between 2D and 3D and to understand why there are some differences for composite materials.

# REFERENCES

Alleyne, D. N.; Cawley, P.(1992) "The interaction of Lamb Waves with Defects", *IEEE Transactions on Ultrasonics, Ferroelectrics, and Frequency Control*, Vol. 39, pp. 381-397, 1992.

Barshinger, J.; Rose, J.L.; Avioli, M.J. (2002) "Guided wave resonance tuning for pipe inspection" *Journal of Pressure Vessel Technology*, Vol. 124, pp. 303-310, 2002.

Blevins, R., (1979), Formulas for natural frequency and mode shape, Litton Educational Publishing, New York, 1979.

Bois, C.; Hochard, C. (2004), "Monitoring of Laminated Composites Delamination Based on Electro-mechanical Impedance Measurement", *Journal of Intelligent Material Systems and Structures*, Vol. 15, pp. 59-67, 2004.

Bois, C.; Herzog, P.;Hochard, C. (2007) "Monitoring a delamination in a laminated composite beam using in-situ measurements and parametric identification" *Journal of Sound and Vibration*, Vol. 299, pp. 786-805, 2007.

Boller, C.; Biemans, C.; Staszewski, W.; Worden, K.; Tomlinson, G. (1999) "Structural Damage Monitoring Based on an Actuator-Sensor System", Proceedings of SPIE Smart Structures and Integrated Systems Conference, Newport, 1999.

Cawley, P., (1984) "The Impedance Method for Non-Destructive Inspection", *NDT International*, Vol. 17, pp. 59-65, 1984.

Chiu, W.K.; Koh, Y.L.; Galea, S.C.; Rajic, N. (2000) "Smart structure application in bonded repairs", *Composite Structure*, Vol. 50, pp. 433-444, 2000.

Clezio, E.L.; Castaings, M.; Hosten, B. (2002) "The interaction of the S0 Lamb mode with vertical cracks in an aluminum plate" *Ultrasonics*, Vol. 40, No. 1-8, pp. 187-192, 2002.

Cuc, A. (2010) "Structural Health Monitoring of Adhesively bonded joints with piezoelectric wafer active sensors, University of South Carolina, 2010.

Ellakany, A.M.; Elawadly, K.M.; Alhamaky, B.N. (2004) "A combined transfer matrix and analogue beam method for free vibration analysis of composite beams", *Journal of Sound and Vibrations*, Vol. 277, No. 4-5, pp 765-781, 2004.

Galea, S. C.; Powlesland, I. G.; Moss, S. D.; Konak, M.; Steve van der Velden, Stade, B.; Baker, A. A. (2001) "Development of Structural Health Monitoring System for Composite Bonded Repairs of Aircraft Structures", *Proceedings of the SPIE Smart Structures and Materials 2001: Smart Structures and Integrated Systems*, Vol. 4327, pp. 246-257, 2001.

Giurgiutiu, V.; Zagrai, A. (2000) "Damage Detection in Simulated Aging-Aircraft Panels Using the Electro-Mechanical Impedance Technique", *Adaptive Structures and Materials Systems Symposium*, *ASME Winter Annual Meeting*, November 5-10, 2000, Orlando, FL, 2000.

Giurgiutiu, V. , Bao, J., Zhao, W. (2001) "Active Sensor Wave Propagation Health Monitoring of Beam and Plate Structures", *Proceedings of the SPIE's 8th International Symposium on Smart Structures and Materials*, Newport Beach, 2001.

Giurgiutiu, V.; Zagrai, A.N. (2001) "Electro-Mechanical Impedance Method for Crack Detection in Metallic Plates", *SPIE's 8th Annual International Symposium on Smart Structures and Materials and 6th Annual International Symposium on NDE for Health Monitoring and Diagnostics*, Newport Beach, 2001.

Giurgiutiu, V.; Zagrai, A. N.; Bao, J. (2002) "Piezoelectric Wafer Embedded Active Sensors for Aging Aircraft Structural Health Monitoring", *Structural Health Monitoring – An International Journal*, Sage Pub., Vol. 1, No. 1, pp. 41-61, 2002.

Giurgiutiu, V. (2003) "Embedded NDE with Piezoelectric Wafer Active Sensors in Aerospace Applications", *Journal of Materials – Special Issue on NDE*, January 2003

Giurgiutiu, V. (2003) "Embedded Ultrasonics NDE with Piezoelectric Wafer Active Sensors", *Journal Instrumentation, Mesure, Metrologie*, Lavoisier Pub., Paris, France, RS series 12M, Vol. 3, No. 3-4, pp. 149-180, 2003.

Giurgiutiu, V.; Zagrai, A. N.; Bao J.; Redmond, J.; Roach, D.; Rackow, K. (2003) "Active Sensors for Health Monitoring of Aging Aerospace Structures", *International Journal of the Condition Monitoring and Diagnostic Engineering Management*, Vol. 6, No. 1, pp. 3-21, 2003.

Giurgiutiu, V.; Bao, J. (2004) "Embedded-Ultrasonics Structural Radar for In-Situ Structural Health Monitoring of Thin-Wall Structures", *Structural Health Monitoring – an International Journal*, Vol. 3, No. 2, pp. 121-140, 2004.

Giurgiutiu, V.; Lyshevski, S. E. (2004) Micromechatronics: modeling, analysis, and design with MATLAB, CRC Press, 2004.

Giurgiutiu, V.; Zagrai, A.; Bao, J. (2004) "Damage Identification in Aging Aircraft Structures with Piezoelectric Wafer Active Sensors", *Journal of Intelligent Material Systems and Structures*, Vol. 15, No. 6, 2004.

Giurgiutiu, V (2008) Structural Health Monitoring with Piezoelectric Wafer Active Sensors, Academic Press, 2008.

Giurgiutiu, V., Gresil, M., Lin, B., Cuc, A., Shen, Y., Roman, C. (2011) "Predictive Modeling of Piezoelectric Wafer Active Sensors Interaction with High-Frequency Structural Waves and Vibration", *Acta Mecanica*, 2011.

Giurgiutiu, V.; Santoni-Bottai, G. (2011) "Structural Health Monitoring of Composite Structures with Piezoelectric Wafer Active Sensors", *AIAA Journal*, Vol. 49, No. 3, March 2011, pp. 565-581, 2011.

Graff, K. F. (1975) Wave Motion in Elastic Solids, Dover Publications Inc., 1975.

Grondel, S.G.; Delebarre, C.; Assaad, J.; Dupuis, J-P.; Reithler, L. (2002) "Fatigue crack monitoring of riveted aluminum strap joints by Lamb wave analysis and acoustic emission measurement techniques" *NDT&E International*, Vol. 35, pp. 137-146, 2002.

Hanneman, S.; Kinra, V.K. (1991) "Ultrasonic nondestructive evaluation (NDE) of adhesively bonded joints: natural frequencies and complex mode shapes", *American Society of Mechanical Engineers, Noise Control and Acoustics Division (Publication) NCA*, Vol. 12, pp. 1-6, 1991.

Ihn, J-B (2003) "Built-in diagnostics for monitoring fatigue crack growth in aircraft structures) PhD dissertation, Stanford University, 2003.

Ihn, J-B; Chang, F-K. (2004) "Detection and monitoring of hidden fatigue crack growth using a built-in piezoelectric sensor/actuator network: I. Diagnostics" *Smart Materials and Structures*, Vol. 13, No. 3, pp. 609-620, 2004.

Jones, R. (1999), "Mechanics of Composite Materials", CRC Press, 1999.

Koh, Y. L.; Chiu, W. K. (2003) "Numerical study of detection of disbond growth under a composite repair patch", *Smart Materials and Structures*, Vol. 12, pp. 633-641, 2003.

Krautkramer, J.; Krautkramer, H (1990) "Ultrasonic Testing of Materials", Springer-Verlag, 1990.

Kreuzer,M.(2007) "Strain Measurement with Fiber Bragg Grating Sensors, HBM, Germany, 2007.

Kwon, J. W.; Chin, W. S.; Lee, D. G. (2003) "Piezoelectric monitoring of the reliability of adhesive joints", *Journal of Adhesion Science and Technology*, Vol. 17, pp. 777-796, 2003.

Lee, B. C.; Palacz, M.; Krawczuk, M.; Ostachowicz, W.; Staszewski, W. J. (2003) "Wave propagation in a sensor/actuator diffusion bond model", *Journal of Sound and Vibration*, Vol. 276, Issue 3-5, p. 671-687, 2003.

Lin, B., (2010), "Power and Energy Transduction in Piezoelectric Wafer Active Sensors for Structural Health Monitoring: Modeling and Applications", *Theses and Dissertations,* Paper 212, 2010.

Lowe, M. J. S.; Cawley, P. (1994) "The applicability of plate wave techniques for the inspection of adhesive and diffusion bonded joints", *Journal of Nondestructive Evaluation*, Vol. 13, pp. 185-199, 1994.

Lowe, M.J.S.; Alleyne, D.N.; Cawley, P. (1998) "Defect detection in pipes using guided waves", *Ultrasonics*, Vol. 36, pp. 147-154, 1998.

Majumdar, P., (2009) Composite Materials, EMCH585 course notes, USC Department of Mechanical Engineering, 2009.

McKeon, J.C.P.; Hinders, M. K. (1999) "Lamb wave scattering form a through hole", *Journal of Sound and Vibration*, Vol. 224, No. 5, pp. 843-862, 1999.

Park, G.; Sohn, H.; Farrar, C. R.; Inman, D.J. (2003) "Overview of Piezoelectric Impedance-Based Health Monitoring and Path Forward", *The Shock and Vibration Digest*, Vol. 35, pp. 451-463, 2003.

Pollock, P. (2011) "Composite Structural Health Monitoring with Piezoelectric Wafer Active Sensors", Master Thesis, 2011.

Rose, J. L.; Rajana, K. M.; Hansch, K.T. (1995) "Ultrasonic guided waves for NDE of adhesively bonded structures", *Journal of Adhesion*, Vol. 50, pp. 71-82, 1995.

Silk, M.G.; Bainton, K.P. (1979) "The propagation in metal tubing of ultrasonic wave modes equivalent to Lamb waves", *Ultrasonics*, Vol. 17, pp. 11-19, 1979.

Thomson, R.B.; Alers, G.A.; Tennison, M.A. (1972) "Application of direct electromagnetic Lamb wave generation to gas pipeline inspection" *Proceedings of the IEEE Ultrasonics Symposium,* pp.91-94, 1972.

Valle, C.; Niethammer, M.; Qu, J.; Jacobs, L. J. (2001) "Crack characterization using guided circumferential waves" *Journal of the Acoustical Society of America*, Vol. 110, No. 3, pp. 1282-1290, 2001.

Zhu, W.; Rose, J.L.; Barshinger, J.N.; Agarwala, V.S. (1998) "Ultrasonic guided wave NDT for hidden corrosion detection", *Research in Nondestructive Evaluation*, Vol. 10, No. 4, pp. 205-225, 19, 1998.